DISSOCIATIVE AND NON DISSOCIATIVE IONIZATION OF H_2, HeH^+ AND H_2^+ BY PHOTONS AND FAST PARTICLES

Jorge Fernández Hernández

Supervisor: Prof. Fernando Martín García

PhD thesis, Universidad Autónoma de Madrid. 2008

Para mis dos amores Marta y Marco

Table of Contents

Resumen

Esta Tesis doctoral se centra en el estudio de la *ionización* de las moléculas H_2, D_2 y HeH^+, mediante la colisión de fotones, electrones e iones de alta energía. Este campo de investigación sigue siendo uno de los más activos de la Física, pese a haber sido extensamente estudiado en el último siglo, tanto desde el punto de vista experimental como teórico, como se podrá comprobar durante la lectura de este trabajo. Dentro de la amplia gama de procesos que existen en la ionización de estas moléculas bielectrónicas, nos centraremos en el papel que desempeñan los estados doblemente excitados presentes en el continuo molecular y su importancia en el estudio de la distribución angular de las partículas finales de este proceso. Asimismo presentaremos los efectos de interferencia y coherencia que aparecen en las moléculas H_2^+ y H_2 mediante el uso de fotones de alta energía. Por último, estudiaremos los procesos de ionización del H_2 y del D_2 mediante colisiones a alta energía de electrones e iones.

En la primera parte de la Tesis se describe el formalismo y los métodos matemáticos utilizados, desarrollados en nuestro laboratorio, necesarios para obtener los parámetros que caracterizan los *estados doblemente excitados* de estas móleculas bielectrónicas. En particular, astudiaremos los estados resonantes del H_2 por encima del segundo y tercer límite de ionización, los estados Q_3 y Q_4. A diferencia del caso atómico, el movimiento vibracional de la molécula complica de manera considerable los desarrollos teóricos necesarios para llegar a una total comprensión de los resultados obtenidos experimentalmente en el estudio de la *ionización disociativa* de estos sistemas. Por ello, introducimos el formalismo necesario para describir el correcto papel que los estados resonantes desempeñan en el estudio de este proceso, haciendo hincapié en las funciones de base de cuadrado integrable *B*-spline utilizadas, cuyo uso es pionero nuestro laboratorio. En concreto presentamos los resultados de la ionización disociativa del H_2 y D_2 en el rango de energía de fotón 35-50 eV, donde los estados resonantes Q_3 y Q_4, así como otros limites de ionización superiores son accesibles, comparándolos con resultados experimentales realizados en paralelo. También mostramos un estudio de la disociación disociativa del H_2 desde el primer estado electrónico excitado E,F$^1\Sigma_g^+$, centrándonos en la influencia que los diferentes estados vibracionales iniciales asociados a este estado electrónico poseen en el proceso de la ionización disociativa, comparando nuestros resultados con los datos experimentales disponibles en la literatura. Para completar esta primera parte de la Tesis, presentaremos los resultados de la ionización disociativa del HeH^+, como ejemplo de sistema bielectrónico heteronuclear, con la intención de poner de manifiesto las principales diferencias con el H_2.

Una vez descritos los procesos arriba mencionados, utilizamos el formalismo desarrollado previamente para estudiar la *distribución angular* de las partículas procedentes de la fotoionización del H_2 y D_2. Dentro de las diferentes expresiones de la sección eficaz que se pueden obtener, cada de las cuales refleja unas condiciones experimentales diferentes, nos centraremos en el estudio la distribución de electrones en el caso en el que la molécula posee una orientación fija en el espacio. Como veremos, a energías de fotón donde los estados doblemente excitados son

accesibles, la distribución angular de electrones proporciona una gran información sobre la física que subyace en este proceso en comparación con los resultados obtenidos en el estudio de secciones eficaces totales. En particular veremos como la simetría inicial de la molécula se puede romper cuando varias vías de disociación son accesibles simultáneamente, produciendo una asimetría Forward-Backward en la distribución angular de electrones, hecho corroborado por los experimentos realizados conjuntamente.

Para completar el estudio de la fotoionización, nos planteamos abordar el problema de la utilización de fotones de altas energías ($\lesssim$ 500 eV). En este caso, la longitud de onda del electrón ionizado es comparable con el tamaño de la molécula, por lo que la naturaleza del electrón se manifiesta a través de patrones de interferencia y difracción, similares al efecto que experimentan las ondas macroscópicas cuando encuentran un objeto macroscópico. Como veremos, estos efectos se manifiestan claramente en el estudio de la distribución angular de electrones y en menor medida en las secciones eficaces totales. En particular, para una orientación de la molécula perpendicular al vector de polarización se observa claramente un efecto de *doble rendija*, mientras que para una orientación paralela un nuevo fenómeno físico entra en juego: el *confinamiento electrónico*. Para esta particular orientación, la función de onda del electrón emitido posee un carácter oscilatorio semejante a de un estado ligado de la molécula inicial, hecho que induce el confinamiento transitorio del electrón en la molécula.

Una vez completado el estudio de la ionización del H_2 mediante fotones, estudiaremos la ionización de esta molécula mediante la *colisión de partículas de alta energía*. Para ello presentaremos los desarrollos teóricos necesarios para llegar a obtener un buen acuerdo con los resultados experimentales desarrollados en paralelo. Mediante la interacción de electrones planteamos un nuevo método de obtener información de la contribución de los estados resonantes, mediante el estudio de la sección eficaz total en función de la energía final del electrón ionizado. En el caso de iones altamente cargados obtenemos una visión mucho mas general del proceso, en el que se estudia en función tanto de la energía del electrón ionizado como del protón procedente de la disociación del ión residual, la contribución de un gran número de resonancias y vías de disociación.

Abstract

The main objective of this Thesis is the study of the *ionization* of diatomic molecules, such as H_2, D_2 or HeH^+ by means of collisions with photons and high-energy particles. Although this field has been a central issue in Physics in the last century, this work and the publications derived from it, as well as other theoretical and experimental research studies developed in other laboratories, show that it is still open and of interest to the Physics community. Within all the physical processes that can be studied, we will focus on the *doubly excited states* that exist in the molecular continuum, paying special attention to the role that these states play in the *angular distribution* of the particles coming from the ionization process. Also we will focus on the interference and coherence effects that appear in the ionization of H_2^+ and H_2 in the high photon energy range. Finally, we will study the ionization process of the H_2 and the D_2 molecules by means of collisions of highly energetic electrons and ions.

We will begin this Thesis describing the formalism and the mathematical methods developed in our laboratory to obtain the parameters that characterize the *doubly excited states* of these bielectronic molecules. We will present results for resonant states of H_2 above the second and third ionization thresholds, the Q_3 and Q_4 states. Unlike the atomic case, the fact that the molecule can vibrate complicates the theoretical developments required to understand completely the last experimental results in the *dissociative ionization* of this molecules. We will present the formalism needed in order to describe the correct role that the resonant states fulfill in the study of this process, making use of *B-splines* functions. Specifically, we will show the results of the dissociative photoionization of H_2 and D_2 in the photon energy range 35-50 eV, where the Q_3 and Q_4 resonant states as well as higher ionization thresholds are accessible, comparing with the experiments developed in parallel. Also, we will present a study of the dissociative photoionization of H_2 from the first excited electronic state E,$F^1\Sigma_g^+$, concentrating on the role that different initial vibrational states associated with this electronic state posses in this process. To complete the first part of this Thesis, we present the results obtained for the dissociative photoionization of the HeH^+ molecule, as an example of a heteronuclear system, with the idea of showing the main differences with the H_2 molecule.

Within this framework we study the *angular distribution* of the particles arising from the photoionization of H_2 and D_2, emphasizing the main mathematical steps required to obtain the fully differential cross section. Within the different expressions that can be obtained for the description of the angular distribution, representing each of them a specific experimental condition, we will pay special attention to the case in which the molecule posseses a fixed orientation at the time of its ionization. At photon energies where the doubly excited states are accessible, the electron angular distribution provides a deeper understanding about the underlying physics than the study of total cross sections. Here we will show that the inversion symmetry of the initial state can be broken by the absorption of a single photon. The emission of a photoelectron with subsequent dissociation of the remaining H_2^+ fragment shows no symmetry with respect to the ionic H^+ and neutral H atomic

fragments, which is the consequence of the entanglement between symmetric and antisymmetric H_2^+ states resulting from autoionization.

To complete the part related to the photoionization of the H_2 molecule, we will study the ionization by high energetic photons ($\lesssim 500$ eV). In this case, the electron wavelength is comparable to the size of the molecule, so the wave nature of the electron should manifest through interference and diffraction patterns, in a similar way to what macroscopic waves experience when they meet a macroscopic object. These effects are clearly manifested in the electron angular distribution and to a lesser extent in the total cross section. For a perpendicular orientation of the molecule with respect to the polarization vector, a clear *double slit* effect is observed, while for the parallel orientation yields a new physical phenomena: the *electronic confinement*. For this particular orientation, the electron that is emitted to the continuum has an oscillatory character similar to the wave function of a bound state of the initial molecule, and therefore, although the electron belongs to the continuum, it is confined temporally within the molecule.

Finally, we will present the results for the ionization of the H_2 molecule by *collision with high-energy particles*. Two different particles will be treated: collision with electrons and collision with highly charged ions. In the former case, we set up a new way of getting information from the contribution of the resonant states, through the calculation of the total cross section as a function of the final energy of the ionized electron. In the latter case, the process is studied simultaneously as a function of both the final electron and proton energies, where the contribution of all the resonant states and dissociative paths are observed simultaneously. In both cases a comparison with experimental results obtained in parallel to our work will be presented.

Acknowledgments

"Es de buen nacido ser agradecido."

Refranero español.

This thesis would not have been possible without the support of many people whom I would like to thank.

This thesis has been developed in the Chemistry Department of the Universidad Autónoma de Madrid in the period 2001-2006, under the supervision of Professor Fernando Martín García, by the FPU (Formación de Profesorado Universitario) Research Fellowship of the Ministry of Education and Science. I thank him for the freedom to choose the projects that were most interesting to me, as well as for his valuable suggestions on my research.

Also, I would like to thank Professor Otilia Mó Romero, since without her support this thesis would have never been written.

I am indebted to Professor Omar Ariel Fojón for many valuable suggestions about my research.

My thanks also go to Doctor Ignacio Sánchez, for the previous work developed in our group, since without his effort my research would have been in vain.

My appreciation also goes to all the Ph.D. and postdoc students of the Chemistry Department for their help, support and friendship, and for all the coffees that we took while we tried to change the world. Especially to my friends Alicia and Luisfe, who shared the struggle as well as the success.

I am also grateful to the rest of the professors and staff of the Chemistry Department of the Universida Autónoma de Madrid.

To the components of the Computational Centre of the Universidad Autónoma de Madrid for helping me to resolve all my computational troubles. Especially to its director Alberto Luna and to the doctors Luis Felipe Ruiz and Pablo Sanz, because without their help this work would have been much harder.

A new research line has been carried out in two stays in the Department of Chemistry Science of Trieste University, Italy, under the supervision of Professor Piero Decleva, to whom I would like to give my gratitude for his hospitality. Specially to my office mates Devis Di Tommasso y Renato De Francesco (*Grazie per tutto!*).

I am very grateful to all the experimentalist groups that I have had the pleasure to work with, specially to Professor Kenji Ito, of the *Photon Factory*, Japan, to Professor Francois Fremon of the *Université de Caen Basse-Normandie*, France, to the group of professors Lamri Adoui y Amine Cassimi of the *Centre Interdisciplinaire de Recherche Ions Lasers (CIRIL)* of Caen, France, to Professor Daniel Dowek of the *Laboratoire des Collisions Atomiques et Moléculaires, Université Paris Sud*, France, and to Professor Reinhard Dörner of the *Institut für Kernphysik Johann Wolfgang Goethe-Universität*, Germany, for teaching me to understand Science through the experimental point of view.

I am also very grateful to my family, especially to my parents and my brother for their constant support and encouragement. I would also like to remember my dear grandparents Pilar and Bernardino.

Finally, I would like to thank my partner Marta for her love, understanding and support, and because without her, I could not have been able to finish this work, and to my new friend, my baby Marco, for not letting me sleep while I was completing this Thesis.

Thank you so much for everything!

Jorge Fernández Hernández

Madrid, 15 de abril de 2008

Chapter 1

Introduction

"The adventure of our science of physics is a perpetual attempt to recognize that the different aspects of nature are really different aspects of the same thing".

Richard Feynman

IONIZATION AND DISSOCIATION of molecules are the most obvious manifestations of both the electronic and nuclear continuum states. The demonstration of these states has been carried out through the interaction of light and different particles, processes that have been one of the main blocks in the understanding of the characteristics of atoms [1], molecules [2] and clusters [3] for more than one century. Most likely the best examples are Einstein's explanation of the photo-effect [4], that was one of the crucial experiments for the birth of Quantum Mechanics, and Ernest Rutherford's discovery of the atomic nucleus using alpha particles [5], that marks the beginning of modern scattering experiments. The calculation of these continuum wave functions may be a formidable task and, in many cases, a direct numerical solution of the Schrödinger equation is not possible even approximately. Although it could seem that this field is totally understood, upcoming new experimental devices [6, 7, 8] and the development of new theoretical methods [9, 10] has motivated this field of Physics to become one of the most attractive research areas.

Resonances in general refer to the energy-dependent enhancement of the inter-particle collision cross section due to the existence of a metastable state. Since the beginning of Quantum Mechanics, such phenomena have been the subject of numerous studies in nuclear [11] as well as atomic and molecular physics [12, 13]. The metastable state may be described in terms of tunneling across a potential energy barrier or coupling a bound level of a subsystem to its environment [14, 15, 16, 17]. These scenarios are referred to as shape and Feshbach resonances, respectively. In the atomic and molecular continuum, there exist resonant states. These states, although they belong to the continuum part of the spectra, could be called quasibound states, since they present a notable concentration of electronic density in the configuration space. In a particular case, the simultaneous excitation of two electrons creates a resonant state, or a doubly excited state, where the electronic correlation plays a crucial role. This doubly excited state possesses a characteristic lifetime, during which it can be considered a bound state embedded in the continuum. When a photon or an incoming particle collides with an atom or a molecule (bielectronic)[1], the energy is absorbed producing the excitation of the system. If the absorbed energy is high enough to overcome the ionization potential, I_p, one of the electrons can be ejected into the continuum, producing the ionization of

[1] See Chapter 13 for the different electronic processes in a polielectronic system.

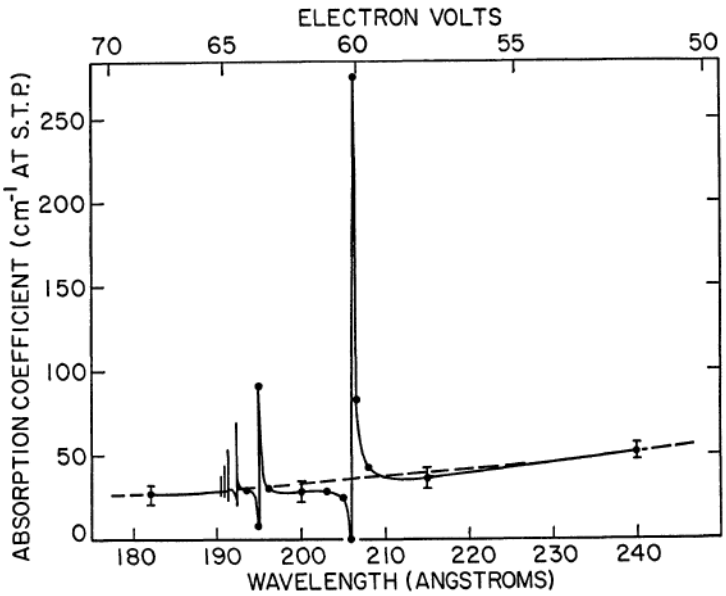

Figure 1.1: Photoionization cross section of He obtained by Madden and Codling [19, 20].

the system. But, due to the presence of doubly excited states in the continuum, several processes can happen simultaneously, which produces interference patterns. So, in the ionization process, either an electron can be expelled directly, or else promote the atom or molecule to a doubly excited state, which then decays after a delay by emission of one electron via autoionization. Because the final state in both of these pathways is the same, the amplitudes for each pathway must be added coherently, leading either to constructive or destructive interference, depending on the phase shift induced by the time delay [18], that manifests as structures in the photoionization cross section.

Resonant states in an atomic system, were observed for the first time by Madden and Codling [19, 20] in 1963 in the photoabsorption spectra of He atom . This result is displayed in Fig. (1.1), and as can be seen, for low photon energies (high wavelength) the cross section presents a quite large plateau associated with the direct ionization of the atom. But for defined photon energies sharp peaks appear as the photon energy is increases. These peaks, called Fano resonances, are the manifestations of the presence of doubly excited states of this atom (see [15] for more details). As in the case for the He atom, one expects the presence of doubly excited states in the continuum of a molecular system. However, because in molecules the excess energy can be distributed among internal nuclear and electron degrees of freedom, the situation is much more complex than in atoms, and a clear cut proof of the interference effects is missing. For the H_2 molecule the role of these states has been extensively studied as intermediate resonance states in different contexts as[2],

1. Elastic scattering [21, 22, 23, 24]
   $e^- + H_2^+ \longrightarrow H_2^{**} \longrightarrow H_2^+ + e^-$.
2. Vibrational excitation [25]
   $e^- + H_2^+(\upsilon) \longrightarrow H_2^{**} \longrightarrow H_2^+(\upsilon') + e^-$.
3. Dissociative recombination [25, 26, 27, 28]
   $H^+ + H^- \longrightarrow H_2^{**} \longrightarrow H + H^*$.

[2] A doubly excited state will be designated as H_2^{**}.

4. Ion-pair formation [29]
   $e^- + H_2^+(\upsilon) \longrightarrow H_2^{**} \longrightarrow H^+ + H^-$.
5. Associative ionization [30, 31]
   $H^+ + H^- \longrightarrow H_2^{**} \longrightarrow H_2^+ + e^-$,
   $H^* + H^* \longrightarrow H_2^{**} \longrightarrow H_2^+ + e^-$.
6. Transfer ionization [32]
   $H^+ + H^- \longrightarrow H_2^{**} \longrightarrow H + H^+ + e^-$.
7. Photodissociation [33, 34, 35, 36, 37]
   $\hbar\omega + H_2 \longrightarrow H_2^{**} \longrightarrow H^* + H^*$.
8. Photoionization [22, 38]
   $\hbar\omega + H_2 \longrightarrow H_2^{**} \longrightarrow H_2^+ + e^-$.
9. Dissociative photoionization [39, 40]
   $\hbar\omega + H_2 \longrightarrow H_2^{**} \longrightarrow H(n\ell) + H^+ + e^-$.
10. Resonantly enhanced multiphoton ionization [41]
    $n\hbar\omega + H_2 \longrightarrow H_2^{**} \longrightarrow H_2^+ + e^-$.
11. Resonantly enhanced multiphoton dissociation [42]
    $n\hbar\omega + H_2 \longrightarrow H_2^{**} \longrightarrow H + H^*$.

and so on.

As a molecular system (in our case a diatomic system) has additional degrees of freedom in comparison with an atom, i.e., the possibility of rotating and vibrating makes even more difficult to treat the role of the resonant states in each specific problem. For example, the inclusion of the vibration motion opens additional final states, such as the dissociation into neutral, excited or ionic fragments as well as producing vibrational bound states of the residual ion. If the deposited energy in the molecule is bigger than the ionization threshold, $energy > I_p$, the main competing channels that characterize the ionization process can be summarized as follows:

- **Non-dissociative ionization**:

  $$\text{energy} + H_2 \longrightarrow H_2^+(\upsilon) + e^-.$$

  The energy is high enough to produce the direct ejection of one electron into the continuum, leaving the residual ion in a bound vibrational state. This is the dominant process as the deposited energy increases.

- **Dissociative ionization**:

  $$\text{energy} + H_2 \longrightarrow H + H^+ + e^-.$$

  In this situation, the deposited energy in the system produces the direct ejection of one electron into the continuum and the residual ion possesses a vibrational energy above the dissociative limit, producing the separation of the nuclei simultaneously with the ionization process.

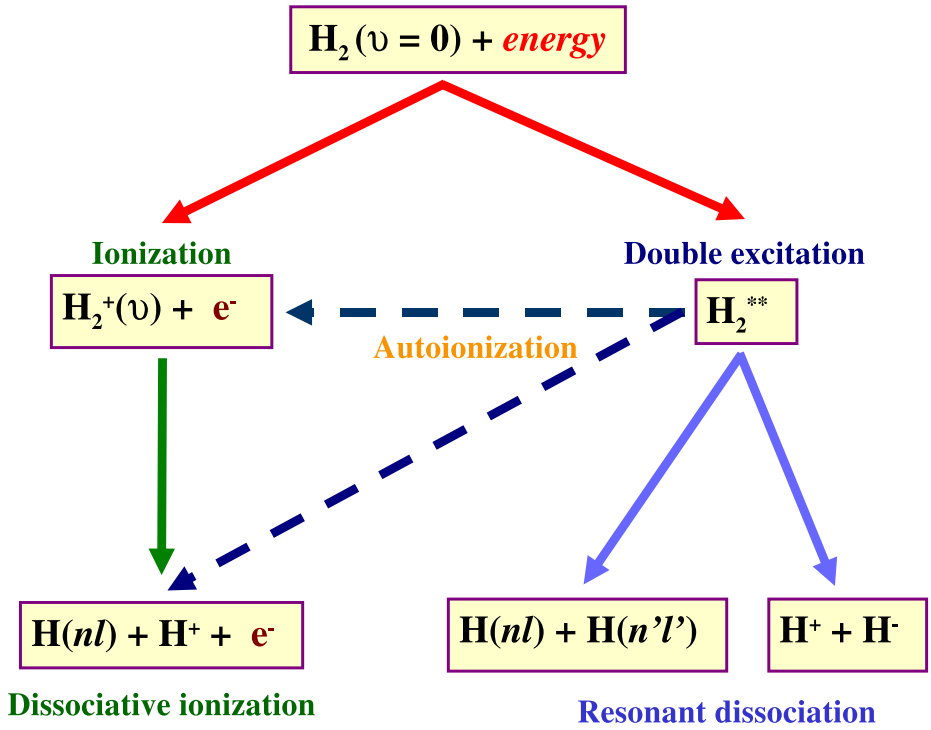

Figure 1.2: Competing paths in the resonant dissociative ionization of the H_2 molecule.

- **Double excitation**:

$$\text{energy} + H_2 \longrightarrow H^{**} \longrightarrow \begin{cases} \longrightarrow H + H, \\ \longrightarrow H_2^+(\upsilon) + e^-, \\ \longrightarrow H + H^+ + e^-. \end{cases}$$

  In this case the energy is able to populate an intermediate resonant state, and it lately decays into several paths depending on its energy position.

- **Double ionization**:

$$\text{energy} + H_2 \longrightarrow H^+ + H^+ + e^- + e^-.$$

  The energy is so high that both electrons can be simultaneously ejected, producing the so called "Coulombic explosion". This extreme case shows up when the energy is greater than the double ionization threshold, and the nuclei separate each other due to the mutual electrostatic repulsion. This process is beyond the scope of this Thesis (see for example [43, 44] for more details).

All these processes can occur simultaneously, so, interference effects appear due to the fact that the same final path can be reached in several different ways. Fig. (1.2) presents a schematic picture of the channels that can compete in the resonant ionization process of the H_2 molecule.

From the theoretical point of view, the characteristics of a doubly excited state, i.e., its width Γ, its energy position E_r and its energy shift ΔE, can be obtained following different procedures. The *stabilization method* proposed by Macías *et al.*[3] [45] has been one of the most used methods devoted to the study of the characteristics of resonant states in atoms [46] and molecules [47], and it has been applied in many other different contexts. Also, the *exterior complex scaling* method has been applied to the study of the characteristics of resonant states of molecular systems (see for example [48]). An alternative method is based on the *Feshbach formalism* [16, 17] and the introduction of *square integrable basis* in order to describe the continuum states. This method, developed in our laboratory (see for example [49, 50]), has been shown to be extremely accurate in order to describe these parameters and the correct description of the role of the doubly excited states in the dissociative photoionization process by a single photon in atoms [50, 51, 52] and molecules [53, 54, 55] as well in the multiphoton case [56, 57]. This method is based in the definition of two projectors, P and Q, that divide the configuration space into two orthogonal subspaces. This definition is performed in such a way that only the "bound states" of the continuum is contained in the subspace defined by Q, while in the subspace defined by P only the "smooth" part of the continuum is contained.

Making use of this method takes several advantages over other theoretical techniques:

1. The resonant state can be visualized as a bound state with a characteristic lifetime, that is related with its width by means of the uncertainty principle.

2. The configuration space is divided into two orthogonal subspaces P and Q, that allows to apply different computational techniques in each subspace.

3. The subspace generated by the projector Q contains the resonant states that can be obtained by means of the common techniques of Quantum Chemistry, as a *configuration interaction* method.

4. The subspace generated by the projector P is formed by continuum states that do not contain any resonant character, i.e. in this subspace we have a smooth continuum that can be discretized in a very easy way.

5. The resonant width is the result of the coupling of a resonant state contained in the Q subspace and a continuum state contained in the P subspace. Therefore, the width of a resonant state can be obtained by a *golden rule* equation (see [18, 58] for more details), and this and other properties of a resonant state can be obtained directly making use of the eigenfunctions of the total electronic Hamiltonian projected into each subspace.

But, as we will show, the knowledge of the characteristics of the doubly excited states by itself is insufficient for understanding the dynamical processes previously described, since the coupling between the electronic and the nuclear motion is essential. Since the role of the doubly excited states of H_2 is quite broad, each specific physical process requires the development of specific theoretical treatments. In particular we will concentrate in the resonant ionization of H_2 by photons and highly energetic particles. In the case of H_2, when the deposited energy in the molecule is greater than the dissociation limit (18.1 eV for the H_2 molecule), the ionization process not only leads to emission of an electron but also to dissociation of the molecule according to the equation H_2 + energy $\longrightarrow$ $H(n\ell)$ + H^+ + e^-, thus leading to the process called dissociative ionization (see Fig. (7.1) in page 118). As we pointed out before, this process can be also carried out through the population of a resonant state. The quantum dynamics of the population and decay of doubly excited states presents an important and fundamental challenge to theory, since the full 4-body problem must be treated fully quantum mechanically without semiclassical approximations for the nuclear motion. This

[3] The term *et al.* comes from the Latin *et alli* and it means "*and others*".

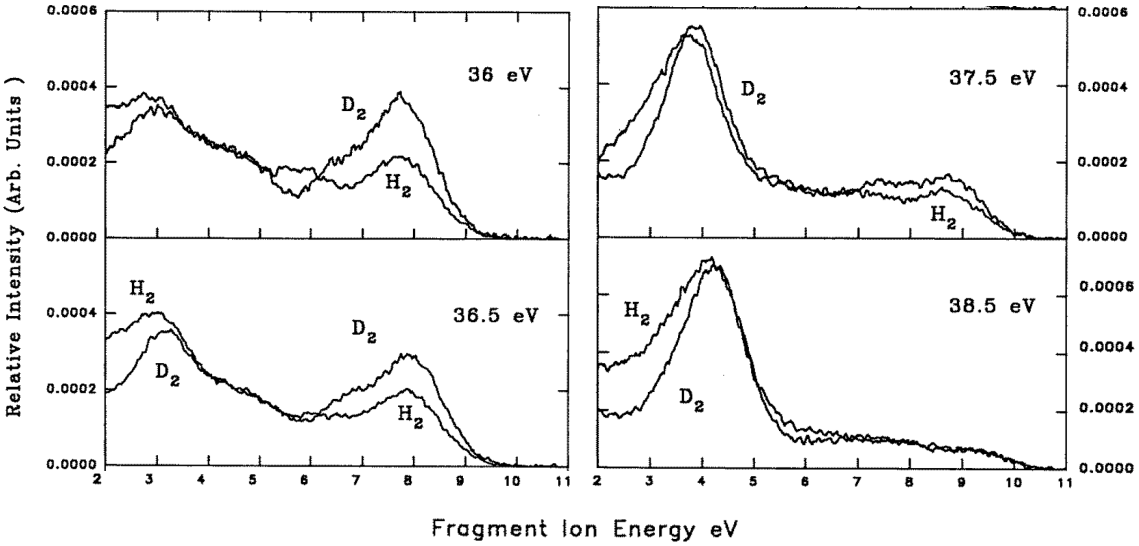

Figure 1.3: Proton kinetic energy distribution obtained by C. J. Latimer *et al.* [59], for H_2 and D_2 observed at 90° with respect to the polarization vector, at photon energies 36.0, 36.5, 37.5 and 38.5 eV.

study was started in our laboratory some years ago making use of photons, in the energy range where the doubly excited states below the second and third ionization thresholds (the $1s\sigma_g$ and $2p\sigma_u$ states of H_2^+, respectively), the Q_1 and Q_2 (see [60, 61]), were responsible for the different structures observed in the proton kinetic energy distributions of the H_2 and D_2 molecules [53, 55]. But the experimental results showed additional structures at higher photon energies whose origin was not totally understood. In particular, for the photon energy range above the third and fourth ionization thresholds, the $2p\pi_u$ and $2s\sigma_g$ states of H_2^+, additional structures were observed in several experimental results [59, 62]. For example, Fig. (1.3) displays the results obtained by C. J. Latimer *et al.* [59] for H_2 and D_2 for several photon energies. As the photon energy increases a peak appears on the left side of the spectra ($\sim$ 4 eV), that was assigned to direct excitation to the $2p\pi_u$ state of the H_2^+ ion. Therefore, this Thesis presents an ab initio calculation that meets the challenge of explaining these experimental findings.

Our second aim will be the study of the angular distribution of the different particles coming from the processes described previously. Angle-resolved photoelectron spectroscopy has been performed for more than 70 years, but only recently its potential to help solving detailed problems in the photoionization dynamics and intramolecular dynamics of gas-phase molecules has been recognized. Measurements of photoelectron angular distributions (PADs) from atoms, the first of which was made in the 1930s [63], have usually been intended to provide information on photoionization dynamics leading ultimately to the so-called complete experiments. Molecular PADs, on the other hand, were used in the past to determine information on molecular orbitals that was complementary to or confirmatory of the photoelectron spectrum [64]. Since the mid-1980s, this situation has changed dramatically, such that on the one hand molecular complete experiments have been attempted, and on the other hand PADs have been used as probes of other dynamical processes of spatial distribution of molecules. The dramatic change in direction of these experiments has been caused by the possibilities opened up by the availability of widely tunable synchrotron radiation, and the use of imagining detectors, which allows to detect in coincidence the momentum of *all* ejected particles. For example, Fig. (1.4) shows the electron angular distribution of CO and N_2 obtained by T. Jahnke *et al.* [6]. In spite of the explosion of new results devoted to the study of electron angular distribution, little attention has been paid to the H_2 molecule, both from the experimental

Figure 1.4: (a), (b) Experimental angular distributions of $C(1s)$ photoelectrons (10 eV kinetic energy, on shape resonance) emitted from a CO molecule by absorption of left and right circularly polarized photons. (c) Analogous distribution of $N(1s)$ photoelectrons (9 eV, on resonance) from N_2. Results obtained by T. Jahnke *et al.* [6].

or theoretical point of view. Only quite recently A. Lafosse *et al.* [65, 66] obtained the first experimental results of the photoelectron angular distribution for the fixed-in-space case, opening a new exciting window to the physical grounds that the study of the proton kinetic proton distribution (KED) was not able to resolve (see Fig. (1.3)). This motivated us to start a new research line in our laboratory devoted to the study of the electron and proton angular distribution. In particular, they found a Forward-Backward asymmetry in the photoelectron distributions, that reflects the break of the symmetry of the molecule, i.e. the emission of a photoelectron with subsequent dissociation of the remaining H_2^+ fragment shows no symmetry with respect to the ionic H^+ and neutral H atomic fragments. What does it take to break this symmetry? The form of a PAD depends sensitively on the particular experiment performed and can therefore be controlled to some extent by experimentalists. The most influential form of control is the manipulation of the relative directions of the polarization vector of the ionizing light and the molecular axis, and the type of polarization. For example, the use of circularly polarized light, instead of the most commonly used linearly polarized one, gives the possibility of obtaining additional information in the ionization process. The circular dichroism effect in diatomic molecules, which is the difference obtained in the PAD between right- and left-handed photons, stands as a new level of challenge to the theory of electron emission from molecules (see Fig. (1.4)). This effect has been studied by D. Dowek *et al.* [66] in the H_2 and D_2, and special attention will be also paid to this effect.

As the photon energy is increased, more and more resonant states are accessible and additional dissociative paths can contribute to the ionization process. When the photon energy is high enough to overcome the double ionization threshold the doubly photoionization is possible. But at even higher photon energies the ionized electron wavelength, λ_e, is comparable to the size of the molecule, and therefore the wave nature of the electron should manifest through interference and diffraction patterns, similarly to what macroscopic waves experience when they meet a macroscopic object. Very recently, interference effects in the ionization of H_2 molecules by energetic ion impact were observed [67, 68]. These pioneering experimental works have motivated several important studies that directly question the basis of Quantum Physics. Inspired by this previous researches, we focus our attention on similar effects on the photoionization process, both in the electron and proton angular distributions. A commonly used image to understand the observed interference patterns is to consider each nuclei as two electron sources, in a similar way as the interference patterns produced by two circular waves, as it is displayed in Fig. (1.5). The interference patterns presented in Fig. (1.5), depend on the distance between the two centers and the wavelength, that can be directly related with the internuclear distance of the molecule and the energy of the ejected electron, respectively. Since the electrons are delocalized in the molecule, is it possible to observe the influence of coherent emission from both sites in the molecule? These effects are fundamental traits of the quantum world and have certain similarities with Young's two slit experiment, although

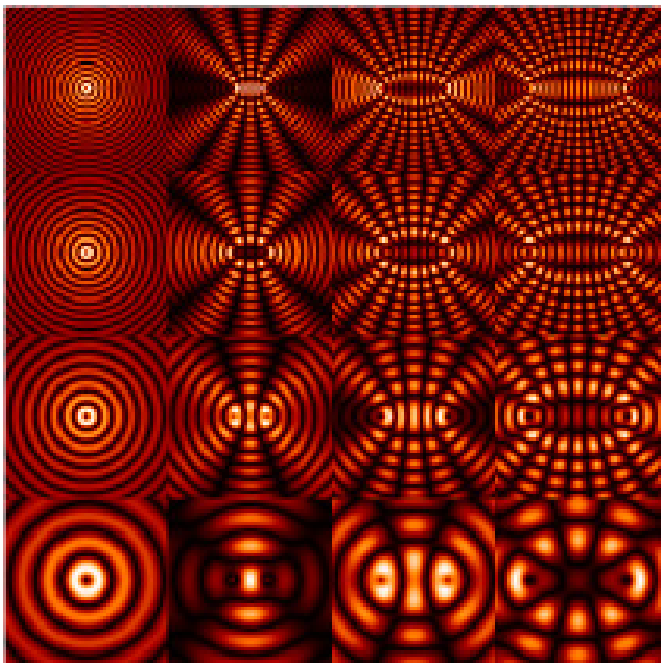

Figure 1.5: Interference of two circular waves - Wavelength (decreasing bottom to top) and wave centers distance (increasing to the right). Absolute value snapshots of the (real-valued, scalar) wave field. As time progresses, the wave fronts would move outwards from the two centers, but the dark regions (destructive interference) stay fixed. Figure obtained from Wikipedia.

one has to keep in mind that the final scattering state of the photoelectron wave in the anisotropic molecular potential differs from the effects derived in a simple two-slit picture. This fundamental idea of such interference effects in molecular photoionization was first brought up by Cohen and Fano in 1966 when discussing total absorption cross section data for H_2, N_2 and O_2 molecules [69]. But Kaplan and Markin [70] were the first who predicted interference effects in the photoelectron angular distribution of oriented H_2 molecules. This theme was then developed by Dehmer and Dill [71] into the K-shell spectroscopy of diatomic molecules. Since then, several experimental and theoretical works have been focused in this item (see for example [72] and references therein); this motivated us to try to clarify these fundamental concepts situated right at the heart of Quantum Mechanics.

Ionization of a target atom by the impact of different types of particles has been the subject of a great number of experimental and theoretical studies for more than five decades [73, 74]. For example, the apparent simple collision of an electron with the hydrogen atom, represents a formidable task that has been resolved only recently [75, 76]. All these elaborated works have been motivated by the importance of the ionization process for basic research in collision physics and for various applications in adjacent fields. Within the field of particle-induced ionization, particular attention has been devoted to the molecular target H_2 [77, 78, 79]. Among all the possible processes coming from the interaction of high energetic particles, in our case electrons, e^-, or ions, X^{z+}, with the H_2 molecule, the main one is the ionization of the system. The main final processes coming from the collision are similar to the ones described in page 3, and in the case of incoming ions, two additional processes can be taken into account[4]:

[4] Although we describe here these two processes, we will not consider them in our calculations presented in Chapter 12, since they can be considered negligible for the energies of the incoming particles considered in this Thesis.

1. **Simple capture**:

$$X^{z+} + H_2 \longrightarrow X^{(z-1)+} + H_2^+(\upsilon).$$

In this case, one of the electrons is taken by the incoming ion, creating a residual ion, that can remain in a bound vibrational (non-dissociative process) or dissociate state (dissociative process).

2. **Double capture**:

$$X^{z+} + H_2 \longrightarrow X^{(z-2)+} + H^+ + H^+.$$

In this case both electrons are taken from the molecular target, producing the Coulomb explosion of the residual ion, similar to the double photoionization process.

For a given projectile, the relative importance of all these processes vary with the ratio $\upsilon_p/Z_p\upsilon_e$, between the velocity of the projectile, υ_p, the velocity of the active electron of the molecule, υ_e, and the charge of the projectile, Z_p. Three different domains of velocities can be distinguished:

- The range of high collisional velocities $\upsilon_p/Z_p\upsilon_e \gg 1$.
- The range of intermediate velocities $\upsilon_p/Z_p\upsilon_e \approx 1$.
- The range of low collisional velocities $\upsilon_p/Z_p\upsilon_e \ll 1$.

Our theoretical methods will be restricted to the *First Born Approximation*, which implies that only the range of high collisional velocities can be taken into account. The main problem encountered when quantum perturbative calculations are attempted beyond the first order is the need to sum over a complete set of intermediate states which are eigenstates of the unperturbed Hamiltonian. In a scattering calculation, the second Born amplitude for electron and positron collisions with atomic hydrogen represents perhaps the simplest example which illustrates this problem (see for example [80, 81]).

The experimental and theoretical results devoted to the study of the collision of different particles with H_2 and D_2 is quite vast, and perhaps the best example is shown in Fig. (1.6), that displays the experimental results obtained by A. K. Edwards *et al.* [82, 83] in the collision of protons of 0.5 MeV/amu with H_2. The experimental results were fitted by the Franck-Condon factors (FC) of the first four dissociative states, i.e., the $1s\sigma_g$, $2p\sigma_u$, $2p\pi_u$ and $2s\sigma_g$ states of H_2^+, the contribution of several resonant states and the double ionization state. Although the theoretical fit provides a good agreement with the experimental results, the method used was quite arbitrary since the intensity of each FC factor, just as the contribution of resonant states, was performed in a "semi-empirical" way. Thus, in this Thesis we will present similar theoretical results, performing full ab initio calculation base in the First Born Approximation, that will reproduce the experimental findings of Fig. (1.6).

This Thesis is structured in two main blocks. The first one is dedicated to the theoretical methods developed in order to describe the different physical processes that we are interested in, while in the second one we present all the results obtained making use of the methods presented in the first part. The first four chapters are devoted to a brief theoretical background that will be used in following chapters. We have tried to include as many key references as possible in case the reader is interested in further details that are beyond the scope of this Thesis. We start the theoretical methods in **Chapter 2** where we present the main characteristics of the *B*-spline functions, since they play a crucial role in order to obtain the different wave functions that describe the ionization process. A general introduction to the methods used to obtain the correct description of the continuum states, both

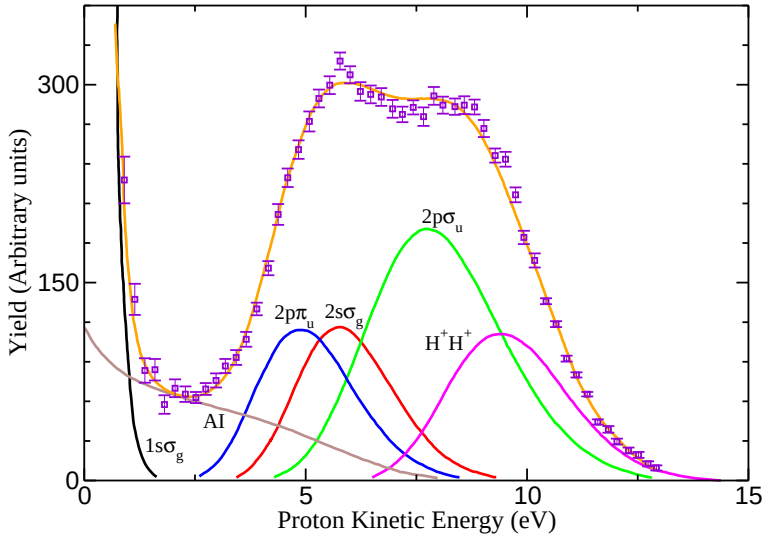

Figure 1.6: Kinetic energy distribution of H^+ produced from the different processes in the dissociative ionization measured by A. K. Edwards *et al.* [82, 83]. The experimental results, squared symbols with error bars, are adjusted to the Franck-Condon factor for the H_2^{**} resonant states, the H_2^+ ($1s\sigma_g$, $2p\sigma_u$, $2p\pi_u$ and $2s\sigma_g$) and for H_2^{2+} (H^+H^+)

electronic and nuclear, is presented in **Chapter 3**. This chapter provides the reader with specific information about the doubly excited states presented in the diatomic bielectronic molecules and the method implemented in order to obtain the characteristics of these states. Also it introduces the theory needed to obtain the continuum wave functions that coherently contain the nuclear motion of the molecule, which is of crucial importance in order to describe the dissociative ionization process. In **Chapter 4**, the angular distribution of the final particles coming from the ionization process is shown and several mathematical developments are described in detail. We will concentrate our attention in the fixed-in-space case, where the molecule possesses a defined orientation in the space with respect to the polarization vector at the ionization instant. To conclude the theoretical part, **Chapter 5** is devoted to the theoretical study of the ionization process by collision of fast particles in the first Born approximation. The results section is opened by **Chapter 6**, where the doubly excited states of H_2 molecule, in particular the families of doubly excited states Q_3 and Q_4, are studied in detail. A brief summary of the main characteristics of the lower resonant states, the Q_1 and Q_2, is also presented, since they will play a crucial role in the study of the photoelectron angular distribution. **Chapter 7** shows the results obtained in the dissociative photoionization of H_2 and D_2, in the 18-50 eV photon energy range, i.e., from the ionization threshold to the double ionization threshold. In **Chapter 8** we show the results for the study of the dissociative photoionization of H_2 from the $E,F^1\Sigma_g^+$ electronic excited state, performing a detailed study of the role of the initial vibrational state posses in this process. **Chapter 9** is devoted to the study of the angular distribution of the final particles coming from the resonant dissociative photoionization of H_2. We present the results for three selected photon energies, in order to highlight the different physical processes relevant in each case: i) At $h\nu = 20$ eV, where only direct ionization is possible; ii) at $h\nu = 27$ eV, where the population and the subsequent decay to the first ionization threshold of the Q_1 states is possible; iii) at $h\nu = 33$ eV, where the decay of the Q_2 states is possible through the first two ionization thresholds. In this latter case, we will discuss the asymmetry observed in the electron distribution. Also, the circular dichroism when circularly polarized light is used, will be discuss. Finally, the results for the proton angular distribution and the electron angular distribution for randomly distributed molecules will be studied in detail. In **Chapter 10** the interference and

coherence phenomena are discussed for the photoionization of the showcase molecules H_2^+ and H_2. To complete the study devoted to the molecular photoionization process, we present in **Chapter 11** the results obtained in the resonant dissociative photoionization of HeH^+, in order to highlight the differences obtained for the homonuclear systems. In **Chapter 12**, the results obtained in the study of the collision of very energetic particles (electrons and highly charged ions) with H_2 and D_2 molecules are provided and analyzed in terms of the the most recent experimental results developed in parallel. A summary of the the main conclusions along with an outlook on future calculations is given in **Chapter 13**. Finally, some additional background information can be found in the **Appendix**. Specifically, we give further information about main mathematical properties of the Clebsch-Gordan coefficients, the Wigner rotations matrices, the Spherical Harmonic functions and the Legendre polynomials.

Atomic units ($m_e = \hbar = e = 1$) will be used throughout this Thesis unless stated otherwise. (see Appendix A for more details about the most useful physical constants).

I hope you enjoy reading!!

Bibliography

[1] P. Lewis, "Ionization in gases from colored flames," *Physical Review*, vol. 21, pp. 2353–2366, 1905.

[2] B. Davis, "Energy necessary to ionize a molecule by impact of negative ions," *Physical Review*, vol. 24, pp. 93–102, 1907.

[3] H. A. Erikson, "On the nature of the ions in air and in carbon dioxide," *Physical Review*, vol. 24, pp. 502–509, 1924.

[4] A. Einstein, "Zur elektrodynamik bewegter körper," *Annalen der Physik. Supplement: Einstein's Annalen Papers*, vol. 14, pp. 194–224, 2005.

[5] E. Rutherford, "The scattering of α and β particles by matter and the strucuture of the atom," *Philosophical Magazine*, vol. 21, pp. 669–688, 1911.

[6] T. Jahnke, T. Weber, A. L. Landers, A. Knapp, S. Schössler, J. Nickles, S. Kammer, O. Jagutzki, L. Schmidt, A. Czasch, T. Osipov, E. Arenholz, A. T. Young, R. D. M. no, D. Rolles, F. J. G. de Abajo, C. S. Fadley, M. A. V. Hove, S. K. Semenov, N. A. Cherepkov, J. Rösch, M. H. Prior, H. Schmidt-Böcking, C. L. Cocke, and R. Dörner, "Circular dichroism in K-shell ionization from fixed-in-space CO and N_2 molecules," *Physical Review Letters*, vol. 88, p. 073002, 2002.

[7] D. Rolles, M. Braune, S. Cvejanović, O. Gener, R. Hentges, S. Korica, B. Langer, T. Lischke, G. Prmper, A. Reinköter, J. Viefhaus, B. Zimmermann, V. McKoy, and U. Becker, "Isotope-induced partial localization of core electrons in the homonuclear molecule N_2," *Nature*, vol. 437, pp. 711–715, 2005.

[8] G. Laurent, J. Fernández, S. Legendre, M. Tarisien, L. Adoui, A. Cassimi, X. Fléchard, F. Frémont, B. Gervais, E. Giglio, J. Grandin, and F. Martín, "Kinematically complete study of dissociative ionization of D_2 by ion-impact," *Physical Review Letters*, vol. 96, p. 173201, 2006.

[9] P. Hohenberg and W. Kohn, "Inhomogeneous electron gas," *Physical Review*, vol. 136, pp. B864–B871, 1964.

[10] H. Bachau, E. Cormier, P. Decleva, J. E. Hansen, and F. Martín, "Applications of B-splines in atomic and molecular physics," *Reports on Progress in Physics*, vol. 64, pp. 1601–1729, 2001.

[11] J. M. Blatt and L. C. Biedenharn, "The angular distribution of scattering and reaction cross sections," *Review of Modern Physics*, vol. 24, pp. 258–272, 1952.

[12] M. S. Child, *Molecular Collision Theory*. Academic, London, 1974.

[13] B. H. Bransden and C. J. Joachain, *Physics of Atoms and Molecules*. Pearson Education, Harlow, 2003.

[14] O. K. Rice, "Predissociation and the crossing of molecular potential energy curves," *The Journal of Chemical Physics*, vol. 1, pp. 375–380, 1933.

[15] U. Fano, "Effects of configuration interaction on intensities and phase shifts," *Physical Review*, vol. 124, pp. 1866–1878, 1961.

[16] H. Feshbach, "Unified theory of nuclear reactions," *Annals of Physics*, vol. 5, pp. 357–390, 1958.

[17] H. Feshbach, "A unified theory of nuclear reactions. II," *Annals of Physics*, vol. 19, pp. 287–313, 1962.

[18] C. Cohen-Tannoudji, B. Diu, and F. Laloe, *Quantum Mechanics vol.* I *and* II. Wiley-Interscience, 1992.

[19] R. P. Madden and K. Codling, "New autoionizing atomic energy levels in He, Ne, and Ar," *Physical Review Letters*, vol. 10, pp. 516–518, 1963.

[20] R. P. Madden and K. Codling, "Two-electron excitation states in Helium," *Astrophysical Journal*, vol. 141, pp. 364–375, 1965.

[21] J. Tennyson, C. J. Noble, and S. Salvini, "Low-energy e-H_2^+ collisions using the R-matrix method," *Journal of Physics B: Atomic, Molecular and Optical Physics*, vol. 17, pp. 905–912, 1984.

[22] J. Tennyson and C. J. Noble, "Low-energy electron-H_2^+ collisions: variation of resonance parameters with internuclear separation," *Journal of Physics B: Atomic, Molecular and Optical Physics*, vol. 18, pp. 155–165, 1985.

[23] H. Takagi and H. Nakamura, "Two-electron excited states and adiabatic quantum defects of H_2: Analysis of elastic scattering of electrons from H_2^+," *Physical Review A*, vol. 27, pp. 691–708, 1983.

[24] L. A. Collins and B. I. Schneider, "Molecular photoionization in the linear algebraic approach: H_2, N_2, NO, and CO_2," *Physical Review A*, vol. 29, pp. 1695–1708, 1984.

[25] K. Nakashima, H. Takagi, and H.Nakamura, "Dissociative recombination of H_2^+, HD^+, and D_2^+ by collisions with slow electrons," *The Journal of Chemical Physics*, vol. 86, pp. 726–737, 1987.

[26] A. P. Hickman, "Dissociative recombination of electrons with H_2^+," *Journal of Physics B: Atomic, Molecular and Optical Physics*, vol. 20, pp. 2091–2099, 1987.

[27] A. Giusti-Suzor, J. N. Bardsley, and C. Derkits, "Dissociative recombination in low-energy e-H_2^+ collisions," *Physical Review A*, vol. 28, pp. 682–691, 1983.

[28] H. Hus, F. Yousif, C. Noren, A. Sen, and J. B. A. Mitchell, "Dissociative recombination of electrons with H_2^+ in low vibrational states," *Physical Review Letters*, vol. 60, pp. 1006–1009, 1988.

[29] B. Peart and K. T. Dolder, "Collisions between electrons and H_2^+ ions VI. Measurements of cross sections for the simultaneous production of $H^+$and H^-," *Journal of Physics B: Atomic, Molecular and Optical Physics*, vol. 8, pp. 1570–1574, 1975.

[30] G. Poulaert, F. Brouillard, W. Claeys, J. W. McGowan, and G. V. Wassenhove, "H_2^+ formation in low energy H^+ -H^- collisions," *Journal of Physics B: Atomic, Molecular and Optical Physics*, vol. 11, pp. L671–L673, 1978.

[31] X. Urbain, A. Giusti-Suzor, D. Fussen, and C. Kubach, "Theoretical study of associative ionisation in H^+ - H^- collisions at low energy (0.001-5 eV)," *Journal of Physics B: Atomic, Molecular and Optical Physics*, vol. 19, pp. L273–L277, 1986.

[32] W. Schön, S. Krüdener, F. Melchert, K. Rinn, M. Wagner, E. Salzborn, M. K. S. Szücs, M. Terao, D. Fussen, R. Janev, X. Urbain, and F. Brouillard, "Transfer ionization in H^+ + H^- collisions," *Physical Review Letters*, vol. 59, pp. 1565–1568, 1987.

[33] S. Arai, T. Yoshimi, M. Morita, K. Hironaka, T. Yoshida, H. Koizumi, K. Shinsaka, Y. Hatano, A. Yagishita, and K. Ito, "Lyman$-\alpha$ excitation spectra in the photodissociation of the doubly excited states of H_2," *Zeitschrift für Physik D Atoms, Molecules and Clusters*, vol. 4, pp. 65–71, 1986.

[34] M. Glass-Maujean, "Electron impact dissociation of H_2 and D_2 studied from the anticrossing signals and by the Doppler-profile technique," *Journal of Physics B: Atomic, Molecular and Optical Physics*, vol. 11, pp. 431–440, 1978.

[35] M. Glass-Maujean, "Photodissociation of doubly excited states of H_2, HD, and D_2," *The Journal of Chemical Physics*, vol. 85, pp. 4830–4834, 1986.

[36] M. Glass-Maujean, "Photodissociation of doubly excited states of H_2: Emission of balmer lines," *The Journal of Chemical Physics*, vol. 89, pp. 2839–2843, 1988.

[37] M. Glass-Maujean, "H_2 doubly-excited-state assignment from the determination of the orbital state of the $H^*(n = 3)$ photodissociation fragments," *Physical Review A*, vol. 52, pp. 4622–4630, 1995.

[38] G. Raşeev, "Variational calculation of the logarithmic derivative of the wavefunction: The electronic autoionisation region in photoionisation of H_2," *Journal of Physics B: Atomic, Molecular and Optical Physics*, vol. 18, pp. 423–439, 1985.

[39] T. Masuoka, "Proton production probability in the dissociative photoionization of H_2," *The Journal of Chemical Physics*, vol. 81, pp. 2652–2656, 1984.

[40] S. Strathdee and R. Browning, "Dissociative photoionization of H_2 at 26.9 eV," *Journal of Physics B: Atomic, Molecular and Optical Physics*, vol. 9, pp. L505–L507, 1976.

[41] W. A. Chupka, "Photoionization of molecular rydberg states: H_2, C $^1\Pi_u$ and its doubly excited states," *The Journal of Chemical Physics*, vol. 87, pp. 1488–1498, 1987.

[42] E. Y. Xu, T. Tsuboi, R. Kachru, and H. Helm, "Four-photon dissociation and ionization of H_2," *Physical Review A*, vol. 36, pp. 5645–5653, 1987.

[43] W. Vanroose, F. Martín, T. N. Rescigno, and C. W. McCurdy, "Complete photo-induced breakup of the H_2 molecule as a probe of molecular electron correlation," *Science*, vol. 310, pp. 1787–1789, 2005.

[44] T. Weber, A. O. Czasch, O. Jagutzki, A. K. Müller, V. Mergel, A. Kheifets, E. Rotenberg, G. Meigs, M. H. Prior, S. Daveau, A. Landers, C. L. Cocke, T. Osipov, R. D. M. no, H. Schmidt-Böcking, and R. Dörner, "Complete photo-fragmentation of the deuterium molecule," *Nature*, vol. 431, pp. 437–440, 2004.

[45] A. Macías, R. Mendizábal, F. Pelayo, A. Riera, and M. Yáñez, "Application of the stabilization method to the molecular states of $LiHe^3+$: Energies and radial couplings," *Physical Review A*, vol. 33, pp. 242–250, 1986.

[46] A. Macías, F. Martín, A. Riera, and M. Yáñez, "Simple discretization method for autoionization widths. I. Theory," *Physical Review A*, vol. 36, pp. 4179–4186, 1987.

[47] A. Palacios, F. Martín, O. Mó, M. Yáñez, and Z. B. Maksić, "Stable doubly charged positive molecular ions formed by direct attachment of alpha particles to HCN and HNC," *Physical Review Letters*, vol. 92, p. 133001, 2004.

[48] F. Morales, C. W. McCurdy, and F. Martín, "Validity of the isolated resonance picture for H_2 autoionizing states," *Physical Review A*, vol. 73, p. 014702, 2006.

[49] F. Martín, "Ionization and dissociation using B-splines: Photoionization of the hydrogen molecule," *Journal of Physics B: Atomic, Molecular and Optical Physics*, vol. 32, pp. R197–R231, 1999.

[50] I. Sánchez, *Métodos de cuadrado integrable para el estudio de colisiones con multiples canales abiertos. Aplicación a la fotoionización del He*. PhD thesis, Universidad Autonoma de Madrid, 1992.

[51] I. Sánchez and F. Martín, "Photoionization of He above the $n = 2$ threshold," *Physical Review A*, vol. 44, pp. 7318–7334, 1991.

[52] M. Cortés and F. Martín, "Multichannel close-coupling method with L^2 integrable bases," *Journal of Physics B: Atomic, Molecular and Optical Physics*, vol. 27, pp. 5741–5760, 1994.

[53] I. Sánchez and F. Martín, "Origin of unidentified structures in resonant dissociative photoionization of H_2," *Physical Review letters*, vol. 79, pp. 1654–1657, 1997.

[54] I. Sánchez and F. Martín, "Representation of the electronic continuum of H_2 with B-spline basis," *Journal of Physics B: Atomic, Molecular and Optical Physics*, vol. 30, pp. 679–692, 1997.

[55] I. Sánchez and F. Martín, "Multichannel dissociation in resonant photoionization of H_2," *Physical Review letters*, vol. 82, pp. 3775–3778, 1999.

[56] A. Palacios, *Ionización y disociación de* H_2^+ *y* H_2 *por pulsos láser ultracortos en la region* XUV. PhD thesis, Universidad Autonoma de Madrid, 2006.

[57] J. L. Sanz-Vicario, H. Bachau, and F. Martín, "Time-dependent theoretical description of molecular autoionization produced by femtosecond xuv laser pulses," *Physical Review A*, vol. 73, p. 033410, 2006.

[58] C. J. Joachain, *Quantum Collision Theory*. North-Holland Publishing Company, 1979.

[59] C. J. Latimer, J. Geddes, M. A. MacDonald, N. Kouchi, and K. F. Dunn, "The photodissociative ionization of hydrogen and deuterium in the VUV via Π states," *Journal of Physics B: Atomic, Molecular and Optical Physics*, vol. 29, pp. 6113–6121, 1996.

[60] I. Sánchez and F. Martín, "The doubly excited states of the H_2 molecule," *Journal of Chemical Physics*, vol. 106, pp. 7720–7730, 1997.

[61] I. Sánchez and F. Martín, "Doubly excited autoionizing states of the H_2 above the second ionization thershold: The Q_2 resonance series," *Journal of Chemical Physics*, vol. 110, pp. 6702–6713, 1999.

[62] K. Ito, P. Lablanquie, P. M. Guyon, and I. Nenner, "Dissociative photoionsation of H_2 at 27-40 eV," *Chemical Physics Letters*, vol. 151, pp. 121–127, 1988.

[63] E. O. Lawrence and M. A. Chaffe, "On the direction of emission of photoelectrons from potassium vapor by ultraviolet light," *Physical Review*, vol. 36, pp. 1099–1100, 1930.

[64] T. A. Carlson and R. M. White, "Study of the angular distribution for the photoelectron spectra of halogen substituted methane molecules," *Faraday Discussions of the Chemical Society*, vol. 54, pp. 285–291, 1972.

[65] A. Lafosse, M. Lebech, J. C. Brenot, P. M. Guyon, L. Spielberger, O. Jagutzki, J. C. Houver, and D. Dowek, "Molecular frame photoelectron angular distributions in dissociative photoionization of H_2 in the region of the Q_1 and Q_2 doubly excited states," *Journal of Physics B: Atomic, Molecular and Optical Physics*, vol. 36, pp. 4683–4702, 2003.

[66] D. Dowek, M. Lebech, and J. C. Houver, "Molecular frame photoemission in photoionization of H_2 and D_2: The role of dissociation on autoionization of the Q_1 and Q_2 doubly exicited states," *24^{th} International Conference on Photonic Electronic and Atomic Collisions*, 2005.

[67] M. E. Galassi, R. D. Rivarola, P. D. Fainstein, and N. Stolterfoht, "Young-type interference patterns in electron emission spectra produced by impact of swift ions on H_2 molecules," *Physics Letters A*, vol. 66, p. 052705, 2002.

[68] D. Misra, U. Kadhane, Y. P. Singh, L. C. Tribedi, P. D. Fainstein, and P. Richard, "Interference effect in electron emission in heavy ion collisions with H_2 detected by comparison with the measured electron spectrum from atomic hydrogen," *Physical Review Letters*, vol. 92, p. 153201, 2004.

[69] H. D. Cohen and U. Fano, "Interference in the photo-ionization of molecules," *Physical Review*, vol. 150, pp. 30–33, 1966.

[70] I. G. Kaplan and A. P. Markin, "Interference phenomena in photoionization of molecules," *Soviet Physics-Docklady*, vol. 14, pp. 36–39, 1969.

[71] J. L. Dehmer and D. Dill, "Shape resonances in K-shell photoionization of diatomic molecules," *Physical Review Letters*, vol. 35, pp. 213–215, 1975.

[72] D. Rolles, *Scattering and Coherence phenomena in the photoionization of small molecules*. PhD thesis, Mathematik und Naturwissenschaften der Technischen Universität Berlin, 2005.

[73] M. E. Rudd, Y. K. Kim, D. H. Madison, and J. W. Gallagher, "Electron production in proton collisions: Total cross sections," *Review Modern Physics*, vol. 57, pp. 965–994, 1985.

[74] M. E. Rudd, Y. K. Kim, D. H. Madison, and T. J. Gay, "Electron production in proton collisions with atoms and molecules: energy distributions," *Review Modern Physics*, vol. 64, pp. 441–490, 1992.

[75] T. N. Rescigno, M. Baertschy, W. A. Isaacs, and C. W. McCurdy, "Collisional breakup in a quantum system of three charged particles," *Science*, vol. 286, pp. 2474–2479, 1999.

[76] C. W. McCurdy, M. Baertschy, and T. N. Rescigno, "Solving the three-body Coulomb breakup problem using exterior complex scaling," *Journal of Physics B: Atomic, Molecular and Optical Physics*, vol. 37, pp. R137–R187, 2004.

[77] C. E. Kuyatt and J. T. Jorgensen, "Energy and angular dependence of the differential cross section for production of electrons by 50-100 keV protons in hydrogen gas," *Physical Review*, vol. 130, pp. 1444–1455, 1963.

[78] W. E. Wilson and L. H. Toburen, "Electron emission in H_2^+-H_2 collisions from 0.6 to 1.5 MeV," *Physical Review A*, vol. 7, pp. 1535–1544, 1973.

[79] M. W. Gealy, I. G. W. Kerby, Y.-Y. Hsu, and M. E. Rudd, "Energy and angular distributions of electrons from ion impact on atomic and molecular hydrogen. I. 20-114-keV H^++H_2," *Physical Review A*, vol. 51, pp. 2247–2255, 1995.

[80] C. J. Joachain and N. J. Kylstra, "Second Born calculations of electron scattering by atomic hydrogen using a B-spline basis," *Journal of Physics B: Atomic, Molecular and Optical Physics*, vol. 28, pp. L477–L482, 1995.

[81] S. Houamer, A. Mansouri, C. D. Cappello, A. Lahmam-Bennani, S. Elazzouzi, M. Moulay, and I. Charpentier, "Second Born approximation for the ionization of H_2 by electron impact," *Journal of Physics B: Atomic, Molecular and Optical Physics*, vol. 36, pp. 3009–3024, 2003.

[82] A. K. Edwards, R. M. Wood, J. L. Davis, and R. L. Ezell, "Collisional ionization and excitation of H_2: Two-electron processes," *Physical Review A*, vol. 42, pp. 1367–1375, 1990.

[83] A. K. Edwards, R. M. Wood, J. L. Davis, and R. L. Ezell, "Erratum: Collisional ionization and excitation of H_2: Two-electron processes," *Physical Review A*, vol. 44, pp. 797–798, 1991.

Part I

Methodology

Chapter 2

The basis of *B*-splines

"It is quite clear that beauty does depend on one's culture and upbringing for certain kinds of beauty, pictures, literature, poetry and so on...But mathematical beauty is of a rather different kind. I should say perhaps it is of a completely different kind and transcends these personal factors. It is the same in all countries and at all periods of time."

Paul Dirac

Table of Contents

2.1 Introduction

B-SPLINES were introduced by Schoenberg in 1946 [1], but it was only with the publication in 1978 of the monograph by de Boor [2] that their application to atomic physics started in earnest, which is now a classic in the field. The book described the most important mathematical properties for *B*-splines of any order and included a set of computer programs that are even used today. In the 1970s Shore published a series of papers [3, 4, 5, 6, 7] where she discussed exclusively different types of single-particle problem. Nevertheless, it took another ten years with the attendant increase in computer power before the next attempt was made to make use of the properties of *B*-splines. First in 1986, on the investigation of Bottcher, Johnson and Sapirstein [8, 9, 10] introduced a *B*-spline basis set for the calculation of second- and higher-order corrections to properties of heavy atoms using many-body perturbation theory.

Since these early works, *B*-splines have been used in many other types of calculation of various properties for both bound and continuum states and this is the main subject of this chapter. As we will see, *B*-splines are able to provide a very accurate representation of continuum states, which makes them superior to more conventional L^2 basis sets (e.g. Gaussian or Slater functions).

Although the first applications were to static properties, it has turned out that *B*-splines are perhaps even more important for the calculation of dynamic properties as multiphoton excitation, above-threshold ionization (ATI) and high-order harmonic generation (HOHG) in atoms and dissociation of molecules for which the use of *B*-splines has meant that effects could be taken into account which were beyond reach from a theoretically point of view earlier.

Therefore, in this chapter we present the main properties of the *B*-spline basis set and its flexibility when one has to obtain the different wave functions solution of the molecular Hamiltonian, and it is based on the review of Martín [11] and Bachau *et al.* [12], and on de Boor's book [2].

2.2 The basis of *B*-splines

The use of basis sets to solve the Schrödinger equation has a long history in physics and chemistry. It transforms the solution of a differential equation into an algebraic eigenvalue problem, and, particularly in conjunction with the introduction of electronic computing, this approach has become popular since linear algebra is one of the best developed branches of numerical computation. In molecular physics, the use of basis sets of different types has been a standard practice for a long time. The introduction of *B*-splines basis set can be considered quite new, despite of the fact its important properties. *B*-splines have the properties of being "complete enough" with a relatively small number of basis functions and, since linear dependences are negligible, even for a large basis, it is possible for such a basis set to compete with the finite-difference methods[1]. This accounts for the recent swing towards the use of *B*-splines in atomic calculations, while also for molecular problems *B*-splines have considerable advantages over the earlier basis sets.

Spline basis functions are compact L^2 integrable functions[2] defined in a restricted space usually referred to as *box*, in contrast to such L^2 basis sets as Gaussian or Slater orbitals that extend to infinity. In a box, a knot sequence is defined and the freedom to define the knots to suit each particular problem, is, as we shall see, another important advantage of the method. The knot sequence defines the extent of the individual splines. *B*-splines are in principle defined as a set (*B* stands for basis) but for convenience we shall also refer to the individual splines in the set as *B*-splines. *B*-splines are positive definite functions[3], which leads to matrices that are easier to diagonalize. This is in contrast to cardinal splines[4], for example, that are different from zero over the whole box and not positive definite functions. Compactness[5] has another advantage in

[1] A method for solving an equation by approximating continuous quantities as a set of quantities at discrete points, often regularly spaced into a so-called grid or mesh. Because finite element methods can be adapted to problems of great complexity and unusual geometry, they are an extremely powerful tool in the solution of important problems in heat transfer, fluid mechanics, and mechanical systems. Furthermore, the availability of fast and inexpensive computers allows problems which are intractable using analytic or mechanical methods to be solved in a straightforward manner using finite element methods.

[2] A function $f(x)$ is said to be square integrable if $\int_{-\infty}^{\infty} |f(x)|^2 dx$ is finite.

[3] A positive-definite function of a real variable x is a complex-valued function $f : R \to C$, such that for any real numbers x_1, ..., x_n, the $n \times n$ matrix A with entries $a_{ij} = f(x_i - x_j)$ is positive semi-definite. It is usual to restrict to the case in which $f(-x)$ is the complex conjugate of $f(x)$, making the matrix A Hermitian. If a function f is positive semi-definite, we find by taking $n = 1$ that $f(0) \geq 0$. By taking $n = 2$ and recognizing that a positive definite matrix has a positive determinant we get $f(x-y)f(y-x) \leq f(0)^2$ which implies $|f(x)| \leq f(0)$.

[4] A cardinal spline is a cubic Hermite spline whose tangents are defined by the points and a tension parameter. This spline creates a curve from one way point to another taking into account the points before and after. By taking into account the way points before and after the current curve, the curves appear to join together making one seamless curve.

[5] In functional analysis, two measures of non-compactness are commonly used; these associate numbers to sets in such a way that compact sets all get the measure 0, and other sets get measures that are bigger according to "how far" they are removed from compactness. The underlying idea is the following: a bounded set can be covered by a single ball of some radius. Sometimes several balls of a smaller radius can also cover the set. A compact set in fact can be covered by finitely many balls of arbitrary small radius, because it is totally bounded. So one could ask: what is the smallest radius that allows to cover the set with finitely many balls?

matrix calculations, since integrals over two *B*-splines for example will be zero if the two splines are different from zero in disjoint intervals. The resulting matrices are sparse and often, but not always, banded, which is advantageous not only in the diagonalization procedure but also when calculating the matrix elements.

2.2.1 Description of *B*-splines

B-splines are functions designed to generalize polynomials for the purpose of approximating arbitrary functions. One can view them as new elementary functions such as $\sin(x)$ or $j_l(x)$. One becomes familiar with them by understanding their qualitative behavior and how to use them, that is how to obtain values of the functions, their derivatives or integrals. A complete description of *B*-splines and their properties can be found in de Boor's book [2]. Just like $\sin(x)$, efficient numerical evaluation can be accomplished by black-box routines, and it is not generally important to know the algorithm for proficient use.

Let us introduce a few definitions.

- The polynomials of order k (maximum degree $k-1$) are

$$p(x) = a_0 + a_1 x + \cdots + a_{k-1} x^{k-1}. \tag{2.1}$$

- A function which is continuous (on a given interval) together with its derivatives up to order n, that is $f(x)$, $Df(x), \ldots, D^n f(x)$, is said to be of class C^n. Then C^0 means that only f is continuous and C^{-1} that f is discontinuous.

- Consider an interval $I = [a,b]$ divided into ℓ subintervals $I_j = [\xi_j, \xi_{j+1}]$ by a sequence of $\ell+1$ points ξ_j in strict ascending order,

$$a = \xi_1 < \xi_2 < \cdots < \xi_{j+1} = b. \tag{2.2}$$

  The ξ_j sequence will be called *breakpoints* (*bps*).

- Let us associate with interior *bps* ξ_j, $j = 2, \cdots, \ell$, a second sequence of non-negative integers ν_j, $j = 2, \cdots, l$, $\nu_j \geq 0$, which define continuity condition $C^{\nu_j - 1}$ at the associated *bps* ξ_j. With the end *bps* ξ_1 and $\xi_{\ell+1}$ we associate $\nu_1 = \nu_{l+1} = 0$, that is we do not require any continuity. This is natural since we are only interested in the interval $[a,b]$. Further restrictions may be dictated by boundary conditions at the endpoints, and are easily implemented as we shall see.

- Finally let us call *knots* another sequence of points t_i in ascending order, not necessarily distinct,

$$\{t_i\}_{i=1,\ldots,m} \qquad t_1 \leq t_2 \leq \cdots \leq t_m, \tag{2.3}$$

  associated with ξ_j and ν_j as follows:

$$\begin{array}{lll} t_1 = t_2 = \cdots = t_{\mu_1} = \xi_1; & \mu_1 = k & \\ t_{\mu_1+1} = \cdots = t_{\mu_1+\mu_2} = \xi_2; & & \\ \cdots & & \\ t_{p+1} = \cdots = t_{p+\mu_i} = \xi_i; & p = \mu_1 + \mu_2 + \cdots + \mu_{i-1} & \\ \cdots & & \\ t_{n+1} = \cdots = t_{n+k} = \xi_{\ell+1}; & \mu_{l+1} = k; & n = \mu_1 \cdots + \mu_\ell \end{array} \tag{2.4}$$

  where μ_j is the multiplicity of the knots t_i at ξ_j and is given by $\mu_j = k - \nu_j$. Actually only multiplicity at the inner *bps* is important, and we shall always choose maximum multiplicity $\nu_1 = \nu_{l+1} = k$ at the endpoints (see Fig. (2.1)).

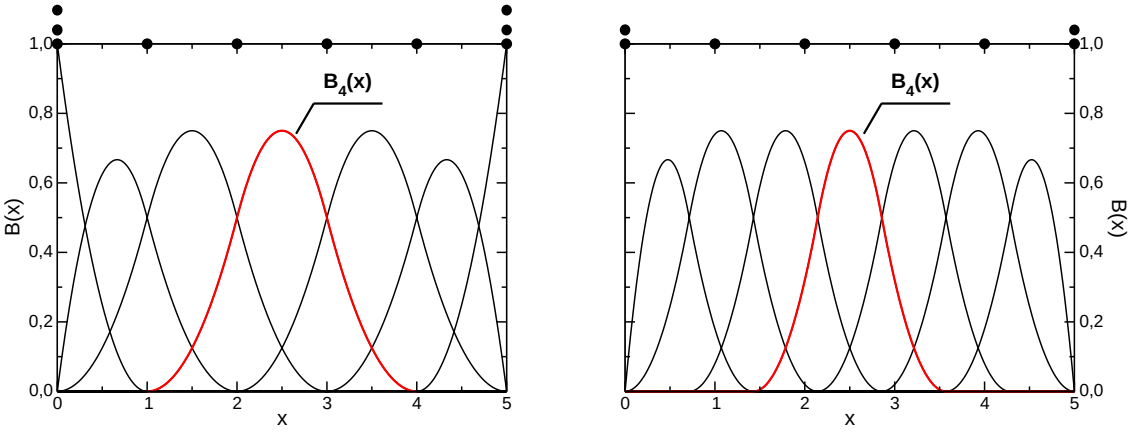

Figure 2.1: The full set of *B*-spline of order $k = 3$ relative to the knot sequence $\{0,0,0,1,2,3,4,5,5,5\}$. Knots are represented by full circles. Left panel, multiplicity in both edges equal to 3. Right panel, same as the left panel, but using a knot sequence of multiplicity equal to 2 at the borders of the box.

The most common choice for knot multiplicity at inner *bps* is unity, corresponding to maximum continuity, that is C^{k-2}. This choice will be employed throughout all the performed calculations carried out in this Thesis. With this choice the number of *B*-spline functions *n*, is given by $n = \ell + k - 1$. Continuity may be relaxed at the inner *bps* by increasing the associated knot multiplicity there. The multiplicity at the edges of the box can be controlled in the same way, which can be used to impose specific boundary conditions on the wave function. For example, the reduced wave function associated with a bound state must be zero at the origin and at very large distance, i.e., at the $r = R_{max}$, therefore, selecting the multiplicity at both edges equal to $k-1$ reproduce the desired behavior (see right panel of Fig. (2.1)). Note that other way to impose this condition is to delete the first and last *B*-spline in the basis set.

A full set of *B*-splines of order $k = 3$ (degree 2, since the order of the *B*-spline corresponds to the degree of the polynomials involved plus one) over the interval $[0,5]$ is shown in Fig. (2.1). The interval is divided into five subintervals by the *bps* $\{0,1,2,3,4,5\}$. Each *B*-spline (consider the fourth *B*-spline, B_4, for example) is a function made up of different polynomial pieces on adjacent subintervals, of a fixed order *k*), joined with a certain degree of continuity at the *bps*. In this case each *B*-spline is continuous together with its first derivative (class C^1) at the interior *bps*, while at x = 0 B_4 is still C^1, but B_2 has discontinuous first derivative, and B_1 is discontinuous (they are C^0 and C^{-1} respectively). The same is true for B_6 and B_7 at $x = 5$, and it will be typical of the *B*-spline bases commonly employed. An explicit representation of $B_4(x)$ in the example is

$$B_4 = \begin{cases} \frac{1}{2}(x^2 - 2x + 1) & 1 \le x < 2 \\ -x^2 + 5x - \frac{11}{2} & 2 \le x < 3 \\ \frac{1}{2}x^2 - 4x + 8 & 3 \le x < 4 \\ 0 & \text{otherwise.} \end{cases} \tag{2.5}$$

In the previous example (left panel of Fig. (2.1)), we therefore have the sequence of points $\{\nu_j\} = \{0,2,2,2,2,0\}$, and the knots sequence, $\{t_i\} = \{0,0,0,1,2,3,4,5,5,5\}$, with the multiplicity of the knots equal to $\{\mu_j\} = \{3,1,1,1,1,3\}$.

2.2.2 The basis of *B*-splines

A single *B*-spline, $B(x)$, is defined by the order $k > 0$, and a set of $k+1$ knots, $\{t_i, \ldots, t_{i+k}\}$, such that $\{t_i < t_{i+k}\}$. The following important properties, apparent in Fig. (2.1), can be extracted:

- $B(x)$ is a pp-function[6] of order k over $[t_i, t_{i+k}]$.
- $B(x) > 0$ for $x \in]t_i, t_{i+k}[$.
- $B(x) = 0$ for $x \notin [t_i, t_{i+k}]$.
- For $x = \xi_j$, $B(x) \in C^{k-1-\nu_j}$, where ν_j is the multiplicity at ξ_j. The maximum multiplicity is k, giving discontinuous functions, the minimum is one, giving $B(x) \in C^{k-2}$.
- The knots need not be equidistant and the shape of $B(x)$ changes smoothly with the change of the knots.

In general a family of *B*-spline functions, B_i, $i = 1, \ldots, n$ is completely defined given $k > 0$, $n > 0$ and a sequence of knots $t = \{t_i\}_{i=1,\ldots,n+k}$ (actually t_i may be infinite at one or both ends). Since k and t are usually fixed, one writes simply $B^k_{t,i}(x) = B_i(x)$. Each $B_i(x)$ is defined over an interval $[t_i, t_{i+k}]$, which contains $i+k$ consecutive knots, and is indexed by the knot where it starts, so exactly one $B_i(x)$ starts at each knot t_i, $i = 1, \ldots, n$, and ends k knots later (see Fig. (2.1)). $B_i > 0$ over the interval $x \in]t_i, t_{i+k}[$, which is called the support of B_i, and $B_i = 0$ outside it. In fact, of all pp-functions, *B*-splines are designed to have minimal support. Some general properties of *B*-splines are the following.

- Over each interval $]t_i, t_{i+k}[$, $t_i < t_{i+1}$, exactly k *B*-spline are nonzero,

  $$B_j(x) \neq 0 \text{ for } j = i-k+1, \ldots, i$$

  the first being B_{i-k+1}, which ends at t_{i+1}, and the last is B_i which starts at t_i. Therefore we have identically

  $$B_i(x) \cdot B_j(x) = 0 \text{ for } |\, i-j \,| \geq k.$$

- In the expansion of an arbitrary function

  $$f(x) = \sum_{j=1}^{n} c_j B_j(x) = \sum_{j=i-k+1}^{i} c_j B_j(x) \text{ for } x \in [t_i, t_{i+k}]$$

  one always has only k terms contributing, so a minimal number of operations is needed.

- Because the *B*-splines are non-negative functions with minimal support, the expansion coefficients of an arbitrary function f are close to the function values at the knots. This means that wild oscillations in the coefficients are avoided, cancellation errors are minimal and numerical stability maximal

- Each interval $I_j = [\xi_j, \xi_{j+1}] = [t_j, t_{j+1}]$ is characterized by a pair of consecutive knots $t_i < t_{i+1}$. t_i is called the left knot of interval $[t_k, t_n]$, and determines the index of the B_i contributing over I_j , which are $B_{i-k+1}, \ldots, B_i$.

- They are normalized as $\sum_i B_i(x) = 1$ over the whole $[t_k, t_n]$.

- For simple equidistant knots each B_i is just a translation by one interval of the previous one. If the knots are not equidistant there is a smooth change in shape.

[6] Any function expressed as a linear combination of the B_i will be called a piecewise polynomial function (pp-function) over $[a, b]$, $f = \sum_{i=1}^{n} c_i B_i$, and it can be shown [2] that f is the most general function made of l polynomial pieces of order k, one for each subinterval I_j joined at the interior *bps* with continuity $C^{\nu_j - 1}$.

- *B*-splines satisfy the recursion relation

$$B_i^1(x) = \frac{x - t_i}{t_{i+k-1} - t_i} B_i^{k-1}(x) + \frac{t_{i+k} - x}{t_{i+k} - t_{i+1}} B_{i+1}^{k-1}(x).$$

  Together with the definition of *B*-spline of order $k = 1$

$$B_1^k = \begin{cases} 1 & t_i \le x \le t_{i+1} \\ 0 & \text{otherwise} \end{cases}$$

  this gives rise to the algorithm employed for the practical evaluation of *B*-splines: given a point x, one generates by recursion the values of all the k *B*-spline which are nonzero at x. The derivative of a *B*-spline of order k, being a pp-function of order $k-1$, can be also expressed as a linear combination of *B*-spline of the same order,

$$DB_i^k(x) = \frac{k-1}{t_{i+k-1} - t_i} B_i^{k-1}(x) + \frac{k-1}{t_{i+k} - t_{i+1}} B_{i+1}^{k-1}(x).$$

Actually there is complete freedom in the choice of the first and last k knots, the only requirement being

$$t_i \leqslant t_k \ldots \leqslant t_k \leqslant \xi_1 \quad \xi_{l+1} \leqslant t_{n+1} \ldots \leqslant t_{n+k}.$$

Their choice affects the behavior of the first and last k *B*-splines, but is of no consequence on their basis set property for pp-functions on $[\xi_1, \xi_{l+1}]$. The standard choice $t_1 = \ldots = t_k = \xi_1$ and $t_{n+1} = \ldots = t_{n+k} = \xi_{l+1}$ is particularly convenient. In this case (see Fig. (2.1)) all $B_i = 0$ outside $[a,b]$. Moreover only the first *B*-spline is discontinuous at $x = a$, $B_1(x) = 0$, the same for DB_1 and DB_2, and likewise for the higher derivatives; the same at $x = b$ for B_n, DB_n and DB_{n-1}, and so on. This makes it very easy to implement boundary conditions at the endpoints. For instance $f(a) = 0$ is satisfied by deleting B_1 from the set, $Df(b) = 0$ by combining B_{n-1} and B_n as $\tilde{B}_{n-1} = c_1 B_{n-1} + c_2 B_n$ so that $D\tilde{B}_{n-1}(b) = 0$, and so on.

Bibliography

[1] I. J. Schoenberg, "Contributions to the problem of approximation of equidistant data by analytic functions. Part A: On the problem of smoothing or graduation," *Quarterly of Applied Mathematics*, vol. 4, pp. 45–99, 1946.

[2] C. de Boor, *A practical Guide to Splines*. New York: Springer, 1978.

[3] B. W. Shore, "Solving the radial Schrödinger equation by using cubic-spline basis functions," *The Journal of Chemical Physics*, vol. 58, pp. 3855–3866, 1973.

[4] B. W. Shore, "Comparison of matrix methods applied to the radial Schrödinger eigenvalue equation: The Morse potential," *The Journal of Chemical Physics*, vol. 59, pp. 6450–6463, 1973.

[5] B. W. Shore, "Use of the Rayleigh-Ritz-Galerkin method with cubic splines for constructing single-particle bound-state radial wavefunctions: The hydrogen atom and its spectrum," *Journal of Physics B: Atomic, Molecular and Optical Physics*, vol. 6, pp. 1923–1932, 1973.

[6] B. W. Shore, "Use of boundary-condition wavefunctions for bound states, continuum states, and resonances," *Journal of Physics B: Atomic, Molecular and Optical Physics*, vol. 7, pp. 2502–2517, 1974.

[7] B. W. Shore, "B-spline expansion bases for excited states and discretized scattering states," *The Journal of Chemical Physics*, vol. 63, pp. 3835–3840, 1975.

[8] W. R. Johnson and J. Sapirstein, "Computation of second-order many-body corrections in relativistic atomic systems," *Physical Review Letters*, vol. 57, pp. 1126–1129, 1986.

[9] W. R. Johnson, M. Idrees, and J. Sapirstein, "Second-order energies and third-order matrix elements of alkali-metal atoms," *Physical Review A*, vol. 35, pp. 3218–3226, 1987.

[10] W. R. Johnson, S. A. Blundell, and J. Sapirstein, "Finite basis sets for the Dirac equation constructed from *B*-splines," *Physical Review A*, vol. 37, pp. 307–315, 1988.

[11] F. Martín, "Ionization and dissociation using B-splines: Photoionization of the hydrogen molecule," *Journal of Physics B: Atomic, Molecular and Optical Physics*, vol. 32, pp. R197–R231, 1999.

[12] H. Bachau, E. Cormier, P. Decleva, J. E. Hansen, and F. Martín, "Applications of B-splines in atomic and molecular physics," *Reports on Progress in Physics*, vol. 64, pp. 1601–1729, 2001.

Chapter 3

Molecular Schrödinger equation

"If anybody says he can think about quantum physics without getting giddy, that only shows he has not understood the first thing about them."

Niels Bohr

Table of Contents

3.1 Introduction

THE ELECTRONIC AND NUCLEAR characteristics of a molecular system implies the resolution of the time-independent Schrödinger equation, that in most cases must be carried out numerically. If one is interested in describing the electron and nuclear characteristics in detail, there is no substitute for quantum mechanics. In this chapter we will present the methods needed to obtain the different wave functions that describe a diatomic molecule with one and two electrons. We will present the Born-Oppenheimer approximation that allows to disentangle the nuclear and electronic movements and to obtain the electronic wave function for different internuclear distances, and making use of the latter, the vibrational wave functions can be obtained. The use of L^2 basis function, as the *B*-splines basis functions (see Chapter 2), implies the discretization of the wave function belonging

to the continuum, so we will present the method developed in our laboratory to treat them correctly. Applications of *B*-splines basis sets in molecular systems are very recent. In 1992, *B*-splines basis sets were used for the first time to describe the electronic states of H_2^+ and HeH^{2+} molecular systems [1, 2, 3, 4, 5, 6, 7]. The proof that *B*-splines could reproduce as accurately as desired the exact result offered a promising perspective and opened the way for subsequent applications in molecules containing several electrons. The subject is now growing very rapidly. The last decade has seen a breakthrough in the description of continuum states of two-electron diatomic molecules, which has been possible through the use of *B*-splines. New theoretical tools have been developed to describe both the electronic and vibrational continuum, and the interferences between them (see [8] for more details).

This Chapter is based on the review of Martín [9] and Bachau *et al.* [8], and on several references cited therein.

3.2 The Born-Oppenheimer approximation

A molecule may be considered as a number of electrons surrounding a set of positively charged nuclei. The Coulombic attraction between these two types of particle forms the basis for atoms and molecules. Since all the particles which make up the molecule are moving relative to each other, a full mechanical description of the molecule is very complicated, even when treated classically. Fortunately, the overall motion of the molecule can be broken down into various types of motions, namely, translational, rotational, vibrational and electronic. To a good approximation, each of these motions can be considered on its own. The basis of this classification was established in a ground-breaking paper written by Born and Oppenheimer [10], just one year after the introduction of wave mechanics. The main objective of this paper was the separation of electronic and nuclear motions in a molecule. Neglecting the Mass polarization terms[1] and relativistic effects, the Hamiltonian of a diatomic molecule in the body-fixed frame can be decomposed according to

$$\mathcal{H}(r,R) = -\frac{1}{2\mu}\nabla_R^2 + \mathcal{H}_{el}(r,R), \tag{3.1}$$

where $-\nabla_R^2/2\mu$ is the relative kinetic energy of the nuclei, μ is the reduced mass and $\mathcal{H}_{el}$ is the electronic Hamiltonian, which depends parametrically on R and contains all the potential energy terms (including the nucleus-nucleus repulsion). The vector r labels all electronic coordinates, and R the internuclear distance. Within this framework, the total wave function can be written as

$$\Psi_{n\nu}(r,R) = \frac{\chi_\nu(R)}{R}\psi_n(r,R), \tag{3.2}$$

[1] The total Hamilton operator can be written as the kinetic and potential energies of the nuclei and electrons,

$$\mathcal{H}_{tot} = T_n + T_{el} + V_{ne} + V_{ee} + V_{nn}.$$

When the Hamilton operator is transformed to the center of mass system, it may be written as:

$$\mathcal{H}_{tot} = T_n + H_{el} + H_{mp},$$

$$\mathcal{H}_{el} = T_{el} + V_{ne} + V_{ee} + V_{nn},$$

$$\mathcal{H}_{mp} = -\frac{1}{2M_{tot}}\left(\sum_{i=1}^{N}\nabla_i\right),$$

where $\mathcal{H}_{el}$ is the electronic Hamilton operator and $\mathcal{H}_{mp}$ is called the mass-polarization (M_{tot} is the total mass of all nuclei and the sum is over all electrons).

where the indexes n and ν label the electronic and nuclear states. The electronic wave function satisfies

$$[\mathcal{H}_{el} - E_n(R)]\psi_n(r,R) = 0, \tag{3.3}$$

and the corresponding nuclear wave function

$$[T(R) + E_n(R) - W_{n\nu}]\chi_\nu(R) = 0, \tag{3.4}$$

where $W_{n\nu}$ is the total energy of the molecule, $E_n(R)$ is the Born-Oppenheimer (BO) potential energy curve of the nth electronic state of the molecule and the nuclear kinetic operator is given by

$$T(R) = -\frac{1}{2\mu}\frac{\mathrm{d}^2}{\mathrm{d}R^2} + \frac{J(J+1)}{2\mu R^2}, \tag{3.5}$$

with J the total orbital angular momentum (electronic plus nuclear). The usual BO separation given by Eq. (3.2) is approximately valid except for very slow electrons in the continuum.

3.3 The monoelectronic Schrödinger equation

Before extending the techniques to multi-electron molecules, we will first focus on the simplest molecular systems: those with one electron. Having stated the limitations (non-relativistic Hamilton operator and the Born-Oppenheimer approximation), we are ready to consider the electronic Schrödinger equation for the H_2^+ molecule.

For a one-electron diatomic molecule, the electronic Schrödinger equation reads

$$\mathcal{H}_{el}\psi_n \equiv \left\{-\frac{1}{2}\nabla^2 - \frac{Z_A}{|r-R_A|} - \frac{Z_B}{|r-R_B|} + \frac{Z_A Z_B}{R}\right\}\psi_n = E_n(R)\psi_n, \tag{3.6}$$

where R_A and R_B are the position vectors of nucleus A and B respectively, and $R = |R_B - R_A|$. Eq. (3.6) can be solved using a one-center expansion (OCE), that is, expanding the electronic wave function ψ_n in a basis of radial B-splines multiplied by spherical harmonic with a well defined value of the quantum number m (note that m defines the value of the projection of the angular momentum over the molecular axis, i.e. L_z):

$$\psi_n^m = \sum_\ell^{\ell_{max}} \sum_i^{N_\ell} c_{i\ell}^n \frac{B_i(r)}{r} Y_\ell^m(\theta,\phi), \tag{3.7}$$

where the B-spline basis is defined in the interval $[0, r_{max}]$ (see Chapter 2). Since different values of m are not coupled, we can drop the index m from ψ_n. Eq. (3.7) can also be written as

$$\psi_n = \sum_\ell^{\ell_{max}} \frac{\mathcal{U}_{n\ell}(r)}{r} Y_\ell^m(\theta,\phi), \tag{3.8}$$

with

$$\mathcal{U}_{n\ell}(r) = \sum_i^{N_\ell} c_{i\ell}^n B_i(r), \tag{3.9}$$

the reduced radial wave function. Substituting Eq. (3.8) in Eq. (3.6) and projection onto $B_i Y_\ell^m$, yields the following matrix equation,

$$Hc = ESc, \tag{3.10}$$

where

$$H_{i\ell,j\ell'} = \int_0^{r_{max}} \int_0^{\pi} \int_0^{2\pi} B_i(r)\overline{Y}_\ell^m(\theta,\phi)\mathcal{H}_{el}B_j(r)Y_{\ell'}^m(\theta,\phi)\,\mathrm{d}r\,\sin\theta\,\mathrm{d}\theta\,\mathrm{d}\phi, \tag{3.11}$$

and[2]

$$S_{i\ell,j\ell'} = \delta_{\ell\ell'}\int_0^{r_{max}} B_i(r)B_j(r)\,\mathrm{d}r. \tag{3.12}$$

The overlap matrix S originates from the fact that B-splines do not form an orthonormal set of basis functions. All matrix elements can be computed exactly using a Gauss Legendre (GL) quadrature[3]. A GL quadrature with n GL points calculates exactly the integral of a polynomial of degree $2n+1$ over a closed interval. Since a B-spline of order k is a particular polynomial of degree $k-1$ on each segment, one easily sees that the integrands of the element $S_{i\ell,j\ell'}$ and the kinetic term of the element $H_{i\ell,j\ell'}$ are polynomials with maximum degree $2k-2$. Applying the GL procedure on each segment leads to an exact numerical evaluation of these two integrals. The case of the centrifugal and the potential term of the element $H_{i\ell,j\ell'}$ is slightly different. Here the integrand is no longer a polynomial of some order but rather a rational fraction and the above statement does not hold. However, it can be shown [8] that a small increment in the number of GL points results in an immediate convergence to machine accuracy. Therefore, all matrix elements are implicitly computed exactly. To ensure the continuity of the bound states, ψ_n in $r=0$ and r_{max}, one can exclude the first and the last B-splines from expansion given by Eq. (3.8) for each ℓ or reduce the multiplicity at the edges of the box (see Fig. (2.1) of Chapter 2). A standard matrix diagonalization procedure provides the eigenfunctions and eigenvalues from Eq. (3.10). The main difference from the atomic case is that terms with different ℓ-values are coupled due to the lack of spherical symmetry. Coupling terms in Eq. (3.11) involve the usual integrals over three spherical harmonics and radial integrals

$$\sum_{\ell''}^{\infty}\sum_{m''=-\ell''}^{\ell''} Y_{\ell''}^{m''}(\theta_1,\phi_1)\frac{4\pi}{2\ell''+1}\int_0^{\pi}\int_0^{2\pi} Y_\ell^m(\theta,\phi)Y_{\ell'}^m(\theta,\phi)\overline{Y}_{\ell''}^{m''}(\theta,\phi)\sin\theta\,\mathrm{d}\theta\,\mathrm{d}\phi$$

$$\times \int_0^{r_{max}} B_i(r)\frac{r_<^{\ell''}}{r_>^{\ell''+1}}B_j(r)\mathrm{d}r, \tag{3.13}$$

[2] Notice that throughout this work the complex value of a function f will be designated by the symbol $\overline{f}$ instead of the most common one f^*.

[3] In numerical analysis, a quadrature rule is an approximation of the definite integral of a function, usually stated as a weighted sum of function values. An n-point Gauss Legendre quadrature rule, is a quadrature rule constructed to yield an exact result for polynomials of degree $2n-1$ by a suitable choice of the n points x_i and n weights w_i, which approximate integrals as

$$\int_{-1}^{1} g(x)dx \simeq \sum_{i=1}^{n} g(x_i)w_i.$$

The previous equation can be generalized to treat definite integrals over an arbitrary interval by scaling the points and weights:

$$\int_{r_m}^{r_{m+1}} g(x)dx \simeq \sum_{i=1}^{n} g(x_i^m)w_i^m,$$

where

$$w_i^m = \frac{(r_{m+1}-r_m)}{2}w_i,$$

$$x_i^m = \frac{(r_{m+1}+r_m)x_i + (r_{m+1}-r_m)}{2}.$$

It can be shown that the evaluation points x_i are just the roots of a polynomial belonging to a class of orthogonal polynomials.

since the molecular potential given in Eq. (3.6) can be written as

$$V^{(\ell)} = \frac{1}{|r - R_i|} = \sum_{\ell=0}^{\infty} \frac{r_<^\ell}{r_>^{\ell+1}} \frac{4\pi}{2\ell+1} \sum_{m=-\ell}^{\ell} \overline{Y}_\ell^m(\theta_i, \phi_i) Y_\ell^m(\theta, \phi), \tag{3.14}$$

where

$$r_< = min(r, R_i), \tag{3.15}$$

and

$$r_> = max(r, R_i), \tag{3.16}$$

with R_i the distance from nucleus i to the origin. Note that θ_i and ϕ_i gives the orientation of the nucleus $i = A$ or B with respect to a reference system, and θ and ϕ the electron angles with respect to the molecular reference system. Since we are dealing with a linear molecule, the coordinates of the first nucleus A are $\theta_A = 0$ and $\phi_A = 0$, while for the second one B, $\theta_B = \pi$ and $\phi_B = 0$. So, the spherical harmonic $\overline{Y}_\ell^m(\theta_i, \phi_i)$ functions in Eq. (3.14) take the values

$$\overline{Y}_\ell^m(\theta_A = 0, \phi_A = 0) = \begin{cases} \sqrt{\frac{2\ell+1}{4\pi}} & \text{iif} \quad M = 0 \\ 0 & \text{iif} \quad M \neq 0 \end{cases} \tag{3.17}$$

and

$$\overline{Y}_\ell^m(\theta_B = \pi, \phi_B = 0) = \begin{cases} (-1)^L \sqrt{\frac{2\ell+1}{4\pi}} & \text{iif} \quad M = 0 \\ 0 & \text{iif} \quad M \neq 0 \end{cases} \tag{3.18}$$

The integration of the three spherical harmonic functions in Eq. (3.13) can be easily performed making use of Eq. (B.49)[4], obtaining a quite simple expression

$$\begin{aligned} &\sum_{\ell''}^{\infty} \sum_{m''=-\ell''}^{\ell''} \frac{1}{(2\ell''+1)^{3/2}} Y_{\ell''}^{m''}(\theta_1, \phi_1) C(\ell, \ell', \ell''; m, m, m'') C(\ell, \ell', \ell''; 0, 0, 0) \\ \times \quad &\sqrt{4\pi(2\ell+1)(2\ell'+1)} \int_0^{r_{max}} B_i(r) \frac{r_<^{\ell''}}{r_>^{\ell''+1}} B_j(r)\, dr, \end{aligned} \tag{3.19}$$

with $m'' = 2m$ and $\ell + \ell' + \ell''$ an even number. For a homonuclear molecule, $Z_A = Z_B = Z$, the electronic wave function must have a specific inversion symmetry, i.e., *gerade* or *ungerade*. Since the inversion symmetry of a spherical harmonic is given by $Y_\ell^m(-\hat{r}) = Y_\ell^m(\phi - \theta, \pi + \phi) = (-1)^\ell Y_\ell^m(\theta, \phi)$, only even values of the angular momentum are allowed for the *gerade* symmetry and odd values for the *ungerade* symmetry in Eq. (3.8). This implies that for this case, ℓ'' in Eq. (3.13) only can take even values. $V^{(\ell)}$ has a discontinuous derivative at R_i (*nuclear cusp*), and becomes highly peaked as ℓ and R_i increase. This is the origin of the slow convergence of the one-center expansion for off-center nuclei which are heavy or distant from the origin. Indeed, the exact wave function has a discontinuous first derivative at R_i which causes many high angular momenta to give a small contribution in a narrow region centered around R_i. As an example of the results obtained resolving Eq. (3.6) by means of a B-splines expansion, Fig. (3.1) displays the wave functions associated to the first six bound states of the H_2^+ molecule of symmetry $^2\Sigma_g^+$ at the equilibrium distance $R = 2$ a.u. in the positive z axis. As can be seen in panel (a) of this figure, which

[4]Reference to equations preceding by a letter corresponds to the Appendices, for example, Eq. (B.49) corresponds to Eq. 56 of the Appendix B.

corresponds to the ground state of the H_2^+ molecule, the cusp is "partially" reproduced in spite of the fact of the limited number of partial waves included in the calculation ($\ell_{max} = 20$, which implies 11 partial waves). In this panel it can also be seen the results obtained including different numbers of partial waves: ℓ_{max}=12 and ℓ_{max}=8. The values at the bottom of each panel gives the energy of each bound state, that can be compared with the ones obtained by L. Laaksonen [11] considered as exacts: $E_1 = -1.10263$ a.u.; $E_2 = -0.36086$ a.u.; $E_3 = -0.23577$ a.u.

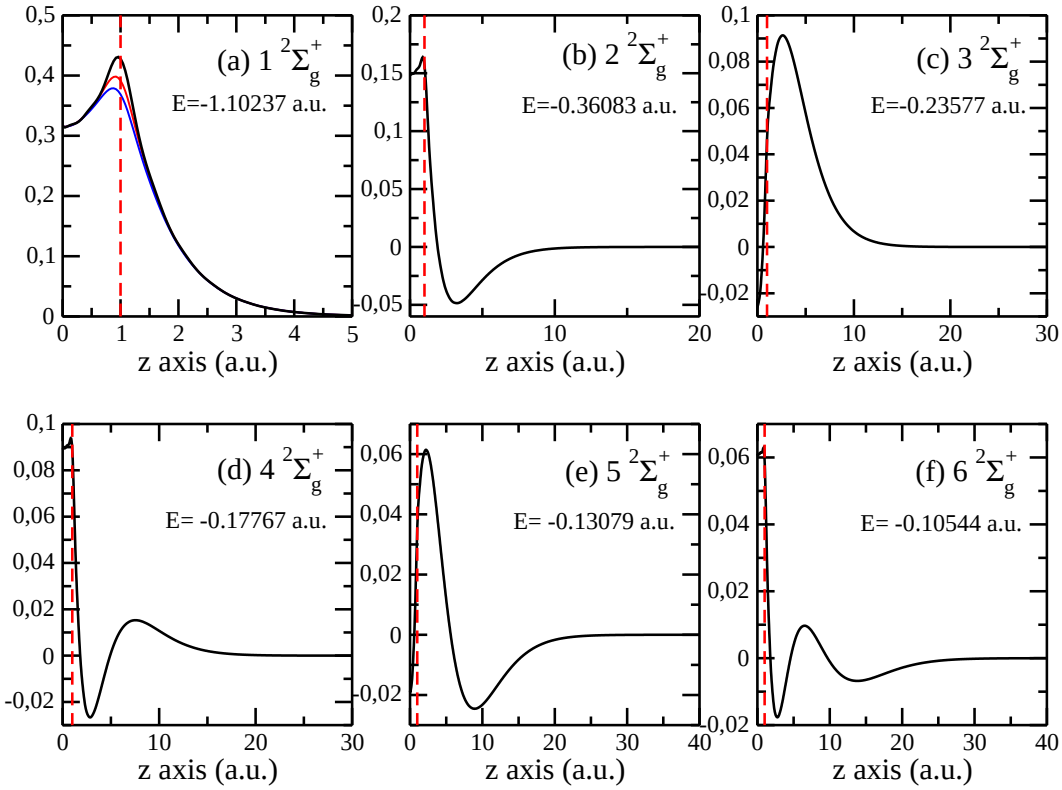

Figure 3.1: Wave functions associated to the first six electronic bound states of the H_2^+ molecule of symmetry $^2\Sigma_g^+$ at the equilibrium distance $R = 2$ a.u. in the positive z axis, obtained with a basis of angular momenta up to ℓ_{max}=20 and 160 B-splines functions of order 8 in a box of 60 a.u., per ℓ. Red dashed vertical line gives the position of the nucleus. In panel (a), red line result obtained with ℓ_{max}=12 and blue line result obtained with ℓ_{max}=8.

3.4 Bielectronic systems

Having stated the problem for the simplest case (monoelectronic systems) we will now present the methods required to solve the bielectronic cases. For molecules containing more than one electron the Hamiltonian reads[5]

$$\mathcal{H}_{el} = -\frac{1}{2}\sum_i \nabla_i^2 - \sum_i \frac{Z_A}{|r_i - R_A|} - \sum_i \frac{Z_B}{|r_i - R_B|} + \sum_{i>j} \frac{1}{|r_j - r_i|} + \frac{Z_A Z_B}{R}. \tag{3.20}$$

In order to obtain the eigenvalues and eigenfunction of the previous Hamiltonian, we can apply a *Configuration Interaction* (CI) procedure[6]. There are two ways to approach this problem. One is to

[5] By neglecting relativistic effects, the electron spin has to be introduced as an *ad hoc* quantum effect.

[6] There are three main methods for calculating electron correlation: ***Configuration interaction*** (CI), ***Many Body Perturbation Theory*** (MBPT) and ***Coupled Cluster*** (CC).

expand a set of single-particle states, for example hydrogenic states, with different ℓ-values in terms of B-splines and use the hydrogenic states to construct the CI matrix in a similar way to what it is done in any other basis. Another approach is to use the B-spline basis directly. The advantage of the first approach is that computer programs constructed for use with conventional basis sets can be used more or less directly when it is kept in mind that the pseudo-continuum functions in the B-spline approach keep oscillating to the boundary at r_{max}. We have applied the former approach, which consists in expanding the electronic wave function in a basis of configurations built from one-electron orbitals [12]:

$$\begin{aligned}\psi^{\Lambda} &= \sum_{n_1,n_2} C^{n_1,n_2}_{m_1,m_2}\Phi^{m_1,m_2}_{n1,n2} \\ &= \frac{1}{2}\left\{\varphi^{m_1}_{n_1}(r_1)\varphi^{m_2}_{n_2}(r_2) \pm \varphi^{m_2}_{n_2}(r_1)\varphi^{m_1}_{n_1}(r_2)\right\}\left\{\alpha(1)\beta(2) \mp \beta(1)\alpha(2)\right\}, \end{aligned} \tag{3.21}$$

where $\Lambda = m_1 + m_2$ is the absolute value of the z-component of the total electronic angular momentum (Σ, Π, ...). The one-electron orbitals are molecular orbitals resulting from Eq. (3.8) and are described in terms of B-splines basis sets as described in the previous section. Therefore Eq. (3.21) can be cast as

$$\begin{aligned}\psi^{\Lambda} &= \sum_{n_1,n_2}\sum_{\ell_1}^{\ell_{1,max}}\sum_{\ell_2}^{\ell_{2,max}}\sum_{m_1=-\ell_1}^{m_1=\ell_1}\sum_{m_2=-\ell_2}^{m_2=\ell_2}\frac{1}{2}C^{n_1,n_2}_{\ell_1,m_1,\ell_2,m_2} \\ &\times \left\{\frac{\mathcal{U}^{n_1}_{i\ell_1}(r_1)}{r_1}\frac{\mathcal{U}^{n_2}_{j\ell_2}(r_2)}{r_2}Y^{m_1}_{\ell_1}(\hat{r}_1)Y^{m_2}_{\ell_2}(\hat{r}_2) \pm \frac{\mathcal{U}^{n_1}_{i\ell_1}(r_2)}{r_2}\frac{\mathcal{U}^{n_2}_{j\ell_2}(r_1)}{r_1}Y^{m_1}_{\ell_1}(\hat{r}_2)Y^{m_2}_{\ell_2}(\hat{r}_1)\right\} \\ &\times \left\{\alpha(1)\beta(2) \mp \beta(1)\alpha(2)\right\}. \end{aligned} \tag{3.22}$$

Substitution of the wave function expansion in the Schrödinger equation leads to a matrix equation similar to Eq. (3.10). All matrix elements involve B-splines and can be reduced to products of one-electron integrals like those given in Eqs. (3.11) and (3.12), except for contributions arising from the electron-electron repulsion term $1/|r_j - r_i|$. In the OCE approach these are the same as in the atomic case (see [8] for more details). As an example, Fig. (3.2) displays the potential energy curve of the H_2 obtained by the CI procedure described previously and the result obtained by K. Wolniewicz *et al.* [13], considered as exact. The figure shows that as the internuclear distance increases the result gets worse, since the one-electron orbitals obtained by the OCE expansion are poorly described at this internuclear distances.

3.5 Electronic continuum states in the fixed-nuclei approximation

Let us turn now to the problem of computation of electronic continuum states. The lowest eigenvalues resulting from diagonalization of Eqs. (3.6) and (3.20) represent bound electronic states of the molecule. Those appearing above the ionization limit correspond to electronic continuum states. Similarly, the solution of the vibrational Schrödinger Eq. (3.4) leads to eigenvalues that lie above the dissociation limit, i.e., they correspond to vibrational continuum states. As the B-spline functions are defined in a finite interval, which is equivalent to enclosing the system in a box, the continuum spectra is replaced by a discrete one. Thus, the use of B-splines to describe continuum states is equivalent to what is called a *discretization technique*. As is well known, discrete states have a finite norm, thus they are usually normalized to unity

$$\langle\psi_i|\psi_j\rangle = \delta_{ij}, \tag{3.23}$$

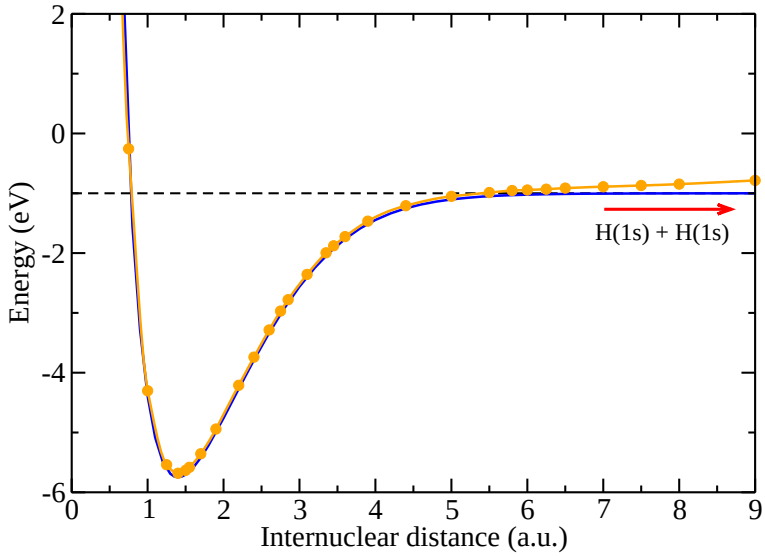

Figure 3.2: Potential energy curve of the ground state of H_2 (symmetry $^1\Sigma_g^+$) obtained by the CI method (orange line), including $\sim$ 800 configurations built with one-electron molecular orbitals, with angular momenta up to ℓ_{max}=26 and 200 *B*-splines functions, per ℓ, of order 8 defined in a box of 60 a.u.. Blue line, result obtained by K. Wolniewicz *et al.* [13].

whereas continuum states have an infinite norm and they are normalized to a delta function

$$\langle \psi_E | \psi_{E'} \rangle = \delta(E - E'). \tag{3.24}$$

Continuum states represent a free particle interacting with a given potential, i.e., they are equivalent to scattering states. The infinite norm is the result of the scattering boundary conditions, which reflect the fact that the free particle is associated with an incoming (or outgoing) flux. The typical textbook example is a plane wave. For a given total energy, different quantum numbers of the ejected or remaining particles imply different boundary conditions. In other words, they correspond to different scattering channels. Discretization methods apply differently to the single- and multichannel cases [14] and, consequently, they must be analyzed separately.

3.5.1 The single-channel case.

Formally, the solutions of the Schrödinger equation for positive energies appear as a family of functions depending on the continuous parameter E. In our approach however, the diagonalization procedure only provides a discrete set of electronic wave functions. Nevertheless, these functions can be interpreted as a representation of the true electronic continuum with a different normalization. So, we have to address a problem known as the normalization problem appearing in any discretization technique [15]. The computed discretized continuum states are normalized on the same level as the bound states, i.e., with respect to their index, because they originate from a diagonalization procedure. Any attempt to compute measurable quantities (such as cross section, ionization rate, ...) involving a continuum state as the final state has to reestablish the correct normalization, that is, to find the coefficient $\mathcal{A}_n$ such that

$$\psi_{E_n} = \mathcal{A}_n \psi_n, \tag{3.25}$$

where ψ_n is a discretized wave function and ψ_{E_n} the corresponding wave function normalized on the energy scale. There exist two methods commonly used with *B*-splines. The first one compares

the discretized state to the exact solution in the asymptotic region ($kr \gg 1$) where the analytical expression is often available. A standard fit will provide the normalization factor $\mathcal{A}_n$ as well as the non-coulombic phase σ_ℓ if the potential is non-coulombic at the origin. This method is actually used in applications involving highly interfering non-perturbative processes [16, 17, 18] to check the accuracy of the discretized wave functions since, apart from the amplitude, it provides the most stringent test on the phase of the wave function. Also, it is generally used in the least-squares algorithm when solutions at any energy are obtained [19]. Note that, as shown below, the square of the normalization factor is no other than the density of discretized continuum states: $\mathcal{A}_n^2 = \rho(E_n)$. The technique used in this Thesis, which is self-consistent with the discretization procedure, extracts the density of states from the set of eigenenergies without the need of external information. It can be shown [15] that switching from a normalization with respect to the index n to a normalization on the energy scale is achieved by means of the relation

$$\psi_{E_n} = \left| \frac{\partial E(n')}{\partial n'} \right|_{n'=n}^{-\frac{1}{2}} \psi_n, \tag{3.26}$$

provided that $E(n)$ is a monotonic function[7] of n, which is satisfied in view of the approximate expression given by Eq. (3.31). Through a Taylor expansion up to third order, one obtains the formal expression

$$\frac{\partial E(n')}{\partial n'} \Big|_{n'=n} = \frac{E_{n+1} - E_{n-1}}{2} + \frac{1}{6} \frac{\partial^3 E(n')}{\partial n'^3} \Big|_{n'=n}. \tag{3.27}$$

The absence of the second-order term together with the weak curvature of the function E_n leads to the rather accurate approximation [15]:

$$\rho(E_i) = \frac{2}{E_{n+1} - E_{n-1}}. \tag{3.28}$$

More accurate expressions for the density of states are obtained by polynomial interpolation of $E(n)$ (see [8, 9] for more details).

One of the great advantages of making use of B-spline functions is that the energy of discretized continuum states can be adjusted with a total degree of freedom simply by modifying the size of the box, r_{max}. continuum states. The value of r_{max} uniquely sets the energy of each discretized continuum state and, consequently, the density of states. This is better understood if one considers the asymptotic behavior of a Coulomb partial continuum wave function, which reads, when $kr \to \infty$,

$$\mathcal{U}_{E,\ell}(r) = \sqrt{\frac{2}{\pi k}} \sin\left(kr + \frac{Z}{k} \ln(2kr) - \frac{\ell\pi}{2} + \arg\Gamma(\ell + 1 - \frac{iZ}{k}) + \sigma_\ell \right), \tag{3.29}$$

where $k = \sqrt{2E}$, ℓ is the angular momentum, Z the nuclear charge, $\arg\Gamma(\ell+1-iZ/k)$ the Coulomb phase and σ_l the non-coulombic phase ($\sigma_\ell = 0$ for hydrogen). Since our method implies that all solutions of the Schrödinger equation vanish at $r = r_{max}$ ($U_{E,\ell}(r_{max}) = 0$), a discretized wave function at energy $E = k^2/2$ satisfies

$$kr_{max} + \frac{Z}{k} \ln(2kr_{max}) - \frac{\ell\pi}{2} + \arg\Gamma(\ell + 1 - \frac{iZ}{k}) + \sigma_\ell = n\pi, \tag{3.30}$$

where n is an integer. Eq. (3.30) defines a relation between the energy and a discrete parameter n, which can be used as a wave function index. In a first approximation (when kr_{max} is bigger than all the other terms) this relation leads to the energy of a particle in a box [20]:

$$E_n = \frac{n^2\pi^2}{2r_{max}^2}. \tag{3.31}$$

[7] A function which is either entirely non-increasing or non-decreasing. A function is monotonic if its first derivative (which need not be continuous) does not change sign.

This latter property makes it possible to compute continuum wave functions at any energy E simply by choosing the proper value of r_{max}. This is achieved either by solving Eq. (3.30) for r_{max} with $k = \sqrt{2E}$, or through an inverse iteration procedure [15], which varies the box size until $E_n = E$. The quality of the continuum discretization improves as the density of states increases (i.e., the energy spacing decreases). The density, defined as

$$\rho(E_i) = \frac{\partial n}{\partial E_n}, \tag{3.32}$$

can be evaluated from Eq. (3.30) as

$$\rho(E) = \frac{1}{\pi\sqrt{2}} \frac{r_{max}}{\sqrt{E}}. \tag{3.33}$$

Thus, the density of states can be adjusted to meet any requirement since it varies linearly with the box size r_{max}.

3.5.2 The multichannel case.

For simplicity, we shall start our discussion with one-electron systems. In contrast with one electron atomic systems, the electronic continuum of one-electron diatomic molecules is a multichannel continuum. Indeed, one can think of the electronic continuum as having an infinite number of channels, one for each value of ℓ of the free electron. For example, the boundary conditions for the continuum states of H_2^+ may be written[8] (see for example [21] and references there in)

$$\psi'_{\ell E}(r;R) \sim \frac{1}{r}\left[f_{\ell E}(r) Y_\ell^m(\theta,\phi) - \sum_{\ell'} \pi K(E;R)_{\ell\ell'} g_{\ell' E}(r) Y_{\ell'}^m(\theta,\phi) \right], \tag{3.34}$$

where $f_{\ell E}$ and $g_{\ell E}$ are regular and irregular Coulomb functions of energy E (see [24, 25]). The K-matrix is related to the usual scattering matrix S by

$$S(E;R) = \frac{I - i\pi K(E;R)}{I + i\pi K(E;R)}. \tag{3.35}$$

The continuum states resulting from diagonalization of the Hamiltonian do not have the above asymptotic behavior, because, as a result of the arbitrary finite normalization of the basis elements, inter-channel coupling is not described properly. They satisfy arbitrary boundary conditions of the form

$$\psi'_{\ell E} \sim \frac{1}{r}\left[a_{\ell\ell' n} f_{\ell' E_n}(r) Y_{\ell'}^m(\theta,\phi) + b_{\ell\ell' n} g_{\ell' E_n}(r) Y_{\ell'}^m(\theta,\phi) \right]. \tag{3.36}$$

Also, only one state is obtained at each energy eigenvalue, in contrast with the infinite set of open channels associated with a single value of E in Eq. (3.34). A possible solution is to employ the least-squares approach [26], which can be applied to the multichannel case giving the full set of N_c independent solutions at each prefixed energy E. The coefficients $a_{\ell\ell' n}$ and $b_{\ell\ell' n}$ define two matrices A and B that can be determined by fitting the obtained solutions to linear combinations of the asymptotic regular and irregular functions with $E = E_n$. Thus, the wave function with the correct boundary conditions of Eq. (3.34) can be related to linear combinations of those with the arbitrary ones through the linear transformation $\psi' = A^{-1}\psi$ (see for example [26] for more details). The resulting wave functions have the proper K-matrix normalization, with $\pi K = -BA^{-1}$. The S-matrix is then obtained from Eq. (3.35). A necessary condition for the method to work is that the basis

[8] The π factor in Eq. (3.34) and (3.35) can differ depending on the source, see for example [2, 21, 22, 23]

set must reproduce the asymptotic region. This condition can be easily satisfied with *B*-splines by choosing a box size large enough to contain a significant part of the asymptotic region; in contrast, it is practically impossible to satisfy with conventional L^2 basis sets (see e.g. [27]). This method has been applied successfully to study photoionization of H^- and He [26, 28, 29] and H_2^+ and HeH^+ [1, 2] and more generally, of polyatomic molecules (see for example [30, 30, 31]).

In this Thesis, the followed approach to the multichannel problem for bielectronic systems has been discussed in [22, 32]. In a first step, one neglects the coupling between the different channels. Thus the multichannel problem is transformed into a sum of single-channel problems that can be trivially discretized following a procedure similar to that described in the previous section. In a second step, the coupling between channels is introduced using a Lippmann-Schwinger formalism which explicitly includes the correct boundary conditions. More specifically, the uncoupled-continuum states, UCSs, are defined for each channel $\alpha\ell_\alpha$:

$$\zeta_{\alpha\ell_\alpha E} = \frac{\mathcal{U}_{\alpha\ell_\alpha E}(r)}{r} Y^m_{\ell_\alpha}(\theta,\phi), \tag{3.37}$$

where α designates the final ionic state, and ℓ_α the electron partial wave associated to α. The UCSs are eigenfunctions of the zero-order uncoupled Hamiltonian:

$$\left(\sum_\alpha \sum_{\ell'_\alpha} P_{\alpha\ell'_\alpha} \mathcal{H}_{e\ell} P_{\alpha\ell'_\alpha} - E\right) \zeta_{\alpha\ell_\alpha E} = 0. \tag{3.38}$$

$P_{\alpha\ell_\alpha}$ is a projection operator defined by $P_{\alpha\ell_\alpha}\zeta_{\alpha\ell_\alpha E} = \zeta_{\alpha\ell_\alpha E}$ and $P_{\alpha\ell_\alpha}P_{\alpha'\ell'_{\alpha'}} = \delta_{\ell_\alpha\ell'_{\alpha'}}\delta_{\alpha\alpha'}P_{\alpha'\ell'_{\alpha'}}$. The radial continuum functions $\mathcal{U}_{\alpha\ell_\alpha E}$ are represented in a basis of *B*-splines. This leads to a discrete spectrum $E_{n\ell}$ and to discretized UCS wave functions $\zeta_{\alpha\ell_\alpha n_{\ell_\alpha}}$. Since the latter are unity-normalized and are associated with a single channel, they are related to those given by Eq. (3.37) through an equation similar to Eq. (3.25):

$$\zeta_{\alpha\ell_\alpha E_n} = \rho^{1/2}_{\alpha\ell_\alpha}(E_{n_{\ell_\alpha}})\zeta_{\alpha\ell_\alpha n_{\ell_\alpha}}. \tag{3.39}$$

In a second step, the coupling between channels is introduced using a Lippmann-Schwinger formalism [33]:

$$\begin{aligned}\psi_{\alpha\ell_\alpha E_n} &= \rho^{1/2}_{\alpha\ell_\alpha}(E_{n_{\ell_\alpha}}) \\ &\times \left(\zeta_{\alpha\ell_\alpha n_{\ell_\alpha}} + \sum_{\alpha\ell''_\alpha n''_{\ell''_\alpha}} \langle\zeta_{\alpha\ell'_\alpha n'_{\ell'_\alpha}}|G^+(E_{n_{\ell_\alpha}})|\zeta_{\alpha\ell''_\alpha n''_{\ell''_\alpha}}\rangle\langle\zeta_{\alpha\ell''_\alpha n''_{\ell''_\alpha}}|V|\zeta_{\alpha\ell_\alpha n_{\ell_\alpha}}\rangle\zeta_{\alpha\ell'_\alpha n'_{\ell'_\alpha}}\right),\end{aligned} \tag{3.40}$$

where

$$G^+(E) = \lim_{\varepsilon\to 0} \frac{1}{E - \mathcal{H}_{el} + i\varepsilon}, \tag{3.41}$$

and

$$V = \sum_{\alpha\alpha'} \sum_{\substack{\ell_\alpha\ell'_{\alpha'} \\ \ell_\alpha \neq \ell'_{\alpha'}}} P_{\alpha\ell_\alpha}\mathcal{H}_{el}P_{\alpha'\ell'_{\alpha'}}, \tag{3.42}$$

and $\rho_{\alpha\ell_\alpha}$ is the density of states associated with the UCS in channel $\alpha\ell_\alpha$. The G^+-matrix elements can be easily obtained following the procedures described in [22, 32], which we briefly summarize

here. One starts by defining the Green operator associated with the uncoupled Hamiltonian of Eq. (3.37):

$$G_0^+(E) = \lim_{\varepsilon\to 0} \frac{1}{(E - \sum_\alpha \sum_{\ell'_\alpha} P_{\alpha\ell'_\alpha} \mathcal{H}_{el} P_{\alpha\ell'_\alpha}) + i\varepsilon}. \tag{3.43}$$

Projecting G_0^+ onto the UCS basis, the latter operator takes the form

$$\begin{aligned} G_0^+(E = E_{n_{\ell_\alpha}}) &= \sum_\alpha \sum_{\ell'_\alpha} \sum_{\substack{n'_{\ell'_\alpha} \\ n_{\ell_\alpha} \neq n'_{\ell'_\alpha}}} \frac{|\zeta_{\alpha\ell'_\alpha n'_{\ell'_\alpha}}\rangle\langle\zeta_{\alpha\ell'_\alpha n'_{\ell'_\alpha}}|}{E_{n_{\ell_\alpha}} - E_{n'_{\ell'_\alpha}}} \\ &+ i\pi \sum_\alpha \sum_{\ell_\alpha} \rho_{\ell_\alpha}(E_{n_{\ell_\alpha}}) |\zeta_{\alpha\ell_\alpha n_{\ell_\alpha}}\rangle\langle\zeta_{\alpha\ell_\alpha n_{\ell_\alpha}}|. \end{aligned} \tag{3.44}$$

The Green functions $G^+(E)$ and $G_0^+(E)$ can be related using standard scattering theory (see for example [23])

$$G^+(E) = G_0^+(E) + G_0^+(E) V G^+(E). \tag{3.45}$$

Then, using Eq. (3.44) and the closure relation written in terms of the UCS, the above formal relation leads to

$$\sum_{\ell''_\alpha n''_{\ell''_{\alpha'}}} C_{\alpha\ell'_\alpha n'_{\ell'_\alpha}\, \ell''_\alpha n''_{\ell''_{\alpha'}}} \langle\zeta_{\alpha\ell''_\alpha n''_{\ell''_\alpha}}|G^+(E)|\zeta_{\alpha\ell_\alpha n_{\ell_\alpha}}\rangle = D_{\alpha\ell'_\alpha n'_{\ell'_\alpha}}, \tag{3.46}$$

where

$$C_{\alpha\ell'_\alpha n'_{\ell'_\alpha}\, \ell''_\alpha n''_{\ell''_\alpha}} = \delta_{\alpha'\alpha}\delta_{\ell'_\alpha\ell''_\alpha}\delta_{n''_{\ell''_\alpha} n'_{\ell'_\alpha}} - \Xi_{\alpha\ell'_\alpha}(E_{n'_{\ell'_\alpha}})\langle\zeta_{\alpha\ell'_\alpha n'_{\ell'_\alpha}}|V|\zeta_{\alpha\ell''_\alpha n''_{\ell''_\alpha}}\rangle, \tag{3.47}$$

$$D_{\alpha\ell'_\alpha n'_{\ell'_\alpha}} = \delta_{\alpha'\alpha}\delta_{\ell_\alpha\ell'_\alpha}\delta_{n'_{\ell'_\alpha} n_{\ell_\alpha}} \Xi_{\alpha\ell'_\alpha}(E_{n'_{\ell'_\alpha}}) \tag{3.48}$$

and

$$\Xi_{\alpha\ell'_\alpha}(E_{n'_{\ell'_\alpha}}) = \begin{cases} i\pi\rho(E_{n'_{\ell'_\alpha}})\delta_{n'_{\ell'_\alpha} n_{\ell_\alpha}} & \text{for} \quad E = E_{n'_{\ell'_\alpha}} \\ 1/(E - E_{n'_{\ell'_\alpha}}) & \text{for} \quad E \neq E_{n'_{\ell'_\alpha}}. \end{cases} \tag{3.49}$$

Therefore, the $G^+(E)$-matrix elements appearing in Eq. (3.40) are the solutions of the system of linear equations given in Eq. (3.47), which can be solved using standard numerical procedures. The coefficient matrix C multiplying the unknowns is the same for all $\alpha\ell_\alpha$, so that each system of equations differs only in the right-hand side column vector D. Therefore, only one matrix inversion is required to solve Eq. (3.47). The need for the closure relation to write Eqs. (3.44) and (3.47) in terms of the UCS basis means that a complete basis is required. This is what makes B-splines superior to other L^2 basis sets because convergence can be easily checked within the box.

3.6 Feshbach approach in the fixed-nuclei approximation

As we have pointed out before, the continuum of many-electron molecules contains resonant states. These states may arise when two or more electrons are excited simultaneously or when an inner-shell vacancy is created (Feshbach resonances). The corresponding energies lie above the ionization threshold and, consequently, belong to the continuum spectrum. The usual picture is that of a

bound state embedded in and coupled to a non-resonant continuum [34, 35]. As a result of the coupling, the bound state has a finite lifetime, i.e., the molecule may eject an electron into the continuum. For this reason, these states are also called autoionizing states. Their properties are fully determined by electron correlation, which plays a more important role here than for bound states. A resonant state can be characterized by its energy position (i.e., the potential energy curve) and its autoionization width. Most theoretical works have concentrated on the evaluation of resonant parameters for simple diatomic molecules, however, this information does not provide a complete description of the resonant molecular continuum (see next section).

In the Feshbach formalism the resonant and non resonant contributions to the wave functions are handled separately and, therefore, one can use specific methods to calculate each part. Furthermore, the Feshbach theory provides the appropriate framework in which resonance parameters (energy position, autoionization width, Fano profiles, etc) can be accurately defined. Evaluation of these resonance parameters in two-electron and three-electron systems was one of the first successful applications of *B*-splines. The theory is based on the definition of two complementary orthogonal subspaces P and Q which contain, respectively, the non resonant and resonant continuum states.

Since the theoretical method has been described in detail in [33, 36], only a brief summary will be given here. Let us call $\Psi^+_{\mu,E}$ the continuum state of energy E in channel μ with outgoing boundary conditions. The channel index μ is defined as $\mu = \alpha, \ell_\alpha, \Lambda, \pi, \sigma, S, M_S$, where α represents the set of quantum numbers describing the H_2^+ target state, ℓ_α is the angular momentum of the continuum electron, Λ is the absolute value of the z-component of the total electronic angular momentum (Σ, Π, ...), π is inversion symmetry (g or u), σ is the reflexion symmetry with respect to the xy plane ($+$ or $-$), S is the total electronic spin and M_S is its z-component.

In Feshbach theory [35, 37], the resonance energy position E_s (including the shift Δ_s) and autoionization width Γ_s are given by [38]

$$E_s = \mathcal{E}_s + \Delta_s = \mathcal{E}_s + \mathrm{Re}\,\langle \phi_s | Q\mathcal{H}PG_P^{(s)+}(E=\mathcal{E}_s)P\mathcal{H}Q|\phi_s\rangle, \tag{3.50}$$

$$\Gamma_s = 2\pi \sum_\mu |\langle P\psi^{0+}_{\mu E=\mathcal{E}_s} | P\mathcal{H}Q|\phi_s\rangle|^2, \tag{3.51}$$

where the sum in Eq. (3.51) runs over all open channels, P is a projection operator satisfying

$$\lim_{r_i\to\infty} P\Psi^+_{\mu E} = \Psi^+_{\mu E}, \tag{3.52}$$

for all open channels μ, with

$$Q = 1 - P, \tag{3.53}$$

$$PQ = 0, \tag{3.54}$$

and where ϕ_s is the resonant wave function solution of a Schrödinger equation in the Q subspace with eigenvalue $\mathcal{E}_s$:

$$(Q\mathcal{H}Q - \mathcal{E}_n)\phi_n = 0. \tag{3.55}$$

$P\psi^{0+}_{\mu E}$ is a non-resonant wave function solution of a Schrödinger equation in P subspace:

$$\left[P\mathcal{H}P + P\mathcal{H}QG_Q^{(s)}(E)Q\mathcal{H}P - E\right] P\psi^{0+}_{\mu E} \equiv (\mathcal{H}' - E)P\psi^{0+}_{\mu E} = 0. \tag{3.56}$$

$G_Q^{(s)}(E)$ is the Green operator in Q subspace in which the s state has been excluded:

$$G_Q^{(s)}(E) = \int\!\!\!\!\!\!\sum_{n\neq s} \frac{|\phi_n\rangle\langle\phi_n|}{E - \mathcal{E}_n} \tag{3.57}$$

and $G_P^{(s)+}(E)$ is the Green operator in P subspace:

$$G_P^{(s)+}(E) = \lim_{\eta\to 0} \frac{1}{E - \mathcal{H}' + i\eta} \equiv G_P^{(s)}(E) + i\pi\delta(E - \mathcal{H}'). \tag{3.58}$$

Thus, in order to obtain the resonance parameters of Eqs. (3.50) and (3.51) one needs to evaluate two kinds of wave functions, ϕ_n and $P\psi_{\mu E}^{0-}$, and their corresponding Green operators, $G_Q^{(s)}(E)$ and $G_P^{(s)+}(E)$ (see Section 3.5.2).

3.7 The vibrational Schrödinger equation

In the BO approximation, the vibrational wave functions are the solutions of the Schrödinger equation (see Eqs. (3.4) and (3.5)):

$$\left\{ -\frac{1}{2\mu}\frac{d^2}{dR^2} + \frac{J(J+1)}{2\mu R^2} + E_n(R) \right\} \chi_\nu(R) = W_{n\nu}\chi_\nu(R). \tag{3.59}$$

where μ is the reduced mass of the molecule, J the rotational quantum number, R the internuclear distance, $E_n(R)$ the electronic potential energy curve and $W_{n\nu}$ the nth eigenvalue solution of Eq. (3.59). This equation can be solved by expanding χ_ν in a basis of B-splines defined in the interval $[0, R_{max}]$:

$$\chi_\nu(R) = \sum_j d_{\nu j} \frac{B_j(R)}{R}. \tag{3.60}$$

Substitution of this expansion into Eq. (3.59) leads to a matrix equation similar to Eq. (3.10), that can be solved with standard diagonalization techniques. As in numerical integration, the accuracy of the results is limited by the number of points used to define the potential $E_n(R)$. In order to obtain accurate results of the vibrational states associated to the different electronic states of the H_2^+ molecule, the potential energy curves of different electronic states are obtained by the code OEDM written by J. D. Power [39], for an internuclear distance in the range from 0 to 100 a.u. For the case of the H_2 molecule, the potential energy curves calculated by K. Wolniewicz *et al.* [13] are used.

The lowest eigenvalues resulting from diagonalization of Eq. (3.59) represent bound vibrational states of the molecule. As an illustration, in Fig. (3.3) we show the first eight bound vibrational wave functions ($J = 1$) of H_2^+ associated to its electronic ground state. In Table (3.1) we compare the energies of these bound vibrational states with the results obtained by H. Wind [40]. The origin of the small differences could come from the different reduced mass used, in [40] they selected a value of 918.045 a.u., from the used energy potential curve or due to the dissociation limit selected, in our case -0.5 a.u. meanwhile in [40] a value equal to -0.49972 a.u. was used. Similar agreement is obtained for the D_2^+ molecule (see for example table III of [41]). Those vibrational states appearing above the dissociation limit correspond to vibrational continuum states that must be renormalized using the appropriate density of states (see references [9, 27] for more details). The discretization method leading to the vibrational continuum is similar to that described in section 3.5.1 for the single-channel electronic continuum. However, notice that, due to the different mass of the nuclei in comparison with that of the electrons (three orders of magnitude), the frequency of the oscillations in the wave function is much larger for the nuclei than for electrons with the same kinetic energy. This means that the asymptotic region is reached much earlier for the nuclear continuum, which explains why, in general, one needs a smaller box than that used to describe the electronic continuum (see Fig. (3.4)).

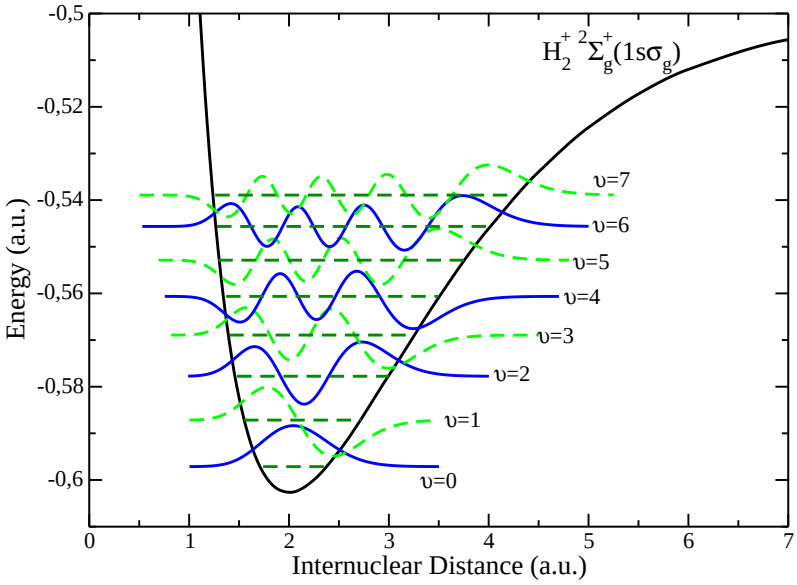

Figure 3.3: Bound vibrational states associated to the electronic potential energy curve of the $^2\Sigma_g^+(1s\sigma_g)$ state of H_2^+. The basis set is the same as the one described in Table (3.1).

Eq. (3.59) can be rewritten as

$$\left\{\frac{\mathrm{d}^2}{\mathrm{d}R^2}+k^2-\frac{J(J+1)}{R^2}-U(R)\right\}\chi_{J,\nu}(k,R)=0, \tag{3.61}$$

where $U(R)=2\mu E_n(R)$ and $k^2=2\mu W_{n\nu}$, which represents the scattering of a spinless particle of mass μ by a real central potential $E_n(R)$[9]. Particular solutions of this equation[10] which are often used in scattering theory are the spherical Bessel function j_ℓ, the spherical Neuman function n_ℓ and the spherical Hankel functions $h_\ell^{(1)}$ and $h_\ell^{(2)}$. The definitions and some important properties of these functions can be found in [23, 24, 42]. The general solution of Eq. (3.61) is then a linear combination of two linearly independent particular solutions:

$$\chi_{J,\nu}(k,R)=kR\left[C_J^{(1)}(k)\,j_J(kR)+C_J^{(2)}(k)n_J(kR)\right] \tag{3.62}$$

or

$$\chi_{J,\nu}(k,R)=kR\left[D_J^{(1)}(k)h_J^{(1)}(kR)+D_J^{(2)}(k)h_J^{(2)}(kR)\right]. \tag{3.63}$$

The examination of the behavior of the spherical Bessel function $j_\ell(\rho)$ as $\rho\to 0$ shows that this function is *regular* at the origin, where it is proportional to ρ^ℓ (see [23, 24, 42]). The other functions n_ℓ, $h_\ell^{(1)}$ and $h_\ell^{(2)}$ have a pole of order $(\ell+1)$ at $\rho=0$ and are called *irregular* solutions. Making use of the asymptotic behavior of the solutions of the Bessel equation,

$$j_\ell(x)\xrightarrow[x\to\infty]{}\frac{1}{x}\sin(x-\frac{1}{2}\ell\pi) \tag{3.64}$$

[9] This equation is known as the "spherical Bessel differential equation", making the replacements: $\rho=kR$ and $f_J(\rho)=\chi_{J,\nu}(k,R)/\rho$.

[10] Note that, for $U(R)=0$, the radial equation for a free particle is obtained.

Table 3.1: Energy levels of the bound vibrational states of H_2^+ associated to the electronic state $^2\Sigma_g^+$ (reduced mass of 918.075 a.u.) with a rotational number $J = 1$, calculated with 300 B-splines set of order 8 defined on a linear knot sequence in box of size 15.0 a.u., and the results obtained by H. Wind [40].

υ	Energy (a.u.)[a]	Energy (a.u.)
0	-0.59687398	-0.59712997
1	-0.58690345	-0.58715648
2	-0.57751216	-0.57776240
3	-0.56868092	-0.56892822
4	-0.56039359	-0.56063824
5	-0.55263686	-0.55288141
6	-0.54540041	-0.54564383
7	-0.53867676	-0.53892001
8	-0.53246140	-0.53270465
9	-0.52675294	-0.52699700
10	-0.52155322	-0.52179814
11	-0.51686762	-0.51711414
12	-0.51270538	-0.51295381
13	-0.50908006	-0.50932976
14	-0.50601008	-0.50626007
15	-0.50351932	-0.50377468
16	-0.50163753	-0.50377468
17	-0.50039855	-0.50066287
18	-0.49982099	-0.50007083
19	-0.499729435	-0.49971636

[a]Results obtained by H. Wind [40].

and

$$n_\ell(x) \underset{x\Rightarrow\infty}{\longrightarrow} -\frac{1}{x}\cos(x-\frac{1}{2}\ell\pi), \tag{3.65}$$

the boundary conditions of Eq. (3.62) can be expressed as

$$\chi_{J,\upsilon}(k,R) \underset{x\Rightarrow\infty}{\longrightarrow} A_J(k)\sin(x-\frac{1}{2}J\pi+\delta_J(k)), \tag{3.66}$$

with

$$A_J(k) = \left\{ \left[C_J^{(1)}(k)\right]^2 + \left[C_J^{(2)}(k)\right]^2 \right\} \tag{3.67}$$

and

$$\tan\delta_J(k) = -C_J^{(2)}(k)/C_J^{(1)}(k). \tag{3.68}$$

Fig. (3.4) displays two continuum vibrational functions for the H_2^+ and D_2^+ molecules for the same energy, obtained by means of an expansion in a B-spline basis set, for the potential energy curve of the ground state of the corresponding molecular ions. The result associated to the D_2^+ molecule oscillates faster that for the H_2^+ case, due to the mass difference. As we have pointed out in previous sections, in the case of the study of the discretization method, the asymptotic behavior of the discretized vibrational wave functions implies that

$$\chi_{J,\upsilon}(k,R=R_{max}) = 0 \tag{3.69}$$

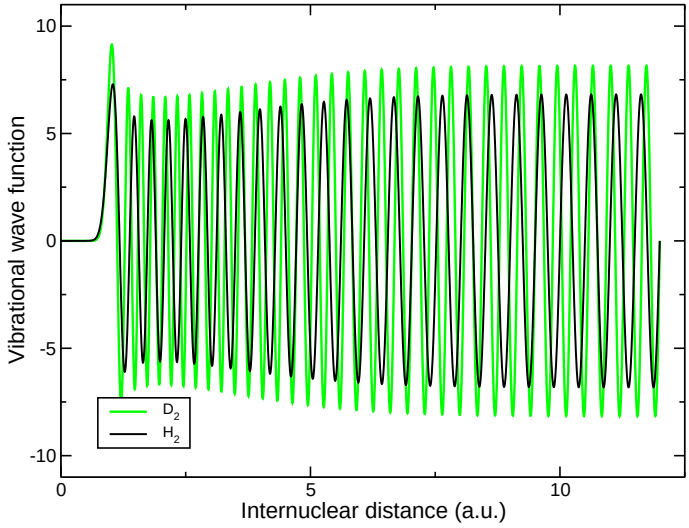

Figure 3.4: Continuum vibrational wave function of H_2^+ (black line) and D_2^+ (green line) associated to the electronic state $^2\Sigma_g^+(1s\sigma_g)$, for an energy of -0.41 a.u. The basis set is the same as the one described in Table (3.1).

since in our expansion given by Eq. (3.60) the last *B*-spline is removed, while the true continuum vibrational states given by Eq. (3.62) are always oscillating functions. The procedure described in section 3.5.1 can be applied, providing the normalization factor, and the comparison of the discretized state to the exact solution in the asymptotic region gives the vibrational phase shift $\delta_J(k)$.

3.8 Beyond the fixed-nuclei approximation: Non resonant continuum states

The simplest description of a continuum state beyond the fixed-nuclei approximation is that of an unbound electron scattered by a positive molecular ion in a given vibrational state and containing all the remaining electrons. In this section we shall neglect the existence of Feshbach resonances, which will be considered in the following section. According to the BO approximation, the wave function can be written as a product of electronic and nuclear wave functions,

$$\Psi^+_{\alpha\upsilon_\alpha\ell_\alpha E} \simeq \psi^{0+}_{\alpha\ell_\alpha\varepsilon_\alpha}(r,R)\chi_{\upsilon_\alpha}(R), \tag{3.70}$$

where $\psi^{0+}_{\alpha\ell_\alpha\varepsilon_\alpha}(r,R)$ is the non resonant electron-scattering wave function as a function of R. The index α includes all electronic quantum numbers of the molecular ion and υ_α stands for either bound or continuum vibrational states of the ion in the α state. The superscript + indicates the usual outgoing boundary conditions in electron-molecule scattering[11], and ℓ_α is the angular momentum of the ejected electron. The ionic nuclear wave function χ_{υ_α} is the solution of the Eq. (3.61) and the energy conservation implies

$$E = \varepsilon_\alpha + W_{\upsilon_\alpha}, \tag{3.71}$$

where ε_α is the electron energy in the continuum associated with the electronic state α of the residual ion and W_{υ_α} is total energy of the vibrational state $\chi_{\upsilon_\alpha}(R)$ solution of Eq. (3.61). So, the total energy

[11] Since calculated quantities involve the square of the appropriate matrix elements, the choice of incoming or outgoing waves is a matter of convenience.

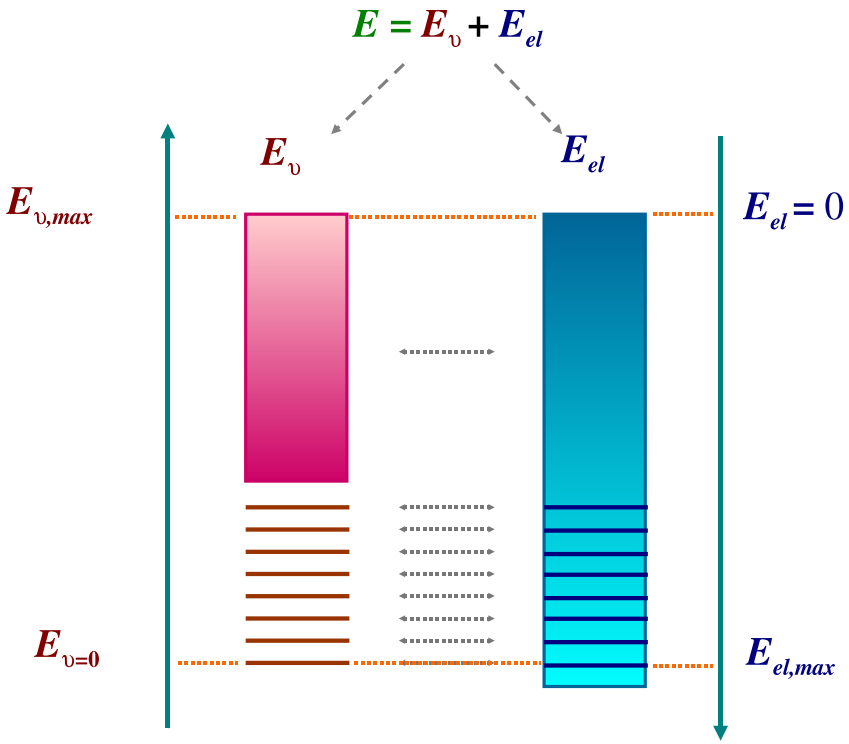

Figure 3.5: Energy sharing in the dissociative photoionization process. The left column represents the final proton energy (from bottom to top) while the right one the final electron energy (from top to bottom). The initial photon energy, E, can be shared in a number (infinity) of different ways.

deposited in the molecule can be shared between the ionized electron and the residual ion (that can remain in a bound or continuum vibrational state), and therefore it can be shared in several different ways, in fact infinite ways. Fig. (3.5) displays this fact, showing the final energy of the residual ion in the red left column and the electron energy in the blue right column. Since the total energy of the system must be conserved, the higher the final electron energy the lower the energy of the residual ion and viceverse. If the ion remains in a bound vibrational state (discontinuous lines in the left column in Fig. (3.5)), the electron energy can only take defined final energies (non-dissociative ionization), but when the energy of the ion remains above the dissociation limit, this can be shared in an infinite number of ways (dissociative ionization).

Eq. (3.70) is often called, in the context of electron-molecule scattering theory, the *adiabatic nucleus approximation* [43]. Evaluation of $\psi^{0+}_{\alpha\ell_\alpha\varepsilon_\alpha}$ can be done with B-spline basis sets following the procedures described in the previous section, for a chosen set of R values. For instance, in the case of the H_2 molecule, for each channel $\alpha\ell_\alpha$, one has to define a set of orthogonal UCSs for each R of the form [36]

$$\zeta_{\alpha\ell_\alpha\varepsilon_\alpha}(r_1,r_2) = \Theta(\Phi_{\alpha\ell_\alpha}(r_1,\theta_2,\phi_2)\rho_{\alpha\ell_\alpha\varepsilon_\alpha}(r_2)), \tag{3.72}$$

where Θ is the symmetrization (antisymmetrization) operator for singlet (triplet) spin multiplicities, $\rho_{\alpha\ell_\alpha\varepsilon_\alpha}$ is the radial wave function of the continuum electron and $\Phi_{\alpha\ell_\alpha}$ is the channel function, which is a state of H_2^+ combined with the angular function of the scattered electron to give the correct channel symmetry (the index α includes all electronic quantum numbers of the molecular ion). This is equivalent to the well known static exchange approximation in electron-atom scattering [44]. The functions $\Phi_{\alpha\ell_\alpha}$ can be described in terms of B-spline functions as in the one-electron case. This procedure leads to discrete spectra $\{\varepsilon_{\alpha\ell_\alpha n_\alpha}\}$ and to discretized UCS wave functions $\zeta_{\alpha\ell_\alpha n_\alpha}$ that must

be used to write the final continuum wave function with the proper asymptotic behavior.

3.9 Beyond the fixed-nuclei approximation: Resonant continuum states

Determination of the resonance positions and autoionization widths is extremely important to understand the behavior of the molecule in many different situations. However, this information does not provide a complete description of the resonant molecular continuum. Indeed, autoionization can lead to the formation of atomic or molecular ions, but it may also lead to dissociation of the molecule in neutral fragments. This is due to the repulsive character of the potential energy curves associated with autoionizing states. These processes may occur simultaneously (see Fig. (1.2) of Chapter 1), leading to complicated interference phenomena such as those recently observed in H_2 and D_2 photoionization experiments [45, 46, 47, 48]. The "standard" Feshbach formalism, defined in the fixed-nuclei approximation, must be modified in order to consider consistently the nuclear motion. The main problem come from the fact, that in the presence of a doubly excited state, the electronic and the nuclear motions cannot be studied separately (as it has been explained in the preceding section). The ionization process happens in the same time scale as the nuclear motion, and both process are completely entangled. It is then clear that, in order to describe all possible ionization and dissociation pathways, the wave function cannot be written as a simple product of an electronic function and a nuclear function. Therefore, the formalism presented in the section 3.6 is only useful for obtaining the parameters that characterized the doubly excited states, the energy position, E_s, given by Eq. (3.50), and its width, Γ_s, given by Eq. (3.51), and for interpretation qualitatively the processes where these states play a relevant role.

The appropriate theoretical framework has been developed by I. Sánchez *et al.* [49, 50, 51], inspired by the ideas of Bardsley [52] and Hazi *et al.* [53]. We summarize here the basic results. In the following, integration over R will be written explicitly, and integration over $\boldsymbol{r}$ will be indicated with the usual bra-ket notation. We assume that there exists a set of orthogonal resonant states ϕ_r embedded in the electronic continuum of the molecule and define two orthogonal projection operators

$$Q = \sum_{r'} |\phi_{r'}(r,R)\rangle\langle\phi_{r'}(r,R)|, \tag{3.73}$$

and

$$P = 1 - Q. \tag{3.74}$$

Notice that these definitions of the projectors P and Q are similar to those given in section 3.6. The resonance energies are given by

$$E_r(R)\delta_{rr'} = \langle\phi_r|\mathcal{H}_{el}|\phi_{r'}\rangle. \tag{3.75}$$

Then the complete final-state wave function can be written

$$\Psi^+_{\alpha\upsilon_\alpha\ell_\alpha E}(r,R) = P\Psi^+_{\alpha\upsilon_\alpha\ell_\alpha E}(r,R) + Q\Psi^+_{\alpha\upsilon_\alpha\ell_\alpha E}(r,R) \tag{3.76}$$

Now, using the definition of Q given by Eq. (3.73), we can write

$$Q\Psi^+_{\alpha\upsilon_\alpha\ell_\alpha E}(r,R) = \sum_{r'} \phi_{r'}(r,R)\xi^{r'}_{\alpha\upsilon_\alpha\ell_\alpha E}(R) \tag{3.77}$$

where the function $\xi^r_{\alpha\upsilon_\alpha\ell_\alpha E}(R)$ describes the relative motion of the nuclei when the system is in the $\phi_r(r,R)$ resonant state. Substituting Eq. (3.76) in the Schrödinger equation

$$[\mathcal{H}(r,R) - E]\,\Psi^+_{\alpha\upsilon_\alpha\ell_\alpha E}(r,R) = 0, \tag{3.78}$$

and projecting into P and Q subspaces, one obtains the system of coupled equations

$$[E - P\mathcal{H}P]\,P\Psi^{+}_{\alpha\upsilon_\alpha\ell_\alpha E}(r,R) = P\mathcal{H}P\Psi^{+}_{\alpha\upsilon_\alpha\ell_\alpha E}(r,R), \tag{3.79}$$

$$[E - Q\mathcal{H}Q]\,Q\Psi^{+}_{\alpha\upsilon_\alpha\ell_\alpha E}(r,R) = Q\mathcal{H}P\Psi^{+}_{\alpha\upsilon_\alpha\ell_\alpha E}(r,R). \tag{3.80}$$

A formal solution of Eq. (3.79) can be written using the Lippman-Schwinger equation

$$P\Psi^{+}_{\alpha\upsilon_\alpha\ell_\alpha E}(r,R) = P\Psi^{0+}_{\alpha\upsilon_\alpha\ell_\alpha E}(r,R) + G^{+}_{P}(E)P\mathcal{H}Q\Psi^{+}_{\alpha\upsilon_\alpha\ell_\alpha E}(r,R), \tag{3.81}$$

where $G^{+}_{P}(E)$ is the Green's operator

$$G^{+}_{P}(E)\lim_{\eta\to 0}\frac{1}{E - P\mathcal{H}P + i\eta}, \tag{3.82}$$

and $P\Psi^{0+}$ is the nonresonant scattering wave function that satisfies the equation

$$[P\mathcal{H}P - E]P\Psi^{0+}_{\alpha\upsilon_\alpha\ell_\alpha E}(r,R) = 0. \tag{3.83}$$

$P\Psi^{0+}$ can also be written as a product of electronic and nuclear wave functions, since we consider the validity of the Born-Oppenheimer approximation,

$$P\Psi^{0+}_{\alpha\upsilon_\alpha\ell_\alpha E}(r,R) = \psi^{0+}_{\alpha\upsilon_\alpha\ell_\alpha E}(r,R)\chi_\upsilon(R), \tag{3.84}$$

where $\psi^{0+}_{\alpha\upsilon_\alpha\ell_\alpha E}(r,R)$ is the nonresonant electron-scattering wave function. It satisfies the equation

$$[P\mathcal{H}_{el}(r,R)P - \mathcal{E}(R)]\psi^{0+}_{\alpha\upsilon_\alpha\ell_\alpha E}(r,R) = 0, \tag{3.85}$$

where $\mathcal{E}_\alpha(R) = E_\alpha + \varepsilon_\alpha$, E_0 is the BO potential energy curve of the residual ion and ε_α is the kinetic energy of the outgoing electron. The corresponding nuclear wave function χ_υ is the solution of the equation

$$[T(R) + E_o(R) - W_\upsilon]\chi_\upsilon(R) = 0, \tag{3.86}$$

where W_υ is the energy of the residual ion and

$$E = \varepsilon + W_\upsilon. \tag{3.87}$$

Eq. (3.84) is often called, in the context of electron-molecule scattering theory, the *adiabatic nuclei approximation* [43]. It results from the validity of the BO approximation for both the molecule and the residual molecular ion, and from the boundary conditions that impose that the latter ion remains in a final vibration state υ. Following the steps described in [54], the total wave function defined in Eq. (3.76) takes the form

$$\begin{aligned}\Psi^{+}_{\alpha\upsilon_\alpha\ell_\alpha E}(r,R) &= \sum_{r'}\phi_{r'}(r,R)\xi^{r'}_{\alpha\upsilon_\alpha\ell_\alpha E}(R) \;+\; \psi^{0+}_{\alpha\upsilon_\alpha\ell_\alpha E}(r,R)\chi_{\upsilon_\alpha}(R)\\ &+ \lim_{\eta\to 0}\sum_{r'}\sum_{\alpha'\ell'_{\alpha'}}\sum_{\upsilon'_{\alpha'}}\int dE'\,\frac{1}{E - E' + i\eta}\int dR' V^{r'*}_{\alpha'_{\alpha'}\upsilon'_{\alpha'}\ell'_{\alpha'}E'}(R')\xi^{r'}_{\alpha\upsilon_\alpha\ell_\alpha E}(R')\\ &\times\psi^{0+}_{\alpha'\ell'_{\alpha'}\varepsilon'_{\alpha'}}(r,R)\chi_{\upsilon'_{\alpha'}}(R).\end{aligned} \tag{3.88}$$

Notice that this wave function is different from that arising form Eq. (3.56). Also in Eq. (3.88), $\chi_{\upsilon_\alpha}(R)$ is the vibrational function of the residual ion, $E = \varepsilon_\alpha + W_{\upsilon_\alpha}$ (in the second term), $E' = \varepsilon'_{\alpha'} +$

$W_{\upsilon'_{\alpha'}}$ (in the third term), $\sum\!\!\!\!\!\!\int dE'$ represents a sum over bound states and an integral over continuum states of the molecule, $\sum\!\!\!\!\!\!\int_{\upsilon'_{\alpha'}}$ represents a sum over all bound vibrational states and an integral over all dissociative states (i.e., the vibrational continuum), $V^r_{\alpha\upsilon_\alpha\ell_\alpha E}(R)$ is a matrix element given by

$$V^r_{\alpha\upsilon_\alpha\ell_\alpha E} = \langle\phi_r|Q\mathcal{H}_{el}P|P\psi^{0+}_{\alpha\ell_\alpha\varepsilon_\alpha}\rangle\chi_{\upsilon_\alpha}(R), \tag{3.89}$$

and $\xi^r_{\alpha\ell_\alpha\upsilon_\alpha E}(R)$ is the solution of

$$\begin{aligned}&[E - E_r(R) - T(R)]\xi^r_{\alpha\upsilon\ell E}(R) = V^r_{\alpha\upsilon_\alpha\ell_\alpha E}(R)\\ +\ &\lim_{\eta\to 0}\sum_{r'}\sum_{\alpha'\ell'_{\alpha'}}\sum\!\!\!\!\!\!\int_{\upsilon'_{\alpha'}}\sum\!\!\!\!\!\!\int dE'\,\frac{V^r_{\alpha'\upsilon'_{\alpha'}\ell'_{\alpha'}E'}(R)}{E - E' + i\eta}\int V^{r'*}_{\alpha'\upsilon'_{\alpha'}\ell'_{\alpha'}E'}(R')\xi^{r'}_{\alpha\upsilon_\alpha\ell_\alpha E}(R')dR'.\end{aligned} \tag{3.90}$$

Eq. (3.88) is derived by assuming that the standard BO approximation is only valid within the P subspace, i.e., for the non resonant continuum states $P\Psi^+_{\alpha\upsilon_\alpha\ell_\alpha E}(r,R)$. The matrix element in Eq. (3.89) represents the coupling between the resonance state and the non resonant wave function of energy ε_α and vibrational state υ_α. Hence, the two terms in the right-hand side of Eq. (3.90) are the result of the autoionizing character of the ϕ_r state. In particular, the last term represents the decay of the resonant state to the adjacent electronic continuum. This term is non-local due to the presence of the $\xi^r_{\alpha\upsilon\ell E}$ functions and it can be split into the usual delta function term and the principal value term. In some cases, Eq. (3.90) can be simplified by using a local approximation and can be written in terms of resonance parameters (see [12] for more details).

All terms defining the wave function given in Eq. (3.88) can be evaluated using B-spline basis sets. We have already shown how $\psi^{0+}_{\alpha\ell_\alpha\upsilon_\alpha}$ and χ_{υ_α} can be calculated. The resonant electronic wave functions ϕ_r can be obtained by solving Eq. (3.55), using the CI technique described in Section 3.4. The most unusual part is the evaluation of the $\xi^r_{\alpha\upsilon\ell E}$ wave functions from Eq. (3.90). A numerical solution of this equation is extremely difficult because it is non-local and the wave functions oscillate strongly. However, Eq. (3.90) can be easily solved in the basis set that results from the diagonalization of the Schrödinger equation (see [50])

$$[T(R) + E_r(R) - \mathcal{W}_k]\tilde{\Upsilon}_k(R) = 0, \tag{3.91}$$

in a basis of B-spline functions. The use of the expansion

$$\xi^r_{\alpha\ell\upsilon E} = \sum_i c^{r,i}_{\alpha\upsilon\ell E}\tilde{\Upsilon}_i(R)\}, \tag{3.92}$$

and a short-range absorbing potential near $R = R_{max}$ leads to a system of linear equations that can be solved using standard methods.

It is worth pointing out that although the formalism leading to Eqs. (3.88) and (3.90) is general, in the sense that is is completely basis independent, its practical implementation has only been possible by using B-splines. The main reason is that autoionization may occur when the molecule is far from its equilibrium geometry, i.e., at relatively large values of R, and consequently one needs an accurate description of both the electronic and nuclear continua in a wide region of space. We would like to point out that, in spite of the complicated mathematical aspect of the continuum wave function given in Eq. (3.88), computation of all the nuclear components (including $\xi^r_{\alpha\upsilon\ell E}$) takes only a few minutes with a personal computer. This is negligible compared with the time required to evaluate the electronic part of the continuum wave function. In fact, for a single value of R, a calculation of the electronic part requires as much computer time as a calculation performed in the fixed-nuclei approximation. The difference is that, in this case one has to repeat calculations for several values of R, while in the fixed-nuclei approximation a single value of R is sufficient.

Bibliography

[1] M. Brosolo and P. Decleva, "Variational approach to continuum orbitals in a spline basis: An application to H_2^+ photoionization," *Chemical Physics*, vol. 159, pp. 185–196, 1992.

[2] M. Brosolo, P. Decleva, and A. Lisini, "Accurate variational determination of continuum wavefunctions by a one-centre expansion in a spline basis. An application to H_2^+ and HeH^{2+} photoionization," *Journal of Physics B: Atomic, Molecular and Optical Physics*, vol. 25, pp. 3345–3356, 1992.

[3] P. D. M. Brosolo and A. Lisini, "Sub-nanohartree accuracy from LCAO expansion with B-spline functions. An application to H_2^+ and HeH^{2+}," *Chemical Physics Letters*, vol. 203, pp. 586–591, 1992.

[4] P. Decleva, M. Brosolo, A. Lisini, and M. Venuti, "Continuum wave functions by least-squares scheme in a B-spline basis: Multicenter and multielectron formulations," *International Journal of Quantum Chemistry*, vol. 52, pp. 507–514, 1994.

[5] M. Brosolo, P. Decleva, and A. Lisini, "LCAO expansion in a spline basis for accurate variational determination of continuum wavefunctions. Applications to H_2^+ and HeH^{2+}," *Chemical Physics*, vol. 181, pp. 85–95, 1994.

[6] C. Chen, H. Chang, and C. Hsue, "A highly accurate calculation for the electronic states of H in B-spline basis," *Chemical Physics Letters*, vol. 217, pp. 486–489, 1994.

[7] A. Apalategui, A. Saenz, and P. Lambropoulos, "Effect of vibration and internuclear axis orientation on multiphoton ionization of H_2^+," *Journal of Physics B: Atomic, Molecular and Optical Physics*, vol. 33, pp. 2791–2807, 2000.

[8] H. Bachau, E. Cormier, P. Decleva, J. E. Hansen, and F. Martín, "Applications of B-splines in atomic and molecular physics," *Reports on Progress in Physics*, vol. 64, pp. 1601–1729, 2001.

[9] F. Martín, "Ionization and dissociation using B-splines: Photoionization of the hydrogen molecule," *Journal of Physics B: Atomic, Molecular and Optical Physics*, vol. 32, pp. R197–R231, 1999.

[10] M. Born and R. Oppenheimer, "Zur quantentheorie der molekule," *Annalen der Physik*, vol. 389, pp. 457–484, 1927.

[11] L. Laaksonen, P. Pyykkö, and D. Sundholm, "Two-dimensional fully numerical solutions of molecular Schrödinger equations. I. One-electron molecules," *International Journal of Quantum Chemistry*, vol. 23, pp. 309–317, 1983.

[12] I. Sánchez and F. Martín, "The doubly excited states of the H_2 molecule," *Journal of Chemical Physics*, vol. 106, pp. 7720–7730, 1997.

[13] K. Wolniewicz, K. Szalewicz, and H. J. Monkhorst, "New Born-Oppenheimer potential energy curve and vibrational energies for the electronic ground state of the hydrogen molecule," *The Journal of Chemical Physics*, vol. 84, pp. 3278–3283, 1986.

[14] P. J. Mohr and J. Sapirstein, "Evaluation of two-photon exchange graphs for excited states of highly charged heliumlike ions," *Physical Review A*, vol. 62, p. 052501, 2000.

[15] A. Macías, F. Martín, A. Riera, and M. Yáñez, "A practical solution to the unknown normalization problem," *International Journal of Quantum Chemistry*, vol. 33, pp. 279–300, 1988.

[16] E. Cormier and P. Lambropoulos, "Journal of physics b: Atomic, molecular and optical physics," *Optimal gauge and gauge invariance in non-perturbative time-dependent calculation of above-threshold ionization*, vol. 29, pp. 1667–1680, 1996.

[17] E. Cormier and P. Lambropoulos, "Above-threshold ionization spectrum of hydrogen using B-spline functions," *Journal of Physics B: Atomic, Molecular and Optical Physics*, vol. 30, pp. 77–91, 1997.

[18] E. Cormier and P. Lambropoulos, "Effect of a strong dressing field on the polarizability of atomic helium at harmonic frequencies," *Journal of Physics B: Atomic, Molecular and Optical Physics*, vol. 30, pp. 3095–3106, 1997.

[19] F. Fischer and M. Idrees, "Spline methods for resonances in photoionisation cross sections," *Journal of Physics B: Atomic, Molecular and Optical Physics*, vol. 23, pp. 679–691, 1990.

[20] E. Cormier, *Etude théorique de l'interaction entre un sytème à 1 ou 2 électrons actifs et un champ laser intense*. PhD thesis, L'Université Bordeaux I, 1994.

[21] H. Park and R. N. Zare, "Molecular-orbital decomposition of the ionization continuum for a diatomic molecule by angle- and energy-resolved photoelectron spectroscopy. i. formalism.," *The Journal of Chemical Physics*, vol. 104, p. 4554, 1996.

[22] M. Cortés and F. Martín, "Multichannel close-coupling method with L^2 integrable bases," *Journal of Physics B: Atomic, Molecular and Optical Physics*, vol. 27, pp. 5741–5760, 1994.

[23] C. J. Joachain, *Quantum Collision Theory*. North-Holland Publishing Company, 1979.

[24] M. Abramowitz and I. A. Stegun, *Handbook of Mathematical Functions with Formulas, Graphs, and Mathematical Tables*. New York: Dover, 1972.

[25] A. R. Barnett, D. H. Feng, J. W. Steed, and L. J. B. Goldfarb, "Coulomb wave functions for all real η and ρ," *Computer Physics Communications*, vol. 8, pp. 377–395, 1974.

[26] P. Decleva, A. Lisini, and M. Venuti, "Multichannel continuum states by a least-squares approach in a spline basis: application to He and H^- photoionization," *Journal of Physics B: Atomic, Molecular and Optical Physics*, vol. 27, pp. 4867–4889, 1994.

[27] F. Martín, A. Riera, and I. Sánchez, "Fully L^2 methods for multichannel scattering problems. Partial widths," *The Journal of Chemical Physics*, vol. 94, pp. 4275–4281, 1991.

[28] M. Venuti, P. Decleva, and A. Lisini, "Accurate multichannel continuum states by a general configuration interaction expansion in a B-spline basis: application to He photoionization," *Journal of Physics B: Atomic, Molecular and Optical Physics*, vol. 29, pp. 5315–5342, 1996.

[29] M. Venuti and P. Decleva, "Convergent multichannel continuum states by a general configuration interaction expansion in a B-spline basis: application to H^- photodetachment," *Journal of Physics B: Atomic, Molecular and Optical Physics*, vol. 30, pp. 4839–4859, 1996.

[30] M. Stener and P. Decleva, "Photoionization of CH_4, SiH_4, BH_3 and AlH_3 by the B-spline one-centre expansion density functional method," *Journal of Electron Spectroscopy and Related Phenomena*, vol. 104, pp. 135–144, 1999.

[31] G. Fronzoni, M. Stener, and P. Decleva, "Theoretical study of the excited and continuum states in the NEXAFS regions of Cl_2," *Physical Chemistry Chemical Physics*, vol. 1, pp. 1405–1414, 1999.

[32] F. Martín, "Completely L^2 integrable method for strong-coupling multichannel photoionization: Photoelectron emission of He between the N=3 and 4 threshold," *Physical Review A*, vol. 48, pp. 331–337, 1993.

[33] I. Sánchez and F. Martín, "Resonant effects in photoionization of H_2 and D_2," *Journal of Chemical Physics*, vol. 107, pp. 8391–8396, 1997.

[34] U. Fano, "Effects of configuration interaction on intensities and phase shifts," *Physical Review*, vol. 124, pp. 1866–1878, 1961.

[35] H. Feshbach, "A unified theory of nuclear reactions. II," *Annals of Physics*, vol. 19, pp. 287–313, 1962.

[36] I. Sánchez and F. Martín, "Representation of the electronic continuum of H_2 with B-spline basis," *Journal of Physics B: Atomic, Molecular and Optical Physics*, vol. 30, pp. 679–692, 1997.

[37] H. Feshbach, "Unified theory of nuclear reactions," *Annals of Physics*, vol. 5, pp. 357–390, 1958.

[38] I. Sánchez and F. Martín, "Photoionization of He above the $n = 2$ threshold," *Physical Review A*, vol. 44, pp. 7318–7334, 1991.

[39] J. D. Power, "Oedm: One-electron diatomic molecules," *Quantum Chemistry Program Exchange*, vol. QCPE Program Number: 233, 1973.

[40] H. Wind, "Vibrational states of the hydrogne molecular ion," *The Journal of Chemical Physics*, vol. 43, pp. 2956–2958, 1965.

[41] G. H. Dunn, "FranckâĂŤcondon factors for the ionization of H_2 and D_2," *The Journal of Chemical Physics*, vol. 44, pp. 2592–2594, 1966.

[42] G. B. Arfken and H. J. Weber, *Mathematical Methods for Physicists*. Academic Press, 1985.

[43] M. Shugard and A. U. Hazi, "Theory of electron-molecule scattering: Comments on the adiabatic-nuclei approximation," *Physical Review A*, vol. 12, pp. 1895–1902, 1975.

[44] N. F. Lane, "The theory of electron-molecule collisions," *Reviews of Modern Physics*, vol. 52, pp. 29–119, 1980.

[45] K. Ito, R. I. Hall, and M. Ukai, "Dissociative photoionization of H_2 and D_2 in the energy region of 25-45 eV," *The Journal of Chemical Physics*, vol. 104, pp. 8449–8457, 1996.

[46] Z. X. He, J. N. Cutler, S. H. Southworth, L. R. Hughey, and J. A. R. Samson, "Zero kinetic energy proton and deuteron production from photoionization of H_2 and D_2," *The Journal of Chemical Physics*, vol. 103, pp. 3912–3916, 1995.

[47] C. J. Latimer, J. Geddes, M. A. MacDonald, N. Kouchi, and K. F. Dunn, "The photodissociative ionization of hydrogen and deuterium in the VUV via Π states," *Journal of Physics B: Atomic, Molecular and Optical Physics*, vol. 29, pp. 6113–6121, 1996.

[48] T. Aoto, Y. Hikosaka, R. I. Hall, K. Ito, J. Fernández, and F. Martín, "Dissociative photoionization of H_2 at high photon energies: Uncovering new series of doubly excited states," *Chemical Physics Letters*, vol. 389, pp. 145–149, 2004.

[49] I. Sánchez and F. Martín, "Origin of unidentified structures in resonant dissociative photoionization of H_2," *Physical Review letters*, vol. 79, pp. 1654–1657, 1997.

[50] I. Sánchez and F. Martín, "Resonant dissociative photoionization of H_2 and D_2," *Physical Review A*, vol. 57, pp. 1006–1017, 1998.

[51] J. Fernández, *Dissertation: Fotoionización disociativa del* H_2. PhD thesis, Universidad Autónoma de Madrid, 2003.

[52] J. N. Bardsley, "Configuration interaction in the continuum states of molecules," *Journal of Physics B: Atomic, Molecular and Optical Physics*, vol. 1, pp. 349–364, 1968.

[53] A. U. Hazi, T. N. Rescigno, and M. Kurilla, "Cross sections for resonant vibrational excitation of N_2 by electron impact," *Physical Review A*, vol. 23, pp. 1089–1099, 1981.

[54] I. Sánchez and F. Martín, "Dissociative photoionization of H_2 and D_2 by (30-37)-eV photons via $^1\Pi_u$ states," *Physical Review A*, vol. 60, pp. 2200–2206, 1999.

Chapter 4

Angular distribution of electrons and ions

"Whatever nature has in store for mankind, unpleasant as it may be, men must accept, for ignorance is never better than knowledge."

Enrico Fermi

Table of Contents

4.1 Introduction

MOLECULAR-frame photoelectron angular distribution (**MFPAD**) provides detailed dynamical information on photoionization processes through the determination of the dipole matrix elements [1, 2]. Taking advantage of dissociative photoionization process, where the molecular orientation can be determined from the recoil direction of the fragment ions, significant steps have been achieved recently towards complete experiments by measuring the photoelectron angular distribution (**PAD**) in terms of the emission angle between the molecular axis and the emission direction of the photoelectron, [3, 4, 5].

In this chapter the physical principles involved in the study of the angular distribution of the particles coming from the photoionization process are given. We begin with a brief summary of the theoretical description of the photoionization process. We will present in much more detail the different differential cross sections, i.e., the angular distribution of the final particles, that reproduce the experimental conditions that we are interested in: the electron and ion angular distribution for fixed-in-space molecules and the electron angular distribution for randomly distributed molecules.

In all these cases the vibrational motion is included and the different developments will be performed as general as possible. In particular, we will use a perturbative and semiclassical treatment of the radiation in order to treat the interaction of the radiation with the molecule [6], and we will make use of the partial wave expansion of the electronic wave function [7], described in the previous chapter.

4.2 Photoionization cross section

In the previous chapters we have concentrated our attention in the description of the methods and the formalism that we need in order to get the different wave functions that describe our molecular system, electronic and nuclear (both, bound and continuum). Now we are interested in describing how to make use of these wave functions in order to reproduce the experimental conditions in the photoionization process.

Photoionization can be considered as an absorption of a photon followed by a half collision between the photoelectron and the ion. The final state reached by the photoabsorption is thus the collision state that describes the scattering event between the photoelectron and the ion. For the atomic case, because a photoelectron always moves under a central potential in the independent electron approximation, the orbital angular momentum quantum number ℓ for the photoelectron is a good number. The fact that the molecular ion has a structure associated with it, introduces two important modifications in the final wave function. First, any wave function for the molecular ionization continuum should be referenced to the molecular-fixed frame. Second, the potential under which the photoelectron moves in the ion-core region is non-central, and the scattering between the photoelectron and the ion core becomes a "multichannel" problem, as we discussed in Chapter 3. Therefore, the molecular photoionization process can be represented schematically as

$$\gamma(j_\gamma = 1, \pi_\gamma = 1, \widehat{R}_{\hat{n}}) \; + \; M_i \rightarrow M_\mu^+ + e^-[k, \pi_e = (-1)^\ell]. \tag{4.1}$$

The electric dipole interaction imparts $j_\gamma = 1$ units of angular momentum and odd parity π_γ to the molecular target M_i, that ejects an electron with the energy and the angular direction given by k. Initially the molecule is in a state characterized by a set of quantum numbers enclosed in the label $i = \{\upsilon_0, \Lambda, \pi, \sigma, S, M_S\}$, where υ_0 represents the initial vibration state, Λ is the absolute value of the z-component of the total electronic angular momentum (Σ, Π, ...), π is inversion symmetry (g or u), σ is the reflexion symmetry with respect to the xy plane ($+$ or $-$), S is the total electronic spin and M_S is its z-component. The final state, composed by the residual ion, M_μ^+, and the electron in the continuum, is characterized by the direction and energy of the electron and a set of quantum numbers that describes the residual ion, $\mu = \{\upsilon', \Lambda, \pi, \sigma, S, M_S\}$, where υ' is the vibrational state of the ion, and the other quantum numbers have been previously described. $\widehat{R}_{\hat{n}}$ gives the orientation of the vector polarization with respect to the molecular reference system at the instant of its ionization. This fact reflects the lack of the spherical symmetry in a molecular system, and, as we will show, implies complications in the description of the process.

Since the spin-orbit coupling will be considered negligible, the spin and angular momentum will be constants of movement, before and after the collision. Likewise, we will suppose that the photon energy is not high enough for ionizing a second electron of the molecule, but we will consider the possibility that the residual molecular ion remains in different electronic and vibrational final states.

We will consider the interaction of the photon with the molecule can be described by a perturbative treatment of the electromagnetic field. This means that the total system, molecule + photon can be written as:

$$\mathcal{H}_{tot} = \mathcal{H}_{mol} + \mathcal{H}_{pert} \tag{4.2}$$

where $\mathcal{H}_{pert}$ gives the interaction of the light with the molecule, given by [8]

$$\mathcal{H}_{pert} = \frac{e}{m}\sum_j A(r,t)\cdot p_j = \frac{ie}{m}\sum_j A(r,t)\cdot \nabla_j. \tag{4.3}$$

$A(r,t)$ is the vector potential given by [9]

$$A(r,t) = A_0\left[e^{i(k\cdot r-\omega t)} - e^{-i(k\cdot r-\omega t)}\right], \tag{4.4}$$

that can be simplified if we take the ***dipole approximation***, that takes into account the fact that the exponential terms can be expanded in a Taylor expansion and takes only the first non zero term. This can be justified by the fact that the vector propagation k is on the order of the inverse of the wavelength of the light, $1/\lambda$, and r of the order of the molecular dimensions, a_o (Bohr radius), so for the usual wavelength, we have $k\cdot r \simeq a_o/\lambda < 1$. For example, for the H_2 molecule the dipole approximation is valid for photon energies $\ll 130$ a.u. The electric dipole contribution is the largest for normal photon intensities. Interference contributions from the next-higher multipoles may affect the differential photoionization cross section by a few percent.

Within this approximation, and performing the integration over time, the fully differential cross section for ionization from the initial state $\Psi_{i\nu}(r,R)$ is given (in atomic units) by

$$\frac{d\sigma_\alpha^{\mu_0}(\omega)}{d\widehat{R}_{\hat{n}}dk_e} = \frac{4\pi^2\omega}{c}\left|\int dR\langle\Psi^+_{\alpha\upsilon_\alpha k_e E}(r,R)|e_{\mu_0}\cdot D|\Psi_{i\nu}(r,R)\rangle\right|^2. \tag{4.5}$$

The initial state is described in the framework of the Born-Oppenheimer (BO) approximation, i.e., $\Psi_{i\nu}(r,R) = \psi_i(r,R)\chi_\nu(R)$, where $\psi_i(r,R)$ is the initial electronic state and $\chi_\nu(R)$ is the initial vibrational state calculated in the potential energy curve $E_i(R)$ associated with $\psi_i(r,R)$. ω is the initial photon energy and c the velocity of the light (see Appendix A). e_{μ_0} is the photon polarization vector where μ_0 defines the polarization vector, for linearly polarized light ($\mu_0 = 0$) and for circularly polarized light ($\mu_0 = \pm 1$). The definition of μ_0 for circularly polarized light is that when $\mu_0 = +1$ the helicity is positive (left circularly polarized light) and when $\mu_0 = -1$ the helicity is negative (right circularly polarized light) (see [6] for more details). D is either (for a bielectronic system) $r_1 + r_2$ (length gauge) or $(\nabla_1 + \nabla_2)/(\omega)$ (velocity gauge). If the wave functions used to calculate the photoionization cross section were exact eigenfunctions of the electronic Hamiltonian, then the dipole length and dipole velocity forms of the cross section would be equivalent [10]. Thus, the equality of these two forms is a necessary but not sufficient condition for the computed cross sections to be accurate. In this sense, the difference between the length an velocity forms can be viewed as an estimate of the minimum error in the calculation. All the calculations presented in this Thesis have been obtained in the velocity gauge since the convergence is faster as a function of the required number of partial waves, although the differences with the results obtained in the length gauge are pretty small. $\Psi^+_{\alpha\upsilon_\alpha k_e E}(r,R)$ represents the molecular electronic final state, asymptotically becoming the product of the remaining ion state $\alpha\upsilon_\alpha$ times a Coulomb wave of energy $\varepsilon_\alpha = E - W_{\upsilon_\alpha}$ and direction k_e describing the photoelectron with respect to the molecular reference system and its final energy, and α and υ_α denote, respectively, the electronic and vibrational states of the residual molecular ion. In the final state, the subscript + indicates the outgoing boundary conditions in electron-molecule scattering, and $E = W_{i\nu} + \omega$ with $W_{i\nu}$ being the total energy of the molecule in the initial state. In Eq. (4.5) we have factored out the rotational wave functions (see [11] for a theoretical treatment of the rotation motion). The rotation has to be considered when the axial recoil approximation is not valid, i.e., when the lifetime of the molecular ion state prior to dissociation is a significant fraction of the rotational period of the molecule [12, 13, 14]. The physical reason for the rotation is that the molecules populating the target gas posses rotational kinetic energy due to the

nonzero rotational temperature of the target. The axial recoil holds[1] when a diatomic ion is formed in a dissociative state, the atoms/ions produced in the dissociation process will move outward along the straight line defined by the internuclear axis of the molecule.

If we impose that the total spin of the system, S, and its projection, M_S, of the global system (ion + electron) will be well defined, this will imply that the corresponding spin components of the ion and the electron will not be well defined. Since the electron possesses a well defined energy and direction, the final wave function, $\Psi^{+}_{\alpha\upsilon_\alpha k_e E}(r,R)$, that describes the electron and the residual ion, will not have spherical symmetry. The photoelectron may considered to be removed from the molecular orbital quantized along the molecular axis, and it is convenient to expand the continuum wave function in terms of function quantized along this axis [15, 16], that implies that the final wave function in Eq. (4.5) can be written in a *partial wave expansion* [7]:

$$\Psi^{+}_{\alpha\upsilon_\alpha k_e E}(r,R) = \sum_{\ell_\alpha} \sum_{m_\alpha=-\ell_\alpha}^{\ell_\alpha} i^{-\ell} e^{i\hat{\sigma}_\ell(k)} \Psi^{+}_{\alpha\upsilon_\alpha \ell_\alpha m_{\ell_\alpha} E}(r,R) \overline{Y}^{m_\alpha}_{\ell_\alpha}(\theta_e,\phi_e). \tag{4.6}$$

where $\hat{\sigma}_{\ell_\alpha}(k)$ is the Coulombic phase shift [23, 24] given by

$$\hat{\sigma}_\ell(k) = \arg\Gamma(\ell+1-iZ_\infty/k), \tag{4.7}$$

with Z_∞ being the total charge of the residual ion. The wave function $\Psi^{+}_{\alpha\upsilon_\alpha \ell_\alpha m_{\ell_\alpha} E}$ is an eigenfunction of the Hamiltonian given in Chapter 3, sections 3.8 and 3.9. Each partial wave represents a final state, so the ionized electron has a well defined angular momentum, but with an undefined direction.

Therefore the general expression of the fully differential cross section, given by Eq.(4.5), for the electronic ionic state α, takes the form

$$\frac{d\sigma^{\mu_0}_\alpha(\omega)}{d\widehat{R}_{\hat{n}} d\Omega_e dW_{\upsilon_\alpha}} = \frac{4\pi^2\omega}{c} \left| \sum_{\ell_\alpha m_{\ell_\alpha}} \int i^{\ell_\alpha} e^{-i\hat{\sigma}_{\ell_\alpha}(\varepsilon_\alpha)} \langle \Psi^{+}_{\alpha\upsilon_\alpha \ell_\alpha m_{\ell_\alpha} E}(r,R) | \hat{e}_{\mu_0} \cdot D | \Psi_{i\nu}(r,R) \rangle \overline{Y}^{m_{\ell_\alpha}}_{\ell_\alpha}(\Omega_e) dR \right|^2, \tag{4.8}$$

where the sum over ℓ_α runs over the electron partial waves associated to the electronic state of the ion, α, and the dependence with k_e has been replaced by $d\Omega_e dW_{\upsilon_\alpha}$, where the final electron energy is expressed in terms of the energy of the residual ion, i.e.,

$$W_{\upsilon_\alpha} = 2 \times [\hbar\omega + W_{i\nu} - W_{\nu_\alpha} - \varepsilon_\alpha]. \tag{4.9}$$

So, in the case of molecules, due to the non-spherical nature of the molecular potential, the wave functions must be presented as an infinite expansion in spherical harmonics with the origin at the center of mass, which means that the orbital angular momentum ℓ is not a good quantum number. Consequently, the dipole selection rules could not restrict the infinite sum in the partial-wave expansion of the continuous spectrum wave function. Therefore, the photoionization process is generally described by an infinite number of complex transition moments, and a complete experiment is not feasible. However, the partial-wave expansion for both bound and continuous spectrum wave functions converges rather rapidly, and to a good approximation one can truncate the relevant sums to a limited number of terms.

[1] For example in H_2^+ the rotational energy of the molecule is of the order of 0.002 eV; the recoil energy at infinity separation of the fragments partners ranges from about 7 to 13 eV if we consider those vertical transitions from the ground vibrational state to repulsive potential curve above, which are permitted in the classical limit of the Franck-Condon principle.

4.3 Photoelectron angular distribution for fixed-in-space molecules

Molecules present a far greater challenge than atoms because (a) there is a greater number of contributing partial waves owing to the lower symmetry; (b) to extract the full information, the resolution of ion internal energy states is desirable; and (c) the radial dipole matrix elements have a dependence on the instantaneous atomic separations. Whereas an atomic PAD can be measured only with respect to an imposed laboratory frame axis, a molecular PAD can, in principle, be measured with respect to an axis in the molecule. This apparently esoteric situation, which was first considered by Dill [1] for diatomic molecules and was latter extended to polyatomic molecules by Chandra [27], has more recently been shown to be realizable in certain situations. As we will see in this section, the general form of the PAD in this case is given by

$$\sigma(\theta_e,\phi_e) \propto \sum_{L_e}\sum_{M_e} A_{L_e,M_e} Y_{L_e}^{M_e}(\theta_e,\phi_e).$$

The contributing terms in this expression reflect the complexity of the molecular structure, and the values of the coefficients give insight into the electron-ion scattering potential. In the molecular frame, a number of additional possibilities arise as the directions of the polarization vector and/or propagation vector of the light can be varied with respect to the molecular axis with consequent variations in the resulting PAD. When PADs from molecules are measured, the aim is either to determine the radial matrix elements and learn about the photoionization process or to make experimental measurements that give information about other dynamical processes that may have purely geometrical effects on the PADs. In the latter case, it is desirable to make measurements that allow the radial dipole matrix elements to be factored out to A_{L_e,M_e} coefficients, thus leaving information about the state that ionized.

In a given photoionization experiment the orientation of the target, or the electron detection direction, or both may be resolved. By ”resolved” we mean ”measured” in the quantum mechanic sense; in particular, an unresolved quantity must be treated theoretically as completely random. Clearly, the most detailed information is available in the experiment which resolves both, either by measuring the angular distribution of electrons from a fixed target (for alternative target orientations), or by measuring it as a function of target orientation of the photoelectron at a fixed detector (for alternative detector-light orientations). Both of these ”fully resolved” processes have been explored quite recently in different experiments [28, 29, 30, 31, 32] and theoretical calculations [1, 26, 33, 34, 35, 36, 37, 38, 39, 40, 41, 42]. The predicted distributions are beautifully rich in structure and detail.

The analysis of the MFPAD for linear molecules within the axis recoil approximation, can be performed in terms of two related coordinate systems[2] defined for the purpose of the present derivation (see Fig. (4.1)). The first coordinate system is defined in the molecular frame where the z axis is the molecular axis at the moment of the photoionization. The angles $\Omega_{\hat{n}} = (\theta_n,\phi_n)$ defines the orientation of the polarized light. If the light is linearly polarized, $\mu_0 = 0$ and $\Omega_{\hat{n}}$ is the direction of the polarization of the light. If the light is circularly polarized, $\mu_0 = \pm 1$ and $\Omega_{\hat{n}}$ is the direction of propagation of the light. The direction of emission of the photoelectron in this reference frame is given by the angles $\Omega_{\hat{e}} = (\theta_e,\phi_e)$. The second coordinate system is associated to the laboratory frame, in which the direction of polarization of linearly polarized light or the direction of propagation of circularly polarized light is along the z' axis. In the laboratory frame coordinate system the direction of propagation of the photoelectron is given by the angles $\Omega'_e = (\theta'_e,\phi'_e)$ and the orientation of the molecular axis is defined by the angles $\Omega'_{\hat{M}} = (\theta'_M,\phi'_M)$. The orientation of

[2] In the case where the axis recoil approximation is not valid, a third reference system can be defined that corresponds to the reference system where the electron is measured [14].

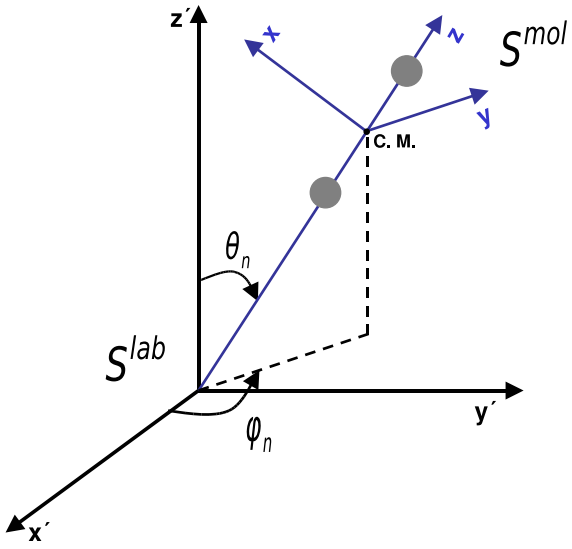

Figure 4.1: Laboratory (S^{lab}) and molecular (S^{mol}) frames for linear molecules.

the laboratory coordinate frame of the light source system with respect to the molecule frame is characterized by the set of Euler angles (see Appendix C)

$$\widehat{R}_{\hat{n}} = \{\alpha, \beta, \gamma\} = \{\phi_n, \theta_n, \pi - \phi_M\}\,, \tag{4.10}$$

which carry the molecular frame into coincidence with the laboratory frame. Note that following the definition of the Euler angles presented in Appendix C, the polar coordinates of the molecular z axis in the $x'y'z'$ laboratory frame are $(\theta_n, \pi - \phi_M)$, while the polar coordinates of the laboratory z' axis in the xyz molecular frame are (θ_n, ϕ_n). In addition, the inverse rotation is

$$\widehat{R}^{-1}_{\hat{n}} = \{-\gamma, -\beta, -\alpha\} = \{\pi - \phi_M, \theta_n, \pi - \phi_n\} = \widehat{R}_{\hat{M}}, \tag{4.11}$$

that defines the set of Euler angles which carry the laboratory frame into the molecular frame.

The dipole matrix elements present in Eq. (4.8) can be defined as

$$T_{\alpha\upsilon_\alpha\ell_\alpha m_{\ell_\alpha}\mu_0 E} = \int \langle \Psi^+_{\alpha\upsilon_\alpha\ell_\alpha m_{\ell_\alpha} E}(r,R)|\hat{e}_{\mu_0}\cdot D|\Psi_{i\nu}(r,R)\rangle \mathrm{d}R \tag{4.12}$$

and they are evaluated in the molecular reference system, while the dipole operator is defined in the laboratory frame. Therefore, making use of the rotations defined previously, that connect both reference systems, the dipole matrix elements can be obtained in the same reference system. The orientation of the polarization direction of the light in the laboratory reference system can be taken along the z' axis, without loss of generality, and taking into account Eq. (C.62), that allows to express the spherical harmonic in the laboratory frame in terms of the ones in the molecular reference system, one can write

$$z' = \sqrt{\frac{4\pi}{3}} r Y_1^0(\theta', \varphi') = \sqrt{\frac{4\pi}{3}} r \sum_{\mu=-1}^{1} Y_1^\mu(\theta, \varphi) D^1_{\mu,\mu_0}(\alpha, \beta, \gamma), \tag{4.13}$$

where we have made use of Eq. (B.58), and $D^1_{\mu,\mu_0}(\alpha, \beta, \gamma)$ is the Wigner rotational matrix, defined in Appendix C.

Replacing Eq. (4.13) in Eq. (4.8), the fully differential cross section takes the form

$$\begin{aligned}\frac{d\sigma_{\alpha}^{\mu_0}(\omega)}{d\widehat{R}_{\hat{n}}d\Omega_e dW_{\upsilon_\alpha}} &= \frac{4\pi^2\omega}{c}\sum_{\mu_a,\mu_b}\sum_{\ell_a,m_a}\sum_{\ell_b,m_b} i^{(\ell_b-\ell_a)}e^{i[\hat{\sigma}_{\ell_a}-\hat{\sigma}_{\ell_b}]}\overline{T}_{\alpha\upsilon_\alpha\ell_a m_a\mu_a E} \\ &\times T_{\alpha\upsilon_\alpha\ell_b m_b\mu_b E}\overline{D}^{1}_{\mu_a,\mu_0}(\alpha,\beta,\gamma)D^{1}_{\mu_b,\mu_0}(\alpha,\beta,\gamma)Y^{m_a}_{\ell_a}(\theta_e,\phi_e)\overline{Y}^{m_b}_{\ell_b}(\theta_e,\phi_e),\end{aligned} \tag{4.14}$$

where, in order to simplify the expression, the index α in ℓ_a, ℓ_b, m_{ℓ_a}, m_{ℓ_b}, $\hat{\sigma}_{\ell_a}$ and $\hat{\sigma}_{\ell_b}$, has been dropped. The dipole matrix elements defined in Eq. (4.12) now can be rewritten as

$$T_{\alpha\upsilon_\alpha\ell_\alpha m_{\ell_\alpha}\mu E} = \sqrt{\frac{4\pi}{3}}\int\langle\Psi^{+}_{\alpha\upsilon_\alpha\ell_\alpha m_{\ell_\alpha}E}(r,R)|rY^{\mu}_{1}(\theta,\varphi)|\Psi_{i\nu}(r,R)\rangle dR. \tag{4.15}$$

In order to simplify the product of the spherical harmonics, we can make use of the relations given by Eqs. (B.46) and (B.47), i.e.,

$$\begin{aligned}Y^{m_a}_{\ell_a}(\theta_e,\phi_e)\overline{Y}^{m_b}_{\ell_b}(\theta_e,\phi_e) &= (-1)^{m_b}\sqrt{\frac{(2\ell_a+1)(2\ell_b+1)}{4\pi}} \\ &\times \sum_{L_e=|\ell_a-\ell_b|}^{\ell_a+\ell_b}\frac{C(\ell_a,\ell_b,L_e;m_a,-m_b)C(\ell_a,\ell_b,L_e;0,0)}{\sqrt{2L_e+1}}Y^{M_e}_{L_e}(\theta_e,\phi_e)\end{aligned} \tag{4.16}$$

where $M_e = m_a - m_b$. Also, the product of the Wigner matrices in Eq. (4.14) can be simplified, making use of Eq. (C.86) and Eq. (C.90), as,

$$\begin{aligned}&\overline{D}^{1}_{\mu_a,\mu_0}(\alpha,\beta,\gamma)D^{1}_{\mu_b,\mu_0}(\alpha,\beta,\gamma) = \\ &(-1)^{\mu_a-\mu_0}\sum_{L_\gamma=0}^{2}C(1,1,L_\gamma;-\mu_a,\mu_b)C(1,1,L_\gamma;-\mu_0,\mu_0)D^{L_\gamma}_{M_\gamma,0}(\alpha,\beta,\gamma),\end{aligned} \tag{4.17}$$

with $M_\gamma = -\mu_a + \mu_b$.

Combining these two equations, Eqs. (4.16) and (4.17), the fully differential cross section given by the Eq. (4.8) becomes

$$\begin{aligned}\frac{d\sigma_{\alpha}^{\mu_0}(\omega)}{d\widehat{R}_{\hat{n}}d\Omega_e dW_{\upsilon_\alpha}} &= \frac{4\pi^2\omega}{c}\sum_{\mu_a,\mu_b}\sum_{\ell_a,m_a}\sum_{\ell_b,m_b} i^{(\ell_b-\ell_a)}e^{i[\hat{\sigma}_{\ell_a}-\hat{\sigma}_{\ell_b}]}(-1)^{m_b+\mu_a-\mu_0} \\ &\times \sqrt{\frac{(2\ell_a+1)(2\ell_b+1)}{4\pi}}\overline{T}_{\alpha\upsilon_\alpha\ell_a m_a\mu_a E}T_{\alpha\upsilon_\alpha\ell_b m_b\mu_b E} \\ &\times \sum_{L_e=|\ell_a-\ell_b|}^{\ell_a+\ell_b}C(\ell_a,\ell_b,L_e;m_a,-m_b)C(\ell_a,\ell_b,L_e;0,0)\frac{Y^{M_e}_{L_e}(\theta_e,\phi_e)}{\sqrt{2L_e+1}} \\ &\times \sum_{L_\gamma=0}^{2}C(1,1,L_\gamma;-\mu_a,\mu_b)C(1,1,L_\gamma;-\mu_0,\mu_0)D^{L_\gamma}_{M_\gamma,0}(\alpha,\beta,\gamma).\end{aligned} \tag{4.18}$$

Now taking the rotational matrix $D^{L_\gamma}_{M_\gamma,0}$ in terms of the spherical harmonics (using Eq. (C.79)), the

previous equation takes the form,

$$\begin{aligned}\frac{d\sigma_\alpha^{\mu_0}(\omega)}{d\Omega_n d\Omega_e dW_{\upsilon_\alpha}} &= \frac{4\pi^2\omega}{c}\sum_{\mu_a,\mu_b}\sum_{\ell_a,m_a}\sum_{\ell_b,m_b} i^{(\ell_b-\ell_a)}e^{i[\hat{\sigma}_{\ell_a}-\hat{\sigma}_{\ell_b}]}(-1)^{m_b+\mu_a-\mu_0} \\ &\times \sqrt{(2\ell_a+1)(2\ell_b+1)}\overline{T}_{\alpha\upsilon_\alpha\ell_a m_a\mu_a E}T_{\alpha\upsilon_\alpha\ell_b m_b\mu_b E} \\ &\times \sum_{L_e=|\ell_a-\ell_b|}^{\ell_a+\ell_b} C(\ell_a,\ell_b,L_e;-m_a,m_b)C(\ell_a,\ell_b,L_e;0,0)\frac{Y_{L_e}^{M_e}(\theta_e,\phi_e)}{\sqrt{2L_e+1}} \\ &\times \sum_{L_\gamma=0}^{2} C(1,1,L_\gamma;-\mu_a,\mu_b)C(1,1,L_\gamma;-\mu_0,\mu_0)\frac{\overline{Y}_{L_\gamma}^{M_\gamma}(\theta_n,\phi_n)}{\sqrt{2L_\gamma+1}},\end{aligned} \tag{4.19}$$

with $M_\gamma = -\mu_a+\mu_b$ and $M_e = m_a - m_b$ and where we have used $\hat{R}_{\hat{n}} = \Omega_n = (\theta_n,\phi_n)$, see Eq. (4.10). The expression given by Eq. (4.19) is the main result of this section. It is quite general, and applies to ionization of diatomic molecules belonging to any point group, taking into account whatever orientation of the arbitrary polarized radiation field. The rank L_e of the spherical harmonics $Y_{L_e}^{M_e}(\theta_e,\phi_e)$ in the previous equation is limited by the number $2\ell_{max}$, where ℓ_{max} is the largest orbital momentum component of the photoelectron amplitude. This equation is the starting point from which one can obtain different angular distributions, depending on the experimental conditions. Following the definitions given by Wallace *et al.* [43], four different situations can be considered:

a. Fixed-target angular distribution (FTAD).

   The orientation of the molecule (or the polarization of the light) is held fixed and the variation of the photoelectron is measured as a function of the detector orientation Ω_e. This is what is commonly called the electron angular distribution for "fixed-in-space" molecules.

b. Fixed-detector angular distribution (FDAD).

   The electron orientation is held fixed and the photocurrent is measured as a function of the target orientation. In this case the ionic particles are studied for a fixed orientation of the ejected electron (see for example [44]).

c. Integrated-target angular distribution (ITAD).

   In this case the net photoelectron for all target orientations along the detector direction is measured. This correspond, e.g., to the usual gas-phase (randomly target) photoelectron-angular-distribution experiment.

d. Integrated-detector angular distribution (IDAD).

   In this case, the net interaction with the target is measured as a function of the orientation of the molecular orientation. This gives the usual ion angular distribution.

Both the FTAD and FDAD are generally very richly structured because of the coherent superposition for the anisotropies in the response of the target to the light and in the distribution pattern of the ejected electrons. The IDAD is substantially simpler because of the limitation of any such coherence and indeed of any dependence on ejection anisotropy whatsoever. In fact, the ITAD, of course, contains no information on target orientation. The IDAD measures directly and exclusively the dependence of the target response on the orientation with respect to the light. This makes the IDAD conceptually and experimentally the most direct probe of target orientation.

4.3.1 Photon and molecular frame in coincidence

Now, let us consider a special case: $\beta = \theta_n = 0$ so that the photon- and molecule-frame z axis coincide [1]. Then $\mu_0 = 0$ corresponds to ionization with the electric vector parallel to the molecular z-axis and $\mu_0 = \pm 1$ corresponds to ionization with the electric vector perpendicular to the molecule z axis. Therefore, making use of the relation

$$Y_{L_\gamma}^{M_\gamma}(0,\phi_n) = \sqrt{\frac{2L_\gamma+1}{4\pi}}\delta_{M_\gamma,0}, \tag{4.20}$$

the condition $\mu_a = \mu_b$ is obtained, since $M_\gamma = -\mu_a + \mu_b$, and the fully differential cross section given by Eq. (4.19) becomes

$$\begin{aligned}\left.\frac{d\sigma_\alpha^{\mu_0}(\omega)}{d\Omega_e dW_{\upsilon_\alpha}}\right|_{\theta_n=0} &= \frac{4\pi^2\omega}{c}\sum_{\mu_a}\sum_{\ell_a,m_a}\sum_{\ell_b,m_b} i^{(\ell_b-\ell_a)}e^{i[\hat{\sigma}_{\ell_a}-\hat{\sigma}_{\ell_b}]}(-1)^{m_b+\mu_a-\mu_0} \\ &\times \sqrt{\frac{(2\ell_a+1)(2\ell_b+1)}{4\pi}}\overline{T}_{\alpha\upsilon_\alpha\ell_a m_a\mu_a E}T_{\alpha\upsilon_\alpha\ell_b m_b\mu_a E} \\ &\times \sum_{L_e=|\ell_a-\ell_b|}^{\ell_a+\ell_b} C(\ell_a,\ell_b,L_e;m_a,-m_b)C(\ell_a,\ell_b,L_e;0,0)\frac{Y_{L_e}^{M_e}(\theta_e,\phi_e)}{\sqrt{2L_e+1}} \\ &\times \sum_{L_\gamma=0}^{2} C(1,1,L_\gamma;-\mu_a,\mu_a)C(1,1,L_\gamma;-\mu_0,\mu_0).\end{aligned} \tag{4.21}$$

with $M_e = -m_a + m_b$. The sum over $\sum_{L_\gamma}$ can be simplified making use of Eq. (C.6), that implies that $\mu_a = \mu_0$, and expressing the spherical harmonic $Y_{L_e}^{M_e}(\theta_e,\phi_e)$ in terms of the Legendre polynomial, Eq. (B.42), the differential cross section takes the form,

$$\begin{aligned}\left.\frac{d\sigma_\alpha^{\mu_0}(\omega)}{d\Omega_e dW_{\upsilon_\alpha}}\right|_{\theta_n=0} &= \frac{4\pi^2\omega}{c}\sum_{\ell_a,m_a}\sum_{\ell_b,m_b} i^{(\ell_b-\ell_a)}e^{i[\hat{\sigma}_{\ell_a}-\hat{\sigma}_{\ell_b}]}(-1)^{m_b} \\ &\times \sqrt{(2\ell_a+1)(2\ell_b+1)}\overline{T}_{\alpha\upsilon_\alpha\ell_a m_a\mu_0 E}T_{\alpha\upsilon_\alpha\ell_b m_b\mu_0 E} \\ &\times \sum_{L_e=|\ell_a-\ell_b|}^{\ell_a+\ell_b} C(\ell_a,\ell_b,L_e;m_a,-m_b)C(\ell_a,\ell_b,L_e;0,0)P_{L_e}(\cos\theta_e).\end{aligned} \tag{4.22}$$

Note that in this result m_a and m_b are restricted to the single value μ_0 due restrictions impose by the dipole selection rules.

So, for a fixed molecular orientation the differential cross section for photon- and molecule-frame z axis in coincidence, can be reorganized in a simple form that directly reflects its angular dependence:

$$\left.\frac{d\sigma_\alpha^{\mu_0}(\omega)}{d\Omega_e dW_{\upsilon_\alpha}}\right|_{\theta_n=0} = \sum_{L_e} B_{L_e}(\omega,W_{\upsilon_\alpha})P_{L_e}(\cos\theta_e), \tag{4.23}$$

where we have defined the $B_{L_e}(\omega, W_{\upsilon_\alpha})$ coefficients as:

$$\begin{aligned} B_{L_e}(\omega, W_{\upsilon_\alpha}) &= \frac{4\pi^2\omega}{c} \sum_{\ell_a, m_a} \sum_{\ell_b, m_b} i^{(\ell_b - \ell_a)} e^{i[\hat{\sigma}_{\ell_a} - \hat{\sigma}_{\ell_b}]} (-1)^{m_b} \\ &\times \sqrt{(2\ell_a+1)(2\ell_b+1)}\, \overline{T}_{\alpha\upsilon_\alpha\ell_a m_a \mu_0 E}\, T_{\alpha\upsilon_\alpha\ell_b m_b \mu_0 E} \\ &\times C(\ell_a, \ell_b, L_e; m_a, -m_b) C(\ell_a, \ell_b, L_e; 0, 0) \end{aligned} \tag{4.24}$$

In Eq. (4.23) the values of L_e are restricted to the values of ℓ_a and ℓ_b due to the relations imposed by the C-G coefficients in Eq. (4.24). Therefore, from an experimental point of view the determination of the $B_{L_e}(\omega, W_{\upsilon_\alpha})$ coefficients opens the possibility of performing a complete experiment, in the sense, that the transition matrix elements and the phase shifts would be obtained (under certain circumstances). Thus, every parameter that is needed to describe the photoionization process would be determined.

The $B_0(\omega, W_{\upsilon_\alpha})$ gives access to the integrated cross section, since the integration of Eq. (4.23) over the electron distribution, i.e. over $d\Omega_e$, implies that only the term $L_e = 0$ gives a contribution different from zero (see Fig. (B.1)). So the integrated cross section is given by

$$\left.\frac{d\sigma_\alpha^{\mu_0}(\omega)}{dW_{\upsilon_\alpha}}\right|_{\theta_n=0} = B_0(\omega, W_{\upsilon_\alpha}) = \frac{4\pi^2\omega}{c} \sum_{\ell} |T_{\alpha\upsilon_\alpha\ell m\mu_0 E}|^2. \tag{4.25}$$

Note that total cross section given by Eq. 4.25 differs from the one obtained for the case where the molecules are randomly distributed in the space (see Eq. 4.84). In this last case the factor $1/3$ reflects the average over the three possible orientation of the polarization vector with respect to the molecular axis consistent with the dipole selection rule.

4.3.2 Azimuthal dependence: The $F_{LN}^{\mu_0}$ functions

Measurements for parallel and perpendicular orientations of the polarization vector with respect to the molecular axis enable one to define separately two independent sets of dipole matrix elements $T_{\ell\sigma}$ and $T_{\ell\pi}$, and two corresponding sets of phase differences for the $\ell\sigma$ and $\ell\pi$ channels, respectively. This is a great advantage compared with the experiment where the ion angular distribution is measured [45] and where such a separation is impossible. The ratios of matrix elements belonging to different sets, for example, $T_{\ell\pi}/T_{\ell\sigma}$, can be defined from the relative measurements of the cross sections corresponding to the σ and π ionization channels, while for determining the phase differences $(\delta_{\ell\pi} - \delta_{\ell\sigma})$ one needs to perform at least one additional measurement, for example, a measurement of the angular distribution of photoelectrons at an angle between the molecular axis and light polarization vector other than 0° and 90°. Therefore, it is quite convenient to obtain an expression for the fully differential cross section that gives both the possibility of obtaining the electron azimuthal dependence and that enables to fix an arbitrary orientation of the polarization vector with respect to the molecular axis. As we will see, this differential cross section can be parametrized by means of only five functions [46], and allows one to obtain both the polar and azimuthal dependence of the electron angular distribution. These functions can be compared in a direct and easy manner with the experimental results. The starting point for the future developments is given by the expression given by Eq. (4.19), which now can be written as:

$$\begin{aligned} \frac{d\sigma_\alpha^{\mu_0}(\omega)}{d\Omega_n d\Omega_e dW_{\upsilon_\alpha}} &= \frac{4\pi^2\omega}{c} (-1)^{-\mu_0} \\ &\times \sum_{L_e, M_e} \sum_{L_\gamma, M_\gamma} A_{L_e, M_e}^{L_\gamma, M_\gamma}(\omega, W_{\upsilon_\alpha}) C(1, 1, L_\gamma; -\mu_0, \mu_0) Y_{L_e}^{M_e}(\theta_e, \phi_e) \overline{Y}_{L_\gamma}^{M_\gamma}(\theta_n, \phi_n), \end{aligned} \tag{4.26}$$

where the $A^{L_\gamma,M_\gamma}_{L_e,M_e}(\omega,W_{\upsilon_\alpha})$ parameters are expressed through the dipole matrix elements (see [41, 47] for more details)

$$A^{L_\gamma,M_\gamma}_{L_e,M_e}(\omega,W_{\upsilon_\alpha}) = \sum_{\mu_a,\mu_b}\sum_{\ell_a,m_a}\sum_{\ell_b,m_b}(-1)^{m_b+\mu_a} i^{(\ell_b-\ell_a)} e^{i[\delta_{\ell_a}-\delta_{\ell_b}]} \overline{T}_{\alpha\upsilon_\alpha\ell_a m_a\mu_a E} T_{\alpha\upsilon_\alpha\ell_b m_b\mu_b E}$$
$$\times\sqrt{\frac{(2\ell_a+1)(2\ell_b+1)}{(2L_e+1)(2L_\gamma+1)}} C(\ell_a,\ell_b,L_e;m_a,-m_b) C(\ell_a,\ell_b,L_e;0,0) C(1,1,L_\gamma;-\mu_a,\mu_b). \tag{4.27}$$

Notice that $M_e = m_a - m_b$ and $M_\gamma = \mu_b - \mu_a$ restrict the m and μ values in the summations in Eq. (4.26). Eq. (4.26) is presented in the very convenient form: it is the product of a geometrical (two spherical functions) and a dynamical term (the parameters $A^{L_\gamma,M_\gamma}_{L_e,M_e}(\omega,W_{\upsilon_\alpha})$, that depend on the photon and final ion/electron energy). The Clebsch-Gordan coefficient in Eq. (4.26) can be written in the following form (see Table (C.1)):

$$C(1,1,L_\gamma;-\mu_0,\mu_0) = \begin{cases} \frac{(-1)^{1-\mu_0}}{\sqrt{3}}, & L_\gamma = 0 \\ \frac{-\mu_0}{\sqrt{2}}, & L_\gamma = 1 \\ \frac{(2-3\mu_0^2)}{\sqrt{6}}, & L_\gamma = 2 \end{cases} \tag{4.28}$$

So, from the previous relations it is clear that for linearly polarized light, ($\mu_0 = 0$), terms with $L_\gamma = 1$ do not contribute.

We can extract some restrictions in the values that the $A^{L_\gamma,M_\gamma}_{L_e,M_e}(\omega,W_{\upsilon_\alpha})$ can take, just considering the symmetry of our molecular system. If a molecular symmetry group contains a center of symmetry, then L_e has to be even. Indeed, due to inversion symmetry both initial and final state wave functions should have a definite parity, therefore in Eq. (4.27) both ℓ_a and ℓ_b should be either even or odd and from the Clebsch-Gordan coefficient it follows immediately that L_e is always even. As a consequence, for molecules having a center of inversion the term $Y^{M_e}_{L_e}(\hat{k}_e)$ can appear in the cross section only in even degrees. If a molecular symmetry group contains a plane of symmetry with the molecular axis in it (for definition we will suppose that if there are planes of symmetry, one of them coincides with the *yz*-plane of the molecular frame), then from the invariance of the dipole matrix element under reflection in this plane it follows that

$$T_{\alpha\upsilon_\alpha\ell_\alpha -m_{\ell_\alpha}-\mu E} = T_{\alpha\upsilon_\alpha\ell_\alpha m_{\ell_\alpha}\mu E}. \tag{4.29}$$

This equality leads also to some relation between the parameters $A^{L_\gamma,M_\gamma}_{L_e,M_e}$. To derive it, one should change the signs of all projections of momenta, and simultaneously also change the signs of all projections in all Clebsch-Gordan coefficients in Eq. (4.27) according to the standard rule. The result is

$$A^{L_\gamma,-M_\gamma}_{L_e,-M_e}(\omega,W_{\upsilon_\alpha}) = (-1)^{L_\gamma} A^{L_\gamma,M_\gamma}_{L_e,M_e}(\omega,W_{\upsilon_\alpha}). \tag{4.30}$$

As a consequence, in the particular case when all projections are equal to zero, $M_e = M_\gamma = 0$, the following relation is obtained:

$$A^{L_\gamma,0}_{L_e,0}(\omega,W_{\upsilon_\alpha}) = 0, \;\; \textit{if } L_\gamma \textit{ is odd}. \tag{4.31}$$

In particular, $A^{0,0}_{0,0}(\omega,W_{\upsilon_\alpha}) = \sum_{\mu,\ell,m}|T_{\ell m\alpha W_{\upsilon_\alpha}\mu}|^2/\sqrt{3}$.

Now we consider the general conclusions which can be drawn from the expression given by Eq. (4.27) for MFPAD. In the Hund's case (a) and (b)[3], which in the absence of rotation coincide,

[3] Hund's case (a) and (b) [15]:

projections of the angular momentum and spin on the molecular axis are conserved separately[4]. Denoting by Λ_0, Σ_0 and Λ_k, Σ_k the corresponding quantum numbers for the initial and final (ionic) states respectively, one obtains

$$\mu_a + \Lambda_0 = \Lambda_k + m_a, \;\; \Sigma_0 = \Sigma_k + s_a, \tag{4.32}$$

$$\mu_b + \Lambda_0 = \Lambda_k + m_b, \;\; \Sigma_0 = \Sigma_k + s_b, \tag{4.33}$$

Subtracting one line from another and combining with the conditions for the Clebsch-Gordan coefficients in Eq. (4.27) to be different from zero, one obtains,

$$M_e + M_\gamma = 0, \;\; M_s = 0. \tag{4.34}$$

For molecules without any plane of symmetry, and if they are optically active (chiral), that is, they have no S_n axis of symmetry, the condition given by Eq. (4.29) is not valid.

Making use of the relations given by Eq. (4.34) in the differential cross section given by Eq. (4.26), the following expression is obtained,

$$\begin{aligned}\frac{d\sigma_\alpha^{\mu_0}(\omega)}{d\Omega_n d\Omega_e dW_{\upsilon_\alpha}} = \;& \frac{4\pi^2\omega}{c}(-1)^{-\mu_0}\sum_{L_e}\sum_{L_\gamma,M_\gamma} A^{L_\gamma,M_\gamma}_{L_e,-M_\gamma}(\omega, W_{\upsilon_\alpha}) \\ & \times C(1,1,L_\gamma;-\mu_0,\mu_0) Y^{-M_\gamma}_{L_e}(\theta_e,\phi_e)\overline{Y}^{M_\gamma}_{L_\gamma}(\theta_n,\phi_n).\end{aligned} \tag{4.35}$$

We can make some considerations about the different values taken by the variables L_γ and M_γ. If linearly polarized light is considered lying in the z' direction, then $\mu_0 = 0$. For this case, the Clebsch-Gordan coefficient $C(1,1,L_\gamma;-\mu_0 = 0,\mu_0 = 0)$ imposes that L_γ must be an even number, so only the $L_\gamma = 0,2$ values are allowed (see Eq. (4.28)). Note that in the case where circularly polarized light is considered ($\mu_0 = \pm 1$), we do not have any restriction over the possible values that L_γ can take. Now, taking into account that $M_\gamma = -\mu_a + \mu_b$, and all the possible values of $\mu_{a,b}$ (-1, 0 and 1), the possible values for M_γ are -1, -2, 0, 1 and 2, as is shown in the Table (4.1). Therefore, the fully differential cross section given by Eq. (4.35) can be written as a sum of terms with different values of L_γ and M_γ:

1. *Hund's case (a): Strong spin coupling.* In Hund's case (a), the electronic angular momenta, both orbital L and spin S, are strongly coupled to the line joining the nuclei and interact very weakly with the rotation of the nuclei [48]. Therefore, their components along the internuclear axis, denoted Λ by and Σ, respectively, form Ω, the total electronic angular momentum about the internuclear axis, with quantum numbers $\Omega = |\Lambda + \Sigma|$, where $\Lambda = 1,2,3,\ldots,L$ and $\Sigma = S, S-1,\ldots,-S$. If Λ is not equal to zero, there are $2S+1$ multiplet components of a given electronic term. States with $\Lambda = 1,2,3,\ldots$ are denoted as Σ, Π, Δ, Φ, etc. Ω and the angular momentum of nuclear rotation R form the resultant total angular momentum J with quantum numbers $J = \Omega, \Omega+1, \Omega+2, \cdot$, resulting in the rotational structure of the multiplet subterm for given Λ and Σ. Therefore, in this case, the multiplet splitting of terms is larger than the rotational splitting.

2. *Hund's case (b): Weak spin coupling.* In Hund's case (b), the orbital angular momentum of the electrons is coupled to the internuclear axis, whereas the spin is either very weakly coupled to the axis or not coupled to it at all [48]. For instance, when $\Lambda = 0$, and $S \neq 0$, the spin is not coupled to the axis and, thus, Σ and Ω are not defined. In Hund's case (b), the orbital angular momentum Λ and the angular momentum of nuclear rotation form N, the total angular momentum excluding spin, with quantum numbers $N = \Lambda, \Lambda+1, \Lambda+2, \ldots$. If $\Lambda = 0$, the angular momentum N is identical with the rotational moment. Finally, the angular momenta N and S form a resultant J, the total angular momentum including spin, with quantum numbers $J = N+S, N+S-1, \ldots, |N-S|$. Thus, in general, each level with a given N consists of $2S+1$ multiplet components. Since the spin is now coupled to rotation, in this case, the rotational splitting of terms is larger than the multiplet splitting.

[4] In the Hund's case (c) only Ω, the projection of the total angular momentum $J = L + S$ on the molecular axis, is defined.

μ_a	-1	-1	-1	0	0	0	1	1	1
μ_b	-1	0	1	-1	0	1	-1	0	1
M_γ	0	-1	-2	1	0	-1	2	1	0

Table 4.1: Possible values of M_γ in terms of the values of μ_a and μ_b.

$$\begin{aligned}\frac{d\sigma_\alpha^{\mu_0}(\omega)}{d\Omega_n d\Omega_e dW_{\upsilon_\alpha}} &= \frac{4\pi^2\omega}{c}(-1)^{-\mu_0}\sum_{L_e}\sum_{L_\gamma,M_\gamma} C(1,1,L_\gamma;-\mu_0,\mu_0)A^{L_\gamma,M_\gamma}_{L_e,-M_\gamma}(\omega,W_{\upsilon_\alpha}) \\ &\times\ Y^{-M_\gamma}_{L_e}(\theta_e,\phi_e)Y^{M_\gamma}_{L_\gamma}(\beta,\alpha) \\ &\times\ \left[\delta_{L_\gamma,0}\delta_{M_\gamma,0}+\delta_{L_\gamma,1}\delta_{M_\gamma,0}+\delta_{L_\gamma,1}\delta_{M_\gamma,1}+\delta_{L_\gamma,1}\delta_{M_\gamma,-1}\right. \\ &\quad \left.+\,\delta_{L_\gamma,2}\delta_{M_\gamma,0}+\delta_{L_\gamma,2}\delta_{M_\gamma,1}+\delta_{L_\gamma,2}\delta_{M_\gamma,2}+\delta_{L_\gamma,2}\delta_{M_\gamma,-1}+\delta_{L_\gamma,2}\delta_{M_\gamma,-2}\right]\end{aligned} \tag{4.36}$$

Note that if we consider the condition imposed by the Eq. (4.31), the term $\delta_{L_\gamma,1}\delta_{M_\gamma,0}$ gives a zero contribution to the differential cross section. We can simplify the previous equation by making explicitly the sum of the terms with opposite M_γ value for the same L_γ value, i.e.,

$$\begin{aligned}\frac{d\sigma_\alpha^{\mu_0}(\omega)}{d\Omega_n d\Omega_e dW_{\upsilon_\alpha}} &= \frac{4\pi^2\omega}{c}(-1)^{-\mu_0}\sum_{L_e}\sum_{L_\gamma,M_\gamma} C(1,1,L_\gamma;-\mu_0,\mu_0)A^{L_\gamma,M_\gamma}_{L_e,-M_\gamma}(\omega,W_{\upsilon_\alpha}) \\ &\times\ Y^{-M_\gamma}_{L_e}(\theta_e,\phi_e)Y^{M_\gamma}_{L_\gamma}(\theta_n,\phi_n) \\ &\times\ \left[\delta_{L_\gamma,0}\delta_{M_\gamma,0}+\delta_{L_\gamma,2}\delta_{M_\gamma,0}+\overbrace{\delta_{L_\gamma,1}(\delta_{M_\gamma,1}+\delta_{M_\gamma,-1})}^{\mathcal{A}}\right. \\ &\quad \left.+\underbrace{\delta_{L_\gamma,2}(\delta_{M_\gamma,1}+\delta_{M_\gamma,-1})}_{\mathcal{B}}+\underbrace{\delta_{L_\gamma,2}(\delta_{M_\gamma,2}+\delta_{M_\gamma,-2})}_{\mathcal{C}}\right]\end{aligned} \tag{4.37}$$

The sums designated as $\mathcal{A}$, $\mathcal{B}$ and $\mathcal{C}$ can be performed explicitly making use of Eqs. (4.30) and (B.46). As an example, we proceed with the term $\mathcal{B}$, since the same steps can be followed for the other two. This term can be written as:

$$\begin{aligned}\mathcal{B} &= (-1)^{M_\gamma}A^{L_\gamma,M_\gamma}_{L_e,-M_\gamma}(\omega,W_{\upsilon_\alpha}) \\ &\times\left[\overline{Y}^{M_\gamma}_{L_e}(\theta_e,\phi_e)Y^{M_\gamma}_{L_\gamma}(\theta_n,\phi_n)+(-1)^{L_\gamma}Y^{M_\gamma}_{L_e}(\theta_e,\phi_e)\overline{Y}^{M_\gamma}_{L_\gamma}(\theta_n,\phi_n)\right]\delta_{L_\gamma,2}\delta_{M_\gamma,1}.\end{aligned} \tag{4.38}$$

In order to perform the sum of the spherical harmonics we can make use of the explicit expression in terms of the Legendre polynomials given by Eq. (B.42)

$$\begin{aligned}\mathcal{B} &= (-1)^{M_\gamma}\sqrt{\frac{2L_e+1}{4\pi}\frac{(L_e-M_\gamma)!}{(L_e+M_\gamma)!)}}\sqrt{\frac{2L_\gamma+1}{4\pi}\frac{(L_\gamma-M_\gamma)!}{(L_\gamma+M_\gamma)!)}}P^{M_\gamma}_{L_\gamma}(\cos\theta_n)P^{M_\gamma}_{L_e}(\cos\theta_e) \\ &\times A^{L_\gamma,M_\gamma}_{L_e,-M_\gamma}(\omega,W_{\upsilon_\alpha})\left[\exp\{-iM_\gamma(\phi_e-\phi_n\}+(-1)^{L_\gamma}\exp\{iM_\gamma(\phi_e-\phi_n)\}\right]\delta_{L_\gamma,2}\delta_{M_\gamma,1}.\end{aligned} \tag{4.39}$$

For an even value of L_γ the sum in the previous equation gives a term $2\cos(M_\gamma(\phi_e-\phi_n))$ while for an odd value we obtain a term equal to $(-2i)\sin(M_\gamma(\phi_e-\phi_n))$. Therefore, Eq. (4.36) can be expressed as,

$$\begin{aligned}\frac{d\sigma_\alpha^{\mu_0}(\omega)}{d\Omega_n d\Omega_e dW_{\upsilon_\alpha}} &= \frac{4\pi^2\omega}{c}(-1)^{-\mu_0}\sum_{L_e}\sum_{L_\gamma,M_\gamma} C(1,1,L_\gamma;-\mu_0,\mu_0)\, f_{L_e,-M_\gamma}^{L_\gamma,M_\gamma}(\omega,W_{\upsilon_\alpha}) \\ &\times \Big\{\left[\delta_{L_\gamma,0}\delta_{M_\gamma,0}+\delta_{L_\gamma,2}(\delta_{M_\gamma,0}+\delta_{M_\gamma,1}+\delta_{M_\gamma,2})\right]\cos(M_\gamma(\phi_e-\phi_n)) \\ &+ \left[\delta_{L_\gamma,1}\delta_{M_\gamma,1}\right]\sin(M_\gamma(\phi_e-\phi_n))\Big\} P_{L_\gamma}^{M_\gamma}(\cos\theta_n), \end{aligned} \tag{4.40}$$

where the $f_{L_e,-M_\gamma}^{L_\gamma,M_\gamma}(\omega,W_{\upsilon_\alpha})$ function is defined as

$$\begin{aligned} f_{L_e,-M_\gamma}^{L_\gamma,M_\gamma}(\omega,W_{\upsilon_\alpha}) &= \frac{2(-i)^{\delta_{L_\gamma,1}\delta_{M_\gamma,1}}\times(-1)^{M_\gamma}}{(1+\delta_{M_\gamma,0})} A_{L_e,-M_\gamma}^{L_\gamma,M_\gamma}(\omega,W_{\upsilon_\alpha}) P_{L_e}^{M_\gamma}(\cos\theta_e) \\ &\times \sqrt{\frac{2L_e+1}{4\pi}\frac{(L_e-M_\gamma)!}{(L_e+M_\gamma)!)}}\sqrt{\frac{2L_\gamma+1}{4\pi}\frac{(L_\gamma-M_\gamma)!}{(L_\gamma+M_\gamma)!)}}. \end{aligned} \tag{4.41}$$

Taking into account the Kronecker's deltas present in the previous equation, the molecular frame fully differential cross section[5] can be expressed by a simple parametrization of four functions[6],

$$\begin{aligned}\frac{d\sigma_\alpha^{\mu_0=0}(\omega)}{d\Omega_n d\Omega_e dW_{\upsilon_\alpha}} &= F_{00}^0(\omega,W_{\upsilon_\alpha},\theta_e)+F_{20}^0(\omega,W_{\upsilon_\alpha},\theta_e)P_2^0(\cos\theta_n) \\ &+ F_{21}^0(\omega,W_{\upsilon_\alpha},\theta_e)P_2^1(\cos\theta_n)\cos(\phi_e-\phi_n) \\ &+ F_{22}^0(\omega,W_{\upsilon_\alpha},\theta_e)P_2^2(\cos\theta_n)\cos(2[\phi_e-\phi_n]), \end{aligned} \tag{4.42}$$

for linearly polarized light, and five functions

$$\begin{aligned}\frac{d\sigma_\alpha^{\mu_0=\pm1}(\omega)}{d\Omega_n d\Omega_e dW_{\upsilon_\alpha}} &= F_{00}^1(\omega,W_{\upsilon_\alpha},\theta_e)+F_{20}^1(\omega,W_{\upsilon_\alpha},\theta_e)P_2^0(\cos\theta_n) \\ &\pm F_{11}^1(\omega,W_{\upsilon_\alpha},\theta_e)P_1^1(\cos\theta_n)\sin(\phi_e-\phi_n) \\ &+ F_{21}^1(\omega,W_{\upsilon_\alpha},\theta_e)P_2^1(\cos\theta_n)\cos(\phi_e-\phi_n) \\ &+ F_{22}^1(\omega,W_{\upsilon_\alpha},\theta_e)P_2^2(\cos\theta_n)\cos(2[\phi_e-\phi_n]), \end{aligned} \tag{4.43}$$

for circularly polarized light, where we have written $F_{11}^1(W_{\upsilon_\alpha},\theta_e)=F_{11}^{\pm1}(W_{\upsilon_\alpha},\theta_e)$, where the positive sign holds for circularly polarized light with positive helicity, $\mu_0=1$, and the minus sign for circularly polarized light with negative helicity, $\mu_0=-1$. Fig. (4.2) shows the reference system

[5] Note that, the sign of the F_{21} and F_{11} functions could depend on the Condon-Shortly factor that appears in the definition of the Legendre polynomials (see Appendix B). On the other hand the fully differential cross section given by Eqs. (4.42) and (4.43) does not depend on this factor.

[6] See [44] for a discussion of "the electron frame photoion angular distribution" and its relation with the $F_{L,N}$ presented in Eq. (4.42).

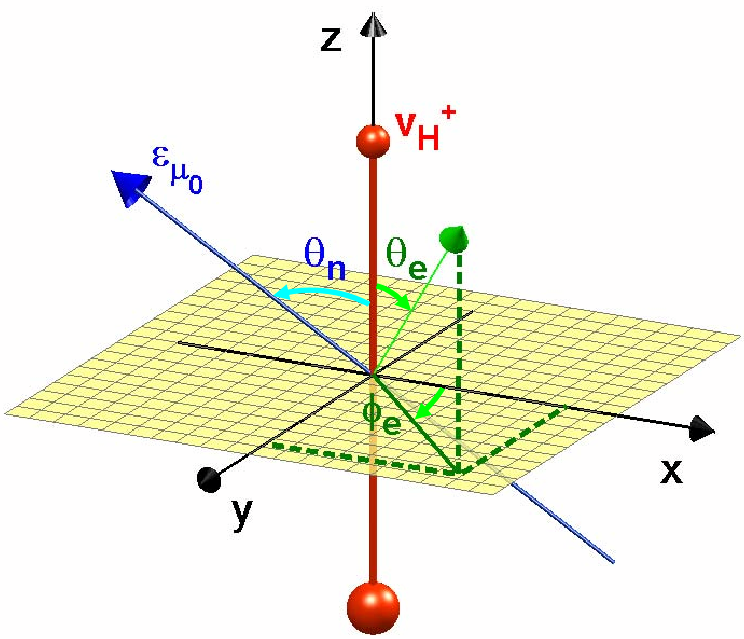

Figure 4.2: Relevant angles in the spatial analysis of the MFPAD. The red vertical bar represents the molecule, where the upper small sphere represents the ion and the lower sphere the residual atom.

used where the description of the polar angles defined in Eqs. (4.42) and (4.43). The $F_{LN}^{\mu_0}(\omega, W_{\upsilon_\alpha}, \theta_e)$ functions are expanded in terms of Legendre polynomials:

$$F_{LN}^{\mu_0}(\omega, W_{\upsilon_\alpha}, \theta_e) = \sum_{L'} C_{L'LN}^{\mu_0}(\omega, W_{\upsilon_\alpha}) P_{L'}^{N}(\cos\theta_e), \tag{4.44}$$

with

$$\begin{aligned} C_{L'LN}^{\mu_0}(\omega, W_{\upsilon_\alpha}) &= \frac{2\pi\omega}{c} \frac{(-1)^N (-i)^{\delta_{L,1}\delta_{N,1}}}{(1+\delta_{N,0})} \sum_{\mu_a,\mu_b} \sum_{\ell_a,m_a} \sum_{\ell_b,m_b} (-1)^{m_b+\mu_a-\mu_0} \\ &\times \sqrt{\frac{(2\ell_a+1)(2\ell_b+1)(L'-N)!(L-N)!}{(L'+N)!(L+N)!}} \\ &\times i^{(\ell_b-\ell_a)} e^{i[\hat{\sigma}_{\ell_a}-\hat{\sigma}_{\ell_b}]} \overline{T}_{\alpha\upsilon_\alpha\ell_a m_a\mu_a E} T_{\alpha\upsilon_\alpha\ell_b m_b\mu_b E} \\ &\times C(\ell_a,\ell_b,L';0,0) C(\ell_a,\ell_b,L';m_a,-m_b) \\ &\times C(1,1,L;-\mu_a,\mu_b) C(1,1,L;-\mu_0,\mu_0), \end{aligned} \tag{4.45}$$

where we have taken into account the explicit form of the $A_{L_e,-M_\gamma}^{L_\gamma,M_\gamma}(\omega, W_{\upsilon_\alpha})$ functions and we have replaced $L_e \to L'$, $L_\gamma \to L$ and $M_\gamma \to N$. Note that in the previous equation, the dependence with the photon energy ω is contained in the the total energy $E = \omega + W_{i\nu}$, where $W_{i\nu}$ is the total energy of the molecule in the electronic state i and in the vibrational state ν. The index N is limited by the restrictions imposed by the Clebsch-Gordan coefficients, i.e., $N = -m_a + m_b = -\mu_a + \mu_b$. The Clebsch-Gordan coefficient $C(\ell_a,\ell_b,L';0,0)$ is different from zero if and only if the sum $\ell_a+\ell_b+L'$ takes an even value (see Appendix C), and this fact ensures that the expansion given by Eq. (4.44) posses a well defined parity if the contribution of the different ionization threshold can be resolved.

The $(L'-N)!$ and $(L-N)!$ terms present in Eq. (4.45), restrict the value of L' and L to values equal or greater than N, that is consequence of the expansion given by Eq. (4.44), since the Legendre polynomial implies that $L' > N$. Since there exists a simple relation in Clebsch-Gordan coefficient $C(1,1,L;-\mu_0,\mu_0)$ for $\mu_0 = 0$ and $\mu = \mp 1$:

$$C(1,1,L;-\mu_0=0,\mu_0=0) = (-1)^{\delta_{L,0}}(1+\delta_{L,2})^{-1}C(1,1,L;-\mu_0=\pm 1,\mu_0=\mp 1) \tag{4.46}$$

for $L = 0,2$ (see for example Table (C.1)), and due to the presence of the term $(-1)^{\mu_0}$ in Eq. (4.45), is easy to show that the $F_{LN}^{\mu_0=0}$ and $F_{LN}^{\mu_0=\pm 1}$ functions follow the relations:

$$F_{00}^{1} = F_{00}^{0}, \tag{4.47}$$

$$F_{20}^{1} = -0.5 \times F_{20}^{0}, \tag{4.48}$$

$$F_{21}^{1} = -0.5 \times F_{21}^{0} \tag{4.49}$$

and

$$F_{22}^{1} = -0.5 \times F_{22}^{0}. \tag{4.50}$$

So the fully differential cross section for circularly polarized light can be also written in terms of the F_{LN}^{0} functions that characterize the process for linearly polarized light:

$$\begin{aligned}\frac{d\sigma_\alpha^{\mu_0=\pm 1}(\omega)}{d\Omega_n d\Omega_e dW_{\upsilon_\alpha}} &= F_{00}^{0}(\omega,W_{\upsilon_\alpha},\theta_e) - \frac{1}{2}F_{20}^{0}(\omega,W_{\upsilon_\alpha},\theta_e)P_2^0(\cos\theta_n) \\ &\pm F_{11}^{1}(\omega,W_{\upsilon_\alpha},\theta_e)P_1^1(\cos\theta_n)\sin(\phi_e-\phi_n) \\ &- \frac{1}{2}F_{21}^{0}(\omega,W_{\upsilon_\alpha},\theta_e)P_2^1(\cos\theta_n)\cos(\phi_e-\phi_n) \\ &- \frac{1}{2}F_{22}^{0}(\omega,W_{\upsilon_\alpha},\theta_e)P_2^2(\cos\theta_n)\cos(2[\phi_e-\phi_n])\end{aligned} \tag{4.51}$$

where $F_{11}^{1}(\omega,W_{\upsilon_\alpha},\theta_e) = F_{11}^{\pm 1}(\omega,W_{\upsilon_\alpha},\theta_e)$.

So, we have found the desired expression for the fully differential cross section that depends on: The photon energy, ω, the vibrational energy, W_{υ_α}, the two incident polarization angles, θ_n and ϕ_n, and the two electron emission angles, θ_e and ϕ_e. These fully differential cross sections given by Eqs. (4.42) and (4.43) were used for the first time by D. Dowek and coworkers in a series of articles devoted to study the electron angular distribution of different diatomic molecules (see for example [46, 49, 50, 51]). As was shown in these experimental-theoretical results, the great advantage of this parametrization of the fully differential cross section is the easy way of comparing theory with experiment through the $F_{L,N}$'s functions. This provides the possibility of getting additional information of the different physical processes that characterizes the ionization process, since the direct comparison of the 3D electron angular distributions can be a very difficult task. This parametrization also gives access to the azimuthal angular dependence, separated from the polar angular, so the interpretation, and the following comparison with the theoretical results, can be performed quite easily. On the other hand, the polarization vector (linear or circularly polarized light) can be fixed for the desired orientation, so the experimental conditions can be reproduced quite easily, which is a great advantage in comparison with the results obtained in Section 4.3.1, where the results were restricted for a parallel or perpendicular orientation of the polarization vector with respect to the molecular axis.

4.4 Ion angular distribution

Let's study now the angular distribution of the ionic fragments coming from the dissociative process of homonuclear diatomic molecules. For the initial state Σ_g^+, the total symmetry for the ionic core plus the photoelectron can be either Σ_u^+ or Π_u in the dipole approximation. The branching ratios to these two states in the ionization processes are directly reflected in the angular distribution of the ions. This branching ratios cannot be obtained from the electron-energy spectrum owing to degeneracy; and the photoelectron angular distribution yields an implicit function of both the branching ratio and the relative phases of the alternative ionization channels form which the branching ratio cannot be isolated without further information. But what is more important, is that the observation direction of the photoions can be equated to the orientation of the internuclear axis at the time of photoionization.

As we have pointed out before, Eq. (4.19) gives the general expression for the fully differential cross section in terms of the orientation of the molecule and the electron emission angles. All the dependence of the electron ejection direction in the molecular frame, is found in the spherical harmonics $Y_{L_e}^{M_e}(\theta_e,\phi_e)$. Since in this case the electron angular distribution is not resolved, these variables must be integrated. This integration can be carried out making use of Eq. (B.43),

$$\int Y_{L_e}^{M_e}(\theta_e,\phi_e)\mathrm{d}\Omega_e = (4\pi)^{1/2}\delta_{M_e,0}\delta_{L_e,0}\,.$$

Taking into account the previous equation and Eq. (C.79), that reflects the cylindrical symmetry of the dipole interaction[7], and evaluating the Clebsch-Gordan coefficients $C(\ell_a,\ell_a,0;-m_a,m_a) = (-1)^{(\ell_a+m_a)}(2\ell_a+1)^{-1/2}$ and $C(\ell_a,\ell_a,0;0,0) = (-1)^{\ell_a}(2\ell_a+1)^{-1/2}$ by means of Eq. (C.24), the differential cross section given by Eq. (4.19) takes the following form:

$$\begin{aligned}\frac{\mathrm{d}\sigma_\alpha^{\mu_0}(\omega)}{\mathrm{d}\Omega_n \mathrm{d}W_{\upsilon_\alpha}} &= \int \frac{\mathrm{d}\sigma_\alpha^{\mu_0}(\omega)}{\mathrm{d}\Omega_n \mathrm{d}\Omega_e \mathrm{d}W_{\upsilon_\alpha}} \sin\theta_e \mathrm{d}\theta_e \mathrm{d}\phi_e = \\ &\frac{4\pi^2\omega}{c}\sum_{\mu_a,\mu_b}\sum_{\ell_a,m_a}(-1)^{\mu_a-\mu_0}\overline{T}_{\alpha\upsilon_\alpha\ell_a m_a\mu_a E}T_{\alpha\upsilon_\alpha\ell_a m_a\mu_b E} \\ &\times\sum_{L_\gamma=0}^{2} C(1,1,L_\gamma;-\mu_a,\mu_b)C(1,1,L_\gamma;-\mu_0,\mu_0)\sqrt{\frac{4\pi}{(2L_\gamma+1)}}\overline{Y}_{L_\gamma}^{M_\gamma}(\theta_n,\phi_n),\end{aligned} \tag{4.52}$$

where we have made use of the triangular condition on the Clebsch-Gordan coefficients, that implies $m_a = m_b$ and $\ell_a = \ell_b$ (since $L_e = 0$ and $M_e = 0$).

As we have pointed out in the previous sections, the orientation of the target is specified by $\hat{R}_{\hat{M}}$, the set of Euler angles which carry the laboratory-frame coordinate system into coincidence with the target-frame system. As in the previous sections, the laboratory frame z' axis is taken as the polarization axis for linear polarization and the propagation direction for circular polarization, and the frame is therefore cylindrically symmetric around z'. Thus, the final Euler rotation, through γ about this axis, is mute and γ may set equal to zero. But the differential cross section given by Eq. (4.19) expresses the orientation of the polarization vector with respect to the molecular-frame system, $\hat{R}_{\hat{n}}$, so making use of the inverse of this transformation given by Eq. (4.11), the relation between the spherical harmonics $Y_{L_\gamma}^{M_\gamma}(\theta_n,\phi_n)$ expressed in terms of the spherical harmonics in the

[7] As we have pointed out before, in this Thesis we will make use of the notation $\overline{Y}_l^m(\theta,\phi)$ to express the complex conjugate of the spherical harmonic functions. This notation must not be mixed up with the definition of the unnormalized spherical harmonics that appears in [43].

laboratory frame polar angles of the target is obtained,

$$\overline{Y}_{L_\gamma}^{M_\gamma}(\theta_n,\phi_n)=\overline{Y}_{L_\gamma}^{M_\gamma}(-\beta_M,-\alpha_M)=(-1)^{M_\gamma}Y_{L_\gamma}^{M_\gamma}(\theta_M,\phi_M). \tag{4.53}$$

Making use of Eq. (4.53) and the replacements $L_\gamma \to L$ and $M_\gamma \to M$, the cross section given by Eq. (4.52) can be expressed as:

$$\frac{d\sigma_\alpha^{\mu_0}(\omega)}{d\Omega_M dW_{\upsilon_\alpha}}=\frac{\pi\omega}{c}\sum_{L=0}^{2}Z_{L,M}^{\mu_0}(\omega,W_{\upsilon_\alpha})\sqrt{\frac{4\pi}{(2L_\gamma+1)}}\overline{Y}_L^M(\theta_M,\phi_M). \tag{4.54}$$

In the previous equation the integration over the third Euler angle γ has been performed, giving a 4π factor in the right part of this equation. The $Z_{L,M}^{\mu_0}(\omega,W_{\upsilon_\alpha})$ functions are given by

$$\begin{aligned}Z_{L,M}^{\mu_0}(\omega,W_{\upsilon_\alpha}) &= (-1)^{-\mu_0}C(1,1,L;-\mu_0,\mu_0)\\ &\times \sum_{\mu_a,\mu_b}\sum_{\ell_a,m_a}(-1)^{\mu_b}\overline{T}_{\alpha\upsilon_\alpha\ell_a m_a\mu_a}T_{\alpha\upsilon_\alpha\ell_a m_a\mu_b}C(1,1,L;-\mu_a,\mu_b).\end{aligned} \tag{4.55}$$

with $M=-\mu_a+\mu_b$. The key features of Eq. (4.54) are the following:

1. There is no interference between ionization amplitudes with alternative orbital momenta ℓ and projection m on the molecular axis, in contrast with the photoelectron angular distribution, both for randomly distributed molecules or in the case of fixed-in-space ones.

2. The maximum harmonic dependence is second order (L), so that the photofragment angular distribution can be relatively easily characterized experimentally.

Since observation direction coincides with the internuclear axis, the molecular frame coincides with the molecule, and, therefore $M=0$. This implies $\mu_a=\mu_b$, and that all nondiagonal terms in μ_a vanish in Eq. (4.55) (see Eq. (4.20)):

$$\frac{d\sigma_\alpha^{\mu_0}(\omega)}{d\Omega_M dW_{\upsilon_\alpha}}=\frac{\pi\omega}{c}\sum_{L=0}^{2}Z_{L,0}^{\mu_0}(\omega,W_{\upsilon_\alpha})P_L(\cos\theta_M), \tag{4.56}$$

where we have used Eq. (B.45). The symmetry properties of the dipole matrix elements given by Eq. (4.29) and the properties of the Clebsch-Gordan coefficients given by Eqs. (C.12), (C.13) and (C.14) imply that the odd term $Z_{1,0}^{\mu_0}(\omega,W_{\upsilon_\alpha})$ vanishes. Therefore, the ion angular distribution takes the form:

$$\frac{d\sigma_\alpha^{\mu_0}(\omega)}{d\Omega_M dW_{\upsilon_\alpha}}=\frac{\pi\omega}{c}\left[Z_{0,0}^{\mu_0}(\omega,W_{\upsilon_\alpha})+Z_{2,0}^{\mu_0}(\omega,W_{\upsilon_\alpha})P_2(\cos\theta_M)\right]. \tag{4.57}$$

The first coefficient $Z_{0,0}^{\mu_0}(\omega,W_{\upsilon_\alpha})$ can be easily obtained making use of the Eq. (C.24) in both Clebsch-Gordan coefficients present in Eq. (4.55):

$$Z_{0,0}^{\mu_0}(\omega,W_{\upsilon_\alpha})=\frac{1}{3}\sum_{\mu_a}\sum_{\ell_a,m_a}\overline{T}_{\alpha\upsilon_\alpha\ell_a m_a\mu_a E}T_{\alpha\upsilon_\alpha\ell_a m_a\mu_a E}. \tag{4.58}$$

The second coefficient $Z_{2,0}^{\mu_0}(\omega,W_{\upsilon_\alpha})$ can be obtained making use of the Eq. (C.26):

$$\begin{aligned}&Z_{2,0}^{\mu_0}(\omega,W_{\upsilon_\alpha})=\\ &\frac{2}{3}\frac{(-1)^{-\mu_0}}{(1+\mu_0)!(1-\mu_0)!}\sum_{\mu_a}\sum_{\ell_a,m_a}\overline{T}_{\alpha\upsilon_\alpha\ell_a m_a\mu_a E}T_{\alpha\upsilon_\alpha\ell_a m_a\mu_a E}\frac{(-1)^{-m_a}}{(1+m_a)!(1-m_a)!}\\ &=\frac{1}{3}\frac{(2-3\mu_0^2)}{2}\sum_{\mu_a}\sum_{\ell_a,m_a}(2-3m_a^2)\overline{T}_{\alpha\upsilon_\alpha\ell_a m_a\mu_a E}T_{\alpha\upsilon_\alpha\ell_a m_a\mu_a E}.\end{aligned} \tag{4.59}$$

The $Z^{\mu_0}_{0,0}(\omega, W_{\upsilon_\alpha})$ coefficient gives access to the total cross section, while $Z^{\mu_0}_{2,0}(\omega, W_{\upsilon_\alpha})$ gives the relative importance of the $\Sigma \rightarrow \Sigma$ transition with respect to the $\Sigma \rightarrow \Pi$ one. The coefficients $Z^{\mu_0}_{0,0}(\omega, W_{\upsilon_\alpha})$ and $Z^{\mu_0}_{2,0}(\omega, W_{\upsilon_\alpha})$ defined in Eqs. (4.58) and (4.59) can be rewritten as,

$$Z^{\mu_0}_{0,0}(\omega, W_{\upsilon_\alpha}) = \frac{1}{3}\sum_{\ell}\left(D^2_{\Sigma}(\omega, W_{\upsilon_\alpha}) + 2D^2_{\Pi}(\omega, W_{\upsilon_\alpha})\right), \tag{4.60}$$

and

$$Z^{\mu_0}_{2,0}(\omega, W_{\upsilon_\alpha}) = \frac{1}{3}\frac{(2-3\mu_0^2)}{2}\sum_{\ell_a} 2\left(D^2_{\Sigma}(\omega, W_{\upsilon_\alpha}) - D^2_{\Pi}(\omega, W_{\upsilon_\alpha})\right), \tag{4.61}$$

where the following functions has been defined:

$$D^2_{\Sigma}(\omega, W_{\upsilon_\alpha}) = \sum_{\ell}\left|T_{\alpha\upsilon_\alpha\ell m=0\mu=0E}\right|^2 \tag{4.62}$$

and

$$D^2_{\Pi}(\omega, W_{\upsilon_\alpha}) = \sum_{\ell}\left|T_{\alpha\upsilon_\alpha\ell m=\pm1\mu=\pm1E}\right|^2. \tag{4.63}$$

Therefore, the differential cross section given by Eq. (4.57) can be now written in the common form

$$\begin{aligned}\frac{d\sigma^{\mu_0}_{\alpha}(\omega)}{d\Omega_M dW_{\upsilon_\alpha}} &= \frac{\pi\omega}{3c}\left[(D^2_{\Sigma}+2D^2_{\Pi}) + \frac{(2-3\mu_0^2)}{2}2(D^2_{\Sigma}-D^2_{\Pi})P_2(\cos\theta_M)\right] \\ &= \frac{\sigma^{\mu_0}(\omega, W_{\upsilon_\alpha})}{4\pi}\left[1+\beta^{\mu_0}_M(\omega, W_{\upsilon_\alpha})P_2(\cos\theta_M)\right],\end{aligned} \tag{4.64}$$

with

$$\sigma^{\mu_0}(\omega, W_{\upsilon_\alpha}) = \frac{4\pi^2\omega}{3c}(D^2_{\Sigma}+2D^2_{\Pi}) \tag{4.65}$$

and

$$\beta^{\mu_0}_M(\omega, W_{\upsilon_\alpha}) = \frac{(2-3\mu_0^2)}{2}\frac{2(D^2_{\Sigma}-D^2_{\Pi})}{D^2_{\Sigma}+2D^2_{\Pi}}, \tag{4.66}$$

and where θ_M is the angle of the molecular-fragment direction relative to the electric vector of the light, $\sigma_{tot}(\omega, W_{\upsilon_\alpha})$ is the integrated total cross section and $\beta_M(\omega, W_{\upsilon_\alpha})$ is the so called *ion beta parameter*. Since the cross section must be a positive quantity, the term $\left[1+\beta^{\mu_0}_M(\omega, W_{\upsilon_\alpha})P_2(\cos\theta_M)\right]$ in Eq. (4.64) must be greater than or equal to zero, which implies that $\beta^{\mu_0}_M(\omega, W_{\upsilon_\alpha})P_2(\cos\theta_M) \geqslant -1$, and since the Legendre polynomial, $P_2(\cos\theta_M)$, oscillates between the values -0.5 and 1 (see Fig. (B.1) of Appendix B), the ion beta parameter is limited to the values $-1 \leqslant \beta^{\mu_0}_M \leqslant 2$.

As we have pointed out before, the knowledge of the ion beta parameter gives access to the relative contribution of the different transitions, so, for example, making use of Eq. (4.66) for linearly polarized light, the the following conclusions can be extracted:

$$\beta^{\mu_0=0}_M(\omega, W_{\upsilon_\alpha}) = \begin{cases} -1 & \Rightarrow \quad D_{\Sigma} = 0 \\ 0 & \Rightarrow \quad D_{\Sigma} = D_{\Pi} \\ 1 & \Rightarrow \quad D_{\Sigma} = 2D_{\Pi} \\ 2 & \Rightarrow \quad D_{\Pi} = 0 \end{cases} \tag{4.67}$$

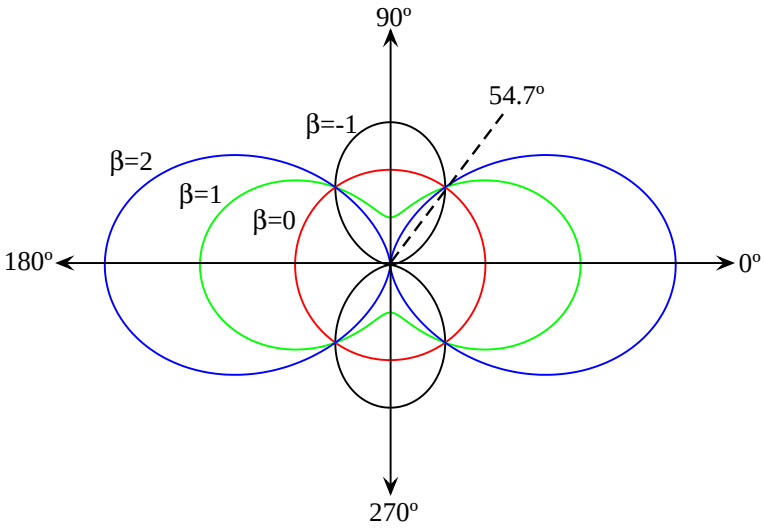

Figure 4.3: Ion angular distribution for different values of the asymmetry parameter β_M, in the $\phi_M = 0$ plane.

Fig. (4.3) displays the ion angular distribution for $\beta_M^{\mu_0=0} = -1$, 0, 1 and 2. For $\beta_M^{\mu_0} = 0$ the angular distribution is completely isotropic, that can be explained by the definition given by Eq. (4.66), since for this value the contribution of both symmetries are equal to each other. For positive values, $\beta_M^{\mu_0} = 1$ and 2, the ion is ejected following the vector polarization, which is consequence of the fact that the Σ transition is more relevant than the Π one, while for negatives values of the beta parameter, $\beta_M^{\mu_0} = -1$, the ion is ejected perpendicular to the polarization vector, since in this case the Π transition dominates the process. There is an angle at which the ion angular distribution takes the same value independently of the value of the ion beta parameter. This angle is known as the "magic angle" and it makes the Legendre polynomial $P_2(\cos\theta_M)$ equal to zero, which implies that $\theta_{mag} = \arccos(1/\sqrt{3}) = 54.7^\circ$ (see Appendix B). The relation between the beta parameter obtained with linearly polarized light ($\mu_0 = 0$) and for circularly polarized light ($\mu_0 = \pm 1$) can be obtained directly looking at the Eq. (4.66): $\beta_M^1 = -0.5 \times \beta_M^0$. Note that the ion beta parameter is independent of the helicity of the circularly polarized light, so, the circular dichroism presented in the case of the electron angular distribution for fixed-in-space molecule, that will be studied in Chapter 9, can not be observed in this case.

When the nuclear motion is included, for each initial photon energy the total cross section and the beta parameter depend on the final ion energy, but if this dependence is not resolved, the differential cross section must be integrated over this variable leading to the following expression:

$$\frac{d\sigma_\alpha^{\mu_0}(\omega)}{d\Omega_M} = \frac{\sigma_{\alpha,tot}^{\mu_0}(\omega)}{4\pi}\left[1 + \beta_{M,\alpha}^{\mu_0,Int}(\omega)P_2(\cos\theta_M)\right], \tag{4.68}$$

where

$$\beta_{M,\alpha}^{\mu_0,Int}(\omega) = \frac{\beta_{M,\alpha}^{\mu_0}(\omega)}{\sigma_{\alpha,tot}^{\mu_0}(\omega)}, \tag{4.69}$$

and $\beta_{M,\alpha}^{\mu_0}(\omega)$ and $\sigma_{\alpha,tot}^{\mu_0}(\omega)$ are given by

$$\beta_{M,\alpha}^{\mu_0}(\omega) = \sum\!\!\!\!\!\!\int \beta_M^{\mu_0}(\omega, W_{\upsilon_\alpha})\sigma^{\mu_0}(\omega, W_{\upsilon_\alpha})dW_{\upsilon_\alpha}, \tag{4.70}$$

and

$$\sigma^{\mu_0}_{\alpha,tot}(\omega) = \sum\!\!\!\!\!\!\int \sigma(\omega, W_{\upsilon_\alpha}) dW_{\upsilon_\alpha}, \tag{4.71}$$

where $\sum\!\!\!\!\!\!\int$ represents a sum over the final vibrational states and/or an integration over the continuum vibrational states. Note that for the dissociative ionization processes, only the integration contributes to the total ion beta parameter.

In the case where several final ionization thresholds are accessible for a given photon energy, but not resolved, the differential cross section takes the form:

$$\begin{aligned}\frac{d\sigma^{\mu_0}(\omega)}{d\Omega_M dW_{\upsilon_\alpha}} &= \frac{1}{4\pi}\left[\sum_\alpha \sigma^{\mu_0}_\alpha(\omega, W_{\upsilon_\alpha})\right] \\ &\times \left[1 + \frac{\left[\sum_\alpha \beta^{\mu_0}_{M,\alpha}(\omega, W_{\upsilon_\alpha})\sigma^{\mu_0}_\alpha(\omega, W_{\upsilon_\alpha})\right]}{\left[\sum_\alpha \sigma^{\mu_0}_\alpha(\omega, W_{\upsilon_\alpha})\right]} P_2(\cos\theta_M)\right].\end{aligned} \tag{4.72}$$

where α runs over the final ionization thresholds. If the ion energy dependence is not observed, and several final ionization paths are accessible but not resolved, the preceding equation have to be substituted by:

$$\frac{d\sigma^{\mu_0}(\omega)}{d\Omega_M} = \frac{1}{4\pi}\left[\sum_\alpha \sigma^{\mu_0}_{\alpha,tot}(\omega)\right] \times \left[1 + \frac{\sum_\alpha \beta^{\mu_0}_{M,\alpha}(\omega)}{\sum_\alpha \sigma^{\mu_0}_{\alpha,tot}(\omega)} P_2(\cos\theta_M)\right]. \tag{4.73}$$

Therefore, the previous equations reflect specific experimental conditions that we have to take into account in order to compare our numerical results.

4.5 Photoelectron angular distribution for randomly distributed molecules

The rotational averaging of the photoionization cross section has been discussed elsewhere [10, 52, 53, 54], since this has been the common method used in the experimental setups until quite recently. The angular distribution of the photoelectrons emitted by a randomly oriented set of molecules is, in general, correlated with the polarization and propagation direction of the incident light. The photoionization cross section for randomly-oriented molecules is obtained from Eq. (4.19) by:

- Expressing the dependence on the molecule-frame ejection direction k_e in terms of the laboratory-frame ejection direction k'_e using the rotational matrix properties.
- Averaging over all orientations of the molecule in the laboratory frame.

Therefore, from the fully differential cross section given by Eq. (4.19), and expressing the electron orientation, given by the spherical harmonic function $Y^{M_e}_{L_e}(\theta_e, \phi_e)$, in terms of the coordinates in laboratory frame by the Wigner rotational matrices,

$$Y^{M_e}_{L_e}(\theta_e, \phi_e) = \sum_\mu D^{L_e}_{\mu,M_e}(-\gamma, -\beta, -\alpha) Y^\mu_{L_e}(\theta'_e, \phi'_e), \tag{4.74}$$

and taking into account Eq. (C.79) in the spherical harmonic $\overline{Y}^{M_\gamma}_{L_\gamma}(\theta_n, \phi_n)$, it is possible to write the dependence of the orientation of the ejected electron and the orientation of the molecule both with

respect to the laboratory reference system:

$$\begin{aligned}\frac{d\sigma_\alpha^{\mu_0}(\omega)}{d\Omega_n d\Omega'_e d\varepsilon_\alpha} &= \frac{4\pi^2\omega}{c\sqrt{4\pi}}\sum_{\mu_a,\mu_b}\sum_{\ell_a,m_a}\sum_{\ell_b,m_b} i^{(\ell_b-\ell_a)}e^{i[\hat{\sigma}_{\ell_a}-\hat{\sigma}_{\ell_b}]}(-1)^{m_b+\mu_a-\mu_0}\\ &\times \sqrt{(2\ell_a+1)(2\ell_b+1)}\overline{T}_{\alpha\upsilon_\alpha\ell_a m_a\mu_a E}T_{\alpha\upsilon_\alpha\ell_b m_b\mu_b E}\\ &\times \sum_{L_e=|\ell_a-\ell_b|}^{\ell_a+\ell_b} C(\ell_a,\ell_b,L_e;m_a,-m_b)C(\ell_a,\ell_b,L_e;0,0)\\ &\times \sum_{L_\gamma=0}^{2} C(1,1,L_\gamma;-\mu_a,\mu_b)C(1,1,L_\gamma;-\mu_0,\mu_0)\\ &\times \sum_{\mu_c=-M_e}^{M_e} D^{L_e}_{\mu_c,M_e}(-\gamma,-\beta,-\alpha)D^{L_\gamma}_{M_\gamma,0}(-\gamma,-\beta,-\alpha)\frac{Y^{\mu_c}_{L_e}(\theta'_e,\phi'_e)}{\sqrt{2L_e+1}},\end{aligned} \tag{4.75}$$

where we have expressed the differential cross section as a function of the final electron energy, ε_α, associated with the state α of the residual ion.

The average over the solid angle is taken by exploiting the orthogonality property of the rotational matrices on the unit sphere, given by Eq. (C.95). Making use of Eqs. (C.84) and (C.86), the differential cross section integrated over the orientation of the molecule can be written as

$$\begin{aligned}\frac{d\sigma_\alpha^{\mu_0}(\omega)}{d\Omega'_e d\varepsilon_\alpha} &= \int d\Omega_M \frac{d\sigma_\alpha^{\mu_0}(\omega)}{d\Omega_M d\Omega'_e dW_{\upsilon_\alpha}}\\ &= \frac{\pi\omega}{c}\sum_{\mu_a,\mu_b}\sum_{\ell_a,m_a}\sum_{\ell_b,m_b} i^{(\ell_b-\ell_a)}e^{i[\hat{\sigma}_{\ell_a}-\hat{\sigma}_{\ell_b}]}(-1)^{m_b+\mu_a-\mu_0}\\ &\times\sqrt{(2\ell_a+1)(2\ell_b+1)}\overline{T}_{\alpha\upsilon_\alpha\ell_a m_a\mu_a E}T_{\alpha\upsilon_\alpha\ell_b m_b\mu_b E}\\ &\times\sum_{L=0}^{2} C(\ell_a,\ell_b,L;m_a,-m_b)C(\ell_a,\ell_b,L;0,0)P_L(\cos\theta'_e)\\ &\times\frac{1}{2L+1}C(1,1,L;-\mu_a,\mu_b)C(1,1,L;-\mu_0,\mu_0)\delta_{m_a+\mu_a,m_b+\mu_b},\end{aligned} \tag{4.76}$$

where we use Eq. (B.42) to express the spherical harmonic in terms of the Legendre polynomials. We can express the previous equation in a much more compact way:

$$\frac{d\sigma_\alpha^{\mu_0}(\omega)}{d\Omega'_e d\varepsilon_\alpha} = \frac{4\pi\omega}{c}\sum_{L=0}^{2}\frac{(-1)^{-\mu_0}}{2L+1}\zeta_L(\varepsilon_\alpha)C(1,1,L;-\mu_0,\mu_0)P_L(\cos\theta'_e) \tag{4.77}$$

where we have defined the function $\zeta_L(\varepsilon_\alpha)$ as

$$\begin{aligned}\zeta_L(\varepsilon_\alpha) &= \sum_{\mu_a,\mu_b}\sum_{\ell_a,m_a}\sum_{\ell_b,m_b} i^{(\ell_b-\ell_a)}e^{i[\hat{\sigma}_{\ell_a}-\hat{\sigma}_{\ell_b}]}(-1)^{m_b+\mu_a}\\ &\times\sqrt{(2\ell_a+1)(2\ell_b+1)}\overline{T}_{\alpha\upsilon_\alpha\ell_a m_a\mu_a E}T_{\alpha\upsilon_\alpha\ell_b m_b\mu_b E}\\ &\times C(\ell_a,\ell_b,L;m_a,-m_b)C(\ell_a,\ell_b,L;0,0)C(1,1,L;-\mu_a,\mu_b)\delta_{m_a+\mu_a,m_b+\mu_b}.\end{aligned} \tag{4.78}$$

In the case of achiral molecules, as it is our case, only the terms $L = 0$ and $L = 2$ survive, as we have discussed in previous sections, so the differential cross section takes the form:

$$\begin{aligned}\frac{d\sigma_\alpha^{\mu_0}(\omega)}{d\Omega_e' d\varepsilon_\alpha} &= \frac{\pi\omega}{c}(-1)^{-\mu_0} \\ &\times \left[C(1,1,0;-\mu_0,\mu_0)\zeta_0(\varepsilon_\alpha) + \frac{1}{5}C(1,1,2;-\mu_0,\mu_0)P_2(\cos\theta_e')\zeta_2(\varepsilon_\alpha)\right]. \end{aligned} \tag{4.79}$$

The ζ_0 function that is given by the expression,

$$\begin{aligned}\zeta_0(\varepsilon_\alpha) &= \sum_{\mu_a,\mu_b}\sum_{\ell_a,m_a}\sum_{\ell_b,m_b} i^{(\ell_b-\ell_a)}e^{i[\hat{\sigma}_{\ell_a}-\hat{\sigma}_{\ell_b}]}(-1)^{m_b+\mu_a} \\ &\times\sqrt{(2\ell_a+1)(2\ell_b+1)}\overline{T}_{\alpha\upsilon_\alpha\ell_a m_a\mu_a E}T_{\alpha\upsilon_\alpha\ell_b m_b\mu_b E} \\ &\times C(\ell_a,\ell_b,0;m_a,-m_b)C(\ell_a,\ell_b,0;0,0) \\ &\times C(1,1,0;-\mu_a,\mu_b)\delta_{m_a+\mu_a,m_b+\mu_b}. \end{aligned} \tag{4.80}$$

can be explicitly calculated by means of the restrictions imposed by the Clebsch-Gordan coefficient, (considering Eq. (C.24), in $C(\ell_a,\ell_b,0;0,0)$ only the diagonal elements with $\ell_a = \ell_b$ are different from zero), and the presence of the delta (this implies $\mu_a = \mu_b$):

$$\begin{aligned}\zeta_0(\varepsilon_\alpha) &= \sum_{\mu_a,\ell_a,m_a}(-1)^{m_a+\mu_a}(2\ell_a+1)\overline{T}_{\alpha\upsilon_\alpha\ell_a m_a\mu_a E}T_{\alpha\upsilon_\alpha\ell_a m_a\mu_a E} \\ &\times C(\ell_a,\ell_a,0;m_a,-m_a)C(\ell_a,\ell_a,0;0,0)C(1,1,0;-\mu_a,\mu_a). \end{aligned} \tag{4.81}$$

Taking the explicit values of the Clebsch-Gordan coefficients, by means of Eq. (C.24), the previous equation is reduced to

$$\zeta_0(\varepsilon_\alpha) = \frac{-1}{\sqrt{3}}\sum_{\mu_a,\ell_a,m_a}\overline{T}_{\alpha\upsilon_\alpha\ell_a m_a\mu_a E}T_{\alpha\upsilon_\alpha\ell_a m_a\mu_a E}, \tag{4.82}$$

The integration of Eq. (4.77) over Ω_e' is quite simple since only the term with $L = 0$ survives,

$$\frac{d\sigma_\alpha^{\mu_0}(\omega)}{d\varepsilon_\alpha} = \frac{4\pi^2\omega}{c}(-1)^{-\mu_0}\zeta_0(\varepsilon_\alpha)C(1,1,0;-\mu_0,\mu_0). \tag{4.83}$$

Now taking into account the expression given by Eq. (4.82) and the value of the Clebsch-Gordan coefficient imposed by Eq. (C.24), we obtain the total cross section for randomly distributed molecules:

$$\sigma_\alpha^{\mu_0}(\omega,\varepsilon_\alpha) = \frac{4\pi^2\omega}{3c}\sum_{\mu,\ell,m}\left|T_{\alpha\upsilon_\alpha\ell m\mu E}\right|^2 \tag{4.84}$$

Therefore, the differential cross section given by Eq. (4.79) can be expressed in the form:

$$\frac{d\sigma_\alpha^{\mu_0}(\omega)}{d\Omega_e' d\varepsilon_\alpha} = \frac{\sigma_\alpha^{\mu_0}(\omega,\varepsilon_\alpha)}{4\pi}\left[1+\beta_e^{\mu_0}(\omega,\varepsilon_\alpha)P_2(\cos\theta_e')\right], \tag{4.85}$$

where have defined the *electron beta parameter* as:

$$\beta_e^{\mu_0}(\omega,\varepsilon_\alpha) = \frac{1}{5}\frac{C(1,1,2;-\mu_0,\mu_0)}{C(1,1,0;-\mu_0,\mu_0)}\frac{\zeta_2(\varepsilon_\alpha)}{\zeta_0(\varepsilon_\alpha)}. \tag{4.86}$$

This angular distribution is cylindrically symmetric around the laboratory frame z' axis. In this case the β_e parameter holds information on photoionization dynamics, but in a locked-up form. It contains the information on the interfering photoelectron partial waves but does not enable us to extract the radial dipole matrix elements or their relative phase shifts. One-photon ionization of isotropically distributed molecules is still used to provide qualitative information about molecular dynamics, resonances, and molecular orbitals, but for maximum information, it is necessary to photoionized anisotropic distributions, as we have shown in Section 4.3. The fact that only the two parameters σ and β_e govern the angular distribution still leaves open two important possibilities for obtaining information from angular-distribution measurements. It must be kept in mind that both are functions of both the photon energy and of the kinetic energy of the outgoing electron, i.e., $\sigma = \sigma(\omega, \varepsilon_\alpha)$ and $\beta = \beta(\omega, \varepsilon_\alpha)$. So, one can expect to see variations in $\sigma(\omega, \varepsilon_\alpha)$ and $\beta(\omega, \varepsilon_\alpha)$ with ω, since when ω approaches to the excitation frequency for an autoionizing state, one can expect σ and β to be dominated or at least strongly affected by the nature of the final state in the autoionizing channel.

Note that the differential cross section given by Eq. (4.85) has the same form as the differential cross section that gives the ion angular distribution, Eq. (4.68), so the same conclusions obtained for this latter case can be applied for the the this case (see Fig. (4.3)), in particular Eqs. (4.70), (4.71), (4.72) and (4.73) can be applied to the case of electron angular distribution.

Bibliography

[1] D. Dill, "Fixed-molecule photoelectron angular distributions," *The Journal of Chemical Physics*, vol. 65, pp. 1130–1133, 1976.

[2] H. Park and R. N. Zare, "Molecular-orbital decomposition of the ionization continuum for a diatomic molecule by angle- and energy-resolved photoelectron spectroscopy. i. formalism.," *The Journal of Chemical Physics*, vol. 104, p. 4554, 1996.

[3] E. Shigemasa, J. Adachi, M. Oura, and A. Yagishita, "Angular distributions of $1s\sigma$ photoelectrons from fixed-in-space N_2 molecules," *Physical Review Letters*, vol. 74, pp. 359–362, 1995.

[4] K. Ito, J. Adachi, R. Hall, S. Motoki, E. Shigemasa, K. Soejima, and A. Yagishita, "Photoelectron angular distributions from dissociative photoionization channels of fixed-in-space molecular hydrogen," *Journal of Physics B: Atomic, Molecular and Optical Physics*, vol. 33, pp. 527–533, 2000.

[5] K. Ito, J. Adachi, Y. Hikosaka, S. Motoki, K. Soejima, A. Yagishita, G. Raseev, and N. A. Cherepkov, "Photoelectron angular distributions from O K shell of oriented CO molecules: A critical comparison between theory and experiment," *Physical Review Letters*, vol. 85, pp. 46–49, 2000.

[6] R. K. Wangsness, *Electromagnetic fields*. John Wiley and Sons, Inc., 1994.

[7] C. J. Joachain, *Quantum Collision Theory*. North-Holland Publishing Company, 1979.

[8] C. Cohen-Tannoudji, B. Diu, and F. Laloe, *Quantum Mechanics vol.* I *and* II. Wiley-Interscience, 1992.

[9] J. D. Jackson, *Classical Electrodynamics*. Wiley; 3th edition, 1998.

[10] I. Cacelli, V. Carravetta, A. Rizzo, and R. Moccia, "The calculation of photoionisation cross sections of simple polyatomic molecules by L^2 methods," *Physics Reports*, vol. 205, pp. 283–351, 1991.

[11] A. Lafosse, J. C. Brenot, P. M. Guyon, J. C. Houver, A. V. Golovin, M. Lebech, D. Dowek, P. Lin, and R. R. Lucchese, "Vector correlations in dissociative photoionization of O_2 in the 20-28 eV range. II. Polar and azimuthal dependence of the molecular frame photoelectron angular distribution," *The Journal of Chemical Physics*, vol. 117, pp. 8368–8384, 2002.

[12] R. N. Zare, "Dissociation of H_2^+ by electron impact: Calculated angular distribution," *The Journal of Chemical Physics*, vol. 47, pp. 204–215, 1967.

[13] R. N. Zare, "Photoejection dynamics," *Molecular Photochemistry*, vol. 4, pp. 1–37, 1972.

[14] R. M. Wood, Q. Zheng, A. K. Edwards, and M. A. Mangan, "Limitations of the axial recoil approximation in measurements of molecular dissociation," *Review of Scientific Instruments*, vol. 68, pp. 1382–1386, 1997.

[15] A. D. Buckingham, B. J. Orr, and J. M. Sichel, "Angular distribution and intensity in molecular photoelectron spectroscopy i. general theory for diatomic molecules," *Philosophical Transactions of the Royal Society of London. Series A, Mathematical and Physical Sciences*, vol. 268, pp. 147–157, 1970.

[16] Y. Itikawa, "Vibrational-rotational structure in the angular distribution and intensity of photoelectrons from diatomic molecules. I. General theory," *Chemical Physics*, vol. 28, pp. 461–471, 1978.

[17] H. A. Bethe and E. E. Salpeter, *Quantum mechanics of one- and two-electron atoms*. Plenum/Rosetta edition, 1977.

[18] A. Messiah, *Quantum mechanics volume* I *and* II. North-Holland publishing company, 1961.

[19] G. B. Arfken and H. J. Weber, *Mathematical Methods for Physicists*. Academic Press, 1985.

[20] M. E. Rose, *Elementary theory of angular momentum*. Dover Publications, 1957.

[21] D. Dill, "Resonances in photoelectron angular distributions," *Physical Review A*, vol. 7, pp. 1976–1987, 1973.

[22] M. Brosolo and P. Decleva, "Variational approach to continuum orbitals in a spline basis: An application to H_2^+ photoionization," *Chemical Physics*, vol. 159, pp. 185–196, 1992.

[23] W. J. Cody and K. E. Hillstrom, "Chebyshev approximations for the Coulomb phase shift," *Mathematics of Computation*, vol. 24, pp. 671–677, 1970.

[24] W. J. Cody and K. E. Hillstrom, "Corrigendum: Chebyshev approximations for the Coulomb phase shift," *Mathematics of Computation*, vol. 26, p. 1031, 1972.

[25] N. F. Mott and H. S. W. Massey, *The Theory of Atomic Collisions*. University Press, Cambridge, 1949.

[26] D. Dill and J. L. Dehmer, "Electron-molecule scattering and molecular photoionization using the multiple-scattering method," *The Journal of Chemical Physics*, vol. 61, pp. 692–699, 1974.

[27] N. Chandra, "Ab initio multichannel photoionisation of H_2: Photoelectron angular distribution for rotationally resolved states of H_2^+," *Journal of Physics B: Atomic, Molecular and Optical Physics*, vol. 19, pp. 1959–1988, 1986.

[28] J. L. Dehmer and D. Dill, "Shape resonances in K-shell photoionization of diatomic molecules," *Physical Review Letters*, vol. 35, pp. 213–215, 1975.

[29] J. L. Dehmer and D. Dill, "Molecular effects on inner-shell photoabsorption. K-shell spectrum of N_2," *The Journal of Chemical Physics*, vol. 65, pp. 5327–5334, 1976.

[30] J. L. Dehmer and D. Dill, "Photoion angular distributions in dissociative photoionization of H_2 at 304 Å," *Physical Review A*, vol. 18, pp. 164–171, 19778.

[31] J. L. Dehmer, D. Dill, and S. Wallace, "Shape-resonance-enhanced nuclear-motion effects in molecular photoionization," *Physical Review Letters*, vol. 43, pp. 1005–1008, 1979.

[32] D. Dill, J. R. Swanson, S. Wallace, and J. L. Dehmer, "Angular distribution of molecular K-shell auger electrons: Spectroscopy of photoabsorption anisotropy," *Physical Review Letters*, vol. 45, pp. 1393–1396, 1980.

[33] D. Dill, S. T. Manson, and A. F. Starace, "Photoelectron angular distributions as a probe of anisotropic electron-ion interactions," *Physical Review Letters*, vol. 32, pp. 971–974, 1974.

[34] D. Dill, J. Siegel, and J. L. Dehmer, "Spectral variation of fixed-molecule photoelectron angular distributions," *The Journal of Chemical Physics*, vol. 65, pp. 3158–3160, 1976.

[35] D. Dill, S. Wallace, J. Siegel, and J. L. Dehmer, "Molecular-photoelectron angular distributions as a probe of dynamic symmetry breaking," *Physical Review Letters*, vol. 41, pp. 1230–1233, 1978.

[36] D. Dill, S. Wallace, J. Siegel, and J. L. Dehmer, "Molecular-photoelectron angular distributions as a probe of dynamic symmetry breaking," *Physical Review Letters*, vol. 42, p. 411, 1979.

[37] S. K. Semenov and N. A. Cherepkov, "Photoionization of the H_2 molecule in the random phase approximation," *Journal of Physics B: Atomic, Molecular and Optical Physics*, vol. 36, pp. 1409–1422, 2003.

[38] N. A. Cherepkov, "Angular distribution and spin polarisation of photoelectrons ejected from oriented molecules," *Journal of Physics B: Atomic, Molecular and Optical Physics*, vol. 14, pp. L623–L627, 1981.

[39] N. A. Cherepkov, "Manifestations of the optical activity of molecules in the dipole photoeffect," *Journal of Physics B: Atomic, Molecular and Optical Physics*, vol. 16, pp. 543–1548, 1983.

[40] N. A. Cherepkov and V. V. Kuznetsov, "Fixed-molecule photoelectron angular distributions with defined spin polarisation," *Journal of Physics B: Atomic, Molecular and Optical Physics*, vol. 20, pp. L159–L163, 1987.

[41] N. A. Cherepkov and V. V. Kuznetsov, "Photoionization of oriented molecules," *Zeitschrift für Physik D Atoms, Molecules and Clusters*, vol. 7, pp. 271–280, 1987.

[42] N. A. Cherepkov and V. V. Kuznetsov, "Optical activity of oriented molecules," *The Journal of Chemical Physics*, vol. 95, pp. 3046–3052, 1991.

[43] S. Wallace and D. Dill, "Detector integrated angular distribution: Chemisorption-site geometry, axial-recoil photofragmentation, and molecular-beam orientation," *Physical Review B*, vol. 17, pp. 1692–1699, 1978.

[44] X.-J. Liu, R. R. Lucchese, A. N. Grum-Grzhimailo, Y. Morishita, N. Saito, G. Prümper, and K. Ueda, "Molecular-frame photoelectron and electron-frame photoion angular distributions and their interrelation," *Journal of Physics B: Atomic, Molecular and Optical Physics*, vol. 40, p. 485, 2007.

[45] P. A. Hatherly, J. Adachi, E. Shigemasa, and A. Yagishita, "The angular distributions of 1s photoelectrons from spatially aligned CO using angle-resolved PEPICO," *Journal of Physics B: Atomic, Molecular and Optical Physics*, vol. 28, pp. 2643–2654, 1995.

[46] A. Lafosse, M. Lebech, J. C. Brenot, P. M. Guyon, O. Jagutzki, L. Spielberger, M. Vervloet, J. C. Houver, and D. Dowek, "Vector correlations in dissociative photoionization of diatomic molecules in the VUV range: Strong anisotropies in electron emission from spatially oriented NO molecules," *Physical Review Letters*, vol. 84, pp. 5987–5990, 2000.

[47] A. N. Grum-Grzhimailo, "Non-dipole effects in magnetic dichroism in atomic photoionization," *Journal of Physics B: Atomic, Molecular and Optical Physics*, vol. 34, pp. L359–L365, 2001.

[48] G. Herzberg, *Molecular Spectra and Molecular Structure: Spectra of Diatomic Molecules*. Krieger Pub. Co., 1989.

[49] A. Lafosse, J. C. Brenot, A. V. Golovin, P. M. Guyon, K. Hoejrup, J. C. Houver, M. Lebech, and D. Dowek, "Vector correlations in dissociative photoionization of O_2 in the 20-28 eV range. I. Electron-ion kinetic energy correlations," *The Journal of Chemical Physics*, vol. 114, pp. 6605–6617, 2001.

[50] A. Lafosse, M. Lebech, J. C. Brenot, P. M. Guyon, L. Spielberger, O. Jagutzki, J. C. Houver, and D. Dowek, "Molecular frame photoelectron angular distributions in dissociative photoionization of H_2 in the region of the Q_1 and Q_2 doubly excited states," *Journal of Physics B: Atomic, Molecular and Optical Physics*, vol. 36, pp. 4683–4702, 2003.

[51] M. Lebech, J. C. Houver, D. Dowek, and R. R. Lucchese, "Molecular frame photoelectron emission in the presence of autoionizing resonances," *Physical Review Letters*, vol. 96, p. 073001, 2006.

[52] C. N. Yang, "On the angular distribution in nuclear reactions and coincidence measurements," *Physical Review*, vol. 74, pp. 764–772, 1948.

[53] J. M. Blatt and L. C. Biedenharn, "The angular distribution of scattering and reaction cross sections," *Review of Modern Physics*, vol. 24, pp. 258–272, 1952.

[54] J. C. Tully, R. S. Berry, and B. J. Dalton, "Angular distribution of molecular photoelectrons," *Physical Review*, vol. 176, pp. 95–105, 1968.

Chapter 5

Collision of highly energetic particles with H_2

"Natural science, does not simply describe and explain nature; it is part of the interplay between nature and ourselves."

Werner Heisenberg

Table of Contents

5.1 Introduction

One of the most fundamental and ubiquitous processes occurring in nature is the collision of an electron with an atom or molecule. An important process with such collisions is ionization, with the ensuring loss of energy and change of direction of the primary electron and the emission of one or more secondary electrons. The first electron-impact ionization experiments with full determination of the angles and energies of the scattered and ejected electrons were done by Ehrhardt *et al.* 1973 at incident energy of 500 eV on helium [1].

As we have seen in Chapter 4, the calculation of the fully differential cross section of a diatomic molecule by photons is not easy to get, and the dissociative particle impact case appears quite formidable for the general case, since in this case we should be able to describe correctly two electrons, the scattered and the ionized one, in the continuum and the dissociation of the remaining molecular ion. The basic difficulty in modeling the single ionization process in particle-molecule collisions at intermediate to high energies arises from the long range of the Coulomb interaction between all the charged particles. In the initial channel, the projectile field will distort the initial bound state, while in the final channel, the emitted particles will travel in the combined fields of the residual target and projectile. Furthermore, there is an additional difficulty introduced by the fact that the target is a multielectronic molecule. So, it is necessary to apply some theoretical approximations

that allow us to get as simple expression for the ionization cross section as possible without loosing good agreement with the actual experimental measurements of this cross section. A convenient way to treat this problem is perturbation theory. In particular, we will focus our attention in the study of the electron and proton energy distribution for single ionization of H_2 molecule by electrons and highly charged ions, in the high energy limit. Since one can find many books (see for example [2, 3] and reference in) and articles devoted to this field, we will only present the main steps that one has to follow in order to obtain the cross section of this process. In particular we will pay special attention to the theoretical developments of Zare [4], who calculated the angular distribution of products in the electron impact dissociation of H_2^+ following closely the Born approximation treatment of Kerner [5].

5.2 Preliminary considerations

Particle-impact ionization of a target molecule M, assumed to be initially in its ground state (both electronic and vibrational), can be described completely by the reaction

$$X(E_0, p_i, \widehat{R}_{\hat{n}}) + M \longrightarrow M^+(s_i, p) + X(E_f, p_f) + e^-(\varepsilon_\alpha, p_e) \tag{5.1}$$

where X designates the incoming particle with kinetic energy E_0, and E_f and ε_α designate the energy of the scattered projectile and the ionized electron, respectively[1]. Similarly, the p's are the momenta of the products, and the label s_i specifies the final state of the ionized target, in the same way as it was described in Chapter 4. $\widehat{R}_{\hat{n}}$ gives the orientation of the incoming particle with respect to the molecular reference system at the instant of its ionization (see Fig. (5.1)). After subtraction of the momentum transferred to the ejected electron by the incident particle, the momenta of the residual ion and ejected electron must sum zero, so that the momentum of the residual ion p, the recoil momentum, is equal and opposite to q, the momentum of the ejected electron at the instant of ionization. The recoil energy of the residual ion, $p^2/2m_{ion}$, is small compared to that of the ejected electron and is neglected in the energy conservation equation.

For the experimental determination of the final momentum of the incoming particle, it is necessary to know the velocities of the final particles and their direction of motion. The velocities are established from the kinetic energies and the directions of motion, generally specified by polar and azimuthal angles with respect to the direction of the incident particle (Fig. (5.1)). In addition to the relation between E_f and ε_α, collisions can also be *coplanar* or *non-coplanar* depending on the azimuthal angles (see Fig. (5.1)).

As we showed in the Introduction, it is convenient to divide the incident-particle velocity into slow, intermediate, and fast regions with respect to the orbital velocity of the target electron in the molecule. Following the previous kinematic combinations, several specific designations can be made. For example, the threshold regime corresponds to incident-particle velocities just sufficient to yield scattered particle and ejected electron with near-zero velocity. On the other hand, for high impact energies, the case considered in this Thesis, the dipole regime derives its name from the close connections between photoabsorption and small-angle electron scattering [6].

The collision experiment involves a measurement, for a given incident particle energy E_0, of the probability that the incident particle is scattered with energy E_f into the solid angle Ω_f, as specified by angles θ_f and ϕ_f, at the same time that the ejected electron, with energy ε_α, is found at solid angle Ω_e, as specified by angles θ_e and ϕ_e. This probability per unit solid angle and per unit energy is proportional to the target density and the path length of the incident particles through the target gas. The constant of proportionality is the eight-fold differential cross section,

[1] In this work the charge transfer processes in the ion collision is not considered.

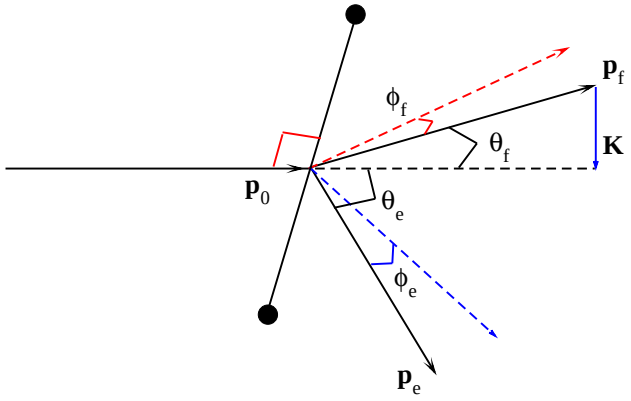

Figure 5.1: Kinematics of a collision. The incident particle has momentum p_0. The scattered particle has momentum p_f, and its direction with respect to the incident electron is defined by the polar angles θ_f and out-of plane angle ϕ_f. The ejected electron has momentum p_e, and its direction with respect to the incident particle is defined by the polar angles θ_e and out-of plane angle ϕ_e

$d\sigma(E_0)/d\widehat{R}_{\hat{n}}d\Omega_f d\Omega_e dE_f dk_\alpha dW_{\upsilon_\alpha}$. So, the cross section for excitation from an initial state Ψ_i to the final state Ψ_f may be written as (see for example Chapter 6 of [3])

$$\frac{d\sigma_\alpha}{d\widehat{R}_{\hat{n}}d\Omega_f d\Omega_e dE_f dk_\alpha dW_{\upsilon_\alpha}} = \frac{\mu^2}{4\pi^2}\frac{k_f}{k_i}\left|T_{if}\right|^2, \tag{5.2}$$

where k_i and k_f are the initial and final relative momenta, $\mu = m_X \cdot m_{mol}/(m_X + m_{mol})$ is the reduce mass of the total system, where m_X and m_{mol} are the rest masses of the incoming particle and the molecule, respectively, and $k_\alpha = \sqrt{2\varepsilon_\alpha}$. The transition element is given by

$$T_{if} = \langle \Psi_i | V | \Psi_f \rangle, \tag{5.3}$$

where the final wave function Ψ_f is normalized to the momentum, i.e.,

$$\int \overline{\Psi}_f(k')\Psi_f(k)dk = \delta(k'-k). \tag{5.4}$$

In the cross section given by Eq. (5.2), $d\widehat{R}_{\hat{n}}$ gives the relative orientation of the incoming particle with respect to the molecular reference system, and the final energy of the residual ion is given by W_{υ_α}, where α designates its final electronic state. Note that E_f, ε_α and W_{υ_α} are not independent variables. For each possible value of the final energy E_f of the scattered particle, there exit infinite ways of sharing the deposited energy in the molecule between the final ionized electron and the residual ion (dissociative ionization), as was explained in Chapter 3 (see Fig. (3.5)). But the collision of a particle with a molecular system is much more difficult in comparison with the photoionization case: Since the final energy E_f of the scattered particle can take values from zero to a maximum value equal to the initial energy of the incoming particle (in our case this maximum value is in the of order of

MeV), this implies that the possible ways that one can combine these three variables is infinite: for each possible value of the variable E_f, ε_α and W_{υ_α} can be combined in infinite ways.

Since k_i and k_f is the momentum of the incident particle before and after the collision, respectively, it is convenient to introduce the momentum transfer, defined as:

$$K = k_i - k_f, \tag{5.5}$$

so the modulus of this momentum transfer vector is determined by the relation

$$K^2 = k_i^2 + k_f^2 - 2k_i k_f \cos\theta_f, \tag{5.6}$$

which proves to be a convenient variable of integration for the evaluation of the total cross section, where θ_f is the angle between k_i and k_f. Ionizing collisions can also be classified according to the relative magnitude of the momentum transferred to the target. Small momentum transfer collisions correspond to small angles of scatter. Ionizing collisions with momentum transfer of the order $\hbar/a_0$ (one unit of momentum in atomic units) are more probable and for these collisions the momentum transferred to the target is just sufficient to knock out a valence electron.

Eq. (5.2) can be converted into the angular distribution of the projectile through Eq. (5.6), since the solid angle $d\Omega_f$ can be expressed by the following relations:

$$2K\mathrm{d}K = 2k_i k_f \sin\theta_f \mathrm{d}\theta_f \longrightarrow \sin\theta_f \mathrm{d}\theta_f = \frac{K\mathrm{d}K}{k_i k_f}. \tag{5.7}$$

Therefore, for the case where the scattered particle is not resolved (measured), the cross section given by Eq. (5.2) may be written as

$$\frac{\mathrm{d}\sigma_\alpha}{\mathrm{d}\widehat{R}_{\hat{n}}\mathrm{d}\Omega_e \mathrm{d}k_\alpha \mathrm{d}W_{\upsilon_\alpha}} = \frac{\mu^2}{4\pi^2}\frac{k_f}{k_i}\int_0^{2\pi}\int_{K_{min}}^{K_{max}} \left|T_{if}\right|^2 \frac{K}{k_i k_f}\mathrm{d}K\mathrm{d}\phi_f, \tag{5.8}$$

with the integration limits given by

$$\begin{aligned} &\cos\theta_f = 1 \Rightarrow K^2 = k_i^2 + k_f^2 - 2k_i k_f \Rightarrow K_{min} = |k_i - k_f|^2 \\ &\cos\theta_f = -1 \Rightarrow K^2 = k_i^2 + k_f^2 + 2k_i k_f \Rightarrow K_{max} = |k_i + k_f|^2 \end{aligned} \tag{5.9}$$

The major contribution to the integral in Eq. (5.8) usually comes from values of K near K_{min}. Consequently, since μ is large, the value of the integral is not altered if K_{max} is assumed to be infinite. The equation of conservation of energy is

$$k_i^2 = k_f^2 + 2\mu\Delta E, \tag{5.10}$$

where ΔE is the energy required to excite the target from state Ψ_i to the final state Ψ_f.

We can define the velocity of the incoming particle as $v = k_i/\mu$, so we can write

$$K_{min}^2 = k_i^2 + k_f^2 - 2k_i k_f, \tag{5.11}$$

and making use of Eq. (5.10) in Eq. (5.11) the following relation is obtained:

$$\begin{aligned} K_{min}^2 &= k_i^2 + (k_i^2 - 2\mu\Delta E) - 2k_i\sqrt{k_i^2 - 2\mu\Delta E} = \\ &= 2k_i^2 - 2\mu\Delta E - 2k_i^2\sqrt{1 - \frac{2\mu\Delta E}{k_i^2}} \\ &= 2\mu^2\left(v^2 - \frac{\Delta E}{\mu} - v^2\sqrt{1 - \frac{2\Delta E}{\mu v^2}}\right). \end{aligned} \tag{5.12}$$

Therefore, provided that v is sufficiently large to ensure the convergence of the expansion in inverse of v^2, the following approximation is obtained[2]:

$$K_{min}^2 = 2\mu^2\left(v^2 - \frac{\Delta E}{\mu} - v^2\left[1 - \frac{1}{2}\frac{2\Delta E}{\mu v^2} - \frac{1}{8}\frac{4\Delta E^2}{\mu^2 v^4} - \ldots\right]\right), \tag{5.13}$$

so,

$$K_{min}^2 \simeq \frac{\Delta E^2}{v^2}. \tag{5.14}$$

It is clear that for heavy particle impact, or highly energetic particles, is little loss of accuracy if one assumes that $K_{min} \simeq \frac{\Delta E}{v}$. The kinetic energy of the projectile in the laboratory frame is $m_X v^2$, where m_X is the projectile mass in units of electron mass. Thus v^2 is the kinetic energy that the projectile would have if its mass were equal to that of the electron, or, in other words, v^2 is the initial kinetic energy of the projectile in the laboratory frame in units of m_X. For proton impact, for example, v^2 is the kinetic energy in the laboratory frame in units of 24.98 KeV.

Eq. (5.14) gives the relation between the minimum value of the momentum transfer in terms of the excitation energy. This relation can be expressed in terms of the final electron and ion energies defining ΔE as

$$\Delta E = k_\alpha^2/2 + W_{\alpha,\upsilon_\alpha} - W_{i\nu}, \tag{5.15}$$

where $W_{\alpha,\upsilon_\alpha}$ is the energy of the residual ion and $W_{i\nu}$ is the energy of the initial state in the electronic state i and in its initial vibrational state ν, so the equation of the conservation energy given by Eq. (5.10) takes the form

$$\frac{k_i^2}{\mu} - 2(W_{\alpha,\upsilon_\alpha} - W_{i\nu}) = \frac{k_f^2}{\mu} + k_\alpha^2, \tag{5.16}$$

provided that the other target electrons remain unexcited. The maximum value of the momentum transfer transmitted to the molecule, corresponds to the values $k_f = 0$, so by relations (5.9) the following condition is obtained:

$$K_{max}^2 = \mu k_\alpha^2 + 2\mu W_{\alpha,\upsilon_\alpha}^0, \tag{5.17}$$

where $W_{\alpha,\upsilon_\alpha}^0 = (W_{\alpha,\upsilon_\alpha} - W_{i\nu})$. Making use of Eq. (5.16) in Eq. (5.12), the K_{min} can be written in terms of k_α and $W_{\alpha,\upsilon_\alpha}^0$,

$$K_{min}^2 = k_i^2 + k_f^2 - 2k_i^2\sqrt{1 - \frac{2\mu(k_\alpha^2/2 + W_{\alpha,\upsilon_\alpha}^0)}{k_i^2}}. \tag{5.18}$$

Because of the large difference between electrons and nuclei it is clear that the projectile is unlikely to transfer more than a small fraction of its energy to the ejected electron. Therefore, a binomial expansion of the square root in Eq. (5.18), similar to that of Eq. (5.13), is valid:

$$K_{min} \simeq \frac{\Delta E}{v} = \frac{\mu(k_\alpha^2/2 + W_{\alpha,\upsilon_\alpha}^0)}{k_i} = \frac{(k_\alpha^2 + 2W_{\alpha,\upsilon_\alpha}^0)}{2v}. \tag{5.19}$$

This equation gives the desired relation between the minimum energy deposited in the system and the sharing between the final particles.

[2] We have made use of the expansion

$$\sqrt{(1-x)} = 1 - \frac{1}{2}x - \frac{1}{8}x^2 - \frac{1}{16}x^3 - \ldots$$

5.3 The Born approximation

A large number of theoretical treatments of particle scattering exists. Our purpose here is not to review all of them in detail, but rather to obtain the simplest one in such a way that the underlying assumptions and the region of validity is clear, since the final test of a theory is the agreement with experiment. Therefore, this section will be devoted to the study of the collision of particles in the framework of the First Born approximation. The Born approximation is a high-energy approximation most applicable when the potential felt by the incoming particle is small compared to the kinetic energies of the projectile particle both before and after scattering. The validity of the assumption of complete screening of the field of the residual ion clearly depends on the relative magnitude of the velocities of the projectile and the ejected electron. There are some definite advantages in using beam energies in the MeV range, since for light projectile at these energies, the time for a typical collision with a target is short enough ($\sim 10^{-17}$ s) compared with the times for molecular vibrations ($\sim 10^{-14}$ s) and rotation ($\sim 10^{-12}$ s). Thus during the collision, the nuclei of a molecular ion may be considered to be stationary in the projectile frame. For high projectile velocities ($v \gg v_o = e^2/\hbar$) it can be expected that, to an excellent approximation, collision-induced dissociation may be treated as a two-step process. First, there occurs a rapid collision with a target during which the target does not move in its center of mass frame. Because of their mass, the electrons associated with the projectile reconfigure themselves in a time scale comparable with the collision time (this process includes the possibility of removal by ionization of some or all the electrons). Then it follows, on a much longer time scale, a dissociation of the resultant excited molecular state into two or more atomic or molecular fragments. There are several other approximations that are also appropriate at MeV bombarding energies. For example, energy losses due to inelastic collision processes may be neglected and the deflection of the projectile's center of mass during the collision may be neglected.

Now let's consider again the excitation of a diatomic molecular target, consisting of $n = 2$ electrons bound to a nucleus of mass M_1 and M_2 and charge Z_1 and Z_2, from an initial state ψ_i to a final state ψ_f, as a result of an encounter with a particle of mass m_X and charge Z_X. The position vectors of the bound electrons with respect to center of mass of the molecular target nuclei are designated r_j, while R is the internuclear distance of the molecule (see Fig. (5.2)). If R_p is the separation between the projectile and the center of mass of the molecule, the position vector of the projectile with respect to the center of mass of the molecule is

$$\sigma = R_p - r' \tag{5.20}$$

where

$$r' = \frac{1}{\mu_{mol}} \sum_{j=1}^{n} r_j. \tag{5.21}$$

The initial and final unperturbed wave functions can be written as

$$\begin{aligned} \psi_i &= \exp(ik_i \cdot \sigma)\Psi_{i\nu}(\mathbf{r}, R) \\ \psi_f &= \exp(ik_f \cdot \sigma)\Psi^{+}_{\alpha\upsilon_\alpha k_e E_0}(\mathbf{r}, R) \end{aligned} \tag{5.22}$$

where i and ν indicate the initial electronic and vibrational states, respectively, and $\Psi^{+}_{\alpha\upsilon_\alpha k_e E_0}(\mathbf{r}, R)$ represents the molecular electronic final state, asymptotically becoming the product of the remaining ion state $\alpha\upsilon_\alpha$ times a Coulomb plane wave of energy ε_α and direction k_e describing the ejected electron, and α and υ_α denote, respectively, the electronic and vibrational states of the residual molecular ion. In the final state, the subscript + indicates the usual outgoing boundary conditions in electron-molecule scattering, and $E = W_{i\nu} + E_0$ with $W_{i\nu}$ the total energy of the molecule in the

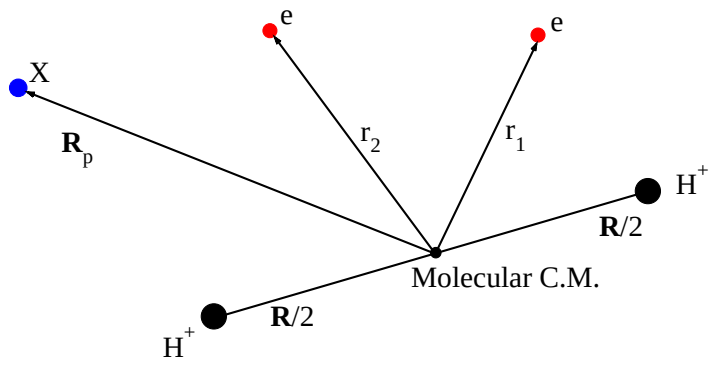

Figure 5.2: Coordinate system describing the collision of and incoming particle along R_p with a hydrogen molecule. The origin is at the midpoint of the molecule.

initial state. The functions $\exp(ik_i \cdot \sigma)$ and $\exp(ik_f \cdot \sigma)$ are plane waves describing the projectile, before and after the collision. Note that more elaborate final wave function can be built in order to improve the results, like Volkov states [7] or Coulomb-Volkov states [8] originally proposed by Cheshire [9] and Vainstein *et al.* [10] for ionizing charged particle collisions. The advantage of this last approximation is that the simultaneous Coulomb interactions of the released electron with the residual ionic core and the charged projectile are taken into account in terms of a product of two two-body Coulomb functions, which leads to a distorted wave function called the continuum-distorted wave (CDW). The CDW allows to include the effect of the two Coulomb fields non-perturbatively yet approximately.

The interaction potential between the projectile and the target is given by

$$V(r_1, r_2, R, R_p) = \frac{Z_X Z_1}{|R_p + \frac{1}{2}R|} + \frac{Z_X Z_2}{|R_p - \frac{1}{2}R|} + \sum_{i=1}^{2} \frac{Z_\rho Z_e}{|R_p - r_i|}, \tag{5.23}$$

where, Z_1 and Z_2 design the charges of the nuclei, $Z_e = 1$ the charges of the electron, and Z_ρ the charge of the incoming particles. The Born approximation to T_{if} in Eq. (5.2) is given by:

$$T_{if} = \int\int \mathrm{d}R\,\mathrm{d}R_p \langle e^{(ik_f \cdot \sigma)} \Psi^+_{\alpha \upsilon_\alpha k_e E_0}(\mathbf{r}, R) | V(r_1, r_2, R, R_p) | e^{(ik_i \cdot \sigma)} \Psi_{i\nu}(\mathbf{r}, R) \rangle. \tag{5.24}$$

where the integration over the electronic coordinates is explicitly denoted by the bra-ket notation.

Taking into account Eq. (5.23), the previous equation can be written as:

$$\begin{aligned} T_{if} &= Z_X Z_1 \int\int \mathrm{d}R\,\mathrm{d}R_p e^{(i(k_i-k_f)\cdot\sigma)} \langle \Psi^+_{\alpha\upsilon_\alpha k_e E_0}(\mathbf{r},R)| \frac{1}{|R_p+\frac{1}{2}R|} |\Psi_{i\nu}(\mathbf{r},R)\rangle \\ &+ Z_X Z_2 \int\int \mathrm{d}R\,\mathrm{d}R_p e^{(i(k_i-k_f)\cdot\sigma)} \langle \Psi^+_{\alpha\upsilon_\alpha k_e E_0}(\mathbf{r},R)| \frac{1}{|R_p-\frac{1}{2}R|} |\Psi_{i\nu}(\mathbf{r},R)\rangle \\ &+ Z_\rho Z_e \sum_{i=1}^{2} \int\int \mathrm{d}R\,\mathrm{d}R_p e^{(i(k_i-k_f)\cdot\sigma)} \langle \Psi^+_{\alpha\upsilon_\alpha k_e E_0}(\mathbf{r},R)| \frac{1}{|R_p-r_i|} |\Psi_{i\nu}(\mathbf{r},R)\rangle. \end{aligned} \tag{5.25}$$

In almost all calculations terms of $1/\mu_{mol}$ are neglected compared with unity. The neglect of terms $1/\mu_{mol}$, which is equivalent to the neglect of nuclear recoil, implies the replacement of σ by R_p in Eq. (5.24). The integration over the variable R_p can be performed making use of the following relation:

$$I(r_j) = \int \frac{e^{iK\cdot R_p}}{|R_p - r_j|} \mathrm{d}R_p \;\; (j = 0, 1, \cdots, n) \tag{5.26}$$

where $r_j = \pm R/2$ for $j = 0$ and $K = k_i - k_f$. On changing the variable of integration to

$$\rho = R_p - r_j, \tag{5.27}$$

Eq.(5.26) takes the form:

$$I(r_j) = e^{(iK\cdot r_j)} \int \frac{1}{\rho} e^{(iK\cdot\rho)} \mathrm{d}\rho = \frac{4\pi}{K} e^{(iK\cdot r_j)} \int_0^\infty \sin(K\rho)\mathrm{d}\rho. \tag{5.28}$$

This integral is "almost convergent" and it may be evaluated by inserting the convergence factor $\exp(-\lambda\rho)$ and taking $\lambda \to 0$ when the integration has been carried out. Thus

$$I(r_j) = \frac{4\pi}{K} e^{(iK\cdot r_j)} \lim_{\lambda\to 0} \int_0^\infty \exp(-\lambda\rho)\sin(K\rho)\mathrm{d}\rho = \frac{4\pi}{K^2} e^{(iK\cdot r_j)}. \tag{5.29}$$

As this result was first derived by Bethe [11], $I(r)$ is referred to as Bethe's integral. So, Eq. (5.24) reduces to

$$\begin{aligned} T_{if} &= \int \mathrm{d}R \langle \Psi^+_{\alpha\upsilon_\alpha k_e E_0}(\mathbf{r},R)| \left\{ \frac{Z_X 4\pi}{K^2} \left[Z_1 \exp\{-i(K\cdot\frac{1}{2}R)\} \right.\right. \\ &\left.\left. + Z_2 \exp\{i(K\cdot\frac{1}{2}R)\} + \sum_{j=1}^{2} \exp\{i(K\cdot r_j)\} \right] \right\} |\Psi_{i\nu}(\mathbf{r},R)\rangle. \end{aligned} \tag{5.30}$$

For a homonuclear molecules, $Z_1 = Z_2 = Z_n$, the previous equation takes the form[3],

$$T_{if} = \frac{Z_X 4\pi}{K^2} \int \mathrm{d}R \langle \Psi^+_{\alpha\upsilon_\alpha \hat{k}_e}(\mathbf{r},R)| \left[2Z_n \cos[\frac{1}{2}K\cdot R] + \sum_{j=1}^{2} \exp\{i(K\cdot r_j)\} \right] |\Psi_{i\nu}(\mathbf{r},R)\rangle. \tag{5.31}$$

The initial and final states, are those described in Chapter 3, i.e., we chose identical Hamiltonians for the entrance-channel Hamiltonian and exit-channel distorted Hamiltonian. Both functions are solutions of the same total Hamilton operator, i.e.,

$$[\mathcal{H}(\mathbf{r},R) - E]\Psi_{i\nu} \simeq [\mathcal{H}(\mathbf{r},R) - E]\Psi^+_{\alpha\upsilon_\alpha k_e E_0} = 0. \tag{5.32}$$

[3]Note, that the presence the term $\cos[\frac{1}{2}K\cdot R]$ presented in Eq. (5.31) is consequence of the bicentric character of the homonuclear molecule, and it is not presented in the atomic case.

This means that both wave functions must be orthogonal. The initial wave function that describes the bound state of H_2 can be written as a product of the initial electron wave function and its corresponding initial vibrational state. As we explained in Chapter 3, when doubly excited states are considered, the final wave function cannot be written in this simple form. Therefore, just the First Born approximation involves a prohibitive amount of labor in the determination of the cross section of the collision of a highly energetic particle with a molecular system, and consequently simpler approximations are desirable. One such approximation is the dipole approximation, due to Bethe. It involves the use of the multipole expansion of the expressions $\cos[\frac{1}{2}K\cdot R]$ and $\exp\{i(K\cdot r_j)$ in Eq. (5.31), and the retention of only the first non-zero term[4].

Taking into account the expansion of both the cosine and the exponential functions present in Eq. (5.31):

$$\cos[\frac{1}{2}K\cdot R]\simeq 1-\frac{(\frac{1}{2}K\cdot R)^2}{2!}+\frac{(\frac{1}{2}K\cdot R)^4}{4!}-\ldots \tag{5.33}$$

$$\exp\{i(K\cdot r_j)\}\simeq 1+i(K\cdot r_j)+\frac{(K\cdot r_j)^2}{2}+\ldots \tag{5.34}$$

Eq. (5.31) can be written as

$$\begin{aligned} T_{if} &= \frac{Z_X 4\pi}{K^2}\int \mathrm{d}R\langle\Psi^+_{\alpha\upsilon_\alpha k_e E_0}|\left[2Z_n+\sum_{j=1}^{2}\{1+i(K\cdot r_j)\}\right]|\Psi_{i\nu}(\mathbf{r},R)\rangle \\ &= \frac{Z_X 4\pi}{K^2}\int \mathrm{d}R\langle\Psi^+_{\alpha\upsilon_\alpha k_e E_0}|\left[2(Z_n+1)+i\sum_{j=1}^{2}(K\cdot r_j)\right]|\Psi_{i\nu}(\mathbf{r},R)\rangle. \end{aligned} \tag{5.35}$$

Since the term $2(Z_n+1)$ does not give any contribution because the initial and final wave functions are orthogonal, the transition matrix element is reduced to

$$T_{if}=\frac{iZ_X 4\pi}{K^2}\int \mathrm{d}R\langle\Psi^+_{\alpha\upsilon_\alpha k_e E_0}|\sum_{j=1}^{2}(K\cdot r_j)|\Psi_{i\nu}(\mathbf{r},R)\rangle. \tag{5.36}$$

Replacing Eq. (5.36) in Eq. (5.8) we obtain the final expression for the cross section

$$\begin{aligned} &\frac{\mathrm{d}\sigma_\alpha}{\mathrm{d}\widehat{R}_{\hat{n}}\mathrm{d}\Omega_e\mathrm{d}k_\alpha\mathrm{d}W_{\upsilon_\alpha}}= \\ &\frac{4Z_X^2}{v^2}\int_{K_{min}}^{K_{max}}\int_0^{2\pi}\left|\int\langle\Psi^+_{\alpha\upsilon_\alpha k_e E_0}|(\hat{K}\cdot D)|\Psi_{i\nu}(\mathbf{r},R)\rangle\mathrm{d}R\right|^2\mathrm{d}\phi_f\frac{\mathrm{d}K}{K}. \end{aligned} \tag{5.37}$$

where we have defined the "operator" $D=r_1+r_2$, and $\hat{K}=K/K$.

The power expansion of Eq. (5.33) and Eq. (5.34) converge for all values of K, r and R and therefore the work so far is exact within the framework of the Born approximation. However, the series is not well represented by its first few terms unless $KR<1$ and $Kr<1$. One therefore chooses a cut-off parameter K_0 such that $K_0R<1$ and $K_0r<1$ for the significant values of R and r, and the integral given by Eq. (5.37) is evaluated between the limit K_{min} and K_0, the basic assumption being that values of K greater than K_0 contribute little to the cross section. The values of K which are significant are those near K_{min}, but at high energies K_{min} is proportional to $1/v$ and is therefore small. Consequently it is reasonable to neglect all but the leading term of the expansions given by Eqs. (5.33) and (5.34). The transition operator $K\cdot D$ resembles to the photoionization transition

[4]Notice that if both wave functions $\Psi^+_{\alpha\upsilon_\alpha k_e E_0}$ and $\Psi_{i\nu}$ were written as a single product of electronic and nuclear wave function (Born-Oppenheimer approximation), the integral involving the term $\cos[\frac{1}{2}K\cdot R]$ would be exactly zero, due to orthogonality of the electronic part.

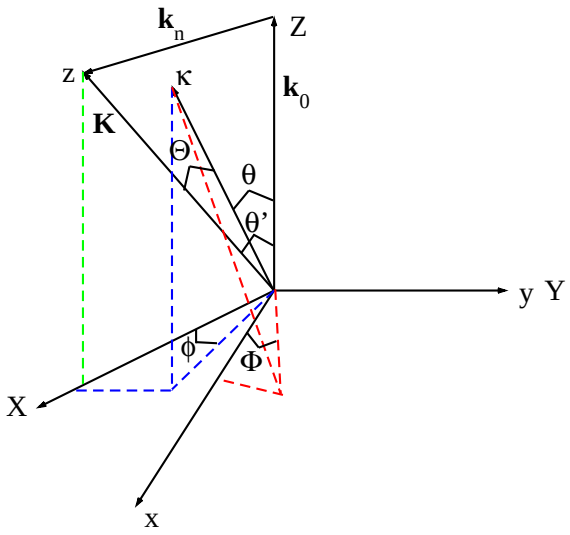

Figure 5.3: Relation between scattering angles in the electron beam and momentum transfer coordinate system. The location of the x' and y' axes in the k_0 frame is chosen so that K lies in the $x'z'$ plane and the y' axes of the k_0 and K frames coincide. Fragments ejected along κ are described by the polar angles (θ,ϕ) and (Θ,Φ) in the two respective frames.

operator (see Chapter 4), where the transfer momentum would play the role of the polarization vector. So, the definition of a 'momentum-transfer" reference frame is necessary in order to express all its possible relative orientations with respect to the molecular system. Thus, the study of the angular distribution of the particles coming from the collision process can be carried out closely to the developments described in Chapter 4. As we pointed out before, it is quite difficult experimentally to determine simultaneously both the distribution of the fragments and the scattering angles of the incoming particle. Rather than making such coincidence measurements, it is customary to observe the angular distribution of products, without regard to the scattered particle. The direction of the particle beam k_0 then serve as a convenient reference coordinates system for reporting the form of the angular distribution, the "particle-beam" frame. So, for the study of the angular distribution of particles coming from the collision process we have an additional reference frame in comparison with the photoionization process (see Chapter 4).

The transformation of the scattering cross section measured in the "momentum-transfer" to the "electron-beam" frame can be carried out in a straight way. From physical considerations it is evident that the flux of particles does not depend on the choice of the coordinate system. Thus the number of particles emitted into corresponding solid angle elements must be the same in the K and k_0 frames. Fig. (5.3) defines the relevant scattering angles (Θ,Φ) and (θ,ϕ) of the molecular axis with respect to these reference systems, where θ' is the angle between K and k_0. We have chosen the X axis of the k_0 frame in Fig. (5.3) so that $\Phi = 0$. Then the scattering angles are related to each other by

$$\cos\Theta = \cos\theta\cos\theta' + \sin\theta\sin\theta'\cos\phi \tag{5.38}$$

and

$$\Phi = \sin^{-1}(\sin\theta \sin\phi / \sin\Theta) \tag{5.39}$$

(see [4] for more details). Fig. (5.3) shows that K and k_0 frames may be transformed into each other thought a simple rotation by θ' about the (Y,y) axis.

Let's now go again to Eq. (5.37), that gives the fully differential cross section of the emitted particles for a defined orientation of the molecule with respect to the momentum-transfer reference frame. Since we have pointed out previously the similarities of this expression with the one obtained for the photoionization process (see Eq. (4.5) of Chapter 4), we can use many of the concepts and ideas described previously in order to obtain a simple expression for the fully differential cross section[5].

The orientation of the momentum transfer vector, K, can be defined in the z' axis, without lost of generalization[6], so we can express $\hat{K}\cdot D$ in the molecular reference frame making use of Eq. (4.13) of Chapter 4:

$$z' = \sqrt{\frac{4\pi}{3}} r Y_1^0(\theta',\varphi') = \sqrt{\frac{4\pi}{3}} r \sum_{\mu=-1}^{1} Y_1^{\mu}(\theta,\varphi) D^1_{\mu,0}(\alpha,\beta,\gamma), \tag{5.40}$$

where $D^1_{\mu,0}(\alpha,\beta,\gamma)$ is the Wigner rotational matrix, defined in Appendix C. Since the final wave function is given by a partial wave expansion (see Eq. (4.6) of Chapter 4), we can follow the same steps described in Section 4.3 of Chapter 4 to obtain the expression of the collision-induced fully differential ionization cross section:

$$\begin{aligned}
\frac{d\sigma_\alpha}{d\widehat{R}_{\hat{n}} d\Omega_e dk_\alpha dW_{\upsilon_\alpha}} &= \frac{4Z_X^2}{v^2} \sum_{\mu_a,\mu_b} \sum_{\ell_a,m_a} \sum_{\ell_b,m_b} i^{(\ell_b-\ell_a)} e^{i[\hat{\sigma}_{\ell_a}-\hat{\sigma}_{\ell_b}]} (-1)^{m_b+\mu_a-\mu_0} \\
\times \quad & \sqrt{(2\ell_a+1)(2\ell_b+1)} \int_{K_{min}}^{K_{max}} \int_0^{2\pi} \overline{Q}_{\alpha\upsilon_\alpha\ell_a m_a\mu_a E} Q_{\alpha\upsilon_\alpha\ell_b m_b\mu_b E} d\phi_f \frac{dK}{K}, \\
\times \quad & \sum_{L_e=|\ell_a-\ell_b|}^{\ell_a+\ell_b} C(\ell_a,\ell_b,L_e;-m_a,m_b) C(\ell_a,\ell_b,L_e;0,0) \frac{Y_{L_e}^{M_e}(\theta_e,\phi_e)}{\sqrt{2L_e+1}} \\
\times \quad & \sum_{L_\gamma=0}^{2} C(1,1,L_\gamma;-\mu_a,\mu_b) C(1,1,L_\gamma;-\mu_0,\mu_0) \frac{\overline{Y}_{L_\gamma}^{M_\gamma}(\theta_n,\phi_n)}{\sqrt{2L_\gamma+1}},
\end{aligned} \tag{5.41}$$

where we have defined the transition matrix elements Q as:

$$Q_{\alpha\upsilon_\alpha\ell_b m_b\mu_b E} = \int \langle \Psi^+_{\alpha\upsilon_\alpha k_e E_0} | (\hat{K}\cdot D) | \Psi_{i\nu}(\mathbf{r},R)\rangle dR \tag{5.42}$$

In Eq. (5.41), θ_e and ϕ_e give the orientation of the ionized electron and θ_n and ϕ_n the orientation of the momentum transfer, both with respect to the molecular axis. The different elements present in this Eq. (5.41) have been described previously in Section 4.3 of Chapter 4. As we have pointed out before, our principal aim is to obtain a expression that allow us to compare with the experimental results obtained in parallel with this theory (see Chapter 12). In these experiments the molecules are randomly distributed in space[7], so we have to get a expression that reproduces this

[5] Note, that the scattered particle is not "measured", so the obtained cross section is not totally fully differential.

[6] As in Chapter 4, all the primed coordinates are designated with respect to the momentum-transfer reference frame.

[7] Some of the results presented in Chapter 12 are obtained for a specific orientation of the molecule with the respect to the beam, results that were not available at the time of writing this Chapter.

experimental condition. This implies that the electron angular distribution must be expressed in the momentum-transfer reference frame (or in the particle-beam reference frame) and the orientation of the molecule must be averaged in this reference frame. Since we are only interested in the study of the total cross section, we can closely follow the steps described in Section 4.5 of Chapter 4. As we showed in that section, the electron angular distribution with respect to the polarization direction was given by Eq. (4.85). As in that case, now we have to express the electron emission angles contained in the spherical harmonic $Y_{L_e}^{M_e}(\theta_e,\phi_e)$ of Eq. (5.41) with respect to the transfer-momentum reference frame, and perform the integration over all possible orientations of the molecule. Then, the following expression is obtained:

$$\frac{d\sigma_\alpha(E_0)}{d\Omega'_e dk_\alpha dW_{\upsilon_\alpha}} = \frac{\sigma_\alpha(\varepsilon_\alpha;E_0)}{4\pi}\left[1+\beta(\varepsilon_\alpha;E_0)P_2(\cos\theta'_e)\right], \tag{5.43}$$

where $\sigma_\alpha(E_f,\varepsilon_\alpha;E_0)$ is the cross section integrated over all directions of the ionized electron and $\beta(E_f,\varepsilon_\alpha)$ is a parameter that characterizes the electron angular distribution, and θ'_e is the polar electron angle measured with respect to the momentum-transfer reference frame. In these functions α designates the electronic state of the residual ion. The cross section σ_α is given by

$$\frac{d\sigma_\alpha(E_0)}{dk_\alpha dW_{\upsilon_\alpha}} = \frac{4Z_X^2}{3v^2}\sum_{\ell,m,\mu}\int_{K_{min}}^{K_{max}}\int_0^{2\pi}|Q_{\alpha\upsilon_\alpha\ell_b m_b\mu_b E}|^2 d\phi_f\frac{dK}{K}, \tag{5.44}$$

The integration over ϕ_f gives a 2π factor since the transition elements have azimuthal symmetry. The integration over K can be obtained making use of the expressions of K_{max} and K_{min} obtained previously:

$$\begin{aligned}\int_{K_{min}}^{K_{max}}\int_0^{2\pi} d\phi_f\frac{dK}{K} &= 2\pi\ln\frac{K_{max}}{K_{min}} = \pi\ln\frac{K_{max}^2}{K_{min}^2} = \pi\ln\frac{\mu k_\alpha^2+2\mu W_{\alpha,\upsilon_\alpha}^0}{\left(\frac{k_\alpha^2+2W_{\alpha,\upsilon_\alpha}^0}{2v}\right)^2}\\ &= \pi\ln\left\{\frac{2\mu v^2}{(\varepsilon_\alpha+W_{\alpha,\upsilon_\alpha}^0)}\right\}.\end{aligned} \tag{5.45}$$

So, the cross section differential in both the final electron and proton energy takes the form:

$$\frac{d\sigma_\alpha(E_0)}{d\varepsilon_\alpha dW_{\upsilon_\alpha}} = \frac{4\pi Z_X^2}{3v^2}\sqrt{2\varepsilon_\alpha}\sum_{l,m,\mu}|Q_{\alpha\upsilon_\alpha\ell_b m_b\mu_b E}|^2\ln\left\{\frac{2\mu v^2}{(\varepsilon_\alpha+W_{\alpha,\upsilon_\alpha}^0)}\right\}. \tag{5.46}$$

Notice that we have changed the depence in k_α in Eq. (5.44) to ε_α in Eq. (5.46) since $d\varepsilon_\alpha = (2k_\alpha)^{-1/2}d\varepsilon_\alpha$, and the factor $\sqrt{2\varepsilon_\alpha}$ appears in the previous equation due to the fact that our continuum wave functions are normalized to the energy (see Section 3) and we want to express this equation as a function of the final electron energy (see for example Chapter 6 of [3]).

As we have explained previously, the initial energy E_0 can be shared between the scattered particle, the final ionized electron and the residual ion, that can remain in a bound vibrational state (non-dissociative process) or in a continuum vibrational state (dissociative process). So, for the case in which the dependence with the final energy of the scattered particle is not observed, the previous differential cross section has to be integrated considering the fact that for a fixed final electron energy, there exist a great number of vibrational states[8]. So the cross section given by Eq. (5.46) takes the form:

$$\begin{aligned}\frac{d\sigma_\alpha(E_0)}{d\varepsilon_\alpha} &= \frac{4\pi Z_X^2}{3v^2}\sqrt{2\varepsilon_\alpha}\sum_{l,m,\mu}\int_0^{W_{\alpha,\upsilon_\alpha}^{max}} dW_{\alpha,\upsilon_\alpha}|Q_{\alpha\upsilon_\alpha\ell_b m_b\mu_b E}|^2\\ &\quad\times\ln\left\{\frac{2v^2}{(\varepsilon_\alpha+W_{\alpha,\upsilon_\alpha}^0)}\right\},\end{aligned} \tag{5.47}$$

[8]Unlike to the photoionization case, there is not a one-to-one relation between the final electron and proton energy, since the initial energy is not fixed.

where $W_{\alpha,\upsilon_\alpha}^{max}$ is the maximum vibrational energy belonging to the channel α compatible with the energy of the incoming particle. Since this energy is very large, the upper limit can be considered as infinity.

Bibliography

[1] H. Ehrhardt, M. Schulz, T. Tekaat, and K. Willmann, "Ionization fo Helium: Angular correlation of the scattered and ejected electrons," *Physical Review Letters*, vol. 22, pp. 89–92, 1969.

[2] N. Stolterfoht, R. Dubois, and R. D. Rivarola, *Electron Emission in Heavy Ion-Atom Collision*. Berlin: Springer, 1997.

[3] M. R. C. McDowell and J. P. Coleman, *Introduction to the Theory of Ion-Atom Collision*. North-Holland Publishing Company, 1970.

[4] R. N. Zare, "Dissociation of H_2^+ by electron impact: Calculated angular distribution," *The Journal of Chemical Physics*, vol. 47, pp. 204–215, 1967.

[5] E. H. Kerner, "The dissociation of H_2^+ by electron impact," *Physical Review*, vol. 92, pp. 1441–1447, 1953.

[6] M. Inokuti, "Inelastic collisions of fast charged particles with atoms and molecules-the Bethe theory revisited," *Review Modern Physics*, vol. 43, pp. 297–347, 1971.

[7] D. M. Wolkow, "Über eine klasse von lösungen der diracschen gleichung," *Zeitschrift für Physik A Hadrons and Nuclei*, vol. 94, pp. 250–260, 1935.

[8] G. Duchateau, E. Cormier, and R. Gayet, "A simple non-perturbative approach of atom ionisation by intense and ultra-short laser pulses," *European Physical Journal D*, vol. 11,, pp. 191–196, 2000a.

[9] I. M. Cheshire, "Continuum distorted wave approximation; resonant charge transfer by fast protons in atomic hydrogen," *Proceedings of the Physical Society*, vol. 84, pp. 89–98, 1964.

[10] L. Vainshtein, L. Presnyakov, and I. Sobelman, "On a certain model for calculation of the effective cross sections for excitation of atoms," *Soviet Physics JETP-USSR*, vol. 18, pp. 1383–1387, 1964.

[11] H. A. Bethe and E. E. Salpeter, *Quantum mechanics of one- and two-electron atoms*. Plenum/Rosetta edition, 1977.

Part II

Results

Chapter 6

Doubly excited states of H_2

"The most exciting phrase to hear in science, the one that heralds new discoveries, is not 'Eureka!' but 'That' funny ...'."

Isaac Asimov

Table of Contents

The work reported in this Chapter has led to the publications [1, 2].

6.1 Introduction

THE DOUBLY EXCITED STATES of hydrogen play an important role in single-photon and multiphoton absorption, electron-impact excitation, associative ionization and $e^- + H_2^+$. As they lie above the ionization threshold (the $X^2\Sigma_g^+(1s\sigma_g)$ state of H_2^+), they may autoionize yielding $H_2^+ + e^-$, $H + H^+ + e^-$ or lead to dissociation into neutral ground and excited H atoms as well as into $H^+ + H^-$ ions. The existence of so many decay channels has motivated a large number of experimental investigations based on the analysis of the different ionic and neutral fragments.

Since the early photoabsorption experiment of Browning and Fryar [3], many other groups have used photon absorption as a way to populate $^1\Sigma_u^+$ and $^1\Pi_u$ doubly excited states of H_2 [4, 5, 6, 7, 8, 9, 10, 11] (see also reference in). Electron-impact excitation of H_2 has also provided valuable information on the latter states and, in addition, has allowed one to explore states that are not accessible by photon absorption [12, 13, 14]. The experimental situation has been reviewed by

Kouchi *et al.* [15]. Although experimental works have been crucial in identifying many doubly excited states of H_2, their energy positions and autoionization widths can only by obtained from theoretical calculations. This is not due to an insufficient experimental precision, but to the presence of interference effects among the different decay channels [16, 17] that makes interpretation of the measured spectra difficult. Several systematic theoretical investigations have been reported in the literature [18, 19, 20, 21, 22, 23]. The latter works have provided potential energy curves and autoionization widths for states of the so-called Q_1 and Q_2 resonances series that lie above the first and second ionization threshold, $X^1\Sigma_g^+(1s\sigma_g)$ and $^2\Sigma_u^+(2p\sigma_u)$. Also, potential energy curves for non-autoionizing doubly excited states of the Q_2 series have been evaluated recently [24].

As for atomic systems, one can expect that there are additional series of autoionizing states converging to higher ionization thresholds. Resonances associated with these autoionizing states should appear 40 eV above the ground state energy of H_2, however, most photoabsorption experiments have concentrated at lower energies. Two exceptions are the experimental works of Latimer *et al.* [11] and Ito *et al.* [10]. These authors have measured the kinetic energy distribution of protons ejected in dissociative photoionization of H_2 over a wide range of photon energies. In particular, Latimer *et al.* considered photon energies of 52 to 60 eV, while Ito *et al.* scanned the photon energy interval 40-45 eV. Recent theoretical efforts [16, 17, 25, 26] have been able to reproduce the experimental findings of [9, 10, 11] up to 36 eV, in particular the resonance structure associated with the Q_1 and Q_2 doubly excited states and the interference effects related to them. At higher photon energies, the experiments show a prominent structures that dominates the spectrum up to 45 eV. Latimer *et al.* and Ito *et al.* have attributed this structure to non-resonant ionization through the $^2\Pi_u(2p\pi_u)$ ionization threshold (this is the third ionization threshold of H_2 in increasing order of energy). The validity of this interpretation was checked in a recent work [27], by explicitly including the $^2\Pi_u(2p\pi_u)$ ionization channel in calculations performed using the theory of [17, 26]. The results of [27] show a good agreement with the experiment up to 40 eV, showing that the $^2\Pi_u(2p\pi_u)$ channel is indeed the dominant channel between 37 and 40 eV. However, at higher energies, the theoretical results underestimate the intensity of the experimental peak. In addition, in the interval 40-45 eV, the experimental peak of [10] exhibits some internal structures which the theory was no able to reproduce and whose origin is still unknown. This is precisely the region where doubly excited states converging to the third and fourth ionization thresholds are expected to appear. So, we have undertaken a theoretical study for doubly excited states above the third and fourth ionization thresholds. Following common use, we will call these states Q_3 and Q_4, respectively.

In this Chapter, we present our predictions for the energy positions, autoionization widths and branching ratios of the lowest Q_3 and Q_4 states of symmetries $^1\Sigma_u^+$ and $^1\Pi_u$ (see the complementary material included in the CD for results of the lowest Q_3 and Q_4 states of symmetries $^{1,3}\Sigma_{g,u}^+$ and $^{1,3}\Pi_{g,u}$ and $^{1,3}\Delta_{g,u}$). As we will show, the autoionization widths of these states are even larger than those reported for the Q_1 and Q_2 states, which suggests that they might play and important role in photoionization of H_2 as well as in electron-impact ionization of H_2 above 40 eV (see Chapters 7 and 12).

6.2 The Q_1 and Q_2 doubly excited states

Although the objective of this Chapter is the study of the Q_3 and Q_4 doubly excited states, we dedicate some words to the two lowest families of resonant states: the Q_1 and Q_2. They will play a crucial role in Chapter 9 devoted to the electron and proton angular distribution. The characteristic of these states have been extensively studied in our laboratory by I. Sánchez *et al.* [20, 21], and in their roles in the dissociative photoionization process [16, 17].

The Q_1 resonant states of H_2 are the lowest doubly excited states. These states are accessible in the 22-33 eV range above the ground state of H_2. Fig. (6.1) displays the energy position of

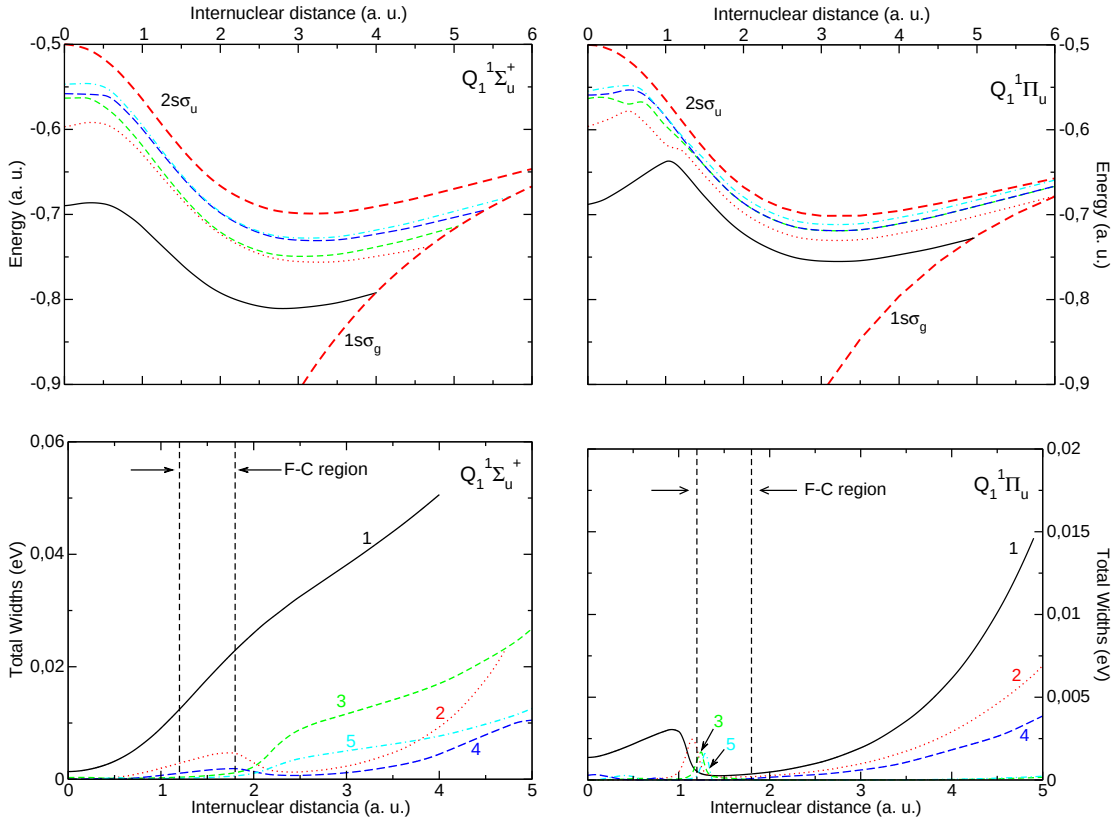

Figure 6.1: Energy position and total withs of the Q_1 doubly excited states of $^1\Sigma_u^+$ (left panel) and $^1\Pi_u$ (right panel) symmetries of H_2, as function of the internuclear distance. Results obtained by I. Sánchez *et al.* [20]. Dashed vertical lines in the lower panel represent the Franck-Condon region.

the first six resonant states of symmetries $^1\Sigma_u^+$ (left panel) and $^1\Pi_u$ (right panel). Notice that the energies do not include the repulsive internuclear-interaction term $1/R$, so that they tend to a finite value in the UA limit. Theses states converge to the second ionization threshold, the $^2\Sigma_u^+(2p\sigma_u)$ state of the H_2^+ molecule. The energy position of these resonant states follows three different patterns. The first one correspond to intermediate internuclear distances: $R \sim 1.5 - 4.0$ u.a. In this region the potential energy curves run parallel to the second ionization threshold, since they are described by the configurations[1] $2p\sigma_u n\ell\lambda$ where $n\ell\lambda$ is an excited molecular orbital. The second region corresponds to large internuclear distances, where the resonant states cross the first ionization threshold, the $X^2\Sigma_g^+(1s\sigma_g)$ state of H_2^+. Thus, for large internuclear distances, the resonant states loose their autoionizing character, in fact, they become excited states H(1s) + H($n\ell$)($n \geq 1$) in the separate atom limit. The third region is described by short internuclear distances, where some potential energy curves run parallel to the second ionization threshold, while others increase their values as function of R. The doubly excited states of $^1\Sigma_u^+$ symmetry belong to two series of doubly excited configurations: $(2p\sigma_u ns\sigma_g)$ and $(2p\sigma_u nd\sigma_g)$ with $n > 1$. As can be observed in Fig. (6.1) there are doubly excited states of $^1\Pi_u$ symmetry whose energy rapidly increase with the internuclear distance in the united atomic limit. These states are described by the configurations $2s\sigma_g np\sigma_u$ that are correlated in the separated atom limit with two excited hydrogen atoms (see figure 1 of [28]).

Fig. (6.1) shows the widths of the Q_1 doubly excited states of H_2 with symmetry $^1\Sigma_u^+$ (left panel)

[1] We make use of the common notation, where a single configuration $(n\ell\sigma_u n'\ell'\sigma_g)$ characterized the molecular states for a given internuclear distance R. Although a single configuration cannot describe by its own the molecular states, it gives the dominant character of the wave function.

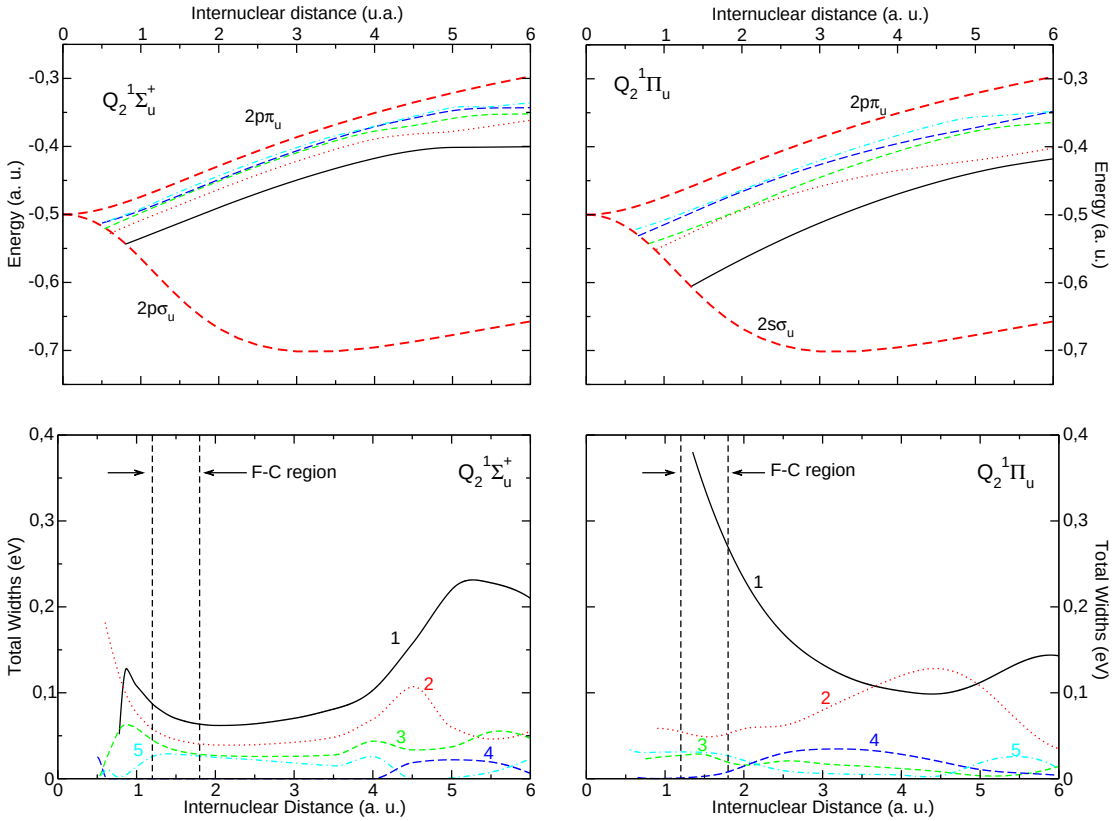

Figure 6.2: Same as Fig. (6.1) for the Q_2 doubly excited states. Results obtained by I. Sánchez *et al.* [21].

and $^1\Pi_u$ (right panel). Generally, the autoionizing widths increase their values in a monotonic way as R is raised, except close to the avoided crossings presented in Fig. (6.1). The values of these widths are larger than for the He atom since the loss of spherical symmetry allows the decay to more final channels than in the atomic case. The widths associated with the resonant states of $^1\Sigma_u^+$ symmetry are larger than for $^1\Pi_u$ symmetry, specially in the Franck-Condon region, which has a dramatic effect in the photoionization of H_2. In the united atom limit, the widths of the lowest states are correlated with the resonant states $^1P^0(2s2p)$ of the He atom.

The Q_2 doubly excited states are accessible in the energy range 30-40 eV over the ground state of H_2. Fig. (6.2) displays the Q_2 doubly excited states of H_2 with symmetry $^1\Sigma_u^+$ (left panel) and $^1\Pi_u$ (right panel), and, as can be seen, they converge to the second ionization threshold, the $^2\Pi_u(2p\pi_u)$ state of H_2^+. Just like for the Q_1 resonant states, three different regions can be distinguished as function of R. In the first one, for values of the internuclear distance $R \sim 1.4 - 4.0$ u.a., the energy positions run parallel to the second third ionization threshold. In this region, the doubly excited states are described by the configuration $2p\pi_u n\ell\lambda$, where $n\ell\lambda$ is the molecular orbital different from $1s\sigma_g$ and $2p\sigma_u$. The second region corresponds to large internuclear distances, where some curves run parallel to the third ionization threshold, while others increase or decrease their values with R. In the last case these states are described by the molecular orbital $3d\sigma_g n\ell\lambda$ since the energy of the orbital $3d\sigma_g$ $3d\sigma_g n\ell\lambda$ decreases with R while the orbitals $2s\sigma_g$ and $2p\pi_u$ increases with R. This fact is also reflected in the behavior of the widths (Fig. (6.2)).

Fig. (6.2) shows the widths of the Q_2 doubly excited states of H_2 with symmetry $^1\Sigma_u^+$ (left panel) and $^1\Pi_u$ (right panel). In this case, the width with $^1\Sigma_u^+$ symmetry are much smaller than for the states with $^1\Pi_u$ symmetry. In relation with the results of the Q_1 state, the widths of the Q_2 of $^1\Pi_u$ symmetry are of the same order of magnitude than the Q_1 $^1\Sigma_u^+$ states, so, we will show in Chapter

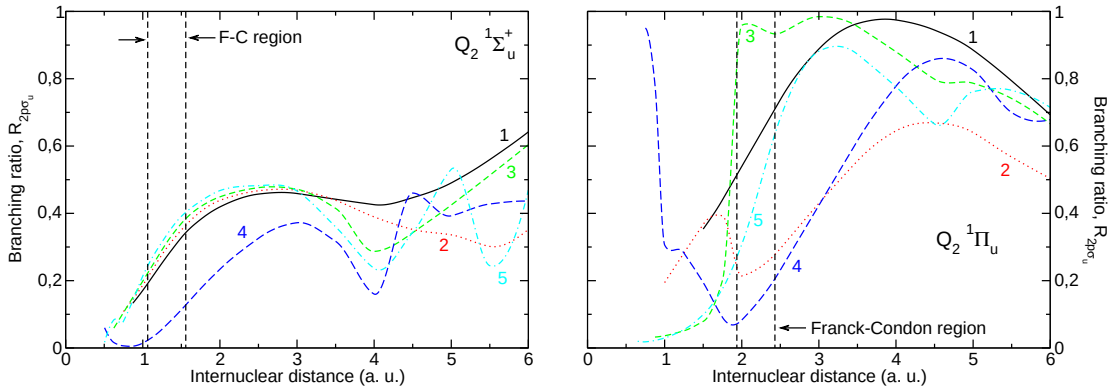

Figure 6.3: Branching ratios though the $2p\sigma_u$ ionization threshold of the Q_2 doubly excited states of $^1\Sigma_u^+$ (left panel) and $^1\Pi_u$ (right panel) symmetries of H_2, as function of the internuclear distance. Results obtained by I. Sánchez *et al.* [21].

7 both resonant states will play an important role in the ionization process. In general, as can be seen from Figs. (6.2) and (6.2), the larger the width the smaller its energy, and the higher the state the smaller its width. These is consequence of a scaling rule that can be applied in the united atom limit. However the avoided crossings in correlation diagram lead to exceptions to this rule.

Since the Q_2 can decay to two ionization thresholds, the $X^2\Sigma_g^+(1s\sigma_g)$ and $^2\Sigma_u^+(2p\sigma_u)$, states, it is convenient to define the branching ration to each threshold. The branching ratios give information about the probability of the decay of a resonant state trough different ionization thresholds, and are essential to interpret experimental results. These branching ratios are defined as

$$\gamma_\alpha = \frac{\Gamma_\alpha}{\sum_{\alpha'}\Gamma_{\alpha'}} \tag{6.1}$$

where $\sum_\alpha \Gamma_\alpha$ is the total width of the resonant state and Γ_α is the partial width associated to the ionization threshold α. The sum of the all branching ratios must be equal to one. Fig. (6.3) displays the branching ratio associated to the $2p\sigma_u$ state. The Q_2 states tend to autoionize, in the Franck-Condon region, through the closer ionization threshold, i.e., to the ionization threshold lying just below it.

6.3 The Q_3 and Q_4 doubly excited states

This section is devoted to the results obtained of the Q_3 and Q_4 doubly excited states of symmetry $^1\Sigma_u^+$ and $^1\Pi_u$, paying special attention to the characteristics of the basis sets used in the calculations. Here we will follow closely the publication [1]. This states are situated above the second ionization threshold, which means that the computational effort is considerable superior to the calculations performed for the Q_1 and Q_2 resonant states.

6.3.1 Computational details

The theoretical method has been described previously in Section 3.9 of Chapter 3, so we refer the reader to this Chapter for more details. Both resonant and non resonant continuum states are written in terms of one-electron basis functions. The calculations have been performed making use of B-spline basis set of order $k = 8$, with a box size of $r_{max} = 60$ a.u., formed by $N_\ell = 210$ basis functions, and a linear knot sequence. We have included angular momenta up to $\ell_{max} = 10$. Since

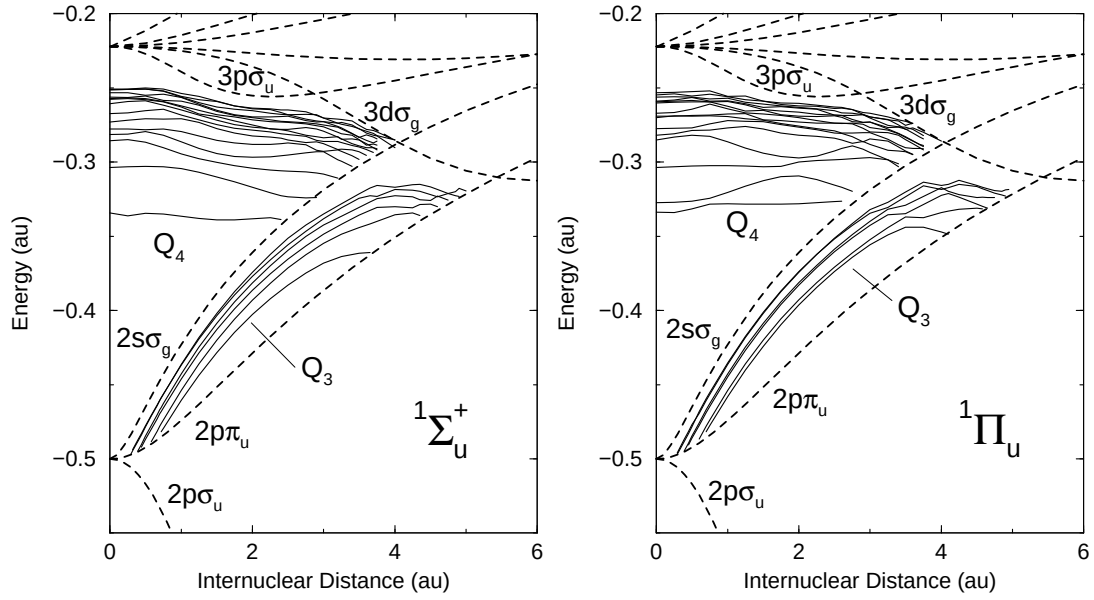

Figure 6.4: Electronic energies for the lowest Q_3 and Q_4 autoionizing $^1\Sigma_u^+$ (left panel) and $^1\Pi_u$ states (right panel) of H_2 as functions of internuclear distance. Dashed lines represent the states of H_2^+, i.e., the ionization thresholds of H_2. Notice that the lowest ionization threshold $1s\sigma_g$ is out of scale.

we have 210 *B*-spline functions per angular momentum, σ_g orbitals are expansions of 1260 terms ($\ell = 0$, 2, 4, 6, 8, and 10), σ_u orbitals of 1050 terms ($\ell = 1$, 3, 5, 7, and 9), π_g orbitals of 1050 terms ($\ell = 2$, 4, 6, 8, and 10), and so on. The present basis set has allowed us to perform reliable calculations in the range of internuclear distances $R = 0 - 5$ a.u.

The resonant wave functions ϕ_n (hence $G_Q^{(s)}(E)$, see Eq. (3.57)) are obtained using standard configuration interaction techniques. The H_2 Hamiltonian is diagonalized in a basis of N_{conf} configurations built from the one electron target orbitals φ_{nm} described in the Chapter 3. For example, in the case of the Q_3 states of the $^1\Pi_u$ symmetry, we have included the configurations $2\sigma_g n\pi_u$ ($n = 2-70$), $2\sigma_u n\pi_g$ ($n = 1-70$), $3\sigma_g n\pi_u$ ($n = 2-70$), $1\pi_g n\sigma_u$ ($n = 3-18$), $1\delta_g n\pi_u$ ($n = 2-18$), $2\pi_u n\sigma_g$ ($n = 4-18$), $4\sigma_g n\pi_u$ ($n = 3-17$), $3\sigma_u n\pi_g$ ($n = 2-16$), $5\sigma_g n\pi_u$ ($n = 3-17$), $4\sigma_u n\pi_g$ ($n = 2-16$), $3\pi_u n\sigma_g$ ($n = 6-20$), $2\pi_g n\sigma_u$ ($n = 5-19$), $2\delta_g n\pi_u$ ($n = 2-16$), $1\delta_u n\pi_g$ ($n = 1-15$), $1\varphi_u n\delta_g$ ($n = 1-15$), $4\pi_u n\sigma_g$ ($n = 6-20$), and $6\sigma_g n\pi_u$ ($n = 5-19$), which amounts to 421 configurations (the index *n* used to label one-electron orbitals in the two-electron basis indicates energy ordering for a given value of *R*). This basis includes all molecular orbitals correlated to the $n = 3$ and $n = 4$ atomic orbitals in the united atom (UA) limit ($R = 0$). For the Q_4 states of $^1\Pi_u$ symmetry and for the Q_3 and Q_4 states of $^1\Sigma_u^+$ symmetry, the quality of the basis set is comparable (352, 402 and 343 configurations, respectively). For the Q_3 states, the lowest target orbitals $1s\sigma_g \equiv 1\sigma_g$, $2p\sigma_u \equiv 1\sigma_u$ and $2p\pi_u \equiv 1\pi_u$ are excluded from the configuration basis in Q subspace in order to ensure orthogonality with the $1s\sigma_g\varepsilon\ell\lambda$, $2p\sigma_u\varepsilon\ell\lambda$ and $2p\pi_u\varepsilon\ell\lambda$ open channels included in P subspace. For the Q_4 states, besides the above orbitals, we have also excluded the $2s\sigma_g \equiv 2\sigma_g$ one to ensure orthogonality with the $2s\sigma_g\varepsilon\ell\lambda$ channel. As we have shown in Chapter 3, the non resonant continuum states $P\psi_{\mu E}^{0+}$ are evaluated for each open channel $\mu = \{\nu, \ell, \Lambda, \pi, \sigma, S, M_S\}$ in three steps. In the first step, we evaluate one-electron orbitals $\{\varphi_{klm}\}$ by diagonalizing the H_2^+ Hamiltonian in the set of basis functions $\{r^{-1}B_i^k(r)Y_l^m(\hat{r})\}$, now restricting the angular momentum ℓ to that of the ejected electron in channel μ. Then, in the second step, we diagonalize the H_2 Hamiltonian for each μ separately, using a basis of configurations built from antisymmetrized

products of the $\{\varphi_{nm}\}$ orbitals with the $\{\varphi_{k\ell m}\}$ ones (the former are the H_2^+ states described in Chapter 3). We have evaluated all open channels μ with angular momentum of the ejected electron up to $\ell = 7$, i.e., 11 and 15 open channels for the $^1\Sigma_u^+$ states lying respectively above the $^2\Pi_u(2p\pi_u)$ and $^2\Sigma_g(2s\sigma_g)$ ionization thresholds, and 14 and 18 open channels for the $^1\Pi_u$ states. For each μ, the number of configurations is 75. Up to this point, the calculated continuum states do not include any kind of mixing between different μ channels. We introduce inter-channel coupling in the third step by using the L^2 close-coupling method of [29]. In other words, we evaluate the $G_P^{(s)+}$ matrix elements (see Eq. (3.58))and the non resonant continuum wave function $P\psi^{0+}_{\mu E_{\mu n}}$ using the above L^2 uncoupled continuum states as a basis for a close-coupling expansion (see [29] for details). This is the same method used in our previous study of the Q_1 and Q_2 series of H_2 [20, 21] and in many other works (see [25, 26, 30] and references therein). Finally, notice that the effect of closed H_2^+ channels on the non resonant continuum is also taken into account through the polarization term $P\mathcal{H}QG_Q^{(s)}Q\mathcal{H}P$ contained in $\mathcal{H}'$ (see Eq. (3.56)) which couples P and Q subspaces. The resulting $P\psi^{0-}_{\mu E_{\mu n}}$ wave functions are used in equations (3.50) and (3.51) to evaluate the shift and the width of the resonances.

The accuracy of the energies and widths calculated with the above basis sets (Basis I) has been checked in three different ways. First, by varying the number of terms in the basis: N_ℓ=170 (Basis II) and ℓ_{max}=8 (Basis III), with N_{conf} and the box size r_{max} fixed. Second, by varying the number of configurations, N_{conf} (Basis IV). In this case, configurations including orbitals with the higher values of n have been eliminated from Basis I. Finally, by increasing r_{max} from 60 to 90 a.u. (and, consequently, N_ℓ from 210 to 315 so that the number of B-splines per atomic unit remains constant) with N_{conf} and ℓ_{max} fixed (Basis V). Table (6.3.1) shows that the energies obtained with Basis we and II differ $\sim 10^{-5}$ a.u. at $R = 2.5$ a.u., and even less at $R = 1.5$ a.u. Basis III and IV provide energies that differ in the fifth significant figure at $R = 1.5$ a.u. and in the fourth significant figure at $R = 2.5$ a.u. The energies obtained by increasing the box size (Basis V) differ again in the fourth significant figure for the two values of R. Although results obtained with Basis V are the most accurate ones, we have chosen Basis we to obtain all our results because the computational effort is much smaller. Hence, the estimated error for the energies in the range of internuclear distances considered in this work is $\sim 10^{-4}$ a.u. Convergence errors for the widths are of the same order, i.e., 10^{-3} eV.

Tables containing energy positions, total autoionization widths and branching ratios for the Q_3 and Q_4 states of $^{1,3}\Sigma^+_{g,u}$, $^{1,3}\Pi_{g,u}$ and $^{1,3}\Delta_{g,u}$ symmetries are available in the additional material included in the CD or upon request. Figs. (6.4) and (6.6) show the variation of the calculated energies and total widths with the internuclear distance R. Notice that the energies do not include the repulsive internuclear-interaction term $1/R$, so that they tend to a finite value in the UA limit.

6.3.2 Q_3 autoionizing states

Fig. (6.4) shows that, for $R < 3$ a.u., the energy curves of the Q_3 states run almost parallel to the fourth ionization threshold $^2\Sigma_g^+(2s\sigma_g)$ because the doubly-excited states are mainly described by $2s\sigma_g nl\lambda$ configurations: $2s\sigma_g nl\sigma_u$ configurations for states of $^1\Sigma_u^+$ symmetry and $2s\sigma_g nl\pi_u$ configurations for states of $^1\Pi_u$ symmetry. This is illustrated by the configuration weights shown in Fig. (6.5) for the lowest Q_3 state of $^1\Sigma_u^+$ and $^1\Pi_u$ symmetries. It can be seen that the weight of the above configurations exceeds 90%. This conclusion is valid for all the Q_3 states evaluated in this work. At short R, the potential energy curves cross the third ionization threshold $^2\Pi_u(2p\pi_u)$ and tend to atomic states that are mainly described by $2lnl'$ configurations. They also cross the $^2\Pi_u(2p\pi_u)$ threshold in the vicinity of $R \simeq 4$ a.u. This is due to a strong mixing with configurations that are dominant for the Q_4 states (see Fig. (6.4) and below), which leads to the series of avoided crossings that can be observed in that region.

I must stress here that the lowest Q_3 state given in Fig. (6.4) does not actually correspond to the

	$R = 1.5$ u.a.				
E_s (u.a.)	I	II	III	IV	V
$1^1\Pi_u$	-0.32845	-0.32845	-0.32842	-0.32842	-0.32835
$2^1\Pi_u$	-0.31262	-0.31261	-0.31263	-0.31261	-0.31233
$3^1\Pi_u$	-0.30311	-0.30311	-0.30310	-0.30306	-0.30293
$4^1\Pi_u$	-0.29410	-0.29410	-0.29405	-0.29409	-0.29408
$5^1\Pi_u$	-0.27790	-0.27790	-0.27785	-0.27788	-0.27789
Γ_s (eV)	I	II	III	IV	V
$1^1\Pi_u$	0.17840	0.17840	0.17840	0.17850	0.18210
$2^1\Pi_u$	0.14310	0.14300	0.14370	0.14380	0.16040
$3^1\Pi_u$	0.30320	0.30320	0.30320	0.30260	0.30400
$4^1\Pi_u$	0.01861	0.01863	0.01868	0.01871	0.01941
$5^1\Pi_u$	0.00864	0.00864	0.00875	0.00860	0.00900
	$R = 2.5$ u.a.				
E_s (a.u.)	I	II	III	IV	V
$1^1\Pi_u$	-0.32675	-0.32672	-0.32660	-0.32670	-0.32693
$2^1\Pi_u$	-0.31544	-0.31543	-0.31538	-0.31539	-0.31553
$3^1\Pi_u$	-0.29846	-0.29842	-0.29826	-0.29845	-0.29839
$4^1\Pi_u$	-0.29262	-0.29261	-0.29264	-0.29260	-0.29178
$5^1\Pi_u$	-0.28392	-0.28390	-0.28382	-0.28391	-0.28392
Γ_s (eV)	I	II	III	IV	V
$1^1\Pi_u$	0.33910	0.33860	0.33460	0.33990	0.34810
$2^1\Pi_u$	0.49810	0.49820	0.50140	0.50180	0.49110
$3^1\Pi_u$	0.02723	0.02731	0.02781	0.02744	0.02363
$4^1\Pi_u$	0.16620	0.16590	0.16460	0.16710	0.19420
$5^1\Pi_u$	0.04137	0.04175	0.04366	0.04205	0.04285

Table 6.1: Convergence of the calculated energies and widths for the lowest five $^1\Pi_u$ Q_4 states of H_2 at $R = 1.5$ and 2.5 a.u. Basis I: $N_\ell = 210$, $\ell_{max} = 10$, $N_{conf} = 352$, $r_{max} = 60$ a. u.; this is the basis used to evaluate all the resonance parameters. Basis II: $N_\ell = 170$, $\ell_{max} = 10$, $N_{conf} = 352$, $r_{max} = 60$ a.u. Basis III: $N_\ell = 210$, $\ell_{max} = 8$, $N_{conf} = 352$, $r_{max} = 60$ a.u. Basis IV: $N_\ell = 210$, $\ell_{max} = 10$ $N_{conf} = 297$, $r_{max} = 60$ a.u. (see text). Basis V: $N_\ell = 315$, $\ell_{max} = 10$, $N_{conf} = 352$, $r_{max} = 90$ a.u.

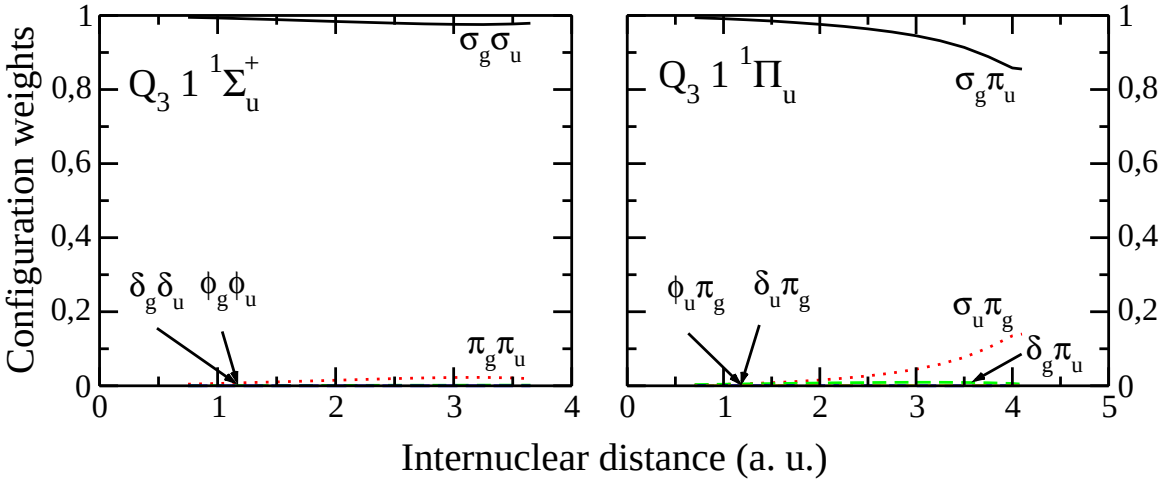

Figure 6.5: Configuration weights for the lowest Q_3 state of $^1\Sigma_u^+$ and $^1\Pi_u$ symmetries.

lowest eigenvalue resulting from solving Eq. (3.55), but to the second lowest eigenvalue. The lowest Q_3 state (whose dominant configuration is $2s\sigma_g 3p\sigma_u$ for the $^1\Sigma_u^+$ symmetry and $2s\sigma_g 3p\pi_u$ for the $^1\Pi_u$ symmetry) lies, in fact, below the $^2\Pi_u(2p\pi_u)$ ionization threshold for all R. This means that this state is completely diluted among the states of the Q_2 series and, therefore, cannot be considered as a member of the Q_3 series. This is in agreement with the results of reference [21], where it was shown that the $2s\sigma_g nl\lambda$ configurations contribute significantly to the wave function of the Q_2 states. As shown in [21], this has a dramatic effect on the Q_2 autoionization widths, since by excluding the latter configurations from the Q_2 states, the calculated widths differ by more than an order of magnitude from the actual ones. Similarly, the dominant configurations for the Q_2 states should contribute to the representation of the Q_3 states, which may rise the question of the pertinence of the $P-$Q partition for the latter states. However, this is not a problem in our formalism because contribution of the latter configurations is fully taken into account through an exact evaluation of the energy shift Δ_s, i.e., of the $G_P^{(s)+}$ Green's function, in Eq. (3.50) (see reference [31] for a detailed discussion). In other words, the $P-$Q coupling is evaluated exactly, while in most applications of the Feshbach theory, where the energy shift is either neglected or evaluated perturbatively, a necessary condition is that the $P-$Q coupling is small. In the latter case, the choice of the $P-$Q partition is a crucial point, but not in the present formalism where any other choice of P and Q would lead to identical results (provided that the same basis set is used, see [31]). Nevertheless, our calculated energy shifts are small, so that even a perturbative approach might lead to reasonable results. Fig. (6.6) shows that, for the Q_3 states, the largest width corresponds to the lowest doubly excited state of each symmetry, and that the more excited the state, the smaller the width. This is the result of the approximate $1/n^3$ scaling of the resonance widths in the UA limit. There are, however, exceptions to this rule that are mainly due to the existence of avoided crossings. It can also be observed that, for each symmetry, the widths vary with R following two different patterns. For instance, in the case of the Q_3 states of $^1\Sigma_u^+$ symmetry below $R = 3$ a.u., the widths of the states labeled 1, 3 and 5 follow more or less the same pattern, while the widths of states 2, 4 and 6 follow a different one. This is the consequence of the different character of the corresponding wave function. For states 1, 3 and 5, the dominant configuration is of the form $2s\sigma_g np\sigma_u$, while for states 2, 4 and 6, it is $2s\sigma_g nf\sigma_u$. The relative weight of these two configurations alternate as n increases along the series because, for a given n, the energy of the $np\sigma_u$ orbital is lower than that of the $nf\sigma_u$ orbital. Above $R = 3$ a.u., there are many different patterns due to the presence of avoided crossings. From the calculated partial autoionization widths, displayed in Fig. (6.7), we conclude

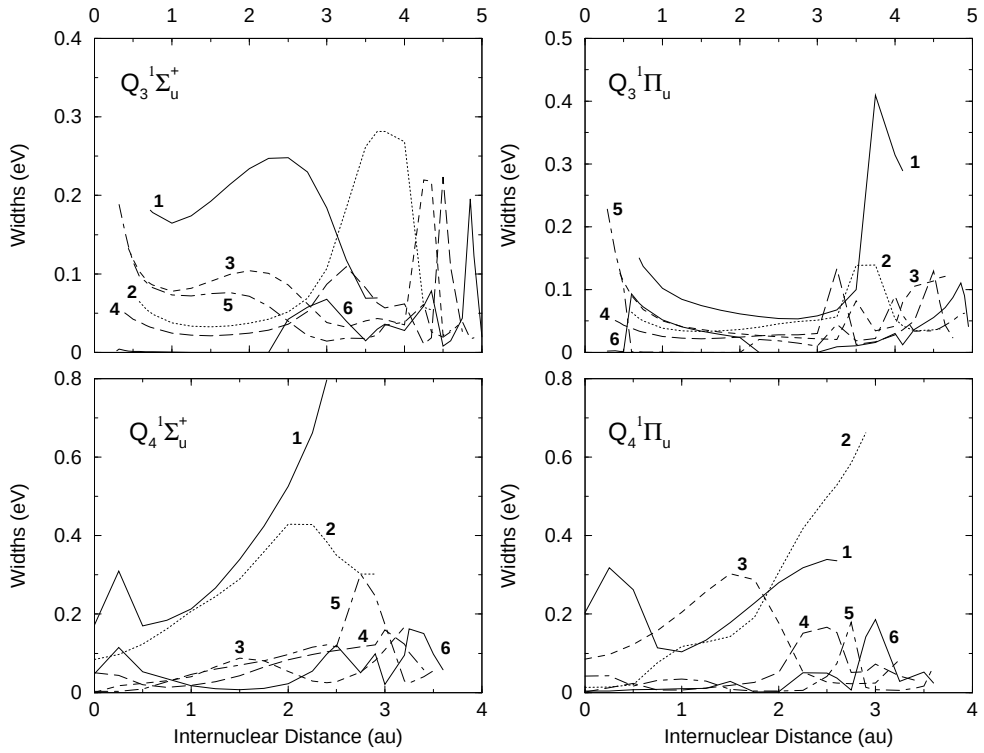

Figure 6.6: Total autoionization widths for the lowest Q_3 and Q_4 states of $^1\Sigma_u^+$ (left panels) and $^1\Pi_u$ symmetry (right panels) of H_2 as functions of internuclear distance. Numbers indicate energy ordering.

that, for all Q_3 states, autoionization leaves preferentially the H_2^+ ion in the highest possible excited state $^2\Pi_u(2p\pi_u)$ (on average, the corresponding partial width is at least $\simeq 80\%$ of the total width). This behaviour is very similar to that of the Q_2 states [21].

6.3.3 Q_4 autoionizing states

In contrast with the Q_3 states, Fig. (6.4) shows that the variation of the Q_4 energy curves with R do not follow a simple pattern. Most of the Q_4 energy curves exhibit avoided crossings in the interval $R = 0 - 3$ a.u., which is the region where these states are expected to be excited from the ground state of H_2. This is also at variance with the rather simple behavior observed in previous works for the Q_1 and Q_2 states.

To understand the origin of the unusual behavior of the Q_4 states, we have plotted in Fig. (6.8) the configuration weights for the two lowest Q_4 states of $^1\Sigma_u^+$ and $^1\Pi_u$ symmetries. The figure shows that there is not a single type of configuration that clearly dominates over the entire range of internuclear distances, especially for the Q_4 states of $^1\Pi_u$ symmetry. For the lowest state of $^1\Pi_u$ symmetry, $\sigma_g\pi_u$- and $\sigma_u\pi_g$-type configurations contribute significantly: none of them exceeds 70% of the wavefunction normalization. Among them, the most important configurations are $3p\sigma_u 3d\pi_g$ and $3d\sigma_g 3p\pi_u$, which are almost degenerate in energy (indeed, the $3p\sigma_u$, $3d\pi_g$, $3d\sigma_g$ and $3p\pi_u$ orbitals of H_2^+ are very close). Furthermore, their relative importance changes around $R = 1$ a.u., which is the consequence of the avoided crossing with the second $^1\Pi_u$ state at this value of the internuclear distance. The structure of the second $^1\Pi_u$ state is even more complicated, because it has significant contributions from $\delta_g\pi_u$-, $\sigma_g\pi_u$- and $\sigma_u\pi_g$-type configurations. Besides the above mentioned $3p\sigma_u 3d\pi_g$ and $3d\sigma_g 3p\pi_u$ configurations, the $3d\delta_g 3p\pi_u$ and $3s\sigma_g 3p\pi_u$ configurations play also a very important role. For the Q_4 states of $^1\Sigma_u^+$ symmetry, Fig. (6.8) shows that the situation

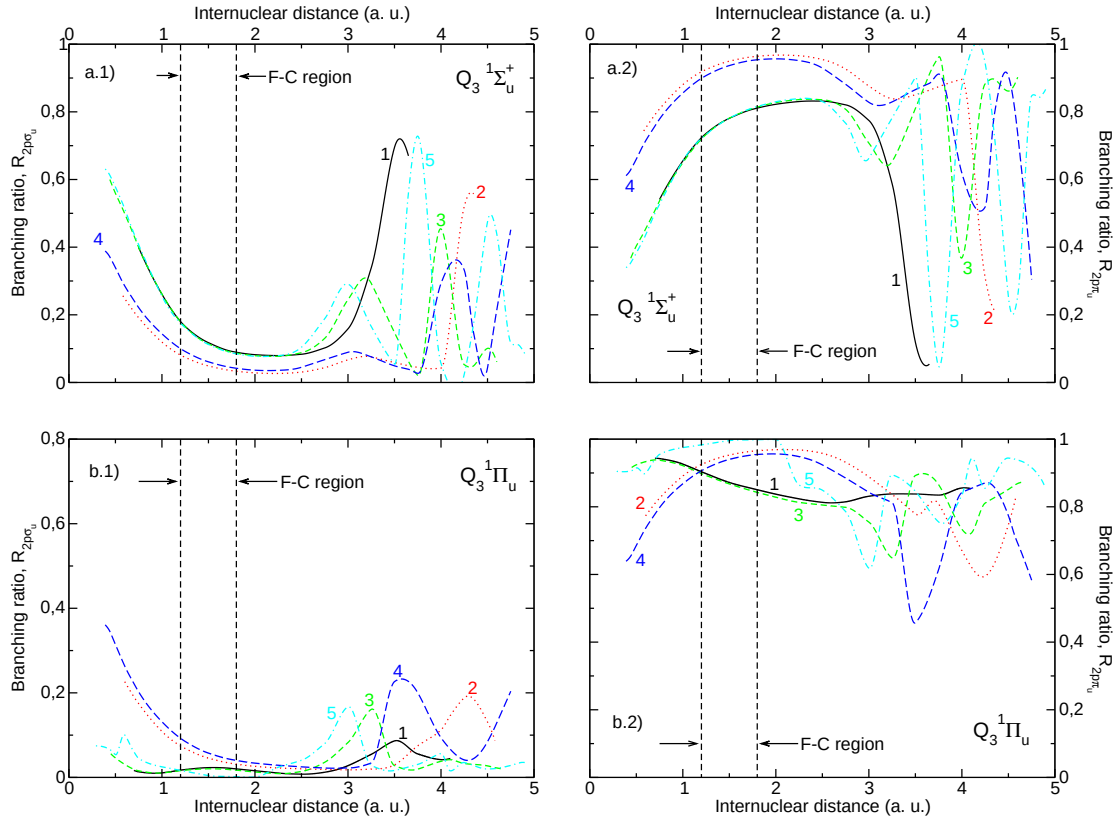

Figure 6.7: Branching ratios though the $2p\sigma_u$ (panels a.1 and b.1) and $2p\pi_u$ (a.2 and b.2) ionization thresholds of the Q_3 doubly excited states of $^1\Sigma_u^+$ (panels a.1 and a.2) and $^1\Pi_u$ (panels b.1 and b.2) symmetry of H_2, as function of the internuclear distance.

is apparently less dramatic, however the dominance of the $\sigma_u\sigma_g$ character is due at least to two configurations: $3p\sigma_u 3s\sigma_g$ and $3p\sigma_u 3d\sigma_g$. Therefore, configurations mixing is as important as for the Q_4 states of $^1\Pi_u$ symmetry.

The main conclusion that can be extracted from this analysis is that the structure of the Q_4 states cannot be explained by assuming that one of the electrons is in the H_2^+ orbital associated to the ionization threshold that lies immediately above in energy. The latter assumption works reasonably well for the Q_1, Q_2 and Q_3 states (see above and references [20, 21]), however it leads to a very poor description of the Q_4 states. This strong configuration mixing is also present in the $3\ell 3\ell'$ doubly excited states of He, nevertheless the present situation is more complicated due to the strong variation of the mixing with internuclear distance. In this respect, it is worth noticing that the configuration weights that we obtain in the limit $R = 0$ are in good agreement with those of the $3\ell 3\ell'$ doubly excited states of helium (see reference [32]), which is a good test of the accuracy of the present calculations. Nevertheless, apart from testing purposes, the knowledge of the configuration mixing at $R = 0$ has no practical utility in predicting the actual mixing of the Q_4 states of H_2 because, as Fig. (6.8) shows, the weights change abruptly with internuclear distance. Therefore, only actual computations can be used to predict the behavior of the Q_4 states. Obviously, this conspicuous behavior has important consequences on the autoionization widths. Fig. (6.6) shows that, in contrast with the Q_3 states, the variation of the total autoionization widths of the Q_4 states is rather unpredictable. This is not only due to the strong variation of the configuration mixing with R, but also to the presence of the avoided crossings. For the $^1\Sigma_u^+$ symmetry, the widths of the two lowest Q_4 states are comparable and larger than those of the rest of states of the series. For the $^1\Pi_u$

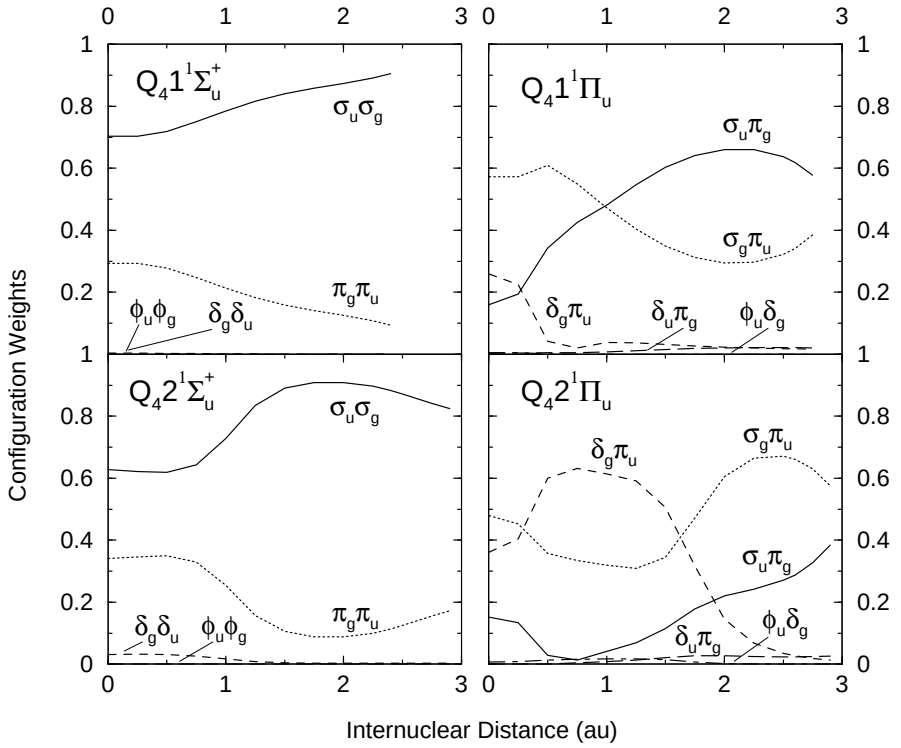

Figure 6.8: Configuration weights for the two lowest Q_4 states of $^1\Sigma_u^+$ and $^1\Pi_u$ symmetries.

symmetry, the widths of the three lowest Q_4 states are comparable. The calculated partial widths, displayed in Fig. (6.9), indicate that there are two dominant autoionization channels, $2p\pi_u$ and $2s\sigma_g$, whose relative importance strongly depends on R.

6.4 Conclusions

In this Chapter we have reported the first theoretical calculations of energy positions and autoionization widths for the Q_3 and Q_4 doubly excited states of H_2 with $^1\Sigma_u^+$ and $^1\Pi_u$ symmetries. Our results show that the autoionization widths of the Q_4 states are larger than those of the Q_1, Q_2 and Q_3 states (except for the lowest Q_1 $^1\Sigma_u^+$ one). The behavior of the Q_3 states follows the general patterns of the known Q_1 and Q_2 states, namely (i) there is a dominant type of configurations in which one of the electrons is in the H_2^+ orbital corresponding to the ionization threshold lying immediately above in energy, (ii) the energy positions and widths exhibit a rather regular behavior as functions of internuclear distance, and (iii) autoionization occurs preferentially through the nearest ionization channel. In contrast, the Q_4 states exhibit a strong configuration mixing (i.e., electron correlation is much more important), no regular behavior is obtained either for energy positions or widths, and autoionization proceeds indistinctly through the two nearest ionization thresholds. The Q_3 and Q_4 states may play an important role in photoionization of H_2 for photon energies above 40 eV (see Chapter 7). Indeed, in a vertical transition from the ground state of H_2 at the equilibrium internuclear distance $R_e = 1.4$ a.u., the Q_3 and Q_4 states lie in the interval 40-44 eV. This is precisely the region where the dissociative photoionization spectrum of reference [10] shows additional structures not explained by the theory [27]. As in reference [27], an explicit comparison with experiment requires the use of the formalism developed in references [25, 26], which includes the nuclear motion. In previous applications of this formalism, the resonance features observed in the spectra could be

explained by including one or at most two doubly excited states. This leads to a great simplification of the coupled equations that have to be solved using the formalism of [25, 26]. Now, the present results show that there are several Q_3 and Q_4 states with large autoionization widths that may contribute significantly to the resonance structures observed above 40 eV. This will be the theme of the next Chapter.

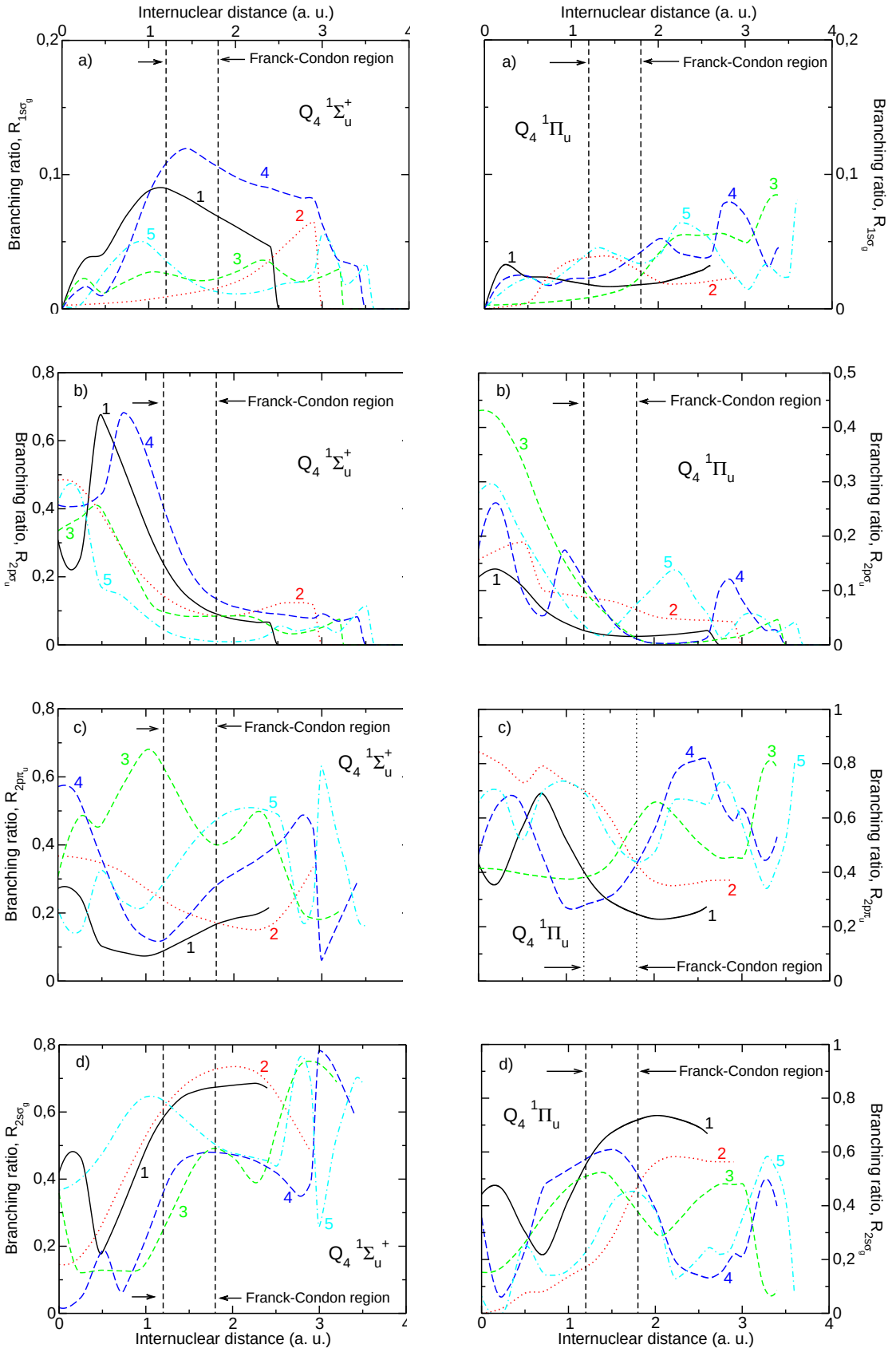

Figure 6.9: Branching ratios though the $1s\sigma_g$ (a), $2p\sigma_u$ (b), $2p\pi_u$ (c) and $2s\sigma_g$ (d) ionization thresholds of the Q_4 doubly excited states of H_2 of $^1\Sigma_u^+$ and Π_u symmetry, as function of the internuclear distance.

Bibliography

[1] J. Fernández and F. Martín, "Autoinizing $^1\Sigma_u^+$ and $^1\Pi_u$ states of H_2 above the third and fourth ionization thrseshols," *Journal of Physics B: Atomic, Molecular and Optical Physics*, vol. 34, pp. 4141–4153, 2001.

[2] J. Fernández, A. Palacios, and F. Martín, "Recent advances in the study of ionization and dissociation of H_2 using B-spline basis sets," *Electron and Photon Impact Ionization and Related Topics (Institute of Physics, London UK) Conference series No. 172*, pp. 1–10, 2003.

[3] R. Browning and J. Fryar, "Dissociative photoionization of H_2 and D_2 through the $1s\sigma_g$ ionic state," *Journal of Physics B: Atomic, Molecular and Optical Physics*, vol. 6, pp. 364–371, 1973.

[4] S. Strathdee and R. Browning, "Dissociative photoionization of H_2 at 26.9 eV," *Journal of Physics B: Atomic, Molecular and Optical Physics*, vol. 9, pp. L505–L507, 1976.

[5] S. Strathdee and R. Browning, "Dissociative photoionisation of H_2: Proton kinetic energy spectra," *Journal of Physics B: Atomic, Molecular and Optical Physics*, vol. 12, pp. 1789–1804, 1979.

[6] M. Glass-Maujean, "Photodissociation of doubly excited states of H_2, HD, and D_2," *The Journal of Chemical Physics*, vol. 85, pp. 4830–4834, 1986.

[7] M. Glass-Maujean, "Photodissociation of doubly excited states of H_2: Emission of balmer lines," *The Journal of Chemical Physics*, vol. 89, pp. 2839–2843, 1988.

[8] Y. M. Chung, E.-M. Lee, T. Masuoka, and J. A. R. Samson, "Dissociative photoionization of H_2 from 18 to 124 eV," *The Journal of Chemical Physics*, vol. 99, pp. 885–889, 1993.

[9] C. J. Latimer, K. F. Dunn, F. P. O'Neill, M. A. MacDonald, and N. Kouchi, "Photoionization of hydrogen and deuterium," *The Journal of Chemical Physics*, vol. 102, pp. 722–725, 1995.

[10] K. Ito, R. I. Hall, and M. Ukai, "Dissociative photoionization of H_2 and D_2 in the energy region of 25-45 eV," *The Journal of Chemical Physics*, vol. 104, pp. 8449–8457, 1996.

[11] C. J. Latimer, J. Geddes, M. A. MacDonald, N. Kouchi, and K. F. Dunn, "The photodissociative ionization of hydrogen and deuterium in the VUV via Π states," *Journal of Physics B: Atomic, Molecular and Optical Physics*, vol. 29, pp. 6113–6121, 1996.

[12] M. Leventhal, R. T. Robiscoe, and K. R. Lea, "Velocity distribution of metastable h atoms produced by dissociative excitation of H_2," *Physical Review*, vol. 158, pp. 49–56, 1967.

[13] L. J. Kieffer and G. H. Dunn, "Dissociative ionization of H_2 and D_2," *Physical Review*, vol. 158, pp. 61–65, 1967.

[14] L. J. Kieffer and G. H. Dunn, "Erratum: Dissociative ionization of H_2 and D_2," *Physical Review A*, vol. 164, p. 270, 1967.

[15] N. Kouchi, M. Ukai, and Y. Hatano, "Dissociation dynamics of superexcited molecular hydrogen," *Journal of Physics B: Atomic, Molecular and Optical Physics*, vol. 30, pp. 2319–2344, 1997.

[16] I. Sánchez and F. Martín, "Origin of unidentified structures in resonant dissociative photoionization of H_2," *Physical Review letters*, vol. 79, pp. 1654–1657, 1997.

[17] I. Sánchez and F. Martín, "Multichannel dissociation in resonant photoionization of H_2," *Physical Review letters*, vol. 82, pp. 3775–3778, 1999.

[18] S. L. Guberman, "The doubly excited autoionizing states of H_2," *The Journal of Chemical Physics*, vol. 78, pp. 1404–1413, 1983.

[19] J. Tennyson, "Resonance parameters and quantum defects for superexcited H_2," *Atomic Data and Nuclear Data Tables*, vol. 64, pp. 253–277, 1996.

[20] I. Sánchez and F. Martín, "The doubly excited states of the H_2 molecule," *Journal of Chemical Physics*, vol. 106, pp. 7720–7730, 1997.

[21] I. Sánchez and F. Martín, "Doubly excited autoionizing states of the H_2 above the second ionization thershold: The Q_2 resonance series," *Journal of Chemical Physics*, vol. 110, pp. 6702–6713, 1999.

[22] S. Lee, M. Iwai, and H. Nakamura, *Molecules in laser fields*. A. D. Bandrauk, 1994.

[23] Y. V. Vanne and A. Saenz, "Numerical treatment of diatomic two-electron molecules using a B-spline based CI method," *Journal of Physics B: Atomic, Molecular and Optical Physics*, vol. 37, pp. 4101–4118, 2004.

[24] F. Martín, "Non-autoionizing doubly excited states of H_2: the Σ^- symmetry," *Journal of Physics B: Atomic, Molecular and Optical Physics*, vol. 32, pp. L181–L187, 1999.

[25] I. Sánchez and F. Martín, "Resonant dissociative photoionization of H_2 and D_2," *Physical Review A*, vol. 57, pp. 1006–1017, 1998.

[26] I. Sánchez and F. Martín, "Dissociative photoionization of H_2 and D_2 by (30-37)-eV photons via $^1\Pi_u$ states," *Physical Review A*, vol. 60, pp. 2200–2206, 1999.

[27] J. Fernández and F. Martín, "In search of new resonance structures in dissociative photoionization of H_2," *International Journal of Quantum Chemistry*, vol. 86, pp. 145–150, 2002.

[28] J. L. Sanz-Vicario, H. Bachau, and F. Martín, "Time-dependent theoretical description of molecular autoionization produced by femtosecond xuv laser pulses," *Physical Review A*, vol. 73, p. 033410, 2006.

[29] F. Martín, "Completely L^2 integrable method for strong-coupling multichannel photoionization: Photoelectron emission of He between the N=3 and 4 threshold," *Physical Review A*, vol. 48, pp. 331–337, 1993.

[30] M. Cortés and F. Martín, "Multichannel close-coupling method with L^2 integrable bases," *Journal of Physics B: Atomic, Molecular and Optical Physics*, vol. 27, pp. 5741–5760, 1994.

[31] I. Sánchez and F. Martín, "Photoionization of He above the $n = 2$ threshold," *Physical Review A*, vol. 44, pp. 7318–7334, 1991.

[32] F. Martín, H. Bachau, P. Galan, A. Riera, and M. Yáñez, "Electron correlation properties of doubly excited states. Berylliumlike vs heliumlike systems," *The Journal of Chemical Physics*, vol. 94, pp. 5011–5020, 1991.

Chapter 7

Resonant dissociative photoionization of H_2

"The task is, not so much to see what no one has yet seen; but to think what nobody has yet thought, about that which everybody sees."

Erwin Schrödinger

Table of Contents

The work reported in this Chapter has led to the publications [1, 2, 3].

7.1 Introduction

PHOTOIONIZATION of H_2 is a fundamental process that plays an important role in interstellar clouds, planetary atmospheres (see for example [4, 5, 6, 7]) and plasma physics. For example, the molecular hydrogen is the dominant species in the space, having a concentration roughly 10^4 times that of the second most abundant molecule, the CO. As mentioned in the introduction, the photon energy can be shared between electronic and nuclear degrees of freedom, so that the outgoing electron may absorb part of the total energy and leave the residual ion in an excited vibrational state. In the case of H_2, absorption of photons with energy $\hbar\omega > 18.1$ eV not only leads to emission of an electron but also to dissociation of the molecule according to the equation $H_2 + \hbar\omega \longrightarrow H(n\ell) + H^+ + e^-$, thus leading to the process called dissociative photoionization. Although the contribution of the latter process to the total photoionization cross section is very small ($\simeq$5% or less of the total cross section), there has beeen significant effort made to understand this dissociative process (see, for instance, [8, 9, 10, 11, 12, 13, 14, 15] and references therein). In recent works, the theory presented in Chapter 3 has been used with *B*-spline functions [16, 17, 18, 19, 20] to study dissociative photoionization of H_2 and D_2, paying particular attention to the role of the doubly

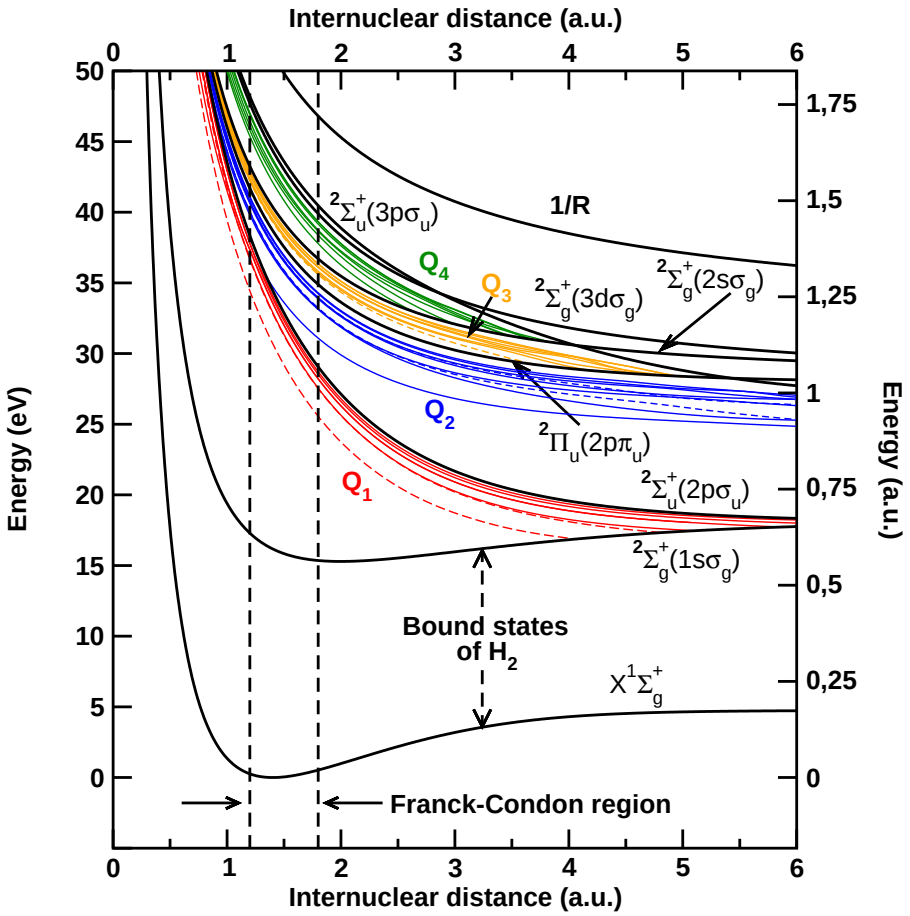

Figure 7.1: Potential energy curves of H_2 and H_2^+ . Q1 states [31]; Q2 states [32]; Q3 and Q4 states [33]. Thin dashed curves: Q states of $^1\Sigma_u^+$ symmetry; thin continuous curves: Q states of $^1\Pi_u$ symmetry.

excited states embedded in the electronic continuum. As expected, when the photon energy is large enough to populate these doubly excited states (DES), the dissociative photoionization spectra exhibit resonant peaks. As a consequence of the coupling between resonant and non-resonant processes, and the interference with the nuclear motion, these peaks are more complex than for atomic systems and much more difficult to assign. In principle, one would expect similar resonant effects for the dominant non-dissociative photoionization process that leads to the formation of H_2^+ . Surprisingly, the experiments [21, 22, 23, 24, 25] show no evidence of resonant structures in this case. In this respect, it is important to point out that theoretical calculations performed in the fixed-nuclei approximation [26, 27, 28] are in contrast with the latter experimental results since they do predict the existence of resonant peaks in the photoionization spectra similar to those observed in atomic photoionization [29]. The fixed-nuclei approximation makes use of the equilibrium geometry of the molecule to evaluate the electronic wavefunction and neglects completely the nuclear degrees of freedom. In a recent work [30] the theory of Chapter 3 has been used to evaluate photoionization cross sections and it has shown that inclusion of the nuclear motion is crucial to account for the experimental observations.

The first experimental evidence of resonant effects was provided by Strathdee and Browning [34] who observed a significant enhancement of the proton production rates at 26.9 and 30.5 eV. This enhancement was immediately related to the existence of doubly excited states in H_2 [15, 34, 35], in particular the lowest $^1\Sigma_u^+$ state, which belongs to the Q_1 resonance series converging to the

$^2\Sigma_u^+(2p\sigma_u)$ ionization threshold (see Fig. (7.1)). The DES of H_2 are embedded in the ionization continuum. These states are both dissociative (the corresponding potential energy curves are repulsive) and autoionizing (they are coupled to the non-resonant electronic continuum). Thus, if autoionization lifetimes are shorter than the time required for the nuclei to separate, DES will contribute significantly to the ionization process and will lead to strong interferences with the non-resonant process (either dissociative or non-dissociative). In contrast, if autoionization lifetimes are very long, the molecule will dissociate into two neutral H atoms, H_2 + energy $\rightarrow$ H + H. Autoionizing states lying above several ionization thresholds (e.g., the Q_2 DES) may decay to different H_2^+ states, most of them dissociative, which leads to proton emission in a wide energy interval. These resonant processes compete efficiently with the non-resonant ones. The Q_1 and Q_2 doubly excited states have been theoretically investigated for more than two decades (see, e.g., [31, 32, 36, 37, 38, 39, 40, 41, 42] and the review [20]). These states lead to the dominant structures observed in the kinetic energy distribution (KED) of protons produced in photoionization [8, 9, 34, 43] and in collisions with electrons (see [44, 45] and reference therein) and ions [46, 47], that will be developed in Chapter 12. They are also responsible for the strong Lyman emission from neutral H atoms [44, 48, 49]. Subsequent experimental works in this energy region revealed additional features that only a theory based on the use of *B*-spline basis sets has been able to explain very recently [16, 18]. For instance, Ito *et al.* [8] reported the existence of several peaks in the KED of protons that had neither been observed in previous works nor predicted theoretically. Also, He *et al.* [9] observed some structure in the zero ion kinetic energy spectrum of H_2 in the region of low photon energies that could not be interpreted satisfactorily in terms of simple energy conservation arguments. At higher photon energies ($\hbar\omega > 35$ eV) the situation is even more complicated because several ionization channels are open (see Fig. (7.1)). In this case, photoionization leaves the H_2^+ ion in the $^2\Sigma_g^+(1s\sigma_g)$, $^2\Sigma_u^+(2p\sigma_u)$, $^2\Pi_u(2p\pi_u)$ and $^2\Sigma_g^+(2s\sigma_g)$ states. This energy region was explored by Ito *et al.* [8] and Latimer *et al.* [10].

The advantage of photoionization experiments is twofold: (i) one knows exactly the amount of energy absorbed by the molecule and (ii) the number of accessible final states is limited by the dipole selection rule (only states of $^1\Sigma_u^+$ and $^1\Pi_u$ symmetries are populated). This greatly simplifies the analysis of the experimental results since individual DES can be revealed by simply scanning the photon energy. The lowest Q_1 and Q_2 DES have been identified in this way by measuring the proton KED for photon energies smaller than 35 eV [8, 16, 18]. Similar experiments at higher photon energies have revealed additional structures but all of them have been attributed to non-resonant dissociative ionization. In this respect, it is worth recalling here that DES have never been observed in photoabsorption spectra because the vibrational motion dilutes resonance effects into the dominant non-resonant ionization background [30]. Thus, dissociative photoionization seems the appropriate tool to look for new DES in H_2. In the previous Chapter, based on [33], has suggested that higher DES, the so called Q_3, Q_4,... states, could contribute significantly to the measured proton KED spectrum at high photon energies (see Chapter 6). We have looked for these states in the proton KED spectra by combining high-energy resolution experiments with accurate theoretical calculations in the photon energy range 36-43 eV. The latter describe both the electronic and nuclear motions and include a large number of ionization channels and DES. In this Chapter we show that Q_3 and, to a lesser extent, Q_4 DES contribute to the measured spectra. In addition, non-resonant dissociative photoionization through very excited ionization thresholds is clearly identified.

As we have mentioned before, the problem of dissociative photoionization, in the photon range of the Q_1 and Q_2, has been investigated systematically by I. Sánchez *et al.* in a series of papers [16, 17, 30] in which they made use of the theory described in Chapter 3. In these papers they were able to explain most of the experimental observations obtained by Ito *et al.* [8].

7.2 The role of the Q_3 and Q_4 doubly excited states

We will present results for the dissociative photoionization in the photon energy range where the Q_3 and Q_4 doubly excited states are accessible energetically. In this Section, the final state $\Psi^+_{\alpha\upsilon_\alpha\ell_\alpha E}$ described in Section 3.9 of Chapter 3 includes contributions from the four lowest ionization thresholds of H_2, namely the $X^2\Sigma^+_g$ $(1s\sigma_g)$, $^2\Sigma^+_u$, $(2p\sigma_u)$, $^2\Pi_u$ $(2p\pi_u)$ and $2\Sigma^+_g$ $(2s\sigma_g)$ threshold states and the Q_1, Q_2, Q_3 and Q_4 doubly excited states, as well as the corresponding vibrational states and nuclear states leading to dissociation.

In the photon energy range considered, fourteen different pathways can be distinguished, all contributing to ionization in the photon energy range of Fig. (7.1) and schematically written as:

$$\hbar\omega + H_2 \rightarrow H_2^+(1s\sigma_g) + e^- \quad , \quad \text{direct} \tag{7.1}$$
$$\hbar\omega + H_2 \rightarrow H_2^+(2p\sigma_u) + e^- \quad , \quad \text{direct} \tag{7.2}$$
$$\hbar\omega + H_2 \rightarrow H_2^+(2p\pi_u) + e^- \quad , \quad \text{direct} \tag{7.3}$$
$$\hbar\omega + H_2 \rightarrow H_2^+(2s\sigma_u g) + e^- \quad , \quad \text{direct} \tag{7.4}$$
$$\hbar\omega + H_2 \rightarrow H_2(Q_1) \rightarrow H_2^+(1s\sigma_g) + e^- \quad , \quad \text{resonant} \tag{7.5}$$
$$\hbar\omega + H_2 \rightarrow H_2(Q_2) \rightarrow H_2^+(1s\sigma_g) + e^- \quad , \quad \text{resonant} \tag{7.6}$$
$$\hbar\omega + H_2 \rightarrow H_2(Q_2) \rightarrow H_2^+(2p\sigma_u) + e^- \quad , \quad \text{resonant} \tag{7.7}$$
$$\hbar\omega + H_2 \rightarrow H_2(Q_3) \rightarrow H_2^+(1s\sigma_g) + e^- \quad , \quad \text{resonant} \tag{7.8}$$
$$\hbar\omega + H_2 \rightarrow H_2(Q_3) \rightarrow H_2^+(2p\sigma_u) + e^- \quad , \quad \text{resonant} \tag{7.9}$$
$$\hbar\omega + H_2 \rightarrow H_2(Q_3) \rightarrow H_2^+(2p\pi_u) + e^- \quad , \quad \text{resonant} \tag{7.10}$$
$$\hbar\omega + H_2 \rightarrow H_2(Q_4) \rightarrow H_2^+(1s\sigma_g) + e^- \quad , \quad \text{resonant} \tag{7.11}$$
$$\hbar\omega + H_2 \rightarrow H_2(Q_4) \rightarrow H_2^+(2p\sigma_u) + e^- \quad , \quad \text{resonant} \tag{7.12}$$
$$\hbar\omega + H_2 \rightarrow H_2(Q_4) \rightarrow H_2^+(2p\pi_u) + e^- \quad , \quad \text{resonant} \tag{7.13}$$
$$\hbar\omega + H_2 \rightarrow H_2(Q_4) \rightarrow H_2^+(2s\sigma_g) + e^- \quad , \quad \text{resonant} \tag{7.14}$$

Asymptotically, the $2p\sigma_u$, $2p\pi_u$ and $2s\sigma_g$ states of H_2^+ always lead to dissociation[1], whereas $1s\sigma_g$ can lead either to H_2^+ in a bound vibrational state or to a dissociative state. All these pathways must be added coherently if they yield the same electron energy and hence the same kinetic energy release (KER)[2]. The interference leads to different complicated patterns presented in the cross section as it was explained by Sánchez et al. [16, 17].

Our theoretical calculations are compared with experimental results performed in parallel obtained in The Photon Factory by Kenji Ito's group. The theoretical cross-sections have been obtained assuming a perfect (100%) linear polarization of the incident radiation. Under this condition, protons observed at 0° and 90° are associated, respectively, with the $^1\Sigma^+_u$ and $^1\Pi_u$ ionization continua [13] (see also Chapter 4). The use of a limited (80%) polarization in the experiment implies that $^1\Sigma^+_u$ and $^1\Pi_u$ symmetries are mixed according to the formulae $I_{obs}(0^\circ) \sim 18\sigma_{^1\Sigma^+_u} + \sigma_{^1\Pi_u}$ and $I_{obs}(90^\circ) \sim \sigma_{^1\Sigma^+_u} + 4.5\sigma_{^1\Pi_u}$. We have used the latter formulae in all the theoretical curves shown below. In addition, to account for the limited energy resolution of the experiment, the calculated crosssections have been convoluted using a gaussian function with half width at half maximum of 0.2 eV (at 0°) and 0.4 eV (at 90°).

The proton KED spectra at 0° are shown in left panel of Fig. (7.2). The experimental results have been normalized to the theoretical cross-sections at a photon energy of 39 eV and a proton kinetic energy of 8.5 eV. The general agreement between theory and experiment is good below 41 eV. At

[1] The $2p\pi_u$ electronic state of the H_2^+ molecule supports two bound states at quite large internuclear distances, ~ 7 a.u. These bound states have a negligible contribution to the process described in this Chapter.

[2] The Kinetic Energy Release is the kinetic energy of the dissociative proton relative to the residual hydrogen atom.

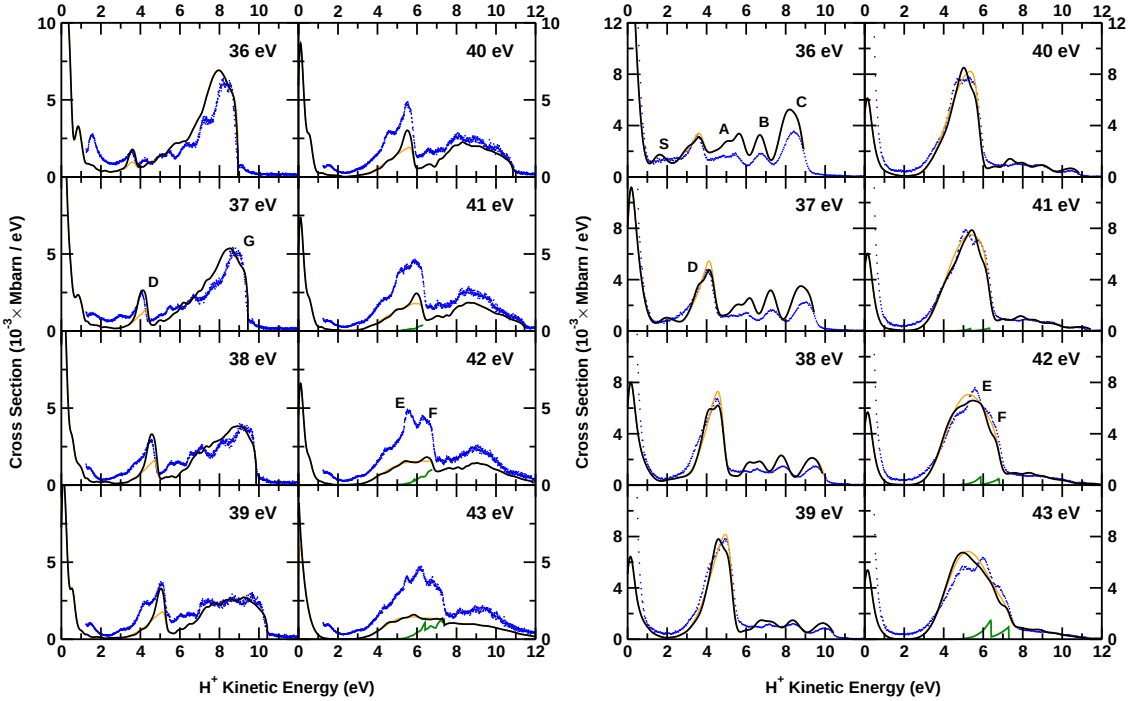

Figure 7.2: Proton kinetic energy spectra of H_2 at 0° (left panel) and 90° (right panel) in the photon energy range 36-43 eV. Dots: experiment; full black curves: theory; dotted red curves: calculated background excluding Q_3 and Q4 DES; full green curves: approximate contribution of higher ionization thresholds (see text).

0°, the two dominant peaks, *D* and *G* are well explained by the theory. Peak *G* is the signature of the autoionizing Q_1 and Q_2 states of $^1\Sigma_u^+$ symmetry. As has been shown in previous works [8, 16] for photon energies smaller than 29 eV, peak G is exclusively due to the lowest Q_1 $^1\Pi_u$ state. At higher photon energies, additional Q_1 states are involved and, at the energies shown in Fig. (7.2), the dominant contribution comes from the higher Q_1 states. It can be seen that the intensity of peak *G* decreases with photon energy, in good agreement with the theory. The origin of peak *D* is quite different. In previous measurements [8], this peak has been attributed to non-resonant ionization through the $^2\Pi_u$ $(2p\pi_u)$ threshold. Now, the present theoretical results show that, between 36 and 40 eV, a substantial part of the peak intensity is due to the autoionizing Q_3 states (and, to a lesser extent, to the Q_4 DES). This is clearly illustrated by calculations in which the Q_3 and Q_4 states have been excluded from the final continuum states (see Fig. (7.2)). Indeed, while in the absence of Q_3 and Q_4 states, the theory leads to a peak in the same proton energy region, its relative intensity compared with peak *G* does not follow the experimental behavior. Fig. (7.2) shows that Q_3 and Q_4 DES account for about 50% of the measured peak intensity. The contribution of these states is very small above 41 eV, where Q_4 states are expected to contribute more importantly. In the latter photon energy region, the theory underestimates the peak intensity and is not able to reproduce the emerging structures *E* and *F* observed in the experiment. We discard that these two structures are due to higher doubly excited states not included in the calculations because dipole matrix elements between the ground state of H_2 and the Q_n states decrease by several orders of magnitudes when *n* increases. In particular, this explains why the Q_4 states are much less visible than the Q_3 ones (a similar effect occurs in He photoionization). Fig. (7.1) shows that above 41 eV, higher ionization threshold are open in the Franck-Condon region. These ionization thresholds are so close in energy that performing meaningful theoretical calculation would require accounting for a large number of

open channels. Inclusion of these channels with the appropriate electronic and nuclear components and the corresponding couplings is far beyond our present capabilities. So, to understand the origin of peaks *E* and *F*, we have used a very simple model in which each additional threshold is considered separately from the rest (i.e. no inter-threshold coupling is included). This procedure cannot provide quantitative results, but is very helpful to interpret the observations. We have chosen all channels associated with the next seven ionization thresholds of H_2. Fig. (7.2) shows the results of the model. It can be seen that the additional channels contribute in the region where peaks *E* and *F* are observed. Although, for obvious reasons, the calculated intensity is not correct, the calculated cross sections exhibit two peaks at the right proton kinetic energy (as discussed below, this is much more apparent at 90°). Thus, the difference between the experimental spectrum and the calculations (full black curve) is due to dissociative ionization through very excited thresholds (full green curve).

Besides the above findings, it is interesting to note that, in the experimental spectrum at 36 eV, there is an additional peak for proton energies between 1 and 2 eV. This peak is reproduced by the theory but at lower proton energies. Similar peaks have been found at lower photon energies [8] and, as discussed in [16], its origin is the interference between direct ionization and autoionization while the molecule dissociates. The shift in the position of this peak is probably due to calibration problems that are common at very low proton energies.

The results at 90° are shown in right panel of Fig. (7.2). In this case, the experimental results have been normalized to the theory at a photon energy of 39 eV and a proton kinetic energy of 4.2 eV. Good agreement between theory and experiment is observed for photon energies smaller than 41 eV. The origin of peaks *A*, *B* and *C* has been discussed in detail in [8, 18, 19]. Here we only notice that they are associated with different autoionization channels of the Q_2 DES. The origin of peak *S* is the same as for the low energy peak observed at 0°: it results from the interference between direct ionization and autoionization while the molecule dissociates (see [16] for details). The intensities of these peaks decrease with photon energy and is practically zero at around 40 eV. It has been shown that below 36 eV, these peaks are mainly due to the lowest Q_2 DES of $^1\Pi_u$ symmetry; however, between 36 and 40 eV, contributions from higher Q_2 states is quite significant. We focus now on peak *D*, which dominates the proton KED spectra. Previous experimental results have assigned this peak to non-resonant ionization through the $^2\Pi_u\ (2p\pi_u)$ threshold [8]. Our theoretical results confirm this interpretation except for a few details. For example, in the photon energy range 38-41 eV, peak *D* exhibits a pronounced shoulder on the left hand side. This shoulder is clearly visible in the theoretical calculations, but it does not appear when the Q_3 and Q_4 resonances are excluded (see "background" curves in Fig. (7.2)). In addition, exclusion of the Q_3 and Q_4 states always leads to theoretical curves with a single maximum, while the experiment and the full calculation show the existence of some structure near the top of the peak. In contrast with the results at 0°, the Q_3 and Q_4 states barely contribute to the peak intensities. At photon energies above 41 eV, additional peaks (*E* and *F*) are observed superimposed on the dominant peak D. As in the case of 0°, these additional peaks are due to non-resonant ionization through more excited ionization thresholds. Again the difference between the measured spectra and the calculated full black curve is well explained by the full green curve (see Fig. (7.2)). In this case, the lower energy peak is mainly due to ionization through the $^2\Pi_u\ (3p\pi_u)$ threshold and the higher energy peak to ionization through the $2^1\Sigma_u^+(3p\sigma_u)$ one.

The previous results presented in Fig. (7.2) can be analyzed in a different manner, studying the correlation diagram between the initial photon energy and the kinetic energy of the final proton. Fig. (7.3) displays this information for H_2 and D_2 in the 29-39 eV photon energy range. In panels a) and b) it can be clearly distinguished different structures due to the population of different resonant states. Panel from c) to f) shows the results for a KER from 0 to 2 eV where the population of the Q_1 and Q_2 doubly excited states and later autoionization through the first ionization threshold is possible(see Chapter 6). The theoretical calculations agree with the experimental results (see

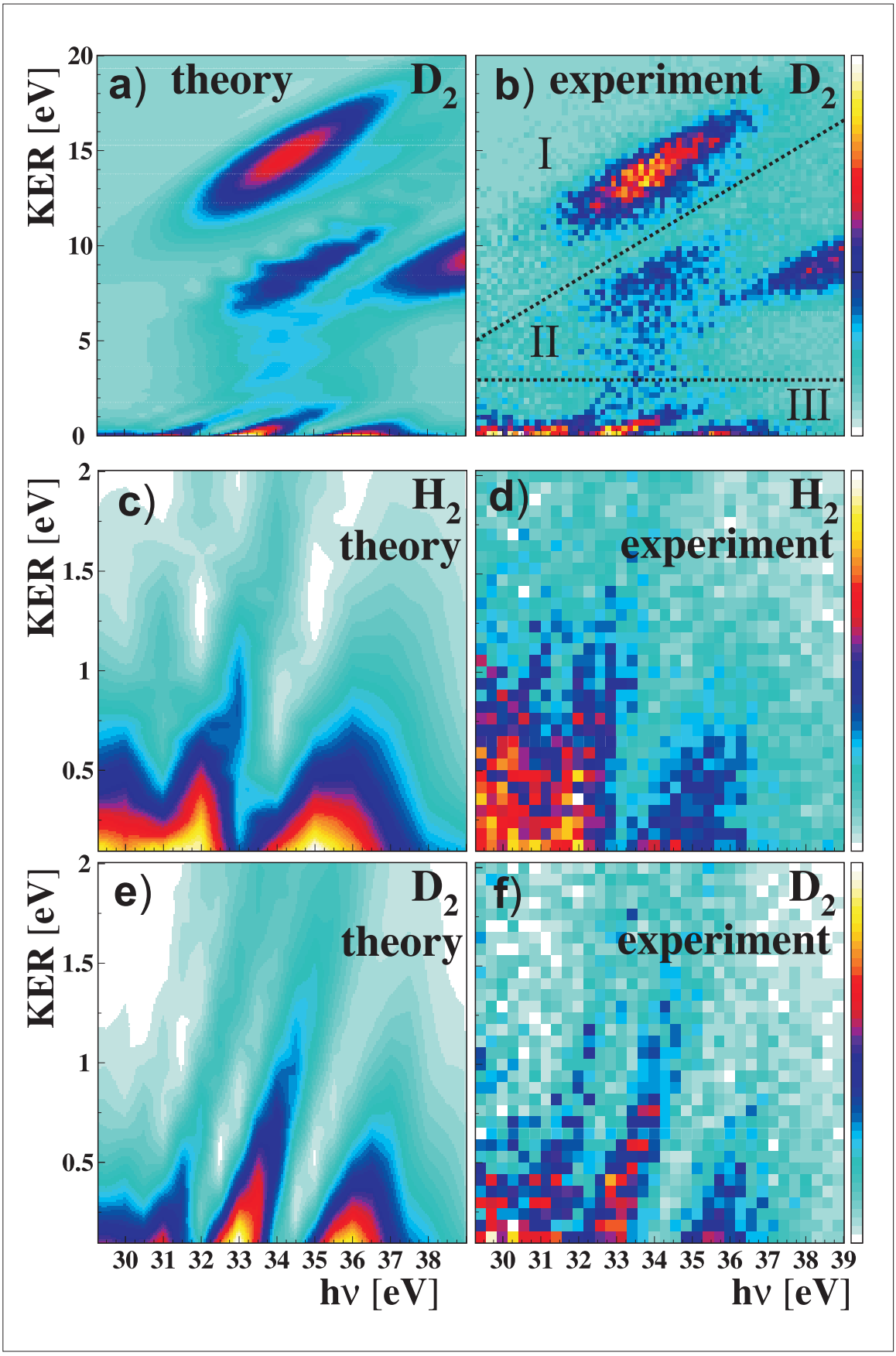

Figure 7.3: Kinetic energy release as a function of photon energy. Left theory, right experiment. (See Chapter 9 for more details about the experimental set up).

Chapter 9 and [3] for more details about the experimental setup).

Three areas with islands can be distinguished (I, II and III in panel (b) of Fig. (7.3)): region I and III can be populated by direct ionization, leaving H_2^+ in the $2p\sigma_u$ or $1s\sigma_g$ state, respectively. However only the latter state contributes significantly, as a direct dipole transition from the H_2 ground state to the $2p\sigma_u k\pi_g$ continuum is very unlikely [19] (in fact, it would be strictly forbidden in an independent electron picture, both for the final Σ_u^+ symmetry, $(1s\sigma_g)^2 \rightarrow 2p\sigma_u k\ell\sigma_g$, and Π_u symmetry, $(1s\sigma_g)^2 \rightarrow 2p\sigma_u k\ell\pi_g$). Thus regions I and II cannot be reached in a single-step direct photoionization. They are the fingerprint of a delayed emission of an Auger electron from H_2 doubly excited states (either Q_1 or Q_2). These states can either dissociate due to the repulsive character of the corresponding potential energy curve or decay by autoionization into the $2p\sigma_u$ or $1s\sigma_g$ states when such a decay is faster than the time required for an effective dissociation. The structure presented in region II, for fast protons is due to the contribution of the Q_3 and Q_4 resonant states.

The interference effect between all the final paths leads to the distinct finger-like structures in the low KER region (Fig. (7.3), panels c-f). The calculated structures (Fig. (7.3) panels c and e) are in excellent agreement with the experimental observations (Fig. (7.3) panels d and f). Our calculations show that the structure is the result of an interference between the processes in Eqs. (7.2) and (7.6), the direct and resonant pathways leading to $1s\sigma_g$ in the same KER region. The finger-like structures are the molecular analogue of the well-known Fano interferences in the atomic case, but there are important differences entirely due to the molecular character of H_2. As the photon energy increases, the position of a particular peak shifts to higher KER, which leads to fingers with a slope approximately equal to one. The number and position of the fingers is controlled by the overlap between the dissociative states associated respectively with processes in Eqs. (7.2) and (7.6), so it is not surprising that the present experimental data and calculations for H_2 and D_2 show a large isotope effect on these structures (the different masses cause very distinct oscillations in the dissociative states).

7.3 Conclusions

In conclusion, first we have presented a combined experimental and theoretical study of dissociative photoionization of H_2 in the photon energy range 36-43 eV. The results show that Q_3 (and to a lesser extent Q_4) doubly excited states of H_2 contribute significantly to the measured proton KED spectrum at 0°. This confirms the existence of the Q_3 and Q_4 states as conjectured by theory. Structural information about these states, in particular energy positions and autoionization widths, has been given in [33]. In addition, the present study shows clear evidence for non-resonant dissociative photoionization through very excited ionization thresholds, namely the $^2\Pi_u\,(3p\pi_u)$ and $2\,^1\Sigma_u^+(3p\sigma_u)$ ones. Experimental results at higher photon energies [50] show that all these structure practically disappear above 45 eV, only a structureless peak remaining whose intensity decreases with photon energy. Most likely, this is due to the strong coupling among open channels and to the nuclear motion that dilutes resonance effects.

Second, we have studied the interference effects that appears in the dissociative photoionization process in the photon energy range 29-39 eV, in combination with experimental results. In this case the contribution of all doubly excited states and different ionization paths accessible at the photon energy considered, can be observed simultaneously, and the interference structures coming from all the final states are observed for the first time and confirmed for the theory developed in our laboratory.

Bibliography

[1] J. Fernández and F. Martín, "In search of new resonance structures in dissociative photoionization of H_2," *International Journal of Quantum Chemistry*, vol. 86, pp. 145–150, 2002.

[2] T. Aoto, Y. Hikosaka, R. I. Hall, K. Ito, J. Fernández, and F. Martín, "Dissociative photoionization of H_2 at high photon energies: Uncovering new series of doubly excited states," *Chemical Physics Letters*, vol. 389, pp. 145–149, 2004.

[3] F. Martín, J. Fernández, T. Havermeier, L. Foucar, T. Weber, K. Kreidi, M. Schöffler, L. Schmidt, T. Jahnke, A. L. Landers, O. Jagutzki, A. Czasch, E. Benis, T. Osipov, A. Belkacem, M. H. Prior, H. Schmidt-Böcking, C. L. Cocke, and R. Dörner, "Single photon-induced symmetry breaking H_2 dissociation," *Science*, vol. 315, pp. 629–633, 2007.

[4] S. Lepp, P. C. Stancil, and A. Dalgarno, "Atomic and molecular processes in the early Universe," *Journal of Physics B: Atomic, Molecular and Optical Physics*, vol. 35, pp. R57–R80, 2002.

[5] E. Herbst, "The chemistry of interstellar space," *Chemical Society Reviews*, vol. 30, pp. 168–176, 2001.

[6] D. J. Hollenbach and A. G. G. M. Tielens, "Photodissociation regions in the interstellar medium of galaxies," *Review Modern Physics*, vol. 71, pp. 173–230, 1999.

[7] J. Braine and F. Herpin, "Molecular hydrogen beyond the optical edge of an isolated spiral galaxy," *Nature*, vol. 432, pp. 369–371, 2004.

[8] K. Ito, R. I. Hall, and M. Ukai, "Dissociative photoionization of H_2 and D_2 in the energy region of 25-45 eV," *The Journal of Chemical Physics*, vol. 104, pp. 8449–8457, 1996.

[9] Z. X. He, J. N. Cutler, S. H. Southworth, L. R. Hughey, and J. A. R. Samson, "Zero kinetic energy proton and deuteron production from photoionization of H_2 and D_2," *The Journal of Chemical Physics*, vol. 103, pp. 3912–3916, 1995.

[10] C. J. Latimer, J. Geddes, M. A. MacDonald, N. Kouchi, and K. F. Dunn, "The photodissociative ionization of hydrogen and deuterium in the VUV via Π states," *Journal of Physics B: Atomic, Molecular and Optical Physics*, vol. 29, pp. 6113–6121, 1996.

[11] A. L. Ford, K. K. Docken, and A. Dalgarno, "Cross-sections for photoionization of vibrationally excited molecular-hydrogen," *The Astrophysical Journal*, vol. 195, pp. 788–789, 1975.

[12] S. V. ONeil and W. P. Reinhardt, "Photoionization of molecular hydrogen," *Journal of Physics B: Atomic, Molecular and Optical Physics*, vol. 69, pp. 2126–2142, 1978.

[13] J. L. Dehmer and D. Dill, "Photoion angular distributions in dissociative photoionization of H_2 at 304 Å," *Physical Review A*, vol. 18, pp. 164–171, 19778.

[14] S. Strathdee and R. Browning, "Dissociative photoionisation of H_2: Proton kinetic energy spectra," *Journal of Physics B: Atomic, Molecular and Optical Physics*, vol. 12, pp. 1789–1804, 1979.

[15] K. Kirby, T. Uzer, A. C. Allison, and A. Dalgarno, "Dissociative photoionization of H_2 at 26.9 and 30.5 eV," *The Journal of Chemical Physics*, vol. 75, pp. 2820–2825, 1981.

[16] I. Sánchez and F. Martín, "Origin of unidentified structures in resonant dissociative photoionization of H_2," *Physical Review letters*, vol. 79, pp. 1654–1657, 1997.

[17] I. Sánchez and F. Martín, "Resonant dissociative photoionization of H_2 and D_2," *Physical Review A*, vol. 57, pp. 1006–1017, 1998.

[18] I. Sánchez and F. Martín, "Multichannel dissociation in resonant photoionization of H_2," *Physical Review letters*, vol. 82, pp. 3775–3778, 1999.

[19] I. Sánchez and F. Martín, "Dissociative photoionization of H_2 and D_2 by (30-37)-eV photons via $^1\Pi_u$ states," *Physical Review A*, vol. 60, pp. 2200–2206, 1999.

[20] F. Martín, "Ionization and dissociation using B-splines: Photoionization of the hydrogen molecule," *Journal of Physics B: Atomic, Molecular and Optical Physics*, vol. 32, pp. R197–R231, 1999.

[21] Y. M. Chung, E.-M. Lee, T. Masuoka, and J. A. R. Samson, "Dissociative photoionization of H_2 from 18 to 124 eV," *The Journal of Chemical Physics*, vol. 99, pp. 885–889, 1993.

[22] C. Backx, G. R. Wight, and M. J. V. der Wiel, "Oscillator strengths (10-70 eV) for absorption, ionization and dissociation in H_2, HD and D_2, obtained by an electron-ion coincidence method," *Journal of Physics B: Atomic, Molecular and Optical Physics*, vol. 9, pp. 315–331, 1976.

[23] J. A. R. Samson, "Photoionization of atoms and molecules," *Physics Reports*, vol. 28, pp. 303–354, 1976.

[24] L. C. Lee, R. W. Carlson, and D. L. Judge, "The absorption cross sections of H_2 and D_2 from 180 to 780 Å," *Journal Quantitative Spectroscopy and Radiative Transfer*, vol. 16, pp. 873–877, 1976.

[25] C. J. Latimer, K. F. Dunn, F. P. O'Neill, M. A. MacDonald, and N. Kouchi, "Photoionization of hydrogen and deuterium," *The Journal of Chemical Physics*, vol. 102, pp. 722–725, 1995.

[26] I. Cacelli, R. Moccia, and A. Rizzo, "Gaussian type orbital basis set for the calculation of continuum properties in molecules: The photoionzation cross section of H_2," *The Journal of Chemical Physics*, vol. 98, pp. 8742–8748, 1993.

[27] I. Sánchez and F. Martín, "Representation of the electronic continuum of H_2 with B-spline basis," *Journal of Physics B: Atomic, Molecular and Optical Physics*, vol. 30, pp. 679–692, 1997.

[28] G. Raşeev, "Variational calculation of the logarithmic derivative of the wavefunction: The electronic autoionisation region in photoionisation of H_2," *Journal of Physics B: Atomic, Molecular and Optical Physics*, vol. 18, pp. 423–439, 1985.

[29] U. Fano, "Effects of configuration interaction on intensities and phase shifts," *Physical Review*, vol. 124, pp. 1866–1878, 1961.

[30] I. Sánchez and F. Martín, "Resonant effects in photoionization of H_2 and D_2," *Journal of Chemical Physics*, vol. 107, pp. 8391–8396, 1997.

[31] I. Sánchez and F. Martín, "The doubly excited states of the H_2 molecule," *Journal of Chemical Physics*, vol. 106, pp. 7720–7730, 1997.

[32] I. Sánchez and F. Martín, "Doubly excited autoionizing states of the H_2 above the second ionization thershold: The Q_2 resonance series," *Journal of Chemical Physics*, vol. 110, pp. 6702–6713, 1999.

[33] J. Fernández and F. Martín, "Autoinizing $^1\Sigma_u^+$ and $^1\Pi_u$ states of H_2 above the third and fourth ionization thrseshols," *Journal of Physics B: Atomic, Molecular and Optical Physics*, vol. 34, pp. 4141–4153, 2001.

[34] S. Strathdee and R. Browning, "Dissociative photoionization of H_2 at 26.9 eV," *Journal of Physics B: Atomic, Molecular and Optical Physics*, vol. 9, pp. L505–L507, 1976.

[35] S. Kanfer and M. Shapiro, "Theory of the dissociative photoionisation of H_2," *Journal of Physics B: Atomic, Molecular and Optical Physics*, vol. 16, pp. L655–L660, 1983.

[36] C. Bottcher, "Dissociative ionization of the hydrogen molecule," *Journal of Physics B: Atomic, Molecular and Optical Physics*, vol. 7, pp. L352–L357, 1974.

[37] S. L. Guberman, "The doubly excited autoionizing states of H_2," *The Journal of Chemical Physics*, vol. 78, pp. 1404–1413, 1983.

[38] L. A. Collins and B. I. Schneider, "Linear algebraic approach to electronic excitation of atoms and molecules by electron impact," *Physical Review A*, vol. 27, pp. 101–111, 1983.

[39] J. Tennyson and C. J. Noble, "Low-energy electron-H_2^+ collisions: variation of resonance parameters with internuclear separation," *Journal of Physics B: Atomic, Molecular and Optical Physics*, vol. 18, pp. 155–165, 1985.

[40] I. Shimamura, C. J. Noble, and P. G. Burke, "Complex quantum defects of superexcited Rydberg states of H_2," *Physical Review A*, vol. 41, pp. 3545–3554, 1990.

[41] L. A. Collins, B. I. Schneider, D. L. Lynch, and C. J. Noble, "Electron scattering from H_2^+: Resonances in the Σ and Π symmetries," *Physical Review A*, vol. 52, pp. 1310–1318, 1995.

[42] J. Tennyson, "Resonance parameters and quantum defects for superexcited H_2," *Atomic Data and Nuclear Data Tables*, vol. 64, pp. 253–277, 1996.

[43] J. Geddes, K. F. Dunn, N. Kouchi, M. A. McDonald, V. Srigengan, and C. J. Latimer, "Isotope effects in the autoionization of superexcited $^1\Sigma_u^+(Q_1)$ states in hydrogen," *Journal of Physics B: Atomic, Molecular and Optical Physics*, vol. 27, pp. 2961–2970, 1994.

[44] Y. Hatano, "Interaction of vacuum ultraviolet photons with molecules. Formation and dissociation dynamics of molecular superexcited states," *Physics Reports*, vol. 313, pp. 109–169, 1999.

[45] J. Y. Chesnel, D. Martina, P. Sobocinski, O. Kamalou, F. Frémont, J. Fernández, and F. Martín, "Autoionization electrons following double excitation of D_2 in 2.4 KeV e^- + D_2 collisions: Experimental and theoretical evidence," *Physical Review A*, vol. 70, p. 010701(R), 2004.

[46] A. K. Edwards, R. M. Wood, J. L. Davis, and R. L. Ezell, "Collisional ionization and excitation of H_2: Two-electron processes," *Physical Review A*, vol. 42, pp. 1367–1375, 1990.

[47] G. Laurent, J. Fernández, S. Legendre, M. Tarisien, L. Adoui, A. Cassimi, X. Fléchard, F. Frémont, B. Gervais, E. Giglio, J. Grandin, and F. Martín, "Kinematically complete study of dissociative ionization of D_2 by ion-impact," *Physical Review Letters*, vol. 96, p. 173201, 2006.

[48] M. Glass-Maujean, "Photodissociation of doubly excited states of H_2, HD, and D_2," *The Journal of Chemical Physics*, vol. 85, pp. 4830–4834, 1986.

[49] M. Glass-Maujean, "Photodissociation of doubly excited states of H_2: Emission of balmer lines," *The Journal of Chemical Physics*, vol. 89, pp. 2839–2843, 1988.

[50] T. Havermeier, *Photoionisation und doppelt angeregte Zustände in Wasserstoff- und Deuterium- Molekülen*. PhD thesis, Institut für Kernphysik Johann-Wolfgang-Goethe-Universität Frankfurt am Main, 2006.

Chapter 8

Dissociative photoionization of H_2 from the $E,F^1\Sigma_g^+$ state

"To know that we know what we know, and know that we do not know what we do not know, that is true knowledge."

Copernicus

Table of Contents

The work reported in this Chapter has led to the publication [1].

8.1 Introduction

MOLECULAR PHOTOIONIZATION is a process in which the excess photon energy is shared by both electrons and nuclei, as we have explained in previous Chapters. Thus the outgoing electron can absorb part of the available energy leading either to a residual molecular ion in a particular vibrational state (non dissociative photoionization) or to dissociation into smaller molecular and/or atomic fragments (dissociative photoionization). Both processes have been extensively investigated in the simplest molecule, H_2, in particular ionization produced by absorption of a single XUV photon from the ground $X^1\Sigma_g^+(\upsilon = 0)$ state (see, e.g., a recent review on the subject [2]). In this case, dissociative photoionization leading to $H + H^+$ is less than 10% of the total cross section. In spite of this, when the photon energy is large enough to populate doubly excited states, the dissociative

photoionization spectra exhibit resonant peaks in the kinetic energy distribution (KED) of ejected protons [3, 4, 5] (see also Chapters 6 and 9). As a consequence of the coupling between resonant and non resonant processes, and the interference with the nuclear motion, the peaks exhibit complex forms and, very often, are difficult to assign [6, 7]. Interestingly, there is almost no trace of resonant effects in the photoelectron energy spectra or in the vibrational energy distribution of H_2^+ ions formed in the non dissociative process (see [2]).

The introduction of moderately intense laser sources have made it possible to populate high lying electronic states of H_2 via multiphoton excitation [8]. From these states, ionization and dissociation can be produced with less energetic photons. Most experiments have concentrated on the E,F$^1\Sigma_g^+$ state [9, 10, 11, 12, 13], which is usually populated by absorption of two identical photons. A subsequent photon can then excite the molecule above the ionization limit and lead to both dissociative and non dissociative photoionization (see Fig. (8.1)). The global process is called (2+1) REMPI (resonant enhanced multiphoton ionization). This process occurs for a photon energy of about 6.4 eV. Pioneering experiments of Anderson at al [9] showed that (2+1) REMPI of H_2 through the E,F$^1\Sigma_g^+$ intermediate state leads to a non Franck-Condon vibrational distribution of the remaining H_2^+ ion. Both this vibrational distribution and the photoelectron angular distribution associated with individual H_2^+ vibrational states were shown to vary significantly with the specific vibrational state that is resonantly populated by absorption of the first two photons. These findings were theoretically interpreted in the late 80s by Rudolph et al [16] and Cornaggia et al [17] using, respectively, the Hartree-Fock frozen core approximation and the multichannel quantum defect theory to describe the molecular continua [17].

In later (2+1) REMPI experiments using 6.4 eV photons, the dissociative ionization channel has also been investigated. In particular, Xu et al [10] and Hill and co-workers [11, 12] have shown that, similarly to ground state H_2 photoionization, non dissociative photoionization produced by absorption of the third photon from the E,F$^1\Sigma_g^+$ state is the dominant process. Xu et al [10] have obtained in addition the detailed H_2^+ vibrational distribution corresponding to H_2 photoionization from different E,F$^1\Sigma_g^+(\upsilon)$ vibronic states. More recently, Bakker et al [13] have measured the KED and the angular distribution of protons produced in one-photon dissociative ionization from the E,F$^1\Sigma_g^+(\upsilon$=6,J=0) state using again 6.4 eV photons. The latter measurements have revealed pronounced oscillations in the proton KED, which has been interpreted as the signature of direct (i.e., non resonant) dissociative ionization.

Simple theoretical models have been used to interpret the latter findings in the dissociative ionization channel. For instance, the interferences between different ionization and dissociation channels were either treated approximately [10] or neglected [13]. Although these model calculations have been very useful to uncover the basic mechanisms behind the experimental observations, there still remain quantitative discrepancies that should be investigated using fully ab initio methods. Furthermore, apart from the work of reference [10], in which different vibrational levels of the E,F$^1\Sigma_g^+$ state have been considered, the most recent experiment to date have concentrated on the E,F$^1\Sigma_g^+(\upsilon$=6,J=0) initial state, which is directly populated from the ground state via a vertical transition. Thus, it is not clear if oscillations as those reported in [13] for the proton KED also exist for other initial vibrational states. Furthermore, we do not know if the above findings change with the energy of the ionizing photon, since all experiments were performed at a fixed wavelength of approximately 190 nm (6.4 eV) corresponding to the ArF excimer laser. Varying the energy of the ionizing photon can be achieved in two-color (2+1) photoionization experiments by using an additional tunable laser. To investigate these problems we have performed fully ab initio calculations of dissociative and non dissociative photoionization of H_2 from the E,F$^1\Sigma_g^+(\upsilon, J=0)$ excited state for υ=0-9 in the photon energy range 3-14 eV. The theoretical method is the same as that successfully used to study dissociative ionization of H_2 from the ground state [6, 7, 18].

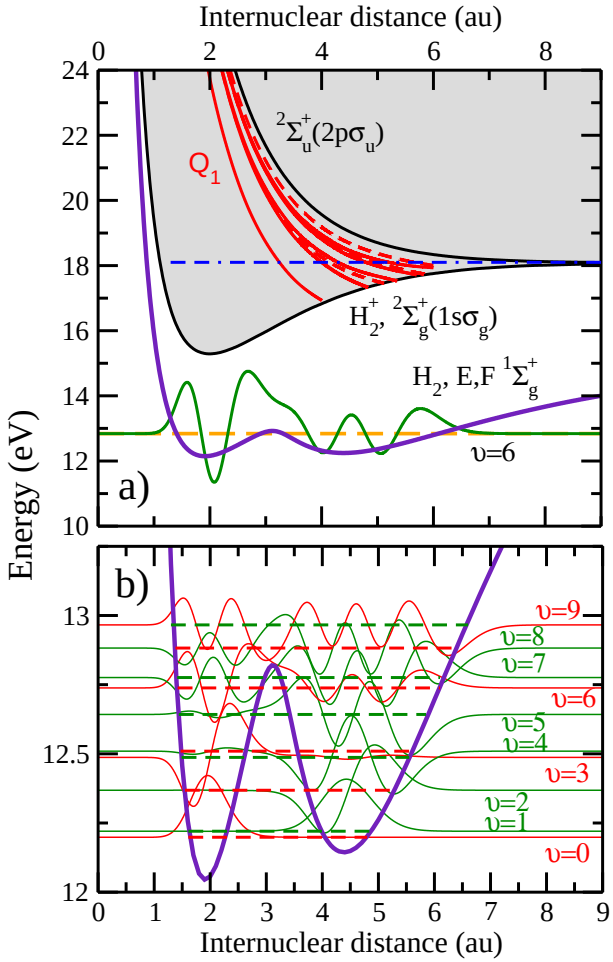

Figure 8.1: (a) Potential energy curves of H_2 relevant for the (2+1) REMPI process described in the text. The potential energy curve of the E,F$^1\Sigma_g^+$ state is taken from [14]. Red lines: Q_1 $^1\Sigma_u^+$ doubly excited states; red dashed lines: Q_1 $^1\Pi_u$ doubly excited states [15]. The energy origin is placed on the lowest rovibrational level of the ground electronic state of H_2. The figure shows a typical vibrational wave function in the E,F$^1\Sigma_g^+$ electronic state (υ=6). (b) Vibrational energies and wave functions associated with the E,F$^1\Sigma_g^+$ state.

8.2 Computational details

The theoretical method has been described in detail in Chapters 2 and 3, so we refer the reader to this chapters for more details.

All electronic wave functions are represented by linear combinations of two-electron configurations built from one-electron molecular orbitals represented in a basis of $B-$spline functions [19] of order 8 in a box of 60 a.u. Bound molecular orbitals include angular momenta up to $\ell_{max} = 26$ and 200 $B-$splines per ℓ. Orbitals associated with a continuum electron include angular momentum up to $\ell = 8$. The nuclear wave functions are represented in a basis of 280 B-splines of order eight defined in a box of 18 a.u.

The initial E,F$^1\Sigma_g^+$ state of H_2 has been evaluated in a basis of two-electron configurations built from $B-$spline representations of Slater-type orbitals (STO) and molecular orbitals (MO). Configurations involving STOs have been built as described in [2]. Configurations involving MOs are: $n_1\sigma_g n_2\sigma_g$ $(n_1 = 1-5, n_2 = 1-25)$, $n_1\sigma_u n_2\sigma_u$ $(n_1 = 1-5, n_2 = 1-25)$, $n_1\pi_g n_2\pi_g$ $(n_1 = 1-4, n_2 = 1-20)$, $n_1\pi_u n_2\pi_u$ $(n_1 = 1-4, n_2 = 1-20)$, $n_1\delta_g n_2\delta_g$ $(n_1 = 1-3, n_2 = 1-15)$ and

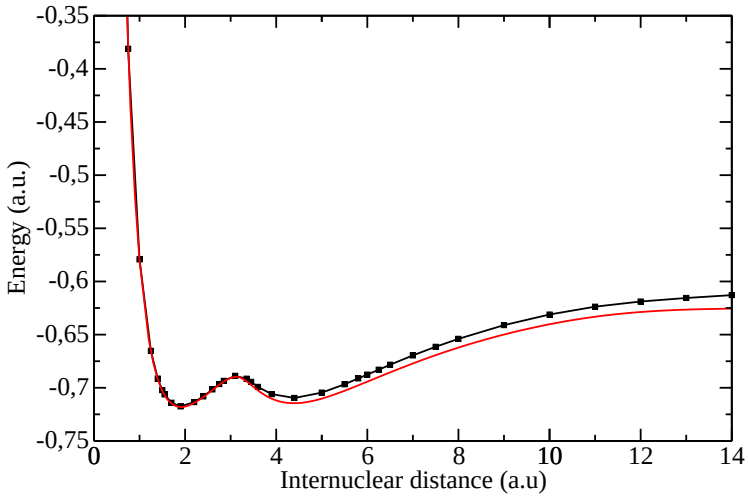

Figure 8.2: Potential energy curve of the E,F$^1\Sigma_g^+$ state of H_2 obtained by a *B*-spline CI method (red line) (see text for details) and the results obtained by Wolniewicz and Dressler [14].

$n_1\delta_u n_2\delta_u$ ($n_1 = 1-3, n_2 = 1-15$). This amounts to 840 configurations. This basis gives an energy for the ground state at the equilibrium distance ($R = 1.4$ a.u.) of -1.171975 a.u., which is 0.002 a.u. higher than the best known value [20]. For the E,F$^1\Sigma_g^+$ excited state, we have obtained an energy of -1.243852 a.u. at the first minimum (R = 1.9 a.u., see Fig. (8.2)), -1.011379 a.u. at the maximum (R = 3.1 a.u.), and -0.936852 a.u. at the second minimum (R = 4.4 a.u.), which are 0.0006 a.u., 0.0009 a.u and 0.0049 a.u. higher, respectively, than the accurate values of reference [14]. We show in Fig. (8.3) the main configurations that characterize the E,F$^1\Sigma_g^+$ state. As can be seen, this state is not described by a dominant type of configuration, in contrast with the ground state. This implies that, as pointed out in previous works, qualitatively assignment of possible transitions in terms of a single configuration picture is much more difficult and probably ambiguous.

The resonant wave functions ϕ_r have been obtained by diagonalizing the H_2 Hamiltonian in a basis of $\simeq 200$ configurations built from $B-$spline representations of MOs as described in [15, 21]. Here we have only considered the lowest six states of the Q_1 series with symmetries $^1\Sigma_u^+$ and $^1\Pi_u$. These states have the largest autoionization widths [15]. Resonant states belonging to the Q_2 and higher series are not relevant except at the higher photon energies considered in this work (14 eV). The Q_1 states lie above the ionization threshold at short and intermediate R (see Fig. (8.1)). At $R = R_c$, their energies cross the ionization threshold and the states lose their autoionizing character. As R increases, the resonant states cross the $1s\sigma_g n\ell\lambda$ Rydberg series and dissociate into H(1*s*)+H(n >1).

The non resonant wave functions $\psi^{0+}_{\alpha\ell_\alpha\varepsilon_\alpha}$ describe a bound electron in either the $1s\sigma_g$ or $2p\sigma_u$ orbitals of H_2^+ and a continuum electron. They have been obtained with the L^2 close-coupling method [2]. The method consists in evaluating the electronic continuum Green's function in the discrete basis of two-electron configurations built from the $B-$spline representations orbitals mentioned above. The use of a discrete basis implies that the Green's function is obtained from the solution of a system of algebraic equations that it is much easier to solve than the original integro differential equation associated with a true electronic continuum. It is important to note that the L^2 close-coupling method allows for inter-channel coupling between different open channels and partial waves, and yields the correct outgoing asymptotic behavior (see [18] for details).

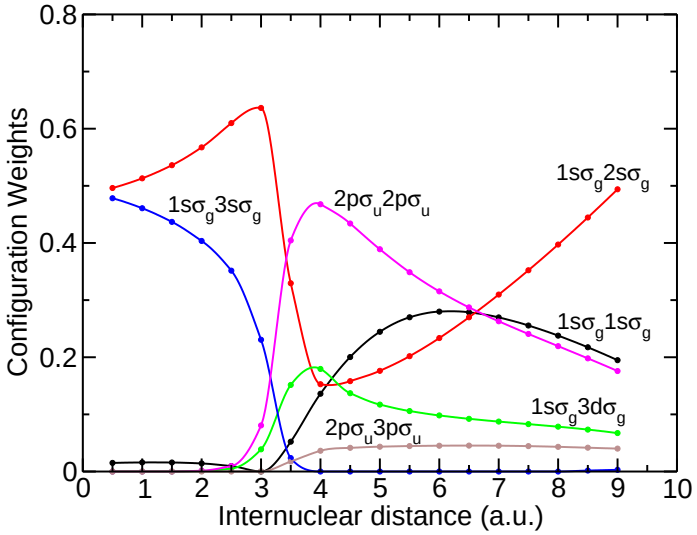

Figure 8.3: Configuration weights for the E,F $^1\Sigma_g^+$ electronic state of the H_2.

8.3 Ionization with 6.4 eV photons

We first present a detailed study at a fixed photon energy of 6.4 eV, which is around the value used in all previously reported experiments. In the next section we will analyze the variation with photon energy.

8.3.1 Non dissociative photoionization

Fig. (8.4) shows the vibrational distribution of H_2^+ molecular ions formed in photoionization of H_2 from the E,F$^1\Sigma_g^+(\upsilon, J=0)$ electronic state for υ=0−9 and a photon energy of 6.4 eV. The final $H_2^+(v)$ vibrational distributions strongly depend on the initial vibrational level υ. For υ=0, 3, and 6, H_2^+ remains in low vibrational states, while for υ=1, 2 and 4, it remains in highly excited vibrational states. For other initial values of υ, H_2^+ is produced in both low and high vibrational states. This complicated behavior is the consequence of the two potential wells in the E,F$^1\Sigma_g^+$ state: initial vibrational states mainly localized around the inner well lead to low-v H_2^+ distributions while initial vibrational states mainly localized around the outer well lead to high-v H_2^+ distributions due to the more favorable Franck-Condon overlap. Those vibrational states with no clear localization lead to much broader $H_2^+(v)$ distributions. Fig. (8.4) also shows the contribution from the non resonant part of the final continuum state [second term in the right hand side of Eq. (3.88)]. It can be seen that, in the case of initial vibrational states clearly localized around the inner minimum ($\upsilon = 0$ and 3), most of the calculated intensity comes from the non resonant term, while the opposite is observed for other initial vibrational states.

Fig. (8.3.1) shows the contribution of the final H_2 $^1\Sigma_u^+$ and $^1\Pi_u$ symmetries to the above vibrational distributions. For most initial values of υ, the largest contributions come from the $^1\Sigma_u^+$ symmetry. Also $H_2^+(v)$ vibrational distributions associated with the $^1\Sigma_u^+$ symmetry are in general much broader (i.e., less Franck-Condon) than those arising from the $^1\Pi_u$ one. This broadening is due to the resonant contribution of the Q_1 states of $^1\Sigma_u^+$ symmetry, which are much more efficiently populated than those of $^1\Pi_u$ symmetry.

Our results are compared in Fig. (8.6) with the experimental measurements reported in reference [10]. Very good agreement is obtained up to υ=6. For υ=9, the absolute values for high v are smaller than those for small v, while they are comparable in the experiment. Nevertheless the relative

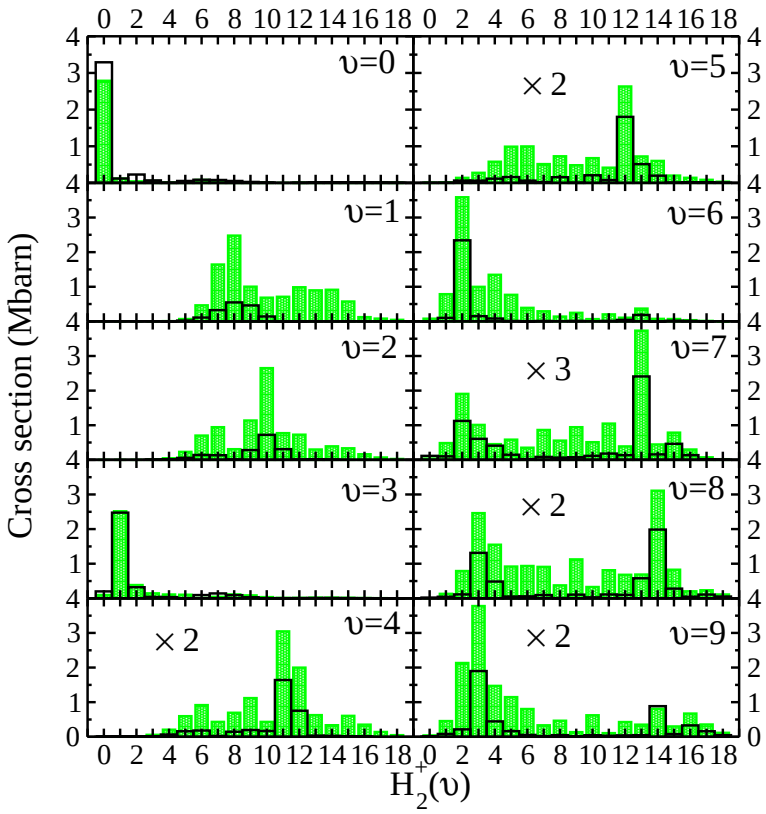

Figure 8.4: Final H_2^+ vibrational distribution in H_2 photoionization from the E,F$^1\Sigma_g^+(\upsilon)$ for $\upsilon = 0-9$ and a photon energy of 6.4 eV. Full bars: total cross section; hollow bars: non resonant contribution.

intensities in both regions taken separately are in qualitative agreement with experiment. It is worth pointing out that, except for the latter case, the present results agree better with experiment than those obtained in early theoretical work [16] or from the simple model reported in [10]. For instance, for υ=6, the experiment and the present theoretical calculations predict a decrease of intensity from v=2 to v=3 and then an increase up to v=4, while the previous theoretical results [10, 16] predict a monotonous decrease in this region. The multichannel quantum defect calculations reported in [16, 17] for $\upsilon = 0$ and 3 are in reasonable agreement with ours.

8.3.2 Dissociative photoionization

Fig. (8.7) shows the KED of protons produced in dissociative photoionization of H_2 from the E,F$^1\Sigma_g^+(\upsilon, J=0)$ state for υ=0−9 and a photon energy of 6.4 eV. Notice that the maximum allowed kinetic energy for ejected protons is given by $T_{max} = (\hbar\omega - E_{th})/2$, where E_{th} is the threshold energy for dissociative photoionization from a given E,F$^1\Sigma_g^+(\upsilon, J=0)$ initial state. Thus the theoretical cross sections go abruptly to zero for $T = T_{max}$. As for non dissociative photoionization, the present results strongly depend on the initial vibrational level υ. For υ=0, 3, and 6, dissociative photoionization is much less important than for other initial values of υ: the calculated cross sections are more than an order of magnitude smaller (notice that, for a better visualization, in Fig. (8.7) the corresponding cross sections have been multiplied by 50, 60 and 8, respectively). Consequently, the ratio of dissociative vs. non dissociative ionization is smaller for υ=0, 3, and 6 (see Fig. (8.11) below). Therefore, for these initial states, experimental determination of the dissociative ionization cross section is most difficult. As mentioned above, these are the initial vibrational states localized

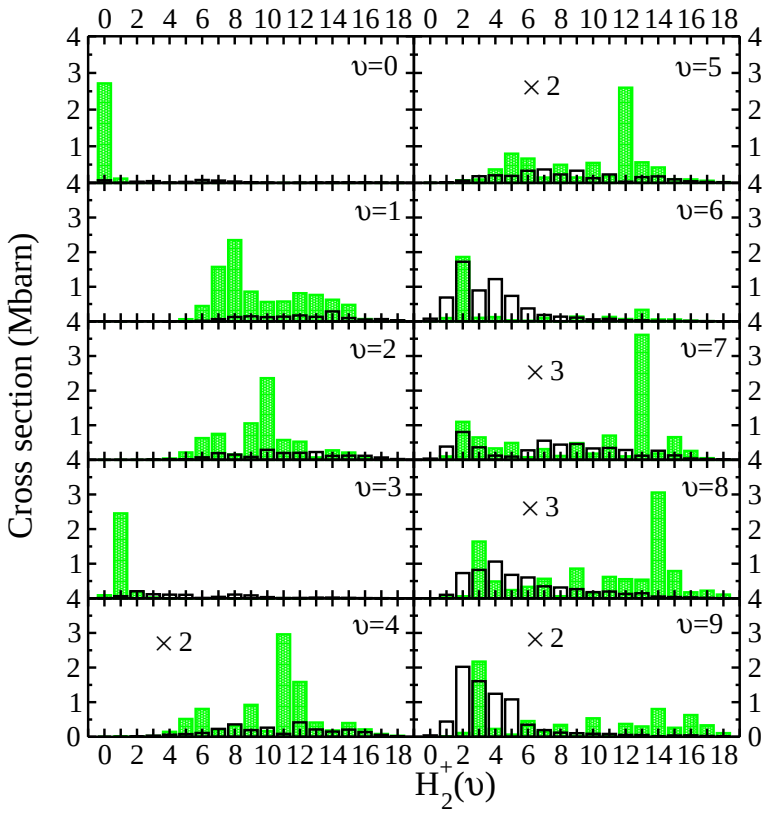

Figure 8.5: $^1\Sigma_u^+$ and $^1\Pi_u$ contributions to the H_2^+ vibrational distribution in H_2 photoionization from the E,F$^1\Sigma_g^+(\upsilon)$ for $\upsilon = 0-9$ and a photon energy of 6.4 eV. Full bars: $^1\Sigma_u^+$ contribution; hollow bars: $^1\Pi_u$ contribution.

around the inner well which favor the production of H_2^+ in a low vibrational state. For vibrational states localized around the outer well, the higher H_2^+ vibrational states, in particular those associated with the vibrational continuum, are favored. This also explains why, for $\upsilon \neq 0$, 3, and 6, the ratio of dissociative vs. non dissociative ionization is significantly larger than in photoionization from the ground X$^1\Sigma_g^+$ state. Fig. (8.7) also shows the contribution from the non resonant part of the final continuum state [second term in the right hand side of Eq. (3.88)]. It can be seen that, except for $\upsilon = 1$, resonance effects induced by the Q_1 doubly excited states are not dominant, but are not negligible. For υ=1, a direct vertical transition from the outer minimum to the second Q_1 $^1\Sigma_u^+$ doubly excited state is possible. For $\upsilon \geq 9$, the vibrational wave function resembles that of a common single-well electronic state, so that excitation to the doubly excited states follows the more traditional behavior based on vertical transitions from the inner classical turning point.

An interesting feature of the KEDs presented in Fig. (8.7) is the existence of pronounced oscillations. These oscillations are present in both the resonant and non resonant contributions. Fig. (8.8a) shows the contribution of the $1s\sigma_g$ and $2p\sigma_u$ ionization channels. The oscillatory behavior is observed in both channels. By comparing Figs. (8.7) and (8.8a), it can be seen that the resonant contribution is very similar to the $1s\sigma_g$ cross section and the non resonant contribution to the $2p\sigma_u$ cross section. This confirms that resonance effects are mostly due to the Q_1 doubly excited states lying below the $^2\Sigma_u^+(2p\sigma_u)$ ionization threshold. The oscillations in the $2p\sigma_u$ channel are a direct consequence of the variation of the Franck-Condon overlap between the initial vibrational state and the dissociative states associated with the $2p\sigma_u$ channel (see [13]). The Franck-Condon factors also explain why the frequency of the oscillations increases with the initial vibrational

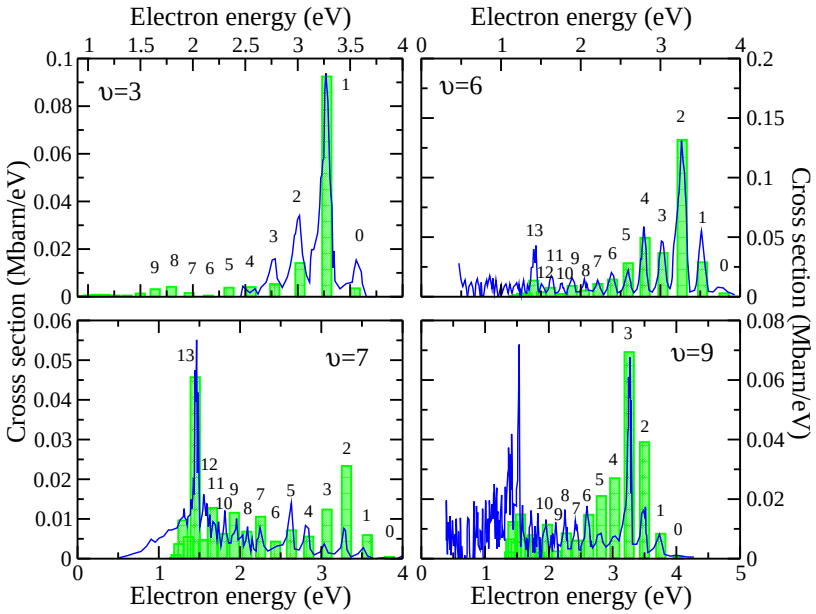

Figure 8.6: Comparison between calculated (bars) and measured (lines, Ref. [10]) H_2^+ vibrational distribution in H_2 photoionization from the E,F$^1\Sigma_g^+(\upsilon)$ state for $\upsilon = 3$, 6, 7 and 9, and a photon energy of 6.4 eV.

quantum number υ. Fig. (8.8b) shows the contribution of the final H_2 $^1\Sigma_u^+$ and $^1\Pi_u$ symmetries to the KEDs. It can be seen that $^1\Sigma_u^+$ and $^1\Pi_u$ contributions are comparable. For $\upsilon \geq 5$, the oscillatory behavior is observed for both symmetries, although it is somewhat distorted in the $^1\Sigma_u^+$ contribution for υ= 6 due to the significant contribution of the Q_1 doubly excited states.

In Fig. (8.9) we compare the calculated spectra from the initial E,F$^1\Sigma_g(\upsilon = 6)$ state with the available experimental results [13]. These measurements correspond to protons observed over all angles with respect to the polarization vector of the incident radiation. Since the measurements are not given in an absolute scale, the experimental data have been normalized to the calculated cross section for a proton kinetic energy of 0.17 eV. It must be stressed again that comparisons for the initial E,F$^1\Sigma_g(\upsilon = 6)$ state are much more difficult than for other initial values of υ because, as shown in Fig. (8.7), the corresponding cross section is one of the smallest ones (remember that this is the consequence of the initial $\upsilon = 6$ vibrational state having the larger maxima in the inner well). In spite of this, the theory reproduces most of the features observed in the experiment: peaks A (0.17 eV), B (0.37 eV), and C (0.57 eV), their shape, and relative intensities (our results slightly overestimate the intensity of peak B). As shown in Fig. (8.7), for the initial $\upsilon = 6$ state, these peaks are present in both the resonant and non resonant contributions. In Ref. [13], all these structures were exclusively attributed to non resonant dissociation though the $^2\Sigma_u^+(2p\sigma_u)$ channel. Although, as we have seen, this is approximately true for most initial υ's, contribution of the Q_1 $^1\Sigma_u^+$ doubly excited states is relatively more important for $\upsilon = 6$.

Using a semiclassical model, we can relate the position of each resonant peak with the internuclear distance R_i at which autoionization is produced by using the formula [5, 7]:

$$2T_i = \hbar\omega + W_{i\upsilon} - E_{H_{1s}} - [E_r(R_i) - E_\alpha(R_i)]\,, \tag{8.1}$$

where T_i and $[E_r(R_i) - E_\alpha(R_i)]$ are the kinetic energies of the ejected proton and electron, respectively, $E_{H_{1s}}$ is the ground-state energy of the H atom, and $W_{i\upsilon} - E_{H_{1s}} \simeq 5.24$ eV. For the lowest Q_1 $^1\Sigma_u^+$ resonant state, we obtain $R > 3.5$ a.u. in the relevant range of T_i. This means that autoionization occurs immediately before the doubly excited state crosses the first ionization limit

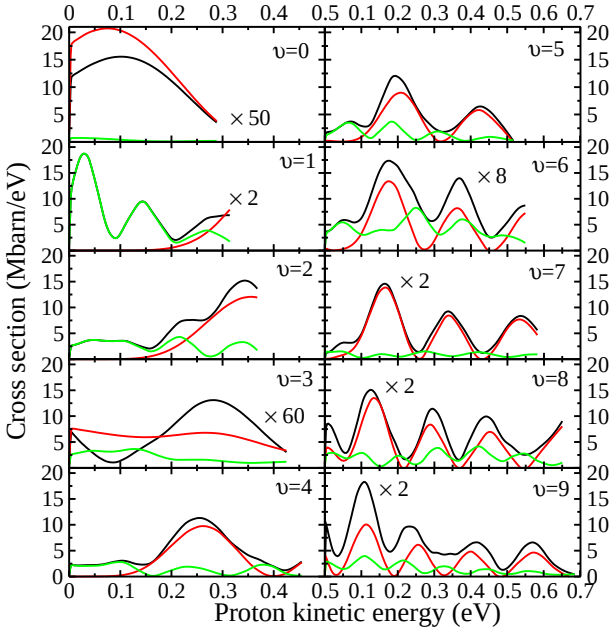

Figure 8.7: Proton kinetic energy distribution in H_2 photoionization from the E,F$^1\Sigma_g^+(\upsilon)$ state for $\upsilon = 0-9$ and a photon energy of 6.4 eV. Black lines: dissociative ionization cross section; red lines: non resonant contribution; green lines: resonant contribution.

(see Fig. (8.1)). This is consistent with the fact that the corresponding autoionization width increases with internuclear distance (see [15]). Contributions from the $Q_1\ ^1\Pi_u$ doubly excited states are much smaller due to the smaller autoionization widths (see [15]).

We now analyze the angular distribution of ejected protons. The differential cross section for proton emission in the solid angle $\Omega_{k_{H^+}}$ along the direction k_{H^+} of the ionic fragments is given by (see Eq. 4.64 of Section 4.4 of Chapter 4 for more details)

$$\frac{d\sigma_{\alpha\nu_\alpha}}{dE\,d\Omega_{k_{H^+}}} = \frac{\sigma_{\alpha\nu_\alpha}(E)}{4\pi}\left[1+\beta_{\alpha\nu_\alpha}(E)\left(\frac{3\cos^2\theta_{k_{H^+}}-1}{2}\right)\right] \tag{8.2}$$

where $\Omega_{k_{H^+}}$ is the angle between the ionic fragment momentum and the incident polarization direction, and $\beta_{\alpha\nu_\alpha}(E)$ is the ion beta parameter given by

$$\beta_{\alpha\nu_\alpha}(E) = 2\frac{D^2_{\alpha\nu_\alpha\Sigma}(E) - D^2_{\alpha\nu_\alpha\Pi}(E)}{D^2_{\alpha\nu_\alpha\Sigma}(E) + 2D^2_{\alpha\nu_\alpha\Pi}(E)} \tag{8.3}$$

where $D^2_{\alpha\nu_\alpha S}(E)$ for $S = \Sigma$ or Π, is the sum of the square of the matrix elements for each partial wave.

When the experimental results cannot distinguish between protons coming from different dissociation paths, one must evaluate an average ion beta parameter. For a photon energy of 6.4 eV, the accessible dissociation paths are those associated with the ground state and the first excited state of H_2^+, which are degenerate at infinite internuclear distance. In this case, the average ion beta parameter is given by Eq. (4.72)

$$\beta^A_{\alpha\nu_\alpha}(E) = \frac{\beta_{1s\sigma_g\nu_{1s\sigma_g}}\sigma_{1s\sigma_g\nu_{1s\sigma_g}} + \beta_{2p\sigma_u\nu_{2p\sigma_u}}\sigma_{2p\sigma_u\nu_{2p\sigma_u}}}{\sigma_{1s\sigma_g\nu_{1s\sigma_g}} + \sigma_{2p\sigma_u\nu_{2p\sigma_u}}}. \tag{8.4}$$

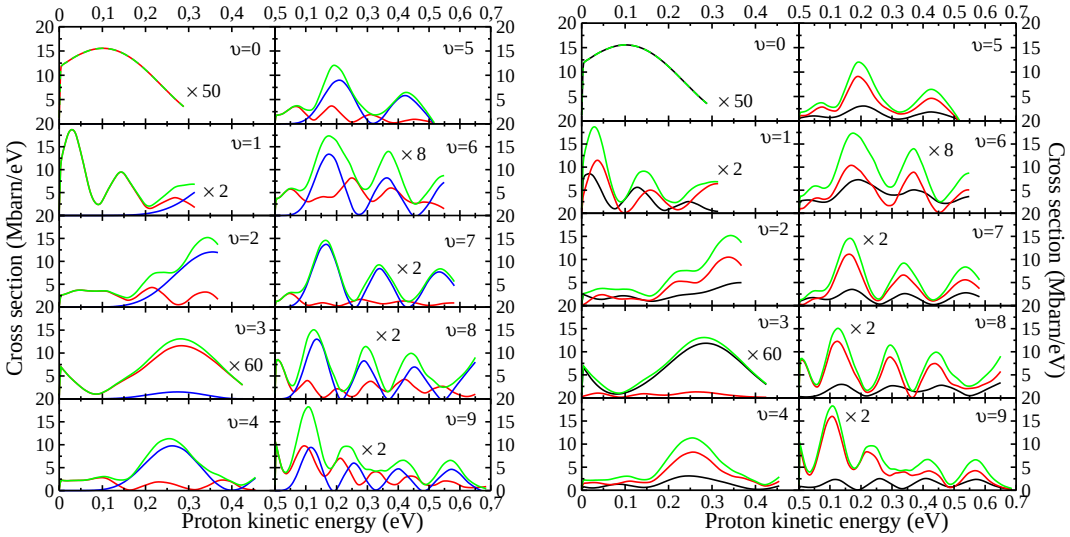

Figure 8.8: Contribution of (a) the $1s\sigma_g$ (red lines) and $2p\sigma_u$ (blue lines) channels, and (b) the $^1\Sigma_u^+$ (black lines) and $^1\Pi_u$ (red lines) symmetries to the proton kinetic energy distribution (green lines) in H_2 photoionization from the E,F$^1\Sigma_g^+(\upsilon)$ for $\upsilon = 0-9$ and a photon energy of 6.4 eV.

Fig. (8.10) shows the calculated proton ion beta parameter for dissociative ionization from the E,F$^1\Sigma_g^+(\upsilon = 6)$ state of H_2 along the $^2\Sigma_g^+(1s\sigma_g)$ channel, the $^2\Sigma_u^+(2p\sigma_u)$ channel, and the average values resulting from Eq. (8.4). In the absence of the Q_1 $^1\Sigma_u^+$ doubly excited states, the value of $\beta_{1s\sigma_g}$ is close to zero in the whole range of proton kinetic energy. However, the $\beta_{1s\sigma_g}$ results shown in Fig. (8.10) clearly differ from this behavior, thus showing the importance of the Q_1 $^1\Sigma_u^+$ doubly excited states in the $^2\Sigma_g^+(1s\sigma_g)$ channel. The $\beta_{2p\sigma_u}$ parameter exhibits a sharp peak at 0.27 eV and a smaller peak at 0.45 eV, which are the consequence of the two minima in the $^2\Sigma_u^+(2p\sigma_u)$ partial cross section (see Fig. (8.8a) for $\upsilon = 6$). As a consequence of the structures observed in the $\beta_{1s\sigma_g}$ and $\beta_{2p\sigma_u}$ parameters, the averaged ion beta parameter $\beta^A_{\alpha v_\alpha}$ exhibits a non monotonous behavior. It can be seen that previous measurements of the average ion beta parameter [13] agree reasonably well with the present calculations. The measurements were performed for proton kinetic energies in the vicinity of the calculated minima. In these minima, $\beta^A_{\alpha v_\alpha}$ is close to zero, but this is more the exception than the rule since $\beta^A_{\alpha v_\alpha}$ is always larger than zero and can reach values even close to the upper bound limit. It is worth noticing that in the absence of the Q_1 $^1\Sigma_u^+$ doubly excited states, $\beta^A_{\alpha v_\alpha} \simeq \beta_{2p\sigma_u}$ and the agreement with the experiment would worsen. In reference [13] it has been argued that a value of $\beta^A_{\alpha v_\alpha}$ close to zero indicates that the electron is mainly ejected in a *d* wave. However, an analysis of the different partial waves in the calculated wave function shows that contributions from the *s* wave are sometimes comparable to those from the *d* wave.

8.4 Variations with photon energy

To obtain photoionization cross sections at energies as high as 14 eV, we have extended our calculations by also including the Q_2 doubly excited states of H_2. Although, as we will see below, these states play a minor role in most cases, there are a few exceptions at the higher photon energies. Fig. (8.11) shows the variation with photon energy of the total photoionization cross sections from the E,F$^1\Sigma_g^+(\upsilon)$ state of H_2 for $\upsilon = 0-9$. The relative contribution of dissociative and non dissociative processes is also shown. Dissociative ionization is only possible for photon energies larger than 5.9 eV (see Fig. (8.1a)). This threshold shifts to higher photon energies as υ increases. The photon

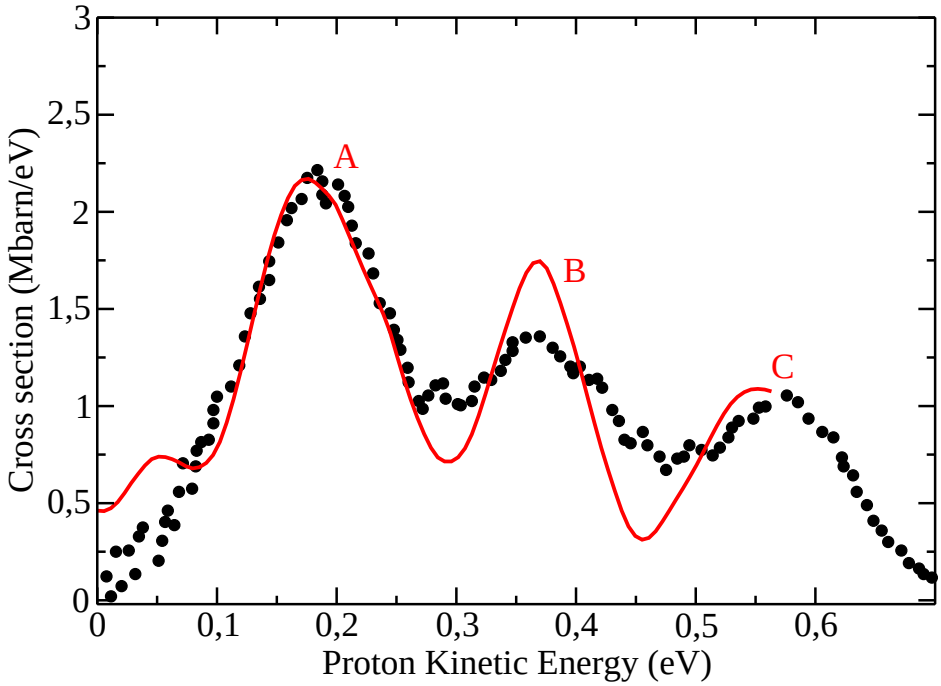

Figure 8.9: Comparison between the calculated (full line) and measured (circles, Ref. [13]) proton kinetic energy distribution in H_2 photoionization from the E,F$^1\Sigma_g^+(\upsilon = 6)$ state and a photon energy of 6.4 eV.

energy considered in the preceding sections (6.4 eV) lies very close to this threshold, especially for the higher υ's. Close to this threshold, the non dissociative ionization process dominates for all initial υ's and the ratio of dissociative vs. non dissociative processes depends very much on this initial υ. However, the situation changes completely when the photon energy is increased. Then the dissociative ionization process becomes dominant for most initial υ's. The only exceptions are υ = 0, 3 and 5, but still the dissociative contribution is comparable to the non dissociative one at the higher photon energies. This is in large contrast with H_2 photoionization from the ground X$^1\Sigma_g^+$ state for which the non dissociative cross section is always an order of magnitude larger than the dissociative one.

Another interesting feature in Fig. (8.11) is the presence of peaks. The origin of these peaks can be understood by looking at Fig. (8.12), which shows the contribution of the non resonant ionization process to the total cross section. It can be seen that the non resonant ionization cross section varies smoothly with photon energy except in the vicinity of the dissociative ionization threshold. For υ = 0 and 3 (i.e., states with dominant inner-well vibrational maxima), there is a broad peak that dominates the photoionization spectrum. The origin of this peak is autoionization from the lowest Q_1 $^1\Sigma_u^+$ doubly excited states of H_2. Population of these states is possible through a vertical transition from the inner well of the initial E,F$^1\Sigma_g^+(\upsilon)$ state (see Fig. (8.1)). The width of the peak corresponds more or less to the difference between the energy of the Q_1 state resulting from a vertical transition from the classical outer turning point and the energy of the Q_1 state resulting from a vertical transition from the classical inner turning point (both classical turning points are defined in the inner well). For the other initial υ's (i.e., those with important vibrational maxima in the outer well), the resonant peaks are much narrower and appear at much lower photon energy. These peaks are also associated with autoionization from the Q_1 $^1\Sigma_u^+$ doubly excited states, but since excitation is mainly produced from the outer well, they can be reached by using less energetic photons (see Fig. (8.1)). Also, since these transitions take place in the region where the Q_1 doubly excited states

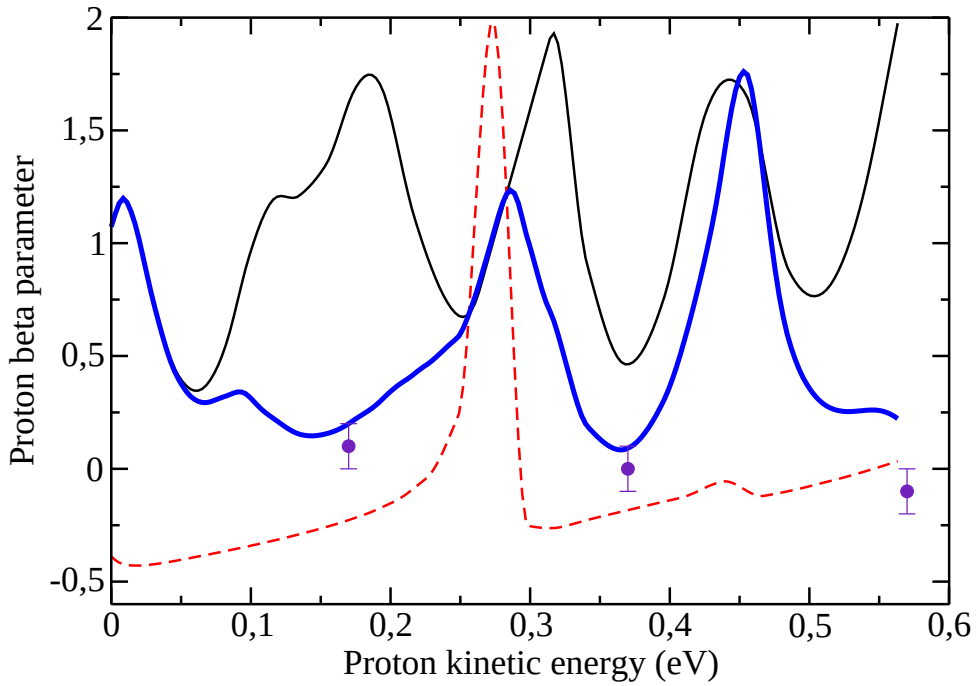

Figure 8.10: Ion beta parameter at 6.4 eV photon energy. Thin full line: ion beta parameter for protons dissociating through the $^2\Sigma_g^+(1s\sigma_g)$ ionic state; dashed line: ion beta parameter for protons dissociating through the $^2\Sigma_u^+(2p\sigma_u)$ ionic state; thick full line: averaged ion beta parameter; circles with error bars: experimental data from [13].

cross the ionization threshold (below which they are no longer autoionizing states), the effective range of photon energies in which these states can autoionize is smaller. At variance with the υ = 0 and 3 cases, many Q_1 $^1\Sigma_u^+$ doubly excited states contribute to the peaks, specially for the higher υ's.

Figs. (8.11) and (8.12) show that, for υ = 6-9, there are also resonant peaks at around 14 eV. These peaks are due to excitation to the lowest Q_2 doubly excited states through vertical transitions from the outer well of the E,F$^1\Sigma_g^+(\upsilon)$ state. For larger photon energies, more and more Q_2 doubly excited states will be populated. It is interesting to note that the Q_2 states are reached at much lower photon energies than in H_2 ground state photoionization, not only because excitation is produced from an excited electronic state but also because, for initial υ's with outer-well maxima, transitions occur at a large value of R (around 5 a.u.), a region where these doubly excited states are much lower in energy due to their dissociative character (see [7] and Fig. (8.1a)).

Figs. (8.13) and (8.14) show, respectively, the vibrational distribution of H_2^+ molecular ions and the KED of protons produced in photoionization of H_2 from the E,F$^1\Sigma_g^+(\upsilon, J=0)$ electronic state for υ=0$-$9 and a photon energy of 10 eV. It can be seen that the results are very different from those shown in Figs. (8.4) and (8.7) for a photon energy of 6.4 eV. In the case of non dissociative photoionization, the largest cross sections are obtained for inner-well vibrational states, $\upsilon = 0$, 3 and 6, which have the largest Franck Condon overlaps with the vibrational states of H_2^+. In contrast with the results obtained at 6.4 eV (Fig. (8.4)), the cross sections for other initial υ's are much smaller at 10 eV. This is because, at variance with the 6.4 eV case, excitation from the outer-well vibrational states using a 10 eV photon does not lead to effective population of the Q_1 doubly excited states. This interpretation is confirmed by analyzing the contribution of the non resonant process. Fig. (8.13) shows that, for the outer-well vibrational states, the non resonant contribution is almost identical to the complete result. It is only for the inner-well vibrational states that the resonant contribution is important, a result that is again in contrast with that obtained at 6.4 eV.

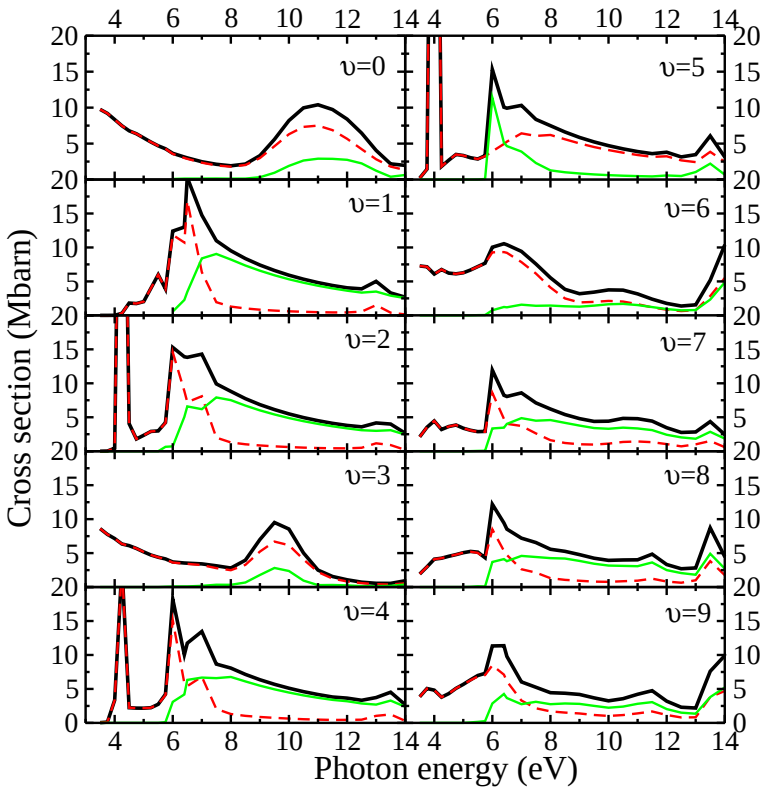

Figure 8.11: Photoionization cross section from the E,F$^1\Sigma_g^+(\upsilon)$ state of H_2 versus photon energy. Full thick line: total cross section; full thin line: non dissociative photoionization cross section; dashed line: dissociative photoionization cross section.

In the case of dissociative photoionization, initial outer-well states lead to oscillatory KED distributions (see Fig. (8.14)). These oscillations are not accidental: they are almost an exact replica of the square of the outer-well vibrational states shown in Fig. (8.1b). Indeed, for these outer-well vibrational states, the contribution of resonant processes through intermediate Q_1 or Q_2 doubly excited states is almost negligible. Therefore, direct ionization maps the initial vibrational distribution of internuclear distances onto the repulsive $^2\Sigma_u^+(2p\sigma_u)$ potential of H_2^+ thus yielding a KED spectrum that looks like the squared nuclear vibrational wave function. A similar mapping of the initial vibrational wave functions has been observed in H_2 double photoionization [22]. Thus inverting this process can be used to determine the squared nuclear vibrational wave function from the measured KED spectrum. The former analysis does not apply to the inner-well states $\upsilon = 0$ and 3, and to a lesser extent to $\upsilon = 6$. For these initial states, photoionization is only possible through the $^2\Sigma_g^+(1s\sigma_g)$ state of H_2^+ (see Fig. (8.1)). Furthermore, as mentioned above, the Q_1 doubly excited states are efficiently populated at this photon energy, thus leading to a KED that is almost entirely due to autoionization. Fig. (8.14) shows indeed that the non resonant contribution is negligible for $\upsilon = 0$ and 3. Also the cross section is significantly smaller.

The main conclusions obtained for a photon energy of 10 eV remain approximately valid in the photon energy range 8 to 12 eV. At higher photon energies, contribution of the Q_2 doubly excited states begin to change this picture, especially for the outer-well initial vibrational states.

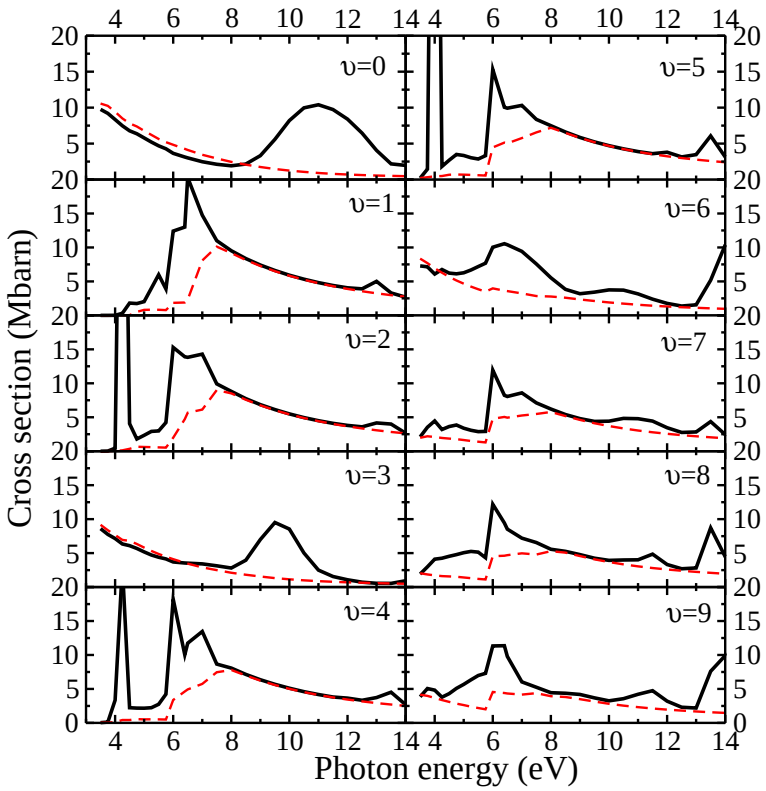

Figure 8.12: Idem to Fig. (8.11) but now the dashed line represents the contribution of non resonant ionization.

8.5 Conclusions

We have performed a theoretical study of dissociative and non dissociative photoionization of H_2 from the E,F $^1\Sigma_g^+(\upsilon, J=0)$ excited state for υ = 0-9 in the photon energy range 3 to 14 eV. The method takes into account both electronic and vibrational degrees of freedom and includes both direct and resonant (through Q_1 and Q_2 doubly excited states) ionization channels as well as the interference between them. Cross sections differential in the energy of the remaining H_2^+ ion or in the proton kinetic energy have been evaluated in the 3-14 eV energy range. We have paid special attention to the case of a photon energy of 6.4 eV corresponding to the wavelength of a ArF excimer laser. Comparison of our results with the available experimental measurements is good. We have shown that contribution of the Q_1 doubly excited states to the measured dissociative ionization cross section is more important than originally believed. At higher photon energies, we have found that, for most initial υ's, dissociative ionization is the dominant process.

Very different results are obtained depending on the initial vibrational state. This is the consequence of the double minimum in the potential energy curve of the initial E,F $^1\Sigma_g^+(\upsilon, J=0)$ state. For the inner-well vibrational states, photon absorption is only effective in an interval around R = 2 a.u., while, for the outer-well vibrational states, photon absorption takes place in an interval around R = 4.5 a.u. This implies that, at a fixed photon energy, very different final states can be reached depending on the initial vibrational state. For instance, at a photon energy of 10 eV, we have found that non resonant dissociative ionization through the $^2\Sigma_u^+(2p\sigma_u)$ threshold is the dominant process for the outer-well initial states, whereas resonant autoionization through the Q_1 doubly excited states is the dominant one for the inner-well initial states. Thus, by just selecting different initial vibrational states one can induce a variety of ionization processes in H_2 that, in

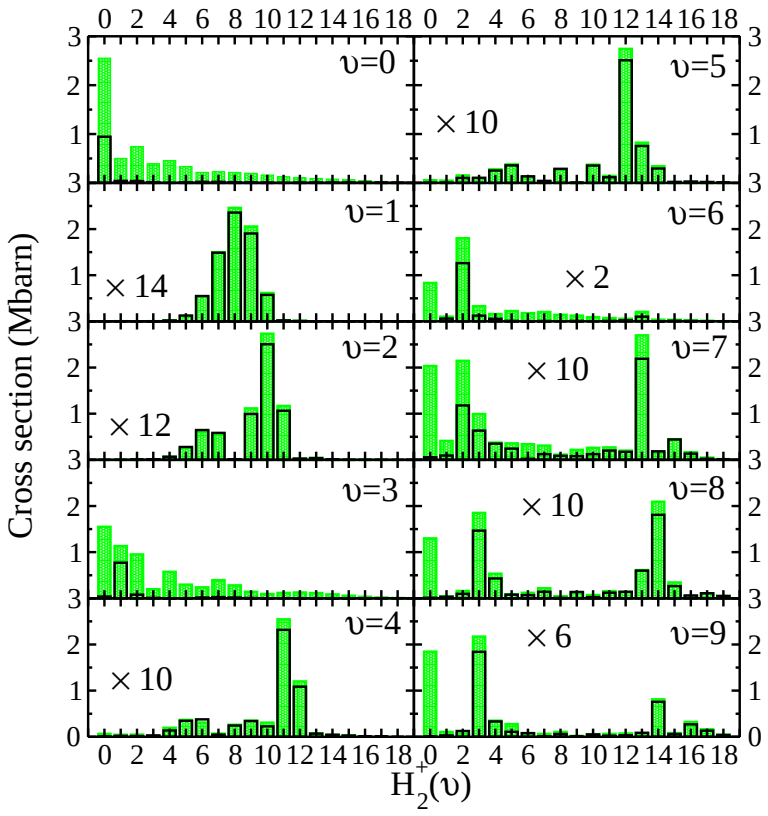

Figure 8.13: Final H_2^+ vibrational distribution in H_2 photoionization from the E,F$^1\Sigma_g^+(\upsilon)$ for $\upsilon = 0-9$ and a photon energy of 10 eV. Full bars: total cross section; hollow bars: non resonant contribution.

ground state photoionization, would only be possible by strongly varying the photon energy.

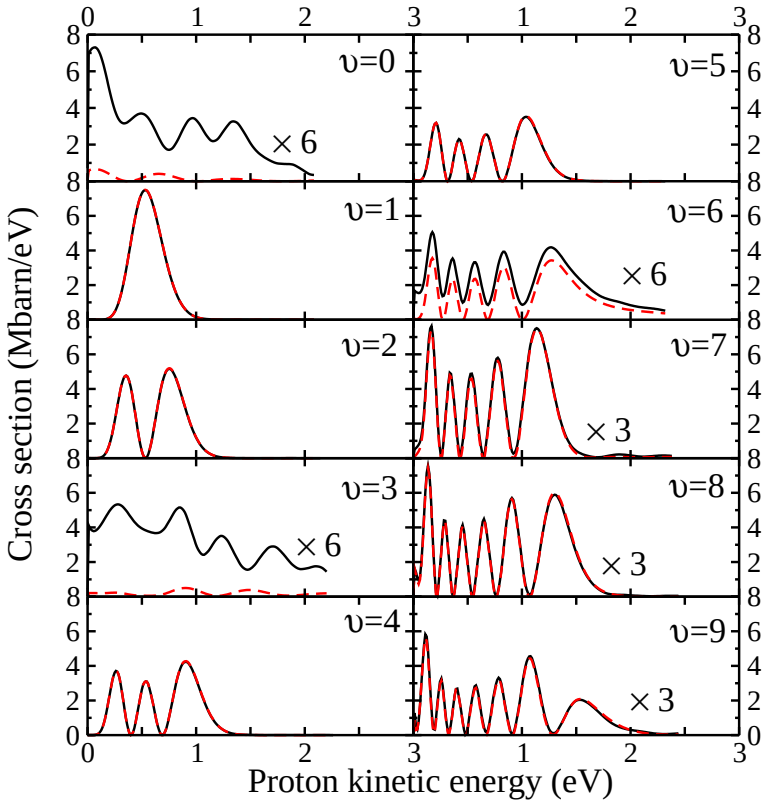

Figure 8.14: Proton kinetic energy distribution in H_2 photoionization from the E,F$^1\Sigma_g^+(\upsilon)$ state for $\upsilon = 0-9$ and a photon energy of 10 eV. Black lines: dissociative ionization cross section; red dashed lines: non resonant contribution.

Bibliography

[1] J. Fernández and F. Martín, "Dissociative and non-dissociative H_2 from the E,F$^1\Sigma_g^+$ excited state," *Physical Review A*, vol. 75, p. 042712, 2007.

[2] F. Martín, "Ionization and dissociation using B-splines: Photoionization of the hydrogen molecule," *Journal of Physics B: Atomic, Molecular and Optical Physics*, vol. 32, pp. R197–R231, 1999.

[3] S. Strathdee and R. Browning, "Dissociative photoionisation of H_2: Proton kinetic energy spectra," *Journal of Physics B: Atomic, Molecular and Optical Physics*, vol. 12, pp. 1789–1804, 1979.

[4] C. J. Latimer, J. Geddes, M. A. MacDonald, N. Kouchi, and K. F. Dunn, "The photodissociative ionization of hydrogen and deuterium in the VUV via Π states," *Journal of Physics B: Atomic, Molecular and Optical Physics*, vol. 29, pp. 6113–6121, 1996.

[5] K. Ito, R. I. Hall, and M. Ukai, "Dissociative photoionization of H_2 and D_2 in the energy region of 25-45 eV," *The Journal of Chemical Physics*, vol. 104, pp. 8449–8457, 1996.

[6] I. Sánchez and F. Martín, "Origin of unidentified structures in resonant dissociative photoionization of H_2," *Physical Review letters*, vol. 79, pp. 1654–1657, 1997.

[7] I. Sánchez and F. Martín, "Multichannel dissociation in resonant photoionization of H_2," *Physical Review letters*, vol. 82, pp. 3775–3778, 1999.

[8] C. A. de Lange, "Laser photoelectron spectroscopy of H_2 and D_2: Competing decay channels in "simple" molecules," *International Reviews in Physical Chemistry*, vol. 20, pp. 1–32, 2001.

[9] S. L. Anderson, G. D. Kubiak, and R. N. Zare, "Resonance-enhanced multiphoton ionization of molecular hydrogen via the E,F$^1\Sigma_g^+$ state: Photoelectron energy and angular distributions," *Chemical Physics Letters*, vol. 105, pp. 22–27, 1984.

[10] E. Xu, A. P. Hickman, R. Kachru, T. Tsuboi, and H. Helm, "Photoelectron spectroscopy of vibrationally excited H_2 (E,F $^1\Sigma_g^+$)," *Physical Review A*, vol. 40, pp. 7031–7038, 1989.

[11] I. W. T. Hill, B. P. Turner, S. Yang, J. Zhu, and D. L. Hatten, "Competition between multiphoton fragmentation channels in H_2 and HD induced by intermediate states," *Physical Review A*, vol. 43, pp. 3668–3674, 1991.

[12] S. Yang and I. W. T. Hill, "Proton angular distribution following multiphoton dissociative ionization of H_2," *Physical Review A*, vol. 51, pp. 2301–2307, 1995.

[13] B. L. G. Bakker, D. H. Parker, and W. van der Zande, "Observation of direct dissociative ionization in molecular hydrogen," *Physical Review Letters*, vol. 86, p. 3272, 2001.

[14] K. Wolniewicz and K. Dressler, "Adiabatic potential curves and nonadiabatic coupling functions for the first five excited $^1\Sigma_g^+$ states of the hydrogen molecule," *Journal of Chemical Physics*, vol. 100, pp. 444–451, 1994.

[15] I. Sánchez and F. Martín, "The doubly excited states of the H_2 molecule," *Journal of Chemical Physics*, vol. 106, pp. 7720–7730, 1997.

[16] H. Rudolph, D. L. Lynch, S. N. Dixit, V. McKoy, and W. M. Huo, "(2+1) resonant enhanced multiphoton ionization of H_2 via the E,F$^1\Sigma_g^+$ state," *The Journal of Chemical Physics*, vol. 86, pp. 1748–1751, 1987.

[17] C. Cornaggia, A. Giusti-Suzor, and C. Jungen, "Photoionization of the EF excited state of H_2: Calculation of vibrational branching ratios and photoelectron angular distributions," *The Journal of Chemical Physics*, vol. 87, pp. 3934–3941, 1987.

[18] I. Sánchez and F. Martín, "Resonant dissociative photoionization of H_2 and D_2," *Physical Review A*, vol. 57, pp. 1006–1017, 1998.

[19] H. Bachau, E. Cormier, P. Decleva, J. E. Hansen, and F. Martín, "Applications of B-splines in atomic and molecular physics," *Reports on Progress in Physics*, vol. 64, pp. 1601–1729, 2001.

[20] K. Wolniewicz, K. Szalewicz, and H. J. Monkhorst, "New Born-Oppenheimer potential energy curve and vibrational energies for the electronic ground state of the hydrogen molecule," *The Journal of Chemical Physics*, vol. 84, pp. 3278–3283, 1986.

[21] I. Sánchez and F. Martín, "Doubly excited autoionizing states of the H_2 above the second ionization thershold: The Q_2 resonance series," *Journal of Chemical Physics*, vol. 110, pp. 6702–6713, 1999.

[22] T. Weber, A. O. Czasch, O. Jagutzki, A. K. Müller, V. Mergel, A. Kheifets, E. Rotenberg, G. Meigs, M. H. Prior, S. Daveau, A. Landers, C. L. Cocke, T. Osipov, R. D. M. no, H. Schmidt-Böcking, and R. Dörner, "Complete photo-fragmentation of the deuterium molecule," *Nature*, vol. 431, pp. 437–440, 2004.

Chapter 9

Molecular frame photoelectron angular distribution of H_2

"The life of a great scientist in his laboratory is not, as many may think, a peaceful idyll. More often, it is a bitter battle with things, with one's surroundings, and above all with oneself. A great discovery does not leap completely achieved from the brain of the scientist, as Minerva sprang, all panoplied, from the head of Jupiter; it is the fruit of accumulated preliminary work."

Marie Curie

Table of Contents

The work reported in this Chapter has led to the publication [1, 2].

9.1 Introduction

ANGLE-RESOLVED photoelectron spectroscopy proved to be a powerful method for studying molecular structure and subtle details of the interaction of photons with molecules. The great majority of theoretical studies of the angular distributions of molecular photoemission is based on the dipole approximation, i.e., neglecting spatial variation of the electric field over the dimensions of the molecule. In this chapter, we report a theoretical determination of the complete photoelectron angular distribution for fixed-in-space H_2 and D_2 diatomic molecules induced by linearly and circularly polarized light, including the nuclear motion. As we have studied in Chapters 7 and 8, dissociative photoionization of $H_2(D_2)$ is the process in which a photon breaks the molecule into three fragments: $H(n\ell) + H^+ + e^-$. Since this is a very sensitive process with the initial photon energy, due to the population of different resonant states and different dissociation paths, we will consider only those photon energies that highlight the main physical mechanisms. So, first we present the results obtained for a photon energy of 20 eV, since the contribution of any doubly excited state is expected to be negligible, and besides, this gives us the possibility of performing a detailed study of the MFPADs, which will be the basis for understanding the more complicated results obtained at higher photon energies. At a photon energy of 27 eV, the role of the Q_1 doubly excited states is of crucial importance in the MFPAD. In particular, we will concentrate our attention on how interference effects, discussed previously by I. Sánchez *et al.* [3, 4] in the proton kinetic energy distribution, affect the electron angular distributions. Finally, we select a photon energy of 33 eV since the Q_2 doubly excited states are also accessible and the dissociation can be carried out through the second ionization threshold. The importance of these doubly excited states will be shown in the backward-forward asymmetry present in the electron angular distribution. In Fig. (9.1) we show the relevant potential energy curves of the H_2 molecule and H_2^+ ion that schematizes the different processes explained previously. Throughout the different sections we will present results for the H_2 and D_2 molecules, in order to highlight its differences. Also results for linearly and circularly polarized light will be presented, and in particular the circular dichroism will be studied in some detail.

Throughout the preceding sections we have shown that there have been many experimental works devoted to the study of the kinetic energy distribution (KED) of the ionic fragments [8, 9, 10, 11, 12, 13, 14, 15, 16, 17, 18, 19, 20, 21, 22, 23, 24, 25, 26, 27, 28, 29, 30, 31] and its angular dependence [32] (see also [33] for a review of this field), and only very recently theoretical calculations have been able to explain the different features presented in the proton KED [3, 4, 34, 35, 36]. In contrast to these vast number of results, minor efforts has been applied to the study of photoelectron angular distribution of H_2 molecule. Although there are several works devoted to electron angular distribution for randomly oriented molecules [37, 38, 39, 40, 41, 42, 43, 44, 45, 46], they were not of great interest in order to explain the different processes present in the dissociative photoionization, mainly because the nuclear motion erase any trace of the contribution of the doubly excited state. Only quite recently a few experimental results have been obtained in the case of fixed oriented H_2 molecules [47, 48, 49, 50, 51], in contract with the large number of studies dedicated to "bigger" diatomic molecules (for example [52, 53, 54, 55, 56], and references therein). From the theoretical part, the numbers of works devoted to the photoelectron angle distribution of oriented H_2 molecules is even scarcer, and to our concern only S. Semenov and N. Cherepkov [57] presented results making use of the Random Phase Approximation in the fixed nuclei approximation, for a photon energy range 21-100 eV.

Within the experimental results, in 2003, Y. Hikosaka and J. Eland [51] studied the photoionization process into the dissociation continuum of the ground state of H_2^+ at photon energies 21.2, 23.1, 26.9 and 40.8 eV, using the VIPCO method. Also they studied the MFPADs for ionization to the $2p\sigma_u$,

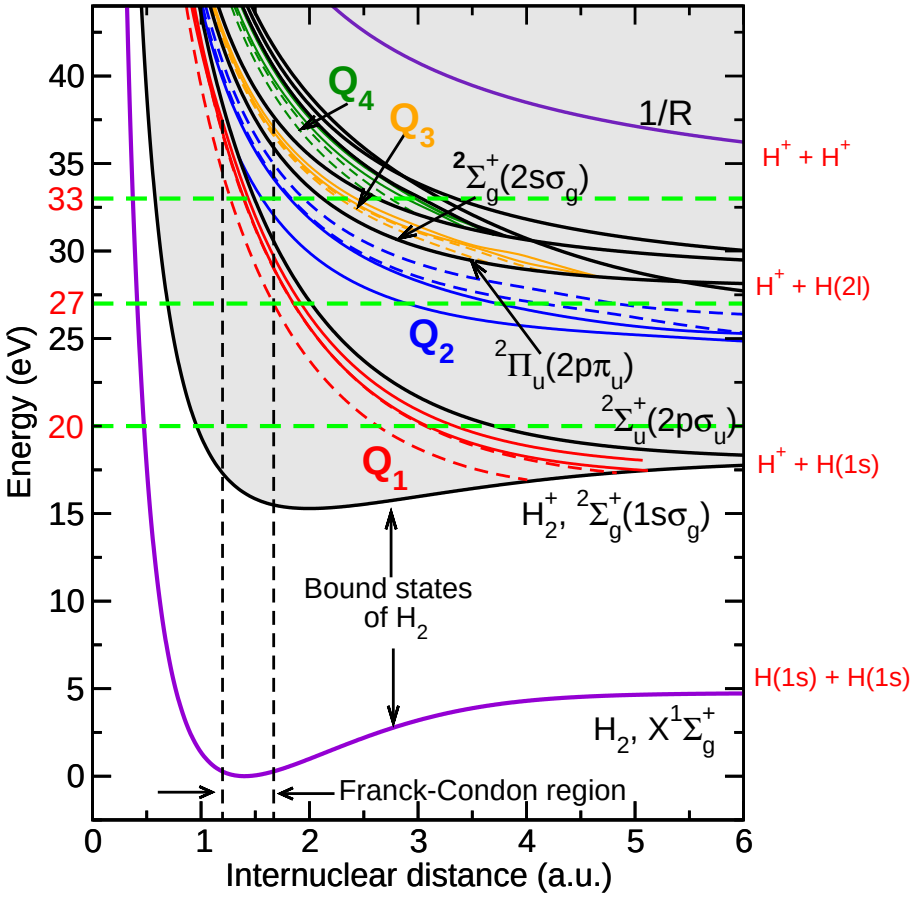

Figure 9.1: Energy level diagram of the H_2 and H_2^+ systems as a function of internuclear distance. Red lines Q_1 states, blue lines, Q_2 states, orange lines Q_3 and green lines Q_4 states, with symmetry $^1\Pi_u$ (full lines) and $^1\Sigma_u^+$ (dashed lines). Doubly-excited states of H_2 from [5, 6, 7]. The Franck-Condon region, which corresponds to classical turning points of the vibrational ground state, is enclosed by two vertical lines. The energy origin is placed on the lowest rovibrational level of the ground electronic state of H_2.

$2s\sigma_g$ and $2p\pi_u$ states of H_2^+ for a photon energy of 40.8 eV [50]. They only presented electron polar distributions for linearly polarized light parallel and perpendicular to the molecular axis (see also [48]). K. Ito *et al.* [49] studied the angular distribution of photoelectrons from fixed-in-space molecular hydrogen in the 44-77 eV photon energy range for an ionic state, with a state energy of 38 eV measured from the ground state of H_2, dissociating to $H^+ + H(n = 2)$. Only very recently, A. Lafosse *et al.* [47] presented a detailed experimental study of the photoelectron angular distribution for the photon energies 20.0, 28.5 and 32.5 eV, using linearly polarized light for any orientation for the molecular axis with respect to the polarization vector, in which the dependence with both the polar and azimuthal angle was obtained. In particular, they observed a backward-forward asymmetry in the MFPAD at photon energies where two dissociative paths are accessible. Also D. Dowek *et al.* [58] studied the electron angular distribution of H_2 and D_2 making use of circularly polarized light, and in particular they studied the circular dichroism. These last experimental works, have been the main motivation of the results presented in this Chapter.

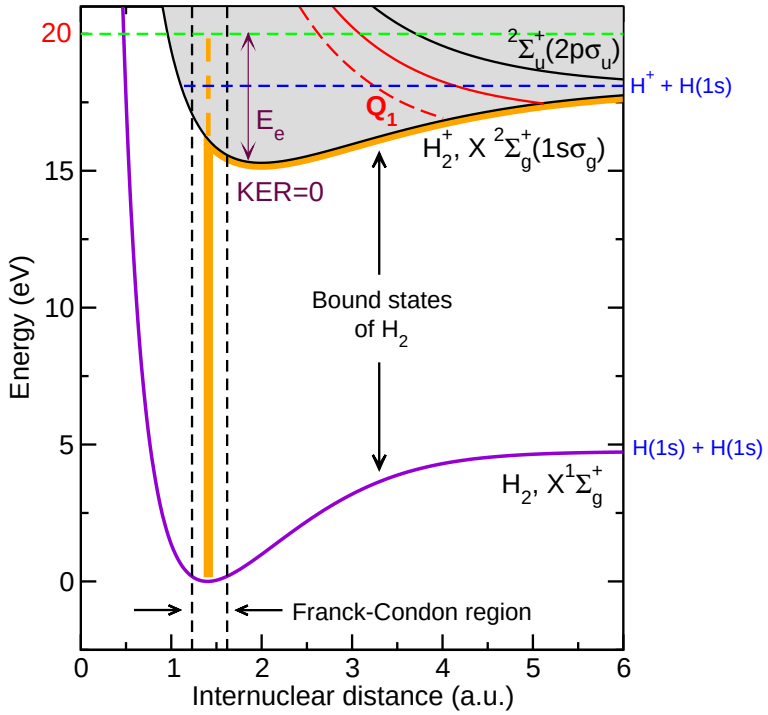

Figure 9.2: Pathways for dissociative ionization by absorption of one 20 eV photon. Direct ionization leading to $H_2^+\ (1s\sigma_g)$ (Eq. (9.1) in the text).

9.2 $\hbar\omega = 20$ eV: direct dissociative photoionization

Photoionization of H_2 leading to the H_2^+ in the $X^2\Sigma_g^+$ state has been studied extensively both experimentally and theoretically, because it is one of the simplest system where fundamental molecular photoionization dynamics can be studied. Total photoionization cross sections have been obtained since early stages of the experimental work [25, 31, 59, 60, 61], and theoretical calculations have generally agreed well [15, 40, 62, 63] with the experimental cross sections except for doubly excited states where an accurate theoretical description has been achieved only recently in our laboratory [33]. However, agreement between experiment and theory is relatively poor on the photoelectron asymmetry parameter β_e ([38] and references there in) which is a complementary quantity to the cross sections. Theoretical calculations have generally yielded β_e values near 2, while experimental values are substantially lower. The discrepancy has led to theoretical improvements of the initial and final states, including the effects of nuclear motion.

For a photon energy of 20 eV, $\alpha = {}^2\Sigma_g^+(1s\sigma_g)$ is the only open channel, and the contribution from doubly excited states is expected to be very small (since these states cannot be reached in a vertical transition from the initial state). Therefore, the photoelectron angular distribution obtained at this photon energy will be useful to reflect the main differences when doubly excited states are populated. Fig. (9.2) shows the pathway to dissociative ionization at this photon energy, that can be described by the reaction:

$$H_2(X^1\Sigma_g^+) + \hbar\omega \rightarrow H_2^+(1s\sigma_g) + e^- \rightarrow H^+ + H(1s) + e^- \tag{9.1}$$

In our theoretical calculations, the $Q_1\ ^1\Sigma_u^+$ and $Q_1\ ^1\Pi_u$ double excited states are included, but, one expects that these states do not play a very important role as they do at higher photon energies. The gerade-ungerade $(g-u)$ selection rule imposed by a single-photon transition restricts the electron in the continuum to the u symmetry, which implies a partial wave expansion with odd terms: $p\sigma_u$,

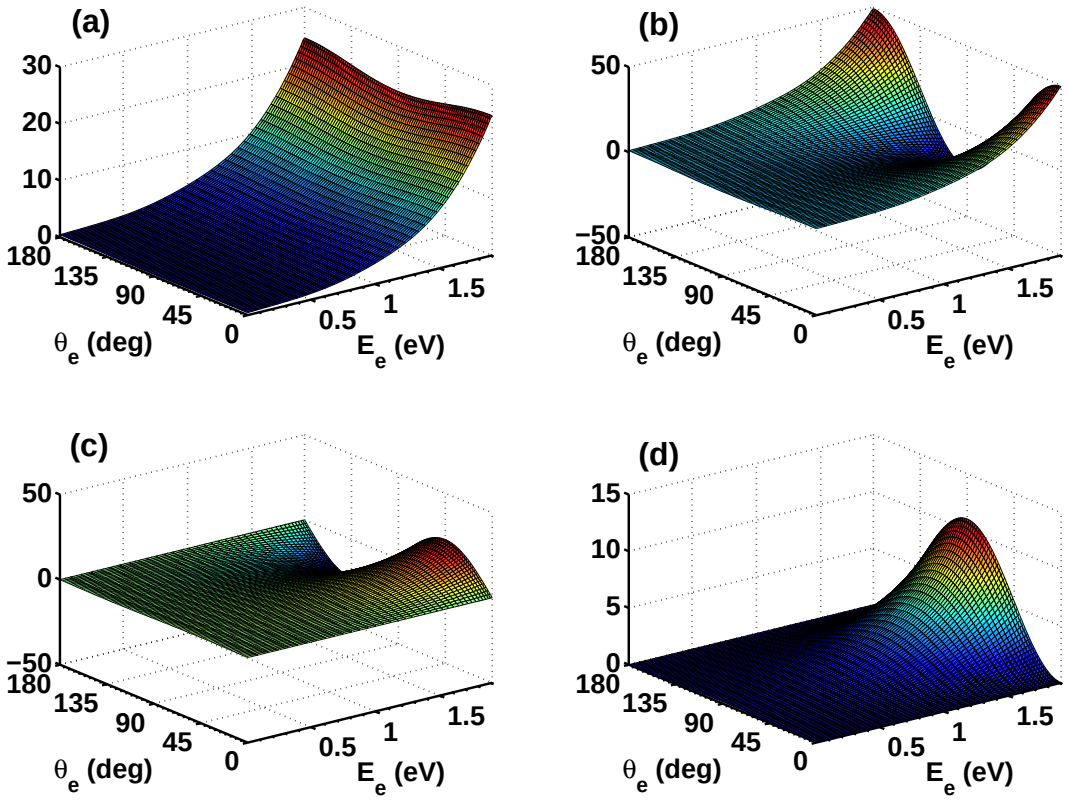

Figure 9.3: $F^0_{LN}(\varepsilon_{1s\sigma_g},\theta_e)$ functions of H_2 as a function of the electron energy $\varepsilon_{1s\sigma_g}$ and the electron polar emission angle θ_e, obtained with linearly polarized light, at $\hbar\omega$=20 eV. (a) $F^0_{00}(\varepsilon_{1s\sigma_g},\theta_e)$. (b) $F^0_{20}(\varepsilon_{1s\sigma_g},\theta_e)$. (c) $F^0_{21}(\varepsilon_{1s\sigma_g},\theta_e)$. (d) $F^0_{22}(\varepsilon_{1s\sigma_g},\theta_e)$. (Atomic units multiplied by 10^3).

$f\sigma_u$, $h\sigma_u$ and $j\sigma_u$ (ℓ=1, 3, 5 and 7) for the parallel and $p\pi_u$, $f\pi_u$, $h\pi_u$ and $j\pi_u$ (ℓ=1, 3, 5 and 7) for the perpendicular transition.

9.2.1 Linearly polarized light

In Chapter 4 we showed that the electron angular distribution for a fixed relative orientation of the polarization vector with respect to the molecule can be expressed through the expressions obtained by Dill given by Eq. (4.23). But this differential cross section is only valid for a perpendicular or parallel orientation of the polarization vector and does not give any information about the azimuthal electron angular distribution. On the other hand, we also showed that the fully differential cross section can be parametrized by four (five) functions for linearly (circularly) polarized light, providing full information about the electron distribution and the possibility of defining arbitrary relative orientations between the molecule and the polarization vector of the light. Therefore, in order to obtain a full description of our problem we have to obtain the $F^{\mu_0}_{LN}(W_{\upsilon_\alpha},\theta_e)$ functions as a function of the polar emission angle θ_e and the proton/electron energy[1] $W_{\upsilon_\alpha}/\varepsilon_\alpha$ as was explained in Chapter 4. Once these functions are obtained, the fully differential cross section, given by Eqs. (4.42)

[1]The electron angular distributions can be expressed as a function of the electron, ε_α, or the proton final energy, W_{υ_α}, since, for a fixed photon energy, the energy conservation implies that

$$W_{\upsilon_\alpha} = 2\times[\hbar\omega + W_{i\nu} - W_{\nu_\alpha} - \varepsilon_\alpha], \tag{9.2}$$

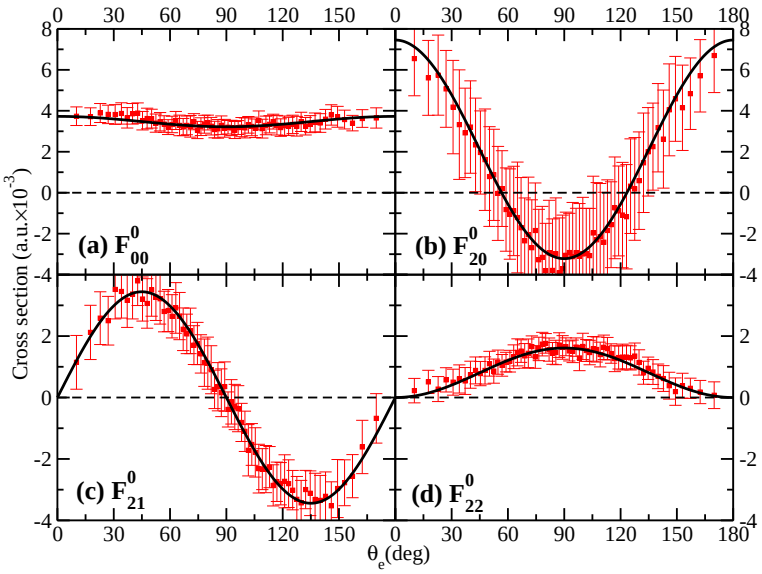

Figure 9.4: Theory-experimental comparison of the $F^0_{LN}(\theta_e)$ functions of H_2 obtained with linearly polarized light, for a fixed final electron energy of 1 eV, at $\hbar\omega$=20 eV. (a) $F^0_{00}(\theta_e)$. (b) $F^0_{20}(\theta_e)$. (c) $F^0_{21}(\theta_e)$. (d) $F^0_{22}(\theta_e)$. Black full line, theoretical calculations; Red square symbols, experimental results presented with error bars taken from A. Lafosse *et al.* [47].

and (4.43), can be calculated in a very easy way in order to compare with the experimental results.

In Fig. (9.3) we present the $F^0_{LN}(\varepsilon_{1s\sigma_g}, \theta_e)$ functions as a function of the ejected electron energy and the electron polar angle with respect to the molecular axis. The F^0_{00} function presents a slight dependence with the polar emission angle, since this function is described mainly by the first coefficient $C^0_{000}(\varepsilon_{1s\sigma_g})P^0_0(\cos\theta_e)$ given by Eq. (4.44), with a minor contribution from the second coefficient (note that $P^0_0(\cos\theta_e) = 1$). The F^0_{20} function has a stronger dependence with the emission angle, and this can also be described by the first coefficient of the expansion $C^0_{020}(\varepsilon_{1s\sigma_g})P^0_2(\cos\theta_e)$. The same conclusions can be apply to the F^0_{21} and F^0_{22} functions, which reflects the fact that all these functions are described mainly by the contribution of the first partial wave $\ell = 1$.

Quite recently, A. Lafosse *et al.* obtained the experimental F^0_{LN} functions collecting electrons in the [0, 2] eV energy range [47]. Fig. (9.4) displays the theory-experiment comparison of the F^0_{LN} functions as a function of the polar emission angle θ_e. Note that the theoretical results are obtained for a final ejected electron energy of 1 eV (same agreements are obtained when the F^0_{LN} functions are integrated over the whole electron energy range). The comparison with the experimental results is practically independent of the selected final electron energy (there exists only a change of absolute value). As can be seen, the agreement is excellent since all the experimental F^0_{LN} functions are renormalized to the single value of the theoretical F^0_{00} function at $\theta_e = 0°$. The $F^0_{LN}(W_{\upsilon_\alpha}, \theta_e)$ functions of the D_2 molecule are presented in Fig. (9.5), for a fixed final electron energy of 1 eV. The patterns for the $F^0_{LN}(W_{\upsilon_\alpha}, \theta_e)$ functions for the D_2 molecule are quite similar to the results obtained for the H_2, but ~ 3 times smaller (although this difference depends slightly on the electron polar angle, for example for the $F^0_{00}(W_{\upsilon_\alpha}, \theta_e)$ function, this difference is bigger at 0 and π polar angles than at $\pi/2$). This reflects the fact that the effective Franck-Condon region is smaller than for H_2.

Once the $F^0_{LN}(\varepsilon_{1s\sigma_g}, \theta_e)$ functions are obtained, the photoelectron angular distribution can be drawn, but, since the expressions given by Eqs. (4.42) and (4.43) are five-fold cross sections, for a

must be hold, where $W_{i\nu}$ is the energy of the initial molecule in the electronic state i and in the initial vibrational state ν, and W_{ν_α} is the dissociative limit of the residual ion. So, the fully differential cross section can indistinctly expressed as a function of the electron or proton energy.

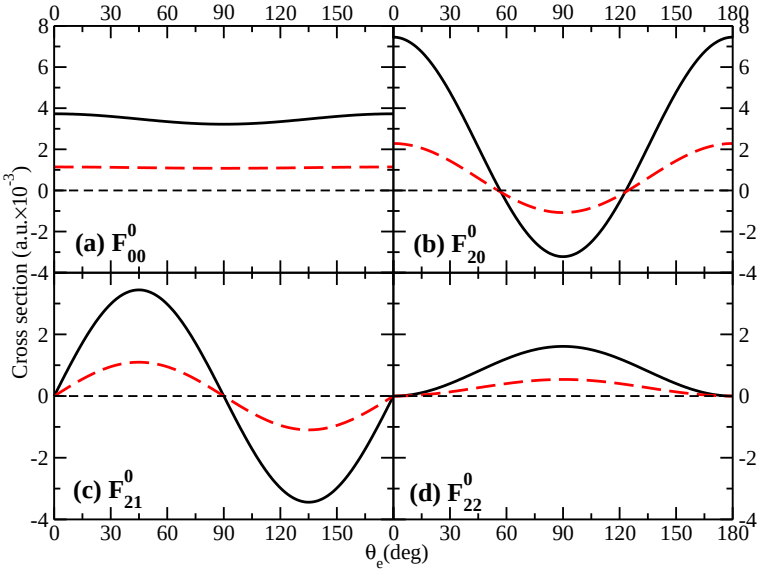

Figure 9.5: The $F^0_{LN}(\varepsilon_\alpha,\theta_e)$ function for H_2 (black lines) and D_2 (red dashed-line), obtained with linearly polarized light, for a fixed final electron energy of 1 eV, at $\hbar\omega$=20 eV (a) $F^0_{00}(\theta_e)$. (b) $F^0_{20}(\theta_e)$. (c) $F^0_{21}(\theta_e)$. (d) $F^0_{22}(\theta_e)$.

fixed initial photon energy, one has to consider several arrangements to highlight the differences due to the geometry of the molecule and the orientation of the light, i.e., some variables must be fixed, specially if we want to compare with the experimental results. In the following we will consider the case where the polarization vector of the linearly polarized light or the incident vector of the circularly polarized light is in the plane defined by the molecular axis and the x axis, i.e., $\phi_n = 0$ (see Fig. (4.2) of Chapter 4). Therefore, the fully differential cross section will depend on the electron emission angles θ_e and ϕ_e, the polarization (incident) angle of the linearly (circularly) polarized light θ_n, and the final proton (electron) energy $W_{\upsilon_\alpha}(\varepsilon_\alpha)$.

In order to get the spatial photoelectron angular distribution, the initial polarization angle of the linearly polarized light θ_n, and a specific energy of the ejected electron/proton have to be selected (or integrated over a specific energy range). For the specific angles $\theta_n = 0^\circ$, $\theta_n = 54.7^\circ$ (the "magic angle"), and $\theta_n = 90^\circ$, the differential cross section given by Eq. (4.42) takes the following forms:

$$\left.\frac{d\sigma_\alpha^{\mu_0=0}(\omega)}{d\Omega_e dW_{\upsilon_\alpha}}\right|_{\theta_n=0^\circ} = F^0_{00}(W_{\upsilon_\alpha},\theta_e) + F^0_{20}(W_{\upsilon_\alpha},\theta_e), \tag{9.3}$$

$$\left.\frac{d\sigma_\alpha^{\mu_0=0}(\omega)}{d\Omega_e dW_{\upsilon_\alpha}}\right|_{\theta_n=54.7^\circ} = F^0_{00}(W_{\upsilon_\alpha},\theta_e) - \sqrt{2}\times F^0_{21}(W_{\upsilon_\alpha},\theta_e)\cos(\phi_e) + 2\times F^0_{22}(W_{\upsilon_\alpha},\theta_e)\cos(2\phi_e), \tag{9.4}$$

and

$$\left.\frac{d\sigma_\alpha^{\mu_0=0}(\omega)}{d\Omega_e dW_{\upsilon_\alpha}}\right|_{\theta_n=90^\circ} = F^0_{00}(W_{\upsilon_\alpha},\theta_e) - \frac{1}{2}\times F^0_{20}(W_{\upsilon_\alpha},\theta_e) + 3\times F^0_{22}(W_{\upsilon_\alpha},\theta_e)\cos(2\phi_e). \tag{9.5}$$

As can be seen from the previous equations, the $F^0_{21}(W_{\upsilon_\alpha},\theta_e)$ function is only accessible when θ_n is different from 0 and 90 degrees, and it gives access to the relative phase between the $^1\Sigma_u^+$ and

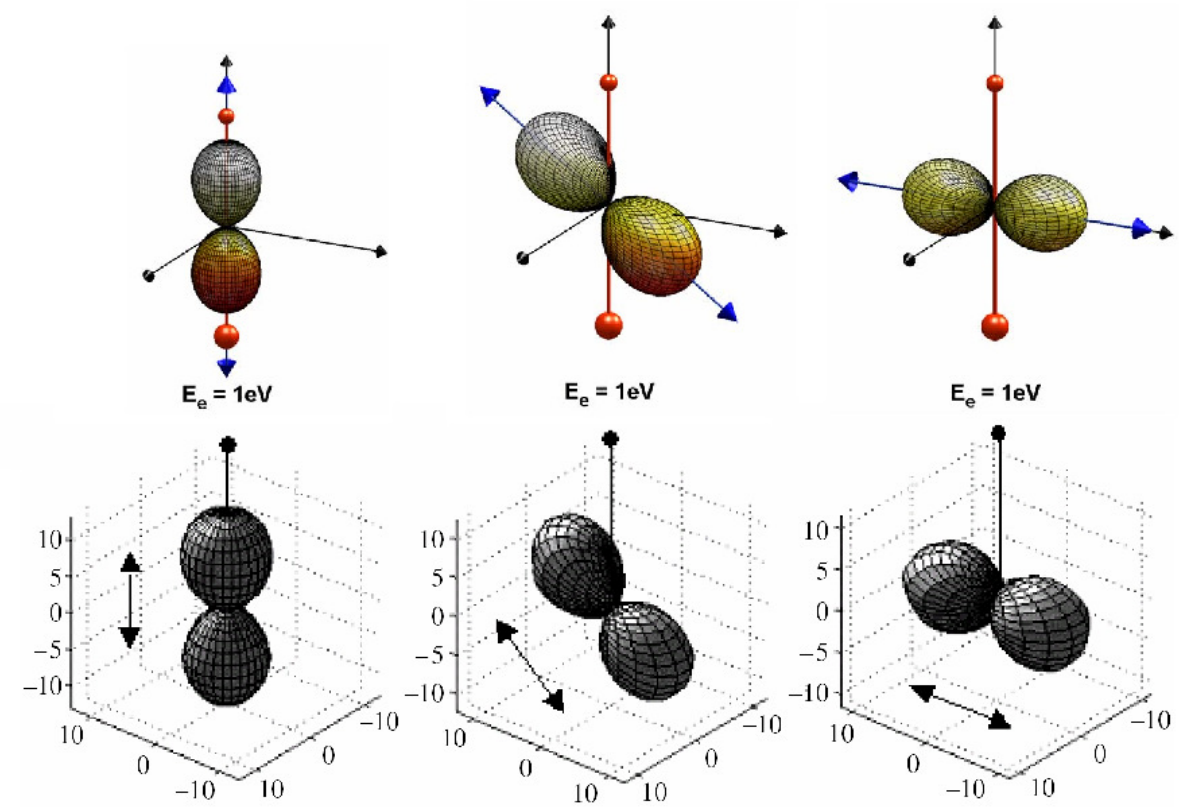

Figure 9.6: (Upper panels) Theoretical MFPAD of H_2 obtained with linearly polarized light, for a fixed final electron energy of 1 eV, for three different orientations of the polarization vector, at $\hbar\omega$=20 eV. (a) $\theta_n = 0°$; (b) $\theta_n = 54.7°$; (c) $\theta_n = 90°$. The smaller sphere in the upper part of the molecule represents the ejected proton and the blue arrow is the vector polarization vector. (Lower panels) Experimental results obtained from A. Lafosse *et al.* [47]. In these figures the proton is represented by the sphere situated in the upper size.

$^1\Pi_u$ matrix elements. Making use of Eqs. (9.3), (9.4) and (9.5), the MFPAD is obtained, selecting an electron/proton energy or a specific energy range. Fig. (9.6) presents the MFPAD for a fixed final electron energy of 1 eV, for the three previous initial orientations of the polarization vector with respect to the molecular frame (upper color panels). For the parallel orientation the electron emission is favored along the molecular/polarization axis, with the shape of the lobes similar to a *p*-wave shape (see Fig. (B.3) of Appendix B), which reflects the fact that the ionization process is described mainly by the first partial wave $\ell = 1$ (see Table (9.1)). This conclusion was also obtained by S. Semenov and N. Cherepkov [57] for this photon energy, in the fixed nuclei approximation. In this figure we also present the MFPAD obtained by A. Lafosse *et al.* For the two other orientations, electron emission is also favored along the polarization axis. Similar experimental results were obtained by Hikosaka *et al.* [51] observing the electron polar angle distribution.

Fig. (9.7) displays the MFPAD integrated over the whole electron/proton energy range, which confirm the fact that the results are similar to the ones showed in Fig. (9.6) for a fixed electron energy of 1 eV. The values at the bottom of each panel give the maximum value of the MFPAD. We have performed a partial wave analysis in $P_\ell(\cos\theta_e)$ Legendre polynomial expansion[2] in the form given

[2]Note that odd terms do not contribute to the expansion due to symmetry restrictions.

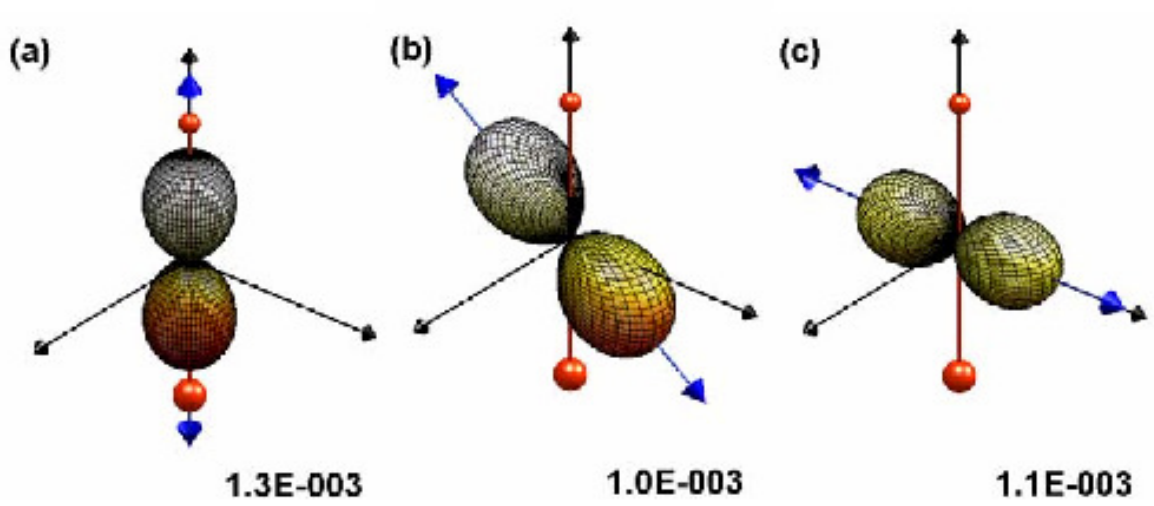

Figure 9.7: MFPAD of H_2 obtained with linearly polarized light, integrated over the whole final proton energy range, for three different orientations of the polarization vector, at $\hbar\omega$=20 eV. (a) $\theta_n = 0°$; (b) $\theta_n = 54.7°$; (c) $\theta_n = 90°$. The different values give the maximum of the MFPAD in atomic units.

by Eq. (4.23):

$$\frac{d\sigma_\alpha^{\mu_0}(\omega)}{d\Omega_e dW_{\upsilon_\alpha}} = \sum_L^{2\ell_{max}} B_L(W_{\upsilon_\alpha}) P_L(\cos\theta_e),$$

for H_2 and D_2. As for the F_{LN}^0 function, the coefficients $B_L(W_{\upsilon_\alpha})$ can be considered practically constant with the electron energy, whose results are presented in Table (9.1) for a final electron energy of 1 eV. Only the $B_2(W_{\upsilon_\alpha})$ takes a relevant value, both for parallel and perpendicular transition, with reflect the fact that the MFPAD is characterized by the *p*-wave contribution. In table (9.2) we present the results integrating over the whole final electron energy range. In this case the B_2 coefficient takes the same value than in the case where the electron energy is fixed to 1 eV, with a minor variation in the other coefficients. The value of the MFPAD given in panel (a) of Fig. (9.7), i.e., for the parallel orientation $\theta_n = 0°$, coincides with the cross section obtained by the expansion in Legendre polynomials presented in Table (9.2), for the electron polar angle $\theta_e = 0°$, which confirms the fact that both theoretical expressions given by Eq. (4.23) and Eq. (4.44) coincides for $\phi_e = 0$.

Performing the integration over the azimuthal angle, ϕ_e, in Eq. (4.42) we obtain the two-fold differential cross section as a function of the polarization orientation Ω_n and the polar emission angle θ_e. This integration can be performed directly:

$$\begin{aligned}\frac{d\sigma_\alpha^{\mu_0=0}(\omega)}{d\theta_n d\theta_e dW_{\upsilon_\alpha}} &= F_{00}^0(W_{\upsilon_\alpha},\theta_e)\phi_e\Big|_{\phi_{e,1}}^{\phi_{e,2}} \\ &+ F_{20}^0(W_{\upsilon_\alpha},\theta_e)P_2^0(\cos\theta_n)\phi_e\Big|_{\phi_{e,1}}^{\phi_{e,2}} \\ &+ F_{21}^0(W_{\upsilon_\alpha},\theta_e)P_2^1(\cos\theta_n)\sin\phi_e\Big|_{\phi_{e,1}}^{\phi_{e,2}} \\ &+ F_{22}^0(W_{\upsilon_\alpha},\theta_e)P_2^2(\cos\theta_n)\frac{1}{2}\sin(2\phi_e)\Big|_{\phi_{e,1}}^{\phi_{e,2}}. \end{aligned} \quad (9.6)$$

Table 9.1: Partial wave analysis in the $P_L(\cos\theta_e)$ Legendre polynomial expansion for H_2 and D_2 for parallel ($\sigma_\parallel$) and perpendicular ($\sigma_\perp$) transitions, for a fixed final electron energy to 1 eV, at $\hbar\omega$=20 eV.

	H_2		D_2	
B_L	$\sigma_\parallel$(a.u.)	$\sigma_\perp$(a.u.)	$\sigma_\parallel$(a.u.)	$\sigma_\perp$(a.u.)
0	0.3720(-02)	0.3223(-01)	0.9704(-03)	0.9185(-03)
2	0.2002(+01)	-0.9986(+00)	0.2002(+01)	-0.9988(+00)
4	0.2726(-02)	-0.1296(-02)	0.3612(-02)	-0.1117(-02)
6	0.2321(-04)	-0.2395(-04)	0.4215(-04)	-0.4107(-04)
8	0.7956(-06)	-0.3849(-06)	-0.8884(-07)	0.1186(-06)
10	-0.1156(-08)	0.1228(-08)	0.2848(-09)	-0.3973(-09)
12	0.1339(-11)	-0.3520(-12)	-0.5017(-12)	0.8476(-12)
14	0.9052(-13)	-0.4765(-13)	0.1740(-14)	-0.4479(-14)

Table 9.2: Same as in Table (9.1) for H_2, but integrating over the whole proton energy range.

B_L	$\sigma_\parallel$(a.u.)	$\sigma_\perp$(a.u.)
0	0.4208(-03)	0.3766(-03)
2	0.2000(+01)	-0.1002(+01)
4	0.4303(-03)	0.1881(-02)
6	0.1000(-03)	-0.5651(-05)
8	0.1562(-05)	-0.8865(-06)
10	0.7731(-09)	0.1887(-08)
12	0.1461(-10)	-0.5419(-11)
14	0.2397(-12)	-0.1666(-12)

Therefore, taking the integration limits from 0 to 2π, the previous differential cross section can be written as:

$$\frac{d\sigma_\alpha^{\mu_0=0}(\omega)}{d\theta_n d\theta_e dW_{\upsilon_\alpha}} = 2\pi\left[F_{00}^0(W_{\upsilon_\alpha},\theta_e) + F_{20}^0(W_{\upsilon_\alpha},\theta_e)P_2^0(\cos\theta_n)\right]. \tag{9.7}$$

In left panel of Fig. (9.8) we present the contour plot of the two-fold differential cross section for H_2, as a function of the polarization orientation θ_n and the electron polar emission angle θ_e, for a fixed electron energy equal to 1 eV. The dependence with the polarization and the electron emission angles is totally symmetric around $\theta_n = \pi/2$ and $\theta_e = \pi/2$, respectively. For an orientation of the polarization vector in the range 0-50 degrees, the electron is mainly emitted along the molecular axis. When θ_n approach to the magic angle the dependence with $F_{20}^0(W_{\upsilon_\alpha},\theta_e)$ function disappears and the differential cross section only depends on the function $F_{00}^0(W_{\upsilon_\alpha},\theta_e)$. For an orientation of the polarization vector in the range 60-90 degrees, the electron emission is performed perpendicular to the molecular axis. By fixing the initial orientation of the polarization vector in Eq. (9.7), the following expressions are obtained:

$$\left.\frac{d\sigma_\alpha^{\mu_0=0}(\omega)}{d\theta_e dW_{\upsilon_\alpha}}\right|_{\theta_n=0^\circ} = 2\pi\left[F_{00}^0(W_{\upsilon_\alpha},\theta_e) + F_{20}^0(W_{\upsilon_\alpha},\theta_e)\right], \tag{9.8}$$

$$\left.\frac{d\sigma_\alpha^{\mu_0=0}(\omega)}{d\theta_e dW_{\upsilon_\alpha}}\right|_{\theta_n=54.7^\circ} = 2\pi F_{00}^0(W_{\upsilon_\alpha},\theta_e), \tag{9.9}$$

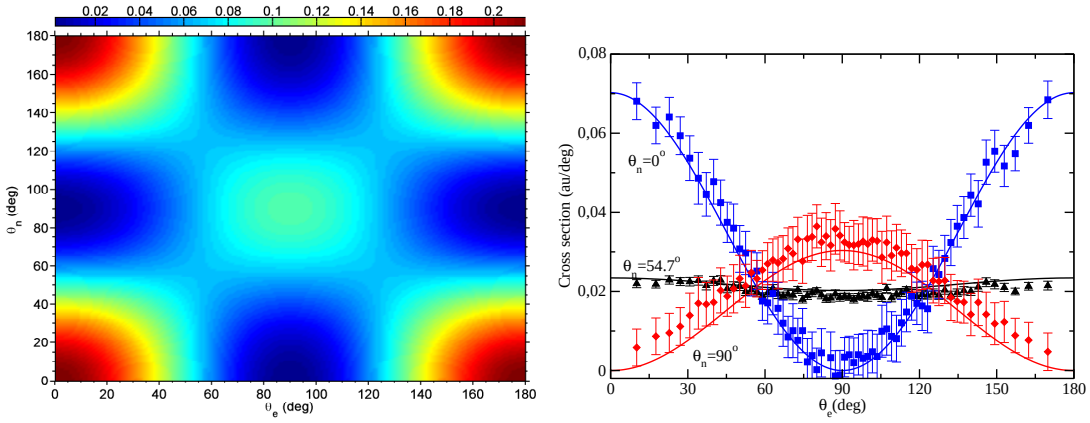

Figure 9.8: (Left panel) Contour plot of the two-fold differential cross section function of θ_n and θ_e for H_2 and the differential cross section as a function of θ_e, for three selected values of θ_n (right panel), at $\hbar\omega$=20 eV.: Blue line: $\theta_n = 0°$; Black line: $\theta_n = 54.7°$; Red line: $\theta_n = 90°$. All the theoretical results obtained for a fixed final electron energy of 1 eV. Experimental results obtained by A. Lafosse *et al.* [47] are presented with square symbols with its corresponding error bars.

and

$$\left.\frac{d\sigma_\alpha^{\mu_0=0}(\omega)}{d\theta_e dW_{\upsilon_\alpha}}\right|_{\theta_n=90°} = 2\pi\left[F_{00}^0(W_{\upsilon_\alpha},\theta_e) - \frac{1}{2}F_{20}^0(W_{\upsilon_\alpha},\theta_e)\right] \tag{9.10}$$

The results for these specific orientations are displayed in the right panel of Fig. (9.7), where the experimental results obtained by A. Lafosse *et al.* [47] are also included. For the magic angle the angular distribution is practically constant over all electron polar angle, since it is proportional to the F_{00}^0 functions, and for both perpendicular or parallel orientations the electron is emitted following the vector polarization, as we pointed out previously.

Another suitable selection of variables in the MFPAD, are the polarization orientation θ_n and the azimuthal emission angle ϕ_e, that can be obtained integrating over the polar angle θ_e in Eq. (4.42). By integrating over θ_e, one can emphasize the ϕ_e dependence for a particular value of θ_n:

$$\begin{aligned}\frac{d\sigma_\alpha^{\mu_0=0}(\omega)}{d\Omega_n d\phi_e dW_{\upsilon_\alpha}} &= G_{00}^0(W_{\upsilon_\alpha}) + G_{20}^0(W_{\upsilon_\alpha})P_2^0(\cos\theta_n) + G_{21}^0(W_{\upsilon_\alpha})P_2^1(\cos\theta_n)\cos(\phi_e) \\ &\quad + G_{22}^0(W_{\upsilon_\alpha})P_2^2(\cos\theta_n)\cos(2\phi_e),\end{aligned} \tag{9.11}$$

where $G_{LN}^{\mu_0}(W_{\upsilon_\alpha}) = \int_0^\pi F_{LN}^{\mu_0}(W_{\upsilon_\alpha},\theta_e)\sin\theta_e d\theta_e$.

Left panel of Fig. (9.9) shows the contour plot of the double differential cross section of H_2 given by Eq. (9.11), for an electron energy of 1 eV. Once again, it can be seen that the results obtained are completely symmetric around $\theta_n = \pi/2$ and $\phi_e = \pi$. For θ_n in the range 0-20 degrees, the double differential cross section is independent of the azimuthal emission angle ϕ_e, which means that only the first two terms of Eq. (9.11) are relevant, due to the fact that the $G_{21}^0(W_{\upsilon_\alpha})$ function takes a zero value and the $G_{22}^0(W_{\upsilon_\alpha})$ is much smaller than the $G_{00}^0(W_{\upsilon_\alpha})$ and $G_{20}^0(W_{\upsilon_\alpha})$ functions. From 20 to 90 degrees, the behavior is completely different, presenting an oscillatory pattern described by the $\cos(2\phi_e)$ function. Fixing the initial angle of the polarization vector, θ_n, in the previous equation the dependence of the cross section with the angle ϕ_e can be studied. As in previous cases we select the particular cases $\theta_n = 0°$, $54.7°$ and $90°$:

$$\left.\frac{d\sigma_\alpha^{\mu_0=0}(\omega)}{d\phi_e dW_{\upsilon_\alpha}}\right|_{\theta_n=0°} = G_{00}^0(W_{\upsilon_\alpha}) + G_{20}^0(W_{\upsilon_\alpha}), \tag{9.12}$$

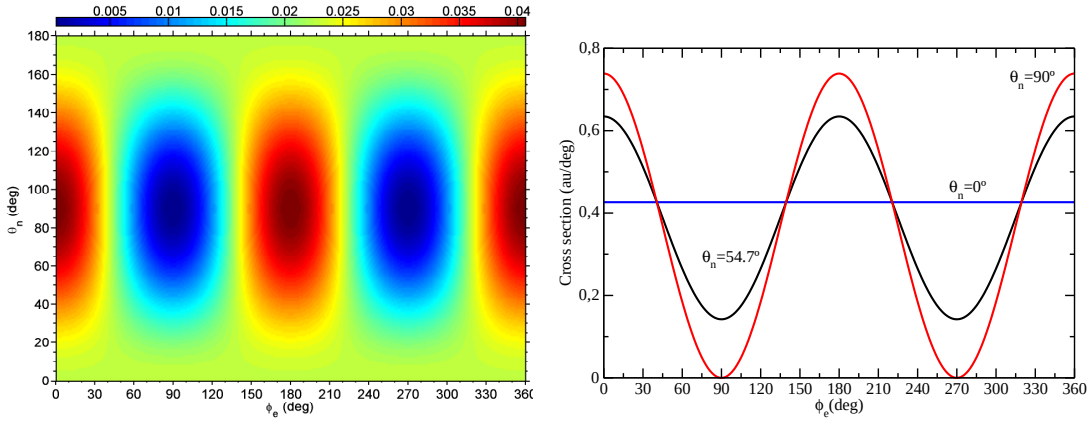

Figure 9.9: (Left panel) Contour plot of the two-fold differential cross section as a function of θ_n and ϕ_e(left panel) for H_2 and the differential cross section as a function of ϕ_e, for three selected values of θ_n (right panel), at $\hbar\omega$=20 eV.: Blue line: $\theta_n = 0°$; Black line: $\theta_n = 54.7°$; Red line: $\theta_n = 90°$. All results obtained for a fixed final electron energy of 1 eV.

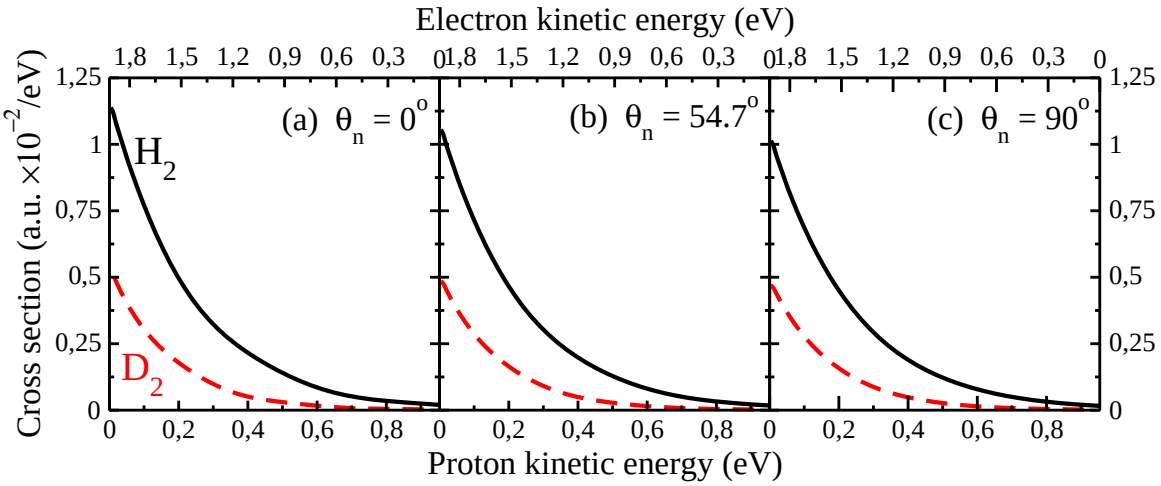

Figure 9.10: Total cross section of H_2 (black line) and D_2 (dashed red line) using linearly polarized light as a function of the proton/electron energy, for three different orientation of the polarization vector, at $\hbar\omega$=20 eV: (a) $\theta_n = 0°$; (b) $\theta_n = 54.7°$; (c) $\theta_n = 90°$.

$$\left.\frac{d\sigma_\alpha^{\mu_0=0}(\omega)}{d\phi_e dW_{\upsilon_\alpha}}\right|_{\theta_n=54.7^\circ} = G_{00}^0(W_{\upsilon_\alpha}) - \sqrt{2}\times G_{21}^0(W_{\upsilon_\alpha})\cos(\phi_e) + 2\times G_{22}^0(W_{\upsilon_\alpha})\cos(2\phi_e) \tag{9.13}$$

and

$$\left.\frac{d\sigma_\alpha^{\mu_0=0}(\omega)}{d\phi_e dW_{\upsilon_\alpha}}\right|_{\theta_n=90^\circ} = G_{00}^0(W_{\upsilon_\alpha}) - \frac{1}{2}\times G_{20}^0(W_{\upsilon_\alpha}) + 3\times G_{22}^0(W_{\upsilon_\alpha})\cos(2\phi_e). \tag{9.14}$$

The right panel of Fig. (9.9) presents the results obtained using the previous equations.

To complete the different information that can be obtained from Eq. (4.42), the integration over the electron emission angle ϕ_e and θ_e can be performed, obtaining the differential cross section as a function of the proton energy W_{υ_α} and the orientation of the polarization vector, θ_n (see results

presented in Chapter 7):

$$\frac{d\sigma_{\alpha}^{\mu_0=0}(\omega)}{dW_{\upsilon_\alpha}} = 2\pi\left[G_{00}^{0}(\omega,W_{\upsilon_\alpha}) + G_{20}^{0}(\omega,W_{\upsilon_\alpha})P_2^0(\cos\theta_n)\right]. \tag{9.15}$$

The previous equation resembles the differential cross section for the proton distribution, presented by Eq. (4.68) of Chapter 4. In fact the proton beta parameter can be written as:

$$\beta_{H^+}^{\mu_0}(\omega,W_{\upsilon_\alpha}) = \frac{G_{20}^{\mu_0}(\omega,W_{\upsilon_\alpha})}{G_{00}^{\mu_0}(\omega,W_{\upsilon_\alpha})}; \tag{9.16}$$

and the total cross section as:

$$\sigma_{tot}^{\mu_0}(\omega,W_{\upsilon_\alpha}) = 3\times G_{00}^{\mu_0}(\omega,W_{\upsilon_\alpha}). \tag{9.17}$$

So, the proton beta parameter non-resolved in the final proton energy is given by:

$$\beta_{H^+}^{\mu_0}(\omega) = \frac{\int G_{20}^{\mu_0}(W_{\upsilon_\alpha})dW_{\upsilon_\alpha}}{\int G_{00}^{\mu_0}(W_{\upsilon_\alpha})dW_{\upsilon_\alpha}}. \tag{9.18}$$

Since $F_{00}^1 = F_{00}^0$ and $F_{20}^1 = -0.5\times F_{20}^0$ (see Eqs. (4.47) - (4.50) of Chapter 4), the relation between the proton beta parameter obtained with circular and linearly polarized light, presented in Section 4.68, is kept.

For the previously selected orientations of the polarization vector, the differential cross section exclusively depends on the proton energy, obtaining the proton kinetic energy distribution (KED) ([64] and references therein):

$$\left.\frac{d\sigma_{\alpha}^{\mu_0=0}(\omega)}{dW_{\upsilon_\alpha}}\right|_{\theta_n=0^\circ} = 2\pi\left[G_{00}^{0}(W_{\upsilon_\alpha}) + G_{20}^{0}(W_{\upsilon_\alpha})\right], \tag{9.19}$$

$$\left.\frac{d\sigma_{\alpha}^{\mu_0=0}(\omega)}{dW_{\upsilon_\alpha}}\right|_{\theta_n=54.7^\circ} = 2\pi G_{00}^{0}(W_{\upsilon_\alpha}) \tag{9.20}$$

and

$$\left.\frac{d\sigma_{\alpha}^{\mu_0=0}(\omega)}{dW_{\upsilon_\alpha}}\right|_{\theta_n=90^\circ} = 2\pi\left[G_{00}^{0}(W_{\upsilon_\alpha}) - \frac{1}{2}\times G_{20}^{0}(W_{\upsilon_\alpha})\right]. \tag{9.21}$$

So the $G_{00}^{0}(W_{\upsilon_\alpha})$ gives access to the total cross section. Fig. (9.10) displays the total cross section for H_2 and D_2 as a function of the proton kinetic energy, for the three selected orientation of the polarization vector. As can be seen, the results are rather insensitive to the polarization vector orientation, in contrast with the results that will be presented in following sections. The cross section follows an exponential decay with the proton energy which is consequence of the fact that the FC factor decreases exponentially with the energy of the final ion state. These results are similar to the ones obtained by I. Sánchez *et al.* [65][3]

[3]Note that the KED obtained by these authors at 90° with respect to the polarization vector is two times larger than the results presented in Fig. (9.10), since those calculations where performed for randomly distributed molecules.

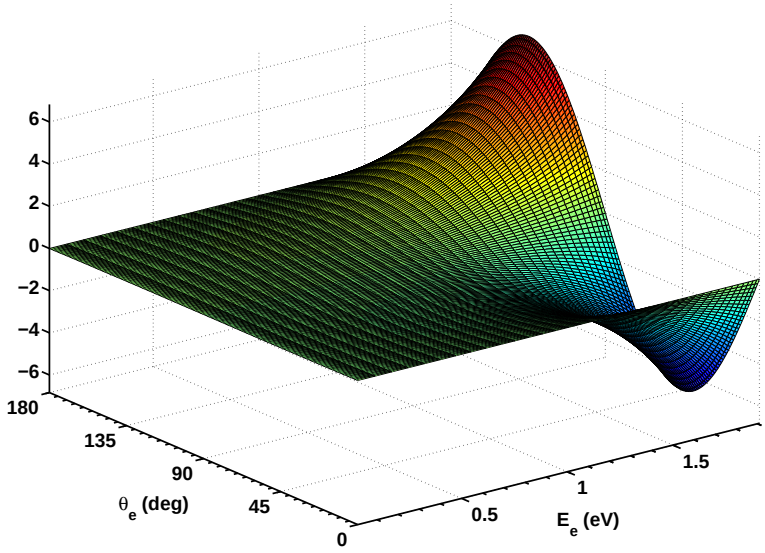

Figure 9.11: The $F^1_{11}(\varepsilon_{1s\sigma_g},\theta_e)$ function of H_2 as a function of the electron energy and the electron emission angle at $\hbar\omega$=20 eV. (Atomic units multiplied by 10^3).

9.2.2 Circularly polarized light

Now let's study the MFPAD of H_2 and D_2 making use of circularly polarized light, where now the angle θ_n represents the incident orientation of the light with respect to the molecular axis. As in the preceding section, the main objective is the calculation of the $F^{\pm1}_{LN}(W_{\upsilon_\alpha},\theta_e)$ functions, but, as we showed previously in Chapter 4, since there exists a simple relation between the $F^{\pm1}_{LN}(W_{\upsilon_\alpha},\theta_e)$ and $F^{0}_{LN}(W_{\upsilon_\alpha},\theta_e)$, for $L = 0,2$ and $N = 0,1,2$, (see Eqs. (4.47) - (4.50) of Chapter 4), only the $F^{\pm1}_{11}(W_{\upsilon_\alpha},\theta_e)$ function must be calculated in order to show up the effects of the circularly polarized light. Moreover, since the only different between making use of left handed and right handed light is a sign change in the $F^{\pm1}_{11}(W_{\upsilon_\alpha},\theta_e)$ functions, i.e., $F^{-1}_{11}(W_{\upsilon_\alpha},\theta_e) = -F^{1}_{11}(W_{\upsilon_\alpha},\theta_e)$, only the results obtained by right handed light ($\mu_0 = 1$) will be considered.

In Fig. (9.11) we present the $F^1_{11}(\varepsilon_{1s\sigma_g},\theta_e)$ function as a function of the electron energy and the electron polar angle for the H_2 molecule. It is characterized by the first coefficient of the expansion given by Eq. (4.44), i.e., the $C^1_{111}(\omega,W_{\upsilon_\alpha})P^1_1(\cos\theta_e)$ (see Fig. (B.2) of Appendix B), since only the first partial wave $\ell = 1$ dominates the ionization the process. As in the case of linearly polarized light, the dependence with the electron energy clearly follows a Franck-Condon pattern, which implies that the differential cross section can be considered independent of the final electron/proton energy. Fig. (9.12) shows the $F^1_{11}(\varepsilon_{1s\sigma_g},\theta_e)$ function for H_2 and D_2 as a function of the electron emission angle θ_e, for an electron energy of 1 eV. Also is included the results for the $F^1_{21}(\varepsilon_{1s\sigma_g},\theta_e)$ functions in order to give the relative magnitude of $F^1_{11}(\varepsilon_{1s\sigma_g},\theta_e)$. The behavior of these two functions, F^1_{21} and F^1_{11}, is quite similar due to the fact that both are mainly described by the $P^2_1(\cos\theta_e)$ Legendre polynomial, and as in the case for linearly polarized light (Fig. (9.4)) the result associated with the D_2 molecule is ~ 3 times smaller than the H_2.

Once the $F^1_{11}(\varepsilon_\alpha,\theta_e)$ function is obtained, we can perform the same study carried out for the case of linearly polarized light. First, in order to obtain the photoelectron angular distribution as a function of the electron emission angles, we must select the initial orientation of the direction of propagation of the light in Eq. (4.43) (remember that we are considering $\phi_n = 0$). As in the case of linearly polarized light, we choose the angles $\theta_n = 0°$, $54.7°$ and $90°$, so the differential cross

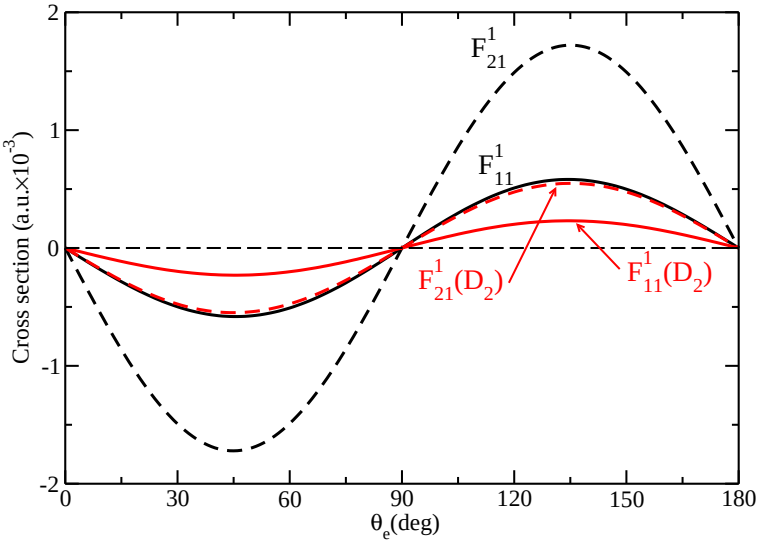

Figure 9.12: The $F^1_{11}(\theta_e)$ function (full line) and the $F^1_{21}(\theta_e)$ function (long dashed line) of H_2 (black line) and D_2 (red line), at $\hbar\omega$=20 eV. (Atomic units multiplied by 10^3).

section takes the form:

$$\left.\frac{d\sigma_\alpha^{\mu_0=\pm1}(\omega)}{d\Omega_e dW_{\upsilon_\alpha}}\right|_{\theta_n=0^\circ} = F^1_{00}(W_{\upsilon_\alpha},\theta_e)+F^1_{20}(W_{\upsilon_\alpha},\theta_e), \tag{9.22}$$

$$\left.\frac{d\sigma_\alpha^{\mu_0=\pm1}(\omega)}{d\Omega_e dW_{\upsilon_\alpha}}\right|_{\theta_n=54.7^\circ} = F^1_{00}(W_{\upsilon_\alpha},\theta_e)\mp\sqrt{\frac{2}{3}}\times F^1_{11}(W_{\upsilon_\alpha},\theta_e)\sin(\phi_e) - \sqrt{2}\times F^1_{21}(W_{\upsilon_\alpha},\theta_e)\cos(\phi_e)+2\times F^1_{22}(W_{\upsilon_\alpha},\theta_e)\cos(2\phi_e), \tag{9.23}$$

and

$$\left.\frac{d\sigma_\alpha^{\mu_0=\pm1}(\omega)}{d\Omega_e dW_{\upsilon_\alpha}}\right|_{\theta_n=90^\circ} = F^1_{00}(W_{\upsilon_\alpha},\theta_e)-\frac{1}{2}\times F^1_{20}(W_{\upsilon_\alpha},\theta_e)\mp F^1_{11}(W_{\upsilon_\alpha},\theta_e)\sin(\phi_e) +3\times F^1_{22}(W_{\upsilon_\alpha},\theta_e)\cos(2\phi_e). \tag{9.24}$$

In particular, the differential cross section given by Eq. (9.22) is equal to the differential cross section obtained by linearly polarized light for an orientation of the polarization vector equal to $\theta_n = 90^\circ$ (see Eq. (9.5)), for the electron azimuthal angle $\phi_e = \pi/4$:

$$\left.\frac{d\sigma_\alpha^{\mu_0=\pm1}(\omega)}{d\Omega_e dW_{\upsilon_\alpha}}\right|_{\theta_n=0^\circ} = \left.\frac{d\sigma_\alpha^{\mu_0=0}(\omega)}{d\theta_e dW_{\upsilon_\alpha}}\right|_{\theta_n=90^\circ,\phi_e=\pi/4}. \tag{9.25}$$

The MFPADs for these particular orientations are displayed in Fig. (9.13), for a fixed final electron energy of 1 eV. In all the cases the electron is emitted following the direction of the polarization vector, which is perpendicular to the orientation of the incoming direction of the light. This fact is clearly manifested for $\theta_n = 0^\circ$, while for the other two orientations the presence of the function F^1_{11} slightly deforms the electron distribution. In this case there are no experimental results to compare with, and only S. Semenov and N. Cherepkov [57] performed a theoretical calculation

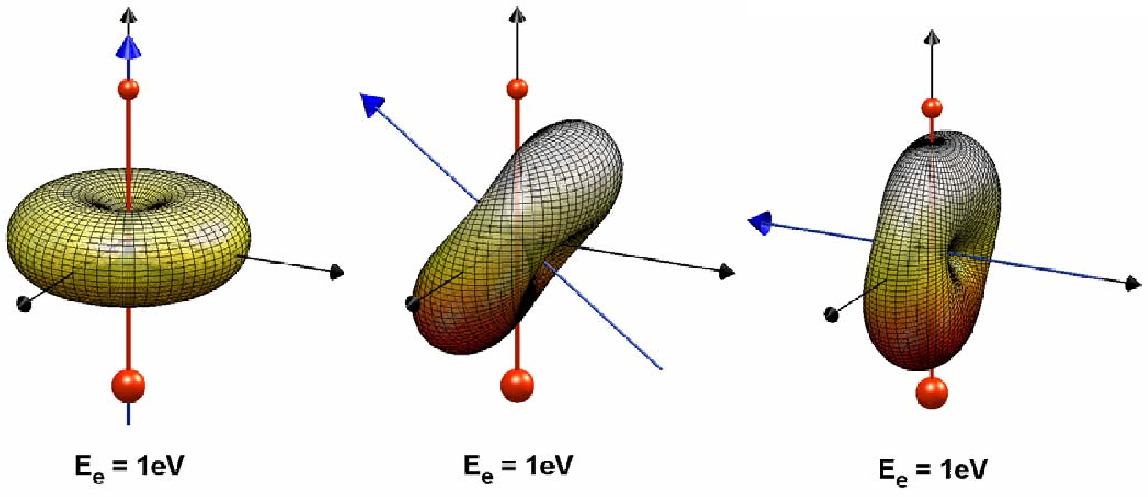

Figure 9.13: Same as Fig. (9.6) but using instead circularly polarized light ($\mu = +1$).

in the fixed nuclei approximation for this photon energy. Their results are presented in panel b) of Fig. (9.14), and can be compared with the MFPAD displayed in Fig. (9.13) for an incident angle $\theta_n = 90°$. Panel a) gives the geometry configuration of the molecular and laboratory reference systems used by these authors. The general features are reproduced by both theoretical results, although there are several differences: the result obtained by Semenov *et al.* presents a much more pronounced node in the *xz* plane (see Fig. (4.2) of Chapter 4.)

Fig. (9.15) shows the MFPAD integrated over the whole electron/proton energy range, and as for the linearly polarized light case, the pattern is equal to the one obtained for a fixed electron energy of 1 eV (Fig. (9.13)). The value at the bottom of each panel gives the maximum of the MFPAD. Making use of the Legendre polynomial expansion presented in Table (9.2), and considering only the results for the perpendicular orientation, for an electron polar angle of $\theta_e = 90°$, the same value in the MFPAD for $\theta_n = 0°$ is obtained (panel (a)).

Let's study the differential cross section as a function of the orientation of incoming circularly polarized light, θ_n, and the electron polar angle θ_e, integrating the fully differential cross section given by Eq. (4.43) over the electron azimuthal angle ϕ_e, as we did for linearly polarized light (see Eq. (9.7)). In this case, the differential cross section takes the form:

$$\frac{d\sigma_\alpha^{\mu_0=\pm1}(\omega)}{d\theta_n d\theta_e dW_{\upsilon_\alpha}} = 2\pi\left[F_{00}^1(W_{\upsilon_\alpha},\theta_e) + F_{20}^1(W_{\upsilon_\alpha},\theta_e)P_2^0(\cos\theta_n)\right], \tag{9.26}$$

which is independent of the F_{11}^1 function. The left panel of Fig. (9.16) presents the contour plot of the previous three-fold differential cross section for the H_2 molecule, for an electron energy equal to 1 eV. The behavior is quite similar to the one obtained with linearly polarized light (see Fig. (9.8)): For smaller angles θ_n than the "magic angle" (greater that 125.3 degrees), it takes the maximum value for θ_e in the 54.7-125.3 range. For θ_n angles in the 54.7-125.3 range, the pattern for circularly polarized light is opposite to the case of linearly polarized, since it takes the maximum values for θ_e angles in the range 0-54.7 and 125.3-180 degrees, which is the consequence of the fact that the polarization of the light and the propagation orientation are perpendicular. Also, it can be seen in Fig. (9.8) that when θ_n or θ_e are equal to the magic angle, the two-fold differential cross section takes a constant value. So, for circularly polarized light, the magic angle divide the contour plot in nine regions (in fact, only six different regions), which was less evident for linearly polarized light.

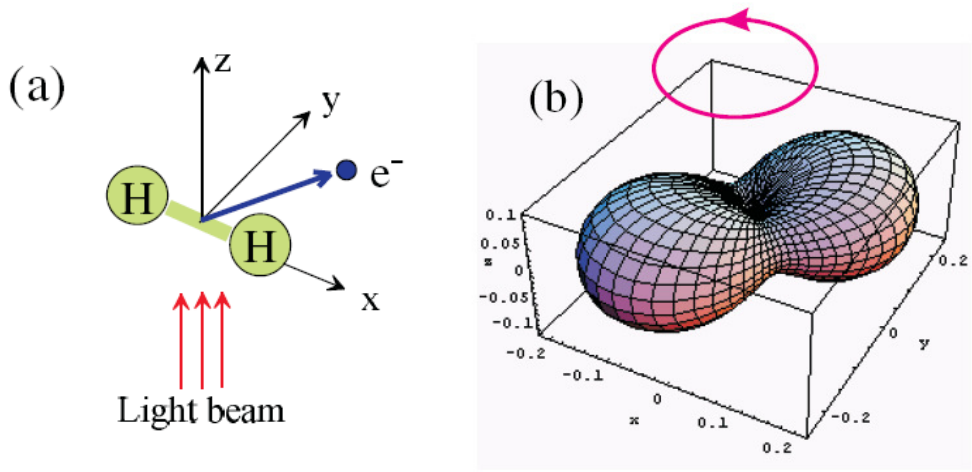

Figure 9.14: (Right panel) MFPAD for circularly polarization light at 20 eV, calculated in the RPA by S. Semenov and N. Cherepkov [57]. (Left panel) The geometry for which the three-dimensional angular distributions are shown. The molecular axis is fixed along the *x* axis of the photon frame; the direction of the light beam is along the *z* axis.

Following the same scheme as in the case of linearly polarized light, the fully differential cross section given by Eq. (9.26) can be studied for different orientations of the incoming light, θ_n:

$$\left.\frac{d\sigma_\alpha^{\mu_0=\pm1}(\omega)}{d\theta_e dW_{\upsilon_\alpha}}\right|_{\theta_n=0^\circ} = 2\pi\left[F_{00}^1(W_{\upsilon_\alpha},\theta_e)+F_{20}^1(W_{\upsilon_\alpha},\theta_e)\right], \tag{9.27}$$

$$\left.\frac{d\sigma_\alpha^{\mu_0=\pm1}(\omega)}{d\theta_e dW_{\upsilon_\alpha}}\right|_{\theta_n=54.7^\circ} = 2\pi F_{00}^1(W_{\upsilon_\alpha},\theta_e) \tag{9.28}$$

and

$$\left.\frac{d\sigma_\alpha^{\mu_0=\pm1}(\omega)}{d\theta_e dW_{\upsilon_\alpha}}\right|_{\theta_n=90^\circ} = 2\pi\left[F_{00}(W_{\upsilon_\alpha},\theta_e)-\frac{1}{2}F_{20}^1(W_{\upsilon_\alpha},\theta_e)\right]. \tag{9.29}$$

The result is presented in the right panel of Fig. (9.16). For the "magic angle" the result is equal to the one obtained making use of linearly polarized light (see Eq. (9.28)), and for 0 and 90 degrees, their behavior as a function of the electron polar angle is similar to the one obtained for linearly polarized light for a orientation of 90 and 0 degrees, respectively.

The cross section as a function of the electron azimuthal angle ϕ_e and the initial incoming orientation θ_n of the light can be obtained, integrating over the electron polar angle θ_e Eq. (4.43). In this case, the three-fold differential cross section takes the following form:

$$\begin{aligned}\frac{d\sigma_\alpha^{\mu_0=\pm1}(\omega)}{d\theta_n d\phi_e dW_{\upsilon_\alpha}} &= G_{00}^1(W_{\upsilon_\alpha})+G_{20}^1(W_{\upsilon_\alpha})P_2^0(\cos\theta_n)\pm G_{11}^1(W_{\upsilon_\alpha})P_1^1(\cos\theta_n)\sin(\phi_e)\\ &\quad +G_{21}^1(W_{\upsilon_\alpha})P_2^1(\cos\theta_n)\cos(\phi_e)+G_{22}^1(W_{\upsilon_\alpha})P_2^2(\cos\theta_n)\cos(2\phi_e).\end{aligned} \tag{9.30}$$

The left panel of Fig. (9.17) displays the contour plot of the two-fold differential cross section given by Eq. (9.30), for an electron energy of 1 eV. As can be seen, the two-fold differential cross

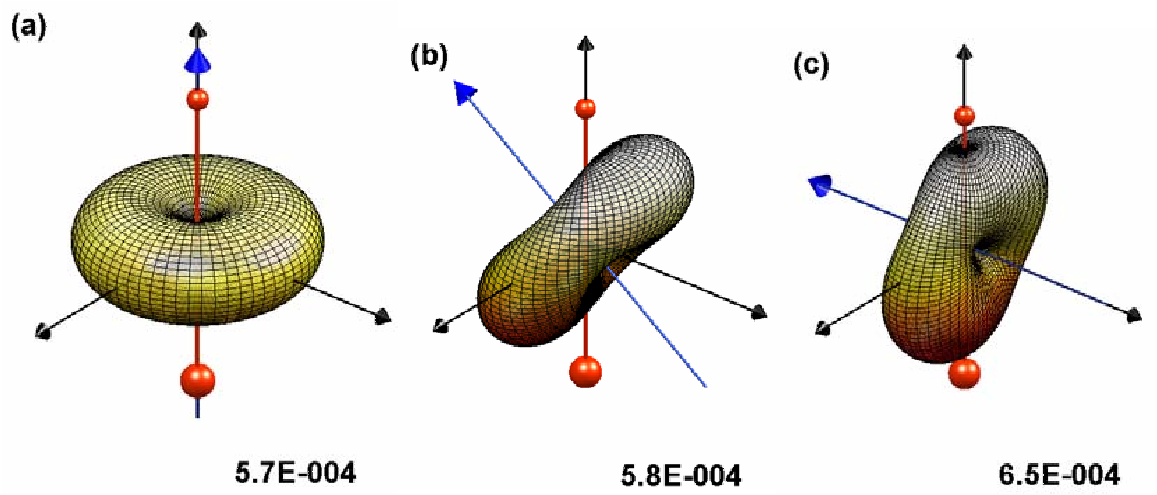

Figure 9.15: Same as Fig. (9.7) but using instead circularly polarized light ($\mu = +1$).

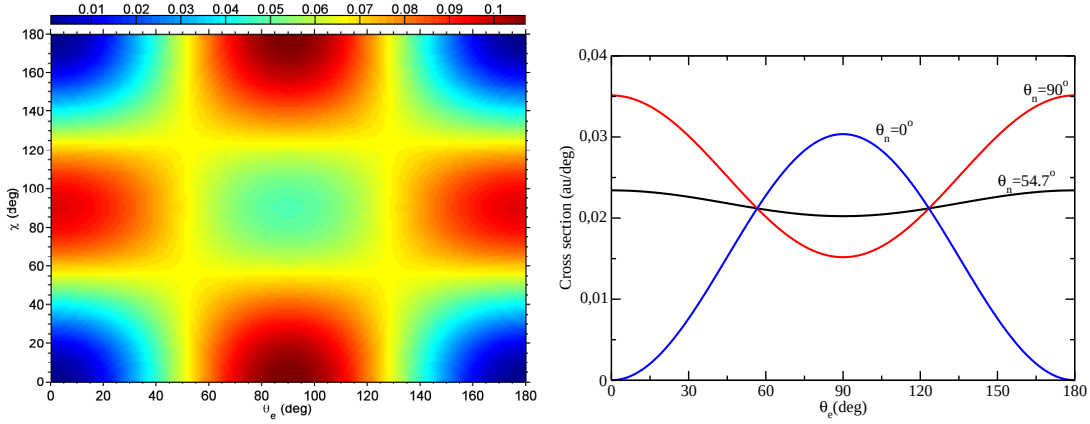

Figure 9.16: Same as Fig. (9.8) but using instead circularly polarized light ($\mu = +1$).

section presents an oscillatory behavior similar to the one obtained for linearly polarized light, but ϕ_e shifted 90 degrees. The G^1_{11} does not contribute, since it is an odd function with respect to $\pi/2$. The previous equation can be simplified by fixing the initial value of θ_n, obtaining the differential cross section as a function of the electron azimuthal angle ϕ_e:

$$\left.\frac{d\sigma_\alpha^{\mu_0=\pm1}(\omega)}{d\phi_e dW_{\upsilon_\alpha}}\right|_{\theta_n=0^\circ} = G^1_{00}(W_{\upsilon_\alpha}) + G^1_{20}(W_{\upsilon_\alpha}), \tag{9.31}$$

$$\left.\frac{d\sigma_\alpha^{\mu_0=\pm1}(\omega)}{d\phi_e dW_{\upsilon_\alpha}}\right|_{\theta_n=54.7^\circ} = G^1_{00}(W_{\upsilon_\alpha}) \mp \sqrt{\frac{2}{3}} \times G^1_{11}(W_{\upsilon_\alpha}) \sin(\phi_e) - \sqrt{2} \times G^1_{21}(W_{\upsilon_\alpha}) \cos(\phi_e) + 3 \times G^1_{22}(W_{\upsilon_\alpha}) \cos(2\phi_e) \tag{9.32}$$

and

$$\left.\frac{d\sigma_\alpha^{\mu_0=\pm1}(\omega)}{d\phi_e dW_{\upsilon_\alpha}}\right|_{\theta_n=90^\circ} = G^1_{00}(W_{\upsilon_\alpha}) - \frac{1}{2} \times G^1_{20}(W_{\upsilon_\alpha}) \mp G^1_{11}(W_{\upsilon_\alpha}) \sin(\phi_e) + 3 \times G^1_{22}(W_{\upsilon_\alpha}) \cos(2\phi_e). \tag{9.33}$$

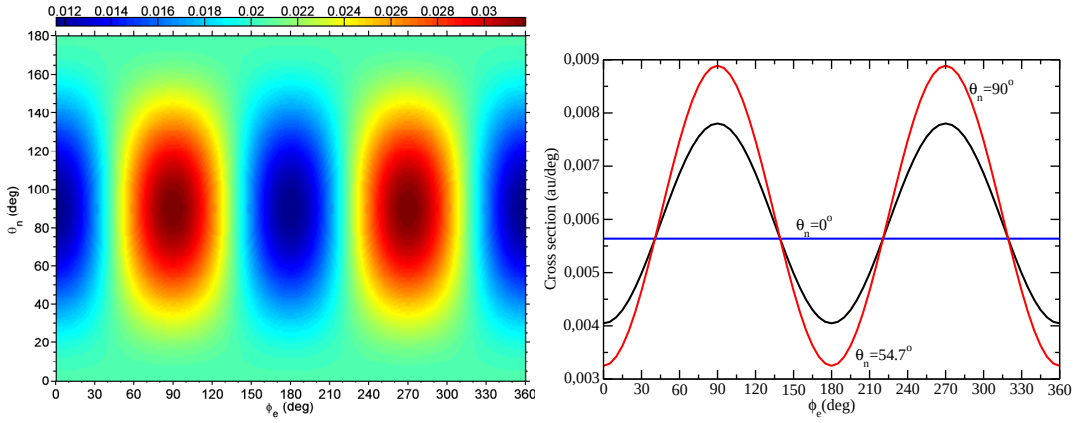

Figure 9.17: Same as Fig. (9.9) but using instead circularly polarized light ($\mu = +1$).

The right panel of Fig. (9.17) shows the differential cross section obtained making use of Eqs. (9.31), (9.32) and (9.33). In this case the results present the same oscillatory behavior as for the case of linearly polarized light, but with a global sign change, with implies a shift of $\pi/2$.

Finally, we complete this study performing an integration over the electron emission angles ϕ_e and θ_e in Eq. (4.43), obtaining the differential cross section as a function of the proton energy W_{υ_α} and the orientation of the incoming light, θ_n:

$$\frac{d\sigma_\alpha^{\mu_0=\pm1}(\omega)}{d\theta_n dW_{\upsilon_\alpha}} = 2\pi\left[G_{00}^1(W_{\upsilon_\alpha}) + G_{20}^1(W_{\upsilon_\alpha})P_2^0(\cos\theta_n)\right], \tag{9.34}$$

that has the same form as the expression for the proton angle distribution given by Eq. (4.68) of Chapter 4. Selecting the orientation of the incoming light, the previous equation gives:

$$\left.\frac{d\sigma_\alpha^{\mu_0=\pm1}(\omega)}{dW_{\upsilon_\alpha}}\right|_{\theta_n=0^\circ} = 2\pi\left[G_{00}^1(W_{\upsilon_\alpha}) + G_{20}^1(W_{\upsilon_\alpha})\right] = 2\pi\left[G_{00}^0(W_{\upsilon_\alpha}) - \frac{1}{2}G_{20}^0(W_{\upsilon_\alpha})\right], \tag{9.35}$$

$$\left.\frac{d\sigma_\alpha^{\mu_0=\pm1}(\omega)}{dW_{\upsilon_\alpha}}\right|_{\theta_n=54.7^\circ} = 2\pi G_{00}^1(W_{\upsilon_\alpha}) = 2\pi G_{00}^0(W_{\upsilon_\alpha}), \tag{9.36}$$

and

$$\begin{aligned}\left.\frac{d\sigma_\alpha^{\mu_0=\pm1}(\omega)}{dW_{\upsilon_\alpha}}\right|_{\theta_n=90^\circ} &= 2\pi\left[G_{00}^1(W_{\upsilon_\alpha}) - \frac{1}{2}\times G_{20}^1(W_{\upsilon_\alpha})\right] \\ &= 2\pi\left[G_{00}^0(W_{\upsilon_\alpha}) + \frac{1}{4}\times G_{20}^0(W_{\upsilon_\alpha})\right]\end{aligned} \tag{9.37}$$

Note that since the $G_{11}^1(W_{\upsilon_\alpha})$ does not contribute to the total cross section, there is no difference in the proton energy distribution between left and right handed polarized light. In previous equations we have written the relation of the total cross section for circularly polarized light as a function of the $G_{NL}^0(W_{\upsilon_\alpha})$ functions obtained making use of linearly polarized light. So, the total cross section for circularly polarized light for a parallel orientation (Eq. (9.35)) is equal to the result obtained by linearly polarized light for a perpendicular orientation of the polarization vector with respect to the molecular axis (see Eq. (9.21)), as it was established in Section 4.3.1 of Chapter 4. At $\theta_n = 54.7^\circ$, the magic angle, the total cross section is equal in both cases. For the perpendicular case,

Eq. (9.37), there is no simple relation with the results obtained for linearly polarized light, since for this specific orientation both symmetries, Σ_u^+ and Π_u, are accessible. As can be seen directly from the previous equations, the cross section for the initial orientation of the circularly polarized $\theta_n = 0^\circ$ takes smaller values than in the case where the polarization vector of linearly polarized light takes the same orientation. On the other hand, for $\theta_n = 90^\circ$ the cross section is greater than the case of linearly polarized light. The total cross section is presented in Fig. (9.18), both for H_2 and D_2.

To complete this section, we study a new physical process: the ***circular dichroism*** . The circular dichroism angular distribution (CDAD) is the difference between the photoionization cross sections for left ($\mu_0 = -1$) and right ($\mu_0 = +1$) circularly polarized light[4] [66, 67]:

$$\frac{d\sigma_\alpha^{\rm CDAD}(\omega, W_{\upsilon_\alpha})}{d\Omega_n d\Omega_e dW_{\upsilon_\alpha}} = \frac{d\sigma_\alpha^{\mu_0=1}(\omega, W_{\upsilon_\alpha})}{d\Omega_n d\Omega_e dW_{\upsilon_\alpha}} - \frac{d\sigma_\alpha^{\mu_0=-1}(\omega, W_{\upsilon_\alpha})}{d\Omega_n d\Omega_e dW_{\upsilon_\alpha}}. \tag{9.38}$$

This is known to be a very powerful probe of the molecular conformations, since in large molecules and especially in biomolecules, it mostly originates from the coupling between the various constituents and is therefore sensitive to their relative positions, and it is routinely use, in particular, to elucidate the secondary structure of proteins. For smaller systems, like diatomic molecules, investigation of circular dichroism at the level of photoemission in the molecular frame is a very sensitive probe of the photoionization dynamics of molecules. Circular dichroism in electron angular distribution (CDAD) in photoionization of gas phase molecules was first reported in rotationally resolved photoelectron angular distributions for molecules aligned by multiphoton absorption [68]. The CDAD observation for randomly oriented achiral molecules was further demonstrated by recording molecular frame photoelectron angular distributions, taking advantage of dissociative photoionization induced by X/VUV one-photon absorption of circularly polarized synchrotron radiation for inner shell [69, 70, 71] and outer shell [55, 56, 72] photoionization. They were motivated by the fact that the MFPADs obtained for photoionization induced by circularly or elliptically polarized light give the most complete access to the dipole matrix elements of the transition, their magnitudes and phase shifts [68, 71]. Quite recently D. Dowek *et al.* [73] have proposed some qualitative features of the CDAD observed in photoionization of small molecules were discussed, addressing in particular the possibility to disentangle the respective role of the spectroscopic properties of the initial and final bound states, and that of the photoelectron scattering dynamics. An exemplary system for which CDAD has been predicted is the emission of one photoelectron from an oriented diatomic molecule such as CO [66, 69, 74] (see also Fig. (1.4) of the Introduction). Its occurrence in photoionization of oriented achiral molecules is a consequence of the spatial non-coplanarity of three vectors: the light propagation vector of elliptically polarized light k, the photoelectron momentum k_e, and the molecular axis n, which creates a handedness for the system [67].

The CDAD defined above can be viewed in a simple physical picture as being proportional to the *sine* of the phase difference between the continuum photoelectron wave created by linearly polarized light parallel and perpendicular to the molecular axis (σ and π transitions) (see, e.g., [66, 69]). Taking into account the fully differential cross section given by Eq. (4.43), the CDAD can be written as:

$$\frac{d\sigma_\alpha^{\rm CDAD}(\omega, W_{\upsilon_\alpha})}{d\Omega_n d\Omega_e dW_{\upsilon_\alpha}} = F_{11}^1(W_{\upsilon_\alpha}, \theta_e) P_1^1(\cos\theta_n) \sin(\phi_e - \phi_n), \tag{9.39}$$

that takes a zero value for $\theta_n = \phi_e = 0, \pi$ and 2π (taking $\phi_n = 0$), and for the cases where $F_{11}^1(W_{\upsilon_\alpha}, \theta_e)$ cancels, and takes its maximum values for $\theta_n = \phi_e = \pi/2$. Fig. (9.19) displays the MFPAD of H_2 for an orientation of the incoming circularly polarized light $\theta_n = 90^\circ$, for a fixed electron energy

[4] In the case of unoriented chiral molecules is the result of the interference between electric-dipole and magnetic-dipole terms.

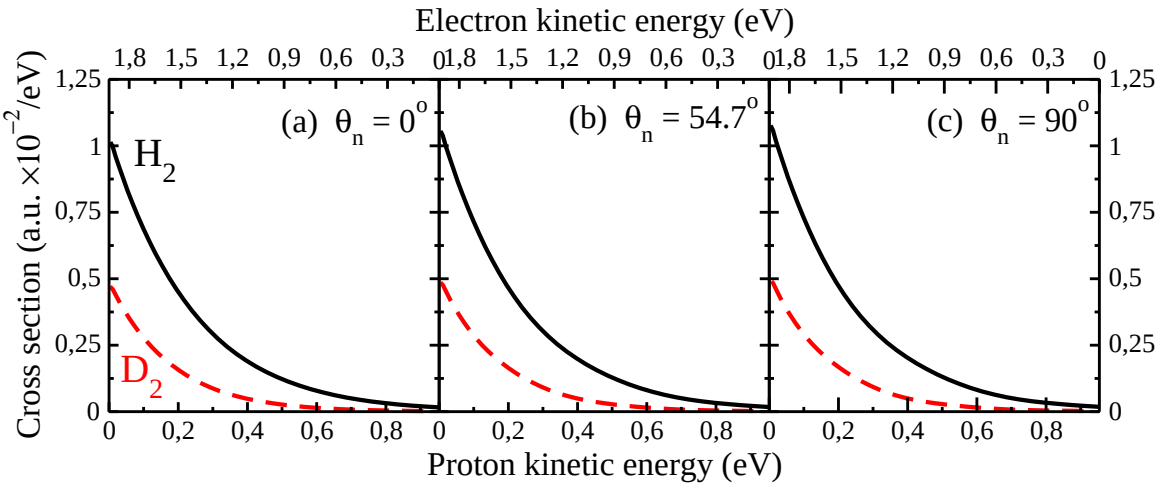

Figure 9.18: Same as Fig. (9.10) but using instead circularly polarized light ($\mu = +1$).

of 1 eV, making use of left- (panel a) and right-handed light (panel b). The different between both results is shown in panel c) of this figure, that follows Eq. (9.39).

The most favorable geometry for the observation of circular dichroism in the molecular frame is obtained for a molecule oriented perpendicular to the light propagation axis ($\theta_n = 90°$). The CDAD is then characterized by the left-right asymmetry of photoelectron emission which is maximum in the plane perpendicular to k ($\phi_e = 90°$ and $\phi_e = 270°$) as described by the $\sin(\theta_e)$ dependence in Eqs. 4.43 and 4.51. We can define the dimensionless CDAD parameter in two equivalent ways, and establish an expression in terms of the $F_{LN}(\theta_e)$ functions as follows [55]:

$$\begin{aligned} CDAD_{(\theta_n=\pi/2,\phi_e=\pi/2)} &= \frac{\sigma_{LHC}-\sigma_{RHC}}{\sigma_{LHC}+\sigma_{RHC}} = \\ &= \frac{2F^1_{11}(W_{\upsilon_\alpha},\theta_e)}{2F^1_{00}(W_{\upsilon_\alpha},\theta_e)-F^1_{20}(W_{\upsilon_\alpha},\theta_e)-6F^1_{22}(W_{\upsilon_\alpha},\theta_e)} \\ &= \frac{2F^1_{11}(W_{\upsilon_\alpha},\theta_e)}{2F^0_{00}(W_{\upsilon_\alpha},\theta_e)+(1/2)F^0_{20}(W_{\upsilon_\alpha},\theta_e)+3F^0_{22}(W_{\upsilon_\alpha},\theta_e)} \end{aligned} \tag{9.40}$$

where the propagation of the light is fixed perpendicular to the molecule axis ($\theta_n = \pi/2$) and the electron emission is observed in the half-plane perpendicular to the propagation axis ($\phi_e = \pi/2$). In the third line of the previous equation we have expressed the CDAD in term of the F^0_{LN} obtained by linearly polarized light.

Fig. (9.20) displays the CDAD parameter for H_2 and D_2 for a fixed electron energy of 1 eV. The maximum (minimum) of the CDAD parameter for H_2 and for D_2 takes place at 133.2 (47.1) with a value of ~ 0.1. At 0, 90 and 180 degrees there is no different of making use of left or right handed circularly polarized light, since the CDAD parameter takes a zero value.

9.2.3 Proton and electron beta parameters

To complete the study of the angular distribution of the particles coming from the photoionization process at the photon energy of 20 eV, we present the results obtained for the proton angular distribution and the electron angular distribution for randomly oriented molecules. As we have

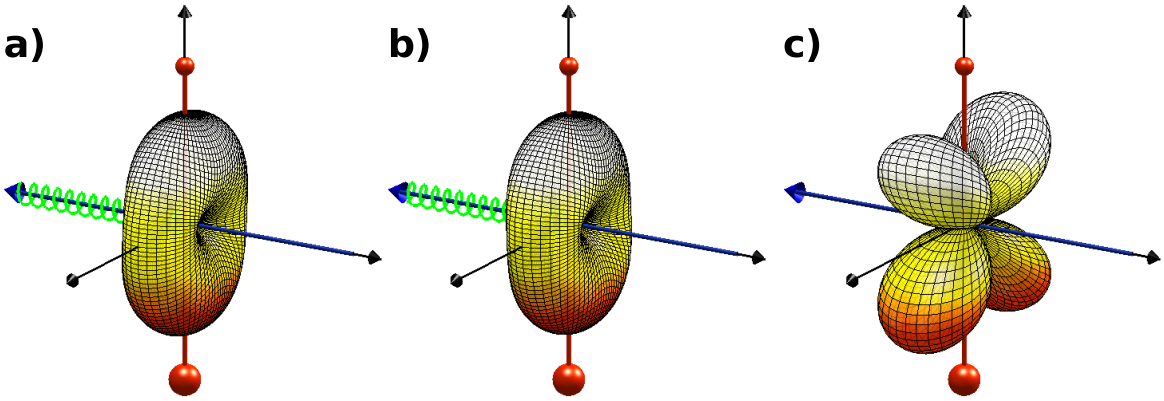

Figure 9.19: Circular dichroism in the MFPAD of H_2 for a fixed final electron energy of 1 eV, at $\hbar\omega$=20 eV. Panels a) and b) display the result obtained with right- ($\mu = +1$) and left-handed ($\mu = -1$) circularly polarized light, respectively; Panel c) displays the different between panels a) and b).

explained previously, the study of theses parameters gives less physical information that the case of fixed-in-space case, and nowadays can be consider as a complementary information. The β_e value includes information on the partial wave composition while the proton beta parameter β_M gives the relative weights of the Σ and Π transitions. The value of electron beta parameter, β_e, is expected to be 2 in the united He atom, and hence deviation from 2 are understood in terms of the molecular field felt by the photoelectron. The photoionization dynamics is completely described by the partial wave composition of the photoelectron, where molecular field effects may appear as population of $\ell > 1$ partial waves

In left panel of Fig. (9.21) we present the photoelectron beta parameter as a function of the electron kinetic energy both for H_2 and D_2, for linearly (upper panel) and circularly polarized light (lower panel). As we have explained in Chapter 4 there exists a simple relation between the electron beta parameter obtained with linearly and circularly polarized light, so the information contained in Fig. (9.21) can be considered redundant. Electrons with energies greater than ~ 2 eV are associated with the formation of bound vibrational states of $H_2^+(\upsilon)$ (non dissociative process). The value of the beta parameter is very close to 2 for the case of linearly polarized light, and to -1 for circularly polarized light, and in both cases the electron beta parameter monotonically decreases (increases) as a function of the electron energy. In this figure the blue lobes represent the electron angular distribution with respect to the polarization vector and the incident orientation for linearly and circularly polarized light, respectively, for $\beta_e \sim 2$ and ~ -1, respectively.

Although the number of experimental results devoted to the study of the β_e is quite large, we will compare only our theoretical results with the experimental results obtained in the last years, without describing the characteristics of the experiments. For example, making use of linearly polarized light, A. Lafosse *et al.* [47] obtained a value of $\beta_e \approx 1.7 \pm 0.1$ for a photon energy of 20.0 eV, while Hikosaka while Eland [51] found a value of $\beta_e \approx 1.83 \pm 0.05$ and Eland *et al.* [48] a value of $\beta_e \approx 1.95 \pm 0.1$ both for a photon energy of 21.2 eV. In order to compare with the previous experimental results, one have to consider the electron energy range over with the electron beta parameter is obtained, as we explained in Chapter 4 (see Eq. (4.70)). The H_2 integrated beta parameter for electrons coming from the dissociative process (electrons with energy less than ~ 2 eV) gives a value of 0.42, while the beta parameter coming from the non-dissociative process (i.e., producing bound vibrational states) gives a value of 1.93. The total beta parameter takes a value of 1.90, which agree with the previous experimental values. Similar results are obtained for the D_2.

The proton angular distribution for H_2 and D_2 molecules, explained previously in Section 4.4 of Chapter 4, is displayed in the right panel of Fig. (9.21) as a function of the proton kinetic energy.

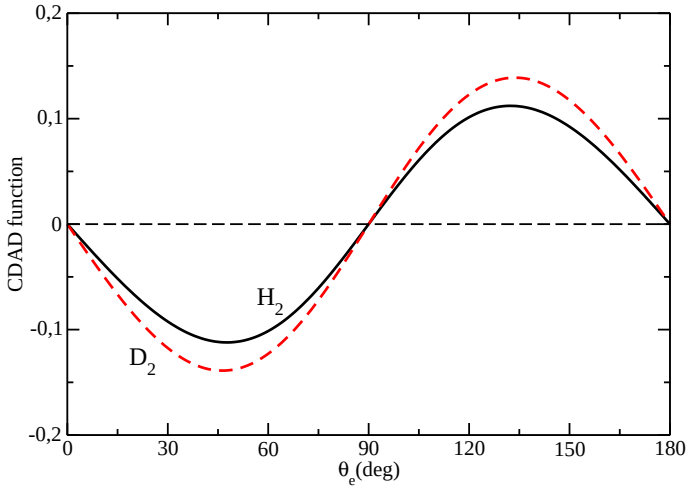

Figure 9.20: The CDAD function of H_2 (black full line) and D_2 (red dashed line) for a fixed final electron energy of 1 eV, at $\hbar\omega$=20 eV.

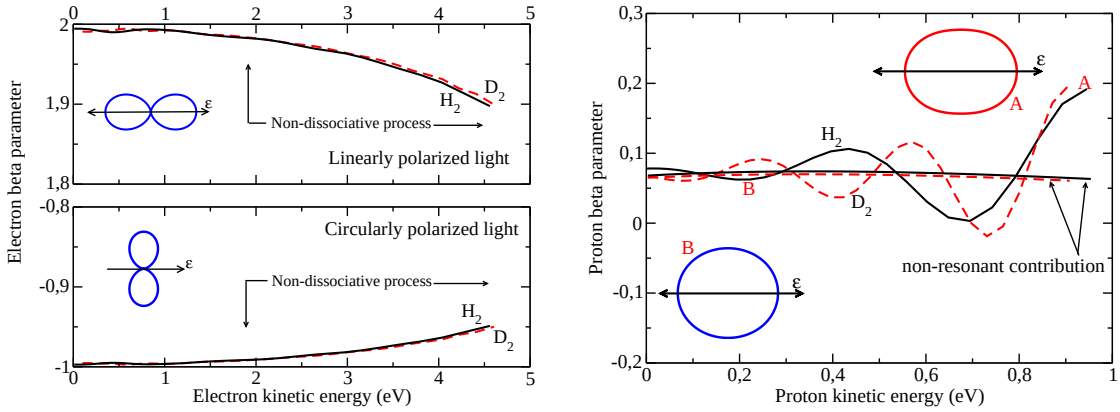

Figure 9.21: (Left panel) Photoelectron beta parameter as a function the electron energy, for linearly polarized light (upper panel) and circularly polarized light (lower panel). Vertical lines indicate the non-dissociative contribution. (Right panel) Proton beta parameter as a function of the proton energy. All results obtained at $\hbar\omega$=20 eV. Full black lines and dashed red lines results for H_2 and D_2, respectively.

Unlike to any previous results obtained in this Section, the proton beta parameter presents a strong dependence with the final proton energy, which is observed neither in the total cross section nor the electron beta parameter, both for H_2 and D_2 molecule. This oscillatory pattern is due to the contribution of the Q_1 $^1\Sigma_u^+$ doubly excited states, although they are not populated by a vertical transition (see Fig. (9.2)). In order to highlight the contribution of the doubly excited states, we have included the proton beta parameter excluding any contribution from these states (considering only the first term of Eq. (3.88)). The proton beta parameter takes values around ~ 0.1 , which implies that the contribution of the $^1\Sigma_u^+$ transition is slightly more relevant than the $^1\Pi_u$ one (see Eq. (4.67)). Although the oscillatory behavior possesses a very small amplitude, ~ 0.2, in comparison with the total scale, from -1 to 2, this result is quite surprising since the population and autoionization of the Q_1 doubly excited state takes part at an internuclear distance of ~ 2.6 a.u. (see Fig. (9.38)). The same oscillatory pattern is also observed for the D_2 molecule, although as the proton energy decreases both results oscillates out of phase, which is consequence of the different oscillatory frequency of the continuum vibrational states. In Fig. (9.21) we have also drawn the proton angular

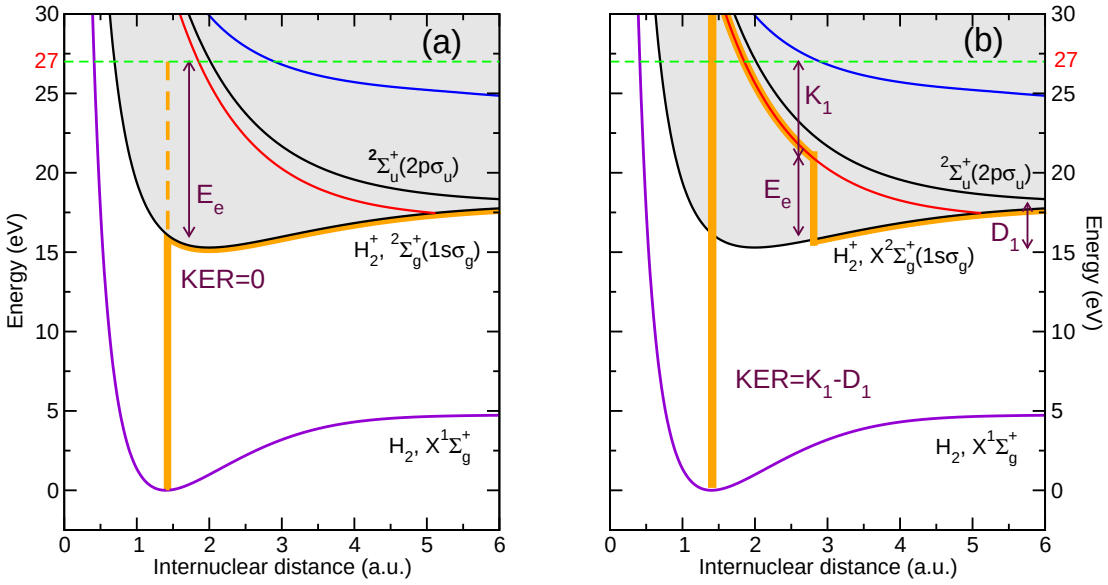

Figure 9.22: Semiclassical pathways for dissociative ionization by absorption of one 27 eV photon. (a) Direct ionization leading to $H_2^+(1s\sigma_g)$ (Eq. (9.41) in the text). (b) Resonant ionization through the lowest Q_1 doubly excited states leading to $H_2^+(1s\sigma_g)$ (Eq. (9.42) in the text).

distribution with respect to the polarization vector, for the values $\beta_M = 0.1$ and $\beta_M = 0.2$, i.e., for slow and fast protons, respectively.

The experimental results are scarcer than for the electron beta parameter. A. Lafosse *et al.* [47] obtained a value of $\beta_{H^+} \approx 0 \pm 0.1$ for a photon energy of 20.0 eV, while Hikosaka and Eland [51] found a value of $\beta_{H^+} \approx 0.2 \pm 0.05$ and Eland *et al.* [48] a value of $\beta_{H^+} \approx 0.14 \pm 0.1$ for a photon energy of 21.2 eV. The integrated proton beta parameter takes a value of 0.073 for H_2 and 0.068 for D_2, which agrees with the previous experimental results. Comparing the results obtained for the electron and proton beta parameters, it can be seen that electrons strongly prefer to be emitted along the electric vector, while H^+ emission is relative isotropic.

9.3 $\hbar\omega = 27$ eV the role of the Q_1 resonant states

In this section we will present the angular distribution of electrons and protons making use of a photon energy of 27 eV. Although at this photon energy there is no experimental results to compare with, to our concern, the results obtained at this photon energy will reveal the effects of the doubly excited states in the MFPAD in comparison with the results obtained in the previous section.

At this photon energy it is possible to populate the Q_1 doubly excited states, as it has been demonstrated in Chapter 7. In particular I. Sánchez *et al.* [3, 4] showed that this resonant states play a crucial role in the proton kinetic energy distribution, and the coupling between the resonant and non-resonant amplitudes was responsible for several peaks observed in several experimental works [27, 29, 30]. Although, the role of the Q_1 doubly excited states of symmetry $^1\Sigma_u^+$ is more important than the Q_1 $^1\Pi_u$ states due to their large autoionization widths, as we showed in Chapter 6, we could expect to observe the contribution of the later states to the MFPAD, since the partial wave decomposition of the process should be manifested through different structures in the MFPAD. So,

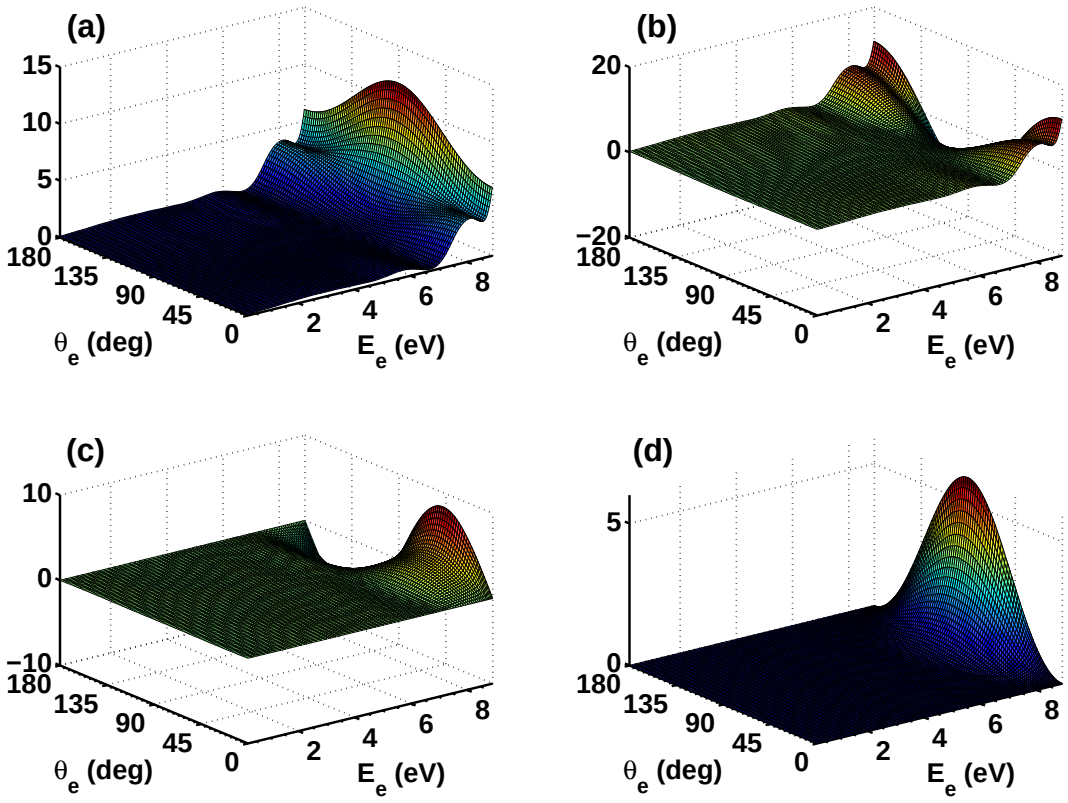

Figure 9.23: The $F^0_{LN}(\varepsilon_{1s\sigma_g},\theta_e)$ functions of H_2 as a function of the electron energy $\varepsilon_{1s\sigma_g}$ and the electron polar emission angle θ_e, at $\hbar\omega$=27 eV. (a) $F^0_{00}(\varepsilon_{1s\sigma_g},\theta_e)$; (b) $F^0_{20}(\varepsilon_{1s\sigma_g},\theta_e)$; (c) $F^0_{21}(\varepsilon_{1s\sigma_g},\theta_e)$; (d) $F^0_{22}(\varepsilon_{1s\sigma_g},\theta_e)$. (Atomic units multiplied by 10^3).

the ionization process can be schematically described as:

$$H_2(X^1\Sigma_g^+)+\hbar\omega \rightarrow H_2^+(1s\sigma_g)+e^- \rightarrow H^+ + H(1s)+e^- \quad (9.41)$$

$$\rightarrow H_2^{**}(Q_1\,{}^1\Sigma_u^+) \rightarrow H^+ + H(1s)+e^- \quad (9.42)$$

$$\rightarrow H_2^{**}(Q_1\,{}^1\Pi_u^+) \rightarrow H^+ + H(1s)+e^- \quad (9.43)$$

with the same partial wave expansion described in the previous section. These paths relative to the Eqs. (9.41) and (9.42) are shown in Fig. (9.22).

9.3.1 Linearly polarized light

Once again, we start with the study of the characteristics of the $F^0_{LN}(W_{\upsilon_\alpha},\theta_e)$, since they are the main blocks in order to understand the MFPADs. Fig. (9.23) displays the $F^0_{LN}(W_{\upsilon_\alpha},\theta_e)$ functions as a function of the ejected electron energy and the electron polar angle with respect to the molecular axis. Unlike the result obtained at 20 eV, presented in Fig. (9.3), these functions present a quite complex behavior, which mainly reflects the role of the $Q_1\,{}^1\Sigma_u^+$ doubly excited states. A magnification of the previous figure highlights the complicated patterns followed by these functions, as is displayed in Fig. (9.24).

The $F^0_{00}(W_{\upsilon_\alpha},\theta_e)$ function is described mainly by the $P_0(\cos\theta_e)$ and the $P_2(\cos\theta_e)$ Legendre polynomial, and in particular, the sign of the coefficient associated with this last polynomial changes

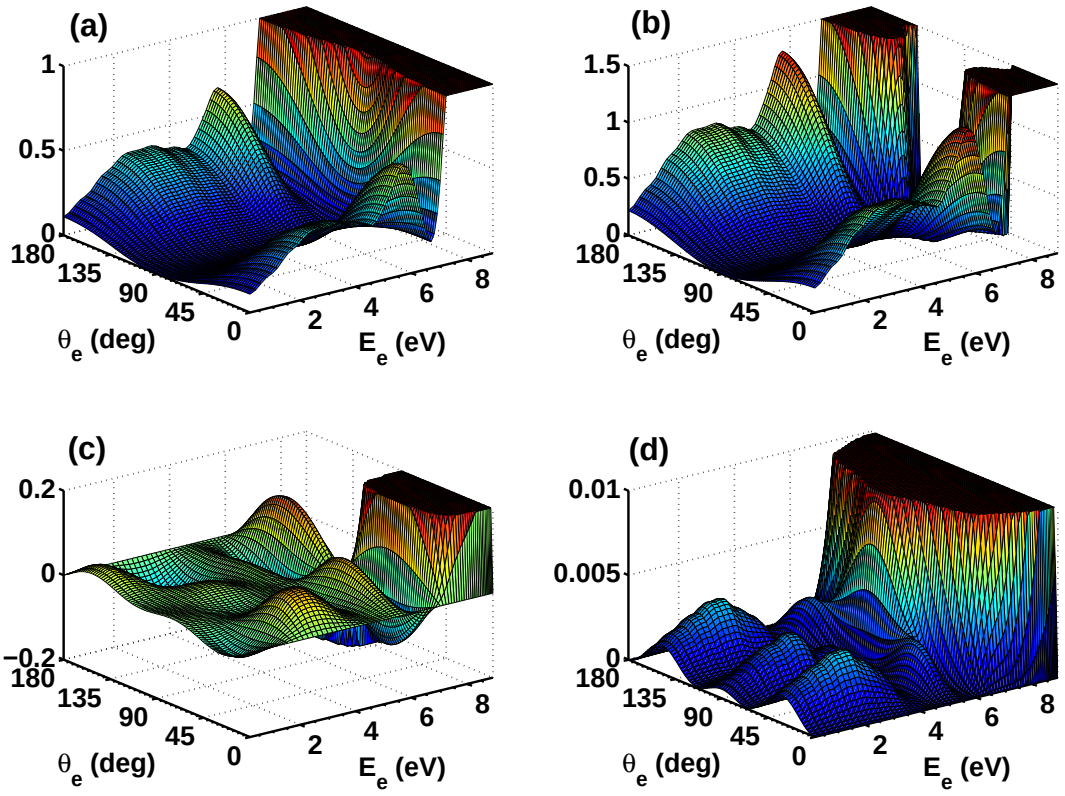

Figure 9.24: Magnification of the $F^0_{LN}(W_{\upsilon_\alpha}, \theta_e)$ functions presented in Fig. (9.23).

drastically for very high electron energies (slow protons), producing an enhancement at $\pi/2$. The $F^0_{20}(W_{\upsilon_\alpha}, \theta_e)$ function is described by the contributions of the same Legendre polynomial, but for high energetic electrons (slow protons), the contribution of the $P_2(\cos\theta_e)$ Legendre polynomial dominates the process with a positive coefficient. On the other hand, the $F^0_{21}(W_{\upsilon_\alpha}, \theta_e)$ function is described by the contribution of the $P_2(\cos\theta_e)$ Legendre polynomial, but the associated coefficient presents and oscillatory pattern for an electron energy less than ~ 6 eV. From ~ 6 to ~ 7 eV the contribution of the $P^1_4(\cos\theta_e)$ Legendre polynomial takes relevance since this function takes a maximum/minimum closer to $\pi/2$. At higher electron energies, the $P^1_4(\cos\theta_e)$ Legendre polynomial dominates again. The $F^0_{22}(W_{\upsilon_\alpha}, \theta_e)$ functions follows a completely different patterns since for an electron energy in the range [0, 4] eV, it is described by the $P^2_6(\cos\theta_e)$ Legendre polynomial. From 4 to 6 eV, the pattern is described by the contribution of the $P^2_4(\cos\theta_e)$ Legendre polynomial and for higher electron energies this is characterized by the contribution of the $P^2_2(\cos\theta_e)$ Legendre polynomial.

All the $F^0_{LN}(W_{\upsilon_\alpha}, \theta_e)$ functions shown in Fig. (9.24) present a common feature: a minimum at an electron energy ~ 6.6 eV (a proton energy ~ 1.1 eV). For an electron energy in the range 0.2 to 5.7 eV (a proton energy in the [1.6, 4.4] energy range), the contribution of the non-resonant process (direct ionization) is practically negligible, $F^0_{00}(W_{\upsilon_\alpha}, \theta_e)$ and $F^0_{20}(W_{\upsilon_\alpha}, \theta_e)$ increase their value at 0 and π degrees as the electron energy increase, and they always take a zero value at $\pi/2$. For electron energies ~ 6.6 eV (proton energies ~ 1.1 eV), the electron emission is drastically reduced at 0 and π. For an electron energy of 8.2 eV, the contribution of the non-resonant process is dominant, and the emission at $\pi/2$ is quite important. The role of the doubly excited state is much more important in

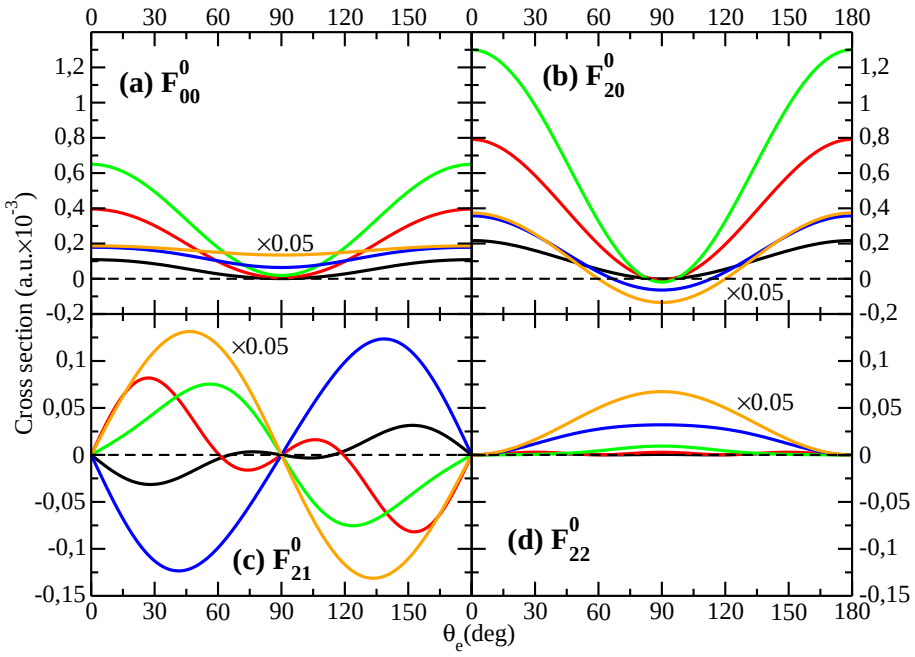

Figure 9.25: The $F^0_{LN}(\theta_e)$ functions of H_2 for different final electron energies, at $\hbar\omega$=27 eV. (a) $F^0_{00}(\theta_e)$ function. Black line electron energy of 0.2 eV; Red line energy of 2.8 eV; Green line energy of 5.7 eV; Blue line energy of 6.6 eV; Orange line energy of 8.2 eV; (b) $F^0_{20}(\theta_e)$; (c) $F^0_{21}(\theta_e)$; (d) $F^0_{22}(\theta_e)$.

$F^0_{21}(W_{\upsilon_\alpha},\theta_e)$, where the form and sign of this function changes drastically with the electron energy. Therefore, one should expect to find a strong dependence with the electron/proton energy in the MFPADs. In Fig. (9.25) we present the $F^0_{LN}(W_{\upsilon_\alpha},\theta_e)$ functions for H_2 for five different electron energies.

Fig. (9.26) displays the evolution of the MFPAD of the H_2 molecule as a function of the final electron energy, for the orientations of the polarization vector $\theta_n = 0°$, $\theta_n = 54.7°$ and $\theta_n = 90°$, panels (a), (b) and (c), respectively. For $\theta_n = 0°$ where the role of the $Q_1\,{}^1\Sigma^+_u$ doubly excited states is clearly manifested in the total cross section (see lower panel of Fig. (9.26)), the MFPAD presents a simple pattern independent of the final electron energy, resembling the same pattern obtained previously for a photon energy of 20 eV (see Fig. (9.6)), i.e., the electrons are ejected following the polarization vector independently of the electron/proton energy. The same results are obtained for the D_2, as can be seen in panel (a) of Fig. (9.27). On the other hand, for a perpendicular orientation of the polarization vector, $\theta_n = 90°$, the angular distribution presents a strong dependence with the electron energy, that is a clearly manifestation of the $Q_1\,{}^1\Pi_u$ doubly excited state. So, although the contribution of this excited state has minimum relevance in the proton kinetic distribution (see right panel of Fig. (9.30)), they are clearly manifested in the MFPAD (although the absolute value is quite small in comparison with the results obtained for the parallel orientation). For a very low electron energy, ~ 0.2 eV (proton energy ~ 4.4 eV), the MFPAD is characterized by the $P^1_2(\cos\theta_e)$ function presented in Eq. (4.44), which reflects the importance of the $f\pi_u$ partial wave. As the electron energy increases ~ 2.8 eV (proton energy ~ 3.0 eV), the contribution of the $p\pi_u$ increases, as the $F^0_{00}(W_{\upsilon_\alpha},\theta_e)$ function increases its value. In the [3.9, 4.9] eV electron energy range ([2.0, 2.5] eV proton energy range), the $p\pi_u$ and $f\pi_u$ partial waves have the same contribution producing a strong interference that is clearly displayed in the MFPAD. At higher electron energy (lower proton energy), the electron distribution is completely characterized by the $p\pi_u$ contribution, and the ejected electron follows the direction of the polarization vector.

For $\theta_n = 54.7°$, the MFPAD also follows complicated patterns as a function of the electron

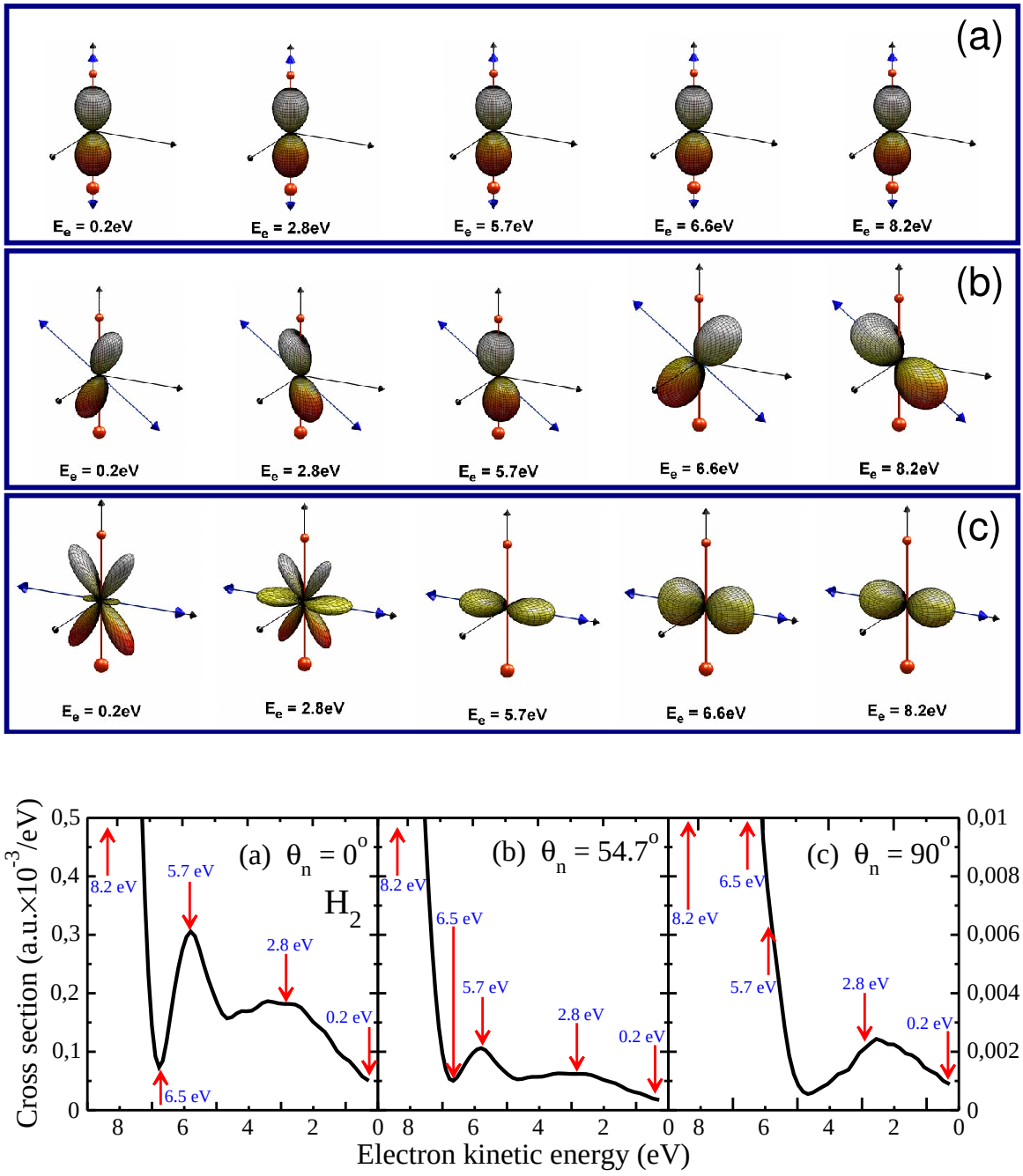

Figure 9.26: Evolution of the MFPAD of H_2 for linearly polarized light as a function of the electron energy, for different initial orientations of the polarization vector, at $\hbar\omega$=27 eV. (a) $\theta_n = 0°$; (b) $\theta_n = 54.7°$; (c) $\theta_n = 90°$. All the MFPADs are normalized to the unit. Lower panels, total cross section as a function of the electron energy for the previous orientations of the polarization vector. The arrows indicate the electron energies at which the MFPADs are obtained.

energy. For electron energies smaller than 7 eV (proton energies greater than 1 eV), the electron is mainly ejected along the molecular axis, and not along the direction of the polarization vector, as happened for a photon energy of 20 eV (see Fig. (9.6)). This is consequence of the low contribution of the $^1\Pi_u$ symmetry, so the ionization process is mainly characterized by the $^1\Sigma_u^+$ transition, that implies that the electron is emitted along the molecular axis. At an electron energy of ~ 6.6 eV the situation changes drastically, the electron is ejected perpendicular to the polarization vector, since the contribution of the Q_1 $^1\Sigma_u^+$ doubly excited state produces a minimum allowing the interference with the contribution of the Π_u symmetry. At this electron energy the MFPAD is characterized mainly by the $F_{21}^0(W_{\upsilon_\alpha}, \theta_e)$ function, which takes its maximum and minimum values at 45° and 135°, respectively (see Fig. (9.25)). For this electron energy, I. Sánchez *et al.* [3, 4] showed that the proton KDE presents a minimum due to the interference between the resonant and non-resonant amplitudes (see also Fig. (9.23)). So this interference pattern is directly reflected in the MFPAD. As the electron energy increases the non-resonant process dominates the process and the usual behavior is restored, i.e., the electron is ejected following the polarization vector.

So, for a parallel orientation the MFPAD follows the expected behavior, i.e., that followed at a photon energy of 20 eV, in spite of the fact doubly excited states play a crucial role in the dissociative photoionization process. On the other hand, for a perpendicular orientation, the electron distributions present a strong dependence with the electron energy, reflecting a strong mixture of the $f\pi_u$ and $p\pi_u$ partial waves, whose origin is the autoionization of the $^1\Pi_u$ double excited state. The obtained distribution reflects the importance of the contribution of the different partial waves, although the intensity of the MFPAD is much smaller. At $\theta_n = 54.7°$, the pattern for each electron energy can be explained as a combination of the results obtained for $\theta_n = 0°$ and $\theta_n = 90°$. Therefore, the electron angular distribution is a clear manifestation of interference effects, i.e., it shows the contribution of the different partial waves that take part in the process and their relative weights. So, although for a parallel orientation the process cannot be described without the inclusion of the Q_1 $^1\Sigma_u^+$ resonant states, its role in the process is not directly reflected in the MFPAD since the interference between different partial waves is negligible. On the other hand, for any other orientation we observe different patters reflecting any change in the contribution of different partial waves. Therefore, the study of the MFPAD gives the possibility of studying effects that can be hardly observable in the proton KED.

The results obtained for the D_2 (Fig. (9.27)) are quite similar to the H_2 case, except at the minimum (electron energy of ~ 8 eV, proton energy of ~ 0.5 eV) present in the proton KED (see Fig. (9.27)), where the electron is ejected perpendicular to the molecular axis for $\theta_n = 54.7°$, instead of being ejected perpendicular to the polarization vector as for H_2. This is consequence of the fact that, at this electron/proton energy, the Σ_u transition takes a smaller value than for the H_2 molecule, so the MFPAD is completely described by the perpendicular transition.

Fig. (9.28) displays the MFPAD of the H_2 molecule integrated over the whole electron/proton energy range for linearly polarized light (panels (a), (b) and (c)). The electron angular distributions shown in this figure resemble the patterns previously obtained for a photon energy of 20 eV (see Fig. (9.7)), which means that any contribution coming from the doubly excited states disappears when the MFPAD is obtained integrating the whole electron/proton energy range. I. Sánchez and *et al.* [5] showed that is not possible to observe any contribution from any resonant state in the total photoionization cross section (contribution of the dissociative and non-dissociative processes), since the nuclear motion of the molecule erases any contribution to the ionization process. In this case we are only considering the dissociative photoionization process in the study of the MFPAD, so the explanation why there is no trace of the resonant states in the integrated (in the final electron energy) MFPAD is different: In this case the non-resonant contribution dominates the process at low(high) electron(proton) energies, so the resonant effect are masked by the direct ionization process.

To conclude this section, we present in Fig. (9.30) the total cross section as a function of the final

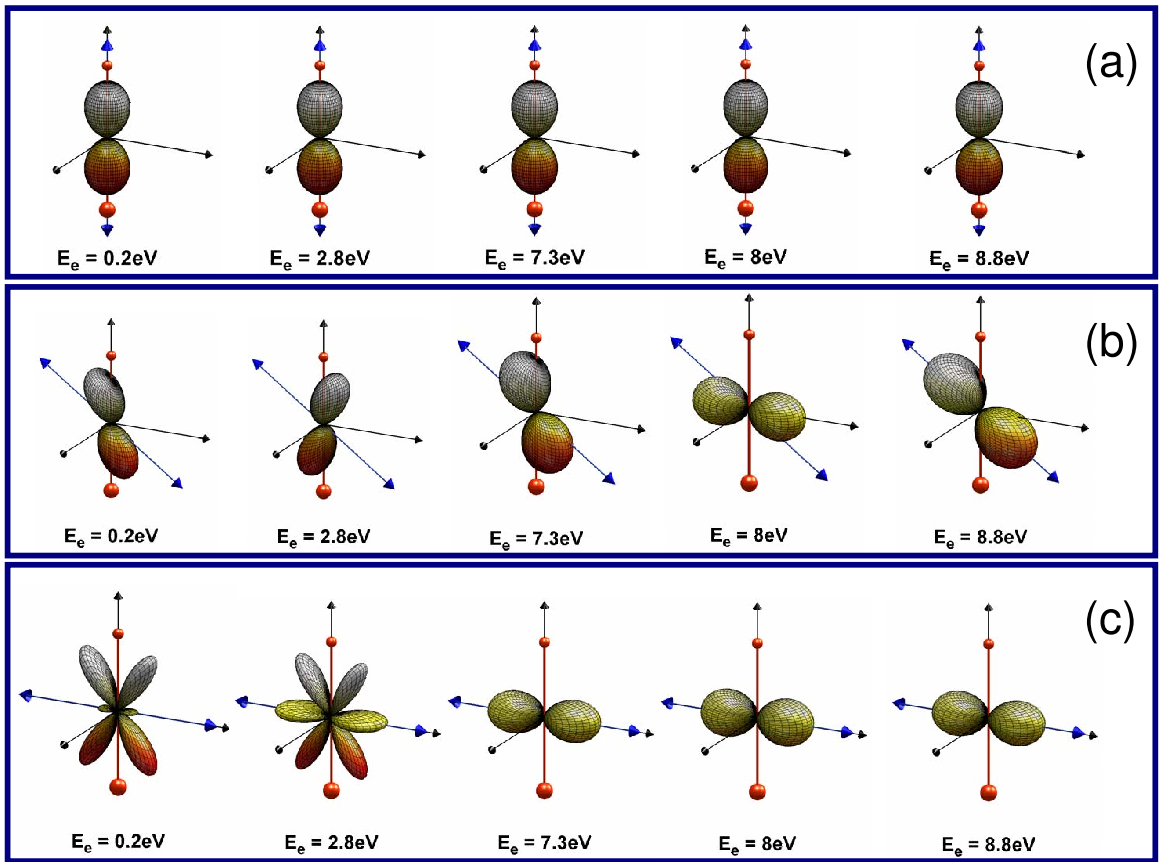

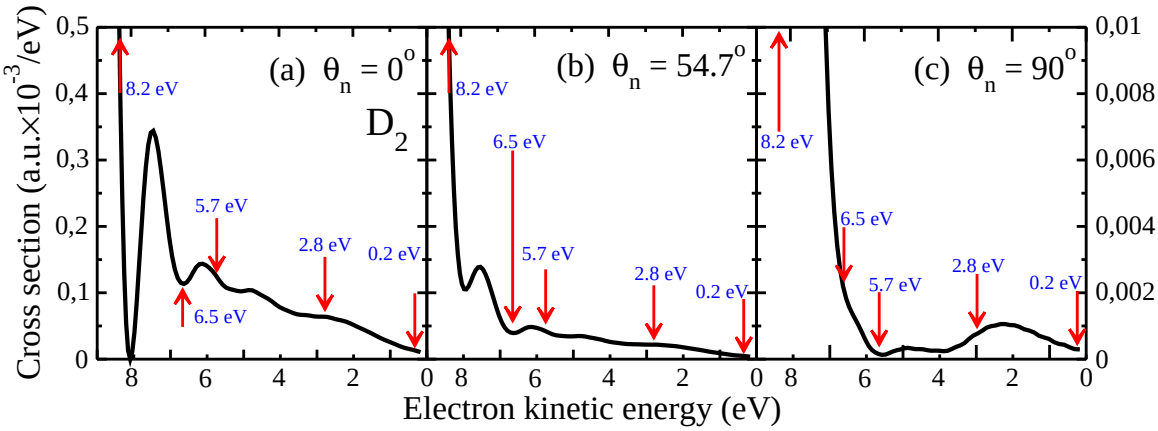

Figure 9.27: Same as in Fig. (9.26) but for the D_2.

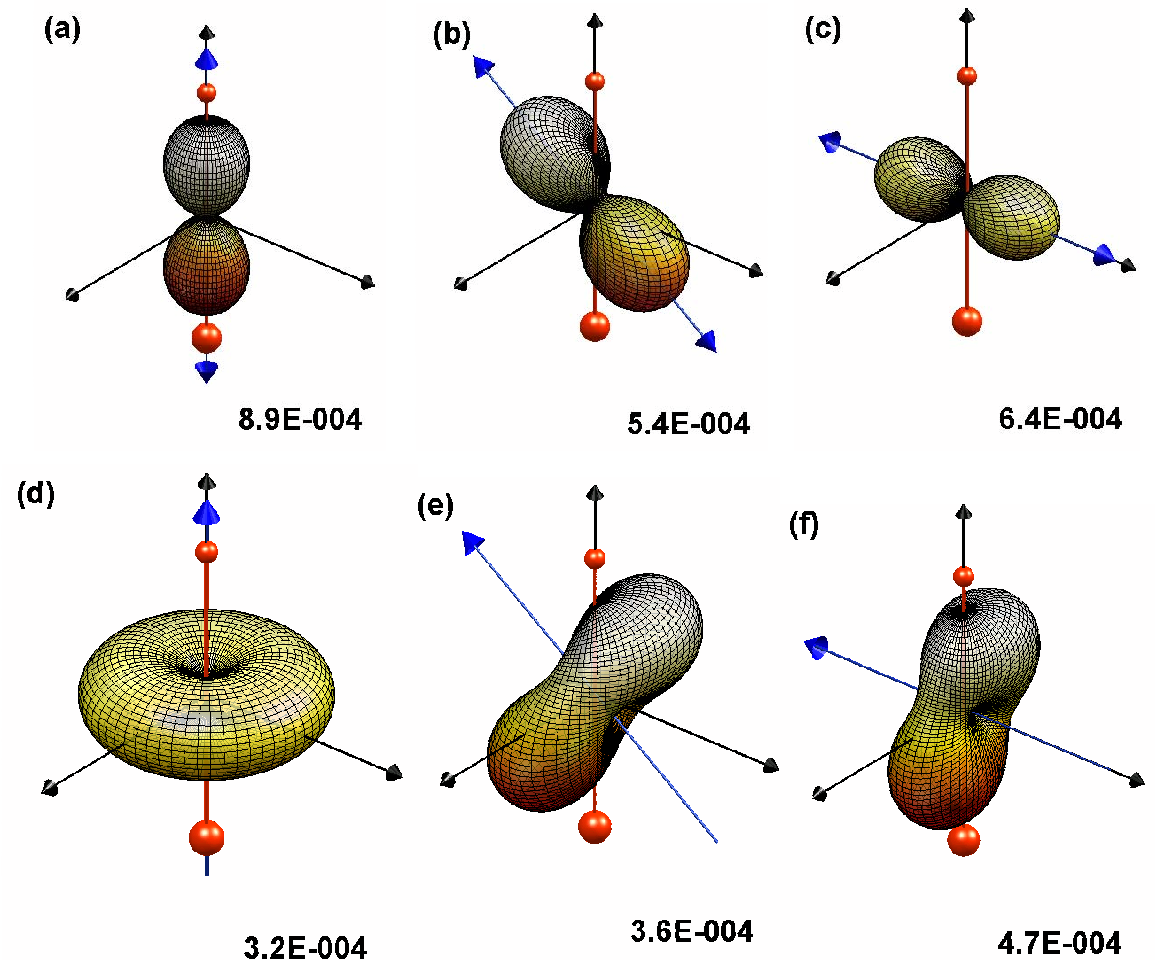

Figure 9.28: MFPAD of H_2 integrated over the whole final proton energy range, for three different orientations of the linearly (circularly) polarized light, at $\hbar\omega$=27 eV. (a, d) $\theta_n = 0°$; (b, e) $\theta_n = 54.7°$; (c, f) $\theta_n = 90°$; (a, b, c) linearly polarized light; (d, e, f) circularly polarized light. The indicated values give the maximum of each MFPAD in atomic units.

proton energy, for three different orientation of the polarization vector, making use of Eqs. (9.19), (9.20) and (9.21), for H_2 and D_2 molecules. The behavior as a function of the initial orientations is quite important, since resonant states play a important role at this photon energy, in contrary to the process at 20 eV (see Fig. (9.30)). For $\theta_n = 0°$ and $\theta_n = 90°$ we reproduce the previous results obtained by I. Sánchez *et al.* [3, 4], with reflects the fact that the $Q_1\,^1\Pi_u$ resonant states have a minor role in the photoionization process in comparison with the $Q_1\,^1\Sigma_u^+$ ones. For the D_2 molecule, the different structures are shifted 1 eV toward higher proton energy (see [4] for more details).

9.3.2 Circularly polarized light

In this section we present the MFPADs obtained with circularly polarized light. As we have pointed out before, it is only necessary to study the behavior of the $F_{11}^1(W_{\upsilon_\alpha}, \theta_e)$ function in order to obtain all the necessary physical information to understand the ionization process. Left panel of Fig. (9.31) shows the $F_{11}^1(W_{\upsilon_\alpha}, \theta_e)$ function as a function of the ejected electron energy and the electron polar angle angle with respect to the molecular axis, and as in the case of linearly polarized light, the

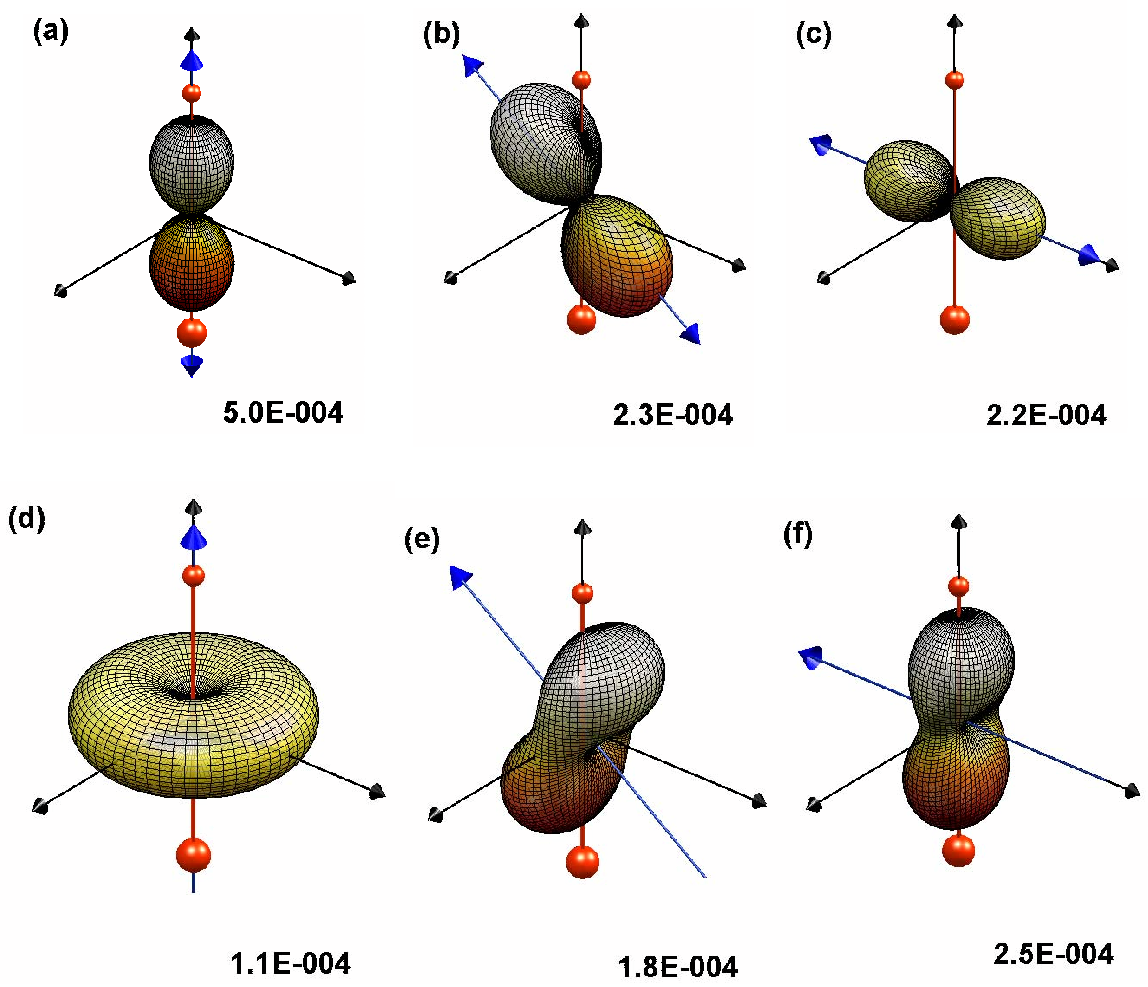

Figure 9.29: Same as Fig. (9.28) for D_2.

dependence with the electron energy presents a quite complicated pattern. In the right panel of Fig. (9.31) we present a magnification of the figure presented in the left panel in order to highlight the dependence with the electron energy. For an electron energy smaller than 6 eV, this function is mainly described by the contribution of the $P_2^1(\cos\theta_e)$ Legendre polynomial, where the associated coefficient presents an oscillatory behavior with the electron energy. For electron energies in the range from 6 to ~ 7 eV the $P_4^1(\cos\theta_e)$ Legendre polynomial dominates, and for higher energies again the $P_2^1(\cos\theta_e)$ recover its importance.

In Fig. (9.32) we present the $F_{11}^1(\theta_e)$ function for H_2 as a function of the electron polar angle θ_e, for the same selected electron energies as in the lower panel of Fig. (9.26). For these electron energies, $F_{11}^1(\theta_e)$ follows a pattern similar to that of the $F_{21}^1(W_{\upsilon_\alpha},\theta_e)$ functions, (see Fig. (9.25) making use of the relation $F_{21}^1 = -0.5 \times F_{21}^0$), except for the electron energy equal to 6.6 eV. As we did in the previous section (Fig. (9.26)), we can study the dependence of the MFPAD with the electron energy in order to study the role of the doubly excited states. Fig. (9.33) shows the evolution of the MFPAD for H_2 as a function of the final electron energy for the three orientations, $\theta_n = 0°$, $\theta_n = 54.7°$ and $\theta_n = 90°$, of the incidence direction of the light. At $\theta_n = 0°$ we obtained similar patterns as the ones obtained previously for linearly polarized light at $\theta_n = 90°$, but rotating these MFPADs around the z axis. So the contribution of the different partial waves are clearly observed in the obtained MFPADs. For $\theta_n = 54.7°$ the results are clearly characterized by the contribution of the

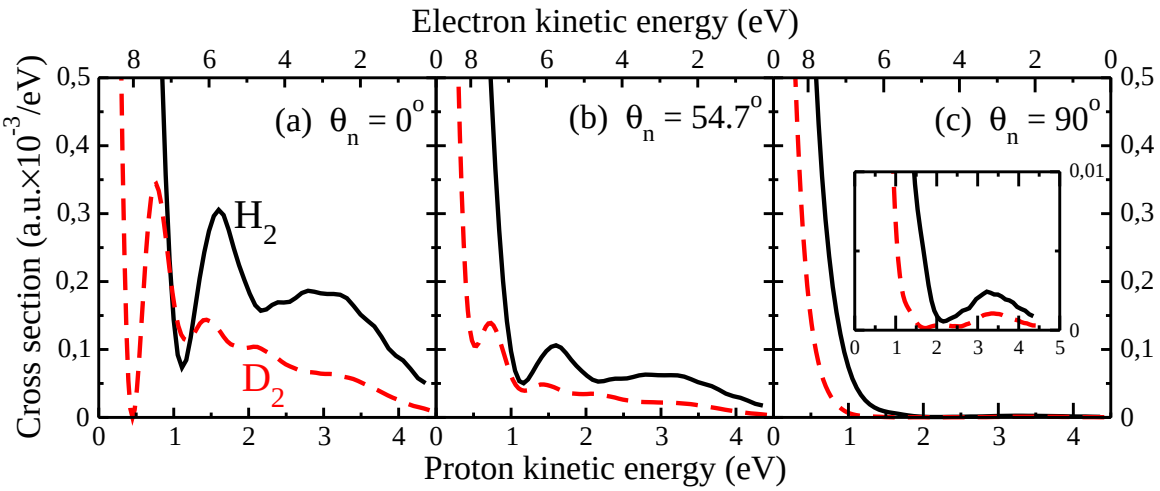

Figure 9.30: Total cross section for H_2 (black line) and D_2 (red dashed line) using linearly polarized light as a function of the proton/electron energy, for three different orientation of the polarization vector, at $\hbar\omega$=27 eV: (a) $\theta_n = 0°$; (b) $\theta_n = 54.7°$; (c) $\theta_n = 90°$.

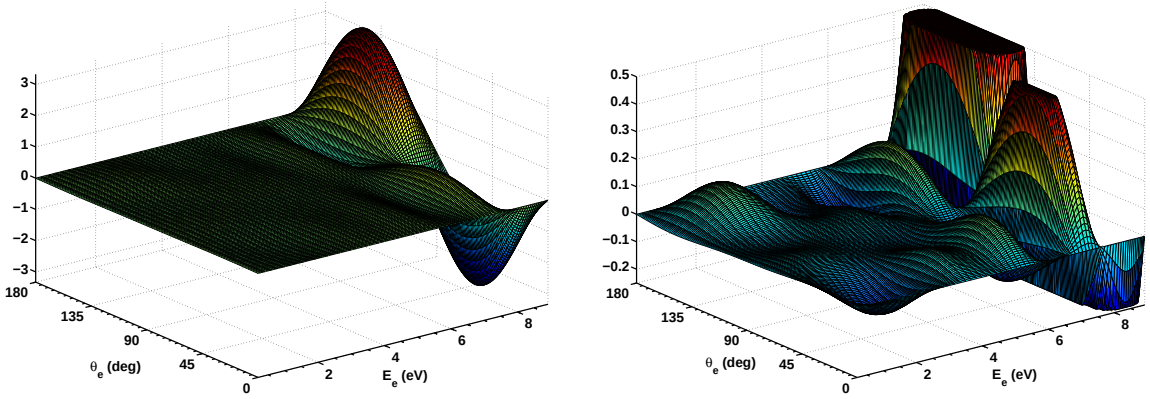

Figure 9.31: The $F^1_{11}(W_{\upsilon_\alpha}, \theta_e)$ function of H_2 as a function of the electron energy and the electron emission angle (left panel), and a magnification of this figure (right panel), at $\hbar\omega$=27 eV. (Atomic units multiplied by 10^3).

$^1\Sigma_u$ symmetry, since the electron are emitted along the molecular axis. For the perpendicular case, where the Q_1 $^1\Sigma^+_u$ doubly excited states can be populated, the MFPAD does not present any variance with the electron/proton final energy, and only close to the maximum value of the electron energy range, there exist a slight variation, that corresponds to the region where the non-resonant process dominates the ionization process. Once again, for an electron/proton energy close to ~ 6.6 (~ 1.1 eV), where the resonant an non-resonant amplitudes interfere, the MFPAD presents a variation for all the selected incident angles of the polarization vector, effect that is more evidence at $\theta_n = 54.7°$. For the D_2 (Fig. (9.34)), this interference effect is much clearly reflected in the MFPADs than in the case of linearly polarized light (see Fig. (9.27)). In this case the electron is ejected out of the plane defined by the direction of the light and the molecular axis, i.e., the plane *xz* plane (see Fig. (4.2)), which implies the dominance of the $F^1_{11}(W_{\upsilon_\alpha}, \theta_e)$ function, since at this electron energy the MFPAD displays a $\sin(\phi_e)$ azimuthal dependence (see Eq. (4.43) and in particular Eqs. (9.22), (9.23) and (9.24)). Since at this electron energy the contribution of the $^1\Sigma_u$ transition matrix gets a zero value, the MFPAD is dominated by the $^1\Pi_u$ symmetry.

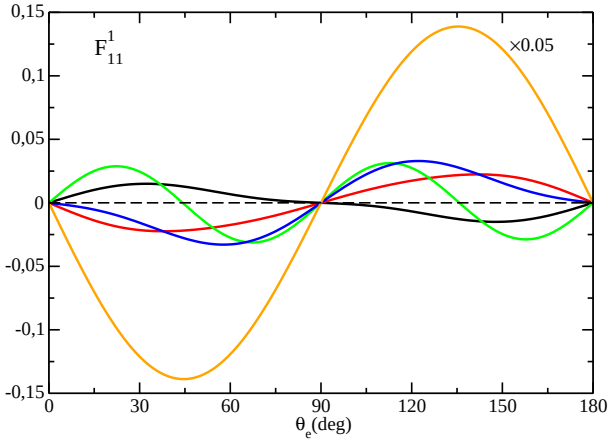

Figure 9.32: The $F^1_{11}(\theta_e)$ function of H_2 for several final electron energies, at $\hbar\omega$=27 eV. Black line electron energy of 0.2 eV; Red line energy of 2.8 eV; Green line energy of 5.7 eV; Blue line energy of 6.6 eV; Orange line energy of 8.2 eV. (Atomic units multiplied by 10^3).

We can study the integrated MFPAD over the whole electron/proton energy range, in order to check if the contribution of the doubly excited states can be observed. The results are displayed in panels (d), (e) and (f) of Figs. (9.28) and (9.29) for H_2 and D_2, respectively. The results associated to the H_2 are similar to the ones obtained for a photon energy of 20 eV, but, on the other hand, the results obtained for the D_2 molecules at the magic angle and at 90 degrees present a slightly tendency to increase the electron emission perpendicular to plane formed by the molecular axis and the direction of the incoming light, since for D_2 the contribution of the $F^1_{11}(W_{\upsilon_\alpha}, \theta_e)$ function is greater than in the H_2 case. So in the case of the D_2 molecules the effects of the resonant states are present even when the MFPAD is obtained integrating over the whole electron/pronto energy range.

In Fig. (9.35) we present the total cross section as a function of the proton (electron) energy, for the three indicated direction of the light (see Eqs. (9.35), (9.36) and (9.37)). At $\theta_n = 90^\circ$ the role of the $Q_1\,{}^1\Sigma_u^+$ doubly excited states is clearly visible, although the value of the cross section is smaller than in the case of linearly polarized light at $\theta_n = 0^\circ$. As the θ_n decreases, the contribution of these resonant states decreases, and since the doubly excited states with ${}^1\Pi_u$ symmetry do not contribute, at $\theta_n = 0^\circ$ the total cross section presents the typical exponential decrease dictated by the overlap of the initial vibrational state with the continuum vibrational states, i.e., a Frank-Condon profile, in the presented scale.

To complete this section let's see what is the effect of the doubly excited states in the study of the circular dichroism, as we did for a photon energy of 20 eV. As we have seen, the MFPAD presents a strong dependence with the electron/proton final energy for several orientation of the polarization vector, therefore one should expect the same dependence in the CDAD parameter. Fig. (9.36) shows the obtained CDAD parameter for the H_2 molecule for several final electron energies. For small electron energies, the CDAD parameter takes the opposite sign in comparison with the other results obtained at higher electron energies, which is consequence of the sign of the F^1_{11} function as a function of the electron energy (see Fig. (9.31). The maximum (minimum) in the CDAD evolves as a function of the electron energy, being close to $\pi/2$ for small electron energies, and as the electron energy increases it approaches to $\pi/4$. For the electron energy close to ~ 6.6 eV, the CDAD takes its maximum value, close to 0.7, since in this case the F^1_{00}, F^1_{20} and F^1_{22} functions take their minimum values (see Eq. (9.40)). Right panel of Fig. (9.36) displays the CDAD parameters for the D_2 molecule for several electron energies. The results are quite different from the results obtained for the H_2, being bigger than for the H_2 molecule. For a small electron energy (panel (a)

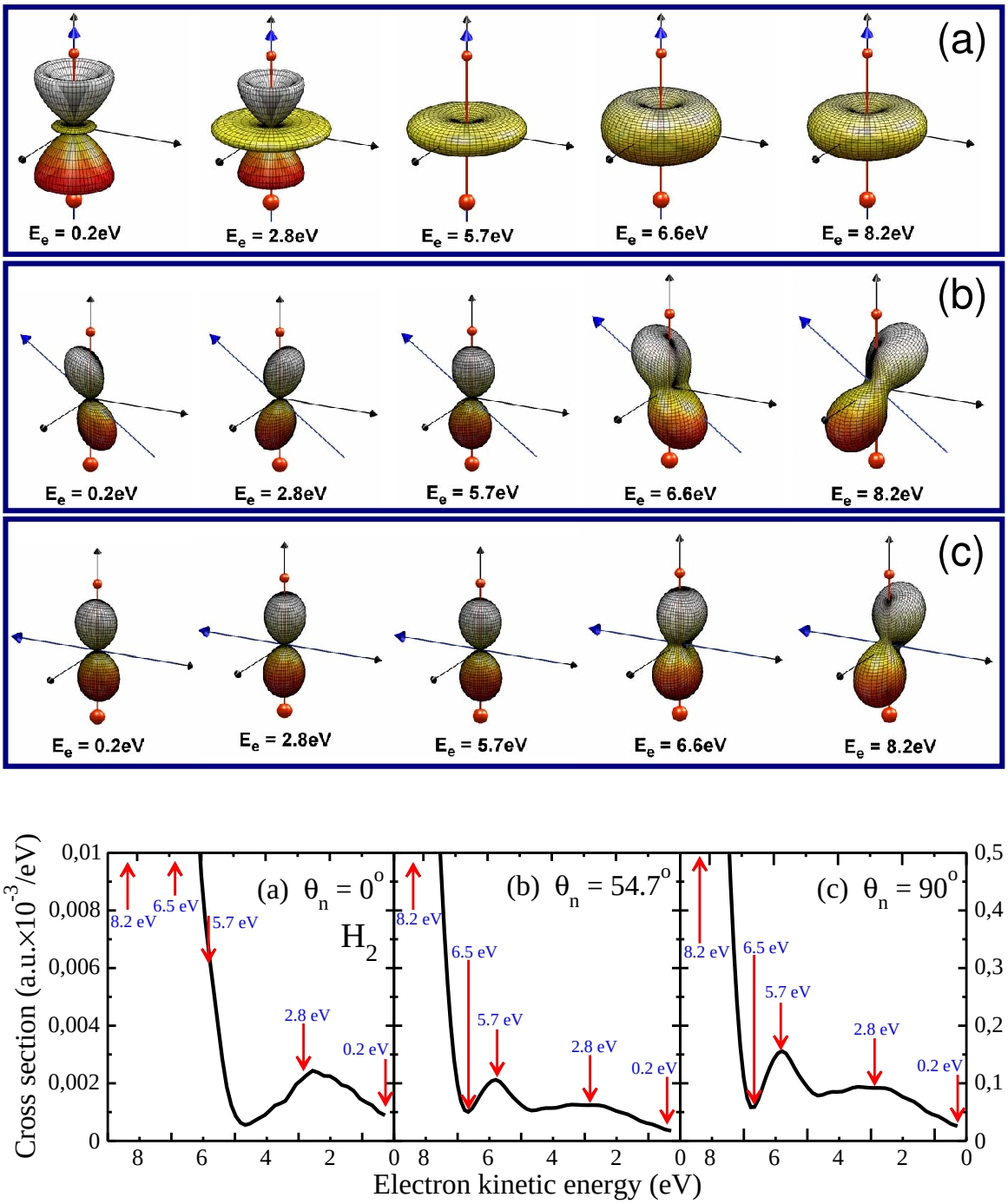

Figure 9.33: Same as Fig. (9.26) but using instead circularly polarized light ($\mu = +1$).

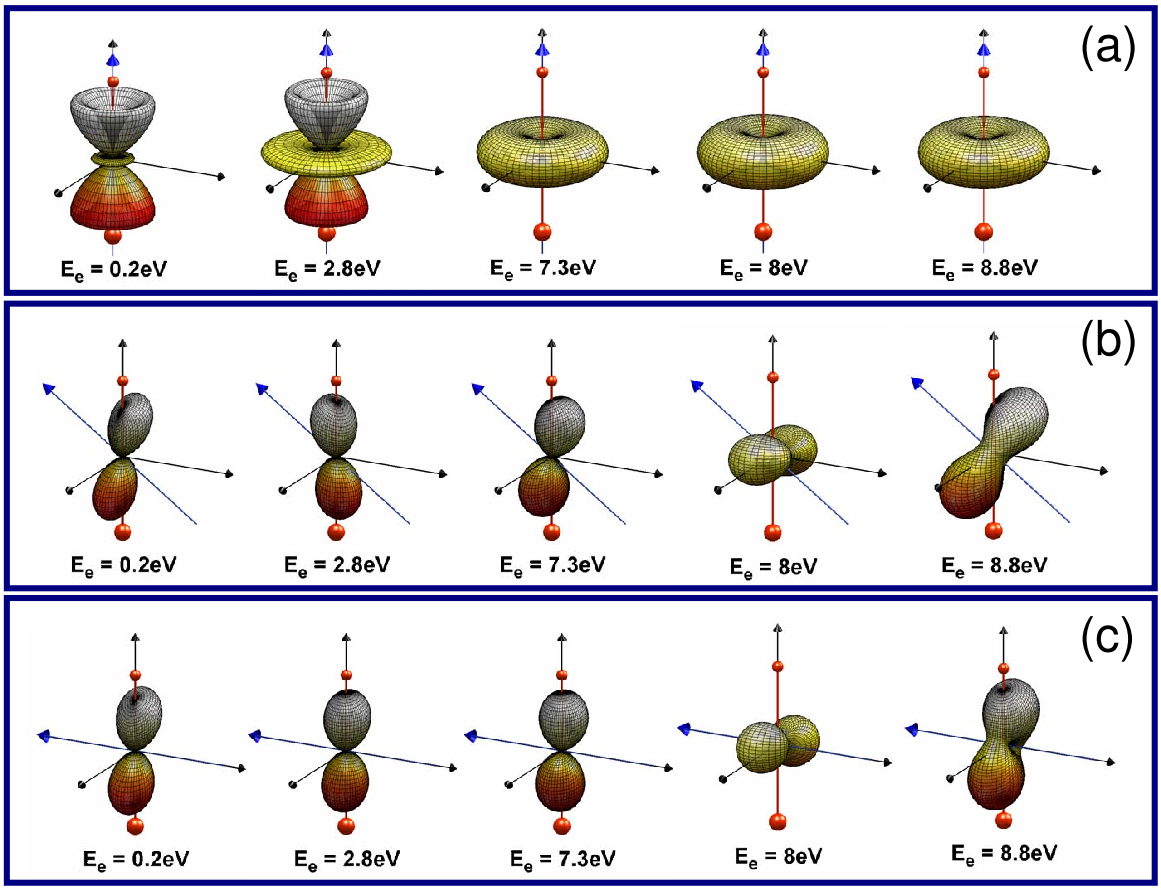

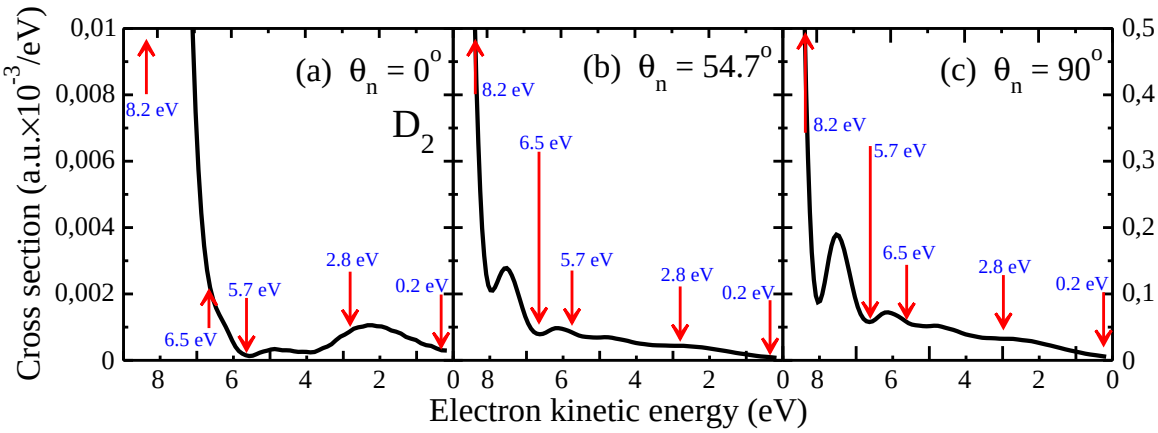

Figure 9.34: Same as Fig. (9.33) but for D_2.

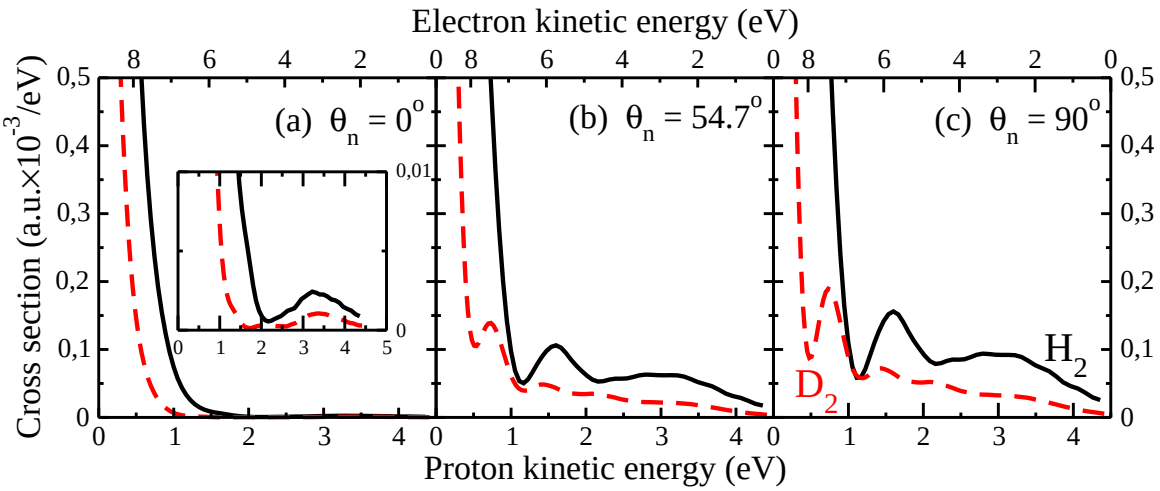

Figure 9.35: Same as in Fig. (9.30) but using instead circularly polarized light ($\mu = +1$).

of Fig. (9.36)), the CDAD presents two maxima (minima): one close to $\pi/4$ ($3\pi/4$), as in the case of a photon energy of 20 eV, and the other close to $\pi/2$. For the electron energy of 8.0 eV (panel (e) of Fig. (9.36)) where the interference effect produces the minimum in the total cross section, not only the CDAD parameter takes its maximum(minimum) value (~ 1) but this maximum(minimum) takes place closer to $0°(180°)$, in contrast with the other results.

9.3.3 Proton and electron beta parameters

The contribution of the doubly excited states also should be reflected in the proton and electron beta parameters. But as we will show, their effects are mainly manifested when these beta parameters are resolved in the final proton and electron energy, respectively. Let's start this section studying the electron angular distribution for randomly oriented molecules, i.e., the electron beta parameter. Left panel of Fig. (9.37) shows the photoelectron beta parameter as a function of the electron kinetic energy for H_2 and D_2 making use of linearly polarized light. The value of the beta parameter always takes positive values, and it is richly structured as a function of the electron energy, due to the contribution of the doubly excited states. Inside this figure we have drawn the electron angular distribution with respect to the polarization vector for the selected electron energies. For an electron energy of 6.6 eV, (see Figs. (9.30) and (9.35)) there is a dip in the electron beta parameter for both H_2 and D_2, whose origin has been previously explained. The only experimental result for the electron beta parameter at this photon energy was reported by Hikosaka and Eland [51], finding a value of $\beta_e \approx 1.7 \pm 0.05$ for a photon energy of 26.9 eV. The integrated beta parameter for H_2 (D_2) for electrons coming from the dissociative process gives a value of 0.23 (0.16), while the beta parameter summed over the electron energy coming from the non-dissociative process (i.e., producing bound vibrational states of the $H_2^+(\upsilon)$ ion) gives a value of 1.90 (1.90). The total beta parameter, which is the contribution of the dissociative and non-dissociative process gives a value of 1.85 (1.88), which is very close to the experimental result of Hikosaka and Eland [51]. The total electron beta parameter takes a value close to the one obtained for a photon energy of 20 eV, since the contribution of the resonant states are diluted in the electron beta parameter when the nuclear motion is included (note that the non-dissociative process is also considered). This fact agrees with the explanation given by I. Sánchez *et al.* [3, 4] in the study of the total cross section.

Right panel of Fig. (9.37) displays the proton beta parameter as a function of the proton kinetic energy for H_2 and D_2 molecules. The dependence of the proton beta parameter with the proton

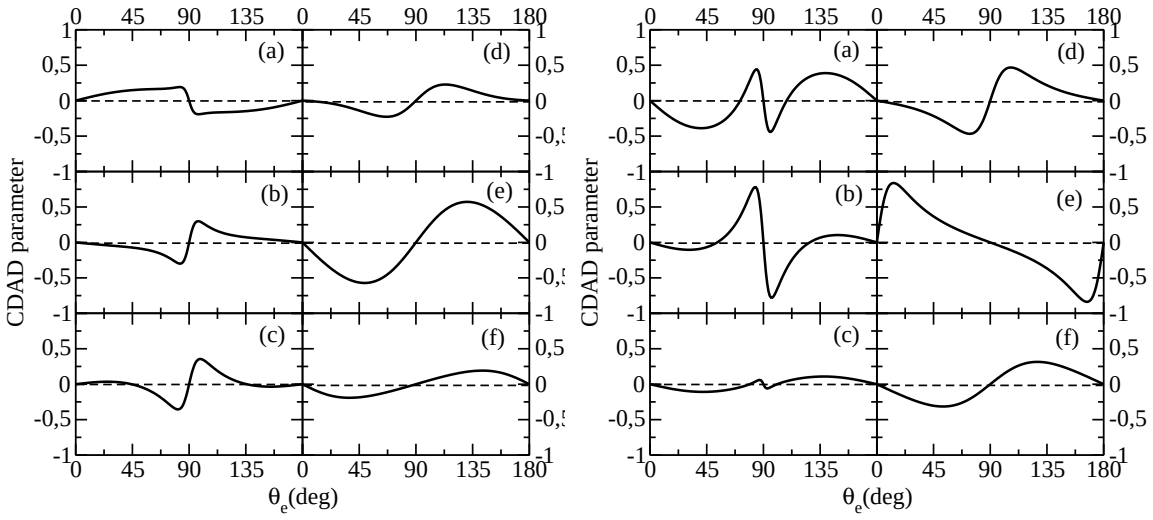

Figure 9.36: The CDAD function of H_2 (left figure) and D_2 (right figure) for several final electron energies, at $\hbar\omega$=27 eV. H_2: (a) Electron energy of 0.2 eV; (b) 2.8 eV; (c) 5.7 eV; (d) 6.6 eV; (e) 8.2 eV; (f) 8.8 eV. D_2: (a) 0.2 eV ; (b) 2.8 eV; (c) 4.8 eV; (d) 7.3 eV; (e) 8.0 eV; (f) 8.8 eV.

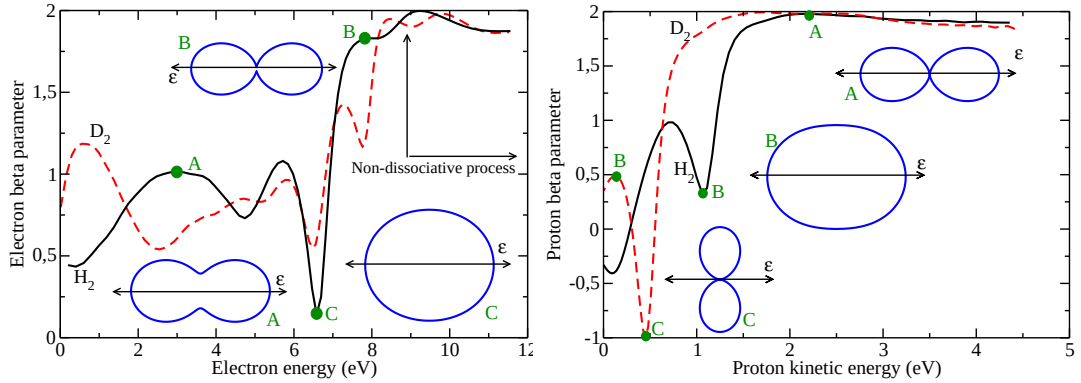

Figure 9.37: (Left panel) Photoelectron beta parameter as a function of the electron energy, for H_2 (black line) and D_2 (red dashed line) for linearly polarized light, at $\hbar\omega$=27 eV. Vertical lines indicate the non-dissociative contribution. (Right panel) Proton beta parameter as a function of the proton energy.

energy is quite small for proton energies greater than 2 eV for both molecules, which takes a value close to 2. Therefore, in this proton energy range, the $^1\Pi_u$ transition can be considered negligible (see Eq. (4.67)). At smaller proton energies the interference between the resonant and non-resonant process (see also Fig. (9.35)), produce a minimum at 2 and 1 eV for H_2 and D_2, respectively. At this electron energy the transition is changed from a pure $^1\Sigma_g^+ \rightarrow {}^1\Sigma_u^+$ transition to a mixture of the $^1\Sigma_g^+ \rightarrow {}^1\Sigma_u^+$ and the $^1\Sigma_g^+ \rightarrow {}^1\Pi_u$ transitions for H_2, and to a pure $^1\Sigma_g^+ \rightarrow {}^1\Pi_u$ transition for the case of D_2, since $\beta_{D^+} \approx -1$. Hikosaka and Eland [51] obtained a value of $\beta_{H^+} \approx 0.16 \pm 0.09$ for the H_2 molecule. The integrated proton beta parameter takes a value of 0.26 for the H_2 and 0.63 for the D_2. In this case, its value is greater than the results obtained at 20 eV (0.073 for the H_2 and 0.068 for the D_2), so the contribution of the doubly excited states are present although the proton beta parameter is integrated over the whole proton energy range. Fig. (9.37) also shows the proton angular distribution with respect to the vector polarization for several proton energies. Note that, at variance with the results at 20 eV, sometimes the protons do not follow the polarization direction (see the results defined by the label *C* in Fig. (9.37)).

9.4 $\hbar\omega = 33$ eV: Breaking symmetry through the Q_2 resonant states

In the previous two sections, the angular distribution of the particles coming from the photoionization process was obtained for the photon energies 20 eV and 27 eV, where only the first ionization threshold was involved, the $X^2\Sigma_g^+$ state of the H_2^+ (see Figs. (9.2) and (9.22)). As we studied in Chapter 7, as the photon energy increases, more doubly excited states can be populated and additional ionization paths can be followed by the residual ion. In this section we will study the MFPAD at a photon energy of 33 eV, where the population of the Q_1 doubly excited states is still possible and the Q_2 doubly excited states are now accessible. Dissociative photoionization can occurs through the first and second ionization thresholds:

$$\begin{aligned} H_2(X^1\Sigma_g^+) + \hbar\omega &\rightarrow H_2^+(1s\sigma_g) + e^- \rightarrow H^+ + H(1s) + e^- && (9.44)\\ &\rightarrow H_2(Q_1) \rightarrow H^+ + H(1s) + e^-, && (9.45) \end{aligned}$$

and

$$\begin{aligned} H_2(X^1\Sigma_g^+) + \hbar\omega &\rightarrow H_2^+(2p\sigma_u) + e^- \rightarrow H^+ + H(1s) + e^- && (9.46)\\ &\rightarrow H_2(Q_2) \rightarrow H^+ + H(1s) + e^- && (9.47)\\ &\rightarrow H_2(Q_2) \rightarrow H^+ + H(n=2) + e^-. && (9.48) \end{aligned}$$

The final wave function is expressed in a partial wave expansion that includes the values $p\sigma_u$, $f\sigma_u$, $h\sigma_u$ and $j\sigma_u$ (ℓ=1, 3, 5 and 7) for the $^1\Sigma_u^+$ transition and $p\pi_u$, $f\pi_u$, $h\pi_u$ and $j\pi_u$ (ℓ=1, 3, 5 and 7) for the $^1\Pi_u$ transition for the reactions given by Eq. (9.44)-(9.45), and $s\sigma_g$, $d\sigma_g$, $f\sigma_g$ and $h\sigma_g$ (ℓ=0, 2, 4 and 6) for the $^1\Sigma_u^+$ transition and $d\pi_g$, $f\pi_u$, $h\pi_u$ and $j\pi_u$ (ℓ=2, 4, 6 and 8) for the $^1\Pi_u$ transition, for the reactions given by Eq. (9.46)-(9.48).

Fig. (9.38) shows the energy diagram for the H_2 and H_2^+ molecules, that schematically represents the possible ionization paths described by the reactions given by Eq. (9.44)-(9.48). The energy difference between the lowest g and u states in H_2^+, $^2\Sigma_g^+(1s\sigma_g)$ and $^2\Sigma_u^+(2p\sigma_u)$ respectively, is about 17eV in the Franck Condon region of H_2. Thus if H_2 is directly ionized in a vertical transition by a photon of energy $\hbar\omega$, the photoelectron will have an energy of about $E_e = \hbar\omega - 16$ eV when the remaining H_2^+ is left in the g state, whereas it will have $E_e = \hbar\omega - 33$eV when it is left in the repulsive u state. Both ionization paths are distinguishable by the energy (Fig. (9.38c) and (9.38d)).

Quite recently A. Lafosse *et al.* obtained the MFPAD for a photon energy of 32.5 eV using linearly polarized light [47]. Fig. (9.39) displays the $F_{NL}(\theta_e)$ functions (upper panels) and the PAD for three different orientations of the polarization vector. These experimental results were obtained collecting electrons in the range 5 eV $\leqslant E_e \leqslant$ 10 eV (2.5 eV $\leqslant E_{H^+} \leqslant$ 5 eV). The most relevant feature of the these results is that both the $F_{NL}(\theta_e)$ functions and the PAD are not symmetric with respect to the emission angle, i.e., the MFPADs present a ***backward-forward asymmetry*** in the electron angle distribution (see for example, panels (d) and (e) of Fig. (9.39)), which suggested the breaking of the symmetry of the system. This is a great difference compared with the results presented in the previous two sections, results for photon energies of 20 and 27 eV, where the dissociative photoionization process can only occur through the first ionization threshold. We showed that for those photon energies, the MFPADs were totally symmetric with respect to the inversion center of the molecule (see for example Figs. (9.4) and (9.6) or Fig. (9.26)).

What does it take to break this symmetry? From the experimental point of view, the orientation of the molecule at its ionization time is determined by observing in coincidence the final ionic state, i.e., the detection of the final proton, and the electron emission. This imposes a specific asymptotic conditions that our final wave functions must reproduce. In the next section we explain how these "new" boundary conditions introduce some modifications in the theory presented in Chapter 3.

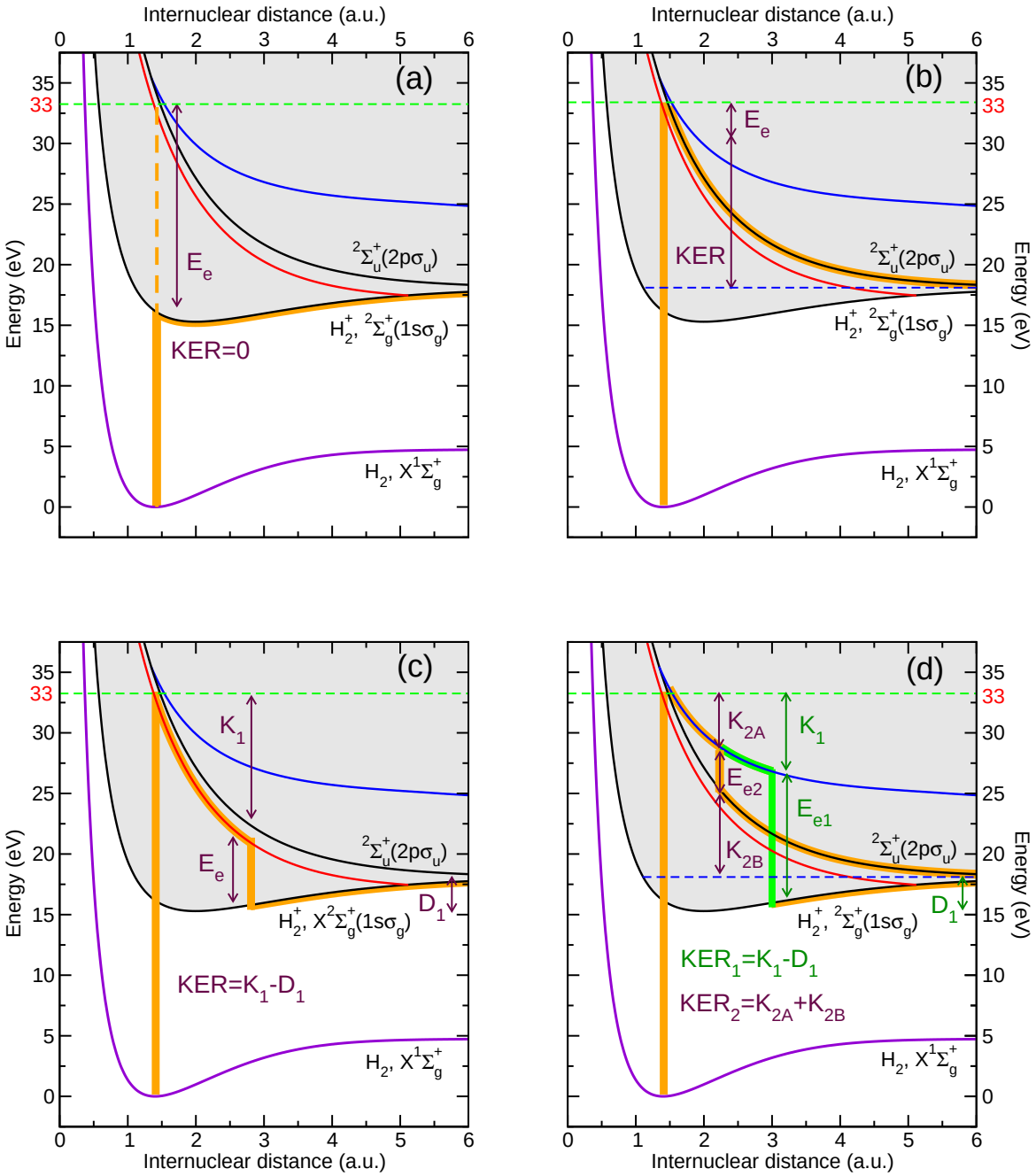

Figure 9.38: Semiclassical pathways for dissociative ionization of one 33 eV photon. Panels (a), (b), (c), (d) show semiclassical pathways for dissociative ionization by absorption of one 33 eV photon. (a) Direct ionization leading to $H_2^+\ (1s\sigma_g)$ (Eq. (9.44) in the text). (b) Direct ionization leading to $H_2^+\ (2p\sigma_u)$ (Eq. (9.46) in the text). (c) Resonant ionization through the lowest Q_1 doubly excited states leading to $H_2^+\ (1s\sigma_g)$ (Eq. (9.45) in the text). (d) Resonant ionization through the lowest Q_2 doubly excited states leading to $H_2^+\ (1s\sigma_g)$ (Eq. (9.47)) in the text) or to $H_2^+\ (2p\sigma_u)$ (Eq. (9.48) in the text).

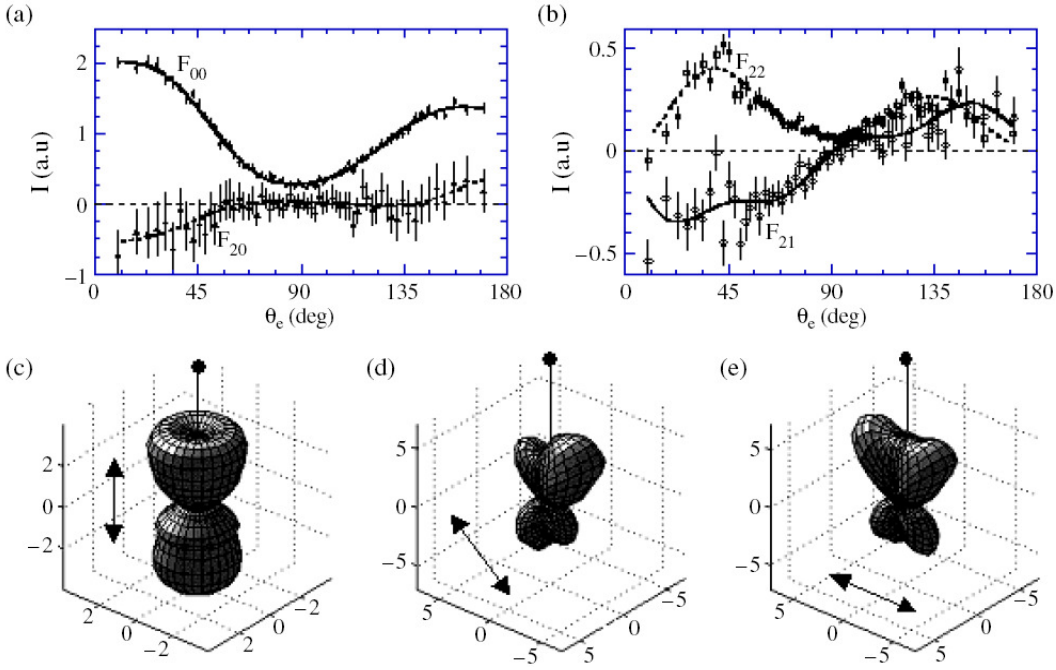

Figure 9.39: The $F_{NL}(\theta_e)$ functions at $h\nu = 32.5$ eV obtained by A. Lafosse *et al.* [47] using linearly polarized light: (a) The F_{00} and F_{20} functions, (b) the F_{21} and F_{22} functions. (c) $I_0(\theta_e)$, (d) $I_{54.7}(\theta_e, \phi_e)$ and (e) $I_{90}(\theta_e, \phi_e)$ MFPADs. The molecular axis is vertical, with the tiny sphere representing the proton direction, and the direction of the polarization axis is as shown.

9.4.1 Boundary conditions imposed by the experimental set-up

Let's study in detail the asymptotic conditions imposed by the experimental setup and how this introduces different modifications in our theoretical developments. In this section, we will compare our theoretical angular distributions with the experimental results obtained by two experimental technique called COLTRIMS and Vector Correlation (VC) method (see for example [58, 75, 76, 77]). The basis idea of these techniques is the determination, both in space and time, of the final velocities that describe the residual particles coming from the ionization process. The COLTRIMS is an imaging technique to measure the complete fragmentation of a few body system (see Fig. (9.40)). All charged fragments from an atomic, molecular or surface reaction are projected by a combination of electric and magnetic fields onto large area position sensitive detectors. From the measured time-of-flight of the particles and their position of impact on the detector the three dimensional momentum vector is obtained. In the VC method, the three components of the nascent velocities vectors of the final ions and electrons are measured in coincidence for each photoionization event, deduced from the arrival time and position of both particles in the VC double velocity spectrometer, and correlated to the quantization light axis Âăof the light propagation vector of elliptically polarized light [55]. Therefore the measurement of the final velocities of each of the final particles (protons and electrons) imposes a strict asymptotic condition that must be exactly reproduced in order to get the right MFPADs, i.e. we have to reproduce the condition in which the final proton is emitted in a defined direction and the residual atom is ejected in the opposite direction. Therefore, our final non-resonant scattering wave function, $P\Psi^{0+}_{\alpha,\upsilon_\alpha,\ell_\alpha,E}$, solution of Eq. (3.83) and that was given in the

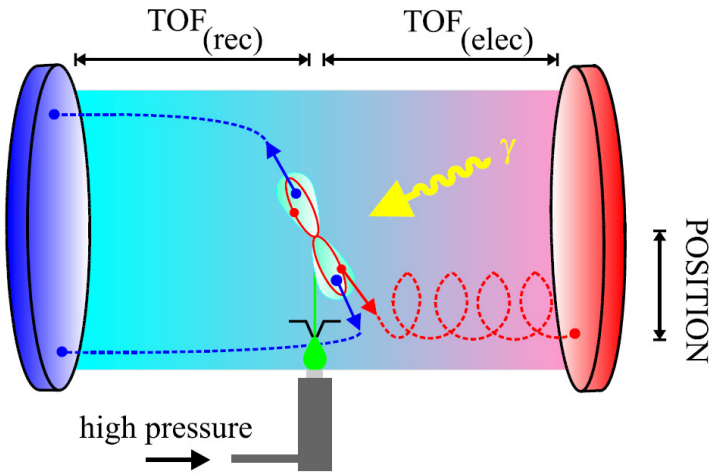

Figure 9.40: COLTRIM Spectrometer set up obtained from [78].

adiabatic nuclei approximation by Eq. (3.84), must now behave asymptotically as:

$$P\Psi^{0+}_{\alpha,\upsilon_\alpha,\ell_\alpha,E} \overset{r,R\to\infty}{\longrightarrow} \Theta[(\psi_{1s_A}(r_1)k\ell_\alpha\varepsilon_\alpha(r_2)]\chi^{\infty}_{\upsilon_\alpha}(R) \tag{9.49}$$
$$\equiv \Theta\left[\left(\psi^{\infty}_{1s\sigma_g}(r_1)+\psi^{\infty}_{2p\sigma_u}(r_2)\right)k\ell_\alpha\varepsilon_\alpha(r_2)\right]\chi^{\infty}_{\upsilon_\alpha}(R),$$

$$P\Psi^{0+}_{\alpha,\upsilon_\alpha,\ell_\alpha,E} \overset{r,R\to\infty}{\longrightarrow} \Theta[(\psi_{1s_B}(r_1)k\ell_\alpha\varepsilon_\alpha(r_2)]\chi^{\infty}_{\upsilon_\alpha}(R) \tag{9.50}$$
$$\equiv \Theta\left[\left(\psi^{\infty}_{1s\sigma_g}(r_1)-\psi^{\infty}_{2p\sigma_u}(r_2)\right)k\ell_\alpha\varepsilon_\alpha(r_2)\right]\chi^{\infty}_{\upsilon_\alpha}(R),$$

where Θ is the symmetrization operator[5], ψ_{1s_A} and ψ_{1s_B} are the wave functions representing the 1s orbital of the hydrogen atom A and B, respectively, and $\psi^{\infty}_{1s\sigma_g}$ and $\psi^{\infty}_{2p\sigma_u}$ are the wave functions representing the $1s\sigma_g$ and $2p\sigma_u$ orbitals of H_2^+ at infinite internuclear distance:

$$\psi^{\infty}_{1s\sigma_g} = \frac{1}{\sqrt{2}}(\psi_{1s_A}+\psi_{1s_B}) \tag{9.51}$$
$$\psi^{\infty}_{2p\sigma_u} = \frac{1}{\sqrt{2}}(\psi_{1s_A}-\psi_{1s_B}) \tag{9.52}$$

In Eq. (9.49), one of the electrons is associated to a proton labeled A producing the emission of a hydrogen atom A in the ground state $1s$ in a given direction (let's say left), while, in Eq. (9.50), the emission occurs in the other direction[6] (to the right). The vibrational wave function $\chi^{\infty}_{\upsilon_\alpha}(R)$ describes the relative motion of the proton and the hydrogen atom in the asymptotic limit $R\to\infty$. The boundary conditions defined by Eqs. (9.49) and (9.50) imply that the non-resonant state given by Eq. (3.83) can be written (in the Born-Oppenheimer approximation) as:

$$P\Psi^{+}_{\alpha,\upsilon_\alpha,\ell_\alpha,E} = \frac{1}{\sqrt{2}}[\psi^{0+}_{1s\sigma_g,\ell_\alpha,E}(r,R)\chi_{\upsilon_{1s\sigma_g}}(R) \pm \psi^{0+}_{2p\sigma_u,\ell_\alpha,E}(r,R)\chi_{\upsilon_{2p\sigma_u}}(R)], \tag{9.53}$$

where $\psi^{0+}_{1s\sigma_g,\ell_\alpha,E}$ and $\psi^{0+}_{2p\sigma_u,\ell_\alpha,E}$ are solutions of Eq. (3.85) with $\mathcal{E}(R)=\mathcal{E}_{1s\sigma_g}(R)$ and $\mathcal{E}(R)=\mathcal{E}_{2p\sigma_u}(R)$, respectively. The previous equation implies that the P projector can be written as

[5] Note that we are considering only singlet states.

[6] We are considering the distinguishability of the final hydrogen atom A from the atom B, since the creation of a hydrogen atom A implies a specific direction emission which is opposite to the creation a hydrogen atom B.

the sum of two orthogonal projectors associated to the $1s\sigma_g$ and $2p\sigma_u$ ionization thresholds, i.e., $P = P_{1s\sigma_g} + P_{2p\sigma_u}$. Notice that, in the above equation, the boundary conditions are fulfilled if

$$\left.\begin{array}{l}\chi_{\upsilon_{1s\sigma_g}}(R)\\ \chi_{\upsilon_{2p\sigma_u}}(R)\end{array}\right\} \longrightarrow \chi^{\infty}_{\upsilon_\alpha}(R). \tag{9.54}$$

which is only true if the non Coulomb phase shifts in the $1s\sigma_g$ and $2p\sigma_u$ ionization channels are identical. This is the case (except for energies very close to the dissociation threshold) provided that the Born-Oppenheimer approximation is a good approximation.

The $V^r_{\alpha\upsilon_\alpha\ell_\alpha E}$ function given by Eq. (3.89), now takes the form

$$V^r_{\alpha\upsilon_\alpha\ell_\alpha E} = \overbrace{\langle\phi_r|Q\mathcal{H}_{el}P_{1s\sigma_g}|\psi^{0+}_{1s\sigma_g,\ell_\alpha,E}\rangle\chi_{\upsilon_{1s\sigma_g}}(R)}^{V^r_{1s\sigma_g,\upsilon_{1s\sigma_g},E}} \pm \overbrace{\langle\phi_r|Q\mathcal{H}_{el}P_{2p\sigma_u}|P_{2p\sigma_u}\psi^{0+}_{2p\sigma_u,\ell_\alpha,E}\rangle\chi_{\upsilon_{2p\sigma_u}}(R)}^{V^r_{2p\sigma_u,\upsilon_{2p\sigma_u},E}}$$

Notice that there are no crossed terms $P_{1s\sigma_g}P_{2p\sigma_u}$ because these projectors are orthogonal. Hence the vibrational state $\xi^r_{\alpha\upsilon\ell E}(R)$ solution of Eq. (3.90) can be written

$$\begin{aligned}[E - E_r(R) - T(R)]\xi^r_{\alpha\upsilon_\alpha\ell_\alpha E}(R) &= \frac{1}{\sqrt{2}}[V^r_{1s\sigma_g,\upsilon_{1s\sigma_g},\ell_\alpha,E}(R) \pm V^r_{2p\sigma_u,\upsilon_{2p\sigma_u},\ell_\alpha,E}(R)]\\ + \lim_{\eta\to 0}\sum_{r'}\sum_{\alpha'\ell'_{\alpha'}}\sum_{\upsilon'_{\alpha'}}\!\!\!\!\!\!\int\!\!\!\!\!\!\int dE' \frac{V^r_{\alpha'\upsilon'_{\alpha'}\ell'_{\alpha'}E'}(R)}{E - E' + i\eta}\int V^{r'*}_{\alpha'\upsilon'_{\alpha'}\ell'_{\alpha'}E'}(R')\xi^{r'}_{\alpha\upsilon_\alpha\ell_\alpha E}(R')dR'.\end{aligned} \tag{9.55}$$

If one neglects second order crossed terms $V^r_{1s\sigma_g,\upsilon_{1s\sigma_g},\ell_\alpha,E}V^r_{2p\sigma_u,\upsilon_{2p\sigma_u},\ell_\alpha,E}$ in the last line of the previous equation, the solution of Eq. (9.55) can be written

$$\xi^r_{\alpha\upsilon_\alpha\ell_\alpha E} \equiv \frac{1}{\sqrt{2}}[\xi^r_{1s\sigma_g,\upsilon_{1s\sigma_g},\ell_\alpha,E} \pm \xi^r_{2p\sigma_u,\upsilon_{2p\sigma_u},\ell_\alpha,E}] \tag{9.56}$$

where $\xi^r_{1s\sigma_g,\upsilon_{1s\sigma_g},\ell_\alpha,E}$ and $\xi^r_{2p\sigma_u,\upsilon_{2p\sigma_u},\ell_\alpha,E}$ are independent solutions of equation Eq. (3.90) for the $1s\sigma_g$ and $2p\sigma_u$ ionization thresholds.

Similarly, the total wave function with the desired boundary conditions can be written:

$$\begin{aligned}\Psi_{1s_A(1s_B),\ell_\alpha,E}(r,R) = \frac{1}{\sqrt{2}}\Bigg[&\sum_{r'}\phi_{r'}(r,R)\xi^{r'}_{1s\sigma_g,\ell_\alpha,E}(R) \pm \sum_{r'}\phi_{r'}(r,R)\xi^{r'}_{2p\sigma_u,\ell_\alpha,E}(R)\\ + &\psi^{0+}_{1s\sigma_g,\ell_\alpha,E}(r,R)\chi_{\upsilon_\alpha}(R) \pm \psi^{0+}_{2p\sigma_u,\ell_\alpha,E}(r,R)\chi_{\upsilon_\alpha}(R)\\ + &\lim_{\eta\to 0}\sum_{r'}\sum_{\alpha'\ell'_{\alpha'}}\sum_{\upsilon'_{\alpha'}}\!\!\!\!\!\!\int\!\!\!\!\!\!\int dE' \frac{1}{E - E' + i\eta}\int dR' V^{r'*}_{\alpha'\upsilon'_{\alpha'}\ell'_{\alpha'}E'}(R')\xi^{r'}_{1s\sigma_g,\ell_\alpha,E}(R')\\ &\times \psi^{0+}_{\alpha'\ell'_{\alpha'}\varepsilon'_{\alpha'}}(r,R)\chi_{\upsilon'_{\alpha'}}(R)\\ \pm &\lim_{\eta\to 0}\sum_{r'}\sum_{\alpha'\ell'_{\alpha'}}\sum_{\upsilon'_{\alpha'}}\!\!\!\!\!\!\int\!\!\!\!\!\!\int dE' \frac{1}{E - E' + i\eta}\int dR' V^{r'*}_{\alpha'\upsilon'_{\alpha'}\ell'_{\alpha'}E'}(R')\xi^{r'}_{2p\sigma_u,\ell_\alpha,E}(R')\\ &\times \psi^{0+}_{\alpha'\ell'_{\alpha'}\varepsilon'_{\alpha'}}(r,R)\chi_{\upsilon'_{\alpha'}}(R)\Bigg]\end{aligned} \tag{9.57}$$

which can be simply written as a combination of the solutions that one would have obtained with boundary conditions that preserve the *g* and *u* symmetries:

$$\Psi_{1s_A(1s_B),\ell_\alpha,E}(r,R) = \frac{1}{\sqrt{2}}\left[\Psi_{1s\sigma_g,\ell_\alpha,E}(r,R) \pm \Psi_{2p\sigma_u,\ell_\alpha,E}(r,R)\right]. \tag{9.58}$$

Thus, in practice, one has to solve the same equations as described in previous sections when the molecular symmetry is preserved in the measurement and combine the solutions as indicated by the previous equation.

9.4.2 Linearly polarized light

In this section we study the results obtained making use of linearly polarized light, considering a photon energy of 33.25 eV (the experimental photon energy), and an orientation of the molecule perpendicular to the polarization axis. Fig. (9.41) shows the key results of this section. Plotted is the angular distribution of the electron with respect to the polarization axis (horizontal). The plane of the figure is defined by the molecular axis and the polarization vector; only electrons in this plane are selected. The molecule is perpendicular to the polarization axis with the proton pointing upwards. The angular distributions are found to vary strongly with the kinetic energy release. Besides a change from a dumbbell to a butterfly shape, a strong asymmetry is found, in particular in a narrow range of KER $\simeq 8$ to 10 eV, corresponding to an electron energy of $E_e \simeq 5$ to 7 eV. All major features predicted by our theory are confirmed by the experimental data. They are also consistent with those reported in a previous experiment [47] by averaging over KER intervals of 2.5 to 3 eV.

The experiments were performed at beam line 9.3.2 of the Advanced Light Source at Lawrence Berkeley National Laboratory. The monochromatized linearly polarized light from the synchrotron was crossed with an internally cold and localized supersonic H_2 and D_2 gas jet. The ions and electrons were directed by a combination of weak electric (20 V/cm) and parallel magnetic (10 Gauss) fields onto two position-sensitive microchannel plate detectors with delayline position encoding [79]. Vector momenta were calculated from the position of impact and the times of flight of each particle. The energies of both ions and electrons were measured. Electron, ion and neutral fragment momenta k_e, k_{p^+}, and k_H are related by momentum conservation: $k_e = -(k_{p^+} + k_H)$. Due to the light electron mass, the electron momentum is about 40 times smaller than the heavy particle momentum, leading to a nearly back-to-back fragmentation of proton and hydrogen atom. The energy deposited by the photon ($\hbar\omega$) in excess of the threshold for dissociative ionization of 18.6 eV is partitioned among the kinetic energy release (KER) of the heavy fragments, the electron energy (E_e) and internal excitation energy of the neutral ($\hbar\omega = KER + E_e - 18.1eV - E_{exc}$). As expected, the hydrogen atom is found only in the ground state ($E_{exc} = 0$) in the photon energy range examined here. The asymptote of the $1s\sigma_g$ and $2p\sigma_u$ curve in Fig. (9.38) corresponds to a proton and a hydrogen atom in its ground state. Because both KER and E_e are measured for each event, energy conservation can be used to very efficiently suppress random background or proton and electron pairs from residual water molecules in the chamber. The overall energy resolution is between 100 meV and 0.5 eV depending on the energy, the angular resolution about 5^o. More detail on the COLTRIMS system can be found in [80].

Our theoretical analysis allows us to distinguish the contributions leading to $1s\sigma_g$ (sum of processes in Eqs. (9.44), (9.45) and (9.47)) from those leading to $2p\sigma_u$ (sum of processes in Eqs. (9.46) and (9.48)). For a fixed photon energy of 33.25 eV, the contributions of the $1s\sigma_g$ and $2p\sigma_u$ channels overlap in the 8 to 10 eV region (Fig. (9.42)), where the largest asymmetry is observed (Fig. (9.41)). How can the $1s\sigma_g$ and $2p\sigma_u$ channels interfere to produce an asymmetric angular distribution? To answer this question we have performed a model calculation in which we have only included the direct ionization channels, $1s\sigma_g k\pi_u$ and $2p\sigma_u k\pi_g$, and the lowest Q_2 state of Π_u symmetry. The angular distributions found in this model calculation are very similar to those obtained from the full calculation (Fig. (9.41)). In particular, the asymmetry is very well reproduced, showing that the Q_1 states are not responsible for its occurrence. We have then additionally excluded the two direct channels (Eqs. (9.44) and (9.46)) and only considered the decay of the Q_2 state through the channels in Eqs. (9.47) and (9.48). The asymmetry remains, thus showing that the origin of the asymmetry is the interference between these two channels, i.e., between the resonant population of

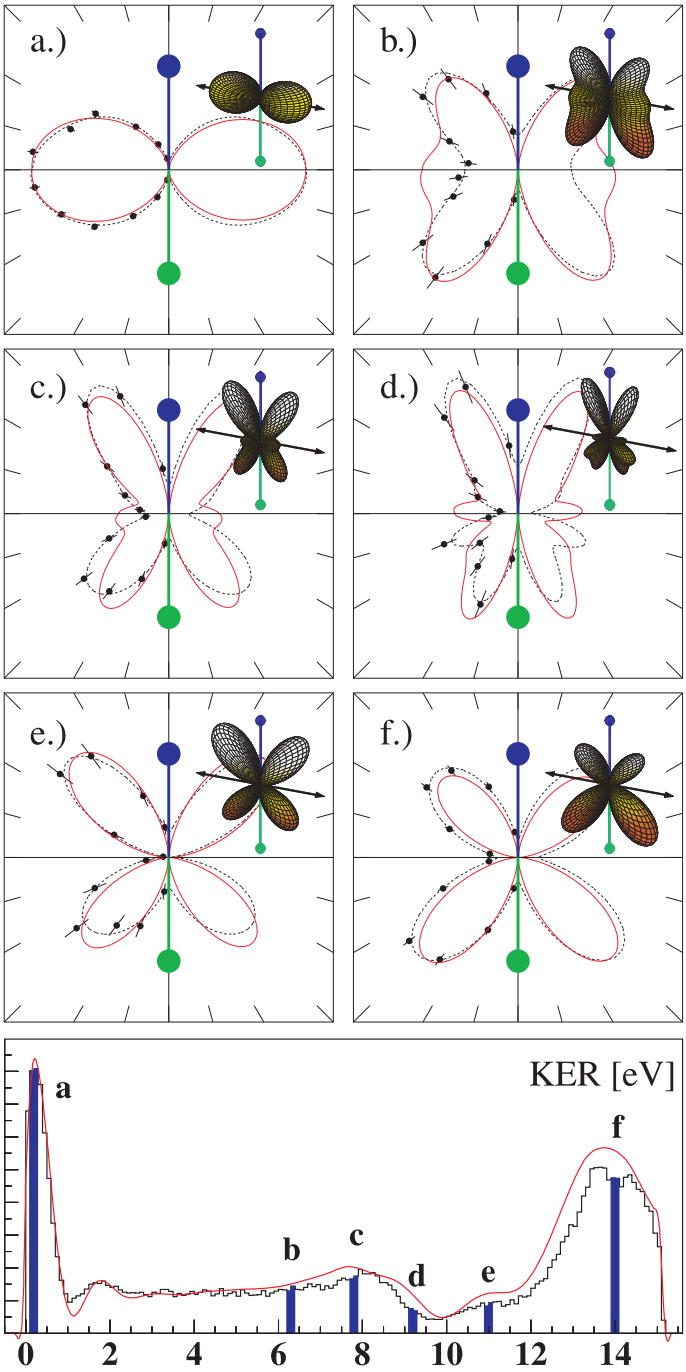

Figure 9.41: (Upper panel) Angular distribution of the electrons as a function of KER at 33.25 eV photon energy, linearly polarized light. For KER intervals see insets (red line: theory, black line: experiment). Infinite resolution theoretical results are shown by the small three-dimensional plots in the upper right: KER = 0.2 (*a*), 6.3 (*b*), 7.8 (*c*), 9.2 (*d*), 11 (*e*), and 14 eV (*f*). The orientation of the molecule at 90 deg to the polarization (theory) and 90 $\pm$ 10 deg (experiment) is indicated by the barbell (blue = deuteron, green = deuterium). The polarization vector, which lies horizontally, and the molecular axis define a common plane. The electron is restricted to this plane by $\pm$ 45 deg. Full red line: theory, circles with error bars: experiment, dotted line: fit of the experimental data with spherical harmonics. The theoretical results have been integrated over the experimental acceptance angles and KER resolution as well as electron resolution. (Lower panel) The angle-integrated KER spectrum. Red line, theory; black line experiment. letters *a* to *f* correspond to *a* to *f* in upper panel; KER intervals are $\pm$0.1 eV. The *x*-axis shows the KER in eV. The *y*-axis shows a cross-section in arbitrary units.

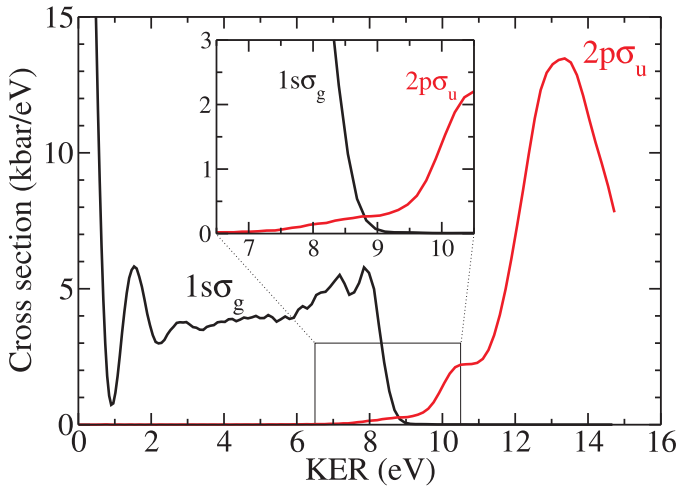

Figure 9.42: Calculated D^+ kinetic energy distribution in dissociative ionization of D_2 by absorption of a 32.25 eV photon. Solid line, $1s\sigma_g$ channel; dashed line, $2p\sigma_u$ channel. The inset is a magnification of the squared region.

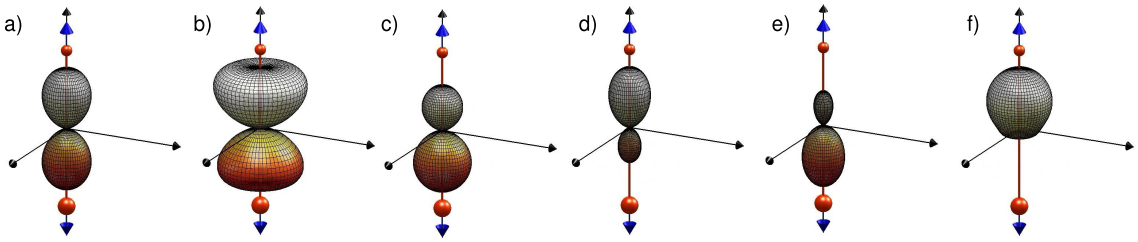

Figure 9.43: Same as Fig. (9.41) but using linearly polarized light parallel to the molecular axis, for KER = 0.45 (*a*), 4.8 (*b*), 8.4 (*c*), 10.0 (*d*), 11.0 (*e*), and 13.8 eV (*f*).

an ungerade and a gerade state. It is only the coherent superposition of these pathways which allows for a localization of the bound electron in the dissociating H_2^+. The transient molecule has broken symmetry and can keep a memory of the direction in which the electron departed. We have also found that the fingers in Fig. (7.3) of Chapter 7 do not appear when the direct channel (Eq. (9.44) is not included in the calculation, thus confirming that their origin is the interference between resonant and non resonant population of the $1s\sigma_g$ state. In any case, the latter interference does not lead to a noticeable asymmetry.

The results of the full quantum calculation completely differ from those of the widely used simple semiclassical model (also used in Fig. (9.38)(a-d) for pedagogical purposes). In this simple model, the system always strictly follows the potential energy curves and only vertical transitions between them are allowed. These vertical transitions may occur as a result of photon absorption (vertical lines on the left) or autoionization decay (vertical lines on the right). In this framework all molecules have an identically well-defined value of the internuclear distance during the transition and, consequently, any possible direct energy exchange between electronic and nuclear motions is neglected. For example, in such a model the electron energy from the path shown by an

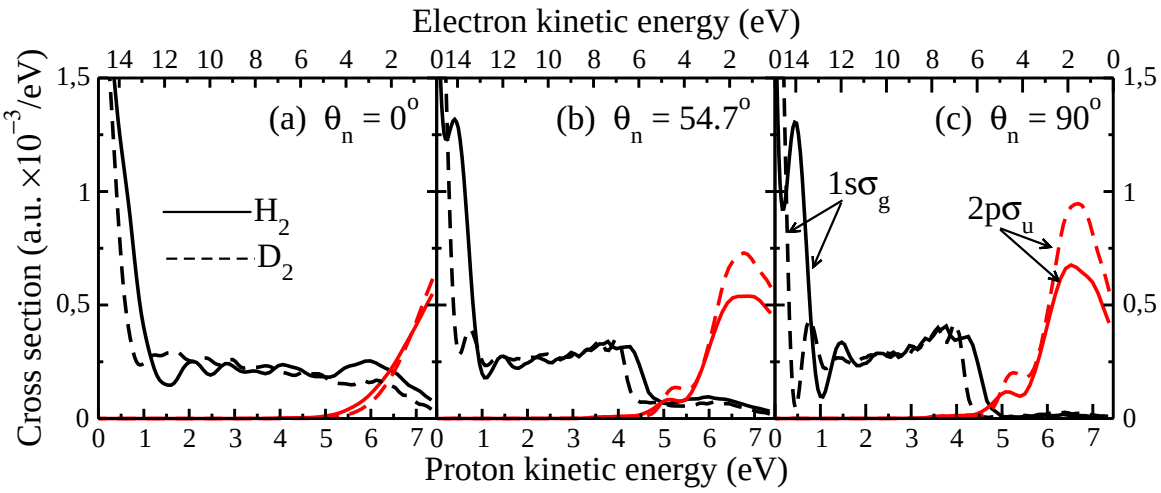

Figure 9.44: Total cross section for the H_2 (full line) and D_2 (dashed line) using linearly polarized light as a function of the proton/electron energy, for three different orientation of the polarization vector, at $\hbar\omega$=33 eV. (a) $\theta_n = 0°$; (b) $\theta_n = 54.7°$; (c) $\theta_n = 90°$. Black line contribution from the $1s\sigma_g$ ionization threshold and red line contribution from the $2p\sigma_u$ ionization threshold.

orange line in Fig. (9.38)(d) (resonant photoionization through the $2p\sigma_u$ channel) would be equal to the energy difference between the Q_2 and the $2p\sigma_u$ curve at the marked internuclear distance. Similar reasoning predicts the electron energy along the path shown by the green line (resonant photoionization through the $1s\sigma_g$ channel). Our calculations show that, in the present case, such simplified models, though of heuristic and pedagogical value, lead to false conclusions. The model predicts that the maximum possible value of the KER in the $1s\sigma_g$ channel is 8.1 eV (corresponding to an autoionization decay at infinite internuclear distance), which is the minimum possible value of the KER in the $2p\sigma_u$ channel (corresponding to autoionization decay at the equilibrium internuclear distance). Therefore, no interference between g and u states can occur within this model because the electron energies and the KER regions for transitions to $1s\sigma_g$ and $2p\sigma_u$ would have no overlap, and hence the electron ejection would always be symmetric. Our fully quantum mechanical treatment shows that transitions to the $1s\sigma_g$ state can occur beyond 8.1 eV and that transitions to the $2p\sigma_u$ state are possible even at zero KER. Thus the angular distribution can exhibit an asymmetry over the whole region of KER. Strictly speaking, a symmetric dissociation in the presence of resonances is the exception rather than the rule. It becomes quantitatively significant in the region where both channels are comparably active, between 8 and 10 eV; however it is also visible in regions where one of the channels dominates (panels b-f in Fig. (9.41)).

It is worth noting that the observed asymmetry has no relation to the direction in which the charged fragment is emitted: sometimes the larger lobes are found on the proton side (panels c, d, and e in Fig. (9.41)), sometimes on the hydrogen side (panels b and f in Fig. (9.41)). Both theory and experiment show that the asymmetry oscillates with the KER, the amplitude of these oscillations being more important in the region where the $1s\sigma_g$ and $2p\sigma_u$ channels overlap. Between consecutive oscillations, there are KER values for which the distribution is practically symmetric. Thus the asymmetry cannot be explained by a preferred attractive interaction between the proton and the escaping electron (the latter is too fast to be efficiently perturbed by the slow proton, except possibly in the region of the maximum allowed KER). Fig. (9.43) displays the MFPAD obtained making use of linearly polarized light parallel to the molecular axis. As can be seen, the electron angular distributions present the similar asymmetry patterns as a function of the final electron energy as the results showed in Fig. (9.41), whose origin can be explained in the same manner. This confirms the

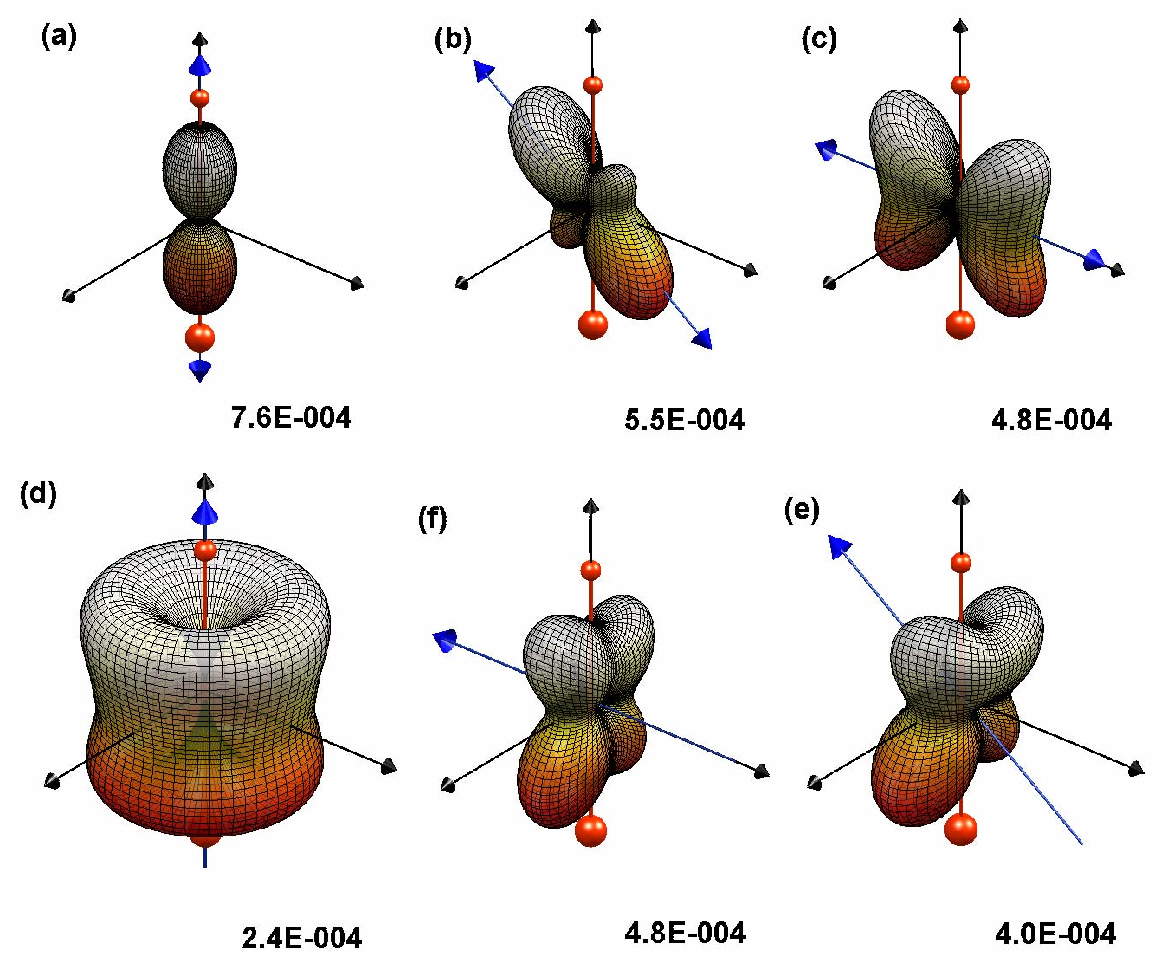

Figure 9.45: MFPAD of H_2 integrated over the whole final proton energy range, for linearly polarized light (a, b, c) and circularly polarized light (d, e, f), at $\hbar\omega$=33 eV. for three different orientations: (a, d) $\theta_n = 0°$; (b, e) $\theta_n = 54.7°$; (c, f) $\theta_n = 90°$.

fact that the origin of the observed asymmetry comes from the interference from the contribution of the first ionization thresholds (see also Fig. (9.44)). Notice that for the parallel situation, the asymmetry is more obvious than for the perpendicular case, since in this case the overlap between both ionization threshold extend towards higher proton energies (see Fig. (9.44)).

In Fig. (9.44) we present the total cross section as a function of the final proton energy, for three different orientation of the polarization vector, for H_2 and D_2 molecules. The cross section presents a clear dependence with the orientation of the polarization vector. For $\theta_n = 90°$ we reproduce the previous results obtained by I. Sánchez *et al.* [3, 4] and also displayed in Fig. (9.41). At this photon energy, the role of the $Q_1\,{}^1\Sigma_u^+$ resonant states is clearly reflected on the results obtained at $\theta_n = 0°$, which are the responsible of the different structures associated to the first ionization threshold. For the D_2 molecule the resonant effects are also present for the same orientation of the polarization vector and the different structures are shifted ~ 1 eV toward higher proton energy as in the results obtained for a photon energy of 27 eV (see Fig. (9.30)).

In order to study the relevance of the resonant states at this photon energy in the MFPAD in comparison with the previous results obtained at lower photon energies, we present in Fig. (9.45) the MFPAD of the H_2 molecule integrated over the whole electron/proton energy range for linearly polarized light (panels (a), (b) and (c)). The angular distributions are completely symmetric,

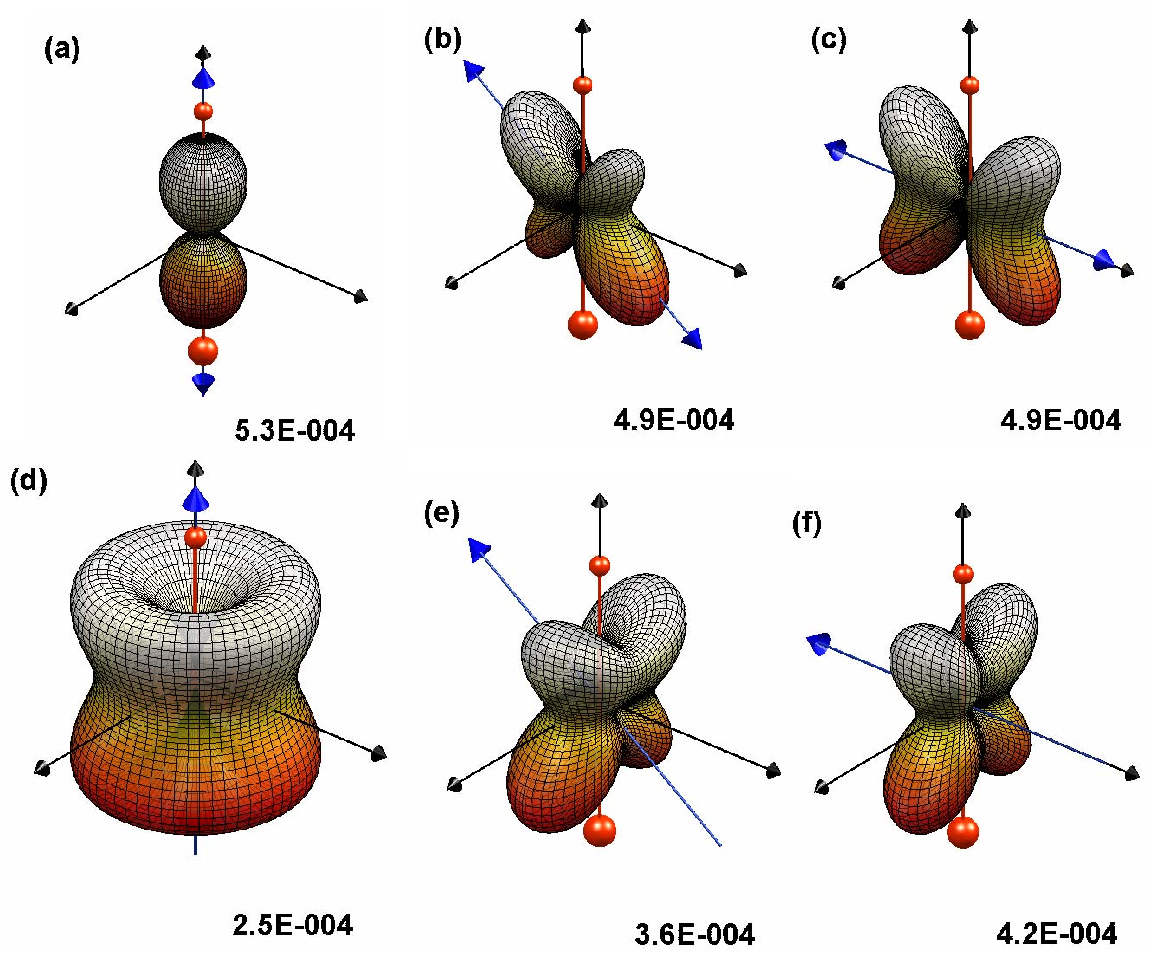

Figure 9.46: Same as in Fig. (9.45) for D_2.

although the trace of the contribution of the doubly excited states is clearly present (see panels b and c of this figure). For the parallel orientation where the $Q_1\ ^1\Sigma_u^+$ resonant states are clearly present in the total cross section, the observed patter is quite similar to previous results obtained at 20 and 27 eV, the shape of the lobes have a *p*-wave shape. For the magic angle, the electron is emitted in the direction of the polarization vector but the contribution of the $^1\Pi_u$ symmetry produces additional lobes perpendicular to the polarization direction. On the other hand, for the perpendicular orientation the observed pattern is completely different in comparison with the previous results displays in Fig. (9.7) and (9.28). The results for the D_2 molecule are displayed in Fig. (9.46) and the patterns of the MFPADs are similar to the results obtained for the H_2.

9.4.3 Circularly polarized light

In the previous section we have seen that the MFPAD obtained by linearly polarized light, present a strong asymmetry that depends on final proton/electron energy, so it is worthy to examine similar effects when circularly polarized light is used. In this section we select some of the parameters obtained in the analysis of photoemission in the molecular frame induced by circularly polarized light and compare the E_{D^+} dependence of the experimental and theoretical results at the level of θ_e integral parameters, taking into account the experimental results obtained by D. Dowek *et al.* [2]. On the experimental side the data analysis is as follows: taking into account the proton

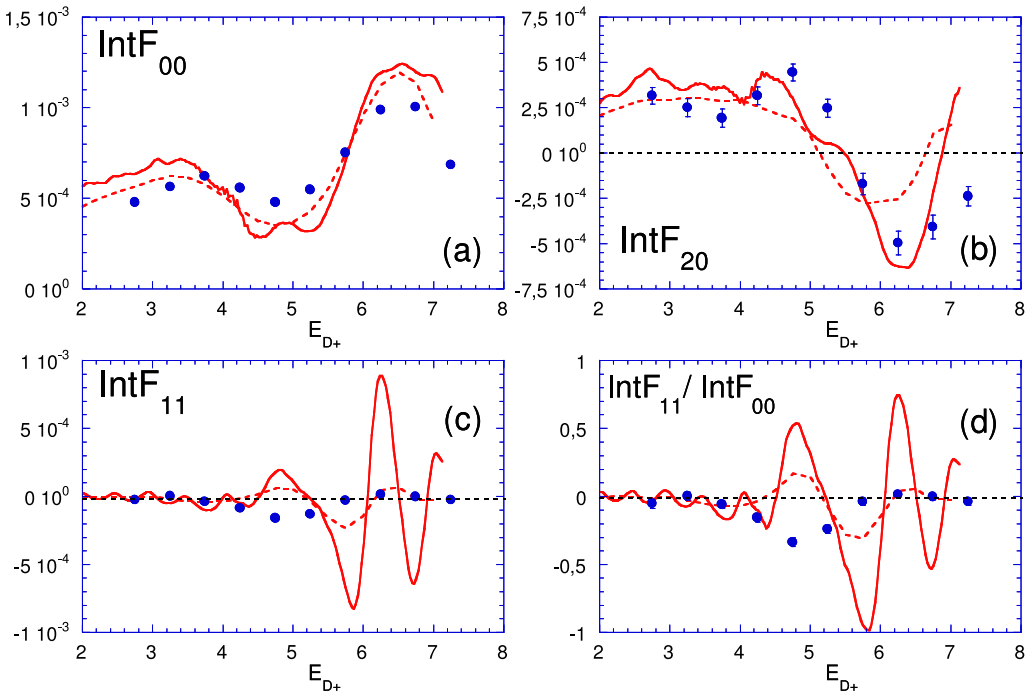

Figure 9.47: Selected angle integrated $F_{LN}^{\mu_0=1}$ functions as a function of the E_{D^+} proton energy: theory (full line), convoluted theory (dashed line), experiment (dots).

energy resolution in the reported experiment, of the order of 0.5 eV, and the statistics enabling the extraction of the $F_{LN}(\theta_e)$ functions for each E_{D^+} selection, the $F_{LN}(\theta_e)$ functions are first determined for sets of events lying along the diagonal in the electron-ion kinetic energy correlation diagram, included between the two straight lines of slope -1 representing pseudo-dissociation limits at 15 eV and 21 eV, in selected intervals of $E_{D^+} = 0.5$ eV, by steps of 0.25 eV. The five integral functions $G_{LN}(E_{D^+}) = IntF_{LN}(E_{D^+})$ are obtained as[7]: $IntF_{LN}(E_{D^+}) = \int_0^\pi F_{LN}(E_{D^+})\sin(\theta_e)d\theta_e$. In Fig. (9.47) we display the E_{D^+} dependence of $IntF_{00}$, $IntF_{20}$, $IntF_{11}$ and the normalized ratio $IntF_{11}/IntF_{00}$ for (i) the present calculations (ii) the calculations convoluted with the apparatus function using a Monte Carlo simulation of the trajectories in the VC spectrometer, and analyzed according to the same procedure as the experimental data in intervals of 0.5 eV (iii) the experimental results. Experiment is normalized to theory such that the integral photoionization cross section over the studied E_{D^+} energy range is identical.

Fig. (9.47) (panels (a) and (b)) shows that the effect of convolution on the $IntF_{00}$ and $IntF_{20}$ E_{D^+} dependence is small and that a good agreement between theory and experiment is achieved. $IntF_{00}$ represents the integral photoionization cross section, in good agreement with previous measurements and calculations [30]. The sign inversion of $IntF_{20}$ for $E_{D^+} \approx 5.5$ eV corresponds to the change from a dominant parallel transition for low proton energies ($\beta_{D^+} \approx 0.5$ along the 2-4 eV plateau, see Fig. (9.50)) to a dominant perpendicular transition for $E_{D^+} \geq 5.5$ eV ($\beta_{D^+} \approx -0.5$ in the range 6-7 eV, see Fig. (9.50)). The same good agreement is obtained when comparing the computed and measured $IntF_{22}$. However the situation is different for the E_{D^+} variation of $IntF_{11}$ shown in Fig. (9.48) (c) (as well as that of $IntF_{21}$ not shown): the computed $IntF_{11}$ and $IntF_{21}$ lie close to zero

[7] Notice that in page 157, we define the functions $G_{LN}(E_{D^+})$ that are equivalent to the $IntF_{LN}(E_{D^+})$ functions defined in this section.

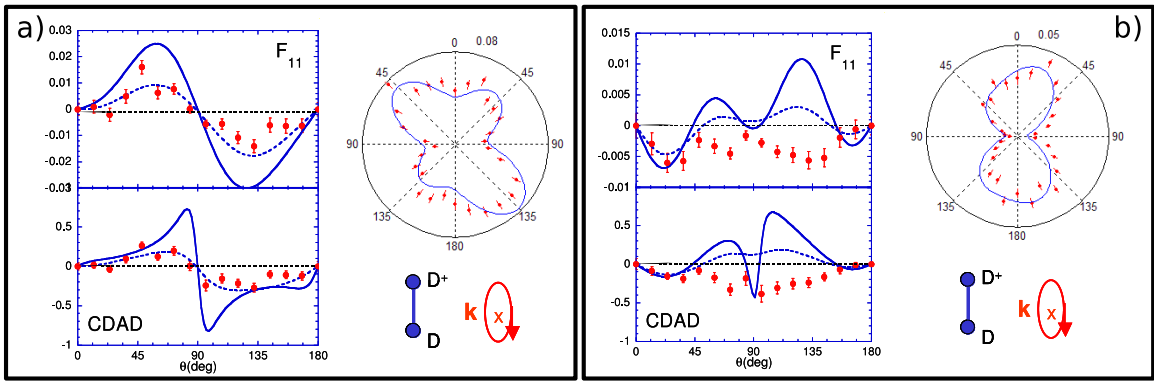

Figure 9.48: Panel a, results collecting deuterons in the energy range $5.5 \leq E_{D^+} \leq 6.5$ eV; left column: The $F_{11}^{\mu_0=1}$ function, the CDAD function: theory (full line), convoluted theory (dashed line), experimental results (dots); right column: cut of the MFPAD induced by LHC polarized light D_2 oriented perpendicular to k ($\theta_n = 90^\circ$) corresponding to electron emission at $\phi_e = 90^\circ$ and $\phi_e = 270^\circ$: convoluted theory (line), experimental results (dots). Panel b, results collecting deuterons in the energy range $4.5 \leq E_{D^+} \leq 5.5$ eV;

for low protons energies $2 \leq E_{D^+} \leq 4$ eV and display strong positive and negative oscillations in the range $4 \leq E_{D^+} \leq 7.5$ eV, with a half-period of the order of 0.5 eV. This result is the first fingerprint that, for the higher E_{D^+} range, the CDAD does not display the inversion symmetry that one expects in photoionization of homonuclear molecules. Indeed this property would imply that $IntF_{11}$, and similarly $IntF_{21}$, would remain equal to zero. The effect of convolution strongly attenuates the contrast of these oscillations. The experimental result is in qualitative agreement with the theoretical prediction in the sense that $IntF_{11}$ and $IntF_{21}$ are close to zero in the $2 \leq E_{D^+} \leq 4$ eV range, take non-zero values for $4 \leq E_{D^+} \leq 6$ eV of comparable amplitude with the convoluted theory, and decrease to zero again for higher energies, consistent with the convolution. However the sign of the measured $IntF_{11}$ values are negative in the region where theory predicts positive values, and the opposite is true for the evolution of $IntF_{21}$.

We also present the $IntF_{11}(\theta_e)$ functions and related MFPADs for two specific proton energy selections: the first one, $5.5 \leq E_{D^+} \leq 6.5$ eV (left panel of Fig. (9.48)), in the region of the maximum of the cross section where the integral CDAD is close to zero, and the second one, $4.5 \leq E_{D^+} \leq 5.5$ eV (right panel of Fig. (9.48)), in the region where the computed and measured $IntF11$ (and $IntF21$) are of significant magnitude. For both examples we present here the experimental and theoretical results in terms of (i) $F_{11}(\theta_e)$, (ii) the CDAD parameter according to equation 6, and (iii) the cuts of the MFPAD induced by LHC polarized light of helicity +1 for a D_2 molecule oriented perpendicular to the light propagation axis ($\theta_e = 90^\circ$) corresponding to electron emission in the half planes $\phi_e = 90^\circ$ and $\phi_e = 270^\circ$ (see Eq. (9.38)) .

In the $5.5 \leq E_{D^+} \leq 6.5$ eV region, the measured and convoluted theoretical differential results are in very good agreement. $F_{11}(\theta_e)$ and the CDAD display the inversion symmetry with respect to $\theta_e = 90^\circ$ expected for homonuclear molecules, which results in a zero integral value, although we note here that this behavior for theory results from the integration over an E_{D^+} interval covering two oscillations of opposite sign. However, in the $4.5 \leq E_{D^+} \leq 5.5$ eV region, both theoretical and experimental differential results demonstrate that $F_{11}(\theta_e)$ and the CDAD violate the inversion symmetry with respect to $\theta_e = 90^\circ$. Nevertheless this agreement in only qualitative since the measurements lead to an opposite sign, than the theoretical predictions. Finally, we note that for the lowest studied proton energies $2 \leq E_{D^+} \leq 3.5$ eV the computed $F_{11}(\theta_e)$ and CDAD satisfy the inversion symmetry, in consistent agreement with the measurements, although the statistics was more limited due to the lower cross section in this region.

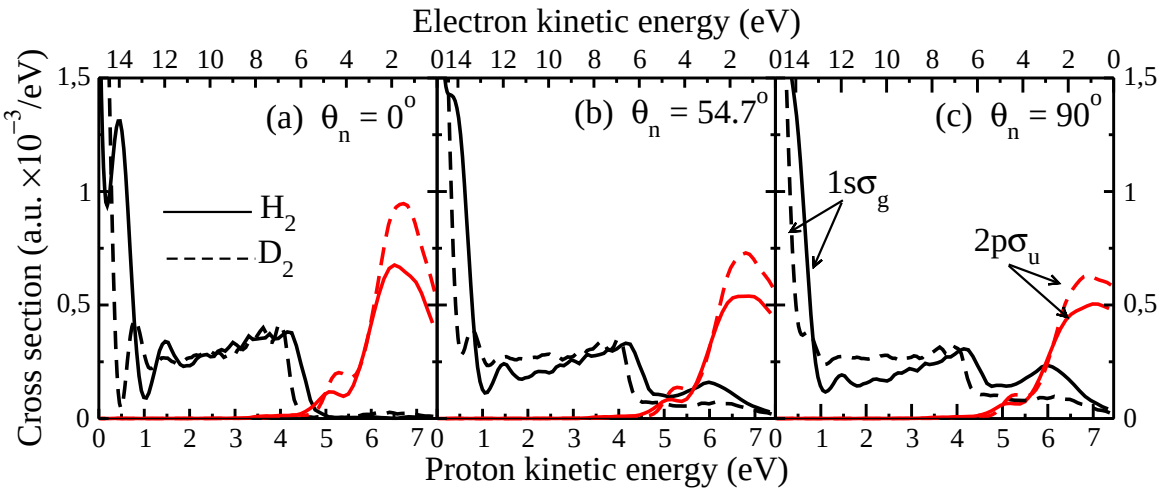

Figure 9.49: Same as Fig. (9.44) but using instead circularly polarized light.

To complete this section and in order to reflect the main differences obtained making use of linearly polarized light, we present in Fig. (9.49) the total cross section for the three indicated orientations as a function of the final electron/proton energy. As we pointed out before, results for $\theta_n = 0°$ are similar to the ones obtained for linearly polarized light at $\theta_n = 90°$, and the responsible of the different structures is the population of the $Q_2\,{}^1\Pi_u$ resonant states. On the other hand for $\theta_n = 90°$, the population of the $Q_1\,{}^1\Sigma_u^+$ and the $Q_2\,{}^1\Pi_u$ is possible, implying that the proton kinetic energy distribution associated with the first ionization threshold extends to larger proton energies. In panels (d), (e) and (f) of Fig. (9.46) we displayed the MFPAD integrated over the whole final proton energy range. For a parallel orientation the results are similar to the ones obtained making use linearly polarized light, in the sense that this electron distribution is characterized by the same partial waves (Notice that we are populating the same symmetry in both cases). For the other two orientations of the polarization vector the role of the resonant states is also clearly reflected. As for the case of linearly polarized light, the asymmetry observed when the proton/electron energy is resolved is completely lost.

9.4.4 Proton and electron beta parameters

To complete this section we study the proton angular distribution and the electron distribution for randomly distributed molecules. In Fig. (9.50) we present the photoelectron beta parameter for H_2 (upper panel) and D_2 (lower panel), given the contribution of the different ionization thresholds and the total result. For electron energies greater than 6 eV the electron beta parameter is mainly described by the contribution of the first ionization threshold, and present strong oscillations due to the population of the $Q_1\,{}^1\Sigma_u^+$ and the $Q_2\,{}^1\Pi_u$ resonant states. For energies ≤ 6 eV the behavior of the electron beta parameter changes drastically presenting a smooth dependence with the electron energy. This region correspond to the contribution of the second ionization threshold, and in this case only the $Q_2\,{}^1\Pi_u$ resonant states are responsible for the structures presented in this energy range. The results for the D_2 molecule, displayed in the lower panel of Fig. (9.50), present a similar behavior as the ones presented for the H_2, but in this case the different structures are shifted ~ 1 eV, as the structures shown in the total cross section (see Fig. (9.49)). In Table (9.50) we summarize the dissociative, non-dissociative and total electron beta parameters for H_2 and D_2, associated to each ionization threshold. For this photon energy, only A. Lafosse *et al.* [47] obtained experimental values of the photoelectron beta parameter. In particular, they obtained a value of $\beta_e \approx 1.0 \pm 0.1$

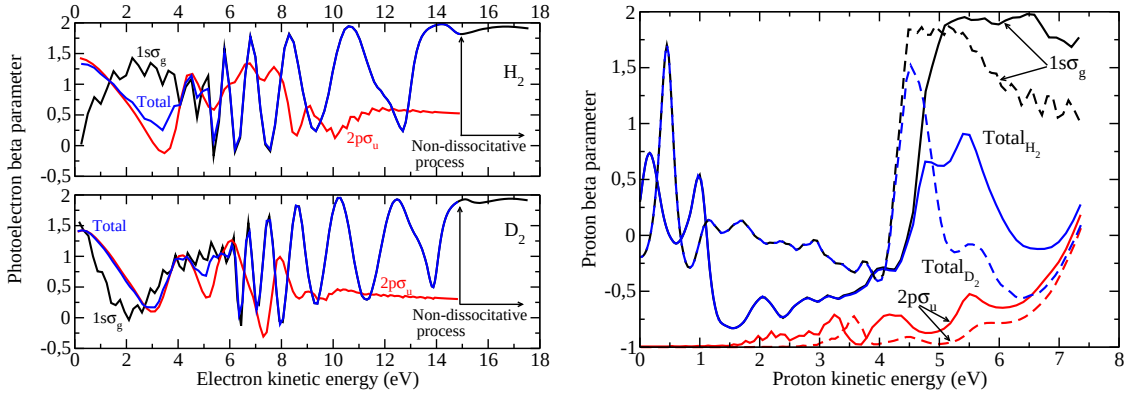

Figure 9.50: (Left panel) Photoelectron beta parameter as a function of the electron energy, for H_2 (upper panel) and D_2 (lower panel). Vertical line indicates the electron energy coming from the non-dissociative process. (Right panel) Proton beta parameter as a function of the proton energy for H_2 (full line) and for D_2 (dashed line). All results obtained at $\hbar\omega$=33 eV.

Table 9.3: Photoelectron beta parameter, for H_2 and D_2 for linearly and circularly light, at $\hbar\omega$=33 eV. β_e^N, beta parameter for the non-dissociative process; β_e^D, beta parameter for the dissociative process; β_e^T, total beta parameter.

H_2				D_2			
$1s\sigma_g$			$2p\sigma_u$	$1s\sigma_g$			$2p\sigma_u$
β_e^N	β_e^D	β_e^T	β_e^D	β_e^N	β_e^D	β_e^T	β_e^D
1.92	0.56	1.83	0.83	1.92	0.52	1.88	0.87

in the electron energy range [0, 5.0] eV, and $\beta_e \approx 0.15 \pm 0.1$ in the electron energy range [5, 10.0] eV. Integrating our theoretical photoelectron beta parameter in the same electron energy ranges, we obtain a value of $\beta_e = 1.16$ and $\beta_e = 0.20$, respectively, which agree with these experimental results.

The proton beta parameter is shown in the right panel of Fig. (9.50) for the H_2 and D_2 molecules, including the contribution of the first two ionization thresholds. The proton beta parameter presents a strong dependence with the proton energy, reflecting the relative contribution of the resonant states to each ionization threshold. The integrated proton beta parameter associated to the first ionization threshold ($1s\sigma_g$) is equal to 0.20 for the H_2 and 0.15 for the D_2, which implies that the Σ_u and Π_u symmetries posses the same relevance (see Eq. (4.67) of Chapter 4). The result for the $2p\sigma_u$ ionization threshold gives a value of -0.44 for the H_2 and -0.58 for the D_2. In the case where the contribution of the different ionization thresholds cannot be resolved, the total beta parameter takes a value of 0.03 for the H_2 and -0.11 for the D_2. A. Lafosse *et al.* [47] obtained the proton beta parameter in two different proton energy ranges: [4.5, 9.0] eV with a value of $\beta_{H^+} \approx 0.25 \pm 0.1$, and [2.5, 5.0] eV with a value of $\beta_{H^+} \approx -0.1 \pm 0.1$. Integrating the theoretical results in the proton energy range [2.5, 5.0] eV we obtain a value of $\beta_{H^+} \approx -0.32$ and for the proton energy in the range [4.5 7.35] eV a value equal to $\beta_{H^+} \approx 0.15 \pm 0.1$ (note that the maximum proton energy of a photon energy of 33 eV is 7.35 eV), which agree quite well with the experimental results.

9.5 Conclusions

In this Chapter we have studied the MPAD of H_2 and D_2 molecule making use of linear and circular polarized light for three different photon energies. At 20 eV, we have presented a detailed study of

the different information that can be extracted from the study of the electron angular distribution. For this photon energy we showed that the electron angular distribution was practically independent of the final electron energy. Also, we have studied the role of the circularly polarized light in the study of the circular dichroism, that gives the different between left and right-handed polarized light. For a photon energy of 27 eV, the presence of the Q_1 doubly excited states responsible for the different structures in the total cross section had no relevance in the MPAD. The results for a photon energy of 33 eV presented a new effect: a forward-backward asymmetry in the electron angular distribution. This effect was explained in terms of a interference process between the two final paths that the residual ion can followed.

For this photon energy, we also reported a comparative theoretical and experimental study of molecular frame photoemission in photoionization of D_2 induced by circularly polarized light. The remarkable evolution of the CDAD predicted by the full four body calculations was in qualitative agreement with the reported experimental results in the sense that both demonstrate a strong evolution of the CDAD as a function of the proton energy, with a violation of the inversion symmetry with respect to $\theta_e = 90^\circ$ that characterizes molecular frame circular dichroism in photoionization of homonuclear molecules.

Asymmetric photoelectron angular distributions should arise in any symmetric molecule that decays through two (or more) dissociative ionization channels associated with different symmetries of the residual molecular ion. When the final electron energy is the same in both channels, the corresponding ionization pathways are indistinguishable. This equivalence leads to interferences that depend on the time delay between the two ionization processes. The time delay implies that the decay in either pathway occurs at different positions of the nuclei. This unique relationship between time delay and nuclear positions makes the problem of molecular autoionization much richer than the atomic case, with the asymmetry of the photoelectron angular distribution the most striking (and so far unexpected) effect. In conclusion, symmetry breaking should be considered a general molecular manifestation of autoionization when several decay channels are effectively accessible.

Bibliography

[1] F. Martín, J. Fernández, T. Havermeier, L. Foucar, T. Weber, K. Kreidi, M. Schöffler, L. Schmidt, T. Jahnke, A. L. Landers, O. Jagutzki, A. Czasch, E. Benis, T. Osipov, A. Belkacem, M. H. Prior, H. Schmidt-Böcking, C. L. Cocke, and R. Dörner, "Single photon-induced symmetry breaking H_2 dissociation," *Science*, vol. 315, pp. 629–633, 2007.

[2] D. Dowek, J. Fernández, M. Lebech, J. C. Houver, and F. Martín, "Electron angular distribution in dissociative photoionization of fixed in space D_2 molecules induced by circularly polarized light," *Journal of Physics B: Atomic, Molecular and Optical Physics*, vol. 88, pp. 12009–12015, 2007.

[3] I. Sánchez and F. Martín, "Resonant effects in photoionization of H_2 and D_2," *Journal of Chemical Physics*, vol. 107, pp. 8391–8396, 1997.

[4] I. Sánchez and F. Martín, "Resonant dissociative photoionization of H_2 and D_2," *Physical Review A*, vol. 57, pp. 1006–1017, 1998.

[5] I. Sánchez and F. Martín, "The doubly excited states of the H_2 molecule," *Journal of Chemical Physics*, vol. 106, pp. 7720–7730, 1997.

[6] I. Sánchez and F. Martín, "Doubly excited autoionizing states of the H_2 above the second ionization thershold: The Q_2 resonance series," *Journal of Chemical Physics*, vol. 110, pp. 6702–6713, 1999.

[7] J. Fernández and F. Martín, "Autoinizing $^1\Sigma_u^+$ and $^1\Pi_u$ states of H_2 above the third and fourth ionization thrseshols," *Journal of Physics B: Atomic, Molecular and Optical Physics*, vol. 34, pp. 4141–4153, 2001.

[8] R. J. V. Brunt and L. J. Kieffer, "Angular distribution of protons and deuterons produced by dissociative ionization of H_2 and D_2 near threshold," *Physical Review A*, vol. 2, pp. 1293–1304, 1970.

[9] A. Crowe and J. W. McConkey, "Experimental evidence for new dissociation channels in electron-impact ionization of H_2," *Physical Review Letters*, vol. 31, pp. 192–196, 1973.

[10] A. Crowe and J. W. McConkey, "Dissociative ionization by electron impact. I. protons from H_2," *Journal of Physics B: Atomic, Molecular and Optical Physics*, vol. 6, pp. 2088–2107, 1973.

[11] A. U. Hazi, "Distribution of final states resulting from the autoionization of the $^1\Sigma_g(2p\sigma_u^2)$ states of H_2 and D_2," *The Journal of Chemical Physics*, vol. 60, pp. 4358–4361, 1974.

[12] J. A. D. Stockdale, V. E. Anderson, A. E. Carter, and L. Deleanu, "Dissociative ionization of molecules by electron impact. I. Apparatus and kinetic energy distributions of D^+ ions from D_2," *The Journal of Chemical Physics*, vol. 63, pp. 3886–3897, 1975.

[13] J. L. Gardner and J. A. R. Samson, "Proton kinetic-energy distributions from dissociative photoionization of hydrogen," *Physical Review A*, vol. 12, pp. 1404–1407, 1975.

[14] A. L. Ford, K. K. Docken, and A. Dalgarno, "Cross-sections for photoionization of vibrationally excited molecular-hydrogen," *The Astrophysical Journal*, vol. 195, pp. 788–789, 1975.

[15] S. V. ONeil and W. P. Reinhardt, "Photoionization of molecular hydrogen," *Journal of Physics B: Atomic, Molecular and Optical Physics*, vol. 69, pp. 2126–2142, 1978.

[16] C. Backx, G. R. Wight, and M. J. V. der Wiel, "Oscillator strengths (10-70 eV) for absorption, ionization and dissociation in H_2, HD and D_2, obtained by an electron-ion coincidence method," *Journal of Physics B: Atomic, Molecular and Optical Physics*, vol. 9, pp. 315–331, 1976.

[17] B. van Wingerden, P. E. van der Leeuw, F. J. de Heer, and M. J. van der Wiel, "artial oscillator strengths (25-40 eV) for repulsive states of $D_2(H_2)$," *Journal of Physics B: Atomic, Molecular and Optical Physics*, vol. 12, pp. 1559–1577, 1979.

[18] S. Strathdee and R. Browning, "Dissociative photoionisation of H_2: Proton kinetic energy spectra," *Journal of Physics B: Atomic, Molecular and Optical Physics*, vol. 12, pp. 1789–1804, 1979.

[19] K. Kirby, S. Guberman, and A. Dalgarno, "Resonant dissociative photoionization of H_2," *The Journal of Chemical Physics*, vol. 70, pp. 4635–4639, 1979.

[20] K. Kirby, T. Uzer, A. C. Allison, and A. Dalgarno, "Dissociative photoionization of H_2 at 26.9 and 30.5 eV," *The Journal of Chemical Physics*, vol. 75, pp. 2820–2825, 1981.

[21] S. Kanfer and M. Shapiro, "Theory of the dissociative photoionisation of H_2," *Journal of Physics B: Atomic, Molecular and Optical Physics*, vol. 16, pp. L655–L660, 1983.

[22] M. Landau, R. I. Hall, and F. Pichou, "Proton production from H_2 by electron impact excitation of autoionising states near threshold," *Journal of Physics B: Atomic, Molecular and Optical Physics*, vol. 14, pp. 1509–1524, 1981.

[23] F. Pichou, R. I. Hall, M. Landau, and C. Schermann, "Observation of autoionising states in H_2 and D_2 above 30 eV by electron impact," *Journal of Physics B: Atomic, Molecular and Optical Physics*, vol. 16, pp. 2445–2456, 1983.

[24] K. Ito, P. Lablanquie, P. M. Guyon, and I. Nenner, "Dissociative photoionsation of H_2 at 27-40 eV," *Chemical Physics Letters*, vol. 151, pp. 121–127, 1988.

[25] Y. M. Chung, E.-M. Lee, T. Masuoka, and J. A. R. Samson, "Dissociative photoionization of H_2 from 18 to 124 eV," *The Journal of Chemical Physics*, vol. 99, pp. 885–889, 1993.

[26] Z. X. He, J. N. Cutler, S. H. Southworth, L. R. Hughey, and J. A. R. Samson, "Zero kinetic energy proton and deuteron production from photoionization of H_2 and D_2," *The Journal of Chemical Physics*, vol. 103, pp. 3912–3916, 1995.

[27] C. J. Latimer, K. F. Dunn, N. Kouchi, M. A. McDonald, V. Srigengan, and J. Geddes, "A dissociative photoionization study of the autoionization lifetime of the lowest $^1\Sigma_u$ superexcited state in hydrogen and deuterium," *Journal of Physics B: Atomic, Molecular and Optical Physics*, vol. 26, pp. L595–L600, 1993.

[28] J. Geddes, K. F. Dunn, N. Kouchi, M. A. McDonald, V. Srigengan, and C. J. Latimer, "Isotope effects in the autoionization of superexcited $^1\Sigma_u^+(Q_1)$ states in hydrogen," *Journal of Physics B: Atomic, Molecular and Optical Physics*, vol. 27, pp. 2961–2970, 1994.

[29] C. J. Latimer, J. Geddes, M. A. MacDonald, N. Kouchi, and K. F. Dunn, "The photodissociative ionization of hydrogen and deuterium in the VUV via Π states," *Journal of Physics B: Atomic, Molecular and Optical Physics*, vol. 29, pp. 6113–6121, 1996.

[30] K. Ito, R. I. Hall, and M. Ukai, "Dissociative photoionization of H_2 and D_2 in the energy region of 25-45 eV," *The Journal of Chemical Physics*, vol. 104, pp. 8449–8457, 1996.

[31] C. J. Latimer, K. F. Dunn, F. P. O'Neill, M. A. MacDonald, and N. Kouchi, "Photoionization of hydrogen and deuterium," *The Journal of Chemical Physics*, vol. 102, pp. 722–725, 1995.

[32] J. L. Dehmer and D. Dill, "Photoion angular distributions in dissociative photoionization of H_2 at 304 Å," *Physical Review A*, vol. 18, pp. 164–171, 19778.

[33] F. Martín, "Ionization and dissociation using B-splines: Photoionization of the hydrogen molecule," *Journal of Physics B: Atomic, Molecular and Optical Physics*, vol. 32, pp. R197–R231, 1999.

[34] I. Sánchez and F. Martín, "Multichannel dissociation in resonant photoionization of H_2," *Physical Review letters*, vol. 82, pp. 3775–3778, 1999.

[35] I. Sánchez and F. Martín, "Dissociative photoionization of H_2 and D_2 by (30-37)-eV photons via $^1\Pi_u$ states," *Physical Review A*, vol. 60, pp. 2200–2206, 1999.

[36] T. Aoto, Y. Hikosaka, R. I. Hall, K. Ito, J. Fernández, and F. Martín, "Dissociative photoionization of H_2 at high photon energies: Uncovering new series of doubly excited states," *Chemical Physics Letters*, vol. 389, pp. 145–149, 2004.

[37] J. C. Tully, R. S. Berry, and B. J. Dalton, "Angular distribution of molecular photoelectrons," *Physical Review*, vol. 176, pp. 95–105, 1968.

[38] A. C. Parr, J. E. Hardis, S. H. Southworth, C. S. Feigerle, T. A. Ferrett, D. M. P. Holland, F. M. Quinn, B. R. Dobson, J. B. West, G. V. Marr, and J. L. Dehmer, "Vibrationally resolved photoelectron angular distributions for H_2 in the range 17 eV$\leq h\nu \leq$ 39 eV," *Physical Review A*, vol. 37, pp. 437–443, 1988.

[39] E. D. Poliakoff, J. L. Dehmer, P. M. Dehmer, and A. C. Parr, "Vibrationally resolved photoelectron angular distributions for H_2," *Chemical Physics Letters*, vol. 96, pp. 52–56, 1983.

[40] C. M. Dutta, F. M. Chapman, Jr., and . F. Hayes, "Theoretical studies of photoionization cross sections and angular distributions for the hydrogen molecule," *The Journal of Chemical Physics*, vol. 67, pp. 1904–1908, 1977.

[41] B. Ritchie and B. R. Tambe, "Theoretical studies in photoelectron spectroscopy: Extraction of dynamical and structural information from the angular distributions for oriented or rotationally resolved unoriented molecular samples," *The Journal of Chemical Physics*, vol. 68, pp. 755–761, 1978.

[42] S. Katsumata, Y. Achiba, and K. Kimura, "Angular distribution of HeII photoelectron spectrum of H_2," *Chemical Physics Letters*, vol. 63, pp. 281–282, 1979.

[43] G. V. Marr, R. M. Holmes, and K. Codling, "The angular distribution of photoelectrons from molecular hydrogen as a function of photon energy," *Journal of Physics B: Atomic, Molecular and Optical Physics*, vol. 13, pp. 283–290, 1980.

[44] S. Southworth, W. D. Brewer, C. M. Truesdale, P. H. Kobrin, D. W. Lindle, and D. A. Shirley, "Photoelectron angular distributions from H_2 and D_2," *Journal of Electron Spectroscopy and Related Phenomena*, vol. 26, pp. 43–51, 1982.

[45] J. A. Richards and F. P. Larkins, "Molecular photoionisation calculations with numerical continuum wavefunctions: Application to the hydrogen molecule," *Journal of Physics B: Atomic, Molecular and Optical Physics*, vol. 17, pp. 1015–1026, 1984.

[46] S. Hara, H. Sato, S. Ogata, and N. Tamba, "Vibrationally and rotationally resolved cross sections and angular distributions of photoelectrons from H_2," *Journal of Physics B: Atomic, Molecular and Optical Physics*, vol. 19, pp. 1177–1186, 1986.

[47] A. Lafosse, M. Lebech, J. C. Brenot, P. M. Guyon, L. Spielberger, O. Jagutzki, J. C. Houver, and D. Dowek, "Molecular frame photoelectron angular distributions in dissociative photoionization of H_2 in the region of the Q_1 and Q_2 doubly excited states," *Journal of Physics B: Atomic, Molecular and Optical Physics*, vol. 36, pp. 4683–4702, 2003.

[48] J. H. D. Eland, M. Takahashi, and Y. Hikosaka, "Photoelectron-fragment ion correlations and fixed-molecule photoelectron angular distributions from velocity imaging coincidence experiments," *Faraday Discussions*, vol. 115, pp. 119–126, 2000.

[49] K. Ito, J. Adachi, R. Hall, S. Motoki, E. Shigemasa, K. Soejima, and A. Yagishita, "Photoelectron angular distributions from dissociative photoionization channels of fixed-in-space molecular hydrogen," *Journal of Physics B: Atomic, Molecular and Optical Physics*, vol. 33, pp. 527–533, 2000.

[50] Y. Hikosaka, M. Ahmad, P. Lablanquie, F. Penent, R. I. Hall, and J. H. D. Eland, "Inner valence region of CO^+ studied by threshold photoelectron-photoion coincidence spectroscopy," *Journal of Electron Spectroscopy and Related Phenomena*, vol. 125, pp. 99–106, 2002.

[51] Y. Hikosaka and J. H. D. Eland, "Photoionization into the dissociation continuum of $H_2^+(X^2\Sigma_g^+)$ studied by velocity imaging photoionization coincidence spectroscopy," *Journal of Electron Spectroscopy and Related Phenomena*, vol. 133, pp. 77–86, 2003.

[52] D. Rolles, M. Braune, S. Cvejanović, O. Gener, R. Hentges, S. Korica, B. Langer, T. Lischke, G. Prmper, A. Reinköter, J. Viefhaus, B. Zimmermann, V. McKoy, and U. Becker, "Isotope-induced partial localization of core electrons in the homonuclear molecule N_2," *Nature*, vol. 437, pp. 711–715, 2005.

[53] A. Lafosse, J. C. Brenot, A. V. Golovin, P. M. Guyon, K. Hoejrup, J. C. Houver, M. Lebech, and D. Dowek, "Vector correlations in dissociative photoionization of O_2 in the 20-28 eV range. I. Electron-ion kinetic energy correlations," *The Journal of Chemical Physics*, vol. 114, pp. 6605–6617, 2001.

[54] A. Lafosse, J. C. Brenot, P. M. Guyon, J. C. Houver, A. V. Golovin, M. Lebech, D. Dowek, P. Lin, and R. R. Lucchese, "Vector correlations in dissociative photoionization of O_2 in the 20-28 eV range. II. Polar and azimuthal dependence of the molecular frame photoelectron angular distribution," *The Journal of Chemical Physics*, vol. 117, pp. 8368–8384, 2002.

[55] M. Lebech, J. C. Houver, A. Lafosse, D. Dowek, C. Alcaraz, L. Nahon, R. R. Lucchese, and D. Dowek, "Complete description of linear molecule photoionization achieved by vector correlations using the light of a single circular polarization," *The Journal of Chemical Physics*, vol. 118, pp. 9653–9663, 2003.

[56] M. Lebech, J. C. Houver, D. Dowek, and R. R. Lucchese, "Molecular frame photoelectron emission in the presence of autoionizing resonances," *Physical Review Letters*, vol. 96, p. 073001, 2006.

[57] S. K. Semenov and N. A. Cherepkov, "Photoionization of the H_2 molecule in the random phase approximation," *Journal of Physics B: Atomic, Molecular and Optical Physics*, vol. 36, pp. 1409–1422, 2003.

[58] D. Dowek, M. Lebech, and J. C. Houver, "Molecular frame photoemission in photoionization of H_2 and D_2: The role of dissociation on autoionization of the Q_1 and Q_2 doubly exicited states," *24th International Conference on Photonic Electronic and Atomic Collisions*, 2005.

[59] J. A. R. Samson and R. B. Cairns, "Total absorption cross sections H_2, N_2 and O_2 in region 550-200 Å," *Journal of the Optical Society of America*, vol. 55, pp. 1035–1040, 1965.

[60] L. C. Lee, R. W. Carlson, and D. L. Judge, "The absorption cross sections of H_2 and D_2 from 180 to 780 Å," *Journal Quantitative Spectroscopy and Radiative Transfer*, vol. 16, pp. 873–877, 1976.

[61] J. Samson and G. Haddad, "Total photoabsorption cross section of H_2 from 18 to 113 eV," *Journal of the Optical Society of America B*, vol. 11, pp. 277–279, 1994.

[62] I. Cacelli, R. Moccia, and A. Rizzo, "Gaussian type orbital basis set for the calculation of continuum properties in molecules: The photoionzation cross section of H_2," *The Journal of Chemical Physics*, vol. 98, pp. 8742–8748, 1993.

[63] S. K. Semenov and N. A. Cherepkov, "Generalization of the atomic RPA method for diatomic molecules: H_2 photoionization cross-section calculation," *Chemical Physics Letters*, vol. 291, pp. 375–380, 1998.

[64] H. Bachau, E. Cormier, P. Decleva, J. E. Hansen, and F. Martín, "Applications of B-splines in atomic and molecular physics," *Reports on Progress in Physics*, vol. 64, pp. 1601–1729, 2001.

[65] I. Sánchez and F. Martín, "Origin of unidentified structures in resonant dissociative photoionization of H_2," *Physical Review letters*, vol. 79, pp. 1654–1657, 1997.

[66] N. A. Cherepkov, "Circular dichroism of molecules in the continuous absorption region," *Chemical Physics Letters*, vol. 87, pp. 344–348, 1982.

[67] N. A. Cherepkov and V. V. Kuznetsov, "Fixed-molecule photoelectron angular distributions with defined spin polarisation," *Journal of Physics B: Atomic, Molecular and Optical Physics*, vol. 20, pp. L159–L163, 1987.

[68] G. Schönhense, "Circular dichroism and spin polarization in photoemission from adsorbates and non-magnetic solids," *Physica Scripta*, vol. T31, pp. 255–275, 1990.

[69] T. Jahnke, T. Weber, A. L. Landers, A. Knapp, S. Schössler, J. Nickles, S. Kammer, O. Jagutzki, L. Schmidt, A. Czasch, T. Osipov, E. Arenholz, A. T. Young, R. D. M. no, D. Rolles, F. J. G. de Abajo, C. S. Fadley, M. A. V. Hove, S. K. Semenov, N. A. Cherepkov, J. Rösch, M. H. Prior, H. Schmidt-Böcking, C. L. Cocke, and R. Dörner, "Circular dichroism in K-shell ionization from fixed-in-space CO and N_2 molecules," *Physical Review Letters*, vol. 88, p. 073002, 2002.

[70] K. L. Reid, D. J. Leahy, and R. N. Zare, "Effect of breaking cylindrical symmetry on photoelectron angular distributions resulting from resonance-enhanced two-photon ionization," *The Journal of Chemical Physics*, vol. 95, pp. 1746–1756, 1991.

[71] S. Motoki, J. Adachi, K. Ito, K. Ishii, K. Soejima, A. Yagishita, S. K. Semenov, and N. A. Cherepkov, "Complete photoionization experiment in the region of the $2\sigma_g \rightarrow \sigma_u$ shape resonance of the N_2 molecule," *Journal of Physics B: Atomic, Molecular and Optical Physics*, vol. 35, pp. 3801–3819, 2002.

[72] O. Geßner, Y. Hikosaka, B. Zimmermann, A. Hempelmann, R. R. Lucchese, J. H. D. Eland, P.-M. Guyon, and U. Becker, "$4\sigma^{-1}$ inner valence photoionization dynamics of NO derived from photoelectron-photoion angular correlations," *Physical Review Letters*, vol. 88, p. 193002, 2002.

[73] D. Dowek, M. Lebech, J. Houver, and R. Lucchese, "Circular dichroism in molecular frame photoemission," *Molecular Physics: An International Journal in the Field of Chemical Physics*, vol. 105, pp. 1757–1768, 2007.

[74] R. L. Dubs, S. N. Dixit, and V. McKoy, "Circular dichroism in photoelectron angular distributions from oriented linear molecules," *Physical Review Letters*, vol. 54, pp. 1249–1251, 1985.

[75] R. Dörner, V. Mergel, O. Jagutzki, L. Spielberger, J. Ullrich, R. Moshammer, and H. Schmidt-Böcking, "Cold target recoil ion momentum spectroscopy: a "momentum microscope" to view atomic collision dynamics," *Physics Reports*, vol. 330, pp. 95–192, 2000.

[76] J. Ullrich, R. Moshammer, A. Dorn, R. Dörner, L. P. H. Schmidt, and H. Schmidt-Böcking, "Recoil-ion and electron momentum spectroscopy: reaction-microscopes," *Reports on Progress in Physics*, vol. 66, pp. 1463–1545, 2003.

[77] A. Lafosse, M. Lebech, J. C. Brenot, P. M. Guyon, O. Jagutzki, L. Spielberger, M. Vervloet, J. C. Houver, and D. Dowek, "Vector correlations in dissociative photoionization of diatomic molecules in the VUV range: Strong anisotropies in electron emission from spatially oriented NO molecules," *Physical Review Letters*, vol. 84, pp. 5987–5990, 2000.

[78] T. Weber, *Untersuchung der verschränkten Bewegung freier Elektronenpaare emittiert aus Ein- und Zweizentren Coulomb-Potentialen in Photoabsorptionsprozessen.* PhD thesis, Institut für Kernphysik Johann-Wolfgang-Goethe-Universität Frankfurt am Main, 2003.

[79] O. Jagutzki, V. Mergel, K. Ullmann-Pfleger, L. Spielberger, U. Spillmann, R. Dörner, and H. Schmidt-Böcking, "A broad-application michochannel plate-detector system or photon detection tasks: large area imagining, precise multi-hit timing information and high detection rate," *Nuclear Instrument and Methods in Physics Research Section A: Accelerators, Spectrometers, Detectors and Associated Equipments*, vol. 477, pp. 244–249, 2002.

[80] T. Jahnke, L. Foucar, J. Titze, R. Wallauer, T. Osipov, E. P. Benis, A. Alnaser, O. Jagutzki, W. Arnold, S. K. Semenov, N. A. Cherepkov, L. P. H. Schmidt, A. Czasch, A. Staudte, M. Schöffler, C. L. Cocke, M. H. Prior, H. Schömidt-Bcking, , and R. Dörner, "Vibrationally resolved K-shell photoionization of CO with circularly polarized light," *Physical Review Letters*, vol. 93, p. 083002, 2004.

Chapter 10

Interferences from fast electron emission in molecular photoionization

"Imagination is more important than knowledge."

Albert Einstein

Table of Contents

The work reported in this Chapter has led to the publications [1, 2, 3].

10.1 Introduction

A DISTINGUISHING aspect of the quantum mechanical description of nature is its non-locality. N. Bohr, for example, stressed the undivided wholeness inherent in the quantum mechanical description of nature. Perhaps the best example is the doubly slit experiment, displayed in Fig. (10.1), since its essential feature is a sort of wholeness in which changes made at one slit, located a macroscopic distance from the other, result in overall changes to the interference pattern. The non-locality inherent in a pair of initially correlated particles that become separated by a macroscopic distance has been investigated by Bell [4] and in a variety of experiments [5]. These experiments demonstrate a non-local correlation that cannot be explained with reference to any "local" theory in classical physics.

At the beginning of the nineteenth century, T. Young carried out his famous experiment that unmistakeably demonstrated the wave nature of light [6]. In a recent poll conducted by R. P. Crease [7], Young's double-slit demonstration, applied to the interference of single electrons instead of

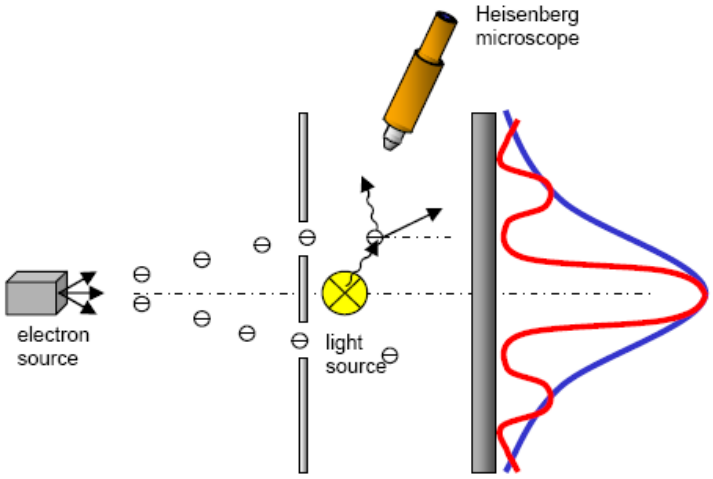

Figure 10.1: Doubly slit experimental set up designed by Feynman [9]. Without any detector, the interference pattern appears at the screen after the electron has gone through both holes (red line). When a detector is placed after the holes, the interference patter disappears (blue line).

light, was devoted the most beautiful experiment in Physics. The double slit scheme, has played a pivotal role in the development of optics and quantum mechanics, and its scope was greatly expanded by Zernike's work and continues to deliver new insights into coherence to the present day [8]. Presented by Feynman as a *gedanken*[1] experiment in his lectures [9], he warned that nobody should try to set these experiment up, and he adds that "the trouble is that the apparatus would have to be made on an impossibly small scale to show the effects we are interested in". Probably Feynman was not aware that a double-slit experiment with electrons had already been carried out in 1961 by Clauss Jönsson [10, 11]. These kind of experiments are of particular importance for interpreting quantum mechanics, specifically the experiments with a single particle at any given time in the apparatus performed by Merli *et al.* [12] and Tonomura *et al.* [13]. More recent works have illuminated the fundamental importance of complementary in which-way experiments [14].

Interpretations based on the double-slit analogy have been used in different contexts. For example, Yudin *et al.* [15] have studied the interference in photoionization of molecules by monochromatic and attosecond x-ray pulses. Using the hydrogen molecule ion as a test case, Linder *et al.* [16] performed a double-slit experiment in the time domain making use of laser pulses (see also [17, 18]). In 1960 Tuan and Gerjuoy[19] formulated the problem of electron transfer in atom-molecule collisions in terms of a separated-atoms picture with interfering electron-transfer amplitudes. A similar description for scattering amplitudes was employed by Deb *et al.* [20] considering the "two-slit" problem of high-velocity electron capture from an oriented hydrogen molecule for which the projectile has to pass close by one of the target nuclei [21]. Abranyos *et al.* [22] connected the wave-particle duality with a two-way interferometer such as Young's double slit experiment. Very recently D. Toffoli *et al.* [23] studied the first-order non dipole terms to the photoelectron angular distribution from randomly oriented nitrogen molecules, finding strong interference effects leading to high-energy oscillations in the dipole and non dipole asymmetry parameters. Eichmann *et al.* [24] reported the first observation of interference effects in the light scattered from two trapped atoms. They presented a version of Young's experiment where the interference of weak laser light scattered from two localized atoms which act as two slits are detected. This experiment resembles the Young's two-slit arrangement with the slits replaced by

[1] A thought experiment (from the German term *Gedankenexperiment*, coined by Hans Christian Ørsted) in the broadest sense is the use of a hypothetical scenario to help us understand the way things actually are.

the two atoms. Swenson *et al.* [25] presented a new interference mechanism, analogous to the double-slit electron scattering, for an ion-atom collision at low energies. An autoionizing states He^{**} formed in a collision He^{+} + He may decay at a time when the collision partners are separated by a distance R. The key observation is that, for a localized source of autoionizing electrons and an attractive potential, there are different paths by which the electrons may merge for the collision with a given laboratory energy E and emission angle θ. Similarly, Barrachina [26] studied the post-collision interaction effect produced on the autoionization of an atom colliding with a molecule. The observed oscillatory pattern was ascribed to the Young's interference effect due to the interaction of the emitted electron with the structured multicenter cluster. Noel and Stroud [27] presented an experiment which is analog to Young's double-slit interferometer using an atomic electron instead of light. They made use a two phase-coherent laser pulses to excite a single electron into a state of the form of a pair of Rydberg wave packets that are initially on opposite sides of the orbit. Couder and Fort [28] studied the oscillatory pattern observed in a droplet bouncing on a vertically vibrated bath. Schouten *et al.* [29] presented an experimental and theoretical study of the optical transmission of a thin metal screen perforated by two sub-wavelength slits, separated by many optical wavelengths.

But, why are we talking about the doubly-slit experiment? A distinguishing feature of molecules, as opposed to atoms, is the existence of multiple atomic centers. When molecules are probed with ions or photons, the presence of these multiple-centers can lead to phenomena quite different from those observed for atoms. In particular, since the atoms that form the H_2 molecule are indistinguishable, their contribution to ionization add coherently and interference effects might be expected in the ionization process. Such electron emission from H_2 may be (or may be not) closely related to Young's two-slit experiment. This idea is not so wild as it might sound, since we are referring to a macroscopic experimental setup by to atomic-size "apparatus" inside it. So, an interesting aspect of molecular ionization by ions and photons is the possibility of interference effects in the ejection of electron and protons. As we have shown throughout the preceding chapters, photoionization of molecular systems is a subject that has received continuous experimental and theoretical attention for more than half a century (see, e.g., Ref. [30] for a review). In particular, the case of homonuclear diatomic molecules has been considered in great detail, since experiments are easier to analyze and the process can be accurately described by theory. Due to limitations in both electron detection efficiency and photon-source intensity, most previous studies have focused on the dominant process, i.e., the production of slow and moderately fast photoelectrons. However, the production of fast electrons offers a very interesting perspective, in particular when the electron wave length λ_e is comparable to the size of the molecule. In this case, the wave nature of the electron should manifest through interferences and diffraction, similarly to what macroscopic waves experience when they meet a macroscopic object, which supposes another example of one of the key postulates of quantum: interference of matter waves, experimentally confirmed by electron diffraction [31, 32]. Quantum superposition lies at the heart of quantum mechanics and gives rise to many of its paradoxes. Superposition of de Broglie matter waves [33] has been observed for massive particles such as electrons [31], atoms and dimers [34], small van der Waals clusters [35], neutrons [36] and fullerens [37] which is the most massive and complex object in which wave behavior has been observed. The typical size of diatomic molecules is given by their internuclear distance, R, and is of the order of 1 Å in most cases (e.g., 0.74 Å for H_2 and 1.06 Å for H_2^+). Therefore, interferences are expected to show up when the photon energy, $h\nu$, is of the order of a hundred eV [$h\nu \sim I_p + h^2/(2m_e\lambda_e^2)$, where I_p is the vertical ionization potential]. These energies correspond to vacuum or extreme ultraviolet radiation, which is currently available in modern synchrotron radiation sources at high enough intensity.

These interference effects were theoretically predicted for ionization by photon impact on H_2 [1, 2, 38, 39, 40, 41], and recently measured indirectly for electron emission by fast multicharged ion impact on the same target [42, 43], where different theoretical models were introduced to

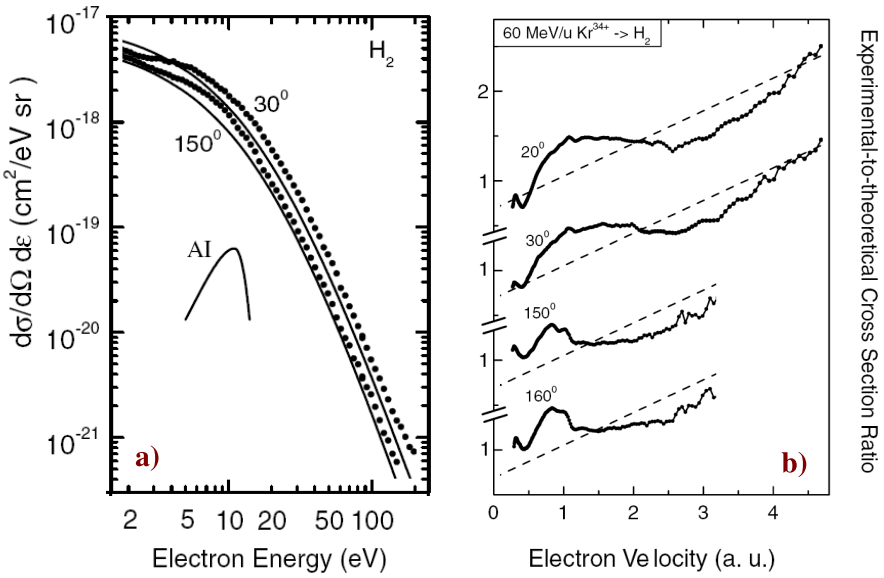

Figure 10.2: Cross sections for electron emission by 60 MeV/*u* Kr^{+34} impacting on H_2, obtained by Stolterfoht *et al.* [42], as a function of the ejected electron energy, panel a). Panel b), experimental-to-theoretical cross section ratios. The electron observation angles are 20°, 30°, 150°, and 160°.

describe these experiments [42, 44, 45, 46, 47, 48]. Pioneering studies by Cohen and Fano [38] showed that the structures observed in the photo-ionization spectra of diatomic molecules were due to interference effects arising from the coherent emission from the two molecular center. From Huygens' point of view one may, for example, regard the two atoms of a diatomic molecules as essentially independent absorbers of light which constitute, in turn, separate sources of photoelectrons (see Fig. (1.5) in the Introduction). Superposition of the emissions from these two sources produces an interference pattern whose properties should depend periodically on the ratio of the internuclear distance to the photoelectron wavelength. This interference may modulate the cross section for photoabsorption by the whole molecule in accordance with its periodicity. So, an indication of the interferences associated with fast electron emission can already be seen in the integral photoionization cross section, which approximately follows the formula [38], $\sigma_A\,[1+\sin(k_eR)/(k_eR)]$, where σ_A is the atomic photoionization cross section (for an effective charge $Z_{\rm eff}$) and $k_e = 2\pi/\lambda_e$ is the electron wave vector. The signature of interferences is, as usual, the oscillatory term within the brackets. However, due to the rapid decrease of σ_A with photon energy, i.e., with k_e, oscillations are usually observed in a rather indirect way, e.g., by dividing the total cross section by a "reasonable" independent estimate of σ_A [42, 49] or by studying the ratio of two rapidly decreasing partial cross sections as in K-shell molecular photoionization [50].

The study of interference effect in diatomic molecules has been renewed by the experimental results obtained by N. Stolterfoht *et al.* [42], where interference effects in the ionization of H_2 molecules by Kr^{34+} ions with a energy of 60 MeV/u were indirectly observed. Left panel of Fig. (10.2) shows the total cross section obtained at the observation angles 30° and 150°, also with the theoretical cross section obtained by means of the continuum-distorted-wave theory [51]. The amplitude of oscillation due to interference, being quite small, was difficult to be observed in such double differential cross section spectrum owing to its steep dependence on the electron energy. To enhance the visibility of the oscillatory structure in the double differentially cross section (DDCS) spectrum of the H_2 target, it was necessary to divide it by twice the DDCS of atomic H (right panel of Fig. (10.2)). As can be seen from this figure, the possible oscillatory pattern is not well defined.

So, to obtain a clearly oscillatory pattern, one need to use different fits and model calculations, with unphysical meanings. Therefore, the shape of the oscillation and its interpretation in terms of theoretical models is subject to the choice of several parameters and depends on the fitting procedure required for normalization (see [49, 52]). What is more, any small systematic error in the measured data may give rise to a spurious structures, which will be otherwise absent if one fully measures the ratio directly. Therefore, are these oscillatory patterns really related with an interference process similar to the doubly slit experiment?

Much clearer evidence of interferences can be obtained from fixed-in-space molecules[2]. This was anticipated in 1969 by Kaplan and Markin [53] and further investigated by Walter and Briggs [39], who used a very simple model in which molecular orbitals were represented by a combination of two atomic orbitals, the continuum electron was described by a plane wave and the nuclei did not move. As we have seen in Chapter 9, experiments with fixed-in-space molecular orientations are now possible since recent imaging techniques allow one to relate the angular pattern of the ejected electrons to the orientation of the molecule at the instant of ionization [54, 55].

During the previous Chapters we have shown the importance of the inclusion of the nuclear motion in the resonant ionization process. At the photon energies considered in this Chapter the molecules also vibrate and this can affect the way electrons are emitted. This is the case, e.g., for very slow ionized electrons, whose motion is strongly affected by the vibronic coupling between the low lying ionization continuum and the Rydberg molecular states [57, 58]. This coupling is the consequence of the ionized electron having a velocity comparable to that of the nuclei; in other words, it results from the breakdown of the Born-Oppenheimer (BO) approximation. However, the faster the electron, the better is the BO approximation. Does it mean that fast electrons and vibrations do not know at all from each other? Since interferences are, in general, very sensitive to the position of the "diffraction" centers, it is worth investigating this question when $\lambda_e \sim R$.

10.2 Linearly polarized light perpendicular to the molecular axis.

As we saw in Chapter 9, the electron angular distribution for different orientations of the polarization vector is a powerful tool to unravel the physical processes responsible for the ionization of atoms and molecules. In this section we present a theoretical study of fast electron emission produced in H_2 and H_2^+ photoionization using linearly polarized light perpendicular to the molecular axis. We focus first our attention on the study of the dissociative photoionization of H_2^+, since one-electron diatomic represents a useful workbench on which to test different approaches and numerical methods. First, because exact numerical solutions of the electronic Schröodinger equation are available through the use of prolate spheroidal coordinates for both bound and continuum states (see Ref. [59], and reference therein). Second, because problems related to the multi-center nature of molecules may be investigated without the complexity introduced by electron correlation in multi-electronic systems. These features make the H_2^+ system an excellent candidate to get a deep insight into dynamical problems involving the ionization continuum as, e.g, photoelectron angular distribution. For the H_2 we will study the dominant non-dissociative process, in which the residual ion, $H_2^+(\upsilon)$, remains in a bound vibrational state. In this case, only the first ionization threshold, the $^2\Sigma_g^+(1s\sigma_g)$ state, contributes to the ionization process since the higher ionization thresholds are all dissociative, although in the theoretical calculation the inclusion of higher ionization thresholds is considered (see Fig. (10.19)).

[2]Note that the experiment results presented in Fig. (10.2) were obtained for the case in which the orientation of the molecule was not determined experimentally at the moment of the collision, which means that electrons were ejected from a randomly distributed H_2 molecules, and the momentum transfer was not controlled.

The dissociative photoionization of the H_2^+ molecule with the polarization vector perpendicular to the molecular axis can be expressed by the following reactions:

$$H_2^+(^2\Sigma_g^+(\upsilon=0))+\hbar\omega \longrightarrow H^+ + H^+ + e^-(\varepsilon\ell\pi_u) \tag{10.1}$$

where ε is the electron energy in the continuum and ℓ its angular momentum at an infinity distance from the molecule. A partial wave expansion with a maximum value of $\ell_{max}=7$ have been taken, which implies four partial waves for the reactions given by Eq. (10.1). Additional calculations have been carried out with higher partial waves ($\ell_{max}=15$), but they have a negligible effect in the photon energy range considered in this work. Since in the case of the H_2^+ molecule, the only final electronic state, $\alpha=1/R$, is purely repulsive , due to the interaction between the residual nuclei (Coulomb explosion), there is no possibility of producing bound vibrational states. On the other hand, the non-dissociative photoionization process in H_2 for the same orientation of the polarization vector can be written as

$$H_2(^1\Sigma_g^+(\upsilon=0))+\hbar\omega \longrightarrow H_2^+(^2\Sigma_g^+(1s\sigma_g)(\upsilon))+e^-(\varepsilon\ell\pi_u). \tag{10.2}$$

In this case, the final continuum state $\Psi^+_{\alpha\upsilon_\alpha\varepsilon lmE}$ (see Eq. (3.88) of Chapter 3) includes contributions from the four lowest ionization thresholds of H_2, $[X^2\Sigma_g^+(1s\sigma_g), {}^2\Sigma_u^+(2p\sigma_u), {}^2\Pi_u(2p\pi_u), {}^2\Sigma_g^+(2s\sigma_g)]$, as well as the corresponding vibrational and dissociative states. Each continuum is described by a partial wave expansion with a maximum value of $\ell_{max}=7$, which implies four partial waves for the preceding reaction given by Eq. (10.1).

As we explained in Chapter 4, the fully differential photoionization cross section $d\sigma_\alpha(\omega)/d\Omega_n d\Omega_e d\varepsilon$, corresponding to leaving the residual molecular ion in a specific electronic state α, is differential in

1. the initial photon energy ω,
2. the photoelectron energy ε,
3. the photoelectron emission direction in the molecular frame $\Omega_e=(\theta_e,\phi_e)$ and
4. the polarization direction with respect to the molecular axis $\Omega_n=(\theta_n,\phi_n)$.

The cross section, restricted to linearly polarized light, given by Eqs. (4.23) and (4.42) of Chapter 4, has been used to obtain the electron angular distribution from fixed-in-space H_2^+ and H_2 molecules at a particular energy sharing between the ejected electron and the remaining ions (3D polar plots in Figs. (10.10) and (10.15)). Integrating that formula over the azimuthal angle ϕ_e leads to the differential cross sections $d\sigma_\alpha/d\Omega_n \sin\theta_e d\theta_e d\varepsilon$ and further integration over the polar angle θ_e gives the cross section for fixed-in-space molecules differential in the energy of the ejected electron $d\sigma_\alpha/d\Omega_n d\varepsilon$ (or, equivalently, differential in the energy of the residual ions υ_α) irrespective of the emission direction. Finally, integration over electron energy leads to the total photoionization cross section for fixed-in-space molecules, $d\sigma_\alpha/d\Omega_n$.

The computational methods to obtain the electronic and vibrational wave functions have been described in Chapters 2 and 3, and are similar to those successfully applied to study a variety of ionization problems in H_2, such as resonant dissociative photoionization, Chapters 6 and 7, and electron and ion impact ionization, Chapter 12. We refer the reader to those chapters for more details, and the references therein. In this Chapter we will study the ionization problem with photon energies up to ~ 500 eV, which means that the ionized electron may posses a quite high energy in the continuum. A fast-electron continuum wave functions present a strong oscillatory behavior, so much care must be taken to reproduce this oscillatory with the enough accuracy, that can only be performed by the used of *B*-spline basis sets. The maximum energy E_{max} of the discretized continuum states will be set by both the *B*-spline order k and the break point spacing, which can be roughly defined as $\Delta r_{max}/N$, where r_{max} is the electronic box size and N the number of *B*-splines. At large distances,

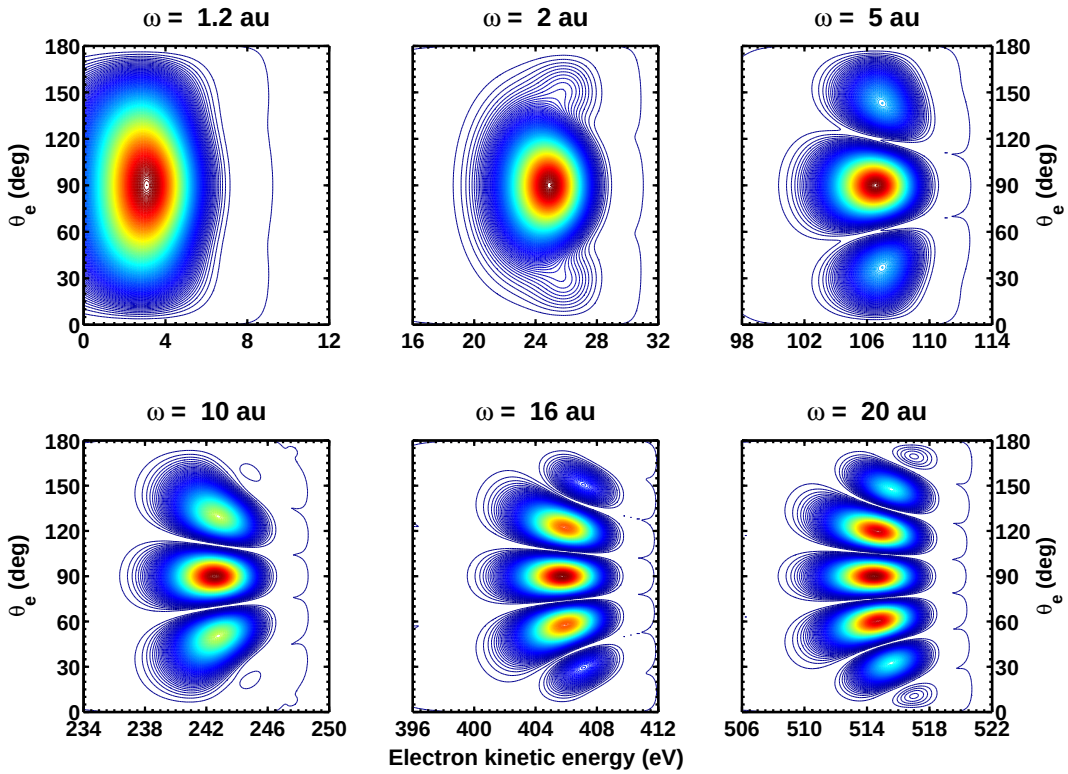

Figure 10.3: Contour plot of the MFPAD of H_2^+ for a perpendicular orientation of the polarization vector with respect to molecular axis, as a function of the electron energy and the polar emission angle of the ionized electron for six photon energies: 1.2 a.u. (32.6 eV), 2 a.u. (54.4 eV), 5 a.u. (136 eV), 10 a.u. (272.1 eV), 16 a.u. (435.4 eV) and 20 a.u. (544.2 eV).

a continuum wave function oscillates with a wavelength $\lambda = 2\pi/\sqrt{2E}$, so the number of B-splines contained in one wavelength has to be large enough to fully reproduce the two sign switches. Due to the high sensitivity of the fully differential cross sections to small deficiencies in the wave functions, convergence has only been achieved by using a much larger number of B-splines (~ 400 per ℓ) within a box of 60 a.u. (which represents a substantially increment in comparison with the basis sets used in Chapters 7 and 9).

Fig. (10.3) shows the contour plot of the MFPADs as a function of the polar emission angle (for $\phi_e = 0$) and the electron kinetic energy, for different initial photon energies, for a perpendicular orientation of the polarization vector with respect to molecular axis. Notice that this figure is equivalent to the momentum distribution in the $k_x - k_z$ plane, since $k_x = \sqrt{2E}\sin\theta_e$ and $k_z = \sqrt{2E}\cos\theta_e$. For low photon energies, < 5 a.u., a broad structure appears centered around $\pi/2$, i.e., perpendicular to the molecular axis. As the photon energy increases, this main structure splits in several narrower structures distributed symmetrically around $\pi/2$. For sufficiently large electron energies, additional structures can be observed, and, as can be seen, the larger the photon energy the larger the relative intensity of the secondary structures, although the central peak is always the dominant one. The energy width of the different structures is ~ 8 eV, which reflects the fact that the energy distribution is approximately characterized by a Frank-Condon factor (see also Section 9.2 of Chapter 9). The appearance of several structures as the photon energy increases is a great different in comparison with the results presented in previous chapters, since one would be expected that, in absence of any resonant state, the electron distribution should follow the same pattern previously obtained for a photon energy of 20 eV(0.74 a.u.) (Section 9.2 of Chapter 9). In order to obtain a clearer image of the electron angular distribution, we can integrate the results presented in Fig. (10.3)

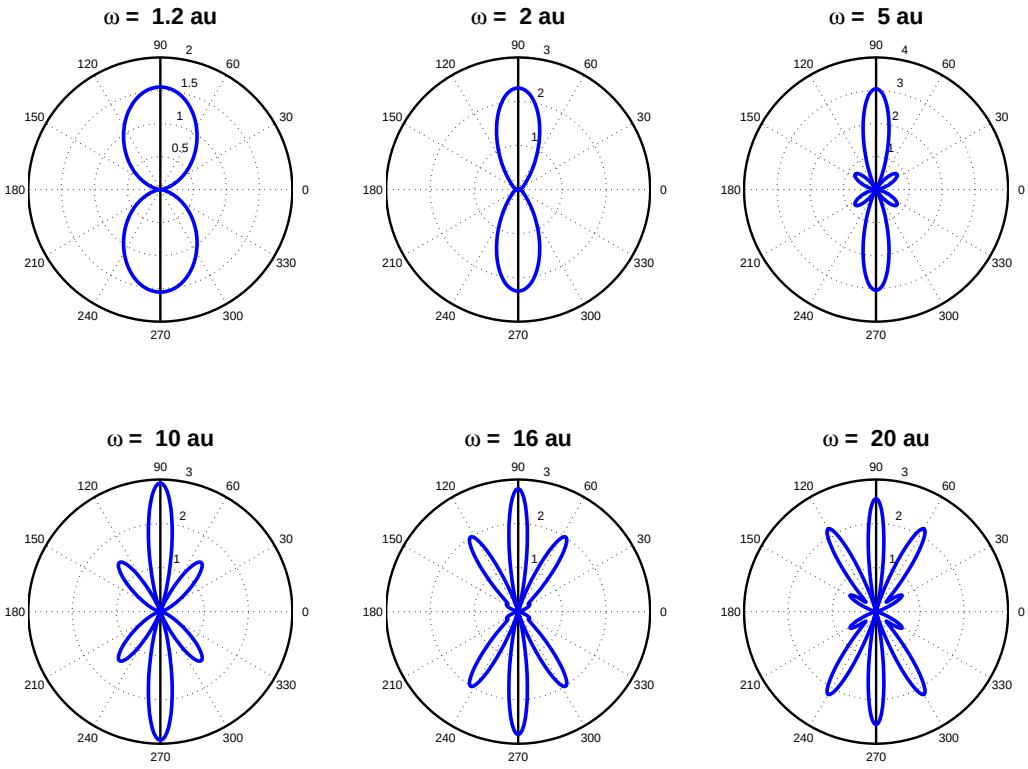

Figure 10.4: MFPADs of H_2^+ integrated over the electron energy, for a perpendicular orientation of the polarization vector at the six indicated photon energies. The results are obtained using Eq. (4.23) of Chapter 4 normalized to the $B_{0,\Pi_u}(\omega)$ coefficient. The molecule axis is situated horizontally.

over the electron energy. These results are displayed in Fig. (10.4) for the same photon energies. For low photon energies, $\lesssim 5$ u.a., the electron distribution shows a characteristic p-wave form where the electron is emitted following the polarization vector, although the angular distribution is stretched as the photon energy increases (compare the results obtained at 1.2 a.u. (32.6 eV) and 2 a.u. (54.5 eV)). As the photon energy increases, additional lobes appear at specific angles: For example for a photon energy of 20 a.u., the electrons are mainly ejected at 90°, 60° and 30°. This fact can be explained as a consequence of a strong mixing between the different partial waves that described the final wave function (see also Fig. (10.9)), but why higher partial waves are more relevant as the photon energy increases? Why the position of the lobes presented in Fig. (10.4) appears at these defined positions?

To answer this fundamental questions, several models and interpretations have been proposed (see for example [38, 39, 60] and references in the introduction of this chapter), here we will analyze some of them. For example, Walter and Briggs (WB) [39, 60] presented a model to explain the different interference effects presented in the electron angular distribution of the H_2^+ molecule. Their model is based on the following assumptions:

1. A LCAO approximation for the initial state, i.e.,

$$\psi_f = \sqrt{\frac{Z^3/\pi}{2(1+S)}}\left[e^{-Zr_a} + e^{-Zr_b}\right], \tag{10.3}$$

where Z is the nuclear charge, S is the overlap integral and r_j gives the distance of the electron to the nucleus $j = a, b$.

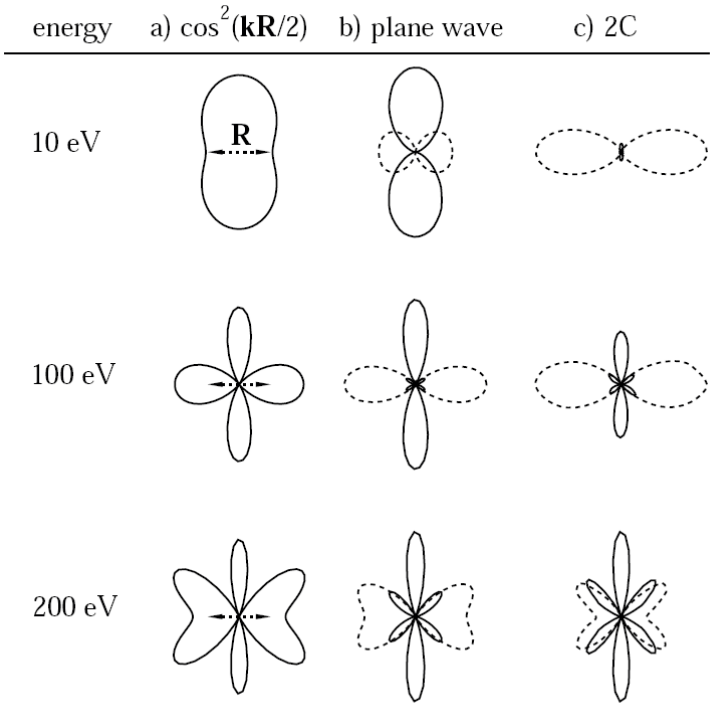

Figure 10.5: H_2^+ electron distribution obtained by J. S. Briggs *et al.* [60], at three different photon energies. **R**, the molecular axis, lies in the horizontal. a) Interference factor only, $\cos^2(\mathbf{k}\cdot\mathbf{R}/2)$. b) Results for a plane wave final state. c) As in b) but for a 2-Coulomb wave final state. Continuous line ε perpendicular to **R**, dashed line parallel to **R**.

2. Final state: a plane wave.

3. Fixed nuclei at a well defined internuclear distance R.

These are, by the way, the same assumptions as in Cohen and Fano model [38]. Making use of the previous considerations, the electron distribution can be approximated by the following formula:

$$I \propto (\mathbf{e}_\mu \cdot \mathbf{k}_e)^2 \cos^2(\mathbf{k}_e \cdot \mathbf{R}/2), \tag{10.4}$$

so, in the united atom limit the electron distribution is proportional to $k^2 \cos\theta_k$, where θ_k is measured relative to the polarization vector, and the electron distribution is modified in the molecular case by the term $\cos^2(\mathbf{k}_e \cdot \mathbf{R}/2)$. The results obtained by these authors are presented in the Fig. (10.5).

As can be seen there exist coincidences between the results presented in this figure (see the results presented by the full lines) and the fully *ab initio* results presented in Fig. (10.4). For example at low photon energies, 1.2 a.u. (32.6 eV) and 2 a.u. (54.5 eV), only one single lobe is obtained and is stretched as the photon energy increases. For higher photon energies additional lobes are obtained at similar angular positions. However much care must be taken in making this comparison, since, for example, one can obtain the same interference patterns if one considers the interference effect produced by two plane waves, which is a very poor description of the ionization process, specially close to the nuclei. On the other hand, when one makes use of the more realistic interference effect produced by two spherical waves, the interference factor $\cos^2(\mathbf{k}\cdot\mathbf{R}/2)$ cannot be obtained. In fact, there exist several physical processes that reproduce similar interference patterns, for example, the interference pattern obtained by an electric dipole [61] or two in-phase dipole antennas [62],

although all of them have to be considered too simple to reproduce the photoionization process since they neglect any molecular effect.

One of the most intuitive models that we can adopt is based on the double-slit[3] analogy (see Fig. (10.1)), as we explain in the introduction of this chapter, however, in the present case, the interplay between the electronic and the nuclear motions, and the molecular character of the electronic states offer a much richer perspective. If we consider the two H atoms that form the molecule as emitters of outgoing waves of momentum k_e associated with the amplitude A_a and A_b (see [63]), respectively, the intensity at large distances will be equal to the coherent sum $I = |A_a + A_b|^2$. If we consider both atoms as identical emission centers, $|A| = |A_a| = |A_a|$ we obtain $I = 2|A|^2 [1 + \cos\delta]^2$, where δ is the relative phase between the amplitudes, whose value is $\delta = k_e \cdot d$, being d the distance between the two atoms and k_e the wave number of the outgoing electron. So the interference pattern follows the equation

$$I(\theta_e) = 2|A|^2 [1 + \cos(k_e \cdot d)]^2, \tag{10.5}$$

with θ_e the electron emission angle. If the ejected electron energy if small, so that $\lambda_e \gg d$ the argument $k_e \cdot d$ takes a very small value, so the intensities takes the value of $2|A|^2$, which means that the cross section should be equal to two times the cross section of the hydrogen atom. So for photon energies less that π^2/d^2 the interference effect should not be present. Making use of the value of the equilibrium internuclear distance of H_2^+ molecule ($R_{eq} = 2.0$ a.u.), for electron energies less than 2.5 a.u. (67 eV) there must be a unique structure centered at 90° with an intensity close to the double value of the H atom cross section. In Fig. (10.3) it can be seen that for energies < 5 a.u. this fact is confirmed. For $\lambda_e \ll d$, the Eq. (10.5) must oscillate between 0 and $2|A|^2$, and vanishes each time $k_e \cdot d$ is half-integral multiple of λ_e/d, and is equal to $2|A|^2$ each time that $k_e \cdot d$ is and integral multiple of λ_e/d. So, the corresponding values of $\cos\theta_e$ gives respectively the directions of minimum an maximum interference. The angular width of the interference structures should be of order λ_e/d, which means that for electrons emitted at high energies the structures should get thinner. As can be see in Fig. (10.3) at a photon energy of 1.2 a.u. the angular width is $\sim 10°$ while for a photon energy of 20 a.u. is 1°, which confirm this fact.

Following with this model, the intensity of the peaks increases as they approach to $\pi/2$, following the relation $[1 + \cos(k_e d \cos\theta_e)]$. The angular position of the maximum value of the peaks is described by the following equation,

$$\cos\theta_e = \frac{2\pi n}{k_e d} = n\frac{hc}{d\sqrt{2m_e c^2 \varepsilon}}, \tag{10.6}$$

being n an integer number[4], c is the speed of light, m_e the electron mass, h the Planck's constant and ε the electron energy. To confirm the analogy between the electron angular distribution in the photoionization process, for a perpendicular orientation of the polarization vector respect to the molecular axis, and the double-slit model, the dependence of the angular position of the peaks (Fig. (10.3)) vs the electron energy can be studied. Nevertheless, we cannot make this study with the first interference order, $n = 0$, since the interference peak always appears at 90°, so we have to study the variation associated to the higher interference peaks. Fig. (10.6) shows the angular position of the maximum of the second order peak, $n = 1$, (see Fig. (10.3)) as a function of its energy position (blue circle-line). The result obtained by Eq. (10.6) is also included (black dashed line), considering

[3] Note that the pure interference effect present in the double-slit experiment predicts all the peaks with the same intensity, and is the diffraction effect between the two holes that is responsible of the dominance of the central peak. So, by the results presented in Fig. (10.4), not only we are observing an interference effects but also diffraction.

[4] Note that the θ_e angle is measured with respect to the z molecule axis, while in the doubly slit result, the emission angle is measured perpendicular to the screen (perpendicular to the molecular axis), so a simply transformation $\Theta = \theta + \pi/2$ recuperates the doubly slit expression.

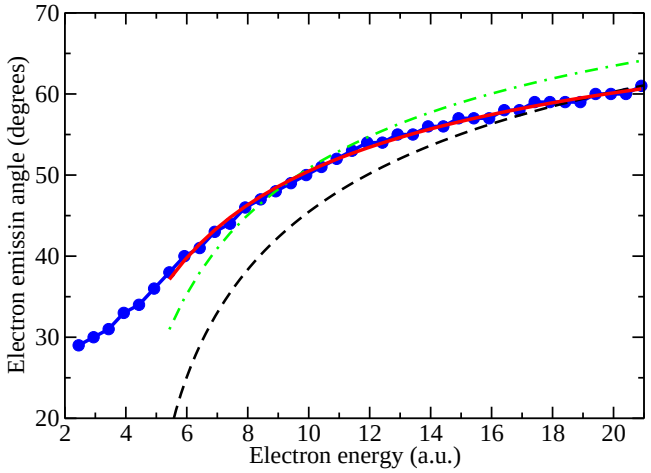

Figure 10.6: Angular position of the second order interference peak of Fig. (10.3) as a function of the electron energy. Blue circular symbols, present results. Black dashed line, result obtained using the double slit model, for an internuclear distance equal to 2.0 a.u. Green dashed and dotted line, fitting curve to double slit model setting the internuclear distance as a free parameter (see text). Full red line, fitting curve to double slit model setting as a free parameters the internuclear distance and an angular shift (see text).

the internuclear distance equal to the equilibrium position. The internuclear distance can be set a as a free parameter, $d = a_0$, in Eq. (10.6) in order to fit our results with the double-slit model. The result of the fit, $a_0 = 2.22$ a.u., is also shown in the figure (green dash-dotted line), and it produces a much more satisfactory result. Finally, the internuclear distance, a_0, and an angular shift[5], a_1, are set as a free parameters:

$$\cos(\theta_e + a_1) = \frac{hc}{a_0\sqrt{2m_e c^2 \varepsilon}}. \tag{10.7}$$

This produces a greater internuclear distance, $a_0 = 2.72$ a.u., and an angular shift $a_1 = 8.5^\circ$, getting and excellent agreement with our results (red line in Fig. (10.6)). Although in Fig. (10.3) can be observed more structures at different angles, which are associated to higher interference order, a similar study cannot be performed since it is necessary to obtain the behavior of these structures at higher photon energies. On the other hand, to assure that these structures correspond to higher interference order, the results for a photon energy of 20 a.u. can be studied in detail. The double-slit model given by Eq. (10.5), predict a separation between the different peaks of 29.7°, for this photon energy. For an internuclear distance equal to $a_0 = 2.22$ a.u., it predicts an angular position of 26.3°, and making use of Eq. (10.7), with the previously obtained parameters, an angular position of 30.0°. It can be directly checked from Fig. (10.3) that the position of the different peaks (interference orders) totally agree with the predicted values. Therefore, the double-slit model predicts the position and the intensity of the different structures present in the MFPAD, which confirms the fact that each nucleus can be considered as a source of electrons, i.e., we can consider the ionization process as a process in which the electron is emitted from two equivalent centers.

If Fig. (10.3) is integrated over the electron energy, the differential cross section as a function of the photon energy and the polar emission angle is obtained. Fig. (10.7) shows the results for a perpendicular orientation of the polarization vector[6], respectively. As can be seen in this figure, the electron is mainly emitted at 90° with respect to the molecule axis, which means that photoelectrons are ionized in the direction of the field. As the photon energy increases, the electrons can be ejected

[5]This variable can be assigned to the incoming photon.

[6]The displayed results are obtained by Eq. (4.23) of Chapter 4 renormalizing the results to the $B_0(\omega)$ coefficient.

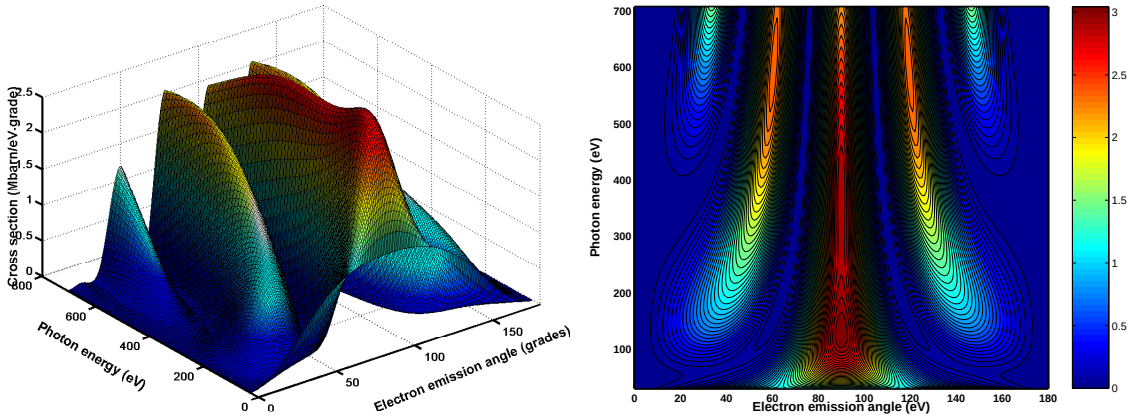

Figure 10.7: Differential cross section (left panel) and contour plot of this figure (right panel), as a function of the electron emission angle and the initial photon energy, for a perpendicular orientation of the polarization vector. All results normalized to the $B_0(\omega)$ coefficient.

at different angles from 90°, which corresponds with higher order interference structures observed in Fig. (10.3). In order to highlight the results obtained in Fig. (10.7), the cross section can be studied as function of the photon energy, selecting a specific electron polar emission angle. Fig. (10.8) displays the results for a perpendicular (black line) and a parallel orientation (red line) of the polarization vector, for the polar emission angles, 0°, 15°, 30°, 60°, 75° and 90° (the cross sections are normalized to the $B_0(\omega)$ coefficient, other wise the oscillatory patters are hidden due to the exponential decay of the total cross section, see also Fig. (10.17)). *n* represents the interference order responsible of the different structures presented in the cross section for a perpendicular orientation of the polarization vector. Note that for $\theta_e = 0°$ and $\theta_e = 90°$ the cross section for a perpendicular and parallel orientation of the polarization vector, is zero, respectively. For $\theta_e = 15°$, the cross section for the perpendicular orientation, takes a very small value due to symmetry restrictions, while for the parallel case the cross section presents a characteristic oscillatory pattern. As the polar emission angle approaches the magic angle, $45° < \theta_e < 60°$, the results for both orientation present similar behavior. For $\theta_e = 75°$ the cross section for the parallel orientation decreases its value without any oscillatory structure, while the result for the perpendicular case is dominant, presenting a monotonic pattern. For the perpendicular case, each structure (or hump) can be directly related to an interference order, *n*, just comparing these results with Fig. (10.7). The main conclusion that can be obtained from the last panel it that for $\theta_e = 90°$, the cross section for the perpendicular orientation presents a very simple behavior, increasing its value from a photon energy of 0 to 4 eV, and then getting a constant value over all the photon energy range; on the hand, for $\theta_e = 0°$, the cross section for the parallel orientation, abruptly increases from 0 to 2 eV, and then presents a strong oscillatory pattern. We previously showed in Figs. (10.4), (10.3) and (10.3) that the double-slit patterns are clearly manifested, but when the cross section is observed as a function of the photon energy for a defined value of the polar emission angle at which the cross section is maximum[7], this pattern disappears. So, several conclusion can be directly obtained: (i) the double-slit interference patterns for the perpendicular orientation can only be observed when the electron angular distribution can be resolved (see Fig. (10.4), (10.3) and (10.3)): (ii), the interference effect disappears when the cross section is calculated at the electron polar angle that maximizes it (i.e., in the total cross section).

These conclusions have a deep implications in the different previous theoretical and experimental results explained in the introduction of this Chapter. For example, are the predicted undulations in

[7]Note that the results for $\theta_e = 90°$ gives the main contribution to the total cross section, since the integration over the polar angle is proportional to $\sin\theta_e$.

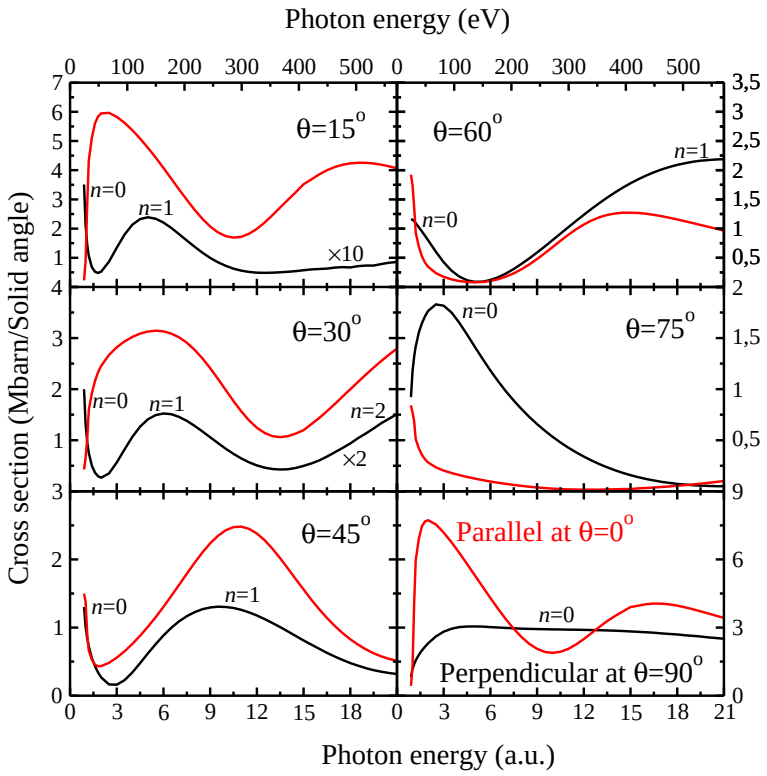

Figure 10.8: Differential cross section integrated over the electron energy, for several electron emission angles. Black full line, results for a perpendicular orientation of the polarization vector with respect to the molecular axis. Red dotted line, results for the parallel case. The results are normalized to the $B_0(\omega)$ coefficient. *n* represents the interference order responsible of the different structures presented in the cross section for a perpendicular orientation of the polarization vector.

the ionization spectra of the H_2^+, described by Cohen and Fano [38], a direct consequence of a double-slit effect in the photoionization process? What is the origin of oscillatory patterns obtained by Stolterfoht *et al.* [42] in cross section?. And, what is more important, why do the results presented in Fig. (10.8) for the parallel orientation not follow the same patters as in the perpendicular case? We should wait until the next chapter in order to answer all these questions.

To confirm the fact that the interference patterns cannot be observed if the electron angular distribution is not resolved, we present in Fig. (10.9) the differential cross section integrated over the electron emission angles, θ_e and ϕ_e, for a perpendicular orientation of the polarization vector. On the right panel, we present the kinetic energy distribution for several photon energies including the partial wave decomposition. It can be seen that the behavior of the cross section follows a characteristic FC pattern, although the contribution of each partial wave changes as the photon energy increases. For example, the third partial wave, $\ell = 5$ takes relevance for photon energies $\geqslant$ 6 a.u. and dominates the process for $\omega = 20$ a.u. So, although the different partial waves present a complicated behavior as a function of the photon energy, the total cross section does not manifest this fact.

To complete this section we present the results obtained for the non-dissociative ionization of the H_2 molecule. Fig. (10.10) presents the results for H_2^+ (upper panel) and H_2 (lower panel), for a perpendicular orientation of the polarization vector (Π_u symmetry) to the molecular axis. Panels (a) show the integrated (in electron energy and solid angle) cross section as a function of the photon energy. At a given photon energy, the electron wave length λ_e depends on the energy sharing between the ionized electron and the residual ion: $W_{g\nu} + h\nu = W_{\upsilon_\alpha} + h^2/(2m_e\lambda_e^2)$. Panels

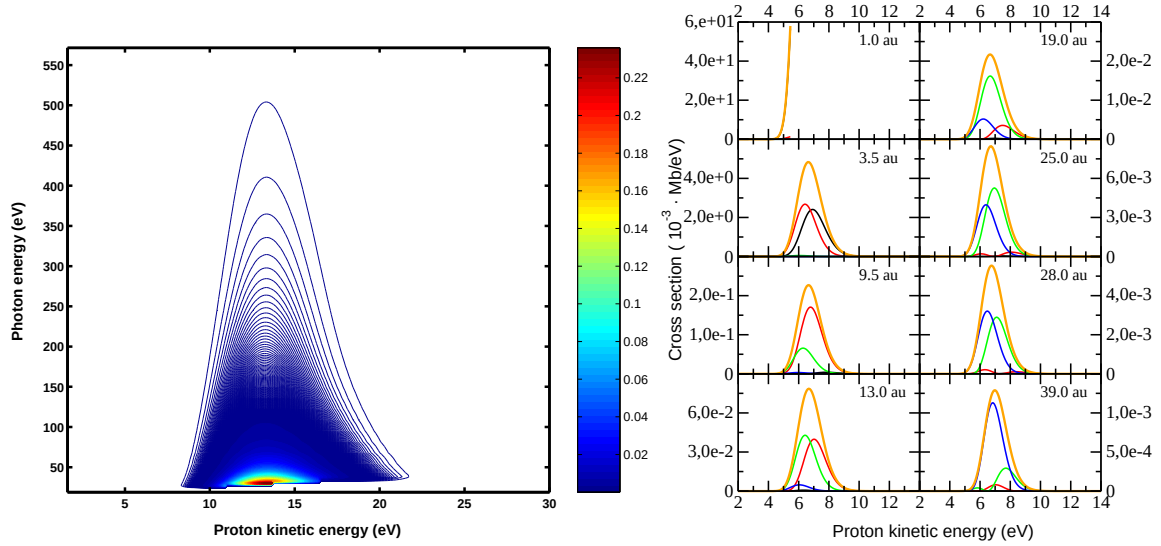

Figure 10.9: (Left panel) Cross section as a function of the photon energy and the proton kinetic energy. (Right panel) Proton kinetic distribution. Black line: partial wave $\ell = 1$; Red line: $\ell = 3$; Green line: $\ell = 5$; Blue line: $\ell = 7$; Orange line: total cross section. Both results obtained for a perpendicular orientation of the polarization vector with respect to the molecular axis

(b) in Fig. (10.10) shows the differential (in λ_e or equivalently in the energy of H_2^+ -for H_2- and H^+ -for H_2^+-) cross sections and the contribution of the different partial waves for the photon energies indicated by vertical dashed lines in panels (a). For both molecules, the angular distributions present a dominant lobe along the polarization direction accompanied by smaller lobes on each side. For the H_2 case, we see that the smaller the residual vibration state the bigger the number of lobes, since the lower the vibrational state the bigger the final electron energy. So not only the interfering patterns are obtained as the photon energy increases (see Fig. (10.4)), but for a fixed photon energy this patterns present a strong dependence on the final electron energy. The comparison between both molecular systems confirms the fact that the coherent emission from the two nuclei that compounds the molecules is a fact, although for the H_2 molecule we are dealing with a bielectronic system.

10.3 Linearly polarized light parallel to the molecular axis.

As we discussed in the previous section, the cross section as a function of the photon energy for different polar emission angles, Fig. (10.8), presents different patterns in comparison with the results obtained for a perpendicular orientation of the polarization vector. In this section we will try to answer the question that were previously presented.

For a parallel orientation of the polarization vector with respect to the molecular axis, only the Σ_u^+ continuum is accessible, so the dissociative photoionization of the H_2^+ molecule can be expressed as:

$$H_2^+(^2\Sigma_g^+) + \hbar\omega \longrightarrow H^+ + H^+ + e^-(\varepsilon\ell\sigma_u), \tag{10.8}$$

and the non-dissociative photoionization process of H_2 can be written as

$$H_2(^1\Sigma_g^+) + \hbar\omega \longrightarrow H_2^+(^2\Sigma_g^+(1s\sigma_g)(\upsilon)) + e^-(\varepsilon\ell\sigma_u). \tag{10.9}$$

In both cases the partial wave expansion that describes the final wave function is identical to the one described for a perpendicular orientation of the polarization vector, so the possible differences

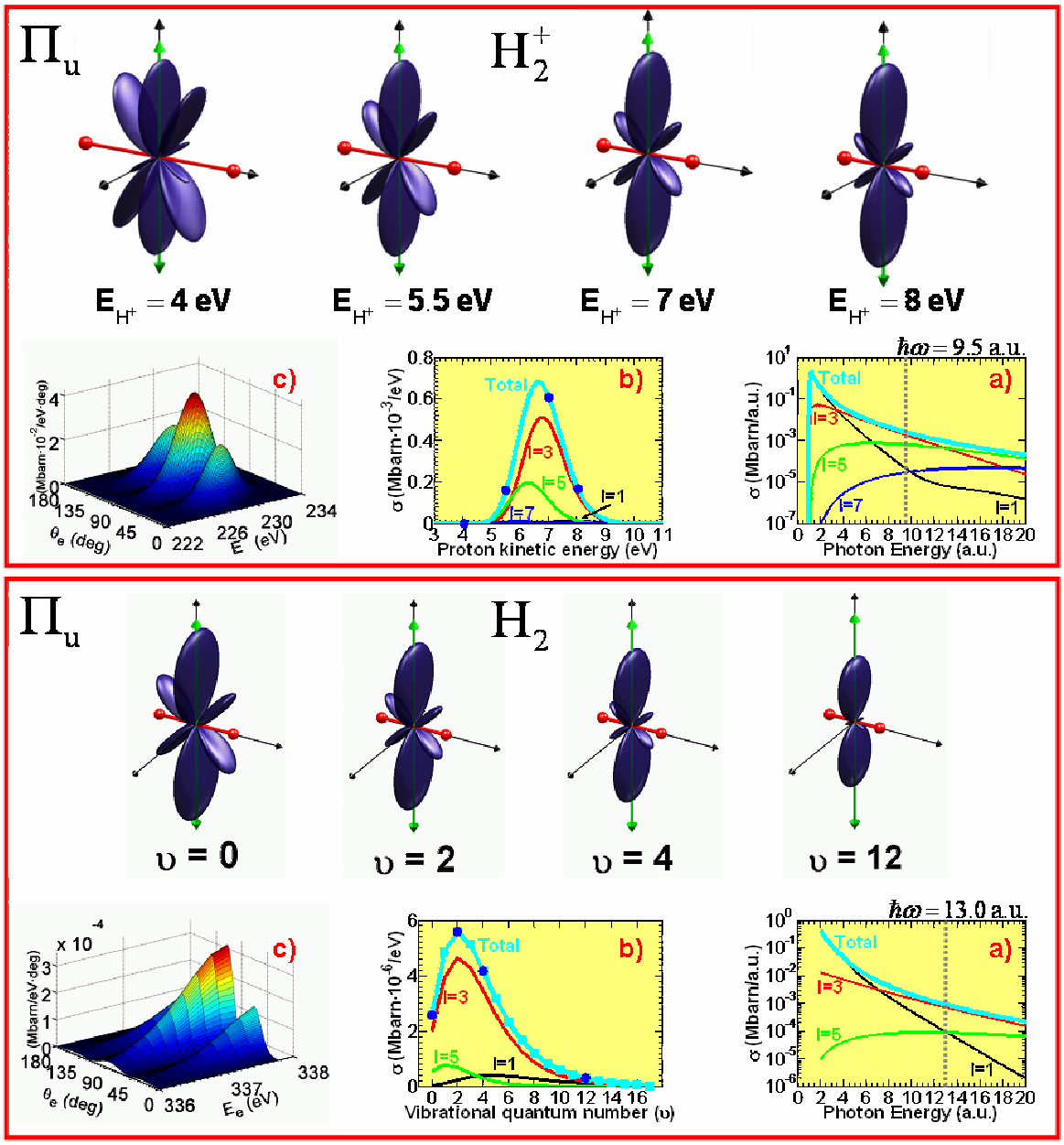

Figure 10.10: Photoionization of H_2^+ and non-dissociative photoionization of the H_2 molecule using linearly polarized light perpendicular to the molecular axis. (a) Integrated photoionization cross section $d\sigma_\alpha/d\Omega_n$ as a function of photon energy; contributions from different partial waves are indicated with different colors; the vertical dashed line indicates a photon energy of 9.5 a.u. ($\sim$ 258 eV) for the H_2^+ molecule and 13 a.u. ($\sim$ 350 eV) for the H_2 molecule. For the chosen photon energies, panel (b) shows the kinetic energy for the H_2^+ molecule and the vibrational distribution of the remaining $H_2^+(\upsilon)$ ions for the H_2 molecule, and the contribution of the different partial waves, and panel (c) shows the differential photoionization cross sections $d\sigma_\alpha/d\Omega_n \sin\theta_e d\theta_e d\varepsilon$. The 3D plots show the fully differential electron angular distribution, $d\sigma_\alpha/d\Omega_n d\Omega_e d\varepsilon$, for the chosen photon energies and four selected energy sharings [indicated by blue circles in panel (b)]. For a better visualization, all 3D plots have been normalized to 1 at the maximum of the electron angular distribution.

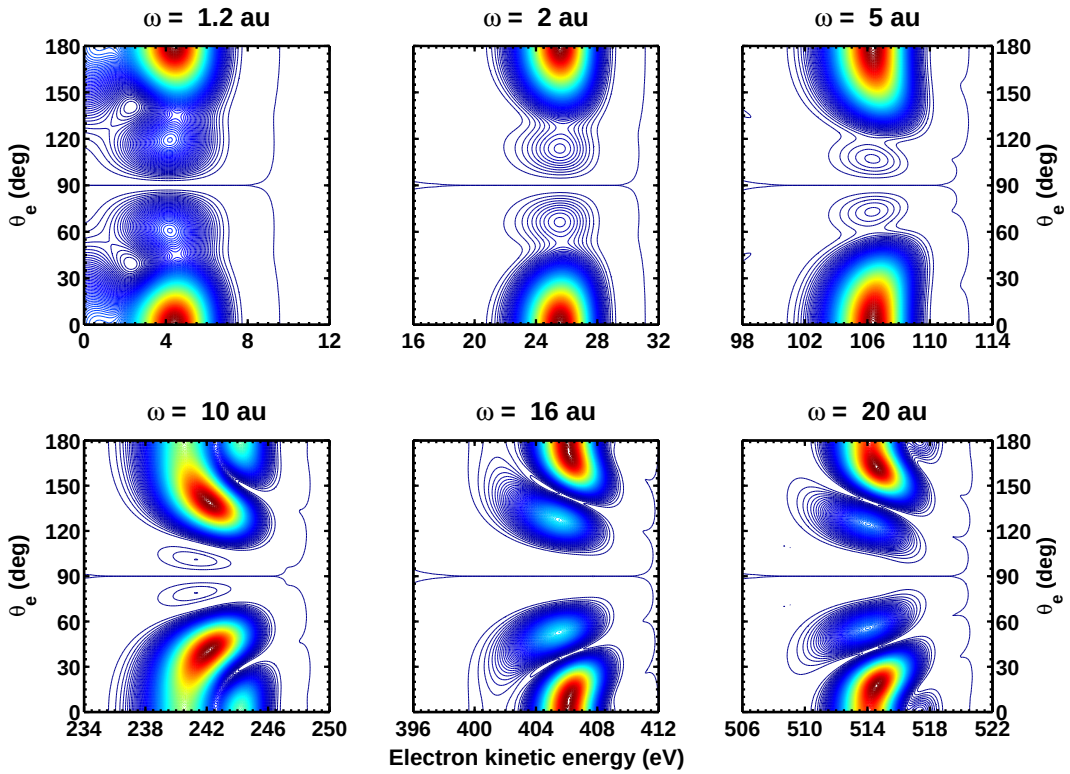

Figure 10.11: Same as Fig. (10.3) but using instead linearly polarized light parallel to the molecular axis.

between the results obtained for a parallel and a perpendicular orientation of the polarization vector cannot be attributed to differences in the description of the final wave functions.

Fig. (10.11) displays the contour plot of the MFPADs between the polar emission angle and the electron kinetic energy, for several initial photon energies, for a parallel orientation of the polarization vector with respect to molecular axis. As can be directly seen in comparison with the results presented in Fig. (10.7), the angular dependence of the difference structures and the evolution of them as a function of the photon energy is completely different. Now the electron is ejected mainly at zero degrees for low photon energies, which is natural since it follows the direction of the field, but, as the photon energy increases, the main structure evolves to higher emission angles (see for example results for a photon energy of 10 a.u., where the electron emission occurs at an angle $\sim 45^{\circ}$) and a second structure appears close to 0°. As we increase the photon energy the main structure approaches an emission angle close to $\sim 60^{\circ}$ decreasing its intensity, while secondary structures begin to grow evolving in the same manner as a function of the photon energy as the first structure did. Although the number of peaks increases with the photon energy, and the energy width of them is of the order $\sim$ 8 eV, neither their angular position nor their evolution with the photon energy agree with the previous results obtained for a perpendicular orientation of the polarization vector (Fig. (10.7)). Integrating over the final electron energy the results presented in Fig. (10.11) we obtained the MFPAD as function of the initial photon energy. Fig. (10.12) displays the electron angular distribution for $\phi_e = 0$. For low photon energies $<$ 10 a.u. the electron is emitted following the direction of the field, consistent with the results obtained for a photon energy of 20 eV(0.74 a.u.) (Section 9.2 of Chapter 9). Note the presence of very small structures oriented 60° for a photon energy equal to 1.2 a.u. (32.6 eV). For a photon energy of 10 a.u. the electron angular distribution changes drastically its patterns: now the electron is emitted with the same probability at 0° and 45°. As the energy increases more, the additional lobes at 45° decrease their intensity and shift to 60°.

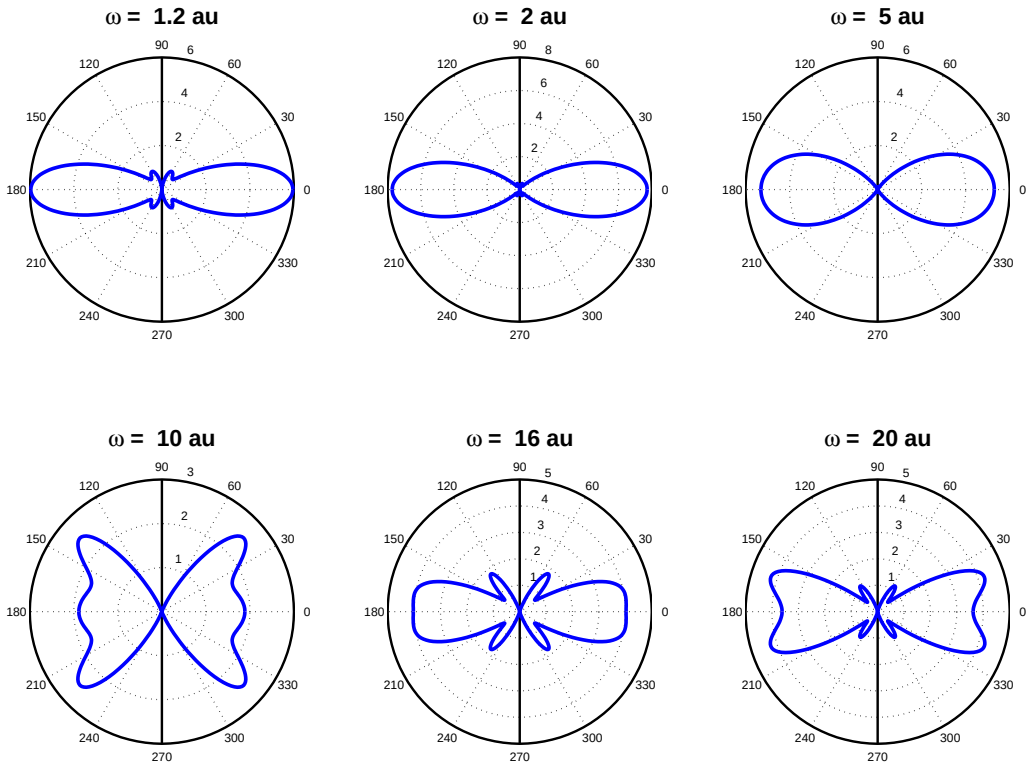

Figure 10.12: Same as Fig. (10.4) but using instead linearly polarized light parallel to the molecular axis. The molecule axis is situated vertically.

Therefore, just looking at the results presented in this figure, one can conclude that the MFPAD for a parallel orientation of the polarization vector presents a complete different behavior in comparison with the results obtained for a perpendicular orientation case (see Fig. (10.4)), and therefore, the physical process that describes the different structures in the MFPAD could be of a completely different nature.

Fig. (10.13) shows the doubly differential cross section as a function of the electron energy and the initial photon energy, similar to the results presented in Fig. (10.7) for a perpendicular orientation of the polarization vector. Now, the electron is mainly emitted parallel to the polarization direction (0° and 180°), and at these specific angles is where the cross section presets oscillatory patterns, i.e., the differential cross section presents a first maximum for low photon energies, a minimum at ~ 11 a.u. (~ 300 eV) and a second maximum at ~ 17 a.u. (~ 460 eV). As can be seen in the right panel of this figure, the maxima and the minimum run parallel as the the polar emission angle varies from 0 to 90°. The differences with the results presented in Fig. (10.7) are much more than evident. Fig (10.8) displays the cross section as a function of the photon energy for selected polar emission angles. In this case, the interference pattern is clearly observed as a function of the initial photon energy (the cross section takes its maximum value for $\theta_e = 0°$). So, when the interference effects are study in the the total cross for randomly distributed molecules, as we will see in the end of this chapter, the observed oscillations are due to the interferences coming from the Σ_u^+ continuum and not from the Π_u one, i.e., the double-slit interference is not responsible of any structure.

In Fig. (10.14) we present the double differential cross section as a function of the final proton kinetic energy and the initial photon energy (left panel) and the kinetic energy distribution for several initial photon energies (right panel). In this case, the profile in the cross section is quite different from that obtained previously for a perpendicular orientation of the polarization vector (see Fig. (10.9)). Now, the cross section presents a broad structure centered at a proton energy of

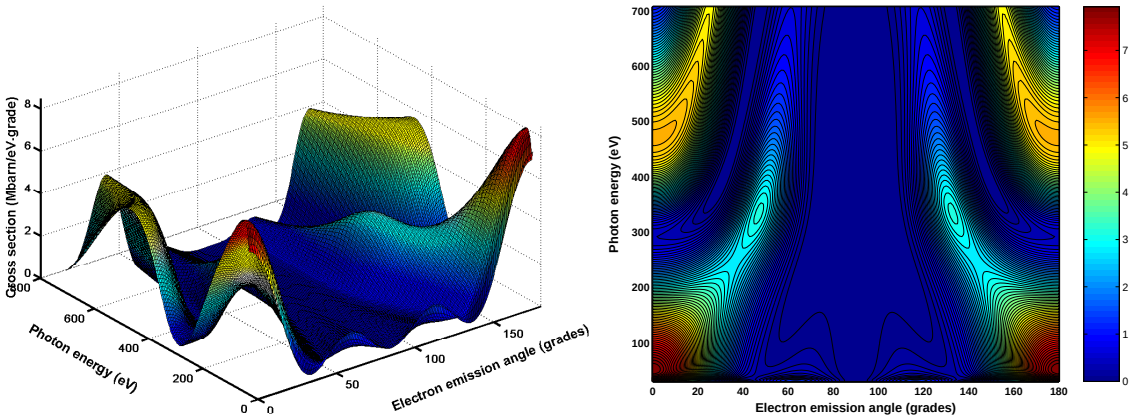

Figure 10.13: Same as Fig. (10.7) but using instead linearly polarized light parallel to the molecular axis.

~ 12 eV that extends for a photon energy from 0 to ~ 150 eV (~ 5.5 a.u.) and in this case, the profile does not resemble a FC pattern. In the right panel of this figure, one can see that the contribution of each partial wave that completely differs from the results obtained for a perpendicular transition (see right panel of Fig. (10.9)). For the parallel case, the cross section is mainly described by the contribution of the first two partial waves $\ell = 1$ and $\ell = 3$ for all the considered photon energies (except at very high photon energy, 30 and 39 a.u.).

Fig. (10.15) displays the the results obtained in the parallel Σ_u^+ arrangement devoted to the H_2^+ molecule (the upper panel) and H_2 molecule (the lower panel). For this arrangement, the different partial waves exhibit pronounced minima at very specific photon energies (panels (a)). These minima lead to shallow dips in the total photoionization cross section. Similar minima have also been found in calculations in which the position of the nuclei is frozen [1, 41, 64]. Inclusion of the nuclear motion barely affects the positions of these minima, but it does change their shape. From the results shown in panels (a) of Fig. (10.15), we find that, for each partial wave, the first minimum appears when the electron wave vector satisfies $k_e R \sim \ell\pi$. According to this simple formula, the $\ell = 1$ minimum should appear at $h\nu \sim 3.1$ a.u. for H_2 and ~ 2.3 a.u. for H_2^+, and the $\ell = 3$ minimum at $\sim$ 23 a.u. and ~ 12 a.u., respectively. These values are in reasonable agreement with the actual ones in the figures. For H_2^+, the $\ell = 1$ minimum appears at such low photon energies that the $\ell = 3$ partial wave unexpectedly dominates in that region (in contrast with the $\ell = 1$ dominance observed in most diatomic molecules at low photon energies, e.g., in H_2). The $k_e R = \ell\pi$ formula describes momentum quantization of an electron moving inside a one-dimensional box of length R. This suggests that the observed minima can be related to electron ***confinement*** at a given internuclear distance. For the k_e values satisfying this condition, the electron continuum wave functions approximately reproduce the nodal structure of the bound $n\ell\sigma_u$ molecular orbitals in the internuclear region (i.e., $2p\sigma_u$, $4f\sigma_u$, ... for $\ell = 1, 3, \ldots$, respectively), as is displayed in Fig. (10.16). For the perpendicular Π_u arrangement (panels (a) in of Figs. (10.10)), a similar effect is not observed.

Fig. (10.16) shows a comparison between bound molecular orbitals of H_2 and H_2^+ and approximated continuum wave functions (particle in a box) in the form $\sin((\ell/2)(2\pi z/R_{eq})$ for the values of k associated with a minimum in the integrated Σ_u cross sections (Fig. (10.15)). The comparison is made along the internuclear axis, the z axis. It can be seen that these approximated continuum wave function looks like a bound molecular orbital in the region between the nuclei. This means that, for these precise values of k, the electron feels as being in a bound state. Hence there is a suppression of ionization due to the transient confinement of the electron between the nuclei. Also we present the real continuum wave function that include the inter-channel coupling.

As in Fig. (10.10), panels (b) in Fig. (10.15) show the differential (in λ_e or equivalently in

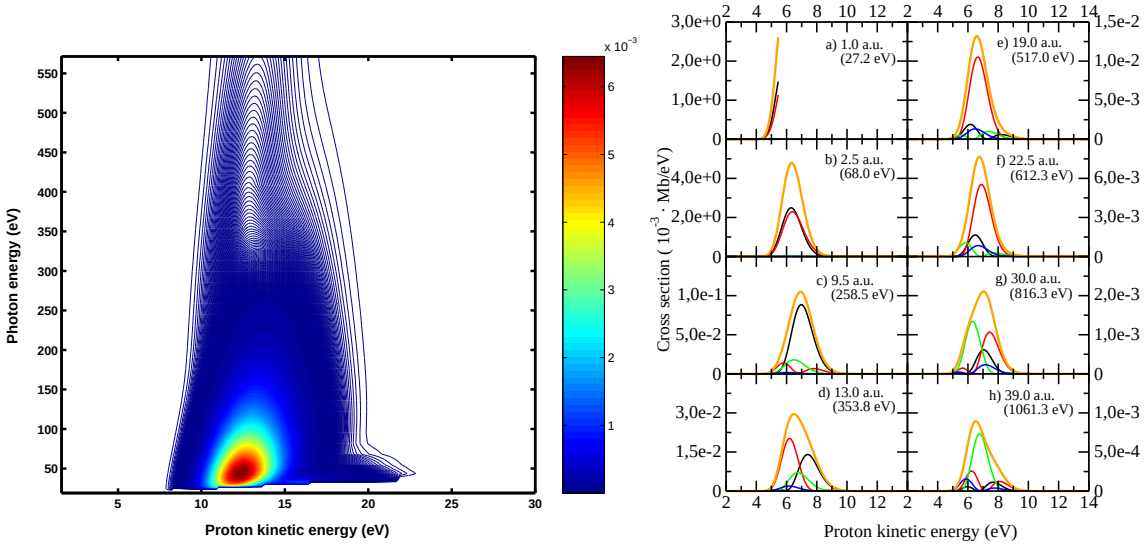

Figure 10.14: Same as Fig. (10.9) but using instead linearly polarized light parallel to the molecular axis.

the energy of H_2^+ -for H_2- and H^+ -for H_2^+-) cross sections and the contribution of the different partial waves for the photon energies indicated by vertical dashed lines in panels (a). The chosen photon energies are close to one of the relevant minima in the partial cross sections (i.e., where confinement is expected to occur). It can be seen that the relative contributions of the different partial waves depend on the energy of the ejected electron (i.e., on the energy of the H_2^+ and H^+ nuclear fragments). This implies very different angular distributions for different energy sharing (see panel (c) and the three dimensional polar plots shown in Figs. (10.10) and (10.15)). In the case of H_2 photoionization with polarized light parallel to the molecular axis (Fig. (10.15)), the angular distribution of the fastest electrons (i.e., of those electrons associated with a residual H_2^+ ion in a low vibrational state) exhibits an almost perfect f shape ($\ell = 3$). As we consider slower and slower electrons (i.e., H_2^+ in higher vibrational states), the $\ell = 1$ and $\ell = 3$ waves interfere leading to a complicated angular pattern, until $\ell = 1$ dominates and an almost pure p wave is found. These variations in the electron angular distribution are also responsible for the non Franck-Condon vibrational distribution of the residual H_2^+ ion (a Franck-Condon distribution decreases much faster with v). Similar strong variations have been obtained in this parallel arrangement for H_2 dissociative ionization (not shown) and for H_2^+ (top of Fig. (10.15)).

As we discussed in the previous section, several simple images can be invoked to understand the observed features. All of them are based on a one-to-one mapping between the energy of the residual ion and R. This is a reasonable assumption in the case of H_2^+ photoionization, since electron emission is followed by the Coulomb explosion of the remaining protons. Assuming that the protons behave classically, it is then possible to relate the observed proton kinetic energy to the R value at which Coulomb explosion takes place, $2E_{H^+} \sim 1/R$ [54]. This is usually called *the reflection approximation*. Thus the analysis of the electron angular distribution for different kinetic energies of the ejected electron (or different energies of the residual protons) at a fixed photon energy allows one to visualize the variation of the interference patterns as the molecule vibrates. Such temporal pictures can be obtained by measuring in coincidence the momentum of all ejected particles [54, 55]. In the context of this approximation, the positions of all the lobes observed in the perpendicular orientation follow, to a very good approximation, Young's formula $R \sin\theta_e = n\lambda_e$, $n = 1, 2, \ldots$. Similarly, for the parallel orientation, electron confinement is only possible when the vibrating H_2^+ is ionized at a value of the internuclear distance compatible with the condition $k_e R = \ell\pi$. Indeed, Fig. (10.15)

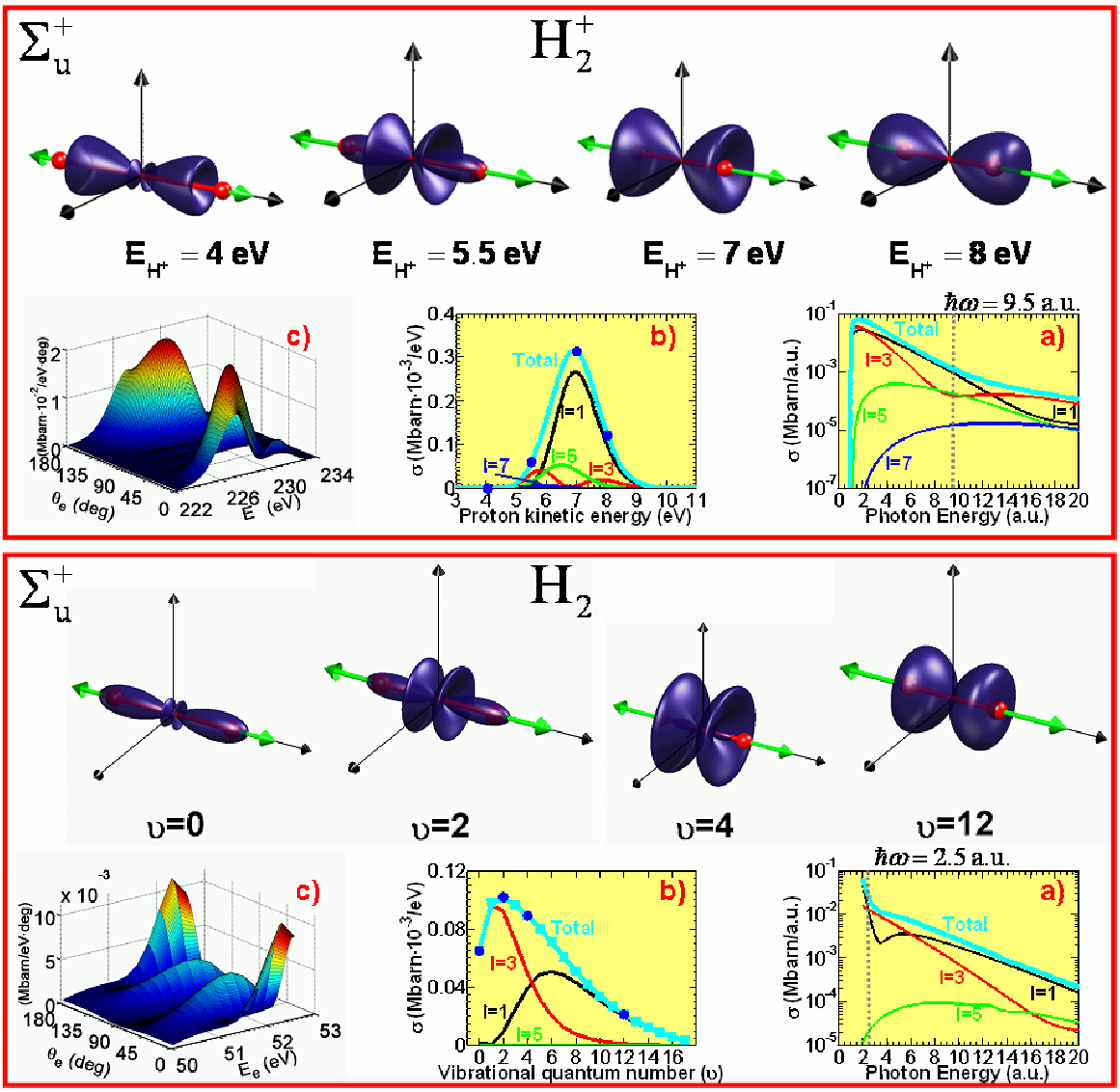

Figure 10.15: Photoionization of H_2^+ and non-dissociative photoionization of the H_2 molecule using linearly polarized light parallel (Σ_u^+ symmetry) to the molecular axis. Conventions as in Fig. (10.10), except that the chosen photon energy is now 9.5 a.u. ($\sim$ 250 eV) for H_2^+ and 2.5 a.u. ($\sim$ 68 eV) for H_2.

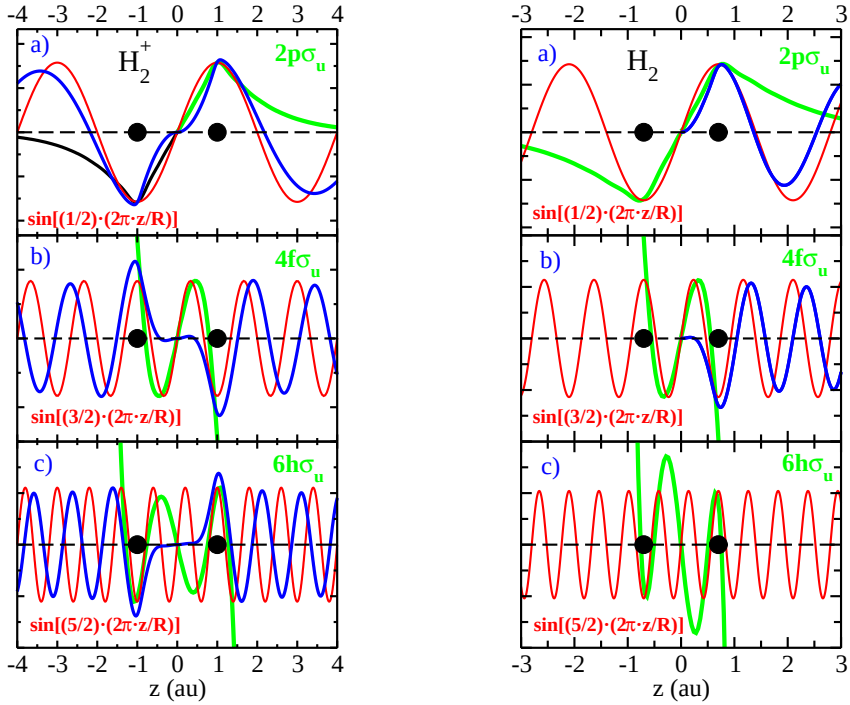

Figure 10.16: Comparison between the bound molecular orbitals of H_2 and H_2^+ (green lines) and an approximated continuum electron wave functions (particle in a box) (red line) for the values of k associated with a minimum in the integrated Σ_u cross sections (Figs. (10.10) and (10.15)). Blue line, represents the real continuum states that include the multichannel coupling. Left panels, results for H_2^+: a) Partial wave $\ell = 1$ for a electron energy of 0.125 a.u. ($k =$); b) Partial wave $\ell = 3$ for a electron energy of 8.4 a.u. ($k =$); c) Partial wave $\ell = 5$ for a electron energy of 22.0 a.u. ($k =$). Right panels, results for H_2: a) Partial wave $\ell = 1$ for a electron energy of 2.6 a.u. ($k =$); b) Partial wave $\ell = 3$ for a electron energy of 19.0 a.u. ($k =$); c) Partial wave $\ell = 5$ for a electron energy of 22.0 a.u. ($k =$)

shows that, for $h\nu = 9.5$ a.u., electron confinement occurs for a proton kinetic energy $E_{H^+} \sim 6$ eV ($k_e \sim 4.1$ a.u., hence $\lambda_e \sim 1.5$ a.u.). According to the reflection approximation, $R \sim 2.3$ a.u., which satisfies $k_e R \sim 3\pi$, in agreement with the fact that the $\ell = 3$ partial wave suffers confinement. When ionization occurs at longer or shorter internuclear distances, there is no confinement, which explains the abrupt variations in the electron angular distribution in a narrow interval of proton kinetic energies around 6 eV. For either orientation, the angular distributions approximately follow the formula [39] given by Eq. (10.4) $(\mathbf{e}_\mu \cdot \mathbf{k}_e)^2 \cos^2(\mathbf{k}_e \cdot \mathbf{R}/2)$. If $\mathbf{e}_\mu$ and $\mathbf{k}_e$ are parallel to the molecular axis, this formula leads to zero when $k_e R = \pi, 3\pi, \ldots$, i.e., no electron emission along the molecular axis in agreement with the image of confinement. A similar formula describes in classical optics the interference produced at long distances by two radiating dipole antennas separated a distance R. Nevertheless, one must be careful in using this analogy for quantitative analysis since it is not valid when $r \sim R$. However, the quantitative value of these images is very limited, at least, as limited as our image based on confinement (which can be justified by the simple particle-in-a-box formula or the similarity of the continuum wave function with a bound molecular orbital). The real behavior is what comes out from the calculation, since it is the solution of the Schrödinger equation with almost no approximations. The WB, two antenna and confinement models are simple images to interpret the results of complicated calculations. The three of them provide qualitative explanations a posteriori.

For H_2, the predictive value of the above models is more limited since the remaining molecular ion is mainly left in a bound vibrational state and one cannot rely on the reflection approximation.

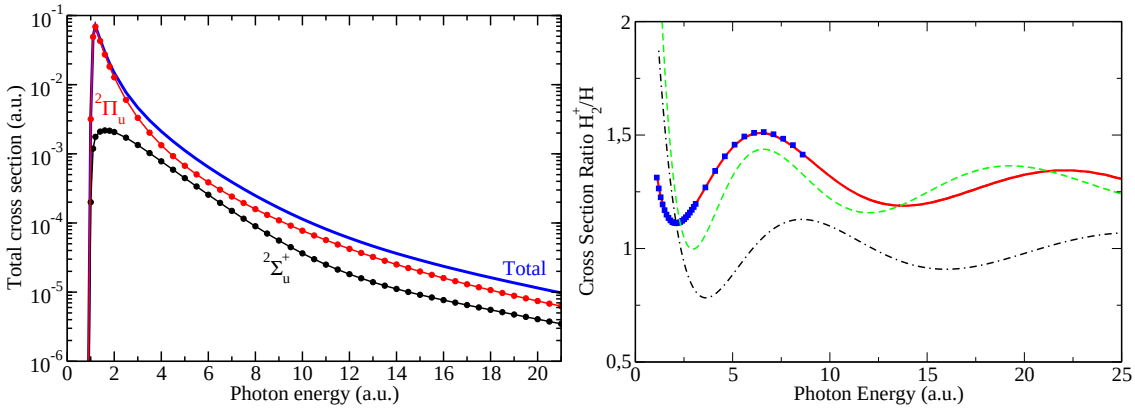

Figure 10.17: Left panel: Total cross section for a parallel orientation of the polarization vector with respect to the molecular axis (black line) and for a perpendicular orientation (red line).Blue line total cross section. Right panel: Photoionization cross section ratio for H_2^+. Red full line, present results. Black dashed and dotted line, Bessel function. Green dashed line, fitting curve (see text). Blue squares, ratios obtained with results from [64].

According to previous work [65, 66], one can expect that different vibrational states of the residual ion sample a narrow enough subset of R values, so that the above picture remains approximately valid. We have checked that this is the case if R is chosen around the mean value of the inner and outer classical turning points associated with the final vibrational state of the residual H_2^+ ion. However, electron correlation, which plays an important role in the bond region, cannot be accounted for by any of the above models.

To complete this Section, we consider the interference effects in the total cross section, i.e., in the cross section integrated over the electron emission angles and its final energy, predicted by the model of Cohen and Fano [38]. The results are presented in left panel of Fig. (10.17) for a parallel and perpendicular orientations of the polarization vector. The result associated to the perpendicular orientation decays monotonically in the entire photon energy range, as we pointed out before (see Fig. (10.8)). On the other hand, the results for the parallel orientation presents a modulation as a function of the photon energy. As was pointed out before, any modulation in the cross section can be reflected using the Cohen and Fano model:

$$\sigma = \sigma_H \left[1 + \sin(k_e R)/(k_e R)\right]/(1+S), \tag{10.10}$$

where σ_H is the photoionization cross section of a hydrogen atom with effective charge Z_{eff}, R is the equilibrium internuclear distance, S is the overlap between the atomic orbitals $1s_A$ and $1s_B$ that describe the initial molecular state, and k_e is the electron wave vector. Right panel of Fig. (10.17) displays the ratio of the H_2^+ total photoionization cross section (TPCS) to the TPCS of atomic hydrogen as a function of photon energy. We also show the ratio obtained from the TPCS calculated by Brosolo *et al* [64](the corresponding ratios from Richards and Larkins are practically identical [67]). The discrepancies are less than 2%, in agreement with the observed discrepancies in the TPCS. Our calculated ratios exhibit a clear oscillatory behavior, which is not present in the TPCS and is much less apparent in previous theoretical results (because the latter do not go beyond 9 a.u.). To analyze the origin of these oscillations, the figure also includes the spherical zeroth order Bessel function resulting from the CF model, $1 + \sin(k_e R)/(k_e R)$. It can be seen that the frequency of the oscillations predicted by the CF model is different from the calculated one. Not only the two curves are out of phase, but the relative magnitude of the ratios at low energy is quite different. We have fitted the calculated TCPS to the CF formula (Eq. 10.10, leaving $a_0 = 1/(2(1+S))$ and $a_1 = R$ as free parameters. The result of the fit ($a_0 = 1.27$ and $a_1 = 2.33$ a.u.) is also shown in

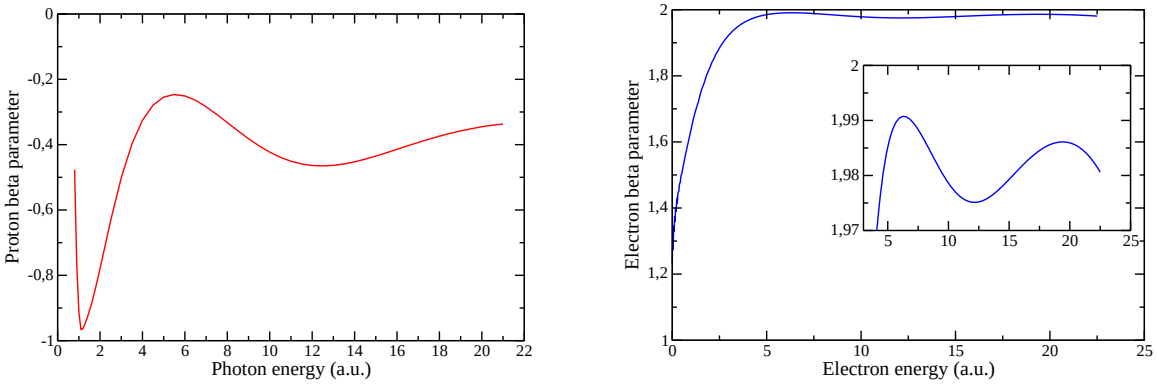

Figure 10.18: Electron beta parameter (left panel) and proton beta parameter (right panel) for the H_2^+ molecule.

the figure. The result of this fit is not satisfactory. This is rather surprising because a similar fitting procedure leads to reasonable results for H_2 and, therefore, seems to support the CF model for H_2 at least qualitatively. In earlier works on H_2 [1], failures of the CF formula to describe the TPCS ratio at low energies were attributed to the use of a simple LCAO and to the absence of screening and correlation effects in the description of the ionization process. As H_2^+ is a one-electron system, screening effects cannot be invoked here. Therefore, the origin of the discrepancy in H_2^+ must be the use of the LCAO approximation or the free wave for the ionized electron [8]. As a matter of fact, an LCAO calculation of the ground state properties of H_2^+ with charge $Z = 1$ gives a poorer description of the geometry of the molecule than in the case of H_2. So once again, these results reveal the deficiencies of the different models that we have proposed during this chapter.

10.4 Proton and electron beta parameters

Could the interference effects be observed in the proton angular distribution or in the electron angular distribution for randomly distributed molecules? In this section we present the proton and electron beta parameter for the H_2^+ and H_2 molecules at very high photon energies. We showed in Chapter 4 that the branching ratios to Σ_u^+ and Π_u states in the ionization processes is directly reflected in the angular distribution of the protons coming from the dissociative process. So, from the results presented in Figs. (10.9) and (10.14) one would expect to observe interference effects in this case. Left panel of Fig. (10.18) displays the proton beta parameter for the H_2^+ molecule as a function of the photon energy. The value of the beta parameter takes negative values all along the photon energy range, which means that the Σ_u^+ transition is smaller than the Π_u one, which is in accordance with the results presented in Fig. (10.17). On the other side, this function present a strong oscillatory pattern as a function of the photon energy, fact that can be easy explained: the observed oscillations comes from the Σ_u^+ transition, since as we showed in Fig. (10.8), this symmetry was the only one that presented oscillations as a function of the photon energy. What happens when the orientation of the molecule is not fixed in the space, i.e., when the molecules are randomly distributed? As we studied in Chapter 4, in this case the electron angular distribution is given by the electron beta parameter. The results are presented in the right panel of Fig. (10.18). In the photon energy range considered, the electron beta parameter does not present a significant oscillatory structures (note, that the oscillations presented in the inset of this figures are not big enough to produce any significant variance in the electron angular distribution). As the photon energy increases the electron beta parameter approaches a value close to 2, which means that the molecular characteristics due to the molecular potential disappears as the photon energy reaches high values. So, the interference

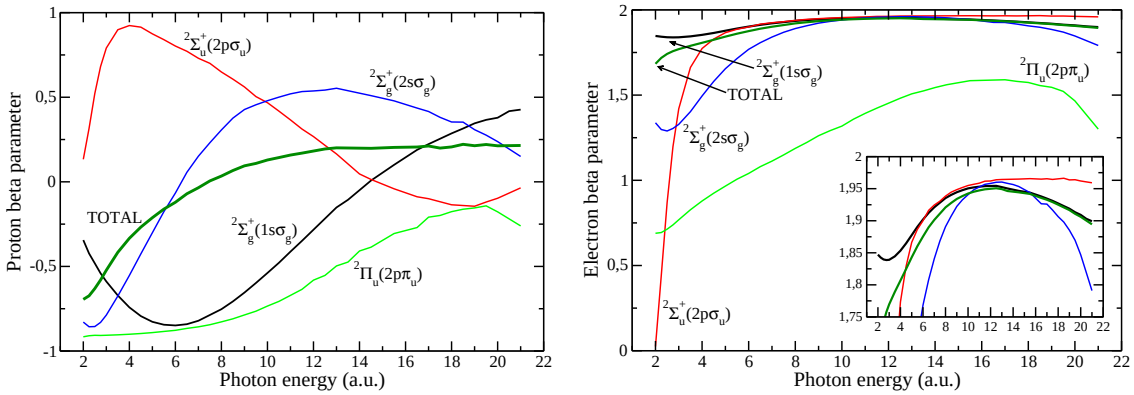

Figure 10.19: (Left panel) Proton beta parameter for the H_2 molecule for the first four ionization thresholds. (Right panel) Total electron beta parameter (dissociative plus non-dissociative process) of H_2 for the first four ionization thresholds.

effects observed previously disappear completely when the orientation of the molecule is not fixed. The proton beta parameter for the H_2 molecule is presented in the left panel of Fig. (10.19) for the contribution of the first four ionization thresholds (although we will focus our attention on the contribution coming from the first one). The behavior is similar to the obtained for the H_2^+, in the sense that this function presents minimum (in that case close to ~ 6 a.u.) and then grows monotonically. The total electron beta parameter for the contribution of the first four ionization threshold is presented in the right panel of Fig. (10.19). The contribution of the first ionization threshold present a monotonic behavior as a function of the photon energy, whose value is close to 2.

So the main conclusions that one can extract from the results presented in the section are that (i) the proton angular distribution present a strong dependence with the photon energy, and the observed oscillatory patterns come from the contribution of the parallel transition (where the double-slit model cannot be applied), and (ii) the electron beta parameter does not present any dependence with the photon energy and its value is close to 2, which implies the fact that no interference effect can be observed in the electron angular distribution when the molecules are not fixed in space.

10.5 Conclusions

We have presented the results of accurate theoretical calculations showing that, when $\lambda_e \sim R$, the angular distributions of electrons arising from fixed-in-space H_2^+ and H_2 molecules exhibit pronounced interference effects that critically depend on orientation and energy sharing between electrons and nuclei. For molecules oriented parallel to the polarization direction, a transient confinement of the escaping electron leads to complicated angular patterns, while for molecules oriented perpendicularly, typical Young's double-slit interferences are observed. More interestingly, we showed that interference patterns change dramatically as the molecule vibrates, which means that the motion of fast electrons strongly depends on the nuclei's positions. These conclusions should be of general validity for any diatomic molecule. We strongly believe these results clarify different previous results published and states some limitations to the different models that can be found in the literature.

Bibliography

[1] O. A. Fojón, A. Palacios, J. Fernández, R. D. Rivarola, and F. Martín, "Interference effects in H_2 photoionisation at high energies," *Journal of Physics B: Atomic, Molecular and Optical Physics*, vol. 37, pp. 1–8, 2004.

[2] O. A. Fojón, A. Palacios, J. Fernández, R. D. Rivarola, and F. Martín, "Interferences in the photoelectron spectrum of H_2^+ molecules at high energy," *Physics Letters A*, vol. 350, pp. 371–374, 2006.

[3] J. Fernández, O. A. Fojón, A. Palacios, and F. Martín, "Interference from fast electron emission in molecular photoionization," *Physical Review Letters*, vol. 98, p. 043005, 2007.

[4] J. S. Bell, "On the Einstein-Podolsky-Rosen paradox," *Physics. Reprinted in Speakable and Unspeakable in Quantum Mechanics, Cambridge University Press, 2004*, vol. 1, pp. 195–200, 1964.

[5] A. Aspect, J. Dalibard, and G. Roger, "Experimental test of Bell's inequalities using time-varying analyzers," *Physical Review Letters*, vol. 49, pp. 1804–1807, 1982.

[6] T. Young, *A Course of Lectures on Natural Phylosophy and the Mechanical Arts.* J. Johnson, 1807.

[7] R. P. Crease, "The most beautiful experiment," *Physics World*, vol. 19, 2002.

[8] L. Mandel and E. Wolf, *Optical Coherence and Quantum optics*. Cambridge, 1995.

[9] R. P. Feynman, R. B. Leighton, and M. Sands, *The Feynman Lectures on Physics*. Addison Wesley Publishing Company, 2005.

[10] C. Jönsson, "Interferenz von elektronen am doppelspalt," *Zeitschrift für Physik*, vol. 161, p. 454, 1961.

[11] C. Jönsson, "Electron diffraction at multiple slits," *American Journal of Physics*, vol. 42, p. 4, 1974.

[12] P. G. Merli, G. F. Missiroli, and G. Pozzi, "On the statistical aspect of electron interference phenomena," *American Journal of Physics*, vol. 44, p. 306, 1976.

[13] A. Tonomura, J. Endo, T. Matsuda, T. Kawasaki, and H. Ezawa, "Demonstration of single-electron buildup of an interference pattern," *American Journal of Physics*, vol. 57, p. 117, 1989.

[14] M. O. Scully, B.-G. Englert, and H. Walther, "Quantum optical tests of complementarity," *Nature*, vol. 351, pp. 111–116, 1991.

[15] G. L. Yudin, S. Chelkowski, and A. D. Bandrauk, "Coulomb continuum effects in molecular interference," *Journal of Physics B: Atomic, Molecular and Optical Physics*, vol. 39, pp. L17–L24, 2006.

[16] F. Lindner, M. G. Schätzel, H. Walther, A. Baltuka, E. Goulielmakis, F. Krausz, D. B. Miloević, D. Bauer, W. Becker, and G. G. Paulus, "Attosecond double-slit experiment," *Physical Review Letters*, vol. 95, p. 040401, 2005.

[17] S. N. Yurchenko, S. Patchkovskii, I. V. Litvinyuk, P. B. Corkum, and G. L. Yudin, "Laser-induced interference, focusing, and diffraction of rescattering molecular photoelectrons," *Physical Review Letters*, vol. 93, p. 223003, 2004.

[18] M. Spanner, O. Smirnova, P. B. Corkum, and M. Y. Ivanov, "Reading diffraction images in strong field ionization of diatomic molecules," *Journal of Physics B: Atomic, Molecular and Optical Physics*, vol. 37, pp. L243–250, 2004.

[19] T. F. Tuan and E. Gerjuoy, "Charge transfer in molecular hydrogen," *Physical Review Letters*, vol. 117, pp. 756–763, 1960.

[20] N. C. Deb, A. Jain, and J. H. McGuire, "Electron capture from a hydrogen molecule at a fixed orientation of the molecular axis," *Physical Review A*, vol. 38, pp. 3769–3772, 1988.

[21] R. Shakeshaft and L. Spruch, "Mechanisms for charge transfer (or for the capture of any light particle) at asymptotically high impact velocities," *Review Modern Physics*, vol. 51, pp. 369–405, 1979.

[22] Y. Abranyos, M. Jakob, , and J. Bergou, "Interference and partial which-way information: A quantitative test of duality in two-atom resonance," *Physical Review A*, vol. 61, p. 013804, 2000.

[23] D. Toffolli and P. Decleva, "Photoelectron angular distribution beyond dipole approximation: a computational study on the N_2 molecule," *Journal of Physics B: Atomic, Molecular and Optical Physics*, vol. 39, pp. 2681–2691, 2006.

[24] U. Eichmann, J. C. Bergquist, J. J. Bollinger, J. M. Gilligan, W. M. Itano, D. J. Wineland, and M. G. Raizen, "Young's interference experiment with light scattered from two atoms," *Physical Review Letters*, vol. 70, pp. 2359–2362, 1993.

[25] J. K. Swenson, J. Burgdöfer, F. W. Meyer, C. C. Havener, D. C. Gregory, and N. Stolterfoht, "Coulomb "path" interference in low-energy ion-atom collisions," *Physical Review Letters*, vol. 66, pp. 417–420, 1991.

[26] R. O. Barrachina and M. Zitnik, "Young's interference effect in the autoionization of atoms colliding with molecules," *Journal of Physics B: Atomic, Molecular and Optical Physics*, vol. 37, pp. 3847–3857, 2004.

[27] M. W. Noel and J. C. R. Stroud, "Young's double-slit interferometry within an atom," *Physical Review Letters*, vol. 75, pp. 1252–1255, 1995.

[28] Y. Couder and E. Fort, "Single-particle diffraction and interference at a macroscopic scale," *Physical Review Letters*, vol. 97, p. 154101, 2006.

[29] H. F. Schouten, N. Kuzmin, G. Dubois, T. D. Visser, G. Gbur, P. F. A. Alkemade, H. Blok, G. W. Hooft, D. Lenstra, and E. R. Eliel, "Plasmon-assisted two-slit transmission: Young's experiment revisited," *Physical Review Letters*, vol. 94, p. 053901, 2005.

[30] Y. Hatano, "Interaction of vacuum ultraviolet photons with molecules. Formation and dissociation dynamics of molecular superexcited states," *Physics Reports*, vol. 313, pp. 109–169, 1999.

[31] C. Davisson and L. H. Germer, "Diffraction of electrons by a crystal of nickel," *Physical Review*, vol. 30, pp. 705–740, 1927.

[32] G. P. Thomson and A. Reid, "Diffraction of cathode rays by a thin film," *Nature*, vol. 119, p. 890, 1927.

[33] L. de Broglie, "Waves and quanta," *Nature*, vol. 112, p. 540, 1923.

[34] G. C. Hegerfeldt and T. Köler, "Atomic versus molecular diffraction: Influence of breakups and finite size," *Physical Review A*, vol. 57, pp. 2021–2029, 1998.

[35] W. Schöllkopf and J. P. Toennies, "Nondestructive mass selection of small van der walls clusters," *Science*, vol. 266, pp. 1345–1348, 1994.

[36] A. Zeilinger, R. Gäler, C. G. Shull, W. Treimer, and W. Mampe, "Single- and double-slit diffraction of neutrons," *Review Modern Physics*, vol. 60, pp. 1067–1073, 1988.

[37] M. Arndt, O. Nairz, J. Vos-Andreae, C. Keller, G. van der Zouw, and A. Zeilinger, "Wave-particle duality of C_{60} molecules," *Nature*, vol. 401, pp. 680–682, 1999.

[38] H. D. Cohen and U. Fano, "Interference in the photo-ionization of molecules," *Physical Review*, vol. 150, pp. 30–33, 1966.

[39] M. Walter and J. Briggs, "Photo-double ionization of molecular hydrogen," *Journal of Physics B: Atomic, Molecular and Optical Physics*, vol. 32, pp. 2487–2501, 1999.

[40] S. K. Semenov and N. A. Cherepkov, "Generalization of the atomic RPA method for diatomic molecules: H_2 photoionization cross-section calculation," *Chemical Physics Letters*, vol. 291, pp. 375–380, 1998.

[41] S. K. Semenov and N. A. Cherepkov, "Photoionization of the H_2 molecule in the random phase approximation," *Journal of Physics B: Atomic, Molecular and Optical Physics*, vol. 36, pp. 1409–1422, 2003.

[42] N. Stolterfoht, B. Sulik, V. Hoffmann, B. Skogvall, J. Y. Chesnel, J. Rangama, F. Frémont, D. Hennecart, A. Cassimi, X. Husson, A. L. Landers, J. A. Tanis, M. E. Galassi, and R. D. Rivarola, "Evidence for interference effects in electron emission from H_2 colliding with 60 MeV/u Kr^{34+} ions," *Physical Review Letters*, vol. 87, p. 023201, 2001.

[43] N. Stolterfoht, B. Sulik, L. Gulyás, B. Skogvall, J. Y. Chesnel, F. Frémont, D. Hennecart, A. Cassimi, L. Adoui, S. Hossain, and J. A. Tanis, "Interference effects in electron emission from H_2 by 68-MeV/u $Kr^3 3+$ impact: Dependence on the emission angle," *Physical Review A*, vol. 67, p. 030702, 2003.

[44] M. E. Galassi, R. D. Rivarola, P. D. Fainstein, and N. Stolterfoht, "Young-type interference patterns in electron emission spectra produced by impact of swift ions on H_2 molecules," *Physics Letters A*, vol. 66, p. 052705, 2002.

[45] L. Nagy, L. Kocbach, K. Póra, and J. P. Hansen, "Interference effects in the ionization of H_2 by fast charged projectiles," *Journal of Physics B: Atomic, Molecular and Optical Physics*, vol. 35, pp. L453–L459, 2002.

[46] G. Laurent, P. D. Fainstein, M. E. Galassi, R. D. Rivarola, L. Adoui, and A. Cassimi, "Orientation and interference effects in single ionization of H_2 by fast ions," *Journal of Physics B: Atomic, Molecular and Optical Physics*, vol. 35, pp. L495–L501, 2002.

[47] L. Sarkadi, "Interference effects in electron emission from H_2 by particle impact," *Journal of Physics B: Atomic, Molecular and Optical Physics*, vol. 36, pp. 2153–2163, 2003.

[48] C. R. Stia, O. A. Fojón, P. F. Weck, J. Hanssen, and R. D. Rivarola, "Interference effects in single ionization of molecular hydrogen by electron impact," *Journal of Physics B: Atomic, Molecular and Optical Physics*, vol. 36, pp. L257–L264, 2003.

[49] D. Misra, U. Kadhane, Y. P. Singh, L. C. Tribedi, P. D. Fainstein, and P. Richard, "Interference effect in electron emission in heavy ion collisions with H_2 detected by comparison with the measured electron spectrum from atomic hydrogen," *Physical Review Letters*, vol. 92, p. 153201, 2004.

[50] X.-J. Liu, N. A. Cherepkov, S. K. Semenov, V. Kimberg, F. Gel'mukhanov, G. Prümper, T. Lischke, T. Tanaka, M. Hoshino, H. Tanaka, and K. Ueda, "Young's double-slit experiment using core-level photoemission from N_2: revisiting Cohen-Fano's two-centre interference phenomenon," *Journal of Physics B: Atomic, Molecular and Optical Physics*, vol. 39, pp. 4801–4817, 2006.

[51] P. D. Fainstein, V. H. Ponce, and R. D. Rivarola, "Two-centre effects in ionization by ion impact," *Journal of Physics B: Atomic, Molecular and Optical Physics*, vol. 24, pp. 3091–3119, 1991.

[52] J. A. Tanis, S. Hossain, B. Sulik, , and N. Stolterfoht, "Comment on "interference effect in electron emission in heavy ion collisions with H_2 detected by comparison with the measured electron spectrum from atomic hydrogen"," *Physical Review Letters*, vol. 95, p. 079301, 2005.

[53] I. G. Kaplan and A. P. Markin, "Interference phenomena in photoionization of molecules," *Soviet Physics-Docklady*, vol. 14, pp. 36–39, 1969.

[54] T. Weber, A. O. Czasch, O. Jagutzki, A. K. Müller, V. Mergel, A. Kheifets, E. Rotenberg, G. Meigs, M. H. Prior, S. Daveau, A. Landers, C. L. Cocke, T. Osipov, R. D. M. no, H. Schmidt-Böcking, and R. Dörner, "Complete photo-fragmentation of the deuterium molecule," *Nature*, vol. 431, pp. 437–440, 2004.

[55] D. Rolles, M. Braune, S. Cvejanović, O. Gener, R. Hentges, S. Korica, B. Langer, T. Lischke, G. Prmper, A. Reinköter, J. Viefhaus, B. Zimmermann, V. McKoy, and U. Becker, "Isotope-induced partial localization of core electrons in the homonuclear molecule N_2," *Nature*, vol. 437, pp. 711–715, 2005.

[56] B. El-Marji, J. P. Doering, J. H. Moore, and M. A. Coplan, "Impulse electron-impact double ionization and two-electron momentum density," *Physical Review Letters*, vol. 83, pp. 1574–1577, 1999.

[57] R. S. Berry and S. E. Nielsen, "Dynamic coupling phenomena in molecular excited states. II. Autoionization and predissociation in H_2, HD, and D_2," *Physical Review A*, vol. 1, pp. 395–411, 1970.

[58] R. S. Berry and S. E. Nielsen, "Dynamic coupling phenomena in molecular excited states. I. General formulation and vibronic coupling H_2," *Physical Review A*, vol. 1, pp. 383–394, 1970.

[59] H. L. Rouzo and G. Raseev, "Finite-volume variational method: First application to direct molecular photoionization," *Physical Review A*, vol. 29, pp. 1214–1223, 1984.

[60] J. S. Briggs and M. Walter, "Oscillatory structure of molecular photoionization cross sections," *Physics Essays*, vol. 13, pp. 297–302, 2000.

[61] J. D. Jackson, *Classical Electrodynamics*. Wiley; 3th edition, 1998.

[62] R. Weilte, "La interacción mutua entre fuentes y las amplitudes anómalas en el fenóeno de interferencia," *Revista Brasileira de Ensino de Física*, vol. 24, pp. 1–6, 2002.

[63] A. Messiah, *Quantum mechanics volume* I *and* II. North-Holland publishing company, 1961.

[64] M. Brosolo, P. Decleva, and A. Lisini, "LCAO expansion in a spline basis for accurate variational determination of continuum wavefunctions. Applications to H_2^+ and HeH^{2+}," *Chemical Physics*, vol. 181, pp. 85–95, 1994.

[65] J. L. Dehmer, D. Dill, and S. Wallace, "Shape-resonance-enhanced nuclear-motion effects in molecular photoionization," *Physical Review Letters*, vol. 43, pp. 1005–1008, 1979.

[66] T. Jahnke, L. Foucar, J. Titze, R. Wallauer, T. Osipov, E. P. Benis, A. Alnaser, O. Jagutzki, W. Arnold, S. K. Semenov, N. A. Cherepkov, L. P. H. Schmidt, A. Czasch, A. Staudte, M. Schöffler, C. L. Cocke, M. H. Prior, H. Schömidt-Bcking, , and R. Dörner, "Vibrationally resolved K-shell photoionization of CO with circularly polarized light," *Physical Review Letters*, vol. 93, p. 083002, 2004.

[67] J. A. Richards and F. P. Larkins, "Molecular photoionisation calculations with numerical continuum wavefunctions: Application to the hydrogen molecule," *Journal of Physics B: Atomic, Molecular and Optical Physics*, vol. 17, pp. 1015–1026, 1984.

Chapter 11

Dissociative photoionization of HeH^+

"Science is facts; just as houses are made of stones, so is science made of facts; but a pile of stones is not a house and a collection of facts is not necessarily science."

Henri Poincare

Table of Contents

The work reported in this Chapter has led to the publication [1].

11.1 Introduction

THE SINGLY CHARGED HELIUM-HYDRIDE ION HeH^+ is one of the most elementary molecular ions. With two electrons, it is isoelectronic with the hydrogen neutral molecule H_2 and the H_3^+ molecular ion and, as the latter, it has been the object of intense experimental and theoretical research. Since it is the only well bound molecular system of the two most abundant elements in the Universe, hydrogen and helium, many researchers have suggested its presence in astronomical objects such as planetary nebulae [2, 3, 4, 5], super novae [6], white dwarfs [7], and quasi-stellar objects [8].

In such rich environments, HeH^+ is expected to participate in a large variety of processes. For example, spontaneous emission of low energy photons from HeH^+ has been suggested as an important factor in primordial star formation [9]. Also, dissociative recombination with electrons, $HeH^+ + e^- \rightarrow He + H$ [10], and dissociative photoionization by extreme ultraviolet or x-ray radiation [11], $HeH^+ + h\nu \rightarrow He^+ + H^+$ or $He^{2+} + H$, may have impact on the calculated abundance of HeH^+ in interstellar space. Formation of the one-electron molecular ion HeH^{2+} might also be possible. However, since the $1s\sigma$ ground state of HeH^{2+} is repulsive and so are most of its excited electronic states [12] (among the lowest 20 states of HeH^{2+} only the $2p\sigma$, $4f\sigma$, and $4f\pi$ ones are bound), dissociative ionization is expected to dominate over non dissociative

ionization. In addition to the above, the electronically equivalent isotope HeT^+ plays a crucial role in the determination of the electron-neutrino mass. The best laboratory determinations of this mass come from measuring the energy spectrum of the β electrons in the decay [13] $T_2 \rightarrow {}^3HeT^+ + \bar{\nu}_e + e^-$. These determinations depend on accurate measurements of the final-state distribution in the molecular product ${}^3HeT^+$. Therefore, these measurements ultimately rely on the accurate knowledge of the ${}^3HeT^+$ electronic states, including the electronic continuum. Thus comparison between measured and calculated HeH^+ photoabsorption spectra has been proposed as an additional test of the measured final-state distributions [11].

Theoretical efforts aiming at providing accurate estimations of absolute photoionization cross sections have mainly focused on the two-electron molecule H_2 (see [14], and references therein). In contrast, little attention has been paid to the simplest heteronuclear two-electron molecular system HeH^+. To our knowledge, the only existing theoretical evaluation of photoionization cross sections in HeH^+ has been reported by Saenz [11]. He has evaluated integral photoionization cross sections by considering linearly polarized light and HeH^+ ions oriented along the polarization direction (final ${}^1\Sigma^+$ symmetry). His calculations include the effect of the nuclear motion through the use of the reflection approximation. More theoretical efforts have been devoted to the evaluation of energy positions and autoionization widths of the doubly-excited states of HeH^+ [11, 15, 16]. As pointed out in [11], these states may play an important role in HeH^+ photoionization, but also in He^{2+}+H^- collisions [17, 18]. The works of [11, 15, 16] have exclusively concentrated on doubly excited states of ${}^1\Sigma^+$ symmetry. Saenz [11] and Froelich et al [16] have only considered doubly excited states lying between the first and the second ionization thresholds, while Tennyson [15] has considered doubly excited states converging up to the fourth ionization threshold.

In this Chapter, we present a theoretical investigation of HeH^+ photoionization in the 40-80 eV photon energy range for molecules oriented both parallel and perpendicular to the polarization direction (final ${}^1\Sigma^+$ and ${}^1\Pi$ symmetries) as well as for molecules randomly oriented. We provide the integral cross sections for these three orientations and the corresponding differential cross sections in the energy of the remaining ions (the kinetic energy release -KER spectrum). In addition, we report energy positions and autoionization widths of the doubly excited states of HeH^+ for both ${}^1\Sigma^+$ and ${}^1\Pi$ symmetries.

11.2 Computational methods

The one-electron functions are defined in an interval $[0, r_{max}]$ in terms of a basis of B-spline functions B_i^k of order k,as was explained in Chapter 2. The HeH^{2+} orbitals φ_{nm} are obtained by diagonalizing the HeH^{2+} Hamiltonian in the above basis.

In this case the origin of electronic coordinates has been placed in the center of charge of the internuclear axis, that is $2R/3$ from the H nucleus. In this work we have used $k = 8$, $r_{max} = 60$ a.u., $\ell_{max} = 12$, and $N_\ell = 160$ (for $\ell = 0, \ldots, \ell_{max}$).

The resonant wave functions ϕ_r were obtained by diagonalizing the HeH^+ Hamiltonian in a basis of N_{conf} configurations built from the above HeH^{2+} orbitals. For example, in the case of the Q_1 states of ${}^1\Pi$ symmetry, we have included the configurations $2\sigma n\pi$ ($n = 2-70$), $1\pi n\sigma$ ($n = 3-18$), $1\delta n\pi$ ($n = 2-18$), $2\pi n\sigma$ ($n = 4-18$), $4\sigma n\pi$ ($n = 3-17$), $3\sigma n\pi$ ($n = 2-16$), $5\sigma n\pi$ ($n = 3-17$), $4\sigma n\pi$ ($n = 2-16$), $3\pi n\sigma$ ($n = 6-20$), $2\pi n\sigma$ ($n = 5-19$), $2\delta n\pi$ ($n = 2-16$), $1\delta n\pi$ ($n = 1-15$), $1\varphi n\delta$ ($n = 1-15$), $4\pi n\sigma$ ($n = 6-20$), and $6\sigma n\pi$ ($n = 5-19$), which amounts to 421 configurations (the index n used to label one-electron orbitals in the two-electron basis indicates energy ordering for a given value of R). This basis includes all molecular orbitals correlated to the $Li^{2+}(n = 2)$ and $Li^{2+}(n = 3)$ atomic subshells in the united atom (UA) limit ($R = 0$). For the Q_2 states of ${}^1\Pi$ symmetry and for the Q_1 and Q_2 states of ${}^1\Sigma^+$ symmetry, the quality of the basis set is comparable (352, 402 and 343 configurations, respectively). For the Q_1 states, the lowest target orbital $1s\sigma$

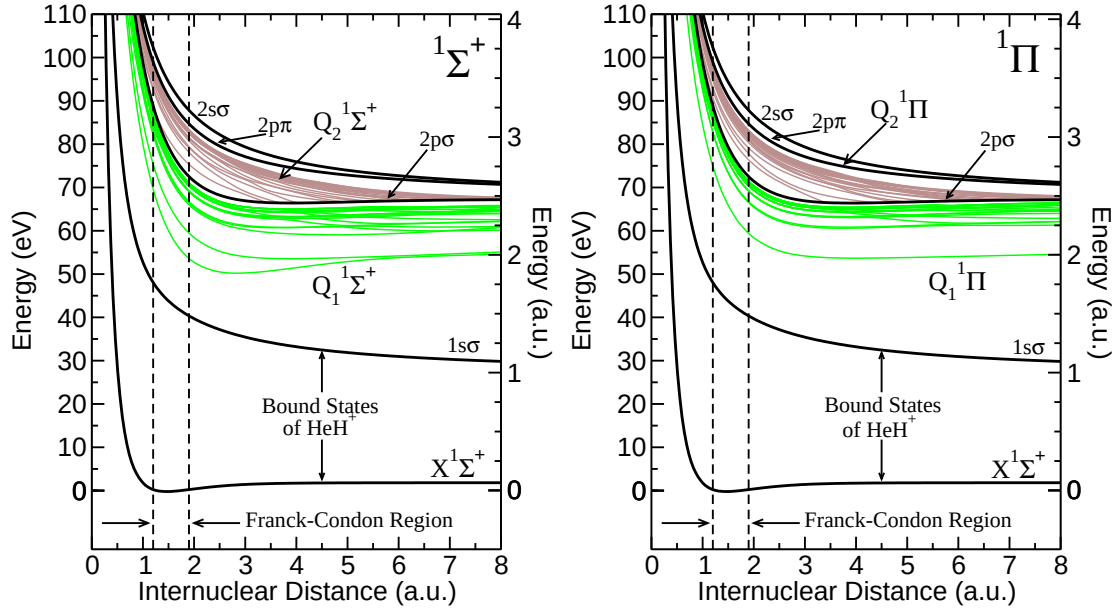

Figure 11.1: Potential energy curves of HeH$^+$ and HeH^{2+}. (a) $^1\Sigma^+$ symmetry of HeH$^+$. (b) $^1\Pi$ symmetry. The energy origin is placed on the lowest rovibrational level of the ground electronic state of HeH$^+$

is excluded from the configuration basis in Q subspace in order to ensure orthogonality with the $1s\sigma\varepsilon\ell\lambda$ non resonant continuum states. For the Q_2 states, besides the above orbital, we have also excluded the $2p\sigma$ one to ensure orthogonality with both the $1s\sigma\varepsilon\ell\lambda$ and $2p\sigma\varepsilon\ell\lambda$ $1s\sigma\varepsilon\ell\lambda$ continuum states. The accuracy of the corresponding energies and autoionization widths has been checked by varying N_ℓ, ℓ_{max}, N_{conf}, and r_{max}. In this work we have only considered the lowest four doubly excited states of the following series: $Q_1\ ^1\Sigma^+$, $Q_1\ ^1\Pi$, $Q_2\ ^1\Sigma^+$ and $Q_2\ ^1\Pi$. These doubly excited states have the largest autoionization widths in each series. The estimated error for the energies and widths of these states in the range of internuclear distances relevant in the present study is $\sim 10^{-4}$ au.

The non resonant wave functions $\psi^{0+}_{\alpha\ell_\alpha\varepsilon_\alpha}(\mathbf{r},R)$ describe a bound electron in either the $1s\sigma$ or $2p\sigma$ orbitals of HeH^{2+}, and a continuum electron with angular momentum ℓ_α. They were evaluated using the L^2 close-coupling method [28], which allows for inter-channel coupling between different partial waves and yields the correct asymptotic behavior [29] (see Chapter 3). The basis set used to represent the ground state of HeH$^+$ is the same as that used in reference [20] for H_2. It consists of 400 two-electron configurations built from both HeH^{2+} molecular orbitals and Li^{2+} Slater-type orbitals (the latter placed on the center of charge) represented in the above mentioned B-spline basis. The initial an final (bound and continuum) vibrational wave functions are written as linear combinations of B-spline functions B^k_j of order k as was described in Section 3.7 of Chapter 3. The B-spline functions are defined in an interval $[0, R_{max}]$ using a linear knot sequence with additional knot points in the borders so that $B_i(0) = B_i(R_{max}) = 0$ for all i. Here we have used $N = 240$, $k = 8$, and $R_{max} = 12$ a.u.

11.3 Results

Fig. (11.1) shows the potential energy curves of the Q_1 and Q_2 doubly-excited states of HeH$^+$ for the two molecular symmetries that are accessible by photon absorption from the HeH$^+$ ground state. The Q_1 and Q_2 states lie above the first and second ionization thresholds, respectively. These

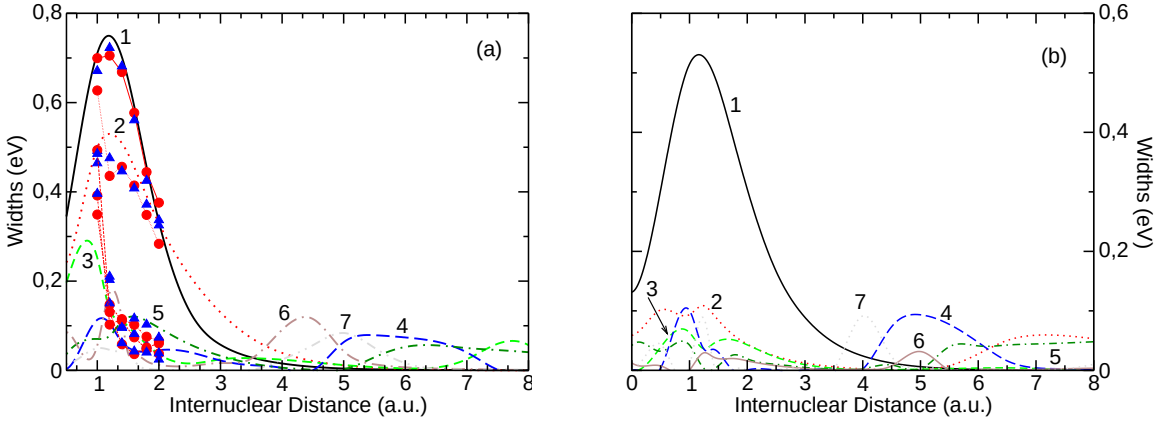

Figure 11.2: Variation of the autoionization widths with internuclear distance for the Q_1 doubly excited states of (a) $^1\Sigma^+$ and (b) $^1\Pi$ symmetries. The results are compared with those previously obtained by Tennyson [15] (circles) and Saenz [11] (triangles).

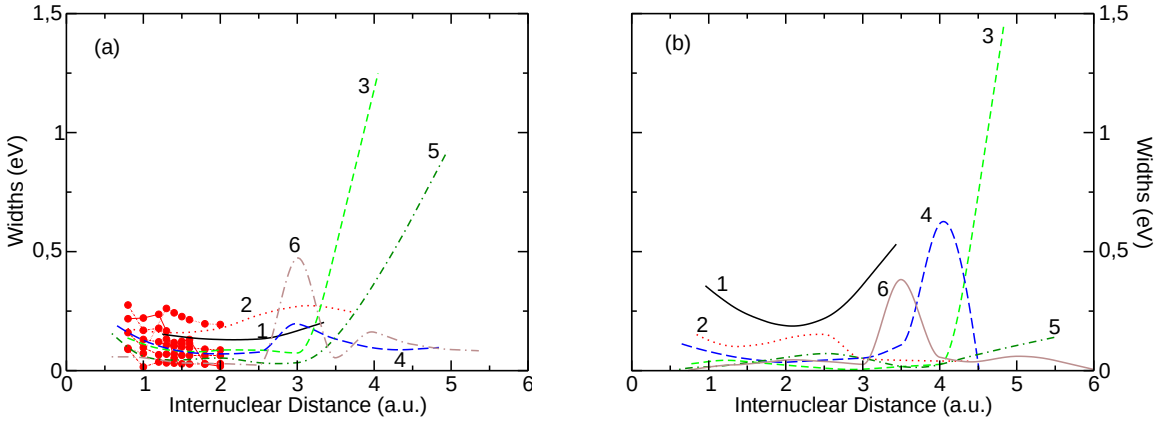

Figure 11.3: Variation of the autoionization widths with internuclear distance for the Q_2 doubly excited states of (a) $^1\Sigma^+$ and (b) $^1\Pi$ symmetries. The results are compared with those previously obtained by Tennyson [15] (circles).

thresholds coincide with the 1sσ and 2pσ states of the one-electron HeH^{2+} molecular ion. The energy positions of these doubly excited states agree fairly well with those previously obtained by Tennyson [15] and Saenz [11]. Fig. (11.1) shows that the energy curves of the Q_1 states run almost parallel to the second ionization threshold $^2\Sigma^+(2p\sigma)$ because the doubly-excited states are mainly described by $2p\sigma nl\lambda$ configurations: $2p\sigma nl\sigma$ configurations for states of $^1\Sigma^+$ symmetry and $2p\sigma nl\pi$ configurations for states of $^1\Pi$ symmetry. The corresponding σσ and σπ configuration weights resulting from our calculations typically exceed 90% (except at very short internuclear distance where avoided crossings with states containing dominant ππ and πδ configurations are important). In contrast with the Q_1 states, the variation of the Q_2 energy curves with R do not follow a simple pattern. Most of the Q_2 energy curves exhibit avoided crossings in the interval $R = 0-4$ a.u., which contains the Franck-Condon region where these states are expected to be excited from the ground state of HeH^+ (see Fig. (11.1)). Thus, for the Q_2 states, there is not a single type of configuration that clearly dominates over the entire range of internuclear distances.

Figs. (11.2) and (11.3) show the calculated autoionization widths for the Q_1 and Q_2 states, respectively. Our results are compared with those previously reported by Tennyson [15] and Saenz

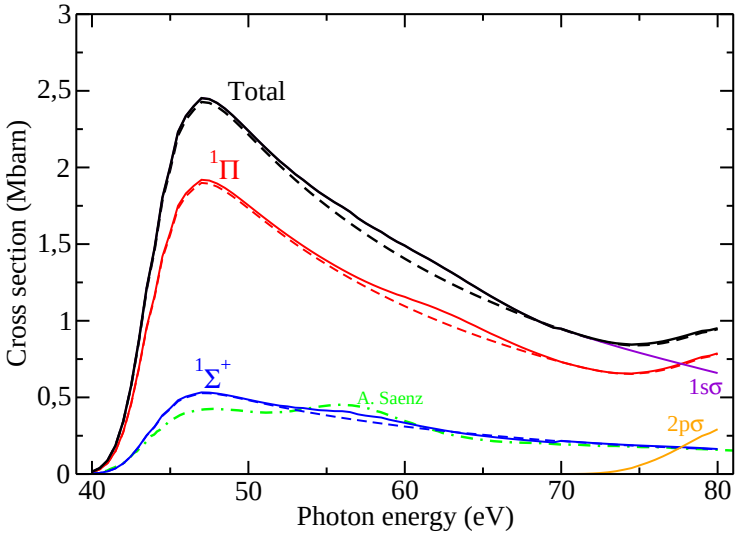

Figure 11.4: Total, $^1\Sigma^+$ and $^1\Pi$ photoionization cross sections of HeH^+ as functions of photon energy. The dashed lines show the corresponding non resonant contributions. The green dot-dashed line represent the result obtained by A. Saenz [11] for the $^1\Sigma^+$ symmetry.

[11]. The agreement is reasonably good. For the Q_1 states it can be seen that, in the region of physical interest (R=0-3 a.u.), the largest autoionization width corresponds to the lowest state. This is not so clear for the Q_2 states, especially for the $^1\Sigma^+$ symmetry, due to the series of avoided crossings between different Q_2 states.

We have calculated the photoionization cross section of HeH^+ from the ionization threshold ($\sim$ 40 eV) up to 80 eV. The results are shown in Fig. (11.4). The photoionization cross section increases with photon energy, reaches a maximum at around 47 eV and then decreases. From the ionization threshold up to 66 eV, photoionization always leads to dissociation of the residual HeH^{2+} ion because the ground state of the latter ion ($1s\sigma$) is entirely repulsive (see Fig. (11.1)). At photon energies higher than 66 eV, ionization can also leave HeH^{2+} in the excited $2p\sigma$ state, which has a sallow minimum of 0.849 eV at R = 3.89 a.u.. However, our calculations show that the probability of producing HeH^{2+} $(2p\sigma)$ in a bound vibrational state is several orders of magnitude smaller than that leading to dissociation of HeH^{2+} $(2p\sigma)$. This is because of the large difference between the equilibrium internuclear distance of this state ($R = 3.89$ a.u.) and that of the $HeH^+(^1\Sigma^+)$ ground state ($R = 1.46$ a.u.). According to Fig. (11.1), a more favorable Franck-Condon overlap is expected for the dissociative states of $HeH^{2+}(2p\sigma)$. However, the contribution of the HeH^{2+} $(2p\sigma)$ channel to the dissociative photoionization cross section is also small (although noticeable above 75 eV) because the dipole transition connecting the ground state of HeH^+ to the HeH^{2+} $(2p\sigma)$+e^- continuum state is much less probable than that connecting the ground state to the HeH^{2+} $(1s\sigma)$+e^- continuum state (the former transition would be strictly forbidden in an independent electron picture). Therefore, for all practical purposes, the photoionization spectrum of HeH^+ is that of dissociative photoionization leading to $He^+(1s) + H^+ + e^-$.

It can be seen that contribution from the $^1\Pi$ symmetry is approximately four times larger than that from the $^1\Sigma^+$ symmetry. This dominance of the $^1\Pi$ component has also been found in H_2 [30]. Also similar to H_2 is the fact that autoionization through the Q_1 and Q_2 doubly excited states is barely visible in the photoionization spectrum: as the figure shows, the spectrum obtained by excluding the resonant contribution to the wave function (the first term in the right hand side of Eq. (3.88) of Section 3.9 of Chapter 3) leads to results that are not significantly different from those including that contribution. The largest differences between the full and the non resonant curves

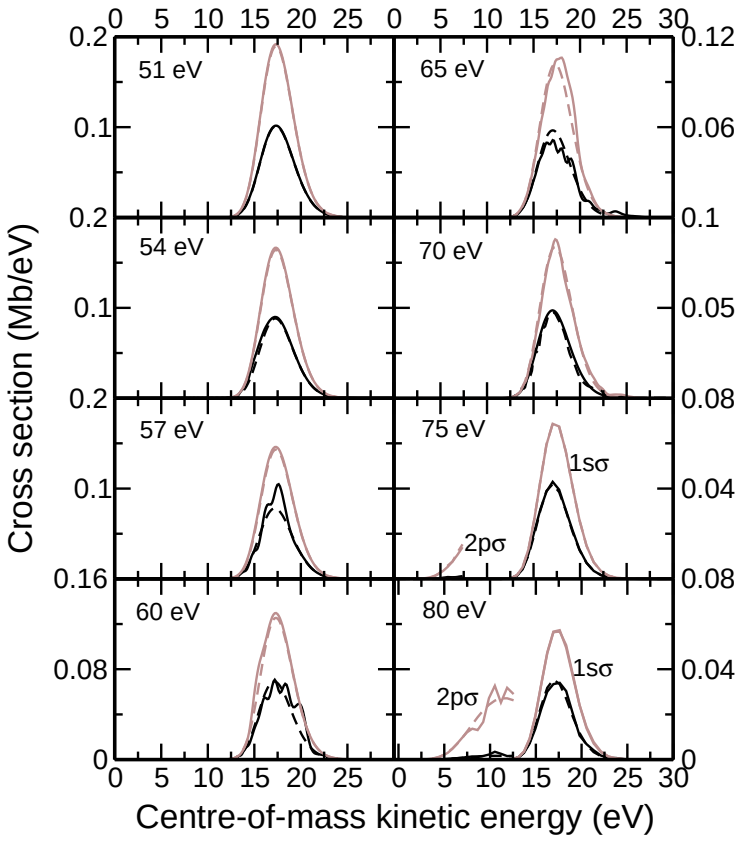

Figure 11.5: Kinetic energy distributions corresponding to dissociative photoionization of HeH^+(full lines). Dashed lines: non resonant contribution. Black lines: $^1\Sigma^+$ contribution; brown lines: $^1\Pi$ contribution.

appear in the region where the lowest Q_1 doubly-excited states are populated. According to the position of the potential energy curves (see Fig. (11.1)), this occurs at lower photon energies for the $^1\Sigma^+$ symmetry than for the $^1\Pi$ one. As shown in Fig. (11.4), previous theoretical results [11] for the $^1\Sigma^+$ symmetry have predicted a more important role of autoionization. This might be due to the use of the reflection approximation in the latter calculation in which it is assumed that the nuclei do not move during the autoionization process. In any case, the general agreement with the results of reference [11] is reasonable.

Fig. (11.5) shows the KER spectra, i.e., the dissociative photoionization cross section differential in the kinetic energy of the ejected atomic fragments, for several choices of the photon energy. Leaving apart the absolute value of the cross sections, the KER spectra are almost identical for all photon energies. The figure shows that these spectra are very similar to those obtained by removing the effect of the autoionizing states. These shapes are very similar to the Franck-Condon factor between the initial vibrational state and the dissociative continua associated with the $1s\sigma$ state of HeH^{2+} (which peaks at around 17.5 eV, see Fig. (11.1)) and the $2p\sigma$ state of HeH^{2+} (which peaks at around 11.5 eV, see Fig. (11.1)). Autoionization through the Q_1 doubly excited states introduces some distortions in the KER spectra, for both $^1\Sigma^+$ and $^1\Pi$ contributions, when these states are effectively populated by photon absorption. However, due to the dominant role of the non resonant dissociative ionization process that appears in the same range of kinetic energies, the resulting resonant structures are nearly invisible. This is at variance with dissociative ionization in H_2, for which resonance peaks are clearly visible since they appear for kinetic energies quite different from those associated with the non resonant dissociative ionization process [19].

11.4 Conclusions

We have investigated photoionization of HeH^+ with linearly polarized light in the 40-80 eV photon energy range by using the theoretical method of Sánchez and Martín [19, 20]. This method includes all electronic and vibrational degrees of freedom as well as the interferences between all possible ionization and dissociation channels. The results show that dissociative ionization leading to $He^+(1s) + H^+ + e^-$ entirely dominates the photoionization spectrum. The calculated integral cross section increases smoothly from the threshold up to 47 eV where it reaches a maximum and then decreases monotonically as the photon energy increases. The same behavior is obtained for both $^1\Sigma^+$ and $^1\Pi$ final symmetries, although the latter is approximately four times larger. Our results for the $^1\Sigma^+$ final symmetry are in reasonable agreement with previously reported ones [11]. Cross sections differential in the energy of the remaining ions exhibit a very simple behavior: for all photon energies they are similar to the Franck-Condon distribution that is obtained from the overlaps between the initial vibronic state and the final dissociative states associated with the HeH^{2+} ionization threshold. The maximum of such distributions appear at around 17.5 eV (center-of-mass energy) in the $1s\sigma$ channel and 11.5 eV in the $2p\sigma$ channel. Energy positions and autoionization widths of the HeH^+ doubly excited states of $^1\Sigma^+$ and $^1\Pi$ symmetries have also been evaluated. However, resonant effects due to autoionization are barely visible either in the integral or the differential cross sections. This is at variance with photoionization of the isoelectronic H_2 molecule.

Bibliography

[1] J. Fernández and F. Martín, "Dissociative photoinisation of HeH^+," *Journal of Physics B: Atomic, Molecular and Optical Physics*, vol. 40, pp. 2471–2480, 2007.

[2] W. Roberge and A. Dalgarno, "The formation and destruction of HeH^+ in astrophysical plasmas," *The Astrophysical Journal*, vol. 255, pp. 489–496, 1982.

[3] I. D. G. Herzberg, "The predicted infrared spectrum of helium hydride$^1+$ ion and its possible astrophysical importance," *Transactions of the New York Academy of Sciences*, vol. 38, pp. 14–25, 1977.

[4] J. H. Black, "Molecules in planetary nebulae," *The Astrophysical Journal*, vol. 222, pp. 125–131, 1978.

[5] C. Cecchi-Pestellini and A. Dalgarno, "Emission of HeH^+ in nebulae," *Astrophysical Journal*, vol. 413, pp. 611–618, 1993.

[6] S. Miller, T. J, S. Lepp, and A. Dalgarno, "dentification of features due to H_3^+ in the infrared spectrum of supernova 1987A," *Nature*, vol. 355, pp. 420–422, 2002.

[7] V. P. Gaur, G. C. Joshi, and M. C. Pande, "A possible presence of HeH^+ in white dwarfs," *Astrophysics and Space Science*, vol. 197, pp. 57–60, 1992.

[8] V. K. Dubrovich and A. A. Lipovka, "Distortions of cosmic blackbody spectrum due to luminescence of H_2D^+ molecules," *Astronomy and Astrophysics*, vol. 296, p. 635, 1995.

[9] S. L. andJ. M. Shull, "Molecules in the early universe," *The Astrophysical Journal*, vol. 280, pp. 465–469, 1994.

[10] S. L. Guberman, "Dissociative recombination without a curve crossing," *Physical Review A*, vol. 49, pp. R4277–R4280, 1994.

[11] A. Saenz, "Photoabsorption and photoionization of HeH^+," *Physical Review A*, vol. 67, p. 033409, 2003.

[12] T. G. Winter, M. D. Duncan, and N. F. Lane, "Exact eigenvalues, electronic wavefunctions and their derivatives with respect to the internuclear separation for the lowest 20 states of the HeH^{2+} molecule," *Journal of Physics B: Atomic, Molecular and Optical Physics*, vol. 10, pp. 285–304, 1977.

[13] E. Holzschuh, "Measurement of the neutrino mass from tritium beta -decay," *Reports on Progress in Physics*, vol. 55, pp. 1035–1091, 1992.

[14] F. Martín, "Ionization and dissociation using B-splines: Photoionization of the hydrogen molecule," *Journal of Physics B: Atomic, Molecular and Optical Physics*, vol. 32, pp. R197–R231, 1999.

[15] J. Tennyson, "Continuum states of HeH^+," *Journal of Physics B: Atomic, Molecular and Optical Physics*, vol. 31, pp. L177–L185, 1998.

[16] P. Froelich, B. Jeziorski, W. Kolos, H. Monkhorst, A. S. A, and K. Szalewicz, "Probability distribution of excitations to the electronic continuum of HeT^+ following the β decay of the T_2 molecule," *Physical Review Letters*, vol. 71, pp. 2871–2874, 1993.

[17] M. H. Cherkani, S. Szucs, M. Terao, H. Hus, and F. Brouillard, "Transfer ionization in He^{2+}-H^- collisions: Cross section measurements in the energy range 0.2-1300 eV," *Journal of Physics B: Atomic, Molecular and Optical Physics*, vol. 24, pp. 209–218, 1991.

[18] M. Terao, C. Harel, A. Salin, and R. J. Allan, "Theoretical study of single-electron capture in He^{2+} - h^- collision," *Zeitschrift für Physik D Atoms, Molecules and Clusters*, vol. 7, pp. 319–332, 1998.

[19] I. Sánchez and F. Martín, "Origin of unidentified structures in resonant dissociative photoionization of H_2," *Physical Review letters*, vol. 79, pp. 1654–1657, 1997.

[20] I. Sánchez and F. Martín, "Resonant dissociative photoionization of H_2 and D_2," *Physical Review A*, vol. 57, pp. 1006–1017, 1998.

[21] I. Sánchez and F. Martín, "Multichannel dissociation in resonant photoionization of H_2," *Physical Review letters*, vol. 82, pp. 3775–3778, 1999.

[22] H. Bachau, E. Cormier, P. Decleva, J. E. Hansen, and F. Martín, "Applications of B-splines in atomic and molecular physics," *Reports on Progress in Physics*, vol. 64, pp. 1601–1729, 2001.

[23] F. Martín, J. Fernández, T. Havermeier, L. Foucar, T. Weber, K. Kreidi, M. Schöffler, L. Schmidt, T. Jahnke, A. L. Landers, O. Jagutzki, A. Czasch, E. Benis, T. Osipov, A. Belkacem, M. H. Prior, H. Schmidt-Böcking, C. L. Cocke, and R. Dörner, "Single photon-induced symmetry breaking H_2 dissociation," *Science*, vol. 315, pp. 629–633, 2007.

[24] J. Fernández, O. A. Fojón, A. Palacios, and F. Martín, "Interference from fast electron emission in molecular photoionization," *Physical Review Letters*, vol. 98, p. 043005, 2007.

[25] G. Laurent, J. Fernández, S. Legendre, M. Tarisien, L. Adoui, A. Cassimi, X. Fléchard, F. Frémont, B. Gervais, E. Giglio, J. Grandin, and F. Martín, "Kinematically complete study of dissociative ionization of D_2 by ion-impact," *Physical Review Letters*, vol. 96, p. 173201, 2006.

[26] W. Vanroose, F. Martín, T. N. Rescigno, and C. W. McCurdy, "Complete photo-induced breakup of the H_2 molecule as a probe of molecular electron correlation," *Science*, vol. 310, pp. 1787–1789, 2005.

[27] C. de Boor, *A practical Guide to Splines*. New York: Springer, 1978.

[28] M. Cortés and F. Martín, "Multichannel close-coupling method with L^2 integrable bases," *Journal of Physics B: Atomic, Molecular and Optical Physics*, vol. 27, pp. 5741–5760, 1994.

[29] I. Sánchez and F. Martín, "Representation of the electronic continuum of H_2 with B-spline basis," *Journal of Physics B: Atomic, Molecular and Optical Physics*, vol. 30, pp. 679–692, 1997.

[30] I. Sánchez and F. Martín, "The doubly excited states of the H_2 molecule," *Journal of Chemical Physics*, vol. 106, pp. 7720–7730, 1997.

Chapter 12

Highly energetic collision of particles with D_2 molecules

"It is also a good rule not to put overmuch confidence in the observational results that are put forward until they are confirmed by theory."

Arthur Stanley Eddington

Table of Contents

The work reported in this Chapter has led to the publications [1, 2].

12.1 Introduction

SINCE the early 70's, extensive experimental and theoretical works have been devoted to the study of doubly excited states of H_2 or D_2 (see Chapters 7 and 8 and reference therein). However, although many of these states decay by autoionization, no previous work has identified electron emission following double excitation of H_2 or D_2. As a result of the collision process, different states of the H_2 molecule as well as those of the H_2^+ and H_2^{2+} can be populated (see Fig. (7.1) of Chapter 7).

In this Chapter we present the collision of highly energetic particles, ions and electrons, with the $H_2(D_2)$ molecule. In the first part, we present a kinematically complete study of dissociative ionization of D_2 by 13.6 MeV/u S^{15+} ions. The experiment allows us to unravel the competing mechanisms, namely direct single ionization, autoionization of doubly-excited states, ionization-excitation and double ionization. The conclusions are supported by theoretical calculations in which the correlated motion of all electrons and nuclei, and interferences between them are described from first principles. The second part of this Chapter is devoted to the electron

spectra originating from ionization of D_2 by impact of 2.4 KeV electrons measured at various emission angles. After subtraction of the direct ionization background, we will see that three peaks are clearly visible in the electron energy range $1-20$ eV. Two of these peaks are due to autoionization of doubly excited states lying above the first and second ionization thresholds. The third peak is attributed to the strong interference between direct ionization and autoionization while the molecule is already dissociating. All the theoretical methods have been described previously in Chapter 5.

12.2 S^{+15} ions collision with D_2 molecules

Ionization of the simplest H_2 molecule by impact of photons [3, 4, 5, 6, 7, 8, 9], electrons [2, 10, 11, 12] and ions [13, 14, 15, 16, 17, 18, 19] has been the subject of extensive experimental and theoretical investigations for almost three decades. With the advent of kinematically complete collision experiments, in which the full momentum vector of all charged particles is determined, it is now possible to investigate these processes with unprecedented detail and precision. So far a few examples have been reported in the literature for photoionization [20, 21, 22, 23, 24] and electron impact ionization [25]. The measurement of the energy distribution of the ionic fragments, formed by the dissociation of the molecule, has been the the object of a great number of works in the preceding years. The first measurement by electron collision [26, 27, 28, 29, 30, 31], and by ions [13, 14]. The main objective of these works have been the study of the molecular state of H_2 and H_2^+ populated in the collision. Thus, the measured kinetic energy distribution is accompanied by theoretical distributions obtained by the projection method [32], which is the Franck-Condon factor calculated from the ground state of H_2 and different final states of H_2^+ state.

In contrast with photoionization (see preceding Chapters), in which a well defined amount of energy is absorbed by the target (the photon energy), the energy absorbed by H_2 in a collision with a fast charged projectile follows a distribution with practically no upper limit. Thus all processes capable of ionizing the molecule are energetically allowed and can, in principle, occur simultaneously. It also means that ionization can involve one or all electrons of the molecule. In the case of ion impact, the only existing electron-ion coincidence experiment has been reported by Dimopoulou *et al*. [33]. In this work both non dissociative and dissociative ionization of H_2 were investigated in the range of very low ion kinetic energy (< 0.04 eV). However, it has been shown in previous experiments [34] that major dissociating processes lead to proton energies as large as 12 eV.

It is known that the dominant ionization process is emission of a single electron that leaves the residual D_2^+ molecular ion in its ground $^2\Sigma_g^+$ electronic state [17]. Most of D_2^+ ions remain in a bound vibrational level (around $\upsilon = 2$), while only a few undergo dissociative single ionization (DSI). Two electron processes also contribute to ionization: ionization-excitation (IE), double ionization (DI), and double excitation followed by autoionization (AI). In DI, both electrons are emitted into the continuum through a direct non-resonant ionization process, leading to a D_2^{2+} molecular ion that dissociates through Coulomb explosion. In IE, only one electron is emitted into the continuum, while D_2^+ is formed in an excited electronic state that dissociates. DSI, IE and DI are direct ionization processes. In contrast, AI is a resonant process that results from the decay of a doubly excited state (DES) into the ionization continuum. The corresponding D_2^+ ion can remain in either the ground or an excited electronic state [5]. Since the DES potential energy curves are repulsive, dissociation into two neutral D atoms also competes with AI. There is a series of DES, Q_n, associated with each ionization threshold, n (i.e., associated with each electronic state of D_2^+). Each series contains an infinite number of DES and there is an infinite number of such series. Previous photoionization experiments have shown that the DES play a crucial role in dissociative ionization of D_2 [9] and the same is expected in the present case.

It is then clear that the number of open channels leading to dissociative ionization is so large

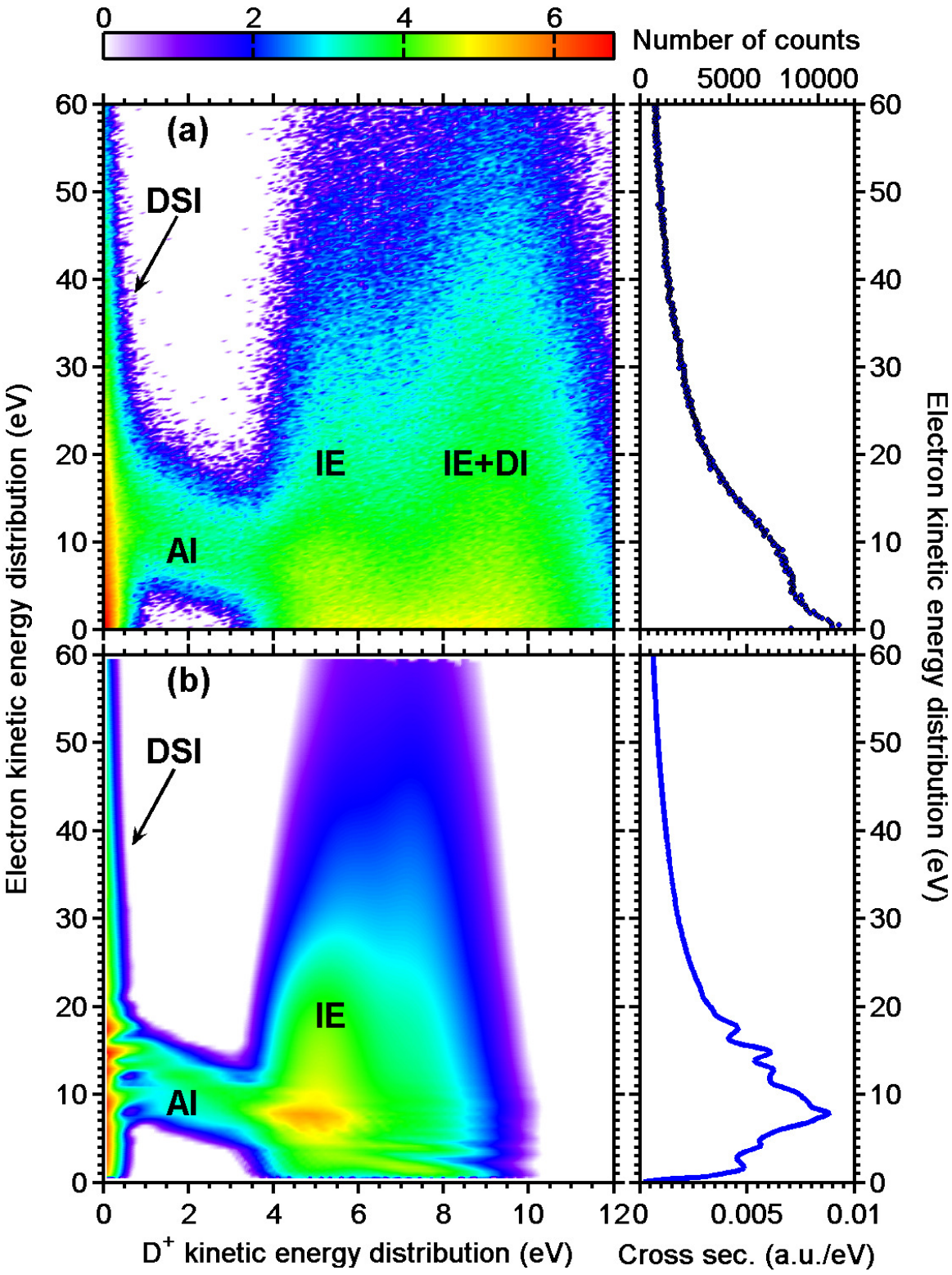

Figure 12.1: Electron and D^+ kinetic energy correlation diagram resulting from 13.6 MeV/u S^{15+}-D_2 collision. (a): experimental results; (b): theoretical results. The right panels show integration over D^+ energy.

that only a experimental approach that images all charged particles in coincidence can disentangle the different mechanisms. Such an experiment was performed in parallel with our theoretical calculations, at GANIL (Grand Accélérateur National d'Ions Lourds) in Caen. A 13.6 MeV/u S^{15+} projectile beam intersected a D_2 supersonic molecular gas jet. The D^+ fragments up to 12 eV are collected by a static electric field (30 V/cm) with 4π solid angle acceptance and directed onto a 80 mm diameter position sensitive channel-plate detector. In addition, a magnetic field (18 Gauss) confines the electrons on helical trajectories, insuring a 4π solid angle coverage for kinetic energies up to 55 eV. From both the time of flight and coordinates of impact position of each particle detected, the complete momentum vector of the electrons and fragment ions were then reconstructed, and the energy deduced ($\Delta E/E$ = 15% and 5% for electrons and ions, respectively).

The complete ion-electron energy correlation diagram is shown in Fig. (12.1a). The result has been integrated over the emission angles of both electron and ion. As expected, the energy sharing between electrons and nuclei is much more complex than in photoionization processes in which an almost linear dependence between electron and ion kinetic energies is observed [22]. The latter behavior is the consequence of energy conservation, $E_{e^-} = -2E_{D^+} + E_T - E_\infty$, where E_{e^-} is the electron kinetic energies, E_{D^+} is the D^+ kinetic energies, E_T is the total energy transferred to the molecule, and E_∞ is the dissociation energy limit. We can see a similar behavior for D^+ energies between 1 and 4 eV. This is because, in the case of resonant dissociative ionization through a DES, E_T is more or less fixed and so is the difference $E_T - E_\infty$.

The electron and D^+ energy distributions are shown in Figs. (12.1a) and (12.2a), respectively. In the latter case, an analysis of the coincidence measurements allows us to extract the contribution of each dissociative process (Fig. (12.2a)). The total D^+ distribution agrees qualitatively with that previously measured by Edwards *et al.* [34] using a different projectile and a different impact velocity (see Fig. (1.6) of Chapter 1). The D^+ energy distribution associated with the AI process is determined by integrating the Auger peaks observed in the electron energy distribution for a specific D^+ energy range. In doing so, one assumes that resonant and non resonant processes sum up incoherently, which is not strictly true [5] but is a reasonable approximation in the present case since DSI and AI appear in separate regions of the e^--D^+ diagram (except for very low D^+ energies) and, therefore, the procedure should give a reasonable estimation of the AI process. Subtraction of this AI contribution from the total D^+ distribution allows us to separate the DSI contribution (localized on the low energy side) from the DI+IE one (localized on the high energy side, see Fig. (12.2a)). The shape of the DI distribution is obtained from coincident detection of two D^+ fragments. We have found that this shape is very close to the corresponding Franck-Condon (FC) factor. The relative contribution of this process has been deduced from the known DI/IE cross section ratio [17], which is $\sim$ 20% for a large variety of projectiles with charge q and velocity v satisfying the condition $0.1 < q/v < 1.5$. In the present experiment, q/v=0.7. All contributions are shown in Fig. (12.2a).

Relative cross sections for each process have been obtained by integrating the D^+ energy distributions. We have found that dissociative ionization is only 6.2$\pm$1.2% of the total ionization cross section. Relative contributions to dissociative ionization from the different processes are: DSI 7.3$\pm$1.8%, AI 13.0$\pm$2.7%, IE 64.6$\pm$7.5%, and DI 15.1$\pm$4.4%. The contribution of DSI to the total non dissociative single ionization is 0.48%, close to the value 0.485% determined by Ben-Itzhak *et al.* [35]. To better understand the origin of the structures observed in the experiment, we have evaluated angle integrated cross sections, differential in both electron and D^+ energies, in the framework of the first Born and dipole approximations using the theory described in Chapter 5. In this case, the final state $\Psi^+_{\alpha\upsilon_\alpha\varepsilon lmW_{\alpha\upsilon_\alpha}}$ results from a close-coupling calculation (see Eq. (3.88) of Chapter 3) that includes contributions from the ten lowest ionization thresholds of D_2, [$X^2\Sigma^+_g(1s\sigma_g)$, $^2\Sigma^+_u(2p\sigma_u)$, $^2\Pi_u(2p\pi_u)$, $^2\Sigma^+_g(2s\sigma_g)$, $^2\Sigma^+_u(3p\sigma_u)$, $^2\Sigma^+_g(3d\sigma_g)$, $^2\Pi_g(3d\pi_g)$, $^2\Delta(3d\delta_g)$, $^2\Pi_u(3p\pi_u)$, $^2\Sigma^+_g(3s\sigma_g)$, $^2\Sigma^+_u(4f\sigma_u)$], the Q_1, Q_2, Q_3 and Q_4 doubly excited states, as well as the corresponding vibrational and dissociative states. The results are shown in Figs. (12.1b) and (12.2b). The calculated

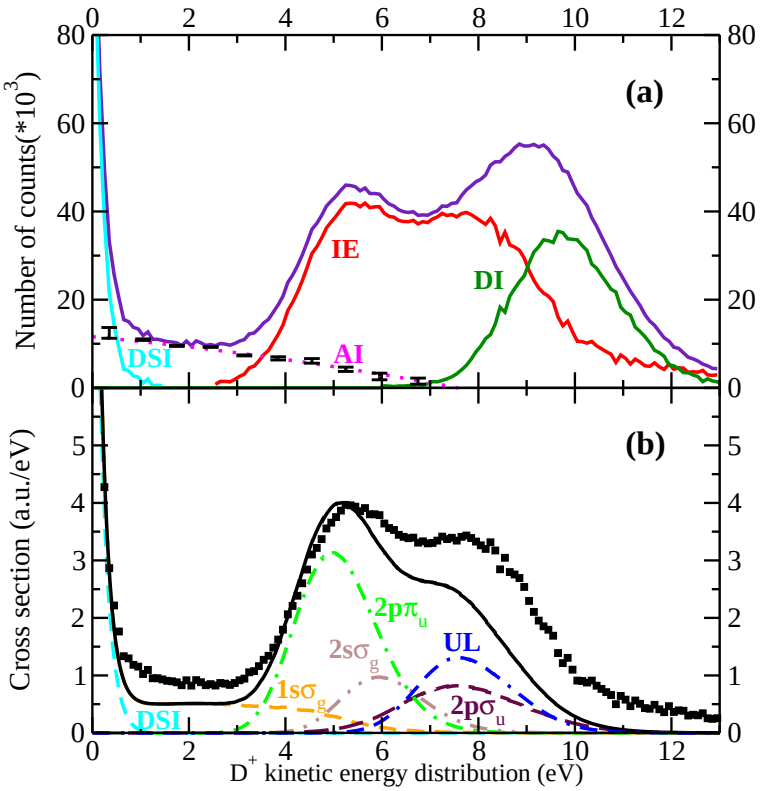

Figure 12.2: D^+ kinetic energy distribution for the 13.6 MeV/u S^{15+}-D_2 collision. (a) Experimental results. DSI, direct single ionization; IE, ionization excitation; AI, autoionization (error bars are shown for illustration); DI, double ionization. (b) Theoretical results for DSI+AI+IE (full line) compared to experimental results (squares). Contributions from the $1s\sigma_g$, $2p\sigma_u$, $2p\pi_u$, and $2s\sigma_g$ ionization thresholds are shown separately. Contributions from upper ionization thresholds (UL) are shown together.

doubly differential cross sections are in reasonable agreement with experiment except for D^+ energies > 8 eV. This is not surprising because this is the region where DI becomes important (Fig. (12.2a)) and the corresponding channels are not included in the calculations. The agreement is also reasonable for the singly-differential cross sections (Figs. (12.1b) and (12.2b)) except for very low electron energies. The AI distribution is obtained by removing the calculated non resonant DSI distribution from the total ${}^2\Sigma_g^+(1s\sigma_g)$ one. It can be seen that both DSI and AI distributions are in good agreement with experiment. This proves that the assumptions made to extract this information directly from experiment (see above) are appropriate. Only at very small D^+ energy, AI is superimposed to DSI, but this is a very small region and, therefore, it has no practical consequence on the ratios given above. The analysis of the final state wave function allows us to separate the individual channels contributing to IE and AI. At D^+ energies of ~ 5 eV, ionization through the ${}^2\Pi_u(2p\pi_u)$ threshold is the dominant process, however its sole contribution is not enough to explain all features observed experimentally. Indeed, higher channels are responsible for the second maximum observed in Fig. (12.2b). The discrepancy with experiment around this second maximum indicates that IE leads to highly excited D_2^+ states not included in the theory (namely, beyond the 11th D_2^+ state). Therefore one has to be very careful in trying to fit the total D^+ distribution to an incoherent sum of FC factors associated to only a few IE channels. Although such a procedure may lead to DSI, IE and DI distributions in qualitative agreement with experiment [34], it fails in predicting the correct contribution of each individual threshold.

The linear behavior observed between 1 and 4 eV in Fig. (12.1) is mainly due to autoionization

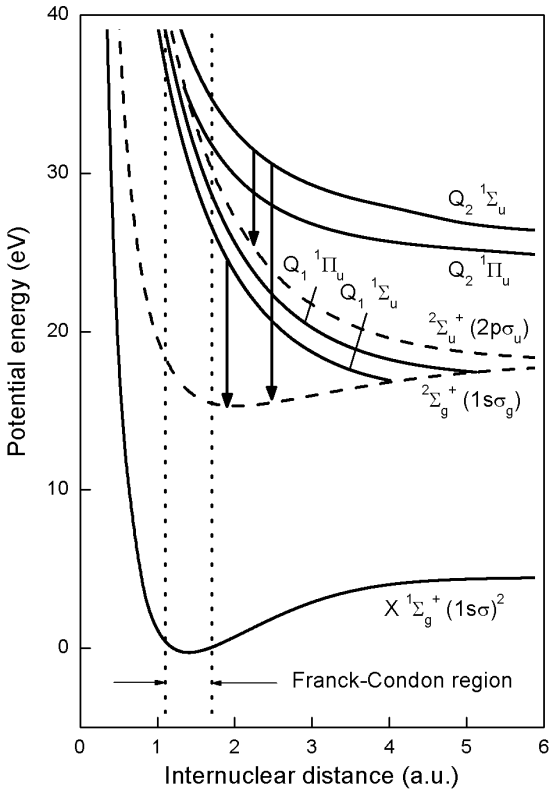

Figure 12.3: Potential energy diagram for D_2. The single-electron (dashed lines) and double-electron (full lines) excited states are taken from [36]. The arrows indicate the possible Auger deexcitation channels following double excitation process.

of the Q_1 states and, to a lesser extent, of the Q_2 ones. The Q_3 and Q_4 states play a minor role. At very low D^+ energy (< 1 eV) and electron energy ≤ 20 eV, the theory shows oscillations that are due to interferences between resonant and non resonant ionization similar to those observed in dissociative photoionization [5]. Such oscillations are not seen in the present experiment due to the limited energy resolution, but they are responsible for the broadening of the linear structure at a D^+ energy of ~ 1 eV.

12.3 Electron collision with D_2 molecules

In this section, we consider the collision of highly energetic electrons with the D_2 target. Fig. (12.3) shows the potential energy curves of some relevant DES of D_2 [5, 37]. The Q_1 DES of D_2 lie above the first ionization threshold (the $X^2\Sigma_g^+(1s\sigma_g)$ state of D_2^+) and may autoionize leading either to (*i*) a bound molecular ion D_2^+ (arrows in Fig. (12.3)) or to (*ii*) a neutral atomic deuterium plus a deuteron (dissociative ionization). Process (*ii*) is possible when most excitation energy is taken by the nuclei instead of by the ejected electron. In this case, the electron kinetic energy is smaller than in process (*i*). Moreover, Fig. (12.3 shows that these DES curves cross the ionization

threshold at large internuclear distances (> 3.5 a.u.) and, therefore, they no longer autoionize in that region. Thus, if the autoionization lifetime is long enough, these states may lead to (*iii*) dissociation of the molecule into two neutral deuterium atoms instead of to ionization. The latter process, called resonant dissociation, competes efficiently with processes (*i*) and (*ii*) [5], but does not lead to electron emission. This means that autoionization can only be observed for those states that autoionize before process (*iii*) occurs. If the autoionization lifetime is very short, the DES will decay in the Franck-Condon region (dotted lines in Fig. (7.1)), but this is not the case in general [5]. The energy position of the Q_2 DES lying above the second ionization threshold $^2\Sigma_u^+(2p\sigma_u)$ can also be shown in Fig. (7.1). These states may decay by autoionization either to the first or to the second ionization threshold. Thus, if e.g. autoionization occurs in the Franck-Condon region, these states lead to slow (< 5 eV) or fast ($\sim 5-20$ eV) electrons corresponding to autoionization through the $^2\Sigma_u^+(2p\sigma_u)$ and $X^2\Sigma_g^+(1s\sigma_g)$ thresholds, respectively. As for the Q_1 states, processes (*ii*) and (*iii*) are also possible.

As mentioned above, in addition to autoionization, DE of D_2 (and H_2) leads to the ejection of deuterons (protons) and/or excited neutral atoms. Hence, to investigate the DES of H_2 and D_2, most previous experimental studies focused on the analysis of both the fragment kinetic energy distributions [9, 38] and the photons emitted by the excited fragments [31, 39]. From these studies, qualitative information on the energy positions of these states has been obtained. An estimate of autoionization widths as functions of internuclear separation has been obtained for the lowest DES from the proton/deuteron ratio in dissociative photoionization of H_2 and D_2 [38]. Also, the relative importance of partial autoionization widths corresponding to different ionization thresholds has been determined [9]. Nevertheless, experimental data for resonance parameters is still very scarce, mainly due to the existence of strong interferences between (*i*), (*ii*) and (*iii*) [40] that complicate the analysis. Hence, most of the information about DES of H_2 and D_2 comes from theoretical works [5, 5, 37, 41, 42, 43].

Observation of autoionization electrons by electron spectroscopy should bring additional and more direct information about the properties of DES. This is an experimental challenge. First of all, because electrons associated with the DE process are much less abundant than those originating from the dominant direct ionization (DI) process. Secondly, because the nuclear motion smooths all resonance peaks associated with the DE process [5]. These difficulties explain why previous attempts in photoionization experiments have failed in identifying autoionization electrons [44, 45]. Very recently, the presence of these electrons has been suggested in electron spectra following 68 MeV/u Kr^{33+} + H_2 collisions [46], however no definite conclusion could be obtained because resonance peaks were absent at several observation angles. Thus, observation of autoionization electrons still remains an open problem.

In this Chapter we present the first clear evidence of autoionization electrons following DE of D_2 after impact of 2.4 keV electrons. These electrons have been observed at angles ranging from 30° to 130°. The key point for a successful observation of autoionization electrons is to perform measurements with high statistics. This is essential to separate the corresponding signal from the background due to the dominant DI process. Besides providing quantitative information on several DES, the results presented in this Chapter opens the door for future experiments in which autoionization electrons are measured in coincidence with the D^+ fragments or with the Lyman-α rays emitted from excited $D(n\ell)$. The latter experiments will be important to obtain direct information on energy positions and lifetimes of individual DES, which is not possible by just analyzing the energy of the D^+ fragments.

The experiment was performed in parallel with our theoretical calculations, at CIRIL (Caen) using an electron gun of simple design. A beam of 2.4-keV electrons collimated to a diameter of ~ 2 mm was directed onto a jet of D_2 molecules. The emitted target electrons were energy analyzed using a single-stage spectrometer, which consists of a 90° parallel-plate analyzer. The voltage on

the plates of the spectrometer was scanned to record the electron yields as a function of the electron emission energy, for several observation angles relative to the beam direction [47].

Fig. (12.4) shows typical doubly differential cross section (DDCS) spectra as functions of the target electron energy for the emission angles of 30° and 90°. The electrons originate mainly from single ionization. It is seen that the cross section decreases strongly when increasing the emitted electron energy. Superimposed on the ionization spectrum, a small structure centered at $\sim 8-10$ eV is clearly observed. It was verified that this structure is not due to the excitation of spurious gases, such as N_2 or O_2. This reproducible structure is thus attributed to double excitation of D_2. A careful inspection of the spectra (inset of Fig. (12.4)) reveals an additional structure at electron energies around 15 eV. Both the latter structure and the one at $\sim 8-10$ eV are systematically observed at each investigated angle. To enhance the visibility of the DE signal, a polynomial function was used (in the logarithmic scale) to reproduce the DI contribution below 2 eV and above 20eV. The quality of the fit was found to be practically independent of the degree of the polynomial function for degrees ranging from 4 to 7. Subtraction of this DI contribution leads to the DE spectrum, as shown in Fig. (12.5)3 for the emission angle of 90°. As mentioned above, the DE spectrum consists mainly of two peaks centered at $\sim$ 8.5 eV and 15 eV. In addition, a low intense structure is also observed at electron energies lower than 5 eV. We have found that the shape of the DE spectrum is nearly independent of the observation angle within the statistical error bars.

The whole spectrum (open circles in Fig. (12.4)) and the direct ionization DDCS (full curves in Fig. (12.4)) have been integrated over the emitted electron energy ε and the emission angle. This gives total and direct ionization cross sections σ_{tot} and σ_I, respectively. The resulting cross section σ_I was then normalized to the value of $1.0\cdot10^{-17}$ cm^2 obtained by extrapolation of previous measurements [34]. In principle, it is not possible to extract absolute DE cross sections from the difference between σ_{tot} and σ_I due to the interference between DI and autoionizing DE [48]. However, one can use this procedure to estimate the order of magnitude of the DE cross section. We have found a value of $(1.9 \pm 0.6)\cdot10^{-19}$ cm^2, which is comparable to the value of $0.64\cdot10^{-19}$ cm^2 obtained by extrapolation of the measurements reported in [34]. This result supports the validity of our fitting procedure to determine the DI background.

The basic formalism to analyze the angular distribution of ionized electrons has been introduced in Chapter 4. To our knowledge, this formalism has only been applied to evaluate photoionization cross sections, which, as we showed in that Chapter, are related to the angle integrated cross section $\sigma(\varepsilon)$ through the usual formula $d\sigma/d\Omega = \sigma(\varepsilon)[1+\beta(\varepsilon)P_2(\cos\theta)]/(4\pi)$. Previous photoionization experiments on H_2 [49, 50] have shown that the β parameter barely depends on ε even in the vicinity of DES. Consequently, the $d\sigma/d\Omega$ and σ spectra are nearly identical at any angle up to a normalization factor. Since dipole transitions govern the entire spectrum at the high impact energy considered in this work ($\sim$ 13 a.u.), a similar behavior is expected in our experiments. As mentioned above, this is exactly what we observe. Thus, in order to understand the origin of the structures observed in the experiment, it is enough to consider the angle integrated cross section. The latter has been evaluated in the framework of the first Born and dipole approximations.

The theoretical results are presented in Fig. (12.5) (right side), normalized to the experimental spectrum at 90° and convoluted with a Gaussian function to account for the 5 % energy resolution in the experiment. The three structures observed in the experiment are also present in the calculated spectrum. More precisely, the dominant peak is centered at 8.5 eV in both spectra, and the widths are close to each other. The peak observed at $\sim$ 15 eV is reproduced more or less by the calculation, although the intensity is slightly larger than in the experiment. This is also the case for the structure observed at energies smaller than 5 eV. Concerning the comparison with experiment, it should be noted that, in addition to the statistical uncertainties, the DI subtraction procedure induces further uncertainties on the final DE spectra. The latter uncertainties are particularly significant ($\sim$ 30 %) in the low energy ($<$ 5 eV) region. Thus, taking into account the difficulties in extracting the

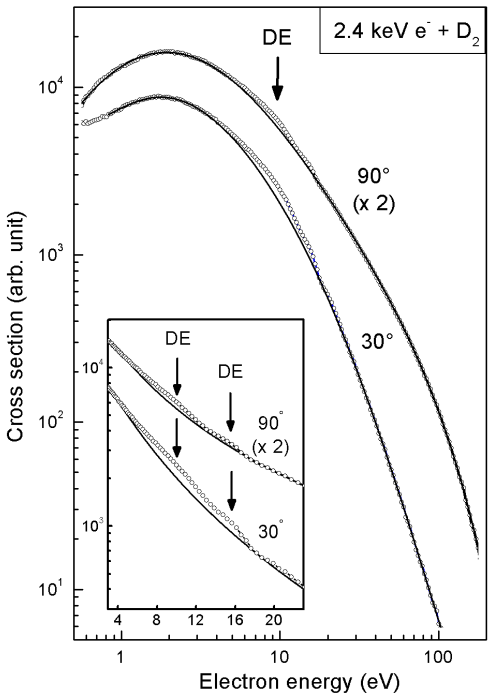

Figure 12.4: Cross section for electron emission by 2.4 keV e^- impacting on D_2, as a function of the ejected electron energy, obtained at the observation angles of 30^o and 90^o. The full curve is a fit of the background. The arrows indicate the positions of the structures due to autoionizing double excitation of D_2.

information from experiment, the agreement between experiment and theory is reasonably good.

The theoretical calculations allow one to understand the origin of the different peaks observed in the experiment. Fig. (12.5) shows the contributions of the $^1\Sigma_u^+$ (dashed line) and $^1\Pi_u$ (dotted line) symmetries (these are the only symmetries allowed in the dipole approximation). Peak (a) is essentially due to autoionization of the lowest Q_2 states of $^1\Pi_u$ symmetry through the excited ionization threshold $^2\Sigma_u^+(2p\sigma_u)$. Autoionization of these states through the lowest threshold $X^2\Sigma_g^+(1s\sigma_g)$ leads to a significant part of peak (b). Another important contribution to peak (b) comes from autoionization of the Q_1 states of $^1\Sigma_u^+$ symmetry through the lowest ionization threshold $X^2\Sigma_g^+(1s\sigma_g)$. In contrast, the contributions of Q_3 and Q_4 states were found to be negligible, so one can expect that higher DES will have a minor effect. Most of the signal associated to the observed peaks correspond to *dissociative* ionization.

The origin of peak (c) is subtle. This peak appears both in the $^1\Sigma_u^+$ and $^1\Pi_u$ symmetries and results from the interference between direct ionization, autoionization and dissociation. Indeed, the autoionized electron is ejected when the two nuclei have already began to separate. This means that the interference between autoionizing DE and DI does not occur in the Franck Condon region or, equivalently, that the interference manifests at electron energies different from those corresponding to a ”vertical” electron decay. The existence of strong interference effects related to molecular dissociation has been theoretically predicted [5] in the case of H_2 photoionization. The interferences are clearly visible in the kinetic energy distribution (KED) of ejected protons and explain, e.g., the

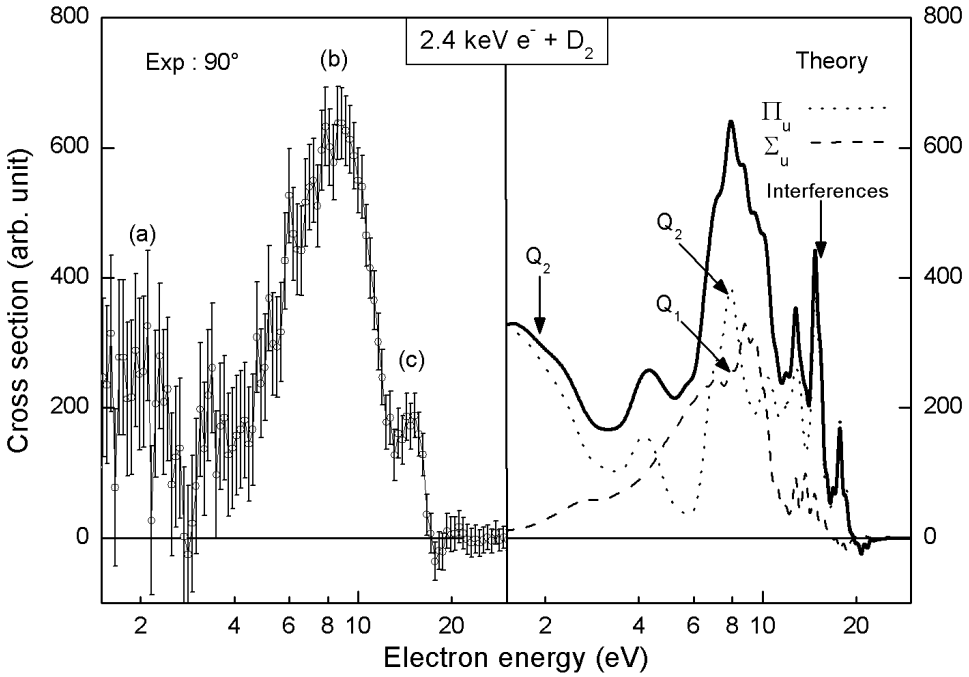

Figure 12.5: Experimental (left side) and theoretical (right side) cross sections for Auger electron emission in 2.4 keV e^- + D_2 collisions, as a function of the ejected electron energy. Statistical error bars for the experimental data are also reported.

presence of unexpected peaks in the spectra measured by Ito *et al.* [9] at low proton energies. Earlier experimental works [34] have not shown any evidence for this phenomenon. Thus, using a totally different approach, i.e., electron spectroscopy, we provide additional evidence for the existence of these interference effects.

12.4 Conclusions

In conclusion, we have performed kinematically complete theoretical calculation of dissociative ionization of D_2 by impact of fast ions and electrons corroborated by different experimental results developed in parallel. As in photoionization, autoionization from DES play a crucial role. In contrast, unusually large contributions from ionization-excitation and double ionization are observed in the electron-D^+ correlation spectra, in agreement with accurate theoretical calculations. These results show that kinematically complete collision experiments are ideal to investigate a large variety of ionization mechanisms, even larger than in photoionization experiments.

Also we have provided clear evidence for electron emission following double excitation of D_2 by fast electron impact. Due to the high statistics of the spectra, the present results give detailed information on the energy distribution of the emitted autoionization electrons. After subtraction of the DI contribution, three structures due to autoionizing double excitation have been revealed at energies lower than 20 eV. Comparison with accurate theoretical calculations allows us to identify the dominant autoionizing states of D_2 as well as the dominant decay channels. Theoretical calculations have shown that Q_1 and Q_2 DES give the major contribution to the double excitation

process. They also show that the peak observed at energies larger than $\sim$ 10 eV results from interference between direct ionization and autoionization while the molecule dissociates. This confirms the observations of Ito *et al*. [9] and shows that a correct assignment of the observed peaks requires the inclusion the nuclear motion.

In both cases, for the first time, autoionization electrons following double excitation of D_2 are clearly detected and separated from other processes. One of the strengths of the presented results is to combine experiment and theory. The excellent agreement between experiment and theory confirms (i) the possibility to observe molecular autoionization electrons (that nobody else have observed), and (ii) the validity of the theoretical method presented in Chapter 5. Therefore, the present results open the door for experimental and theoretical investigations not considered so far. For example, new generations of experimental set-ups now available (e.g. coincidence measurements) could be used to get finer details on molecular doubly excited states (such as partial autoionization lifetimes) that are not accessible through current experimental approaches based on the analysis of heavy fragments. From the theoretical side, this is the first time that fully *ab initio* calculations on highly energetic particle impact ionization on H_2 have been successfully performed including both the doubly excited states of the molecule and the nuclear motion. All previous attempts were based on the fixed nuclei approximation. Therefore these works gives the possibility for realistic theoretical descriptions of electron impact ionization in more complicated molecules (see Chapter 13). This is very important because, as mentioned before, some of the observed structures result from the interference between ionization and dissociation. Such structures cannot be obtained if one ignores the nuclear motion.

Bibliography

[1] G. Laurent, J. Fernández, S. Legendre, M. Tarisien, L. Adoui, A. Cassimi, X. Fléchard, F. Frémont, B. Gervais, E. Giglio, J. Grandin, and F. Martín, "Kinematically complete study of dissociative ionization of D_2 by ion-impact," *Physical Review Letters*, vol. 96, p. 173201, 2006.

[2] J. Y. Chesnel, D. Martina, P. Sobocinski, O. Kamalou, F. Frémont, J. Fernández, and F. Martín, "Autoionization electrons following double excitation of D_2 in 2.4 KeV e^- + D_2 collisions: Experimental and theoretical evidence," *Physical Review A*, vol. 70, p. 010701(R), 2004.

[3] S. Strathdee and R. Browning, "Dissociative photoionisation of H_2: Proton kinetic energy spectra," *Journal of Physics B: Atomic, Molecular and Optical Physics*, vol. 12, pp. 1789–1804, 1979.

[4] C. J. Latimer, J. Geddes, M. A. MacDonald, N. Kouchi, and K. F. Dunn, "The photodissociative ionization of hydrogen and deuterium in the VUV via Π states," *Journal of Physics B: Atomic, Molecular and Optical Physics*, vol. 29, pp. 6113–6121, 1996.

[5] I. Sánchez and F. Martín, "Origin of unidentified structures in resonant dissociative photoionization of H_2," *Physical Review letters*, vol. 79, pp. 1654–1657, 1997.

[6] I. B. Jr. and C. E. Bielschowsky, "Doubly excited states of molecular hydrogen: theoretical absorption and photodissociation cross sections," *Journal of Physics B: Atomic, Molecular and Optical Physics*, vol. 33, pp. 1713–1724, 2000.

[7] K. Ito, J. Adachi, R. Hall, S. Motoki, E. Shigemasa, K. Soejima, and A. Yagishita, "Photoelectron angular distributions from dissociative photoionization channels of fixed-in-space molecular hydrogen," *Journal of Physics B: Atomic, Molecular and Optical Physics*, vol. 33, pp. 527–533, 2000.

[8] W. Vanroose, F. Martín, T. N. Rescigno, and C. W. McCurdy, "Complete photo-induced breakup of the H_2 molecule as a probe of molecular electron correlation," *Science*, vol. 310, pp. 1787–1789, 2005.

[9] K. Ito, R. I. Hall, and M. Ukai, "Dissociative photoionization of H_2 and D_2 in the energy region of 25-45 eV," *The Journal of Chemical Physics*, vol. 104, pp. 8449–8457, 1996.

[10] N. Lermer, B. R. Todd, N. M. Cann, Y. Zheng, C. E. Brion, Z. Yang, and E. R. Davidson, "Electron momentum spectroscopy of H_2 and D_2: Ionization to ground and excited final states," *Physical Review A*, vol. 56, pp. 1393–1402, 1997.

[11] N. Kouchi, M. Ukai, and Y. Hatano, "Dissociation dynamics of superexcited molecular hydrogen," *Journal of Physics B: Atomic, Molecular and Optical Physics*, vol. 30, pp. 2319–2344, 1997.

[12] A. K. Edwards and Q. Zheng, "Excitation of the $Q_1\ ^1\Sigma_g^+$ doubly excited state of H_2 by electron impact," *Journal of Physics B: Atomic, Molecular and Optical Physics*, vol. 34, pp. 1539–1548, 2001.

[13] A. K. Edwards, R. M. Wood, and M. F. Steuer, "Production of H^+ fragments from H_2 by fast projectiles," *Physical Review A*, vol. 16, pp. 1385–1389, 1977.

[14] R. M. Wood, A. K. Edwards, and M. F. Steuer, "Dissociative ionization of H_2 and D_2 produced by bombardment with fast He^+ ions," *Physical Review A*, vol. 15, pp. 1433–1437, 1977.

[15] B. G. Lindsay, F. B. Yousif, F. R. Simpson, and C. J. Latimer, "The dissociative ionisation of hydrogen by 5-25 keV protons: Energy spectra and angular distribution of fragment ions," *Journal of Physics B: Atomic, Molecular and Optical Physics*, vol. 20, pp. 2759–2771, 1987.

[16] E. Y. Kamber, C. L. Cocke, S. Cheng, J. H. McGuire, and S. L. Varghese, "Differential cross sections for single ionisation of He and D_2 by fast protons," *Journal of Physics B: Atomic, Molecular and Optical Physics*, vol. 21, pp. L455–L459, 1988.

[17] E. Wells, I. Ben-Itzhak, K. D. Carnes, and V. Krishnamurthi, "Effect of the projectile charge on the ionization and excitation of hydrogen molecules by fast ion impact," *Physical Review A*, vol. 60, pp. 3734–3739, 1999.

[18] I. Ben-Itzhak, E. Wells, D. Studanski, V. Krishnamurthi, K. D. Carnes, and H. Knudsen, "Double and single ionization of hydrogen molecules by fast-proton impact," *Journal of Physics B: Atomic, Molecular and Optical Physics*, vol. 34, pp. 1143–1161, 2001.

[19] W. Wolff, I. Ben-Itzhak, H. E. Wolf, C. L. Cocke, M. A. Abdallah, and M. Stöckli, "Comparative study of the ground-state dissociation of H_2^+ and D_2^+ induced by ionizing and electron-capture collisions with He^+ at velocities of 0.25 and 0.5 a.u.," *Physical Review A*, vol. 65, p. 042710, 2002.

[20] R. Dörner, H. Bräuning, O. Jagutzki, V. Mergel, M. Achler, R. Moshammer, J. M. Feagin, T. Osipov, A. Bräuning-Demian, L. Spielberger, J. H. McGuire, M. H. Prior, N. Berrah, J. D. Bozek, C. L. Cocke, and H. Schmidt-Böcking, "Double photoionization of spatially aligned D_2," *Physical Review Letters*, vol. 81, pp. 5776–5779, 1998.

[21] Y. Hikosaka and J. H. D. Eland, "Molecular frame photoelectron angular distributions in photoionization of H_2 into the H_2^+ (n=2) states," *Chemical Physics*, vol. 277, pp. 53–59, 2002.

[22] A. Lafosse, M. Lebech, J. C. Brenot, P. M. Guyon, L. Spielberger, O. Jagutzki, J. C. Houver, and D. Dowek, "Molecular frame photoelectron angular distributions in dissociative photoionization of H_2 in the region of the Q_1 and Q_2 doubly excited states," *Journal of Physics B: Atomic, Molecular and Optical Physics*, vol. 36, pp. 4683–4702, 2003.

[23] T. Weber, A. O. Czasch, O. Jagutzki, A. K. Müller, V. Mergel, A. Kheifets, E. Rotenberg, G. Meigs, M. H. Prior, S. Daveau, A. Landers, C. L. Cocke, T. Osipov, R. D. M. no, H. Schmidt-Böcking, and R. Dörner, "Complete photo-fragmentation of the deuterium molecule," *Nature*, vol. 431, pp. 437–440, 2004.

[24] T. Weber, A. Czasch, O. Jagutzki, A. Müller, V. Mergel, A. Kheifets, J. Feagin, E. Rotenberg, G. Meigs, M. H. Prior, S. Daveau, A. L. Landers, C. L. Cocke, T. Osipov, H. Schmidt-Böcking, and R. Dörner, "Fully differential cross sections for photo-double-ionization of D_2," *Physical Review Letters*, vol. 92, p. 163001, 2004.

[25] M. Takahashi, N. Watanabe, Y. Khajuria, Y. Udagawa, and J. H. D. Eland, "Observation of a molecular frame $(e,2e)$ cross section: An $(e,2e+m)$ triple coincidence study on H_2," *Physical Review Letters*, vol. 94, p. 213202, 2005.

[26] G. H. Dunn and L. J. Kieffer, "Dissociative ionization of H_2: A study of angular distributions and energy distributions of resultant fast protons," *Physical Review*, vol. 132, pp. 2109–2117, 1963.

[27] L. J. Kieffer and G. H. Dunn, "Dissociative ionization of H_2 and D_2," *Physical Review*, vol. 158, pp. 61–65, 1967.

[28] A. Crowe and J. W. McConkey, "Experimental evidence for new dissociation channels in electron-impact ionization of H_2," *Physical Review Letters*, vol. 31, pp. 192–196, 1973.

[29] A. Crowe and J. W. McConkey, "Dissociative ionization by electron impact. I. protons from H_2," *Journal of Physics B: Atomic, Molecular and Optical Physics*, vol. 6, pp. 2088–2107, 1973.

[30] J. A. D. Stockdale, V. E. Anderson, A. E. Carter, and L. Deleanu, "Dissociative ionization of molecules by electron impact. I. Apparatus and kinetic energy distributions of D^+ ions from D_2," *The Journal of Chemical Physics*, vol. 63, pp. 3886–3897, 1975.

[31] M. D. Burrows, L. C. McIntyre, Jr., S. R. Ryan, and J. W. E. Lamb, "Dissociative ionization of H_2, D_2, and HD using electron-impact excitation," *Physical Review A*, vol. 21, pp. 1841–1847, 1980.

[32] A. S. Coolidge, H. M. James, and R. D. Present, "A study of the Franck-Condon principle," *The Journal of Chemical Physics*, vol. 4, pp. 193–211, 1936.

[33] C. Dimopoulou, R. Moshammer, D. Fischer, C. Höhr, A. Dorn, P. D. Fainstein, J. R. C. L. Urrutia, C. D. Schröter, H. Kollmus, R. Mann, S. Hagmann, and J. Ullrich, "Breakup of H_2 in singly ionizing collisions with fast protons: Channel-selective low-energy electron spectra," *Physical Review Letters*, vol. 93, p. 123203, 2004.

[34] A. K. Edwards, R. M. Wood, J. L. Davis, and R. L. Ezell, "Collisional ionization and excitation of H_2: Two-electron processes," *Physical Review A*, vol. 42, pp. 1367–1375, 1990.

[35] I. Ben-Itzhak, J. P. Bouhnik, B. D. Esry, I. Gertner, O. Heber, and B. Rosner, "Mean lifetime measurements of $HeH^{2+}(2p\sigma)$ isotopes," *Physical Review A*, vol. 54, pp. 474–479, 1996.

[36] I. Sánchez and F. Martín, "Resonant effects in photoionization of H_2 and D_2," *Journal of Chemical Physics*, vol. 107, pp. 8391–8396, 1997.

[37] I. Sánchez and F. Martín, "Multichannel dissociation in resonant photoionization of H_2," *Physical Review letters*, vol. 82, pp. 3775–3778, 1999.

[38] C. J. Latimer, K. F. Dunn, N. Kouchi, M. A. McDonald, V. Srigengan, and J. Geddes, "A dissociative photoionization study of the autoionization lifetime of the lowest $^1\Sigma_u$ superexcited state in hydrogen and deuterium," *Journal of Physics B: Atomic, Molecular and Optical Physics*, vol. 26, pp. L595–L600, 1993.

[39] M. Glass-Maujean, "Photodissociation of doubly excited states of H_2: Emission of balmer lines," *The Journal of Chemical Physics*, vol. 89, pp. 2839–2843, 1988.

[40] F. Martín, "Ionization and dissociation using B-splines: Photoionization of the hydrogen molecule," *Journal of Physics B: Atomic, Molecular and Optical Physics*, vol. 32, pp. R197–R231, 1999.

[41] C. Bottcher, "Dissociative ionization of the hydrogen molecule," *Journal of Physics B: Atomic, Molecular and Optical Physics*, vol. 7, pp. L352–L357, 1974.

[42] J. Tennyson, "Resonance parameters and quantum defects for superexcited H_2," *Atomic Data and Nuclear Data Tables*, vol. 64, pp. 253–277, 1996.

[43] J. Fernández and F. Martín, "Autoinizing $^1\Sigma_u^+$ and $^1\Pi_u$ states of H_2 above the third and fourth ionization thrseshols," *Journal of Physics B: Atomic, Molecular and Optical Physics*, vol. 34, pp. 4141–4153, 2001.

[44] Y. M. Chung, E.-M. Lee, T. Masuoka, and J. A. R. Samson, "Dissociative photoionization of H_2 from 18 to 124 eV," *The Journal of Chemical Physics*, vol. 99, pp. 885–889, 1993.

[45] C. J. Latimer, K. F. Dunn, F. P. O'Neill, M. A. MacDonald, and N. Kouchi, "Photoionization of hydrogen and deuterium," *The Journal of Chemical Physics*, vol. 102, pp. 722–725, 1995.

[46] N. Stolterfoht, B. Sulik, L. Gulyás, B. Skogvall, J. Y. Chesnel, F. Frémont, D. Hennecart, A. Cassimi, L. Adoui, S. Hossain, and J. A. Tanis, "Interference effects in electron emission from H_2 by 68-MeV/u $Kr^3 3+$ impact: Dependence on the emission angle," *Physical Review A*, vol. 67, p. 030702, 2003.

[47] F. Frémont, K. Sommer, D. Lecler, S. Hicham, P. Boduch, X. Husson, and N. Stolterfoht, "Angular distribution of auger-electron emission following double-electron capture in C^{6+}+He collisions," *Physical Review A*, vol. 46, pp. 222–229, 1992.

[48] A. Bordenave-Montesquieu, P. Moretto-Capelle, A. Gleizes, S. Andriamonje, F. Martin, and A. Salin, "Double excitation of helium by ion impact. II. Experiment and theory for 2-3 Mev proton impact," *Journal of Physics B: Atomic, Molecular and Optical Physics*, vol. 28, pp. 653–670, 1995.

[49] A. C. Parr, J. E. Hardis, S. H. Southworth, C. S. Feigerle, T. A. Ferrett, D. M. P. Holland, F. M. Quinn, B. R. Dobson, J. B. West, G. V. Marr, and J. L. Dehmer, "Vibrationally resolved photoelectron angular distributions for H_2 in the range 17 eV$\leq h\nu \leq$ 39 eV," *Physical Review A*, vol. 37, pp. 437–443, 1988.

[50] S. Southworth, W. D. Brewer, C. M. Truesdale, P. H. Kobrin, D. W. Lindle, and D. A. Shirley, "Photoelectron angular distributions from H_2 and D_2," *Journal of Electron Spectroscopy and Related Phenomena*, vol. 26, pp. 43–51, 1982.

Chapter 13

Conclusions and Perspectives

"No human investigation can be called real science if it cannot be demonstrated mathematically".

Leonardo da Vinci

In this final Chapter the main conclusions obtained in this Thesis and some future lines that can be followed are presented.

The first objective of this work was to investigate the role of the double excited states in the dissociative photoionization of H_2, D_2 and HeH^+ molecules, and in particular, their importance in the photoelectron angular distribution for fixed-in-space molecules. The angular distribution has revealed new and detailed insights into the electronic structure and the dynamics of the photoionization process that were inaccessible by previous studies, for example, by the proton kinetic energy distribution. The role of these states has also been revealed by the collision of highly energetic particles, and it has been shown that fully theoretical calculations are necessary in order to interpret correctly the experimental findings performed in parallel. Coherence and interference phenomena play an essential part in molecular photoionization, as was shown for the showcase molecules H_2^+ and H_2. Their study reveals the role played by quantum mechanical indistinguishability. In this Thesis we have shown that this effects, although small, can be observed in the electron angular distribution for the fixed-in-space case.

Following on from the studies reported here, several research lines suggest themselves. Above we have seen only a very small fraction of the rich and informative research field of resonant and non-resonant electron spectroscopy of free molecules. Before ending this Thesis, we would like to take the opportunity to think about what could be done in the future.

Related to the photoelectron angular distribution results presented in Chapters 4 and 9, several questions are still open. The first line that could be followed would be the study of the effect of the Q_3 and Q_4 doubly excited states in the electron angular distribution. Since these states can autoionized through the first four ionization thresholds, the $1s\sigma_g$, $2p\sigma_u$, $2p\pi_u$ and $2s\sigma_g$ (see for example Fig. (6.1) of Chapter 6), the patterns of the MFPAD should be completely different from from presented in Chapter 9. For example, Fig. (13.1) shows the experimental results obtained by K. Ito *et al.* [1], for different photon energies above the third and fourth ionization thresholds. In particular at 44 eV, it can be observed that the MFPAD obtained by these authors differs considerably with the results obtained at a photon energy of 33 eV, whose origins could come from the contribution of higher resonant states and ionization thresholds. As shown in Chapter 6 devoted to the role of these resonant states in the the study of the proton kinetic energy distribution, their contribution

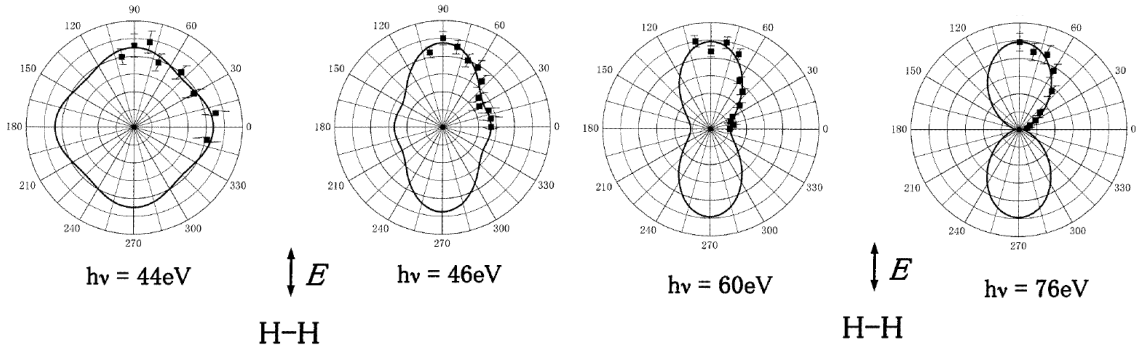

Figure 13.1: Angular distributions of photoelectrons ejected from fixed-in-space molecular hydrogen, aligned perpendicular to the electric vector, measured at four different photon energies; 44, 46, 60 and 76 eV. The molecular axis is oriented along the $0-180^\circ$ line, while the electric vector is along the $90-270^\circ$ line. The full curves are fits to the data. Results obtained by K. Ito *et al.* [1].

is quite small although not negligible. This fact can be checked in Fig. (13.2) that displays the contribution of the first ionization thresholds to the total electron beta parameter (dissociative plus non-dissociative contributions). Clearly the contribution of the Q_3 and Q_4 resonant states should be observed in the MFPADs.

All the calculations presented in this Thesis are performed in the adiabatic approximation. What happens beyond the adiabatic approximation? (e.g., when one looks at very slow electrons). In this case, non adiabatic couplings between continuum states involving the gerade and ungerade states of the residual H_2^+ ion can lead to a symmetry breaking. The importance of non adiabatic effects might also be studied by analyzing the autoionizing decay of doubly excited states that avoid crossings with other doubly excited states.

What is the influence of rotational motion? The theoretical methods could be extended to included the breaking of the axial approximation. For the homonuclear molecules like H_2 and D_2 one could also take into account the difference between the ortho- and para-states[1]. To this respect Fig. (13.3) shows the total electron beta parameter associated to the first ionization threshold including the experimental results obtained by A. C. Parr *et al.* [2]. Our results show no structures as a function of the photon energy, while the experimental are richly structurated, whose origin is not clear.

The results presented in Chapter 10, dedicated to the description of the interference patterns in the electron angular distribution by highly energetic photons, were obtained in the dipole approximation. The pure electric dipole contribution is the largest for long wave length. Interference contributions from the next-higher multipoles may affect the differential photoionization cross section by a few percent [3]. As to our concern, no publication has studied the contribution of these non-dipole contributions to the H_2 molecule. Their contribution could be manifested at high photon energies, and could affect the results obtained in Chapter 10. Also, it could be interesting to study the described interference process making use of circularly polarized light, since in this case more information about this process could be obtained.

As we have shown in Chapter 12, the treatment of the collision between highly energetic

[1]The proton has an associated magnetic moment, which we can treat as being generated by the proton's spin. The spins of the two hydrogen atoms can either be aligned the same direction (this is orthohydrogen) or in opposite directions (this is parahydrogen). The ratio between the ortho and para forms is about 3:1 at standard temperature and pressure, but the para form dominates at low temperatures (approx. 99.95% at 20 K). Other molecules and functional groups containing two hydrogen atoms, such as water and methylene, also have ortho and para forms, although their ratios differ from that of the hydrogen molecule.

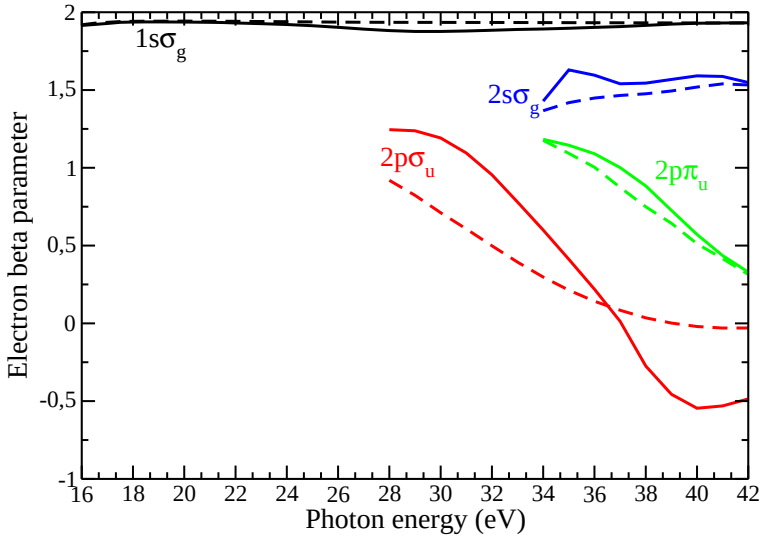

Figure 13.2: Total photoelectron beta parameter for H_2 as function of the photon energy for the first four ionization threshold, $1s\sigma_g$ (black line), $2p\sigma_u$ (red line), $2p\pi_u$ (green line), $2s\sigma_u$ (blue line). Full line, total results; dashed line, non-resonant results.

particles with H_2 molecule, was performed in the frame of the first Born and the dipole approximations. These approximations do not allow the interaction between the ionized particles with the scattered particle, so going beyond this approximation would be convenient, although not easy. Also, it would be interesting to study theoretically the angular distribution of the final particles coming from the collision process, since some interesting experimental results were presented in [4].

Related to all the preceding points, it would be also interesting to study the spin angular distributions of the final particles. This could open the possibility of getting more details about the ionization process. Several theoretical works have been published, although no experiment has yet focused on this topic.

All the theoretical developments described in this work have been related to bielectronic diatomic molecular systems. One of the most challenging search line would be the application of the theory presented in this Thesis to polyelectronic molecular systems, like Li_2, CO or N_2. These systems open a variety of molecular effects that are not present in bielectronic molecules: The electronic structure of a molecule can be divided into valence levels and core levels, where the valence levels correspond to the outer electronic shells and the core levels to the inner electronic shells (see Fig. (13.4)), and this electronic structure of the system can be studied in different ways. Making use of photons and depending on their energies, we can either directly remove a valence electron or a core electron, leading to singly-ionized electronic state configurations (see Fig. (13.4a), or we can resonantly promote a core electron to one of the unoccupied valence orbitals, leading to neutral excited electronic state configurations as schematically shown in Fig. (13.4). Both the core ionization and the core excitation processes create a hole in one of the inner orbitals, a “core-hole”. Core-holes are rather short-lived (a typical lifetime of core holes is in the order of a few femtoseconds) and will be filled by one of the outer electrons. The released energy will either create an X-ray photon (radiative decay channel) or cause another valence electron to be thrown out of the atom or molecule (non-radiative decay channel). The latter process was discovered in 1925 by Pierre Auger [5] and is named after him as the ”Auger effect”. The radiative decay channel can be investigated by means of ”X-ray emission spectroscopy” as developed in the 1920’s by Manne Siegbahn [6], whereas the Auger decay can be studied with an electron spectrometer. If the initial process is core ionization, the subsequent non-radiative decay process is denoted as ”normal

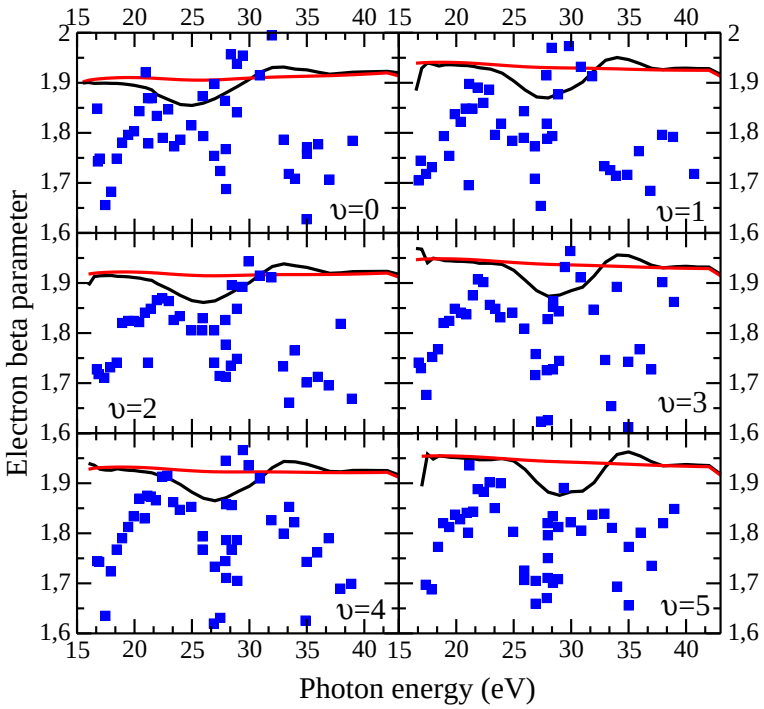

Figure 13.3: Vibrationally resolved photoelectron angular distributions for H_2. Full black line, resonant results. Red dashed line, non-resonant results. Blue symbols, experimental results obtained by A. C. Parr *et al.* [2].

Auger effect", leaving the system in a doubly ionized (2-holes) final state configuration. If the initial process is core excitation, the non-radiative decay process is referred to as "autoionization" or "resonant Auger effect". Depending on whether the excited core electron participates in the decay or it remains in the valence orbital and "watches" the filling of the core-hole by another electron, the decay mechanisms are distinguished as "participator" and "spectator" decays, leaving the system singly-ionized either in a 1-hole final state configuration or in a 2-holes 1-particle final state configuration. The participator decay mechanism apparently leads to singly-ionized final state configurations which are also directly reached by valence photoionization, but due to the presence of an intermediate electronic state in the case of autoionization, the intensity distribution in the resulting electron spectra will be different. Indeed, a comparison between valence photoionization spectra and resonant Auger spectra is commonly done. The classification in terms of "participator" and "spectator" transitions relies upon a rather simple model, which may not always be applicable, in particular in cases where the final electronic state under investigation is interacting with a neighboring electronic state of the same symmetry. A case like this was found for the N_2 molecule [7].

The different process described previously can be studied theoretically with several methods, whose validity and applicability depends on the number of electrons of the molecule. For example the application of a CI method for molecules with more that 4 or 5 electrons can be a very hard task, since the number of configurations needed to obtain accurate results exploits. So the applications of Density Functional Theory (DFT) methods are much more useful for polyelectronic systems (although this theory is formally a one-electron theory).

To sum up this Thesis, we believe that the theory and the results presented so far reveal that this

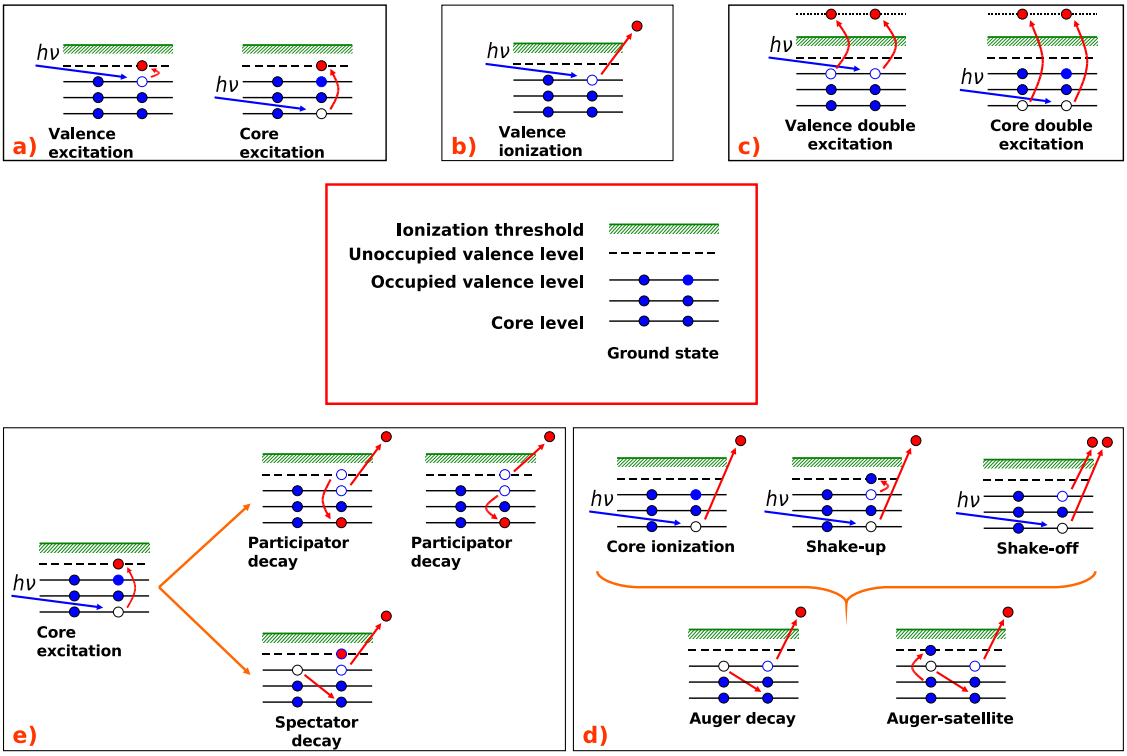

Figure 13.4: A schematic figure illustrating possible processes occurring upon photon impact. Depending on the energy of the incoming photon, several processes can happen: a) Single electron valence and core electron excitation; b) Single electron ionization; c) Double excitation; d) Core excitation, followed by Auger decay. The resonant Auger processes can be classified into participator decays, leading to single-hole final state configurations (singly-ionized), and spectator decays, leading to two-holes one-particle final state configurations (singly-ionized). e) Core ionization, shake-up and shake-off, followed by non-resonant decay process. The normal Auger process leads to two-holes final state configurations (doubly-ionized).

field is a very active branch of Physics, and we hope that this will be the start up of new promising theoretical and experimental developments.

Bibliography

[1] K. Ito, J. Adachi, R. Hall, S. Motoki, E. Shigemasa, K. Soejima, and A. Yagishita, "Photoelectron angular distributions from dissociative photoionization channels of fixed-in-space molecular hydrogen," *Journal of Physics B: Atomic, Molecular and Optical Physics*, vol. 33, pp. 527–533, 2000.

[2] A. C. Parr, J. E. Hardis, S. H. Southworth, C. S. Feigerle, T. A. Ferrett, D. M. P. Holland, F. M. Quinn, B. R. Dobson, J. B. West, G. V. Marr, and J. L. Dehmer, "Vibrationally resolved photoelectron angular distributions for H_2 in the range 17 eV$\leq h\nu \leq$ 39 eV," *Physical Review A*, vol. 37, pp. 437–443, 1988.

[3] D. Toffolli and P. Decleva, "Photoelectron angular distribution beyond dipole approximation: a computational study on the N_2 molecule," *Journal of Physics B: Atomic, Molecular and Optical Physics*, vol. 39, pp. 2681–2691, 2006.

[4] G. Laurent, J. Fernández, S. Legendre, M. Tarisien, L. Adoui, A. Cassimi, X. Fléchard, F. Frémont, B. Gervais, E. Giglio, J. Grandin, and F. Martín, "Kinematically complete study of dissociative ionization of D_2 by ion-impact," *Physical Review Letters*, vol. 96, p. 173201, 2006.

[5] P. Auger, "Sur les rayons β secondaires praduit dans un gaz par des rayons X," *Comptes rendus de L'Academie Bulgare des Sciences*, vol. 180, pp. 65–68, 1925.

[6] M. Siegbahn, *The spectroscopy of* X-*ray*. Oxford University Press, 1925.

[7] M. N. Piancastelli, R. F. Fink, R. Feifel, M. Bässler, S. L. Sorensen, C. Miron, H. Wang, I. Hjelte, O. Björneholm, A. Ausmees, S. Svensson, P. Salek, F. K. Gel'mukhanov, and H. Ågren, "Bond-distance-dependent decay probability of the N 1s $\rightarrow \pi^*$ coreexcited state in N_2," *Journal of Physics B: Atomic, Molecular and Optical Physics*, vol. 33, p. 1819, 2000.

Chapter 14

Conclusiones y Perspectivas

"Ninguna ciencia, en cuanto a ciencia, engaña; el engaño está en quien no la sabe."

Don Quijote de la Mancha de Miguel de Cervantes

En este último Capítulo presentamos las principales conclusiones que se pueden extraer de este trabajo de tesis, así como diferentes líneas de trabajo que se pueden seguir en el futuro.

El primer objetivo de este trabajo fue el estudio del papel que juegan los estados doblemente excitados en el proceso de la fotoionización disociativa de las moléculas de H_2, D_2 y HeH^+, y en particular, su implicación en la distribución angular electrónica. El estudio de la distribución angular ha revelado nuevos detalles sobre la fśica que describe la dinámica del proceso de fotoionización que previamente eran inaccesibles, por ejemplo, en el estudio de la distribución de la energía de los protones.

El papel de estos estados también se ha puesto de manifiesto a través de la colisión de partículas de alta energía, y se ha demostrado la necesidad de desarrollar cálculos teóricos elevarodos para interpretar correctamente los hallazgos experimentales obtenidos en paralelo.

Los fenómenos de coherencia e interferencia juegan un papel esencial en la fotoionización molecular, como se ha demostrado para las moléculas de H_2^+ y H_2. Su estudio ha revelado la importancia de la indistinguibilidad cuántica. En esta Tesis hemos demostrado que sus efectos, aunque pequeños, pueden observarse en la distribución angular para el caso de moléculas fijas en el espacio.

A partir de los resultados presentados, hemos visto sólamente una pequeña fracción de lo que el campo de la espectroscopía electrónica molécular puede ofrecernos. Antes de finalizar esta Tesis, me gustaría sugerir algunas posibles líneas de trabajo para el futuro.

En relación con los resultados de la distribución angular fotoelectrónica presentados en los capítulos 4 y 9, quedan todavía algunas cuestiones por resolver. La primera línea que podría seguirse es el estudio del efecto de los estados doblemente excitados Q_3 y Q_4 en la distribución angular electrónica. Ya que estos estados pueden autoionizarse a través de los primereros cuarto límite de ionización, los límites $1s\sigma_g$, $2p\sigma_u$, $2p\pi_u$ y $2s\sigma_g$ (ver por ejemplo Fig. (6.1) del Capítulo 6), las distribuciones angulares deberían ser completamente diferentes de los presentados en el Capítulo 9. Por ejemplo, Fig. (14.1) muestra los resultados experimentales obtenidos por K. Ito *et al.* [1], para diferentes energías de fotón por encima del tercer y cuarto límite de ionización. En particular, para una energia de 44 eV, se puede observar the la distribución electrónica obtenida por estos autores difiere considerablement con los resultados obtenidos previamente a una energía de 33 eV, lo que refleja la contribución de estados resonantes, así como límites de ionización, adicionales. Como

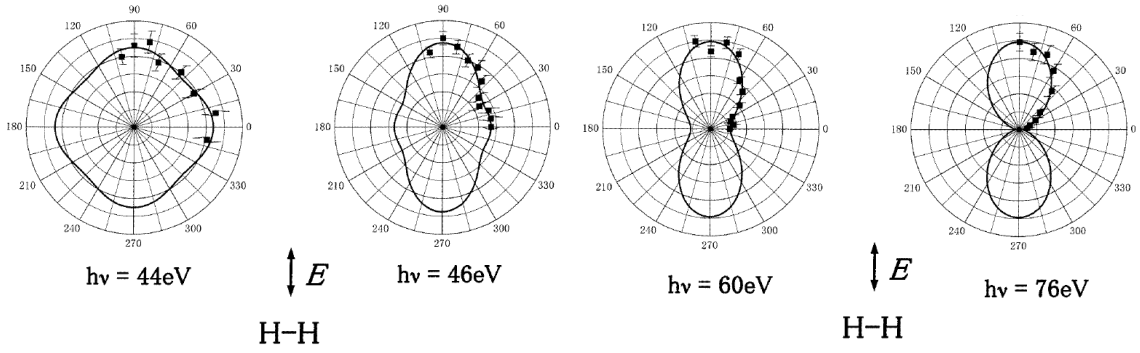

Figure 14.1: Distribución angular electrónica para moleculas de hidrógeno fijas en el espacio, alineadas perpendicularmente con el campo eléctrico, medidas a cuatro energías de fotón diferentes; 44, 46, 60 y 76 eV. El eje molecular está orientado a lo largo de la líniea $0 - 180°$, mientras que el campo electríco está situado a lo largo de la línea $90 - 270°$. Las differentes curvas son ajustes a los datos experimentales. Resultados obtenidos por K. Ito *et al.* [1].

se vio en el Capítulo 6, dedicado al papel que juegan estos estados resonantes en el estudio de la distrubición de la energía cinética del protón, su contribución es bastante pequeña aunque no despreciable. Pero cualquier pequeña contribución de estos estados resonantes debería manifestarse en la distribución angular electrónica (ver por ejemplo, la Sección 9.3 del Capítulo 9). Este hecho puede ser comprobado en la Fig. (14.2), que muestra la contribución de los cuatro primeros límites de ionización al parámetro electrónico beta total (contribución disociativa y no disociativa). Se puede observar claramente que la contribución de los estados resonantes Q_3 and Q_4 se deberían observar en la distribución angular electrónica

Todos los cálculos presentados en esta Tesis se han realizado en la aproximación adiabática. Â£Qué sucede más allá de esta aproximación? (Es decir, cuando se tiene en cuenta los electrones muy lentos). En este caso, los acoplamientos no-adiabáticos entre estados continuos que tienen en cuenta los estados *gerade* y *ungerade* del ión residual H_2^+ pueden conducir a una ruptura de la simetría. La importancia de los efectos no adiabáticos también podría estudiarse mediante el análisis de la autoionizaciíon de los estados doblemente excitados que evitan cruces con otros estados doblemente excitados.

Â£Cuál es la influencia del movimiento rotacional? Lso métodos teóricos pueden extenderse para incluir la ruptura de la aproximación axial. Para moléculas homonucleares tales como H_2 y D_2 también se puede tener en cuenta la diferencia entre los estados orto- y para-[1]. A este respecto, Fig. (14.3) muestra el parámetro beta electrónico total asociado al primer límite de ionización, incluyendo los resultados obtenidos por A. C. Parr *et al.* [2]. Nuestros resultados no muestran grandes variaciones en función de la energía del fotón, mientras que los resultados experimentales presentan una gran dependencia con la energía del fotón, cuyo origen no está completamente entendido.

Los resultados presentados en el Capítulo 10, dedicados a la descripción de los patrones de interferencia en la distribución angular electrónica para fotones altamente energéticos, fueron obtenidos en la aproximación dipolar. La contribución dipolar es la más importante para longitudes

[1] El protón tiene un momento magnético asociado, que se puede tratar como si fuera generado por el espín del protón. Los espines de los dos átomos de hidrógeno pueden estar alineados bien en la misma dirección (ortohidrógeno) bien en direcciones opuestas (parahidrógeno). La relación entre las formas orto y para es de aproximadamente 3:1 a presión y temperatura estándar, aunque la forma para domina a temperaturas bajas (approx. 99.95% a 20 K). Otras moléculas y grupos funcionales que contienen dos átomos de hidrógeno, tales como el agua y el metileno, también presentan formas orto y para, aunque en proporciones diferentes a las de la molécula de hidrógeno

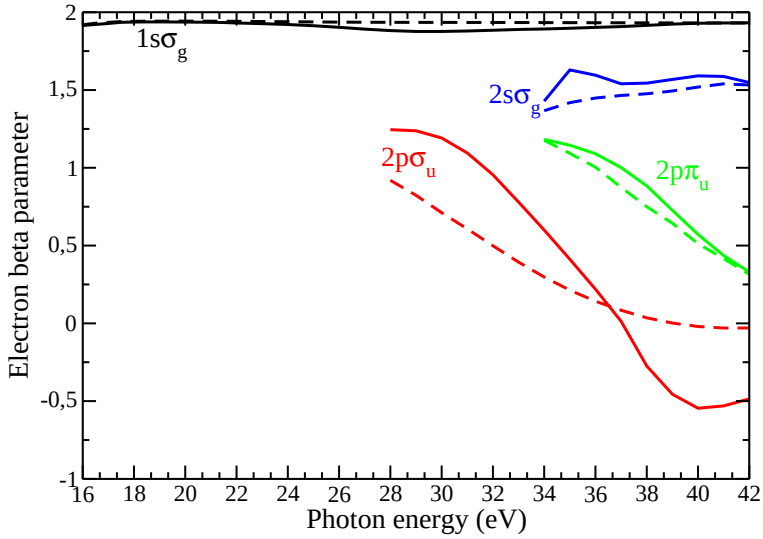

Figure 14.2: Parámetro beta electrónico total del H_2 en función de la energía del fotón para los cuatro primeros límites de ionización, $1s\sigma_g$ (línea negra), $2p\sigma_u$ (línea roja), $2p\pi_u$ (línea verde), $2s\sigma_u$ (línea azul). La contribución resonante (línea llena) y la no resonante (línea a trazos) también están incluidas.

de onda larga. Las contribuciones de las interferencias para los siguientes multipolos podría afectar a la sección eficaz de la fotoionización diferencial en un pequeño porcentaje [3]. Que nosotros sepamos, ninguna trabajo previo ha estudiado la contribución de las contribuciones no-dipolares en la molécula de H_2. Podría manifestarse a altas energías del fotón, y afectaría a los resultados obtenidos en el Capítulo 10. Asimismo, podría ser interesante estudiar el proceso de interferencia ya descrito utilizando diferentes polarizaciones, ya que en este caso se obtendría informació adicional a la ya presentada.

Como ya se ha mostrado en el Capítulo 12, el tratamiento de la colisión entre partículas de altas energías y la molécula de H_2, se realizón en el marco de la primera aproximación de Born y la aproximación dipolar. Esto no permite tener acceso a la interacción entre las partículas ionizadas con la partícula dispersada, por lo que ir más allá de esta aproximación sería altamente interesante, aunque no sea fácil. Igualmente, sería interesante estudiar teoricamente la distribucíon angular de las partículas finales, ya que se tienen a disposición los resultados experimentales presentados en [4].

En relación con todos los puntos precedentes podría analizarse las distribuciones angulares del espin de las partículas finales. Este estudio permitiría obtener mayores detalles sobre el proceso de ionización. Varios trabajos teóricos han sido publicados aunque no hay resultados experimentales relacionados con este tema.

Todos los desarrollos teóricos descritos en este trabajo se han realizado para sistemas moleculares diatómicos bielectrónicos. Para entender los diferentes resultados experimentales, es necesario describir correctamente el papel de los dobles estados excitados. Una de las líneas de trabajo que presentan un mayor reto es la aplicación de la teoría presentada en esta Tesis a sistemas moleculares polielectrónicos tales como Li_2, CO o N_2. Estos sistemas permitirían estudiar una gran variedad de efectos moleculares que no están presentes en sistemas bielectrónicos: La estructura electrónica de una molécula puede dividirse entre niveles de valencia y nivel (core), donde los niveles de valencia corresponden a las capas más externas y los del núcleo a las capas más internas (ver Fig. (14.4)). Esta estructura electrónica puede estudiarse de mediante diferentes tipos de interacciones. Por ejemplo, mediante la utilización de fotones, y dependiendo de sus energías, es posible extraer bien un electrón de valencia o bien un electrón de núcleo, obteniendo configuraciones de estados electrónicos de

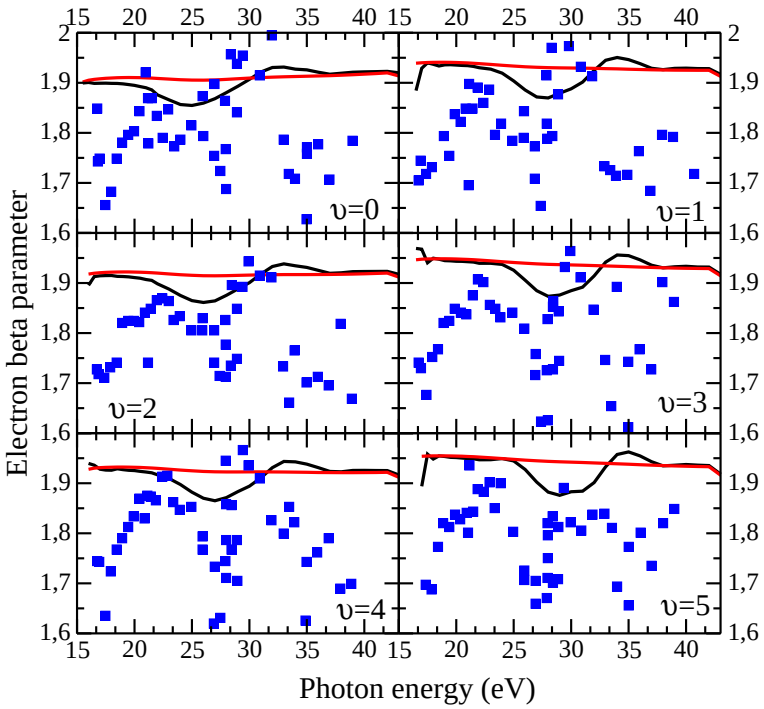

Figure 14.3: Parámetro beta electrónico total resuelto vibracionalmente del H_2. Línea negra, resultados totales. Línea a trazos, contribución no resonantets. Símbolos en azul, resultados experimentales obtenidos por A. C. Parr *et al.* [2].

ionización simple (ver Fig. (14.4a). También se puede promocionar resonantemente un electrón del núcleo a uno de los orbitales de valencia desocupados, obteniendo configuraciones de estados electrónicos neutralmente excitadas, tal y como se muestra en la Fig. (14.4). Tanto el proceso de ionización del núcleo como la de excitación del núcleo crean un "agujero" en uno de los orbitales internos un "core-hole". Estos agujeros tienen generalmente una vida corta (típicamente del orden de unos pocos milisegundos) y acaban llenándose por uno de los electrones externos. La energía liberada crea bien un fotón de rayos-X (canal de decaimiento radiativo) o permite que otro de los electrones de valencia salga del átomo o molécula (canal de decaimiento no radiativo). Este último proceso fue descubierto por Pierre Auger en 1925 [5] y se conoce como "efecto Auger". El canal de decaimiento radiativo puede ser investigado mediante la "espectroscopía de emisión de rayos X" que fue desarrollada en los años 20 por Manne Siegbahn [6], mientras que el efecto Auger se puede estudiar con un espectrómetro electrónico. Si el proceso inicial es la ionización del núcleo el subsiguiente proceso de decaimiento no radiativo se conoce como "efecto Auger normal", que deja al sistema en un estado final doblemente excitado (2 huecos). Si el proceso inicial es la excitación del núcleo, el proceso de decaimiento no-radiativo se conoce como "autoionización" o "efecto Auger resonante". Dependiendo de si el electrón excitado del núcleo participa en el decaimiento o permanece en el orbital de valencia y "observa" como se llena el hueco del núcleo por otro electrón, el mecanismo de decaimiento se distingue entre "participante" o "espectador", dejando el sistema simplemente ionizado bien en un estado final de 1-hueco , bien en una configuración de estado final de 2-huecos y una partícula. El mecanismo de decaimiento participativo conduce aparentemente a una configuarción de estados finales ionizada simplemente, que también se puede alcanzar mediante fotoionización de valencia, pero debido a la presencia de un estado electrónico en el caso de la autoionización, la distribución de intensidades en el espectro electrónico resultante será diferente. En realidad generalmente se comparan los espectros de fotoionización de valencia y los de Auger

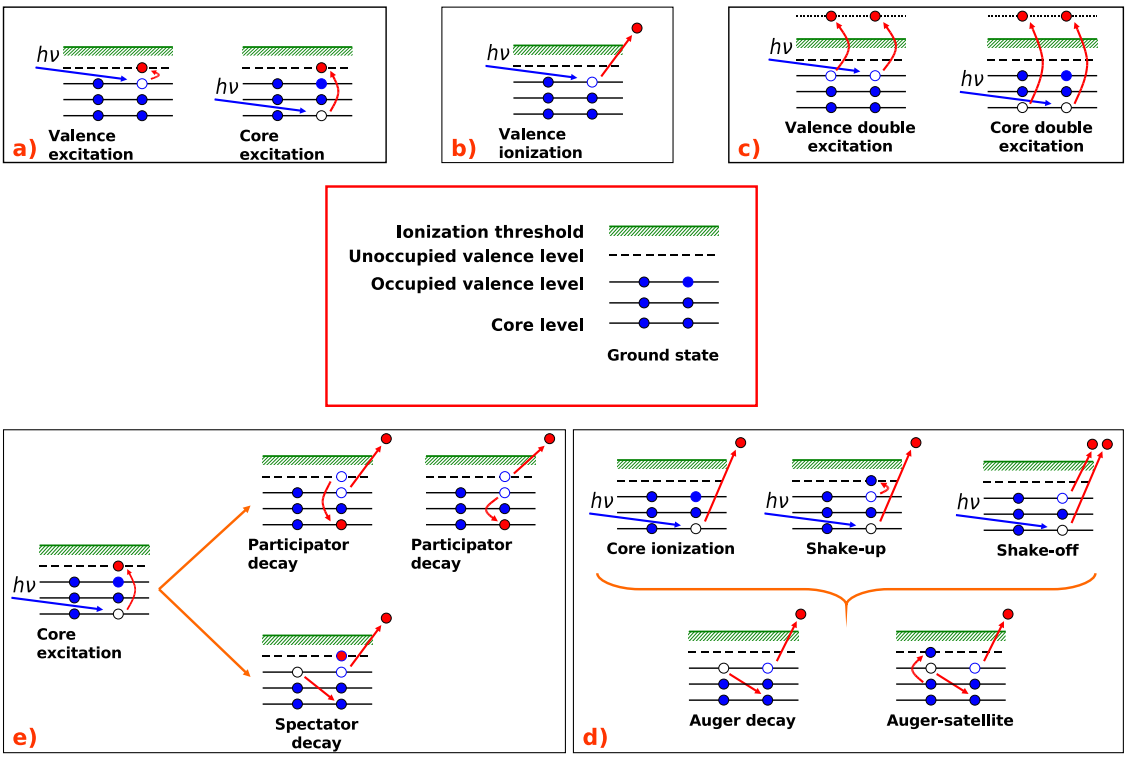

Figure 14.4: Esquema en el que se muestran los posibles procesos que tienen lugar a partir del impacto de un fotón. Dependiendo de la energía del fotón incidente, tienen lugar los siguientes procesos: a) Excitación simple de un electrón de valencia y del núcleo; b) Ionización electrónica simple; c) Excitación doble; d) Excitación del núcleo seguida de decaimiento Auger. El proceso resonante Auger puede clasificarse en decaimientos participativos, que llevan a configuraciones de huecos únicos (ionización simple), y decaimientos expectativos, que llevan a estados finales de dos huecos (ionización simple); e) Ionización del núcleo, shake-up y shake-off, seguidos de un decaimiento no resonante. El proceso Auger normal conduce a un estado final con dos huecos (doblemente-ionizado).

resonante. La clasificación en términos de transiciones de “participante” o “ espectador” depende de un modelo muy simple que no siempre se puede aplicar, especialmente cuando el estado final electrónico interacciona con un estado electrónico vecino de la misma simetría. Un caso como este se encontró en el caso de la molécula de N_2 [7].

Los diferentes procesos descritos anteriormente se pueden estudiar teóricamente con diferentes métodos, cuya validez y aplicabilidad dependen del número de electrones de la molécula. Por ejemplo, la aplicación de un método CI para moléculas con más de 4 ó 5 electrones puede ser una tarea ardua, ya que el número de configuraciones necesarias para obtener resultados exactos es muy elevada. Así que la aplicación de los métodos de la Teoría del Funcional de la Densidad (DFT) son mucho más útiles para sistemas polielectÅŢonicos (aunque esta teoría formalmente es para un sólo electrón).

Como resumen final de este trabajo de Tesis, pensamos que la teoría y los resultados expuestos ponen de manifiesto que este campo de la física es hoy en día uno de los más activo y esperamos que este trabajo permita el desarrollo de nuevos experimentos y resultados teóricos.

Bibliografia

[1] K. Ito, J. Adachi, R. Hall, S. Motoki, E. Shigemasa, K. Soejima, and A. Yagishita, "Photoelectron angular distributions from dissociative photoionization channels of fixed-in-space molecular hydrogen," *Journal of Physics B: Atomic, Molecular and Optical Physics*, vol. 33, pp. 527–533, 2000.

[2] A. C. Parr, J. E. Hardis, S. H. Southworth, C. S. Feigerle, T. A. Ferrett, D. M. P. Holland, F. M. Quinn, B. R. Dobson, J. B. West, G. V. Marr, and J. L. Dehmer, "Vibrationally resolved photoelectron angular distributions for H_2 in the range 17 eV$\leq h\nu \leq$ 39 eV," *Physical Review A*, vol. 37, pp. 437–443, 1988.

[3] D. Toffolli and P. Decleva, "Photoelectron angular distribution beyond dipole approximation: a computational study on the N_2 molecule," *Journal of Physics B: Atomic, Molecular and Optical Physics*, vol. 39, pp. 2681–2691, 2006.

[4] G. Laurent, J. Fernández, S. Legendre, M. Tarisien, L. Adoui, A. Cassimi, X. Fléchard, F. Frémont, B. Gervais, E. Giglio, J. Grandin, and F. Martín, "Kinematically complete study of dissociative ionization of D_2 by ion-impact," *Physical Review Letters*, vol. 96, p. 173201, 2006.

[5] P. Auger, "Sur les rayons β secondaires praduit dans un gaz par des rayons X," *Comptes rendus de L'Academie Bulgare des Sciences*, vol. 180, pp. 65–68, 1925.

[6] M. Siegbahn, *The spectroscopy of* X-*ray*. Oxford University Press, 1925.

[7] M. N. Piancastelli, R. F. Fink, R. Feifel, M. Bässler, S. L. Sorensen, C. Miron, H. Wang, I. Hjelte, O. Björneholm, A. Ausmees, S. Svensson, P. Salek, F. K. Gel'mukhanov, and H. Ågren, "Bond-distance-dependent decay probability of the N 1s $\rightarrow \pi^*$ coreexcited state in N_2," *Journal of Physics B: Atomic, Molecular and Optical Physics*, vol. 33, p. 1819, 2000.

Part III

Appendices

Appendix A

Fundamental constants

A new best set of the fundamental constants has been compiled by the National Institute of Standards and Technology (NIST). A selected set is given in the following table.

quantity	symbol	value	unit
Planck constant in eV s	h	4.13566743(35)	10^{-15} eV s
Planck constant over 2π in eV s	$\hbar$	6.58211915(56)	10^{-16} eV s
elementary charge	e	1.60217653(14)	10^{-19} C
electron rest mass	m_e	9.1093826(16)	10^{-31} kg
proton rest mass	m_p	1.67262171(29)	10^{-27} kg
deuteron mass	m_d	3.34358335(57)	10^{-27} kg
atomic mass constant	$u = m_u$	1.66053886(28)	10^{-27} kg
Avogadro constant	N_A	6.0221415(10)	10^{23} mol^{-1}
Bohr radius	a_0	0.5291772108(18)	10^{-10} m
		0.529177	Å
Hartree energy	E_h	4.35974417(75)	10^{-18} J
Hartree energy in eV	E_h	27.2113845(23)	eV
Rydberg constant	R_∞	10973731.568525(73)	m^{-1}
speed of light (vacuum)	c	299792458	m s^{-1}
magnetic constant	μ_0	$4\pi^{-7} = 12.566370614...$	10^{-7} N A^{-2}
vacuum permittivity	ε_0	8.854187817...	10^{-12} F m^{-1}
	$4\pi\varepsilon_0$	1.112650056...	10^{-10} F m^{-1}
proton-electron mass ratio	m_p/m_e	1836.15267261(85)	
deuteron-electron mass ratio	m_d/m_e	3670.4829652(18)	
proton charge to mass quotient	e/m_p	9.57883376(82)	10^7 C kg^{-1}
electron volt	eV	1.60217653(14)	10^{-19} J
classical electron radius	r_e	2.817940325(28)	10^{-15} m
Compton wavelength	λ_C	2.426310238(16)	10^{-12} m
fine-structure constant	α	$7.297352568(24) \times 10^{-3}$	
inverse fine-structure constant	α^{-1}	137.03599911(46)	

Table A.1: Fundamental constants. See http://physics.nist.gov/cuu/index.html.

Appendix B

Legendre Polynomials and Spherical Harmonics

Table of Contents

B.1 Introduction

LEGENDRE POLYNOMIALS are the essential elements in the study of the electron angular distribution (see chapters (4) and (9)), that in conjunction with the partial wave expansion, describe the geometric part of this process. So, we consider necessary to present a brief summary of the main characteristics of the Legendre polynomials and the spherical harmonic functions. Since there exist an innumerable number of bibliography where different descriptions of these functions can be found (see for example [1, 2, 3, 4]), we present in this appendix the information obtained from [5, 6], since it is quite simple and concise.

B.2 Legendre Polynomials

The Legendre polynomials, sometimes called Legendre functions of the first kind, Legendre coefficients, or zonal harmonics (Whittaker and Watson [2], p. 302), are solutions to the Legendre differential equation. If ℓ is an integer, they are polynomials. The Legendre polynomials $P_n(x)$ are illustrated in Fig. (B.2), for $x \in [-1,1]$ and $n = 0,1,2,...,5$. The Legendre polynomial $P_n(z)$ can be defined by the contour integral

$$P_n(z) = \frac{1}{2\pi i}\oint (1-2tz+t^2)^{-1/2} t^{-n-1} dt, \tag{B.1}$$

where the contour encloses the origin and is traversed in a counterclockwise direction (Arfken [1], p. 416).

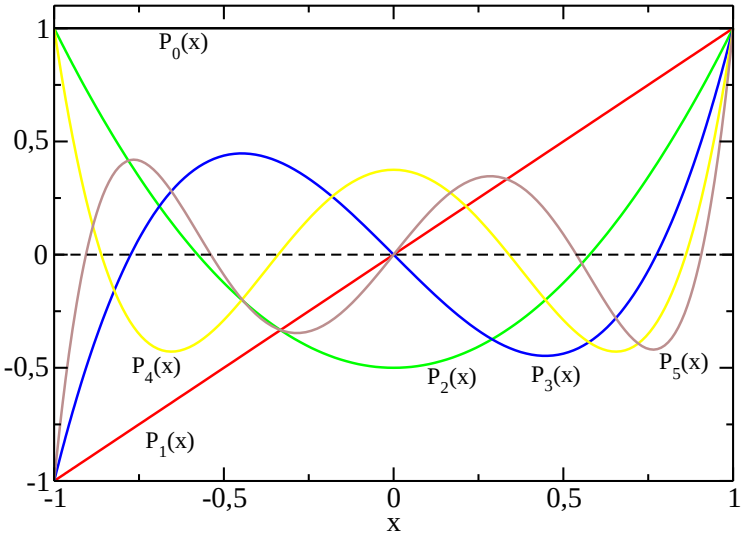

Figure B.1: Legendre polynomials $P_n(x)$. Black line, $P_0(x)$; Red line, $P_1(x)$; Green line, $P_2(x)$; Blue line, $P_3(x)$; Yellow line, $P_4(x)$; Brown line, $P_5(x)$.

The Legendre polynomials are orthogonal over $(-1,1)$ with weighting function 1 and satisfy

$$\int_{-1}^{1} P_n(x)P_m(x)dx = \frac{2}{2n+1}\delta_{m,n}, \tag{B.2}$$

where $\delta_{m,n}$ is the Kronecker delta.

The associated Legendre polynomials $P_\ell^m(x)$ and $P_\ell^{-m}(x)$ are solutions to the associated Legendre differential equation, where ℓ is a positive integer and $m = 0,...,\ell$. For positive m, they can be given in terms of the unassociated polynomials by

$$\begin{aligned} P_\ell^m(x) &= (-1)^m(1-x^2)^{m/2}\frac{d^m}{dx^m}P_\ell(x) \\ &= (-1)^m 2^\ell \ell!(1-x^2)^{m/2}\frac{d^{\ell+m}}{dx^{\ell+m}}(x^2-1)^\ell, \end{aligned} \tag{B.3}$$

where $P_\ell(x)$ are the unassociated Legendre polynomials. The associated Legendre polynomials for negative m are then defined by

$$P_\ell^{-m}(x) = (-1)^m\frac{(\ell-m)!}{(\ell+m)!}P_\ell^m(x). \tag{B.4}$$

There are two sign conventions for the associated Legendre polynomials. Some authors (e.g., Arfken 1[1], pp. 668-669) omit the Condon-Shortley phase $(-1)^m$, while others include it (e.g., Abramowitz and Stegun [7]). Care is therefore needed in comparing polynomials obtained from different sources. One possible way to distinguish the two conventions is due to Abramowitz and Stegun [7](p. 332), who use the notation

$$P_{\ell m}(x) = (-1)^m P_\ell^m(x), \tag{B.5}$$

to distinguish the two.

If $m = 0$, the associated polynomials reduce to the unassociated polynomials. The associated Legendre functions are part of the spherical harmonics, which are the solution of Laplace's equation in spherical coordinates. They are orthogonal over $[-1,1]$ with the weighting function 1.

$$\int_{-1}^{1} P_\ell^m(x) P_{\ell'}^m(x) dx = \frac{2}{2\ell+1}\frac{(\ell+m)!}{(\ell-m)!}\delta_{\ell,\ell'}, \tag{B.6}$$

and orthogonal over $[-1,1]$ with respect to m with the weighting function $(1-x^2)^{-1}$,

$$\int_{-1}^{1} P_\ell^m(x) P_\ell^{m'}(x)\frac{dx}{1-x^2} = \frac{(\ell+m)!}{m(\ell-m)!}\delta_{m,m'}. \tag{B.7}$$

The associated Legendre polynomials also obey the following recurrence relations

$$(\ell-m)P_\ell^m(x) = x(2\ell-1)P_{\ell-1}^m(x) - (\ell+m-1)P_{\ell-2}^m(x). \tag{B.8}$$

Additional identities are

$$P_\ell^\ell(x) = (-1)^\ell(2\ell-1)!!(1-x^2)^{\ell/2} \tag{B.9}$$

$$P_{\ell+1}^\ell(x) = x(2\ell+1)P_\ell^\ell(x). \tag{B.10}$$

Including the factor of $(-1)^m$, the first few associated Legendre polynomials are

$$P_0^0(x) = 1, \tag{B.11}$$

$$P_1^0(x) = x, \tag{B.12}$$

$$P_1^1(x) = -(1-x^2)^{1/2}, \tag{B.13}$$

$$P_2^0(x) = \frac{1}{2}(3x^2-1), \tag{B.14}$$

$$P_2^1(x) = -3x(1-x^2)^{1/2}, \tag{B.15}$$

$$P_2^2(x) = 3(1-x^2), \tag{B.16}$$

$$P_3^0(x) = \frac{1}{2}x(5x^2-3), \tag{B.17}$$

$$P_3^1(x) = \frac{3}{2}(1-5x^2)(1-x^2)^{1/2}, \tag{B.18}$$

$$P_3^2(x) = 15x(1-x^2), \tag{B.19}$$

$$P_3^3(x) = -15(1-x^2)^{3/2}, \tag{B.20}$$

$$P_4^0(x) = \frac{1}{8}(35x^4-30x^2+3), \tag{B.21}$$

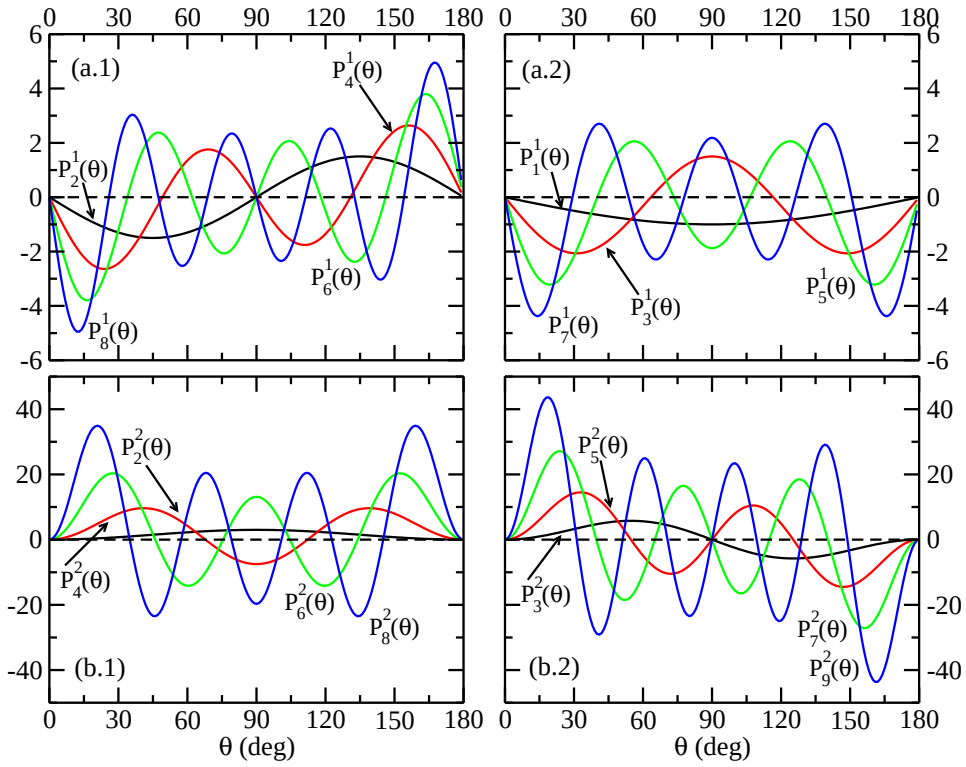

Figure B.2: Legendre polynomials: panel a.1, Legendre polynomial $P_\ell^1(x)$ of ℓ even values; panel a.2, Legendre polynomial $P_\ell^1(x)$ of ℓ odd values; panel b.1, Legendre polynomial $P_\ell^2(x)$ of ℓ even values; panel b.2, Legendre polynomial $P_\ell^2(x)$ of ℓ odd values.

$$P_4^1(x) = \frac{5}{2}x(3-7x^2)(1-x^2)^{1/2}, \tag{B.22}$$

$$P_4^2(x) = 152(7x^2-1)(1-x^2), \tag{B.23}$$

$$P_4^3(x) = -105x(1-x^2)^{3/2}, \tag{B.24}$$

$$P_4^4(x) = 105(1-x^2)^2, \tag{B.25}$$

$$P_5^0(x) = \frac{1}{8}x(63x^4-70x^2+15). \tag{B.26}$$

Written in terms $x = \cos\theta$ (commonly written $\mu = \cos\theta$), the first few become

$$P_0^0(\cos\theta) = 1, \tag{B.27}$$

$$P_1^0(\cos\theta) = \cos\theta, \tag{B.28}$$

$$P_1^1(\cos\theta) = -\sin\theta, \tag{B.29}$$

$$P_2^0(\cos\theta) = \frac{1}{2}(3\cos^2\theta-1), \tag{B.30}$$

$$P_2^1(\cos\theta) = -3\sin\theta\cos\theta, \tag{B.31}$$

$$P_2^2(\cos\theta) = 3\sin^2\theta, \tag{B.32}$$

$$P_3^0(\cos\theta) = \frac{1}{2}\cos\theta(5\cos^2\theta - 3), \tag{B.33}$$

$$P_3^1(\cos\theta) = -\frac{3}{2}(5\cos^2\theta - 1)\sin\theta, \tag{B.34}$$

$$P_3^2(\cos\theta) = 15\cos\theta\sin^2\theta, \tag{B.35}$$

$$P_3^3(\cos\theta) = -15\sin^3\theta. \tag{B.36}$$

B.3 Spherical Harmonics

The spherical harmonics $Y_\ell^m(\theta,\phi)$ are the angular portion of the solution to Laplace's equation in spherical coordinates where azimuthal symmetry is not present. Some care must be taken in identifying the notational convention being used. In this entry, θ is taken as the polar (colatitudinal) coordinate with $\theta \in [0,\pi]$, and ϕ as the azimuthal (longitudinal) coordinate with $\phi \in [0,2\pi)$. This is the convention normally used in physics, as described by Arfken [1] (in mathematical literature, theta usually denotes the longitudinal coordinate and phi the colatitudinal coordinate).

Spherical harmonics satisfy the spherical harmonic differential equation, which is given by the angular part of Laplace's equation in spherical coordinates. Writing $F = \Phi(\phi)\Theta(\theta)$ in this equation gives

$$\frac{\Phi(\phi)}{\sin\theta}\frac{d}{d\theta}\left(\sin\theta\frac{d\Theta}{d\theta}\right) + \frac{\Theta(\theta)}{\sin^2\theta}\frac{d^2\Phi(\phi)}{d\phi^2} + \ell(\ell+1)\Phi(\phi)\Theta(\theta) = 0. \tag{B.37}$$

Multiplying by $\sin^2\theta/\Phi(\phi)\Theta(\theta)$ gives

$$\left[\frac{\sin\theta}{\Theta(\theta)}\frac{d}{d\theta}\left(\sin\theta\frac{d\Theta}{d\theta}\right) + \ell(\ell+1)\sin^2\theta\right] + \frac{1}{\Phi(\phi)}\frac{d^2\Phi(\phi)}{d\phi^2} = 0. \tag{B.38}$$

Using separation of variables by equating the ϕ-dependent portion to a constant gives

$$\frac{1}{\Phi(\phi)}\frac{d^2\Phi(\phi)}{d\phi^2} = -m^2, \tag{B.39}$$

which has solutions

$$\Phi(\phi) = Ae^{(-im\phi)} + Be^{(im\phi)}. \tag{B.40}$$

Plugging in Eq. (B.39) into Eq. (B.38) gives the equation for the θ-dependent portion, whose solution is

$$\Theta(\theta) = P_\ell^m(\cos\theta), \tag{B.41}$$

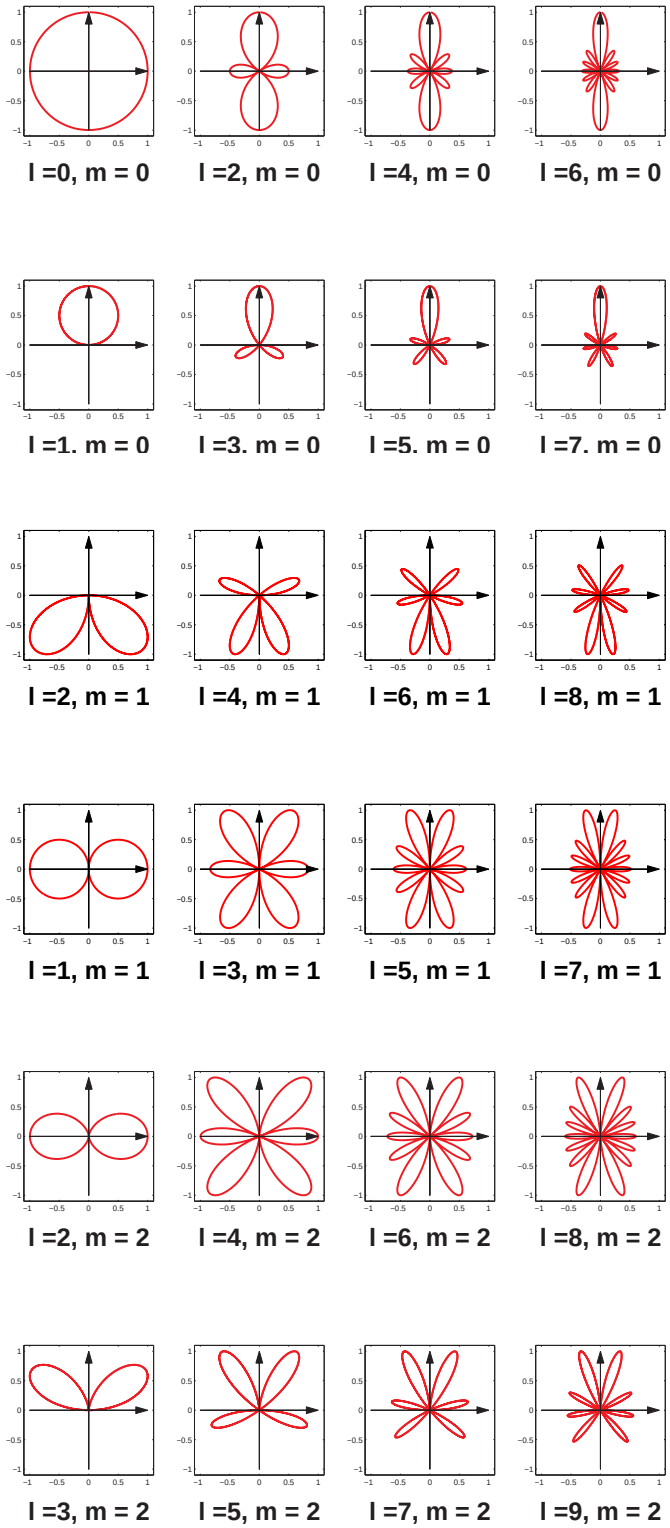

(c) $m = 2$

Figure B.3: Legendre polynomials of order $m = 0$, $m = 1$ and $m = 2$ normalized to its maximum, in Cartesian coordinate system.

where $m = -\ell, -(\ell-1), ..., 0, ..., \ell-1, \ell$ and $P_\ell^m(z)$ is an associated Legendre polynomial. The spherical harmonics are then defined by combining $\Phi(\phi)$ and $\Theta(\theta)$,

$$Y_\ell^m(\theta,\phi) = \sqrt{\frac{2\ell+1}{4\pi}\frac{(\ell-m)!}{(\ell+m)!)}} P_\ell^m(\cos\theta) e^{(im\phi)}, \tag{B.42}$$

where the normalization is chosen such that

$$\int_0^{2\pi}\int_0^{\pi} Y_\ell^m(\theta,\phi)\overline{Y}_{\ell'}^{m'}(\theta,\phi)\sin\theta d\theta d\phi = \delta_{m,m'}\delta_{\ell,\ell'}, \tag{B.43}$$

(Arfken [1], p. 681). Here, $\bar{z}$ denotes the complex conjugate and $\delta_(m,n)$ is the Kronecker delta. Sometimes (e.g., [1]), the Condon-Shortley phase $(-1)^m$ is prepended to the definition of the spherical harmonics.

The spherical harmonics obey

$$Y_\ell^{-\ell}(\theta,\phi) = \frac{1}{2^\ell \ell!}\sqrt{\frac{(2\ell+1)!}{4\pi}}\sin^\ell\theta e^{-i\ell\phi}, \tag{B.44}$$

$$Y_\ell^0(\theta,\phi) = \sqrt{\frac{2\ell+1}{4\pi}} P_\ell(\cos\theta), \tag{B.45}$$

$$Y_\ell^{-m}(\theta,\phi) = (-1)^m \overline{Y}_\ell^m(\theta,\phi), \tag{B.46}$$

where $P_\ell(x)$ is a Legendre polynomial.

The coupling rule for spherical harmonics is giving by the relation,

$$Y_{\ell_1}^{m_1}(\theta,\varphi)Y_{\ell_2}^{m_2}(\theta,\varphi) = \sum_\ell \left[\frac{(2\ell_1+1)(2\ell_2+1)}{4\pi(2\ell+1)}\right]^{\frac{1}{2}} C(\ell_1,\ell_2,\ell;m_1,m_2)C(\ell_1,\ell_2,\ell;0,0)Y_\ell^{m_1+m_2}(\theta,\varphi). \tag{B.47}$$

The coupling rule for spherical in Eq. (B.47) permits an easy evaluation of the integral of three spherical harmonics. Multiplication of Eq. (B.47) by $\overline{Y}_{\ell_3}^{m_3}(\theta,\varphi)$ and integration over the full solid angle gives

$$\int \overline{Y}_{\ell_3}^{m_3} Y_{\ell_2}^{m_2} Y_{\ell_1}^{m_1} d\Omega = \sum_\ell \left[\frac{(2\ell_1+1)(2\ell_2+1)}{4\pi(2\ell+1)}\right]^{\frac{1}{2}} C(\ell_1,\ell_2,\ell;m_1,m_2)C(\ell_1,\ell_2,\ell;0,0)\int \overline{Y}_{\ell_3}^{m_3} Y_\ell^{m_1+m_2} d\Omega. \tag{B.48}$$

The spherical harmonics are orthonormal and, therefore, only $\ell = \ell_3$ term of the sum contributes. Consequently,

$$\int \overline{Y}_{\ell_3}^{m_3} Y_{\ell_2}^{m_2} Y_{\ell_1}^{m_1} d\Omega = \left[\frac{(2\ell_1+1)(2\ell_2+1)}{4\pi(2\ell_3+1)}\right]^{\frac{1}{2}} C(\ell_1,\ell_2,\ell_3;m_1,m_2,m_3)C(\ell_1,\ell_2,\ell_3;0,0,0). \tag{B.49}$$

Again the angular momentum and parity selection rules are operative through the Clebsch-Gordon coefficients $C(\ell_1,\ell_2,\ell_3;m_1,m_2,m_3)$ and $C(\ell_1,\ell_2,\ell_3;0,0,0)$, respectively. And elementary example

of the usefulness of this expression is in the matrix elements of dipole radiation between angular momentum sates for spinless particles. The dipole operator is essentially the spherical harmonic of first order so that the matrix elements is proportional to

$$\left[Y_{\ell_f}^{m_f},\left(\frac{4\pi}{3}\right)^{\frac{1}{2}}Y_1^m Y_{\ell_i}^{m_i}\right]=\left(\frac{2\ell_i+1}{2\ell_f+1}\right)C(\ell_i,1,\ell_f;m_i,m,m_f)C(\ell_i,1,\ell_f;0,0,0). \tag{B.50}$$

The subscripts f and i refer, of course, to the final and initial states, respectively. The Clebsch-Gordon coefficients lead to the familiar angular momentum and parity selection rules

$$\ell_f-\ell_i=\pm 0 \quad \text{and} \quad m_f-m_i=0,\pm 0 \quad . \tag{B.51}$$

Angular momentum conservation alone would also permit the transition $\ell_f-\ell_i=0$ with $\ell_i=0\rightarrow \ell_f=0$ absolutely forbidden in a single quantum jump.

Making use of Eq. (B.49), we have the following relations:

$$\int_0^{2\pi}\int_0^{\pi}Y_L^M(\theta,\phi)Y_0^0(\theta,\phi)\overline{Y}_L^M(\theta,\phi)\sin\theta d\theta d\phi=\frac{1}{\sqrt{4\pi}}, \tag{B.52}$$

$$\begin{aligned}&\int_0^{2\pi}\int_0^{\pi}Y_L^M(\theta,\phi)Y_1^0(\theta,\phi)\overline{Y}_{L+1}^M(\theta,\phi)\sin\theta d\theta d\phi\\&=\sqrt{\frac{3}{4\pi}}\sqrt{\frac{(L+M+1)(L-M+1)}{(2L+1)(2L+3)}},\end{aligned} \tag{B.53}$$

$$\begin{aligned}&\int_0^{2\pi}\int_0^{\pi}Y_L^M(\theta,\phi)Y_1^1(\theta,\phi)\overline{Y}_{L+1}^{M+1}(\theta,\phi)\sin\theta d\theta d\phi\\&=\sqrt{\frac{3}{8\pi}}\sqrt{\frac{(L+M+1)(L+M+2)}{(2L+1)(2L+3)}},\end{aligned} \tag{B.54}$$

$$\begin{aligned}&\int_0^{2\pi}\int_0^{\pi}Y_L^M(\theta,\phi)Y_1^1(\theta,\phi)\overline{Y}_{L-1}^{M+1}(\theta,\phi)\sin\theta d\theta d\phi\\&=-\sqrt{\frac{3}{8\pi}}\sqrt{\frac{(L-M)(L-M-1)}{(2L-1)(2L+1)}},\end{aligned} \tag{B.55}$$

(Arfken [1], p. 700).

The first few spherical harmonics are

$$Y_0^0(\theta,\phi)=\frac{1}{2}\frac{1}{\sqrt{\pi}}, \tag{B.56}$$

$$Y_1^{-1}(\theta,\phi)=\frac{1}{2}\sqrt{\frac{3}{2\pi}}\sin\theta e^{-i\phi}, \tag{B.57}$$

$$Y_1^0(\theta,\phi)=\frac{1}{2}\sqrt{\frac{3}{\pi}}\cos\theta, \tag{B.58}$$

$$Y_1^1(\theta,\phi)=-\frac{1}{2}\sqrt{\frac{3}{2\pi}}\sin\theta e^{i\phi}, \tag{B.59}$$

$$Y_2^{-2}(\theta,\phi) = \frac{1}{4}\sqrt{\frac{15}{2\pi}}\sin^2\theta e^{-2i\phi}, \tag{B.60}$$

$$Y_2^{-1}(\theta,\phi) = \frac{1}{2}\sqrt{\frac{15}{2\pi}}\sin\theta\cos\theta e^{-i\phi}, \tag{B.61}$$

$$Y_2^{0}(\theta,\phi) = \frac{1}{4}\sqrt{\frac{5}{\pi}}(3\cos^2\theta - 1), \tag{B.62}$$

$$Y_2^{1}(\theta,\phi) = -\frac{1}{2}\sqrt{\frac{15}{2\pi}}\sin\theta\cos\theta e^{i\phi}, \tag{B.63}$$

$$Y_2^{2}(\theta,\phi) = \frac{1}{4}\sqrt{\frac{15}{2\pi}}\sin^2\theta e^{2i\phi}, \tag{B.64}$$

$$Y_3^{-3}(\theta,\phi) = \frac{1}{8}\sqrt{\frac{35}{\pi}}\sin^3\theta e^{-3i\phi}, \tag{B.65}$$

$$Y_3^{-2}(\theta,\phi) = \frac{1}{4}\sqrt{\frac{105}{2\pi}}\sin^2\theta\cos\theta e^{-2i\phi}, \tag{B.66}$$

$$Y_3^{-1}(\theta,\phi) = \frac{1}{8}\sqrt{\frac{21}{\pi}}\sin\theta(5\cos^2\theta - 1)e^{-i\phi}, \tag{B.67}$$

$$Y_3^{0}(\theta,\phi) = \frac{1}{4}\sqrt{\frac{7}{\pi}}(5\cos^3\theta - 3\cos\theta), \tag{B.68}$$

$$Y_3^{1}(\theta,\phi) = -\frac{1}{8}\sqrt{\frac{21}{\pi}}\sin\theta(5\cos^2\theta - 1)e^{i\phi}, \tag{B.69}$$

$$Y_3^{2}(\theta,\phi) = \frac{1}{4}\sqrt{\frac{105}{2\pi}}\sin^2\theta\cos\theta e^{2i\phi}, \tag{B.70}$$

$$Y_3^{3}(\theta,\phi) = -\frac{1}{8}\sqrt{\frac{35}{\pi}}\sin^3\theta e^{3i\phi}. \tag{B.71}$$

Bibliography

[1] G. B. Arfken and H. J. Weber, *Mathematical Methods for Physicists.* Academic Press, 1985.

[2] E. T. Whittaker and G. N. Watson, *A Course in Modern Analysis*. Cambridge University Press, 1990.

[3] C. J. Joachain, *Quantum Collision Theory*. North-Holland Publishing Company, 1979.

[4] A. Messiah, *Quantum mechanics volume* I *and* II. North-Holland publishing company, 1961.

[5] E. W. Weisstein, *Spherical Harmonic*. MathWorld-A Wolfram Web Resource. http://mathworld.wolfram.com/LegendrePolynomial.html, 2006.

[6] E. W. Weisstein, *Legendre Polynomial*. MathWorld-A Wolfram Web Resource. http://mathworld.wolfram.com/SphericalHarmonic.html, 2006.

[7] M. Abramowitz and I. A. Stegun, *Handbook of Mathematical Functions with Formulas, Graphs, and Mathematical Tables*. New York: Dover, 1972.

Appendix C

Angular momentum theory

Table of Contents

C.1 Introduction

ANGULAR MOMENTUM properties are the main blocks of this thesis, since they are needed to obtain the total and differential cross section in term of the partial wave expansion. We present the main characteristics of the Clebsch-Gordan coefficients, the Wigner $3j$ symbols and the rotational matrix. So, this appendix provides a brief algebraic background needed for a deeper understanding of the previous chapters. We only present a brief résumé of the elementary theory of angular momentum obtained from Rose's [1], Edmonds's [2] and Varshalovich's book [3].

C.2 Elementary theory of angular momentum

We will start with the definition of the Clebsch-Gordan (CG) coefficients, specifying the notation used in this work and the principal characteristics of these mathematical objects.

Let the eigenfunctions for the angular momenta j_1 and j_2 be Ψ_{j_1,m_1} and Ψ_{j_2,m_2}, respectively. Then

$$\begin{aligned} \mathbf{J}_1^2\Psi_{j_1,m_1} &= j_1(j_1+1)\Psi_{j_1,m_1}; & \mathbf{J}_2^2\Psi_{j_2,m_2} &= j_2(j_2+1)\Psi_{j_2,m_2} \\ J_{1z}\Psi_{j_1,m_1} &= m_1\Psi_{j_1,m_1}; & J_{2z}\Psi_{j_2,m_2} &= m_1\Psi_{j_2,m_2} \end{aligned} \tag{C.1}$$

The CG coefficients are the consequence of the seeking of a representation in which $\mathbf{J}^2$ and J_z, as well as $\mathbf{J}_1^2$ and $\mathbf{J}_2^2$, are diagonal with eigenvalues $j(j+1)$ and m, respectively, where $\mathbf{J}=\mathbf{J}_1+\mathbf{J}_2$ is the total angular momentum operator, J_z is its z component, and $\mathbf{J}_1$ and $\mathbf{J}_2$ are the total angular momentum

of two uncoupled states, $\psi_{j_1 m_1}$ and $\psi_{j_2 m_2}$. The coupled representation of $\psi_{j,m}$ is connected with the uncoupled representation $\psi_{j_1 m_1}\psi_{j_2 m_2}$ by a unitary transformation

$$\psi_{jm} = \sum_{m_1 m_2} C(j_1, j_2, j; m_1, m_2, m)\psi_{j_1 m_1}\psi_{j_2 m_2}. \tag{C.2}$$

The elements of the transformation $C(j_1, j_2, j; m_1, m_2, m)$ are called Clebsch-Gordan coefficients. The CG coefficients must fulfill the basis condition:

$$C(j_1, j_2, j; m_1, m_2, m) = 0 \quad \text{unless} \quad m = m_1 + m_2. \tag{C.3}$$

Therefore, not all three projection quantum numbers are independent and the double sum in Eq. (C.3) is actually a single sum. We shall usually take the advantage of this by replacing m_2 by $m - m_1$ and suppressing the third projection quantum number in the CG-coefficient:

$$\psi_{jm} = \sum_{m_1} C(j_1, j_2, j; m_1, m - m_1)\psi_{j_1 m_1}\psi_{j_2 m - m_1}. \tag{C.4}$$

It should be remembered, however, that the third projection quantum number is always the sum of the first two. We can show that the inverse expansion of Eq. (C.4) is

$$\psi_{j_1 m_1}\psi_{j_2 m - m_1} = \sum_{j} C(j_1, j_2, j; m_1, m - m_1)\psi_{jm} \tag{C.5}$$

As consequence that the CG-coefficients are elements of a unitary transformation they have the following relationships:

$$\sum_{j} C(j_1, j_2, j; m_1, m_2)C(j_1, j_2, j; m_1', m_2') = \delta_{m_1, m_1'}\delta_{m_2, m_2'}, \tag{C.6}$$

$$\sum_{m_1} C(j_1, j_2, j; m_1, m_2)C(j_1, j_2, j'; m_1, m_2) = \delta_{j, j'}. \tag{C.7}$$

When m_1 and m_2 take the maximum possible values, $m_1 = j_1$ and $m_2 = j_2$, the corresponding values of j and m are equal to $j_1 + j_2$, and the CG-coefficients take the value,

$$C(j_1, j_2, j_1 + j_2; j_1, j_2) = 1. \tag{C.8}$$

As we mentioned before the eigenvalues of the $\mathbf{J}^2$ operator are $j(j+1)$ where

$$j = j_1 + j_2, j_1 + j_2 - 1, \cdots, |j_1 - j_2|. \tag{C.9}$$

The numbers j_1, j_2, and j are said to form a triangle, and this relation is denoted by $\Delta(j_1, j_2, j)$, which is symmetric in the three angular momenta. The CG-coefficients must vanish if this condition is not fulfilled, and the results obtained below verify that, in agreement with the definition, this is indeed the case. Thus it is not necessary to specify the limits of the sums like those in Eqs. (C.6) and (C.7), for the terms outside the permissible limits will contain vanishing CG-coefficients.

$$C(j_1, j_2, j; m_1, m - m_1) = 0 \quad \text{unless} \quad \Delta(j_1, j_2, j). \tag{C.10}$$

In addition, we have the restrictions

$$|m_1| \leq j_1, \qquad |m| \leq j, \qquad |m - m_1| \leq j_2. \tag{C.11}$$

There are an almost embarrassing number of notation for the CG-coefficients in the literature. Condon and Shortley [4] use $(j_1, j_2, m_1, m_2|j_1, j_2, j, m) = (j_1, j_2, j, m|j_1, j_2, m_1, m_2)$ for our $C(j_1, j_2, j; m_1, m -$

m_1), $(m_2 = m - m_1)$. This notation has the advantage of clearly indicating what is diagonal in the two representations corresponding to the two coupling schemes. However, it is slightly more cumbersome and, for an information viewpoint, rather redundant. In the Varshalovich's book [3] the notation used is $C^{c\gamma}_{a\alpha b\beta}$ where $a = j_1$, $\alpha = m_1$, $b = j_2$, $\beta = m_2$, and $c = j_3$, $\gamma = m_3$. They use Latin letters to represent the angular momentum and Greek letters for their projections.

If we want to emphasize the symmetry properties of the CG-coefficients we can replace j, m by j_3 and m_3. It evident that among the three number pairs j_1, m_1; j_2, m_2; j_3, and $m_3 = m_1 + m_2$, there is a certain symmetry as evidenced by the triangular relation between j_1, j_2 and j_3 and the m-sum rule. We may therefore expect that some simple relations exist between CG-coefficients when the roles of the participating angular momenta are interchanged. As defined, the CG-coefficients posses a higher degree of symmetry between j_1 and j_2 then between j_3 and either of the other angular momenta. For example, a change in the order in which j_1 and j_2 are compounded to give the resultant j will introduce only a change in phase in the CG-coefficient. On the other hand, interchange of j_1 or j_2 with j_3 introduces factors depending on statical weights, $2j_1 + 1$, etc. This symmetry is not essential, and a redefinition of the coefficients, would remove this unbalance. It must be understood that, whenever the total angular momenta are interchanged, their projection must also be but with such sign changes as are needed to keep the sum rule $m_1 + m_2 = m_3$ inviolate. Three independent symmetry relations are

$$C(j_1, j_2, j_3; m_1, m_2, m_3) = (-1)^{j_1+j_2-j_3} C(j_1, j_2, j_3; -m_1, -m_2, -m_3) \tag{C.12}$$

$$(-1)^{j_1+j_2-j_3} C(j_2, j_1, j_3; m_2, m_1, m_3) \tag{C.13}$$

$$(-1)^{j_1-m_1} \left(\frac{2j_3+1}{2j_2+1}\right)^{\frac{1}{2}} C(j_1, j_3, j_2; m_1, -m_3, -m_2). \tag{C.14}$$

The first relation given by Eq. (C.12) shows that an overall change in the sign of the projection quantum numbers is equivalent to a change in phase. According to Eq. (C.13), the same change of phase is obtained on interchanging the roles of two angular momenta j_1 and j_2 which are being added, together with their projections m_1 and m_2. The third symmetry relation Eq. (C.14) shows that, when the resultant j is interchanged with an addend, here j_2, the square root of a statistical weight ratio as well as a phase factor is introduced. The lack of symmetry is not surprising in view of the special role played by the resultant j_3 and its projection m_3. In the three previous relations, it should be noted that the third projection quantum number is always the sum of the first two, since otherwise the coefficients vanish.

Some other useful symmetry relations, which can be derived from those given in Eqs. (C.12), (C.13) and (C.14), are the following:

$$C(j_1, j_2, j_3; m_1, m_2, m_3) = (-1)^{j_2+m_2} \left(\frac{2j_3+1}{2j_1+1}\right)^{\frac{1}{2}} C(j_3, j_2, j_1; -m_3, m_2, -m_1), \tag{C.15}$$

$$C(j_1, j_2, j_3; m_1, m_2, m_3) = (-1)^{j_1-m_1} \left(\frac{2j_3+1}{2j_2+1}\right)^{\frac{1}{2}} C(j_3, j_1, j_2; m_3, -m_1, m_2), \tag{C.16}$$

$$C(j_1, j_2, j_3; m_1, m_2, m_3) = (-1)^{j_2+m_2} \left(\frac{2j_3+1}{2j_1+1}\right)^{\frac{1}{2}} C(j_2, j_3, j_1; -m_2, m_3, m_1). \tag{C.17}$$

Whenever j_3 is interchanged with either j_1 or j_2, the projection quantum number m_3 associated with it changes sign, and the projection quantum number associated with the angular momentum which is not interchanged with j_3 remains the same. The phase factor depends on the quantum numbers not

involved in the interchange. The statistical weights in the square root involve j_3 (in the numerator) and the j-number which is interchanged with j_3 in the denominator.

Some properties of frequently encountered CG-coefficients can be deduced from the symmetry relations. If the three angular momenta are integers and if all the projection quantum numbers vanish, we have the relation,

$$C(j_1,j_2,j_3;0,0,0)=0 \quad \text{unless} \quad j_1+j_2+j_3 \quad \text{is even.} \tag{C.18}$$

Next, consider the CG-coefficient with $j_2=0$, and therefore $m_2=0$. From the conservation rules $\Delta(j_1,j_2,j)$ and $m_3=m_1+m_2$, we know that $C(j_1,0,j_3;m_1,0,m_3)$ vanishes unless $j_1=j_3$ and $m_1=m_3$, so

$$\begin{aligned} C(j_1,0,j_3;m_1,0,m_3) &= \delta_{j_1,j_3}\delta_{m_1,m_3}C(j_3,0,j_1;-m_3,0,-m_1) && \text{(C.19)}\\ &= \delta_{j_1,j_3}\delta_{m_1,m_3}C(j_1,0,j_1;m_1,0,m_1). && \text{(C.20)}\\ & && \text{(C.21)} \end{aligned}$$

This CG-coefficient occurs for the case when no angular momentum is added to the angular momentum j_1, i.e.,

$$\psi_{j_1,m_1}=C(j_1,0,j_1;m_1,0,m_1)\psi_{j_1,m_1}, \tag{C.22}$$

and so

$$C(j_1,0,j_3;m_1,0,m_3)=\delta_{j_1,j_3}\delta_{m_1,m_3}. \tag{C.23}$$

By means of the symmetry relations and Eq. (C.23) we can evaluate any CG-coefficient when any one of j_1, j_2, or j_3 is zero.

$$C(j_1,j_2,0;m_1,m_2,0)=\frac{(-1)^{j_1-m_1}}{\sqrt{2j_1+1}}\delta_{j_1,j_2}\delta_{m_1,-m_2}, \tag{C.24}$$

$$C(j_1,0,j_3;m_1,0,m_3)=\delta_{j_1,j_3}\delta_{m_1,m_3}. \tag{C.25}$$

If $j_3=j_1+j_2$, then we have

$$\begin{aligned} &C(j_1,j_2,j_1+j_2;m_1,m_2,m_1+m_2)=\\ &\left[\frac{(2j_1)!(2j_2)!(j_1+j_2+m_1+m_2)!(j_1+j_2-m_1-m_2)!}{(2j_1+2j_2)!(j_1+m_1)!(j_1-m_1)!(j_2+m_2)!(j_2-m_2)!}\right]^{1/2}. \end{aligned} \tag{C.26}$$

In particular,

$$C(j_1,j_2,j_1+j_2;j_1,j_2,j_1+j_2)=1, \tag{C.27}$$

$$C(j_1,j_2,j_1+j_2;j_1,-j_2,j_1-j_2)=\left[\frac{(2j_1)!(2j_2)!}{(2j_1+2j_2)!}\right]^{1/2}, \tag{C.28}$$

If $j_1=j_2$ and $m_1=m_2$, then

$$C(j_1,j_1,j_3;m_1,m_1,m_3)=$$

$$\begin{cases} 0 & ,\text{if } 2j_1+j_3=2g+1\\ \delta_{m_3,2m_1}\frac{(-1)^{g-j_3}\sqrt{2j_3+1}g!}{\left(\frac{j_3+m_3}{2}\right)!\left(\frac{j_3-m_3}{2}\right)!(g-j_3)!}\left[\frac{(j_3+m_3)!(j_3-m_3)!(2g-2j_3)!}{(2g+1)!}\right]^{1/2} & ,\text{if } 2j_1+j_3=2g, \end{cases}$$

(C.29)

where g in integer an positive.
For $m_1 = m_2 = m_3 = 0$, we have

$$C(j_1, j_2, j_3; 0, 0, 0) =$$

$$\begin{cases} 0 & ,\text{if } j_1 + j_2 + j_3 = 2g+1 \\ \frac{(-1)^{g-j_3}\sqrt{2j_3+1}\,g!}{(g-j_1)!(g-j_2)!(g-j_3)!}\left[\frac{(2g-2j_1)!(2g-2j_2)!(2g-2j_3)!}{(2g+1)!}\right]^{1/2} & ,\text{if } 2j_1 + j_3 = 2g, \end{cases} \tag{C.30}$$

where g in integer an positive. In particular,

$$C(j_1, j_2, j_1 + j_2; 0, 0, 0) = \frac{(j_1 + j_2)!}{j_1! j_2!}\left[\frac{(2j_1)!(2j_2)!}{(2j_1 + 2j_2)!}\right]^{1/2}, \tag{C.31}$$

$$C(j_1, j_2, j_1 - j_2; 0, 0, 0) = (-1)^{j_2}\frac{(j_1)!}{j_2)!(j_1 - j_2)!}\left[\frac{(2j_2)!(2j_1 - 2j_2 + 1)!}{(2j_1 + 1)!}\right]^{1/2}. \tag{C.32}$$

If $m_3 = j_3$ or $m_1 = j_1$ we have

$$C(j_1, j_2, j_3; m_1, m_2, j_3) = \delta_{m_1+m_2, j_3}(-1)^{j_1 - m_1}$$
$$\times\left[\frac{(2j_3+1)!(j_1 + j_2 - j_3)!(j_1 + m_1)!(j_2 + m_2)!}{(j_1 + j_2 + j_3 + 1)!(j_1 - j_2 + j_3)!(-j_1 + j_2 + j_3)!(j_1 - m_1)!(j_2 - m_2)!}\right]^{1/2}, \tag{C.33}$$

$$C(j_1, j_2, j_3; j_1, m_2, m_3) = \delta_{m_3 - m_2, j_1}$$
$$\times\left[\frac{(2j_3+1)!(2j_1)!(-j_1 + j_2 + j_3)!(j_2 - m_2)!(j_3 + m_3)!}{(j_1 + j_2 + j_3 + 1)!(j_1 - j_2 + j_3)!(j_1 + j_2 - j_3)!(j_2 + m_2)!(j_3 - m_3)!}\right]^{1/2}. \tag{C.34}$$

In particular,

$$C(j_1, j_2, j_3; j_1, j_2, j_3) = \delta_{j_1 + j_2, j_3}, \tag{C.35}$$

$$C(j_1, j_2, j_3; j_1, -j_2, j_3) = \delta_{j_1 - j_2, j_3}\left[\frac{2j_3 + 1}{2j_1 + 1}\right]^{1/2}, \tag{C.36}$$

$$C(j_3, j_2, j_3; j_3, 0, j_3) = (2j_3)!\left[\frac{2j_3 + 1}{(2j_3 - j_2)!(2j_3 + j_2 + 1)!}\right]^{1/2}. \tag{C.37}$$

In table (C.1) we present the values of the most common Clebsh-Gordan coefficients.

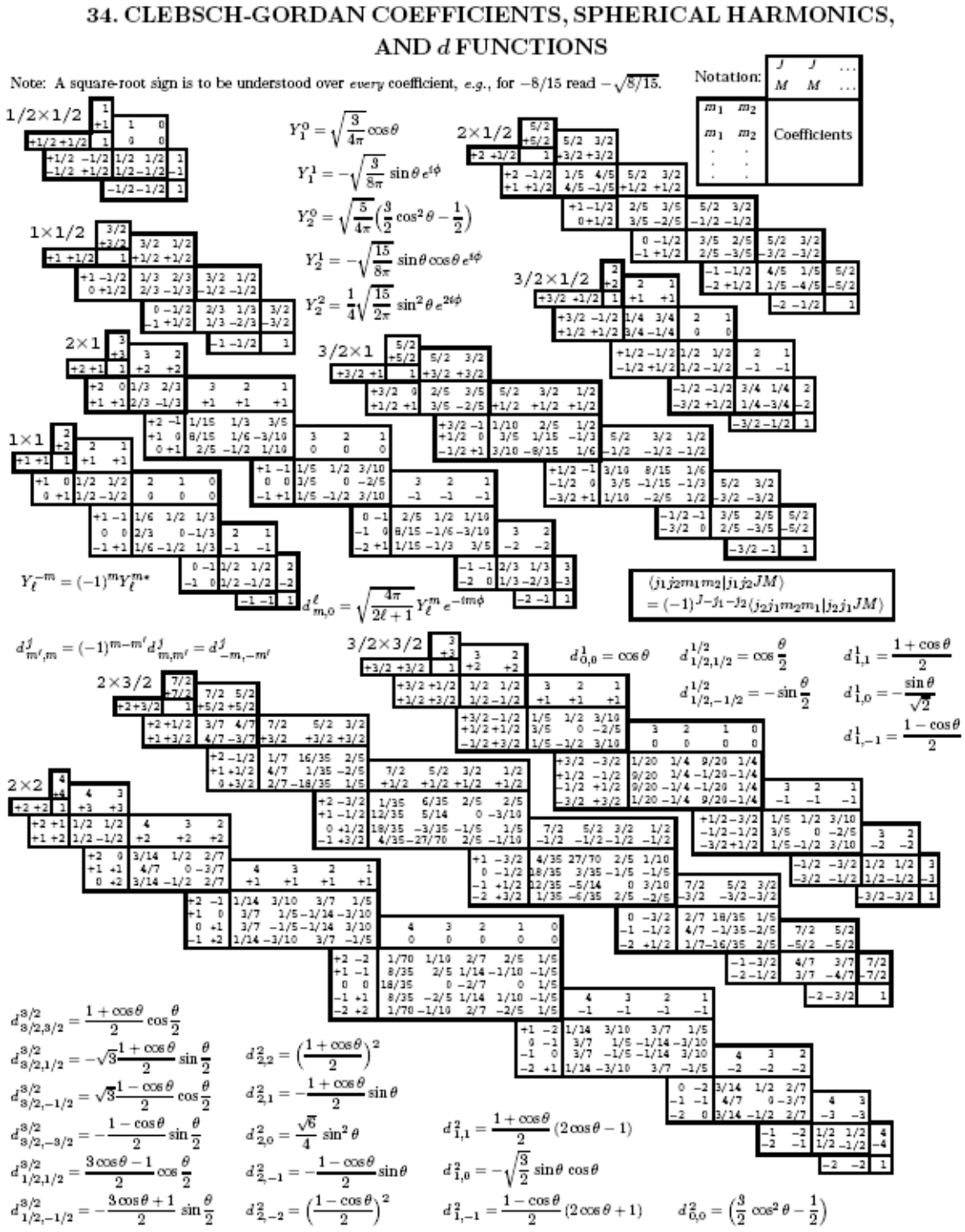

Figure C.1: The sign convention is that of Condon and Shortley [1, 4]. The coefficients here have been calculated using computer programs written independently by Cohen at LBNL.

C.3 The Wigner 3-j symbol

The 3-j symbols are related to the Clebsch-Gordan coefficients by

$$\begin{pmatrix} j_1 & j_2 & j_3 \\ m_1 & m_2 & m_3 \end{pmatrix} = (-1)^{j_1-j_2-m_3}(2j_3+1)^{-1/2}C(j_1,j_2,j_3;m_1,m_2,-m_3). \tag{C.38}$$

Frequently the 3-j symbols are used instead of the Clebsch-Gordan coefficients. These symbols posses simpler symmetry properties. It symmetry properties are easily derived from those of the Clebsch-Gordan coefficients. We have that an even permutation of the columns leaves the numerical values unchanged:

$$\begin{pmatrix} j_1 & j_2 & j_3 \\ m_1 & m_2 & m_3 \end{pmatrix} = \begin{pmatrix} j_2 & j_3 & j_1 \\ m_2 & m_3 & m_1 \end{pmatrix} = \begin{pmatrix} j_3 & j_1 & j_2 \\ m_3 & m_1 & m_2 \end{pmatrix}, \tag{C.39}$$

while an odd permutation is equivalent to multiplication by $(-1)^{j_1+j_2+j_3}$:

$$\begin{aligned} (-1)^{j_1+j_2+j_3}\begin{pmatrix} j_1 & j_2 & j_3 \\ m_1 & m_2 & m_3 \end{pmatrix} &= \begin{pmatrix} j_2 & j_1 & j_3 \\ m_2 & m_1 & m_3 \end{pmatrix} \\ &= \begin{pmatrix} j_1 & j_3 & j_2 \\ m_1 & m_3 & m_2 \end{pmatrix} \\ &= \begin{pmatrix} j_3 & j_2 & j_1 \\ m_3 & m_2 & m_1 \end{pmatrix}, \end{aligned} \tag{C.40}$$

The analogue of Eq. (C.12) is

$$\begin{pmatrix} j_1 & j_2 & j_3 \\ m_1 & m_2 & m_3 \end{pmatrix} = (-1)^{j_1+j_2+j_3}\begin{pmatrix} j_1 & j_2 & j_3 \\ -m_1 & -m_2 & -m_3 \end{pmatrix}. \tag{C.41}$$

The orthogonality properties are not so convenient. They are

$$\sum_{j_3,m_3}\begin{pmatrix} j_1 & j_2 & j_3 \\ m_1 & m_2 & m_3 \end{pmatrix}\begin{pmatrix} j_1 & j_2 & j_3 \\ m_1' & m_2' & m_3 \end{pmatrix} = (2j_3+1)^{-1}\delta_{m_1,m_1'}\delta_{m_2,m_2'}, \tag{C.42}$$

$$\sum_{m_1,m_2}\begin{pmatrix} j_1 & j_2 & j_3 \\ m_1 & m_2 & m_3 \end{pmatrix}\begin{pmatrix} j_1 & j_2 & j_3' \\ m_1 & m_2 & m_3' \end{pmatrix} = (2j_3+1)^{-1}\delta_{j_3,j_3'}\delta_{m_3,m_3'}\Delta(j_1,j_2,j_3), \tag{C.43}$$

where $\Delta(j_1,j_2,j_3)=1$ if j_1,j_2,j_3 satisfy the triangular condition, and is zero otherwise.

The formulas given in the previous section for certain values of the arguments of the Clebsch-Gordan coefficients are repeated here for the $3-j$ symbol.

$$\begin{pmatrix} j & j & 0 \\ m & -m & 0 \end{pmatrix} = (-1)^{j-m}(2j+1)^{-1/2}, \tag{C.44}$$

$$\begin{aligned} &\begin{pmatrix} j_1 & j_2 & j_1+j_2 \\ m_1 & m_2 & -m_1-m_2 \end{pmatrix} = (-1)^{j_1-j_2+m_1+m_2} \\ &\times\left[\frac{(2j_1)!(2j_2)!(j_1+j_2+m_1+m_2)!(j_1+j_2-m_1-m_2)!}{(2j_1+2j_2+1)!(j_1+m_1)!(j_1-m_1)!(j_2+m_2)!(j_2-m_2)!}\right], \end{aligned} \tag{C.45}$$

$$\begin{pmatrix} j_1 & j_2 & j_3 \\ m_1 & -j_1-m_3 & m_3 \end{pmatrix} = (-1)^{-j_1+j_2+m_3}$$
$$\times \left[\frac{(2j_1)!(-j_1+j_2+j_3)!(j_1+j_2+m_3)!(j_3-m_3)!}{(j_1+j_2+j_3+1)!(j_1-j_2+j_3)!(j_1+j_2-j_3)!(-j_1+j_2-m_3)!(j_3-m_3)!} \right]. \tag{C.46}$$

We can write the explicit expression for the $3-j$ symbols with $m_1 = m_2 = m_3 = 0$. We have first

$$\begin{pmatrix} j_1 & j_2 & j_3 \\ 0 & 0 & 0 \end{pmatrix} = 0 \text{ if } j_1+j_2+j_3 \text{ is odd.} \tag{C.47}$$

This is a consequence of the symmetry Eq. (C.41) of the $3-j$ symbol. If $J = j_1+j_2+j_3$ is even, we have

$$\begin{pmatrix} j_1 & j_2 & j_3 \\ 0 & 0 & 0 \end{pmatrix} = 2\left[\frac{j_2(j_2+1)(j_3-1)j_3}{(J+1)(J-2j_1)(J-2j_2)(J-2j_3+1)} \right]^{1/2}$$
$$\times \begin{pmatrix} j_1 & j_2 & j_3-1 \\ 0 & +1 & -1 \end{pmatrix}. \tag{C.48}$$

We also can express the last relation in the following way:

$$\begin{pmatrix} j_1 & j_2 & j_3 \\ 0 & 0 & 0 \end{pmatrix} = \left[\frac{(J-2j_2-1)(J-2j_3+2)}{(J-2j_2)(J-2j_3+1)} \right]^{1/2} \begin{pmatrix} j_1 & j_2+1 & j_3-1 \\ 0 & 0 & 0 \end{pmatrix}. \tag{C.49}$$

C.4 Transformation properties under rotation

The explicit functions $\psi_{j,m}$ which diagonalize the square and one component of the angular momentum, with eigenvalues $j(j+1)$ and m, respectively, presuppose a definite choice of the quantization axis. This is so because m the eigenvalue of the angular momentum component of that axis. It is often necessary to consider rotations of the axis of quantization an this section will be devoted to a study of the transformation properties of the angular momentum eigenfunctions under these rotations. Let us consider a rotation of the coordinate system through an angle θ about an axis defined by the direction $\mathbf{n}$, a unit vector. The wave function ψ in the original system is related to the wave function ψ' in the rotated system by a unitary transformation

$$\psi' = R(\mathbf{n},\theta)\psi. \tag{C.50}$$

The unitary transformation operator $R(\mathbf{n},\theta)$ depends, of course, on three angles in the general case-two to define the direction of $\mathbf{n}$ and another, which is θ, to give the magnitude of the rotation. Of course, $R(\mathbf{n},\theta)$ must approach unity in the limit $\theta \to 0$, and it is convenient to write it in exponential form,

$$R(\mathbf{n},\theta) = e^{-iS(\mathbf{n},\theta)}, \tag{C.51}$$

with the understanding that $S(\mathbf{n},\theta) \to 0$ for $\theta \to 0$. More important, since R must be unitary it follows that S must be Hermitian. It can be shown ([1], pg. 17), that S has the value $S = (\mathbf{n}\cdot\mathbf{J})\theta$, where $\mathbf{J}$ is the angular momentum. So the angular momentum $\mathbf{J}$ is defined by the equation

$$R\psi = e^{-i\theta(\mathbf{n}\cdot\mathbf{J})}\psi, \tag{C.52}$$

where **n** defines the rotation axis, and θ is the rotation angle. The angular momentum thus determines the transformation properties of a system under rotations of the coordinates system. Inversely, the angular momentum operator **J** (that is, three operators) can be determined from the transformation properties of the system. The eigenvalues of the square of the angular momentum is unchanged by a rotation, since $\mathbf{J}^2$ commutes with the rotation operator $\exp^{-i\theta(\mathbf{n}\cdot\mathbf{J})}$, the coordinate system being rotated through an angle θ about the direction **n**. Expressed formally,

$$\left[\mathbf{J}^2, e^{-i\theta(\mathbf{n}\cdot\mathbf{J})}\right] = 0. \tag{C.53}$$

Hence the rotated function (C.52),

$$R\psi_{j,m} = e^{-i\theta(\mathbf{n}\cdot\mathbf{J})}\psi_{j,m}, \tag{C.54}$$

is an eigenfunction of $\mathbf{J}^2$ with unchanged eigenvalue $j(j+1)$. This result expresses the well-known fact that the total angular momentum has nothing to do with a particular direction of a particular coordinate system.

The rotated function $R\psi_{j,m}$ does not diagonalize J_z, in general, and is a superposition of eigenfunctions $\psi_{j',m'}$ with different projection quantum numbers m' but the same total angular momentum j.

$$R\psi_{j,m} = \sum_{m'} \langle j,m'|e^{-i\theta(\mathbf{n}\cdot\mathbf{J})}|j,m\rangle \psi_{j,m'}. \tag{C.55}$$

If we want to determine the matrix representation $\langle j,m' \exp -i\theta(\mathbf{n}\cdot\mathbf{J})|j,m\rangle$ of the rotation operator $R = \exp -i\theta(\mathbf{n}\cdot\mathbf{J})$, we first review some elementary facts about rotations of coordinate systems. It is well known that three parameters are needed to specify a rotation. These may be the three components of the vector θ**n**, where θ gives the magnitude and **n** the direction of the rotation. The most useful description is, however in terms of the Euler angles, which we shall call α, β and γ. The Euler angles is the most useful way of defining the rotation of a rigid body by three real numbers, i.e., of parametrizing the rotation group, $SO(3)$. There are, however, several conventions in existence for choosing the so-called Euler angles. We shall consider this choice with some care,for ambiguities in the definitions of the Euler angles entail confusion in questions of the phases of matrix elements of finite rotations, etc. The general displacement of a rigid body due to a rotation about a fixed point may be obtained by performing three rotations about two of three mutually perpendicular axes fixed in the body. We shall assume a right-handed frame of axes; we shall further define a *positive* rotation about a given axis to be one which would carry a right-handed screw in the positive direction along the axis. Thus a *z*-axis which carried the *x*-axis in the original position of the *y*-axis would be considered to be positive. The rotations are defined by performing the rotation of the coordinate system in three steps, the original coordinate being *x*, *y*, *z*:

1. A rotation is made about the *z*-axis through an angle α ($0 \leq \alpha \leq 2\pi$); the new coordinate axes are x', y', z'; see Fig. (C.4a).

2. A rotation is made about the y'-axis through an angle β ($0 \leq \beta \leq \pi$); the new coordinate axes are x'', y'', z'', as in Fig. (C.4b).

3. A rotation is made about the z'' through an angle γ ($0 \leq \gamma \leq 2\pi$); the new coordinate axes are x''', y''', z'''; see Fig. (C.4c);

In the diagrams of Fig. (C.4) the Euler rotations have been illustrated as positive rotations. As we have said before, a positive rotation is defined here as one that advances a right-hand screw along the axis of rotation. Although the possible values α, β and γ are restricted, we do not have a 1:1

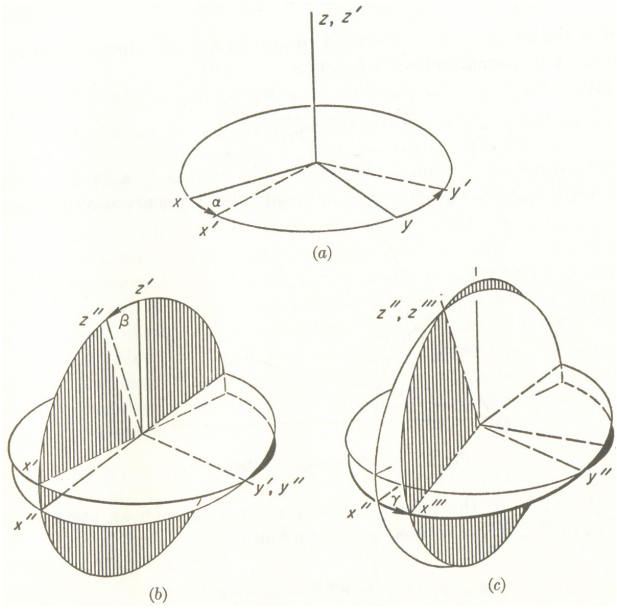

Figure C.2: The Euler angles α, β and γ and the three Euler rotations which carry the initial (x,y,z) coordinate system into the final (x''',y''',z''') coordinate system. This figure is extracted from [1].

correspondence between rotations and parameters for all possible rotations; for example a rotation symbolized by (α,0,γ) is identical that symbolized by (α′,0,γ′) if $\alpha+\gamma=\alpha'+\gamma'$. It should be noted that the polar coordinates φ and θ with respect to the original frame S of the z-axis in its final position are identical with the Euler angles α, β respectively. In the description of the general rotation just given, the rotations β and γ have been defined with respect to the frame of reference carried with the moving body. It is convenient in many applications always to refer rotations to the original fixed frame of axes S. The rotation operator in Eq. (C.54) is now a product of three operators

$$e^{-i\theta(\mathbf{n}\cdot\mathbf{J})} = R(\theta\mathbf{n}) = R_\gamma R_\beta R_\alpha, \tag{C.56}$$

with the R_α operating on the wave function first. Obviously, the subscripts are the Euler angles of rotation. But R_α, R_β, and R_γ are successive rotations about the z, y', and z''. therefore,

$$R = R_\gamma R_\beta R_\alpha = e^{-i\gamma J_{z''}} e^{-i\beta J_{y'}} e^{-i\alpha J_z}. \tag{C.57}$$

Here $J_{y'}$ and $J_{z''}$ are the components of $\mathbf{J}$ along y' and z'' axes, respectively. However, a unitary transformation U transforms an operator Ω into $U\Omega U^{-1}$ (see [1] section 2). Thus $R_\beta = e^{-i\beta J_{y'}}$ is the transform of $\exp -i\beta J_y$ under the previous rotation $R_\alpha = \exp(-i\alpha J_z)$ which carried the y-axis into the y'-axis; and $R_\gamma = \exp(-i\gamma J_{z''})$ is the transform of $\exp(-i\gamma J_{z'})$ under the previous rotation $R_\beta = \exp(-i\beta J_{y'})$ which carried z' into z''. Accordingly, to express R_β in terms of the original coordinate system we use $U = R_\beta$ and

$$e^{-i\beta J_{y'}} = e^{-i\alpha J_z} e^{-i\beta J_y} e^{i\alpha J_z}. \tag{C.58}$$

In the same way

$$e^{-i\gamma J_{z''}} = e^{-i\beta J_{y'}} e^{i\gamma J_{z'}} e^{-i\beta J_{y'}}, \tag{C.59}$$

which express R_γ in the coordinate system that results after the R_α rotation is performed. If we use Eq. (C.59), the rotation operator R in Eq. (C.57) is now

$$R = e^{-i\beta J_{y'}} e^{i\gamma J_{z'}} e^{i\alpha J_z}. \tag{C.60}$$

Applying Eq. (C.58) and a similar equation for $\exp(-i\gamma J_{z'})$ gives, finally,

$$R = e^{i\alpha J_z} e^{i\beta J_y} e^{i\gamma J_z}. \tag{C.61}$$

Eq. (C.57) expresses the fact that the rotation R is carried out by the three successive Euler rotations: The first is a rotation α along the z-axis, the second a rotation β about the y'-axis, and the third a rotation γ about the z''-axis. Thus, the axes of rotation are coordinates axes of different coordinates systems, namely the coordinates system obtained by the precious rotation. Eq. (C.61) says that these rotations may all be carried out in the same coordinate system if the order of the rotations is inverted. That is, the rotation R of the coordinate system may also be performed in this way: First a rotation γ is made about the z-axis, then a rotation β is made about the y-axis, and, finally, a rotation α is made about the z-axis.

The dependence on α and γ of the matrix representation of the rotation operator R can now be determined very simple. We call this matrix $D^j_{m',m}(\alpha,\beta,\gamma)$ so that Eq. (C.55) becomes

$$R\psi_{j,m} = \sum_{m'} D^j_{m',m}(\alpha,\beta,\gamma)\psi_{j,m'}. \tag{C.62}$$

If we use Eq. (C.61) for R, the elements of the rotation matrix $D^j_{m',m}(\alpha,\beta,\gamma)$ are

$$D^j_{m',m}(\alpha,\beta,\gamma) = \langle j,m'|e^{-i\alpha J_z} e^{-i\beta J_y} e^{-i\gamma J_z}|j,m\rangle. \tag{C.63}$$

Letting $\exp(-i\gamma J_z)$ operate on the right and $\exp(-i\alpha J_z)$ on the left, we find

$$D^j_{m',m}(\alpha,\beta,\gamma) = e^{-im'\alpha}\langle j,m'|e^{-i\beta J_y}|j,m\rangle e^{-im\gamma}. \tag{C.64}$$

Of course, $e^{-i\beta J_y}$ is not diagonal in this representation. Calling its matrix elements $d^j_{m',m}(\beta)$, that is

$$d^j_{m',m}(\beta) = \langle j,m'|e^{-i\beta J_y}|j,m\rangle, \tag{C.65}$$

the (factored) dependence of $D^j_{m',m}(\alpha,\beta,\gamma)$ on the Euler angles is

$$D^j_{m',m}(\alpha,\beta,\gamma) = e^{-im'\alpha} d^j_{m',m}(\beta) e^{-im\gamma}. \tag{C.66}$$

Wigner has given the following expression for $d^j_{m',m}(\beta)$:

$$\begin{aligned} d^j_{m',m}(\beta) &= \left[(j+m)!(j-m)!(j+m')!(j-m')!\right]^{\frac{1}{2}} \\ &\times \sum_{\chi} \frac{(-1)^{\chi}\left(\cos\frac{\beta}{2}\right)^{2j+m-m'-2\chi}\left(-\sin\frac{\beta}{2}\right)^{m'-m+2\chi}}{(j-m'-\chi)!(j+m-\chi)!(\chi+m'-m)!\chi!}, \end{aligned} \tag{C.67}$$

where the sum is over the values of the integer χ for which the factorial arguments are greater than or equal to zero. Using this relation, can be proven that

$$d^j_{m',m}(\beta) = d^j_{m,m'}(-\beta), \tag{C.68}$$

$$d^j_{m,m'}(\pi+\beta) = (-1)^{j+m} d^j_{-m,m'}(\beta), \tag{C.69}$$

$$d^j_{m,m'}(\pi-\beta) = (-1)^{j+m} d^j_{m',-m}(\beta), \tag{C.70}$$

$$d^j_{m,m'}(0) = \delta_{m,m'}. \tag{C.71}$$

That is, the inverse to $\exp(-i\beta J_y)$ is $\exp(i\beta J_y)$, a rotation about y through $-\beta$. But a rotation is a unitary transformation, and the inverse operator is the Hermitian adjoint. Thus, in finding $d^j_{m,m'}(-\beta)$ we have transposed the indices and taken the complex conjugate of $d^j_{mm'}(\beta)$. The last operation is unnecessary, however, since inspection of Eq. (C.67) reveals that $d^j_{m',m}(\beta)$ is real. Now a replacement of β with $-\beta$ in Eq. (C.67) leads only to a phase change $(-1)^{m'-m+2\chi}$ in the sum over χ. But χ is an integer and $(-1)^{2\chi} = 1$, so that changing the sign of β is equivalent to an overall phase change of $(-1)^{m'-m}$,

$$d^j_{m',m}(-\beta) = (-1)^{m'-m} d^j_{m',m}(\beta). \tag{C.72}$$

Application of this result to Eq. (C.68) leads to this very useful relation

$$d^j_{m',m}(\beta) = (-1)^{m'-m} d^j_{m,m'}(\beta). \tag{C.73}$$

Another important relation can be derived from inspection of Eq. (C.67). It states that $d^j_{mm'}(\beta)$ is invariant to an interchange of m' and m accompanied by a change in sign of both m' and m,

$$d^j_{m',m}(\beta) = d^j_{-m,-m'}(\beta). \tag{C.74}$$

Coupled with Eq. (C.73), this means that

$$d^j_{m',m}(\beta) = (-1)^{m'-m} d^j_{-m',-m}(\beta). \tag{C.75}$$

We can also express Eq. (C.67) in term of the the Jacobi polynomial:

$$\begin{aligned} d^j_{m',m}(\beta) &= \left[\frac{(j+m')!(j-m')!}{(j+m)!(j-m)!}\right]^{\frac{1}{2}} \\ &\times \left(\cos\frac{\beta}{2}\right)^{m'-m} \left(-\sin\frac{\beta}{2}\right)^{m'-m} P^{(m'-m,m'+m)}_{j-m'}(\cos\beta). \end{aligned} \tag{C.76}$$

The value of $d^j_{m,0}(\beta)$ may be obtained easily by consideration of the above expression. We make use of the Rodrigues formulas for the Jacobi polynomial and for the associated Legendre functions to show that

$$P^{(m,m)}_{l-m}(x) = (-2)^m \frac{l!}{(l-m)!}(1-x^2)^{-m/2} P^{-m}_l(x). \tag{C.77}$$

Hence

$$d^j_{m,0}(\beta) = (-1)^m \left[\frac{(l+m)!}{(l-m)!}\right]^{1/2} P^{-m}_l(\cos\beta) = \left[\frac{(l-m)!}{(l+m)!}\right]^{1/2} P^m_l(\cos\beta). \tag{C.78}$$

It follows from Eq. (C.64) the relation between the spherical harmonics that

$$D^l_{m,0}(\alpha,\beta,\gamma) = \left[\frac{4\pi}{(2l+1)}\right]^{1/2} \overline{Y}^m_l(\beta,\alpha), \tag{C.79}$$

$$D^l_{0,m}(\alpha,\beta,\gamma) = \left[\frac{4\pi}{(2l+1)}\right]^{1/2} Y^m_l(\beta,\gamma). \tag{C.80}$$

In particular

$$D^{l}_{0,0}(\alpha,\beta,\gamma) = P^{0}_{l}(\beta\gamma). \tag{C.81}$$

We have made use of the fact that any rotation of the coordinate system can be carried out by three successive Euler rotations. But the inverse of a product of operators is the product of the inverse operator in inverse order

$$R^{-1} = e^{i\gamma J_z} e^{i\beta J_y} e^{i\alpha J_z}. \tag{C.82}$$

Thus the inverse rotation is accomplished by performing the rotations through negative angles (about the same angles) but in opposite order to Eq. (C.61). The unitary property of the rotation operator R means that the matrix elements of R^{-1} are identical with those of the Hermitian adjoint

$$\langle j,m'|R^{-1}|j,m\rangle = \langle j,m|R|j,m'\rangle^{*}. \tag{C.83}$$

Using Eq. (C.82), this means that

$$D^{j}_{m',m}(-\alpha,-\beta,-\gamma) = \overline{D}^{j}_{m,m'}(\alpha,\beta,\gamma). \tag{C.84}$$

The generalization of Eq. (C.75) is obtained in the following way

$$\overline{D}^{j}_{m',m}(\alpha,\beta,\gamma) = e^{im'\alpha} d_{m',m}(\beta) e^{im\gamma} = (-1)^{m'-m} e^{im'\alpha} d_{-m',-m}(\beta) e^{im\gamma}, \tag{C.85}$$

where we have used Eq. (C.75); therefore,

$$\overline{D}^{j}_{m',m}(\alpha,\beta,\gamma) = (-1)^{m'-m} D^{j}_{-m',-m}(\alpha,\beta,\gamma). \tag{C.86}$$

C.5 The Clebsch-Gordan series

The discussion of the previous section on the general properties of the rotation matrices can now be applied to the derivation of some very useful results. In the section XXX we treated the coupling of two angular momenta j_1 and j_2 to give a resultant j. The connection between the uncoupled and coupled representations is given, for example, by Eq. (C.5),

$$\psi_{j_1,m_1}\psi_{j_2,m_2} = \sum_{j} C(j_1,j_2,j;m_1,m_2)\psi_{j,m_1+m_2}. \tag{C.87}$$

If the coordinate system is rotated through the Euler rotation $\alpha\beta\gamma$ as described in the previous section, each angular momentum eigenfunction transforms under the appropriate rotation according to Eqs. (C.62), and (C.87) becomes

$$\sum_{\mu_1}\sum_{\mu_2} D^{j_1}_{\mu_1,m_1} D^{j_2}_{\mu_2 m_2} \psi_{j_1,m_1}\psi_{j_2,m_2} = \sum_{j}\sum_{\mu} C(j_1,j_2,j;m_1,m_2) D^{j}_{\mu,m_1+m_2}\psi_{j,\mu}. \tag{C.88}$$

The common arguments $\alpha\beta\gamma$ of the D-matrices have been dropped for the purposes of brevity. If we use Eq. (C.4) for $\psi_{j,\mu}$ is now

$$\begin{aligned}&\sum_{\mu_1}\sum_{\mu_2} D^{j_1}_{\mu_1,m_1} D^{j_2}_{\mu_2 m_2}\psi_{j_1,m_1}\psi_{j_2,m_2} = \\ &\sum_{j}\sum_{\mu}\sum_{\mu_1'} C(j_1,j_2,j;m_1,m_2) C(j_1,j_2,j;\mu_1',\mu_2') D^{j}_{\mu,m_1+m_2}\psi_{j_1,\mu_1'}\psi_{j_2,\mu-\mu_1'}.\end{aligned} \tag{C.89}$$

The sum over μ can be replaced by a sum over $\mu_2 = \mu - \mu_1'$, but the primes on μ_1' and μ_2' can be dropped since they are only summation indices. Comparison of these coefficients of $\psi_{j_1,m_1}\psi_{j_2,m_2}$ yields the following result:

$$D^{j_1}_{\mu_1,m_1} D^{j_2}_{\mu_2,m_2} = \sum_j C(j_1,j_2,j;\mu_1,\mu_2) C(j_1,j_2,j;m_1,m_2) D^{j}_{\mu_1+\mu_2,m_1+m_2}. \tag{C.90}$$

This is known as the Clebsch-Gordan series, and is a coupling rule for the D-matrices. The arguments of all D-matrices elements are the same, and the sum is over those values of j for which $\Delta(j_1,j_2,j)$ holds. The inverse of the Clebsch-Gordan series is

$$D^{j}_{\mu,m} = \sum_{\mu_1}\sum_{m_1} C(j_1,j_2,j;\mu_1,\mu-\mu_1) C(j_1,j_2,j;m_1,m-m_1) D^{j_1}_{\mu_1,m_1} D^{j_2}_{\mu-\mu_1,m-m_1}, \tag{C.91}$$

C.6 Orthogonality and normalization of the rotation matrices

The rotation matrices possess the usual orthonormality properties

$$\sum_m \overline{D}^{j}_{m'm}(\alpha,\beta,\gamma) D^{j}_{m''m}(\alpha,\beta,\gamma) = \delta_{m'm''}, \tag{C.92}$$

$$\sum_m \overline{D}^{j}_{mm'}(\alpha,\beta,\gamma) D^{j}_{mm''}(\alpha,\beta,\gamma) = \delta_{m'm''}. \tag{C.93}$$

These are an expression of the fact that the $D^{j}_{m'm}(\alpha,\beta,\gamma)$ are the matrix elements of a unitary transformation from one set of $2j+1$ orthonormal eigenfunctions $\psi_{j,m}$ to another set, the rotated eigenfunctions $R(\alpha,\beta,\gamma)\psi_{j,m}$. Here we show that $D^{j}_{m'm}(\alpha,\beta,\gamma)$ are orthonormal on the surface of the unit sphere. Therefore, the integration of two rotation matrices is given by

$$\int \overline{D}^{j_1}_{\mu_1 m_1}(\alpha,\beta,\gamma) D^{j_2}_{\mu_2 m_2}(\alpha,\beta,\gamma)\, \mathrm{d}\Omega = \frac{8\pi^2}{2j_1+1}\delta_{\mu_1,\mu_2}\delta_{m_1,m_2}\delta_{j_1,j_2}, \tag{C.94}$$

where the symbol $\int \mathrm{d}\Omega$ stands for integration over the full range of the three Euler angles; that is,

$$\int \mathrm{d}\Omega = \int_0^{2\pi} \mathrm{d}\alpha \int_0^{\pi} \sin\beta \mathrm{d}\beta \int_0^{2\pi} \mathrm{d}\gamma, \tag{C.95}$$

gives the orthogonality property of the rotation matrices on the unit sphere.

The factor $8\pi^2$ is the volume of the region of integration and the factor $2j_1+1$ is the dimensionality of the set of eigenfunctions ψ_{j_1,m_1}. Through Eq. (C.79) this reduces to the usual orthonormality of the spherical harmonics:

$$\frac{1}{2\pi}\int \overline{D}^{l}_{m,0}(\alpha,\beta,0) D^{l'}_{m',0}(\alpha,\beta,0)\, \mathrm{d}\Omega = \frac{4\pi}{2l+1}\delta_{m,m'}\delta_{l,l'}, \tag{C.96}$$

and, changing β to θ and α to φ, this is

$$\int_0^{2\pi} \mathrm{d}\varphi \int_0^{\pi} \mathrm{d}\theta \sin\theta \overline{Y}^{m'}_{l'}(\theta,\varphi) Y^{m}_{l}(\theta,\varphi) = \delta_{m,m'}\delta_{l,l'}. \tag{C.97}$$

With the aid of the Clebsch-Gordan series we can also evaluate the integral of three rotation matrices:

$$\begin{aligned}
&\int \overline{D}^{j_3}_{\mu_3 m_3}(\alpha,\beta,\gamma) D^{j_2}_{\mu_2,m_2}(\alpha,\beta,\gamma) D^{j_1}_{\mu_1,m_1}(\alpha,\beta,\gamma)\, \mathrm{d}\Omega = \\
&= C(j_1,j_2,j;\mu_1,\mu_2) C(j_1,j_2,j;m_1,m_2) \int \overline{D}^{j_3}_{\mu_3 m_3}(\alpha,\beta,\gamma) D^{j}_{\mu_1+\mu_2,m_1+m_2}(\alpha,\beta,\gamma) \\
&= C(j_1,j_2,j;\mu_1,\mu_2) C(j_1,j_2,j;m_1,m_2) \frac{2}{2j_3+1} \delta_{\mu_1+\mu_2,\mu_3} \delta_{m_1+m_2,m_3} \delta_{j,j_3}. \qquad \text{(C.98)}
\end{aligned}$$

Therefore,

$$\begin{aligned}
&\int \overline{D}^{j_3}_{\mu_3 m_3}(\alpha,\beta,\gamma) D^{j_2}_{\mu_2,m_2}(\alpha,\beta,\gamma) D^{j_1}_{\mu_1,m_1}(\alpha,\beta,\gamma)\, \mathrm{d}\Omega = \\
&= \frac{2}{2j_3+1} \delta_{\mu_1+\mu_2,\mu_3} \delta_{m_1+m_2,m_3} C(j_1,j_2,j_3;\mu_1,\mu_2) C(j_1,j_2,j_3;m_1,m_2). \qquad \text{(C.99)}
\end{aligned}$$

A special case of this is the integral of three spherical harmonics. This can be obtained from Eq. (C.99) by using Eq. (C.79), and the result checks that give in Eq. (B.49).

Bibliography

[1] M. E. Rose, *Elementary theory of angular momentum*. Dover Publications, 1957.

[2] A. R. Edmonds, *Angular Momentum in Quantum Mechanics*. Princeton University Press, 1957.

[3] D. A. Varshalovich, A. N. Moskalev, and V. K. Khersonskii, *Quantum Theory of Angular Momentum*. World Scientific Publication, 1988.

[4] E. U. Condon and G. H. Shortey, *The theory of atomic spectra*. Cambridge University Press, 1935.

Appendix D

Publications

1. Autoionizing $^1\Sigma_u^+$ and $^1\Pi_u$ states of H_2 above the third and fourth ionization thresholds.
   J. Fernández and F. Martín, *Journal of Physics B: Atomic Molecular and Optical Physics* **34**, pp. 4141-4153 (2001)

2. In search of new resonance structures in dissociative photoionization of H_2.
   J. Fernández and F. Martín, *International Journal of Quantum Chemistry* **86**, pp. 145-150 (2002)

3. Recent advances in the study of ionization and dissociation of H_2 using B-spline basis sets.
   J. Fernández, A. Palacios and F. Martín, *Proceedings of the International Conference on "Electron and Photon Impact Ionization and Related Topics"* Ed. L.U. Ancarani, pp. 1-10 (2002)

4. Autoionization electrons following double excitation of D_2 in 2.4 KeV e^- + D_2 collisions: Experimental and theoretical evidence.
   J. -Y. Chesnel and D. Martina and P. Sobocinski and O. Kamalou, F. Freémont, J. Fernández and F. Martín, *Physical Review A* **70**, pp. 010701 (R) (2004)

5. Interference effects in H_2 photoionisation at high energies.
   O. A. Fojón, J. Fernández, A. Palacios, R. D. Rivarola and F. Martín, *Journal of Physics B: Atomic Molecular and Optical Physics* **37**, pp. 1-8 (2004)

6. Dissociative photoionization of H_2 at high photon energies: uncovering new series of doubly excited states.
   T. Aoto, Y. Hikosaka, R. I. Hall, K. Ito, J. Fernández and F. Martín, *Chemical Physics Letters* **389**, pp. 145-149 (2004)

7. Kinematically complete study of dissociative ionization of D_2 by ion-impact.
   G. Laurent, J. Fernández, S. Legendre, M. Tarisien, L. Adoui, A. Cassimi, X. Fléchard, F. Frémont, B. Gervais, E. Giglio, J. P. Grandin and F. Martín, *Physical Review Letters* **96**, pp. 173201 (2006)

8. Interferences in the photoelectron spectrum of H_2^+ molecules at high energy.
   O. A. Fojón, A. Palacios, J, Fernández, R. D. Rivarola and F. Martín, *Physics Letters A* **350**, pp. 371-374 (2006)

9. Single photon induced symmetry breaking H_2 dissociation.
   F. Martín, J. Fernández, T. Havermeier, L. Foucar, Th. Weber, K. Kreidi, M. Schöffler, L.

Schmidt, T. Jahnke, A. L. Landers, O. Jagutzki, A. Czasch, E. Benis, T. Osipov, A. Belkacem, M. H. Prior, H. Schmidt-Böcking, C. L. Cocke, and R. Dörner, *Science* **315-633**, pp. 629 (2007)

10. Interference from fast electron emission in molecular photoionization.
J. Fernández, O. A. Fojón, A. Palacios and F. Martín, *Physical Review Letters* **98**, pp. 043005 (2007)

11. Electron angular distribution in resonance enhanced two-photon ionization of H_2^+ by ultrashort laser pulses.
S. Selstø, A. Palacios, J. Fernández and F. Martín, *Physical Review A* **75**, pp. 33419-33424 (2007)

12. Dissociative and non-dissociative ionization of H_2 from the E,F$^1\Sigma_g^+$ excited state.
J. Fernández and F. Martín, *Physical Review A* **75**, pp. 042712 (2007)

13. Photoionization of the HeH^+ molecular ion.
J. Fernández and F. Martín, *Journal of Physics B: Atomic, Molecular and Optical Physics* **40**, pp. 2471-2480 (2007)

14. Electron angular distribution in dissociative photoionization of fixed in space D_2 molecules induced by circularly polarized light.
D. Dowek, J. Fernández, M. Lebech, J. C. Houver and F. Martín, *Journal of Physics: Conference Series* **88**, pp. 12009-12015 (2007)